



HAL
open science

Variabilité spatio-temporelle de la composition des fluides hydrothermaux (observatoire fond de mer EMSO-Açores, Lucky Strike) : traçage de la circulation hydrothermale et quantification des flux chimiques associés

Thomas Leleu

► **To cite this version:**

Thomas Leleu. Variabilité spatio-temporelle de la composition des fluides hydrothermaux (observatoire fond de mer EMSO-Açores, Lucky Strike) : traçage de la circulation hydrothermale et quantification des flux chimiques associés. Sciences de la Terre. Université Paul Sabatier - Toulouse III, 2017. Français. NNT : 2017TOU30023 . tel-01874701

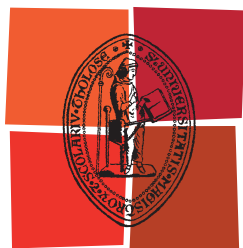
HAL Id: tel-01874701

<https://theses.hal.science/tel-01874701>

Submitted on 14 Sep 2018

HAL is a multi-disciplinary open access archive for the deposit and dissemination of scientific research documents, whether they are published or not. The documents may come from teaching and research institutions in France or abroad, or from public or private research centers.

L'archive ouverte pluridisciplinaire **HAL**, est destinée au dépôt et à la diffusion de documents scientifiques de niveau recherche, publiés ou non, émanant des établissements d'enseignement et de recherche français ou étrangers, des laboratoires publics ou privés.



Université
de Toulouse

THÈSE

En vue de l'obtention du

DOCTORAT DE L'UNIVERSITÉ DE TOULOUSE

Délivré par :

Université Toulouse 3 Paul Sabatier (UT3 Paul Sabatier)

Présentée et soutenue par :

Thomas LELEU

Le vendredi 27 janvier 2017

Titre :

Variabilité spatio-temporelle de la composition des fluides hydrothermaux
(Observatoire Fond de mer EMSO-Açores, Lucky Strike): Traçage de la
circulation hydrothermale et quantification des flux chimiques associés

ED SDU2E : Sciences de la Terre et des Planètes Solides

Unité de recherche :

UMR 5563

Directeur(s) de Thèse :

Valérie CHAVAGNAC

Georges CEULENEER

Rapporteurs :

Rachael H. JAMES, Javier ESCARTIN, Pierre-Marie SARRADIN

Autre(s) membre(s) du jury :

Christine DESTRIGNEVILLE, Marc De RAFELIS

Mathilde CANNAT, Anne BRIAIS

VARIABILITE SPATIO-TEMPORELLE DE LA COMPOSITION DES
FLUIDES HYDROTHERMAUX (OBSERVATOIRE FOND DE MER
EMSO-AÇORES, LUCKY STRIKE): TRAÇAGE DE LA
CIRCULATION HYDROTHERMALE ET QUANTIFICATION DES
FLUX CHIMIQUES ASSOCIES

Résumé

Cette thèse présente une étude détaillée de la composition des fluides de haute température du champ hydrothermal de Lucky Strike (37°N, dorsale médio atlantique) s'appuyant sur 3 campagnes d'échantillonnage réalisées dans le cadre de l'observatoire fond de mer EMSO–Açores. Ce champ hydrothermal s'est développé autour d'un lac de lave fossile bordé au Nord-Ouest, Nord Est et Sud Est par des cônes volcaniques plus anciens. En 2013, la découverte du site hydrothermal de Capelinhos à l'Est, et présentant des compositions de fluides inédites à Lucky Strike (concentration faible en Cl et forte en Fe et Mn), nous permet de proposer un nouveau modèle de circulation hydrothermale basé sur l'application de géothermobaromètres (Si ; Si–Cl ; Fe–Mn) chimiques sur 13 événements hydrothermaux. Nous avons défini 5 groupes de sites selon leur chlorinité et leur position par rapport au lac de lave. Les fluides de Capelinhos, dominés par la phase vapeur, sont rapidement extraits de la zone de séparation de phase (estimée à 2600 m sous le plancher océanique). Les fluides à proximité du lac de lave, avec des chlorinités variables, suggèrent un rééquilibrage à des pressions et températures plus faibles qu'à Capelinhos, cohérent avec des processus de refroidissement conductif et/ou d'entraînement de saumures prenant place lors de la remontée des fluides jusqu'à la base de la couche 2A. La fluctuation de la chlorinité témoigne de la variabilité du temps de résidence du fluide dans la zone de remontée, et ses relations avec les caractéristiques physiques de la croûte océanique.

Nous avons évalué la variabilité temporelle de la composition des fluides collectés au cours des campagnes effectuées entre 2009 et 2015. Deux échelles de temps sont mises en évidence. (1) l'échelle de l'échantillonnage, i.e. de l'heure, répond à des phénomènes de subsurface, et révèle qu'un fluide hydrothermal refroidi conductivement ($T < 150^{\circ}\text{C}$) est stocké dans la roche poreuse entourant le site de décharge. (2) l'échelle de temps pluri-annuelle montre une fluctuation des conditions de P et T apparentes de la zone de séparation de phase et du degré d'altération du substratum dans la zone de réaction. Les variations intersites du rapport Ca/Na (indicateur du degré d'albitisation) sont dues à la séparation de phase, à l'exception des sites du Sud–Est du lac de lave qui indiquent un degré d'altération plus élevé.

La concentration en Li et sa composition isotopique indiquent que le basalte du substratum est relativement frais avec des rapports W/R proches de 1 pour tous les groupes, avec des $\delta^7\text{Li}$ du fluide identiques au substratum. Pour le Sr nous calculons des rapports W/R plus

élevés, autour de 7-8, qui sont dus au Sr de l'eau de mer initiale qui est partiellement stocké et à la formation de minéraux secondaires (l'albite et l'anhydrite) lors des interactions eau-roche dans le faciès schiste vert. La faible teneur en métaux des fluides situés autour du lac de lave est probablement due à un piégeage en subsurface, équivalent à ~65% du Fe mobilisé dans la zone de réaction (basé sur les teneurs des fluides de Capelinhos).

La variabilité de chlorinité des fluides de Lucky Strike offre l'opportunité d'étudier le comportement des terres rares à l'échelle d'un site hydrothermal. Ainsi, nous montrons l'effet de la séparation de phase sur les terres rares légères et lourdes ainsi que le lien entre l'Eu et le cycle géochimique du Sr. Les terres rares dissoutes dans le panache hydrothermal montrent une perte au cours du mélange ainsi que des phénomènes de redissolution visible via la signature isotopique en Nd. Cette modification des compositions isotopiques en Nd de l'eau de mer profonde est similaire au « boundary exchange » observé aux interfaces océan–plateforme continentale. Au vue de la répartition des champs hydrothermaux sur les dorsales océaniques, ce phénomène pourrait avoir un impact sur le bilan océanique du Nd et donner lieu à un phénomène de « ridge exchange ».

Mots-clés : Fumeur noir ; séparation de phase ; isotope ; circulation hydrothermale ; variabilité spatio-temporelle.

Abstract

This thesis presents a detailed study of the composition of high temperature fluid from the Lucky Strike hydrothermal field (37°N, Mid Ocean Ridge) collected during three sampling campaigns within the framework of the deep sea observatory EMSO-Azores. The hydrothermal field has developed around a fossil lava lake framed by three ancient volcanic cones. In 2013, the discovery of a new active site to the East of the system, and presenting an unprecedented fluid composition at Lucky Strike (low Cl concentration and high Fe and Mn concentration), led to a new model of hydrothermal circulation based on chemical geothermobarometer (Si; Si-Cl) and geothermometer (Fe-Mn) applied to 13 venting sites. We defined 5 groups of sites based on their chlorinity and location around the lava lake. It appears that vapor-dominated Capelinhos fluids were extracted relatively fast from the phase separation zone (estimated at ~2600mbsf). Nevertheless, fluids in the vicinity of the lava lake, both vapor and brine dominated, display P and T conditions of equilibration lower than for Capelinhos fluids. This highlights on-going equilibration process through conductive cooling and/or brine entrainment in the upflow zone up to the layer 2A of the oceanic crust. Chlorinity variations highlight the varying residence time in the upflow of the fluids between vents which depends on physical characteristics of the crust.

We studied the temporal variability of fluid composition collected between 2009 and 2015. Two time scales have been evidenced. The first is the sampling scale, i.e. ~1h, and corresponds to subsurface processes indicating that a hydrothermal fluid, conductively cooled ($T < 150^{\circ}\text{C}$), was stored in the porous substratum close to the discharge. The second is at the scale of the year. It shows fluctuations of P and T conditions in the phase separation and different degree of alteration of the substratum in the reaction zone. Intersites variations of Ca/Na ratios (proxies for albitisation) are related to phase separation expected the South Eastern sites that display a more altered substratum. To avoid this issue, we use Li and Sr isotopes which are not affected phase separation.

Li concentration and isotopic composition indicates that basalt substratum is relatively fresh with W/R ratio close to 1 calculated for all groups with $\delta^7\text{Li}$ of fluid equivalent to substratum. Sr concentration and isotopic composition suggest higher W/R ratio (~7-8) because of seawater Sr partially removed in the recharge. Moreover, other parameters are at play such as secondary mineral formation (albite, anhydrite) during water rock

interaction in the greenschist facies. Because the basalt is relatively fresh, the low metal content in the fluid around the lava lake is due to storage, in the subsurface, of approximately ~60–70% of Fe that is mobilized in the reaction zone compared to Fe–Mn rich Capelinhos fluids.

Furthermore, the Cl variability from the fluids at Lucky Strike brings a unique opportunity to study the REE distribution from the reaction zone to the discharge into the deep ocean. We show that the LREE are preferentially concentrated into the brine phase. Furthermore, the Eu is linked to the Sr geochemical cycle. Dissolved REE from buoyant plume fluids highlight a scavenging effect. The Nd isotopic compositions indicate redissolution process. This Nd isotopes modification of the deep seawater is similar to the process of “boundary exchange” that occurs at the ocean/continents interface. Considering the global distribution of submarine hydrothermalism, the Nd modification at the ridge could have an impact on the global Nd cycle in the oceans and act as a “ridge exchange”.

Keywords: Black Smoker; phase separation; isotope; hydrothermal circulation; time-serie.

Remerciements

Je suis un peu embêté, je sais bien que j'ai déjà écrit cette partie en partie mais pas moyen de mettre la main dessus, j'ai pourtant parcouru tous mes dossiers, et rangé tous les fichiers par « modifié le », rien y fait. Je me vois donc résigné à les réécrire.

Il est difficile de penser à tous, et de n'oublier personne, mais je vais faire de mon mieux. Comme c'est en plus une partie qui est lue de tous, je vais essayer d'y placer quelques jeux de mots.

Un romain entre dans un bar et dit : « je voudrais V bières ».

Évidemment il peut y avoir des ratés.

J'aimerais d'abord remercier les membres du Jury (invités compris), qui ont bien voulu lire et « juger » ce manuscrit de thèse. Les trois rapporteurs Rachael James, Pierre-Marie Sarradin et Javier Escartin qui par leurs questions m'ont donné des pistes de réflexion pour la rédaction des futures publications (Ch. 4, 5 et 6). En particulier Javier Escartin qui m'a fourni ce manuscrit rigoureusement et précieusement annoté. Les deux examinateurs, Marc de Rafélis et Christine Destrigneville, j'ai beaucoup apprécié les discussions que l'on a pu avoir au cours de ces dernières années autour d'un café matinal ou autour du tricot. Merci beaucoup à Anne Briaïs qui, bien qu'absente lors de la soutenance, m'a aidée dans la correction du manuscrit. Je remercie également Mathilde Cannat qui m'a accompagnée tout au long de la thèse via le comité de thèse, les missions MoMAR et ODEMAR, ainsi qu'à l'écriture du papier soumis. Tu as le chic pour poser le doigt où cela fait mal, et on en ressort grandi.

Enfin évidemment mes deux directeurs de thèse, Valérie Chavagnac et Georges Ceuleneer. Georges est assez éloigné des fluides hydrothermaux, ce qui a donné aux discussions que l'on a eu une grande valeur. Merci surtout pour ta bienveillance. J'ai appris beaucoup grâce à Valérie qui a toujours été très disponible au cours de cette thèse que ce soit pour discuter de problème d'ordre scientifique ou autre. Par la suite pour corriger des trucs rédigés. Grâce à toi, j'ai eu une grande liberté (un peu déroutante au départ) au cours de ce travail.

Je vais maintenant remercier toutes les personnes rencontrées lors des missions océanographiques auxquelles j'ai participé. J'ai beaucoup apprécié chacune de ces missions, à savoir MoMAR 13, ODEMAR, MoMAR 14 et MoMAR 15, n'étant pas ennuyé par la durée fatidique d'une semaine et demie qui définit la fin de la salade fraîche en entrée.

J'ai profité des commodités du « Pourquoi Pas ? », pendant les quelques temps mort que l'on trouve en mission. Et à ce propos je recommande chaudement *Histoire d'un Allemand* de Sébastien Haffner chez Actes Sud, c'est un livre que j'ai lu au hasard de la bibliothèque du « Pourquoi Pas? » et qui m'a tenu à la main no matter what. J'aimerais remercier particulièrement Alain Castillo et Ludovic Menjot qui nous ont accompagnés avec Valérie lors des missions. La première mission avec Ludo reste la plus belle, pour le temps, pour la piscine, et surtout pour la découverte. Merci Ludo d'être toujours aussi positif. Alain et Valérie ont formé, pendant MoMAR 14 et 15, un duo pseudo-parental flanqué d'un gamin un peu niais et barbus. Merci pour tout !

Chronologiquement, après l'échantillonnage et le « terrain », vient le temps des dilutions et des analyses. Ainsi en chapitre 3 du présent ouvrage, je fais état d'un nombre de techniques et d'instruments de mesures absolument fou. Avec un éventail aussi important, il est impossible de tout maîtriser. J'ai ainsi eu la chance de collaborer avec beaucoup de chercheurs, techniciens, et ingénieurs très sympathiques. Au service chimie, je tiens à remercier Philippe Besson, Carole Causserand et Stéphanie Mounic pour leurs conseils sur la préparation des échantillons et pour l'analyse elle-même. Plus particulièrement Philippe qui m'a accompagné à l'ICP AES et m'a expliqué comment préparer des magrets séchés (que je n'ai toujours pas fait tiens !).

Le rire est le propre de l'Homme, pour un géochimiste c'est la salle blanche.

Cette salle blanche, où l'on doit faire attention à tout ce que l'on touche et la manière dont on le touche m'a beaucoup impressionné dans les premiers temps. J'ai pu passer beaucoup de temps avec Jonathan Prunier et Manuel Henry. Ils m'ont aidé à effectuer les séparations chimiques du Sr et du Li, à nettoyer une pipette qui avait aspiré de l'acide concentré (HNO_3 7N, oups !), 3 fois de suite (oups !). Et pendant que je suis dans la salle blanche, merci beaucoup à Catherine Pradoux et Catherine Jeandel pour m'avoir accueilli dans celle du LEGOS, c'était super. Deux salles, deux ambiances !

Une fois les échantillons préparés, l'heure est à l'analyse. Ainsi je remercie grandement Pierre Brunet, Jérôme Chmeleff, Aurélie LanzaNova et Frédéric Candaubap du service ICP-MS du GET pour m'avoir guidé lors de la préparation et de l'analyse des éléments et isotopes. Pierre Brunet m'a beaucoup aidé dans les premiers temps de la thèse et même avant pour les analyses au TIMS. Jérôme m'a beaucoup aidé dans l'élaboration du protocole de mesure des isotopes du Li. Merci aussi à Emmanuel Ponzevera et Céline

Liorzou à Brest (Ifremer et IUEM) avec qui j'ai eu le plaisir de faire quelques analyses, ainsi qu'à Rémi Freyrier de Montpellier (laboratoire Hydroscience).

Place maintenant aux collègues doctorants et post doctorant qui ont fait pétiller ces trois années et un peu plus. Mes co-bureaux qui ont tardé à le devenir. Antonin Laurent pour une langue pointue et râpeuse, qui sait dire « ferme la ! » comme personne, merci pour la cannette, les beignets et Capitaine. Il a notamment été responsable d'une certaine homogénéisation du parler doctorant. Bryan Cochelin, qui possède un « y », ne l'oublie pas, et qui est grand amateur de Cochelinchine endiablée. Tu as aussi eu une influence sur le parler doctorant avec tes célèbres « , » mais surtout tu as apporté la lumière sur les Pyrénées. Jing Ye, tu seras peut être surprise de lire ces mots mais je ne t'appréciais pas trop. « Oh oui ? » Bien sûr que non. Tu as quand même survécu à 3 ans de thèse avec 3 barbus sans changer d'un poil ta bonne humeur et ton joli sourire (même après l'appareil), ce qui constitue un exploit notable. Bon tu en es ressortie enceinte mais nous déclinons toute responsabilité dans cette histoire.

Il y a aussi les autres doctorants, Alexandre qui a été notre mentor et nourrice à tous. Le grand ordonnateur des ACDC et de la vie sociale GET. Quand j'y repense c'était vraiment une belle cage. Sylvain qui va bientôt soutenir et qui aime crier dans le couloir, merci pour ces pauses café, le Rugby et ma Rylou (cela te va très bien la paternité). Léandre, qui est toujours là pour donner un coup de main, pour un volley éructant des « qu'est ce qu'on boit ? ». Laetitia Gal pour la parité et un grand sourire qui fait douter de la taille de tes cotons-tiges. Gillou, pour l'Orval, la musique et les boulets. Merci aux mouflettes ! Mélody pour ton perpétuel étonnement et ta curiosité, ça te dit on fait du tricot ? oh oui !!! on fait du pilates ? ohh oui !!! C'est promis, si je me rase un jour, je te donne ma barbe. Raticchon pour sa bonne volonté, ses huiles essentielles et saga. Alice pour ton armée à minitrooper, tes efforts au flat foot clog dancing et un pantalon d'été qui m'étonne encore aujourd'hui. Pierremafre pour Kurozawa, tes couilles bleu et blanche (la blanche est plus juste) et ton décalage. Loïsmoier pour ton sens des nuances, et tes inspirations à rallonge. Le plus ancien des jeunes, jeune Maxine, pour ta jeunesse, tes beaux cheveux et ton col en laine doublé polaire. Merci à Tristan pour le coup de main sur les spikes, j'ai trouvé plus bordelique que moi et ça fait plaisir. Merci à Alexandra pour ton aide pour des trucs mais surtout pour ta bonne humeur, et les weekends end chez toi qui sont mémorables. J'en oublie sûrement mais tant que ça ?

Merci à ma famille qui malgré une certaine opacité sur ce que je faisais ne m'ont pas tenu rigueur des anniversaires oubliés, des coups de fil rares etc... mince je n'ai plus d'excuses maintenant. De vous voir arriver 5 minutes avant la soutenance sans que je sois au courant, m'a fait très plaisir, et un peu stressé, mais je crois que cela ne s'est pas vu.

Merci évidemment à Juliette qui a suivi l'intégralité de la thèse par les coulisses, qui m'a remonté le moral dans les moments de doutes, qui est venu passer de super vacances dans les Açores !! oui !! qui a supporté toute mes lubies de rédaction, et qui s'y est même mise pour certaines ! Merci pour tout ce que tu m'as fait découvrir pendant cette période, la montagne, le théâtre, la danse (bon ça..., c'était intéressant), et tout ce qui est à venir. Ton tour approche, et je serais là pour tout ça.

Merci à Capitaine.

Il n'y a pas de fumée sans Fe.

TABLE DES MATIERES

Résumé	i
Abstract	iii
Remerciements	v
Introduction.....	1
Introduction (english)	7
Chapitre I	15
Geological context and hydrothermal circulation.....	15
1 Mid Ocean ridges	17
1.1 Morphology	17
1.2 Structure of the oceanic crust	19
2 Hydrothermal Circulation	22
2.1 Discovery.....	22
2.2 High temperature hydrothermal systems.....	25
2.3 Low temperature hydrothermal systems.....	42
References	44
Chapitre 2.....	53
The Lucky Strike hydrothermal field.....	53
1 Discovery and geological context	55

2 Geological setting.....	55
3 Basalt chemistry at Lucky Strike	58
4 Seafloor.....	58
5 Hydrothermal deposits	59
6 Hydrothermal fluid venting at Lucky Strike	60
7 Hydrothermal fauna at the LSHF	63
8 The EMSO Azores node: a multidisciplinary deep sea observatory.....	64
9 First results from the observatory.....	66
Chapitre 3.....	75
Materials and methods	75
1 Hydrothermal fluid sampling and processing	77
2 On board analyses	86
3 On shore analyses.....	86
3.1 Anions.....	86
3.2 Major cations	87
3.3 Trace elements	88
3.4 Rare Earth Elements (REE).....	89
3.5 Sr isotopes.....	94
3.6 Li concentration analysis	94
3.7 Li isotopes determination	101
3.8 Nd isotopes	106
Chapitre 4.....	111
Spatial variations in vent chemistry at the Lucky Strike hydrothermal field, Mid Atlantic Ridge (37°N): Implications for seafloor flow geometry.	111
Abstract	113
Résumé.....	114

1. Introduction	115
2. Geological setting.....	117
3. Sampling and analytical method	121
3.1 Sampling.....	121
3.2 Analytical methods	122
4. Results	125
Chloride, Sulfate, Bromide	125
Iron and Manganese.....	126
Silica	126
Sodium, Calcium and Potassium	126
Rubidium, Strontium, Cesium and Lithium	127
Sr isotopes.....	128
5. Origin of the end-member hydrothermal fluids diversity	128
6. Pressure and temperature of the reaction zone.....	132
6.1 P–T conditions of phase separation	133
6.2 P–T conditions in the upflow zone	135
6.3 P–T fluid pathway at LSHF	138
7. Chloride variability within the LSHF.....	142
Conclusion.....	144
Chapitre 5.....	155
Time-serie study of hot vent chemistry from the Lucky Strike hydrothermal field (37°N): contribution from the EMSO-Azores deep sea observatory.	155
Abstract	157
Résumé	158
1. Introduction	160
2. Geological context.....	161

3. Materials and methods	165
3.1 Sampling.....	165
3.2. Elemental concentration measurement.....	165
3.3. Sr and Li isotopic compositions	166
4. Results	167
4.1. Group of sites between 2013 and 2015	168
4.2. Time-series of hot vent chemistry since 1993	169
5 Discussion	179
5.1 Time-series of hot vent chemistry: a matter of time-scale	179
5.2 Proxy of phase separation conditions and its reliability: Application to SE group from 1993 to 2015.	182
5.3 Alteration state of the substratum.....	187
5.4 Apparent temperature of greenschist mineral equilibration (Fe-Mn variations per sites).....	190
5.5 Three years isotopic variations	193
5.6 Water–Rock determination.....	200
Conclusion.....	202
References	204
Chapitre 6.....	211
REE and Nd isotope signatures of hydrothermal fluids and their impact on the North Atlantic Deep Water: a case study of the Lucky Strike hydrothermal field (37°N, Mid- Atlantic Ridge).....	211
Abstract	213
Résumé	213
1 Introduction	214
2 Geological and hydrothermal setting	215
2.1. Geological context.....	215

2.2. Focused hydrothermal fluids	217
3 Method	218
3.1 Sample collection	218
3.2 Sample processing and determination of REE concentrations	220
3.3 Nd isotopic compositions	221
3.4 REE End-member calculation and Normalization	222
4 Results	223
4.1 REE concentrations of pure hydrothermal end-member fluids	223
4.2 REE concentrations of the buoyant hydrothermal plume fluids.....	224
4.3 Nd Isotopic composition of hydrothermal fluids.....	224
5 Discussion	224
5.1 Subsurface controls.....	224
5.2 Fate of REE within the proximal buoyant hydrothermal plume:	232
5.3 Isotopic evolution within the plume	241
Conclusion.....	242
References	243
Conclusion et perspectives.....	249
Conclusion and perspectives.....	257
Liste des figures	265
Annexe 1:.....	277
Accepted article in Journal of Sedimentary Research	277

INTRODUCTION

Les fumeurs noirs représentent, dans le milieu marin, les manifestations naturelles du mélange entre un fluide hydrothermal chaud (généralement supérieur à 300°C), réducteur et riche en métaux, ayant réagi avec la croûte océanique et l'eau de mer profonde, oxydante et froide (entre 2 et 4°C). Lors de ce mélange, des réactions chimiques d'oxydo-réduction provoquent la précipitation de particules poly-métalliques et d'oxyhydroxides qui forment ces volutes de « fumées » noires qui leur ont valu leur nom et leur célébrité (Corliss et al., 1979). La consolidation de ces particules au niveau de la zone de sortie des fluides chauds conduit à la formation de cheminées hydrothermales dont la hauteur peut atteindre plus de 10m (Haymon, 1983).

L'observation directe de ces curiosités naturelles par une équipe de chercheurs américains et français a eu lieu pour la première fois à la fin des années 1970 dans le bassin des Galápagos dans l'Océan Pacifique (Corliss et al., 1979). Cette découverte n'était pas le fruit du hasard, mais visait bien à mettre en évidence par observation directe la circulation de fluide dans la lithosphère océanique au niveau des dorsales. L'existence de l'hydrothermalisme marin était soupçonnée au vu des données géophysiques et géochimiques. Par exemple, les flux de chaleur mesurés dans les sédiments déposés sur la croûte océanique étaient systématiquement plus faibles que ceux prédits par les modèles de refroidissement conductif de la lithosphère (Bostrom and Peterson, 1966; Lister, 1972; Stein and Stein, 1994). Certains auteurs avaient alors invoqué un refroidissement convectif liée à la circulation hydrothermale au niveau des dorsales pour expliquer ce refroidissement plus rapide (Lister, 1974, 1972). D'autres études, géochimiques cette fois-ci, avaient montré la présence d'enrichissement en fer et en manganèse dans les sédiments marins à proximité des dorsales océaniques. Ces auteurs avaient alors invoqué des émanations de

fluide riche en métaux et d'origine profonde (Bostrom and Peterson, 1966; Muray and Renard, 1891).

Depuis cette première observation, la recherche et la détection de ces objets géologiques se sont affinées et ont conduit à la découverte de nouveaux systèmes hydrothermaux sur les dorsales à fort taux d'accrétion telle qu'à l'East Pacifique Rise (EPR), à faible–ultra-faible taux d'accrétion telles que la dorsale medio atlantique et les dorsales sud-est et sud-ouest indienne (German et al., 2016). Très vite, d'autres systèmes hydrothermaux sous-marins ont été découverts dans les bassins d'arrière arc d'une zone de subduction (Craddock and Bach, 2010). Ces systèmes de haute température sont omniprésents sur les quelques 60000 km de dorsale et 23000 km de zone de subduction.

Dans les années 1990, l'importance d'un hydrothermalisme de basse température a émergé avec la découverte, suite à des anomalies de flux de chaleur, des sources de Baby Bare dans le bassin de Cascadia (Wheat and Mottl, 2000). Baby Bare est un mont volcanique sous-marin qui sert de résurgence à des sources à ~60°C qui sont marquées par l'altération du basalte à cette température ainsi que par les sédiments avoisinant. Un autre système hydrothermal de basse température (<120°C) a été découvert en 2000 par hasard sur le flanc d'un ancien « oceanic core complex » en dehors de l'axe de la dorsale medio atlantique (Kelley et al., 2001). Ce système plus connu sous le nom de Lost City, s'exprime par une composition chimique très différente des systèmes de hautes température (Früh-Green et al., 2003; Von Damm, 2001). Ces systèmes sont des analogues directs de l'hydrothermalisme actuel bien connu dans les ophiolites. Les fluides issus de ces systèmes sont particuliers avec des pH supérieurs à 9 (jusqu'à 12) et forment, sur le site de leur décharge, des cheminées carbonatées en milieu immergé et des travertins dans les ophiolites (Barnes et al., 1978; Chavagnac et al., 2013a, 2013b; Früh-Green et al., 2003).

Ainsi, l'ubiquité des systèmes hydrothermaux a été observée et démontrée dans chaque océan. Les fluides hydrothermaux se trouvent ainsi à l'interface entre la lithosphère, siège des processus tectoniques et magmatiques d'accrétion océanique et l'hydrosphère. Ils participent à la fois à l'échange de chaleur entre ces deux réservoirs mais aussi à l'échange de matière. Ainsi, Resing et al. (2015) ont montré que le panache hydrothermal pouvait être suivi jusqu'à 4300 km de la dorsale EPR, soulignant ainsi l'impact des activités hydrothermales sur les cycles biogéochimiques globaux en tant que source de matière. De plus, plusieurs études ont montré le lien entre l'activité magmatique et la composition des fluides hydrothermaux sur les dorsales rapides. Ce lien et le type de réponse en termes de

variabilité des compositions des fluides hydrothermaux restent à déterminer en contexte de dorsale à faible taux d'accrétion, où les processus tectoniques jouent un rôle plus important du fait que les épisodes magmatiques sont moins fréquents. Il apparaît donc nécessaire pour comprendre à la fois le bilan chimique de la lithosphère et de l'océan et les processus profonds d'accrétion océanique d'étudier les fluides hydrothermaux qui se trouvent à l'interface entre ces deux réservoirs.

D'une manière générale, un système hydrothermal sous-marin est constitué de trois compartiments : 1) une zone de recharge, qui est la zone où l'eau de mer froide et oxydante pénètre le long de fractures/fissures dans la lithosphère océanique ; 2) une zone dite de réaction, où l'eau de mer, déjà modifiée à basse et moyenne température au sein de la croûte océanique, va acquérir sa composition chimique finale via les interactions eau-roche à des conditions de pression et température élevées ; 3) la zone de décharge, qui voit le fluide hydrothermal descendant de la zone de réaction se décharger dans l'eau de mer profonde.

La remontée de ces fluides hydrothermaux profonds vers le plancher océanique, est due à une différence de densité et de flottabilité entre les fluides ascendants chauds et les fluides et/ou eau de mer environnant-e-s (Bischoff, 1991; Fontaine and Wilcock, 2007; Lowell et al., 1995). Cette différence de densité est souvent associée à un phénomène appelé la séparation de phase (Bischoff, 1991; Bischoff and Rosenbauer, 1984), qui est liée à la salinité du fluide, et aux conditions de pression et de température atteintes dans la zone de réaction (Bischoff and Rosenbauer, 1988; Driesner, 2007; Driesner and Heinrich, 2007; Foustoukos and Seyfried, 2007). La séparation de phase est marquée par la formation d'une phase vapeur peu salée ainsi que d'une phase saumure plus salée. Les proportions des phases vapeur et saumure sont dépendantes des conditions pression et température atteintes au cours des interactions eau-roche. Ces processus engendrent une grande diversité de compositions chimiques des fumeurs noirs qui dépendent à la fois des conditions de pression, température et des interactions eau-roche. Le couple pression et température provoque la remontée des fluides depuis la zone de réaction vers la surface du plancher océanique. Les interactions eau-roche de la zone de réaction engendrent leurs diversité chimiques (German and Seyfried, 2014).

Les fluides hydrothermaux émanant à la surface sont d'excellents indicateurs de processus profonds auxquels il est difficile d'avoir accès à moins de forer la lithosphère océanique, comme cela s'est fait au cours du Leg ODP 158 au niveau du champ hydrothermal TAG (MAR, 26°N) , et de les comparer aux analogues continentaux comme les ophiolites dont

l'histoire tectonique complexe limite les possibilités de comparaison directe. En raison des hautes températures, le forage ne peut pas atteindre les régions profondes d'où le fluide. Des indicateurs chimiques existent et sont utilisés pour évaluer les conditions de température et de pression, telle que la solubilité du quartz via les concentrations en Si dans le fluide ainsi que les conditions de température enregistrées par le fluide hydrothermal via le rapport Fe/Mn, qui est lui-même contrôlé par la formation de minéraux du faciès schiste vert.

Le site hydrothermal de Lucky Strike situé à 400 km au Sud Est de l'archipel des Açores (Faial) sur la dorsale medio atlantique (37°N) a été découvert en 1992 lors d'une campagne scientifique nommée FAZAR (French and American Zaps and Rocks) qui visait à étudier, par une approche multidisciplinaire, plusieurs segments de la ride (Langmuir et al., 1997, 1992). Lors de la première drague de cette expédition, des cheminées hydrothermales associées à des verres basaltiques frais ont été collectées, attestant d'une activité volcanique et hydrothermale au centre du segment récente. L'année suivante a été organisée une campagne de plongée en submersible pour observer et échantillonner les fluides provenant de ce champ hydrothermal. Celui-ci s'est révélé être un des plus développés au monde, couvrant une superficie $\sim 1 \text{ km}^2$ (Langmuir et al., 1997; Von Damm et al., 1998). Depuis 1992, de nombreuses études menées en biologie, géochimie et géophysique ont contribué à caractériser le champ hydrothermal de Lucky Strike (Fouquet et al. 1995; Lee Van Dover et al. 1996; Singh et al. 2006 ; Dziak et al., 2004 ; Escartin et al., 2008 ; Barreyre et al., 2012). Malgré ces études, la dynamique de circulation hydrothermale et ses conséquences sur le développement des processus profonds restent élusives.

C'est une des raisons qui ont motivé le projet d'observatoire fond de mer en cet endroit. Cet observatoire issu d'un projet européen formant le nœud EMSO Açores a développé une technologie permettant une transmission quasi-continue de données biologiques, chimiques et géophysiques via communication satellitaire et acoustique (Colaço et al., 2011). Ce programme contribue à une caractérisation très fine du fonctionnement et de la dynamique du système hydrothermal à Lucky Strike. Dans le cadre de cet observatoire, les fluides hydrothermaux ont été collectés chaque année depuis 2009 assurant un suivi temporel de la composition chimique couplée à une couverture spatiale de la diversité des fluides qui reste inégalée sur une dorsale lente (Chavagnac et al., 2015). Ma thèse est une contribution à l'étude de cet observatoire en alimentant cette base de données par 3 années d'échantillonnage des sites permettant de mieux caractériser les processus profonds et de

les relier aux observations d'autres domaines comme la géophysique et la microbiologie. Le manuscrit se compose de six chapîtres.

Dans un premier chapître, je présente l'état de l'art de la structure de la croûte océanique et des produits de son altération par l'eau de mer en lien avec la formation et la diversité des systèmes hydrothermaux.

Dans le deuxième chapître, je présente en détail les connaissances acquises au niveau du champ hydrothermal de Lucky Strike depuis sa découverte et en particulier les composantes de l'observatoire fond de mer qui ont apporté une gamme de connaissances diversifiées et à haute résolution.

Le troisième chapitre présente en détail le matériel et les méthodes utilisés au cours de cette thèse pour échantillonner et analyser les fluides hydrothermaux. Cette partie est primordiale pour attester de la qualité des données présentées dans ce travail. La stratégie et le protocole d'échantillonnage y sont présentés en détail ainsi que les protocoles de préparation des fluides en vue des analyses chimiques, aussi bien en terme de concentration (Cl, SO₄, Br, Ca, Na, K, Si, Mg, Fe, Mn, Sr, Rb, Cs, Li, REE) qu'en terme de composition isotopique (⁸⁷Sr/⁸⁶Sr, ⁷Li/⁶Li, et ¹⁴³Nd/¹⁴⁴Nd).

Les trois chapitres suivants présenteront tous les résultats acquis lors de cette thèse sous un format de publications scientifiques qui font/feront l'objet de soumission/publication dans des revues scientifiques.

Le chapitre 4 a été soumis pour publication à la revue *Geochimica et Cosmochimica Acta* en Juillet 2016. Cet article concerne la variation spatiale des compositions chimiques des fluides et pose les bases d'un modèle de circulation hydrothermale à l'échelle de l'ensemble du champ hydrothermal. Pour ce faire, une classification a été faite en fonction de la salinité et de la position géographique des événements. Cela répond à la réinterprétation des données de la littérature via des outils géochimiques d'estimation de pression et de température. Cette réinterprétation est grandement enrichie par la découverte d'un nouveau site hydrothermal nommé Capelinhos, lors de ma première campagne océanographique. Celui-ci fait partie du champ hydrothermal de Lucky Strike mais son éloignement par rapport au lac de lave fossilisé et de sa composition chimique en fait un site particulier au sein de cette diversité d'événements hydrothermaux. Les fluides de Capelinhos sont les plus appauvris en Cl par rapport aux autres sites et les indicateurs Fe/Mn de température de la zone de réaction indiquent des températures bien supérieures à ce qui a été publié auparavant (Pester et al.,

2012). Ces résultats ne suggèrent pas une origine plus profonde pour ce fluide mais plutôt une extraction plus rapide de ceux-ci depuis la zone de séparation de phase ainsi qu'une ségrégation de la phase saumure plus efficace.

Le chapitre 5 se base sur les interprétations du chapitre 4 pour suivre l'évolution temporelle de la composition des fluides du champ hydrothermal depuis 1993 jusqu'en 2015 (avec un hiatus de 11 ans entre 1997 et 2008). Il se penche, dans un premier temps, sur des éléments diagnostiques des pressions et températures permettant de repérer des perturbations magmatiques et/ou tectoniques au cours du suivi temporel, ainsi qu'à des indicateurs d'altération du plancher océanique et du stockage de métaux dans la zone de décharge. Ainsi, nos résultats mettent en lumière un cycle d'altération à la suite du remplissage de la chambre magmatique en 2008, et d'évènements sismiques en 2009, 2011 et 2012. La deuxième partie de ce chapitre dresse un éventail des compositions isotopiques en Sr et en Li, en lien avec les processus de subsurface. Il montre un substratum relativement peu altéré mais dont le cycle géochimique du Sr est perturbé pour 2 groupes de sites par l'influence de minéraux incorporant le Sr comme l'albite ou l'anhydrite.

Le chapitre 6 se concentre sur des éléments particuliers que sont les terres rares. Les terres rares dans les fluides hydrothermaux ont été étudiées seulement ponctuellement à quelques systèmes hydrothermaux à l'échelle mondiale mais assez peu à l'échelle d'un champ hydrothermal présentant une forte variabilité de chlorinité. Le champ hydrothermal de Lucky Strike rend possible une telle étude de ces éléments dans un contexte géologique solidement établi (Chapitre 2, 4 et 5). L'autre volet de ce chapitre concerne le devenir immédiat de ces éléments en présentant pour la première fois des concentrations de terres rares dissoutes dans le panache hydrothermal et qui peuvent avoir une influence sur le bilan chimique et isotopique de l'eau de mer à grande échelle.

Enfin, pour conclure ce travail de thèse, je résume les avancées en termes de connaissance du système hydrothermal de Lucky Strike.

INTRODUCTION (ENGLISH)

Black-smokers represent the natural manifestations of the mixing between hot, reduced and metal-rich hydrothermal fluid ($>300^{\circ}\text{C}$), which has reacted with the oceanic crust, and deep cold ($2\text{--}4^{\circ}\text{C}$), oxidized and metal-depleted seawater. During this mixing, redox reactions induce precipitation of poly-metallic and oxy-hydroxides particles that compose the typical “black smoke” (Corliss et al., 1979). When consolidating, these particles can form hydrothermal chimneys that can reach over 10m above the seafloor (Haymon, 1983).

These geological objects were observed by American and French scientists for the first time at the end of the 1970s in the Galapagos basin of the Pacific Ocean (Corliss et al., 1979). This expedition was looking for these objects that were suspected to exist through geophysical and geochemical indicators. Heat fluxes measured in sediments above the oceanic crust show systematically lower values than the ones predicted provided by conductive cooling models of the oceanic lithosphere (Bostrom and Peterson, 1966; Lister, 1972; Stein and Stein, 1994). To explain these discrepancies between the calculated and measured heat fluxes, some authors have invoked the possibility of hydrothermal circulation at the ridge crest (Lister, 1974, 1972). Other geochemical studies revealed Fe and Mn enrichment in sediments collected near the Pacific Ocean ridge crests. It was then suggested that metal rich fluid of deep origin was flowing through these sediments (Bostrom and Peterson, 1966; Muray and Renard, 1891).

Since this first observation, the exploration techniques to detect these geological objects have significantly improved and lead to the discovery of numerous high temperature hydrothermal systems on fast spreading ridges (East Pacific Rise), slow to ultra-slow spreading ridge like the Mid Atlantic ridge and the South West Indian Ridge (German et al., 2016). Other submarine hydrothermal systems have been discovered in back arc basin of subduction zone (Craddock and Bach, 2010). These high temperature hydrothermal systems are ubiquitous along the ~ 60000 km of ocean ridge and ~ 23000 km of subduction zone.

Since the 1990s, the impact of low temperature venting ($<120^{\circ}\text{C}$) has been also questioned with the discovery of hydrothermal springs at the Baby Bare seamount in the Cascadia basin, which were found by heat flux anomalies near the seamount (Wheat and Mottl, 2000). Baby Bare is a volcanic seamount where hydrothermal water springs out at 60°C .

The chemical compositions of these fluids are marked by basalt alteration and sediment interactions at this temperature (~60°C). Another low temperature hydrothermal system has been discovered surprisingly, in 2000, during the exploration of a fossil Ocean Core Complex outside the ridge axis in the North Atlantic (Kelley et al., 2001). This system is called Lost City, and has a different chemical composition of fluids compared to high temperature systems with pH values higher than 9 (up to 12) and high alkali concentrations (Früh-Green et al., 2003; Von Damm, 2001). It represents a direct analog of the actual hyperalkaline springs that can be found on ophiolites; note withstanding that percolating water is of meteoric origin rather than seawater at Lost City. This type of fluids leads to the formation of carbonated chimneys at submarine discharge and travertines on the ophiolites (Barnes et al., 1978; Chavagnac et al., 2013a, 2013b; Früh-Green et al., 2003).

Hydrothermal systems are ubiquitous and the discharging fluids are located at the interface between the lithosphere (which hosts tectonic and magmatic process) and the hydrosphere (which regulates the thermohaline circulation). These fluids participate in the heat and matter exchange between these two reservoirs. Recently, Resing et al., (2015) showed that traces of hydrothermal plumes indicated by high Fe concentration in the water column, are found as far as 4300 km off the EPR axis. This highlights the impact of hydrothermal activities on the biogeochemical cycles on a wide/global scale. Moreover, several studies have linked magmatic activity at the ridge axis to changes of fluid compositions on fast spreading ridges. The chemical response recorded by hydrothermal fluids are still to be identified on the slow spreading ridge context where tectonic processes are more important than magmatic ones. It thus appears necessary to study the hydrothermal fluids at the interface between the lithosphere and the ocean in slow spreading ridge in order to better constrain the chemical exchange between them and as a response of crust accretion process.

A submarine hydrothermal system can be summarized into three areas: 1) the recharge zone, where cold and oxidizing seawater percolates into the ocean crust through cracks/fractures; 2) a reaction zone, where seawater already modified at low temperature, will acquire its final composition at high temperature and pressure conditions during water–rock interactions; 3) the discharge zone, where the ascending hydrothermal fluid discharges into and mix with deep seawater.

The upflow of these fluids is triggered by density difference with proximal fluids and their relative buoyancy (Bischoff, 1991; Fontaine and Wilcock, 2007; Lowell et al., 1995). This difference originates from the phase separation process, linked to the salinity, the

temperature and the pressure of the fluid in the reaction zone (Bischoff, 1991; Bischoff and Rosenbauer, 1984; Bischoff and Rosenbauer, 1988; Driesner, 2007; Driesner and Heinrich, 2007; Foustoukos and Seyfried, 2007). The phase separation process is characterized by the formation of a vapor phase with low salinity and a brine phase with high salinity. The proportions of vapor and brine are dependent on the P and T conditions of phase separation. This process leads to a wide diversity of fluid compositions of black smokers depicting the various P and T conditions governing the reaction zone of the systems, and the extent of water-rock reactions (German and Seyfried, 2014).

Hydrothermal fluids emanating at the seafloor are excellent indicators of deep processes which are difficult to attain otherwise, as it would require drilling a too high temperature, e.g. Leg ODP 158 at the TAG hydrothermal field (26°N MAR), or a direct comparison to ophiolites, whose complex tectonic histories severely limit inter comparisons. Chemical indicators do exist and are used to assess the P and T conditions of water-rock interactions, such as a geothermobarometer based on Quartz solubility estimated through Si concentrations in the fluid, and a geothermometer based on Fe/Mn ratios in fluids, the latter being controlled by the equilibria with greenschist facies minerals.

The Lucky Strike hydrothermal field (LSHF) is located 400 km south-east of the Azores islands on the Mid Atlantic Ridge (37°N). It was discovered in 1992 during the FAZAR cruise (French and American Zaps and Rocks) that aimed at studying ridge segments via a multidisciplinary approach (Langmuir et al., 1997, 1992). During the first dredge, hydrothermal chimneys were collected together with pieces of fresh basaltic glass, which indicated that recent volcanic activity and hydrothermal activity were present at the segment center. The following year, a sampling cruise was organized to study this hydrothermal field. It revealed that the LSHF was the largest hydrothermal field known worldwide (~1 km²; Langmuir et al., 1997; Von Damm et al., 1998). Since 1992, the field has been characterized for biology, geochemistry and geophysical surveys which made the Lucky Strike hydrothermal field one of the best known on the MAR (Fouquet et al. 1995; Lee Van Dover et al. 1996; Singh et al. 2006; Escartin et al., 2008 ; Barreyre et al., 2012). However the dynamic of hydrothermal circulation and its response to deep crustal processes are still to be characterized.

These observations have motivated the scientific community to monitor continuously seafloor processes by installing a deep-sea observatory at Lucky Strike. This observatory, as part of the EMSO project, benefited from the development of the technology for near

real time transmission of biological, chemical and geophysical data through acoustic and satellite communications (Colaço et al., 2011). This program contributes to the fine characterisation of the hydrothermal dynamic at Lucky Strike. In the frame of this observatory, hydrothermal fluids have been collected since 2009, providing a wide spatial and temporal survey, which is unique on a slow spreading ridge (Chavagnac et al., 2015). This thesis is aimed to characterize deep processes as recorded by chemical composition of focused fluids and acquired within this observatory, and to link these variations to other geophysical and/or biological monitoring. This thesis is composed of 6 chapters.

In a first chapter, I review the state of the art on the oceanic crust and its alteration products by interaction with seawater. I also summarize the hydrothermal circulation in terms of fluid types (i.e. hot vs. cold) and the anatomy of a hydrothermal cell.

In a second chapter, I present in detail the knowledge of the Lucky Strike hydrothermal field since its discovery till the set-up of the deep-sea observatory that allowed high resolution characterisation of the hydrothermal system from different domains. Indeed the multidisciplinary approach used at this deep sea observatory leads to an excellent characterization of the geophysical, geological, biological and geochemical features of this hydrothermal field.

The third chapter presents in details the material, the instruments and the methods used during this thesis to sample and analyze hydrothermal fluids. This chapter is a prerequisite to attest on the quality of presented datasets regarding elemental concentrations (Cl, SO₄, Br, Ca, Na, K, Si, Mg, Fe, Mn, Sr, Rb, Cs, Li, and REE) and isotopic composition (⁸⁷Sr/⁸⁶Sr, ⁷Li/⁶Li, and ¹⁴³Nd/¹⁴⁴Nd).

The three following parts present the results from this thesis in the form of scientific publication that are either submitted or in preparation for submission in international scientific journals.

Chapter 4 was submitted to *Geochimica et Cosmochimica Acta* in July 2016. This article focuses on the spatial variation of fluid composition to propose a new model of hydrothermal circulation at the scale of the whole Lucky Strike hydrothermal field. Venting sites were classified according to their chlorine concentrations and their location compared to a central fossil lava lake. Geochemical indicators are used to infer pressure and temperature conditions taking place during water-rock interactions. The discovery in 2013 of a new active site named Capelinhos, located far from the fossil lava lake, allows the

reinterpretation of the hydrothermal pathways underneath the Lucky Strike hydrothermal field. Capelinhos fluids are the most depleted in Cl compared to the other sites and have higher Fe and Mn, which indicates a higher temperature in the reaction zone. These results are not indicative of a deeper origin of the fluid but rather a rapid upflow toward the seafloor with a limited re-equilibration and efficient brine segregation.

Chapter 5 is based on the model proposed in chapter 4, and focuses on the chemical variabilities of focused fluids since its discovery in 1992 till 2015, with our dataset obtained through the deep-sea observatory between 2009 and 2015. First, we assess the temporal variability of the phase separation P and T conditions through Si-Cl indicators. These results highlight an alteration cycle following a magmatic replenishment of the axial magma chamber in 2008 and 2010, as well as seismic activity in 2009, 2011 and 2012. The second part presents the isotopic compositions of Sr and Li analyzed for the fluid samples. The Li isotopes indicate a relatively fresh substratum whereas the Sr geochemical cycle indicates a more complicated behavior for 23 sites probably due to subsurface processes.

The chapter 6 investigates the REE and Nd isotopic signatures of focused and buoyant hydrothermal fluids at the Lucky Strike hydrothermal field. Previous REE studies have been performed either at the scale of one single hydrothermal field or by comparison to other hydrothermal fields on the global scale. The Lucky Strike hydrothermal field is a unique opportunity to investigate the distribution of REE over a wide range of chlorinity and at the scale of a hydrothermal field. The other part of the chapter focuses on the buoyant plume forming at the mixing zone between pure hydrothermal fluid and seawater. This is the first study, to provide the dissolved REE concentrations in this zone. The results show that these fluids have an impact on the REE elemental and Nd isotopic composition of the deep seawater.

To conclude, I will summarize the main progress this thesis brought to our knowledge of the Lucky Strike hydrothermal field system.

Reference

- Barnes, I., O'neil, J.R., Trescases, J.-J., 1978. Present day serpentinization in New Caledonia, Oman and Yugoslavia. *Geochim. Cosmochim. Acta* 42, 144–145.
- Barreyre T., Escartín J., Garcia R., Canna, M., Mittelstaedt E., Prados R. (2012) Structure, temporal evolution, and heat flux estimates from the Lucky Strike deep-sea hydrothermal field derived from seafloor image mosaics: Hydrothermal outflow and image mosaics. *Geochem. Geophys. Geosystems* 13. doi:10.1029/2011GC003990
- Bischoff, J., 1991. Densities of liquids and vapors in boiling NaCl-H₂O solutions: A PVTX summary from 300° to 500°C. *Am. J. Sci.* 291, 309–338.
- Bischoff, J.L., Rosenbauer, R.J., 1984. The critical point and two-phase boundary of seawater, 200-500°C. *Earth Planet. Sci. Lett.* 68, 172–180.
- Bischoff, J., Rosenbauer, R.J., 1988. Liquid-vapor relations in the critical region of the system NaCl-H₂O from 380 to 415°C: A refined determination of the critical point and two-phase boundary of seawater. *Geochim. Cosmochim. ACTA* 52, 2121–2126.
- Bostrom, K., Peterson, A., 1966. Precipitates from hydrothermal exhalations on the East Pacific Rise. *Econ. Geol.* 61, 1258–1265.
- Chavagnac, V., Ceuleneer, G., Monnin, C., Lansac, B., Hoareau, G., Boulart, C., 2013a. Mineralogical assemblages forming at hyperalkaline warm springs hosted on ultramafic rocks: A case study of Oman and Ligurian ophiolites: Mineral Precipitate at Alkaline Springs. *Geochem. Geophys. Geosystems* 14, 2474–2495. doi:10.1002/ggge.20146
- Chavagnac, V., Leleu, T., Boulart, C., Barreyre, T., Castillo, A., Menjot, L., Cannat, M., Escartín, J., Sarradin, P.-M., 2015. Deep-Sea Observatory EMSO-Azores (Lucky Strike, 37°17'N MAR): Impact of Fluid Circulation Pathway on Chemical Hydrothermal Fluxes, in: *Follow the Fluids: Integrating Multidisciplinary Observations of Deep-Sea Hydrothermal Systems II*. Presented at the AGU Fall Meeting, San Francisco.
- Chavagnac, V., Monnin, C., Ceuleneer, G., Boulart, C., Hoareau, G., 2013b. Characterization of hyperalkaline fluids produced by low-temperature serpentinization of mantle peridotites in the Oman and Ligurian ophiolites: Hyperalkaline Waters in Oman and Liguria. *Geochem. Geophys. Geosystems* 14, 2496–2522. doi:10.1002/ggge.20147
- Colaço, A., Blandin, J., Cannat, M., Carval, T., Chavagnac, V., Connelly, D., Fabian, M., Ghiron, S., Goslin, J., Miranda, J.M., Reverdin, G., Sarrazin, J., Waldmann, C., Sarradin, P.M., 2011. MoMAR-D: a technological challenge to monitor the dynamics of the Lucky Strike vent ecosystem. *ICES J. Mar. Sci.* 68, 416–424. doi:10.1093/icesjms/fsq075
- Corliss, J.B., Dymond, J., Gondon, L.I., Edmond, J.M., Von Herzen, R.P., Ballard, R.D., Green, K., Williams, D., Brainbridge, A., Crane, K., van Andel, T.H., 1979. Submarine Thermal Springs on the Galapagos Rift. *Science* 203, 1073–1083.
- Craddock, P.R., Bach, W., 2010. Insights to magmatic–hydrothermal processes in the Manus back-arc basin as recorded by anhydrite. *Geochim. Cosmochim. Acta* 74, 5514–5536. doi:10.1016/j.gca.2010.07.004
- Driesner, T., 2007. The system H₂O–NaCl. Part II: Correlations for molar volume, enthalpy, and isobaric heat capacity from 0 to 1000°C, 1 to 5000bar, and 0 to 1 XNaCl. *Geochim. Cosmochim. Acta* 71, 4902–4919. doi:10.1016/j.gca.2007.05.026

Driesner, T., Heinrich, C.A., 2007. The system H₂O–NaCl. Part I: Correlation formulae for phase relations in temperature–pressure–composition space from 0 to 1000°C, 0 to 5000bar, and 0 to 1 XNaCl. *Geochim. Cosmochim. Acta* 71, 4880–4901. doi:10.1016/j.gca.2006.01.033

Escartín, J., R. García, O. Delaunoy, J. Ferrer, N. Gracias, A. Elibol, X. Cufi, L. Neumann, D. J. Fornari, S. Humphris and J. Renard, Globally-aligned photo mosaic of the Lucky Strike hydrothermal Vent Field (Mid-Atlantic Ridge, 37°18.5'N): release of geo-referenced data, mosaic construction and viewing software, *G-cubed*, 9, Q12009, doi:10.1029/2008GC002204, 2008.

Fontaine, F.J., Wilcock, W.S.D., 2007. Two-dimensional numerical models of open-top hydrothermal convection at high Rayleigh and Nusselt numbers: Implications for mid-ocean ridge hydrothermal circulation: hydrothermal convection. *Geochem. Geophys. Geosystems* 8. doi:10.1029/2007GC001601

Fouquet, Y., Ondréas, H., Charlou, J.L., Donval, J.P., Radford-Knoery, 1995. Atlantic lava lakes and hot vents. *Nature* 377, 201.

Foustoukos, D.I., Seyfried, W.E., 2007. Fluid Phase Separation Processes in Submarine Hydrothermal Systems. *Rev. Mineral. Geochem.* 65, 213–239. doi:10.2138/rmg.2007.65.7

Früh-Green, G., Kelley, D.S., Bernasconi, S.M., Karson, J.A., Ludwig, K.A., Butterfield, D.A., Boschi, C., Proskurowski, G., 2003. 30,000 Years of Hydrothermal Activity at the Lost City Vent Field. *Science* 301, 495–498.

German, C.R., Petersen, S., Hannington, M.D., 2016. Hydrothermal exploration of mid-ocean ridges: Where might the largest sulfide deposits be forming? *Chem. Geol.* 420, 114–126. doi:10.1016/j.chemgeo.2015.11.006

German, C.R., Seyfried, W.E., 2014. Hydrothermal Processes, in: *Treatise on Geochemistry*. Elsevier, pp. 191–233.

Haymon, R., 1983. Growth history of hydrothermal black smoker chimneys. *Nature* 301.

Kelley, D. S., Karson, J. A., Blackman, D. K., Früh-Green G. I., Butterfield, D. A., Lilley, M. D., Olson, E. J., Schrenk, M. O., Roe, K. K., Lebon, G. T., Rivizzigno P., AT3-60 shipboard party, 2001. An off-axis hydrothermal vent field near the Mid-Atlantic Ridge at 30°N. *Nature*, v. 412.

Langmuir, C.H., Klinkhammer, G.P., Bougault, H., 1992. Evaluation of the relationships among segmentation, hydrothermal activity and petrological diversity on the mid-Atlantic ridge: FAZAR (French American Zaps and Rocks) (Cruise report). Lamont-Doherty Earth Observatory of Columbia University, R/V Atlantis II.

Langmuir, C., Humphris, S.E., Fornari, D.J., Van Dover, C., Von Damm, K.L., Tivey, M.K., Colodner, D., Charlou, J.L., Desonie, D., Wilson, C., Fouquet, Y., Klinkhammer, G.P., Bougault, H., 1997. Hydrothermal vents near a mantle hot spot: the Lucky Strike vent field at 37°N on the Mid-Atlantic Ridge. *Earth Planet. Sci. Lett.* 148, 69–91.

Lee Van Dover, C., Desbruyères, D., Segonzac, M., Comtet, T., Saldanha, L., Fiala-Medioni, A., Langmuir, C., 1996. Biology of the Lucky Strike hydrothermal field. *Deep Sea Res. Part Oceanogr. Res. Pap.* 43, 1509–1529.

Lister, C.R.B., 1974. On the penetration of water into hot rock. *Geophys. J. Int.* 39, 465–509.

Lister, C.R.B., 1972. On the thermal balance of a mid-ocean ridge. *Geophys. J. Int.* 26, 515–535.

Lowell, R.P., Rona, P., Von Herzen, R.P., 1995. Seafloor hydrothermal systems. *J. Geophys. Res.* 100, 327–352.

Murray, J., Renard, A.F., 1891. *Deep Sea Deposits, Report "Challenger3 Expedition (1873-1876)*.

Resing, J.A., Sedwick, P.N., German, C.R., Jenkins, W.J., Moffett, J.W., Sohst, B.M., Tagliabue, A., 2015. Basin-scale transport of hydrothermal dissolved metals across the South Pacific Ocean. *Nature* 523, 200–203. doi:10.1038/nature14577

Singh, S.C., Crawford, W.C., Carton, H., Seher, T., Combier, V., Cannat, M., Pablo Canales, J., Düsünür, D., Escartin, J., Miguel Miranda, J., 2006. Discovery of a magma chamber and faults beneath a Mid-Atlantic Ridge hydrothermal field. *Nature* 442, 1029–1032. doi:10.1038/nature05105

Stein, C.A., Stein, S., 1994. Constraints on hydrothermal heat flux through the oceanic lithosphere from global heat flow. *J. Geophys. Res.* 99, 3081–3095.

Von Damm, K.L., Bray, A.M., Buttermore, L.G., Oosting, S.E., 1998. The geochemical controls on vent fluids from the Lucky Strike vent field, Mid-Atlantic Ridge. *Earth Planet. Sci. Lett.* 160, 521–536.

Wheat, C.G., Mottl, M.J., 2000. Composition of pore and spring waters from Baby Bare: global implications of geochemical fluxes from a ridge flank hydrothermal system. *Geochim. Cosmochim. Acta* 64, 629–642.

CHAPITRE I

GEOLOGICAL CONTEXT AND HYDROTHERMAL CIRCULATION

1 Mid Ocean ridges

The mid-ocean ridges (MOR) are submarine mountains that extend over ~60000 km long and 5 to 30 km width (Macdonald, 2001). The chain is the most active volcanic system on earth and, together with subduction zones and transform faults, define the boundaries of tectonic plates (Fig I - 1). They mark the location where oceanic crust is formed by the ascension of mantle rock by advection. However, the MOR have shown to be crosscut by numerous transform faults tens to hundreds of km in length

1.1 Morphology

The morphology of Mid Ocean Ridges depends on the spreading rate and of the rate of melt production, which are generally related, although there may be exceptions to the rule. This spreading rate varies from 18 cm/year along some segments of the East Pacific Rise (EPR) to 0.7 cm/year at the South West Indian Ridge. On the basis of the spreading rates, a classification of 3 types of ridge has been drawn (Fig I - 2, Macdonald, 2001).

The ridges with a full spreading rate between 1 and 5 cm/year are called “slow spreading ridges”. They are characterized by a deep axial valley, the “rift”, coinciding with the spreading axis. The rift is 30 km wide and 1 to 2 km deep, bordered by elevated lithosphere (MAR 37°N, Fig I - 2).

From 5 to 9 cm/year spreading rate are called “intermediate spreading ridges”. They are characterized by a pronounced rift with a slightly elevated platform.

Ridges with a spreading rates between 9 and 18 cm/year are “fast spreading ridges”. They are characterized by an axial dome or axial high structure elevated by several hundred meters and by a discrete rift valley.

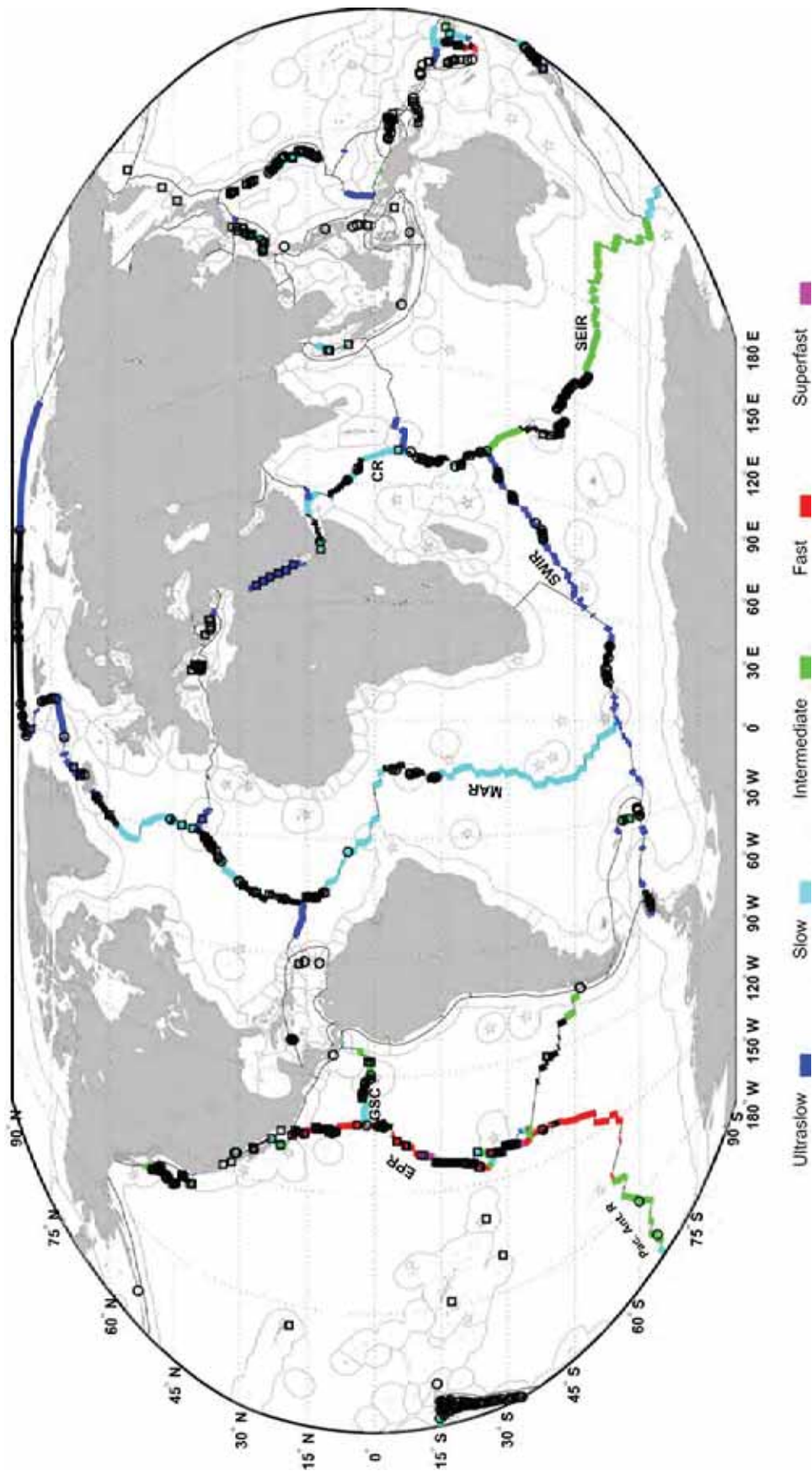


Figure 1 - 1 From Beaulieu et al., 2015. The map shows the repartition of hydrothermal vents on the mid-ocean ridge at different spreading rates.

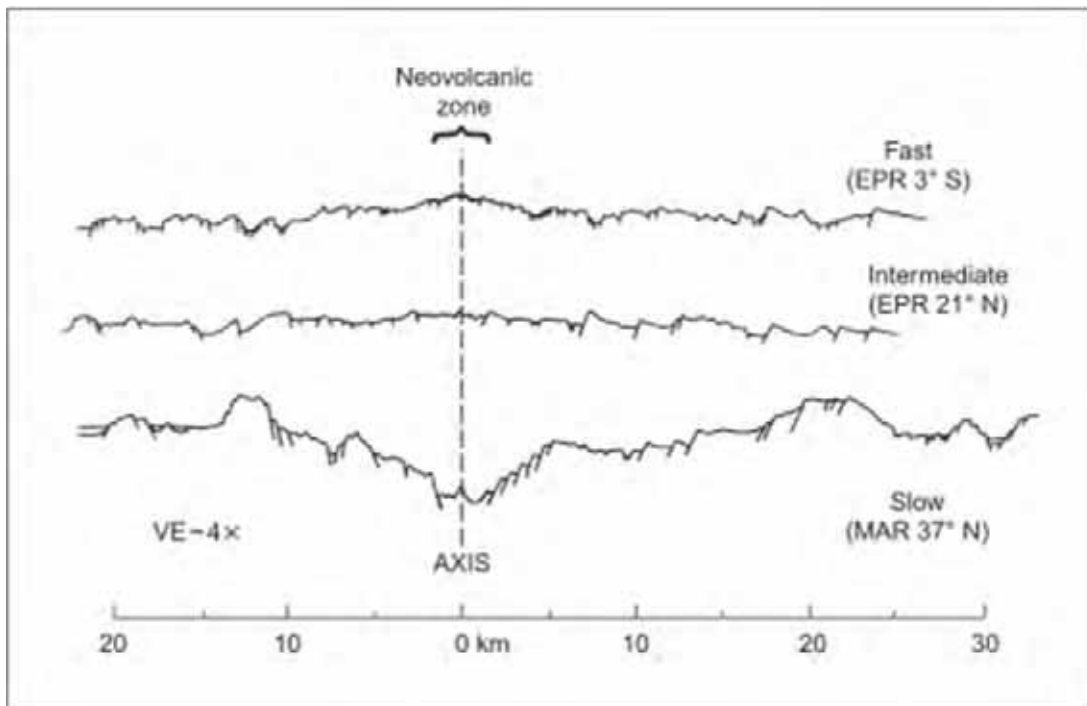


Figure 1 - 2 Cartoon of the ridge morphology dependent on the spreading rate. This show the fast, intermediary and slow spreading ridge type (modified from MacDonald 2001).

1.2 Structure of the oceanic crust

Most of our knowledge on the oceanic crust comes from seismic refraction data. Direct sampling is done by dredging but offers very limited knowledge on structure of the seafloor as for the exact positioning, representativeness of the samples recovered and structural relations between samples from a same dredge. Another part of the seafloor knowledge comes from ophiolite studies but superimposed complex tectonic history might bias their structure and composition.

Therefore, for a long time, the global data available to study the oceanic crust structure were seismic velocity profiles. The crust was shown to be ~7 km thick and rather constant in thickness over the oceans. Studies of the propagation rates of the P waves provided evidence for a model composed by different layers, named layer 1, 2 and 3, which are supposed to reflect a change in the nature of the rocks: sediments, basalts and gabbros respectively. Sub layers were also identified, especially within the layers 2 and 3.

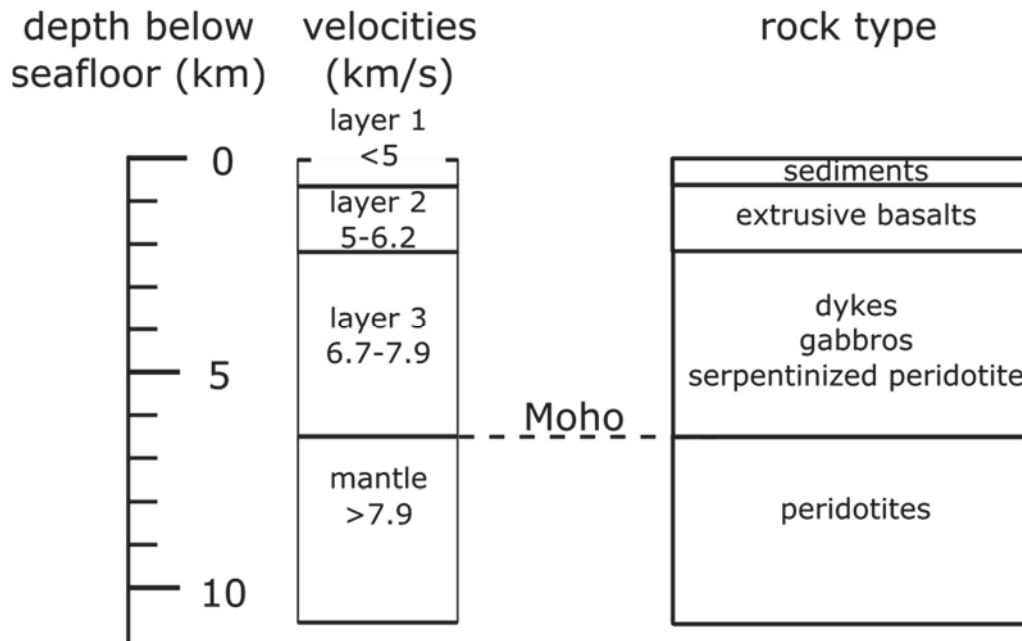


Figure I - 3 Classical representation of the oceanic structure associated to P wave's velocity. Modified from Pomerol et al., 2006.

The layer 2 is composed of 2 sublayers: 2A and 2B. The layer 2A has a maximum thickness of 1 km and has density lower than the underlying sublayer 2B (0.5 to 1 km thick). This low density is probably due to higher porosity rather than to a change in the nature of the rocks: pillow basalts and basaltic flows for the layer 2A and basaltic dikes (the sheeted dike complex) for layer 2B. Off the ridge, aging tends to minimize the differences between layers 2A and 2B due to precipitation of hydrothermal minerals reducing the porosity. However, the conversion of primary minerals into secondary minerals concurs to lower the density, illustrating the difficulty to infer lithology from seismic data alone. Layer 3 represents the gabbroic section of the crust (Fig I -3). This section is the deepest part of the crust. The separation between gabbros and mantle rocks is inferred to be observed on seismic profiles by a sharp increase in seismic wave speed. This boundary was named after its first observer, and is called Moho. This defines the limit between the crust and the upper mantle.

The precise lithology of the oceanic crust has been known thanks to scientific drilling programs. The first one was the MoHole project in the late 50's and early 60's that developed the instrumentation to drill the seafloor, especially dynamic positioning of the vessels that allows a perfectly stationary position. Although the MoHole project did not reach its primary objective (to drill a well down to the Moho), it motivated scientists to launch an international program with less ambitious but more realistic targets. These

drilling expeditions last since 1968 with different administrative forms (Deep Sea Drilling Project 1968-1983; Ocean Drilling Program 1985-2003; Integrated Ocean Drilling Program 2003-2013 and International Ocean Discovery Program 2013-2023).

Along with the drilling and detailed actual ocean crust lithologies, the general structural model, which is based on seismic layers, has been enriched by field truth as shown by Figure I - 4.

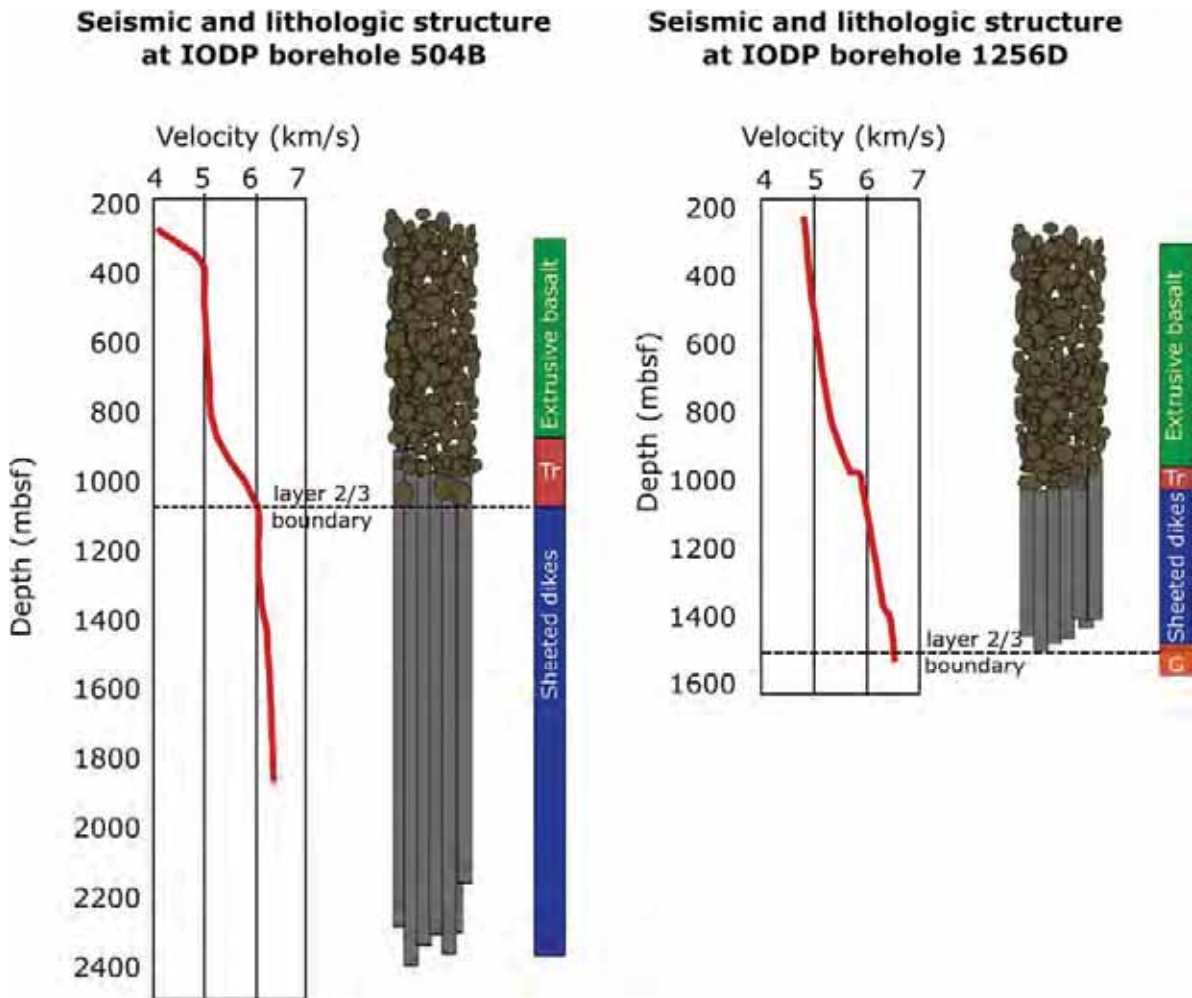


Figure I - 4 Modified from Carlson (2011). Seismic and lithologic profile from 2 IODP core, 504B on the Nazca plate and 1256D on the Cocos plate. Tr: Transition zone; G: Gabbros section.

This figure confronts the seismic profile and observed lithologies (determined on drill cores) of two drill-holes of the oceanic crust, the hole 504B from the Nazca plate and 1256D from Cocos plate. The lithology of the oceanic crust is not as homogeneous as indicated by the model (Fig I -3), at least in terms of thickness of the lithologies. Especially, these profiles show a normal correlation between seismic layer and lithologies for the 1256D hole while the layer2/3 boundary at 504B hole is found in the sheeted dikes section (Fig I

-4). At 504B, the 2300m thick core doesn't show gabbros but has seismic profile indicating the layer 3 is present. This highlights the fact that the oceanic crust is more heterogeneous than previously thought based on seismic profiles alone. Seismicity reflect physical properties rather than lithologies such as porosity/cracks *vs.* rock type.

2 Hydrothermal Circulation

2.1 *Discovery*

The first description of metalliferous deposits appeared in 1891 from sediments sampled by the HMS Challenger expedition at the Eastern flank of the East Pacific Rise (39°N; Muray and Renard, 1891). These deposits were described as brown to red sediments. These observations will only be re-investigated in the middle of the 19th century. Iron and Manganese enrichments were again found in sediments near the crest of the East Pacific Rise (Bostrom and Peterson, 1966) and elsewhere near the mid-ocean ridges (Arrhenius and Bonatti, 1965; Dymond et al., 1973; Skornyakova, 1965; Von der Borsch and Rex, 1970, among others).

In parallel in 1947, a Swedish Deep Sea Expedition was organized to perform the first Heat Flux measurement on the Ocean Floor. After this pioneering expedition, a whole body of measurements accumulated. The emergence of the plate tectonics concept offered a conceptual frame to interpret this wealth of data. Surprisingly, it revealed an inconsistency between measured heat fluxes and the ones predicted by models of conductive cooling of the plate in a spreading context. Especially, measurements conducted at ridge crests revealed a wide range of values, globally lower than expected by modelling (Fig I -5; Davis and Elderfield, 2004; Elderfield and Schultz, 1996; McKenzie, 1967; Stein and Stein, 1994). These observations led scientists to propose other mechanisms than conductive cooling to explain the heat fluxes of the oceanic crust and find the “missing heat”.

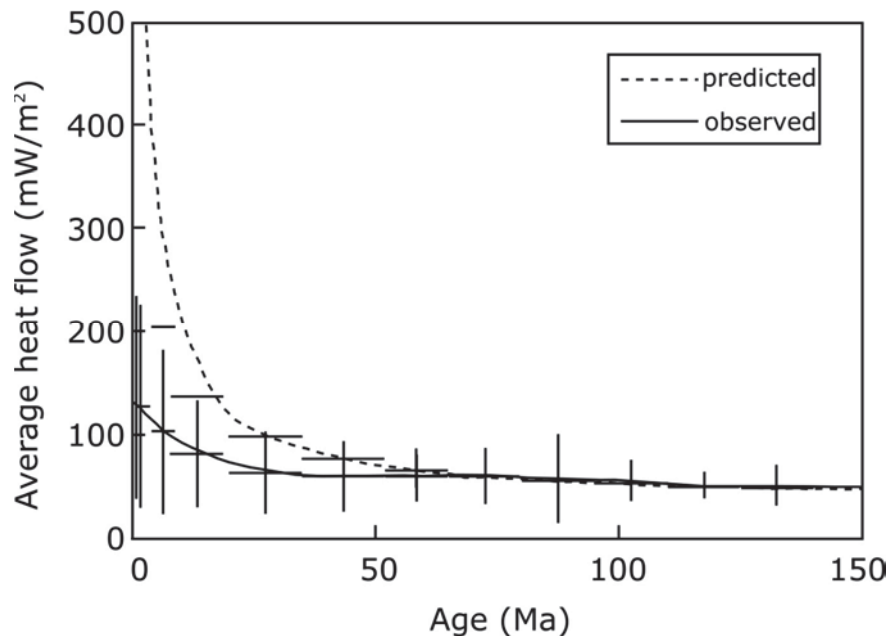


Figure I - 5 Measured Heat Flux as a function of Age of the oceanic crust. From Elderfield and Schultz (1996). Dashed line is the predicted heat flux based on geophysical model based on (McKenzie, 1967). Solid line is average measurements of heat flux by thermistor. The discrepancy between observed and predicted heat fluxes is very low after 65 Ma and maximal for Age < 1Ma, at ridge axis.

Bostrom and Peterson (1966) linked the occurrence of Fe and Mn with high heat flux at and near the crests. They proposed that a deep seated hydrothermal fluid originating from magmatic processes was responsible for this enrichment. This interpretation was supported by Lister (1972) who proposed hydrothermal circulation as a vector of heat in the crust, and developed models of circulation for variable physical setting, e.g. permeability of the substratum. As opposed to the magmatic solution, he proposed that circulation of cold seawater penetrating into the crust was taking place at the ridge valleys while the hot and focused discharge was taking place at seamounts due to physical constraints.

Soon after, the first hydrothermal site at mid-ocean ridge (MOR) was discovered in 1977 at the Galapagos Spreading center with fluids as high as 17°C discharging in a 2°C seawater (Corliss et al., 1979) and a specific chemo-synthetic fauna. Over decades, many hydrothermal vents were discovered over the 60000 km of mid ocean ridges but also in back-arc basin, and especially at higher temperature (up to 400°C) with hydrothermal field composed by the well-known black smokers (Fig I -6; Bowers et al., 1985; Edmonds, 2008; James et al., 1995; Koschinsky et al., 2008; Schmidt et al., 2007; K. L. Von Damm et al., 1985; among others). The discovery of the hydrothermal vents along the MORs has been one of the major discoveries during the last 40 years in terms of geophysical, biological and geochemical processes.

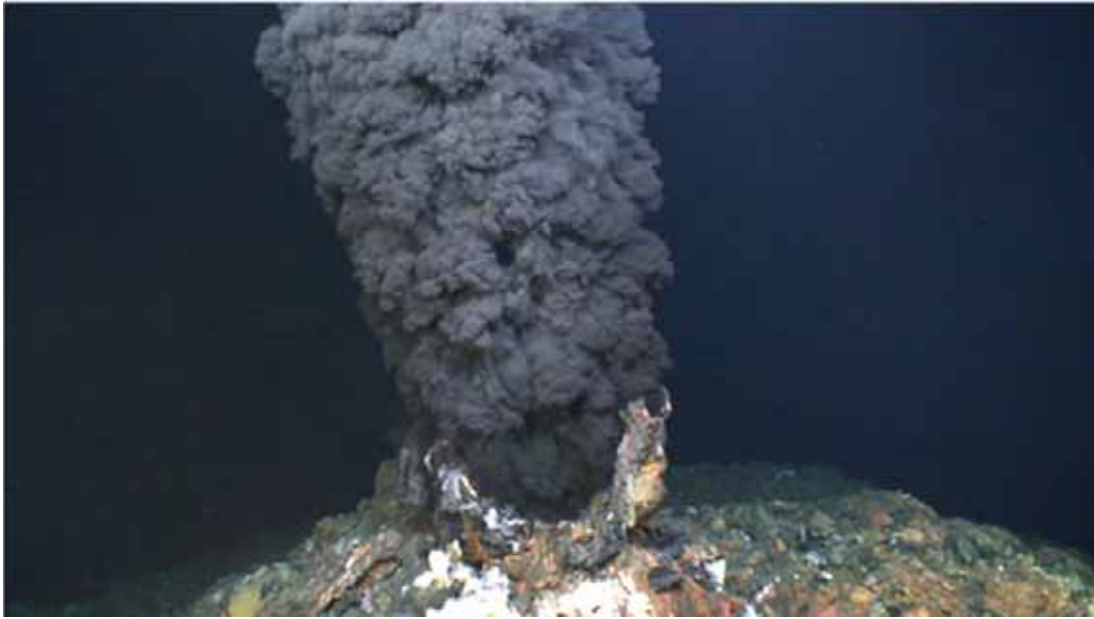


Figure I - 6 Photograph of « Active Pot » black smoker in the Irinovskoe hydrothermal field (13°N) taken during the ODEMAR cruise in 2013 by ROV dive Ifremer/CNRS.

Later another form of hydrothermalism has been discovered. This is the low temperature systems as for example the Baby Bare hydrothermal systems (Davis et al., 1999; Wheat et al., 2002), and the Lost City hydrothermal field (Delacour et al., 2008; Früh-Green et al., 2003; Seyfried et al., 2015). These are harder to detect because they don't lead to the formation of a wide plume or temperature anomaly. Furthermore, obducted oceanic crust can be found on the continent, they are named ophiolite. The ophiolite often shows hydrothermal springs of low temperature (Barnes et al., 1978; Neal and Stanger, 1983; Launay and Fontes 1985; Abrajano et al., 1988; Monnin et al., 2014; Chavagnac et al., 2013b) and are an analog of the Lost City hydrothermal field. Nevertheless, these systems lead to a new hydrothermal model for the oceanic crust which shows that water circulation and hydrothermalism occur everywhere in the ocean crust (Fig I -7).

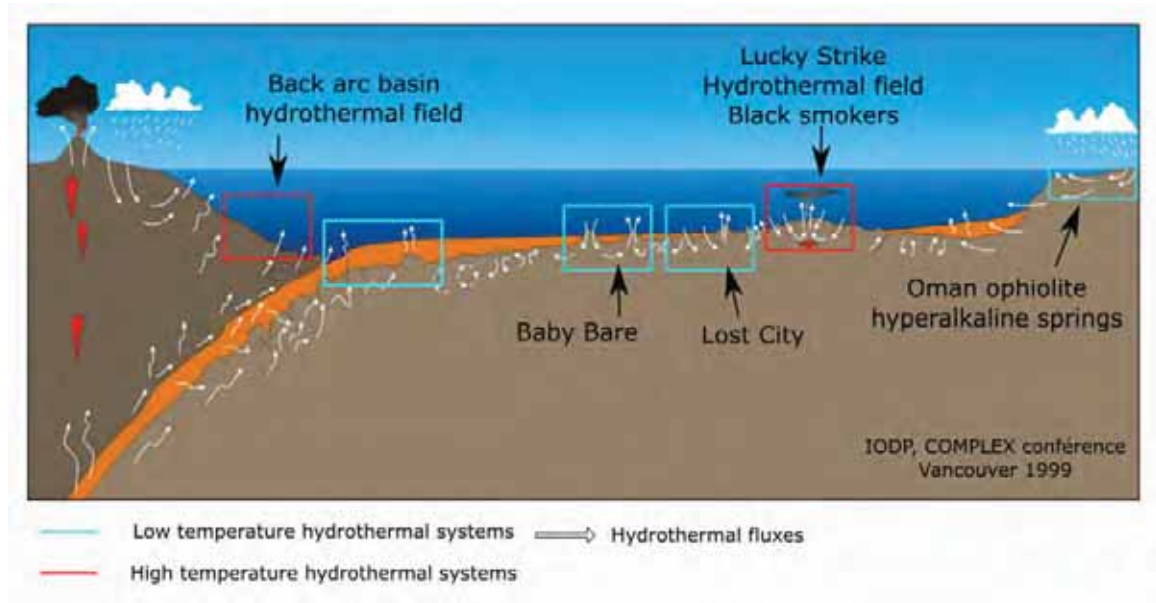


Figure I - 7 Cartoon of hydrothermal circulation illustrating the geographical extent of fluid (High or low temperature) within the crust.

2.2 High temperature hydrothermal systems

The hydrothermal circulation is due to the penetration and percolation of deep seawater into the ocean crust as schematized in Fig I - 8 for homogeneous magmatic crust. The penetrating seawater chemistry is changed during this process as water-rock interaction takes place. The whole hydrothermal circulation path is composed of 3 main compartments: (1) the recharge zone; (2) the reaction zone; (3) the upflow zone.

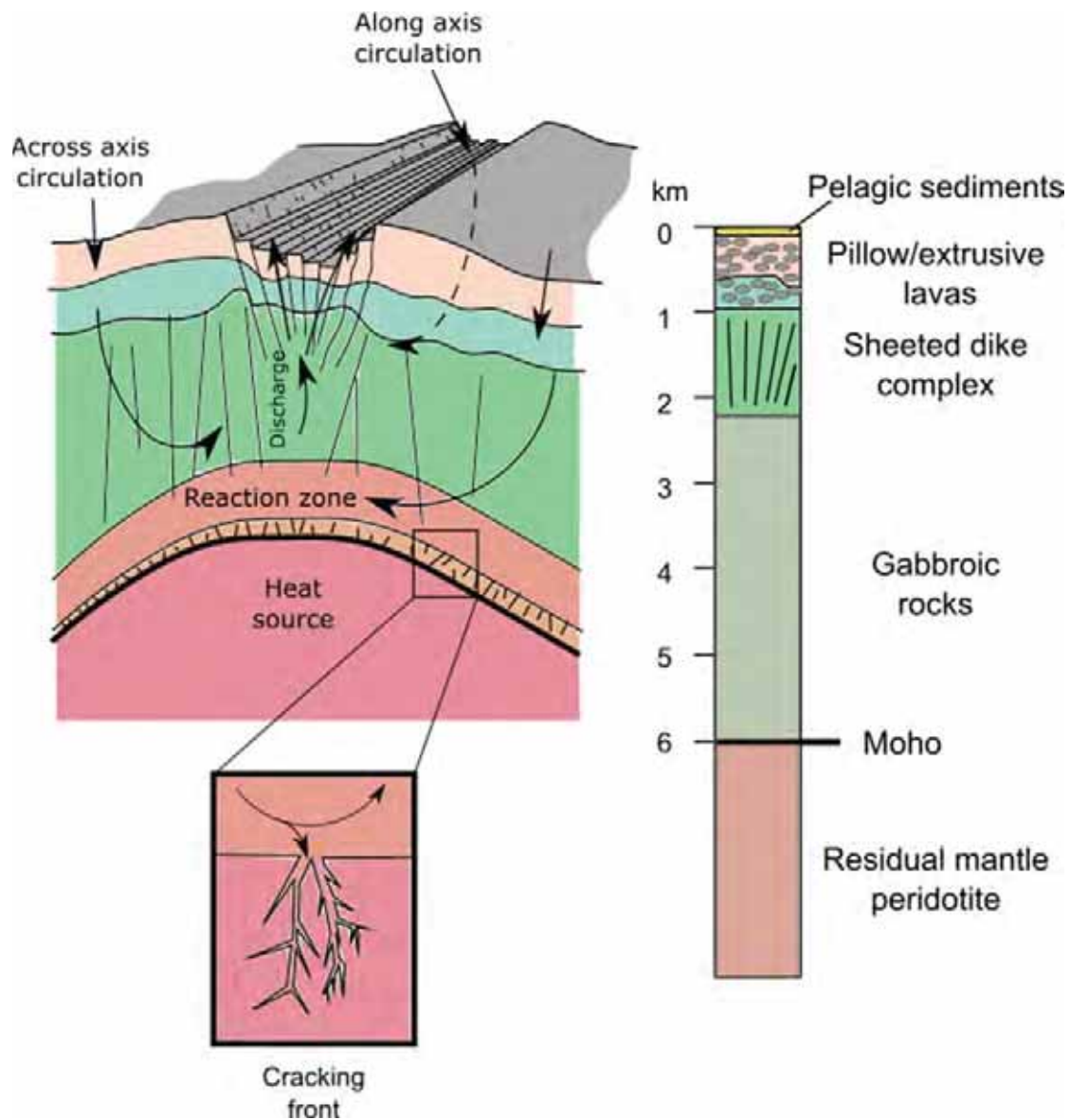


Figure 1 - 8 Cartoon of the general hydrothermal circulation cell (modified from Alt, 1995). This shows the general composition of the oceanic crust.

Recharge zone

The recharge zone begins with penetration of a cold (2–4°C) oxidizing deep seawater into the oceanic crust. Seawater will interact with the basaltic substrate and will progressively be transformed into a higher temperature fluid and eventually into a black smoker type hydrothermal fluid (Kawahata et al., 2001; Magenheim et al., 1995; Teagle et al., 1998, 2003). The infiltration is made possible thanks to important fracture networks and high porosity into the shallowest layers of extrusive volcanic crust. A distinction can be made between the “open” and the “confined” circulation. The superficial fractured part of the seafloor constitutes the “open” circulation and is associated to low-temperature water-rock

interaction (<40°C; Alt, 1995; Alt and Teagle, 2003) and the “confined” circulation only concerns the lower porosity substrate (a few percent of total seawater infiltrated) at higher temperature. This model of percolation is illustrated in Fig I -9.

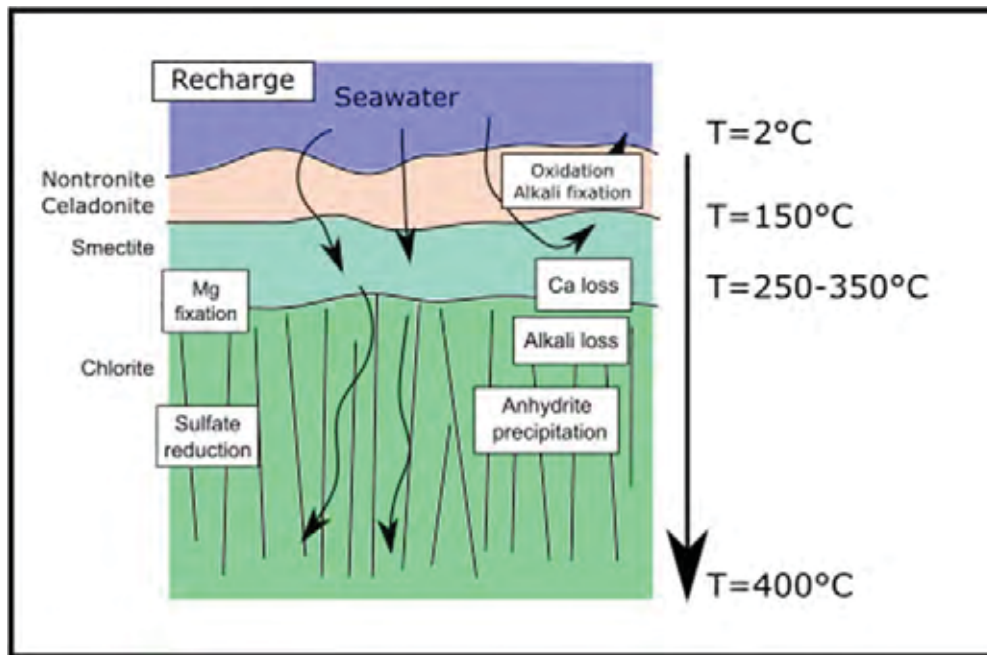


Figure I - 9 Cartoon of the recharge zone of a hydrothermal system (modified from Alt, 1995)

The figure I - 9 shows an oxidizing cold seawater interacting with the basaltic substrate and forming secondary mineral of iron oxy-hydroxides (Goethite and Hematite; Fig I -5, 6) which replace the Fe rich olivine and confers a reddish coloration to the rock. In the altered rock, these Fe oxy-hydroxides are found associated with smectite and other clay-like minerals (celadonite and nontronite; Fig I -9, 10). This affects the chemistry of seawater by up-taking Mg, K, Li, Rb and Cs (Wheat et al., 2010).

As the fluid penetrates deeper in the crust, it meets more reducing conditions at higher temperature which trigger the precipitation of sulfur (pyrite and chalcopyrite). Oxygen isotope studies of these mineral assemblages show temperatures as high as 170°C, which is the limit of seawater infiltration within the extrusive volcanic layer (Alt 1995; Fig I -9).

The transition between the extrusive volcanic layer and the sheeted dike layer is accompanied by steep temperature and permeability gradient. The bottom temperature of the extrusive layer ranges from 100 to 150°C while the top sheeted dike layer is marked by temperature ranging between 250-350°C in the greenschist facies (Alt, 1995; Teagle et al., 1998). Above 200°C the Mg fixation will result from chlorite precipitation (Saccocia and

Seyfried Jr, 1994). The formation of hydrated minerals will lead to acidification of the fluid, enhancing the chemical alteration of the substrate. Many reactions occur in the sheeted dike complex such as replacement of igneous plagioclase by hydrothermal albite, olivine is replaced by serpentine (by chlorite if Al is available) and clinopyroxene by actinote (Bach et al., 2006; Berndt et al., 1988). Pores and veins are filled with sulfides (pyrite, pyrrhotite and chalcopyrite, Delaney et al., 1987; Hannington et al., 1998).

Furthermore, anhydrite precipitates when the seawater temperature exceeds 150°C (Bischoff and Seyfried, 1978), a reaction which leads to extensive Ca, Sr and SO₄ fixation. The remaining SO₄ is reduced to sulphide form. The extent of Sr fixation and its implications in the resulting isotopes are not well constrained (Berndt and Seyfried Jr, 1993; Palmer, 1992). Anhydrite recovered from drilling programs shows precipitation temperatures as high as 250°C (oxygen isotopes).

Alkali metals as K, Li, Rb and Cs are incorporated into secondary minerals at relatively low temperature (up to 150°C) and are leached from the host rock at higher temperature (above 150°C). At 150°C, Li is still incorporated in secondary minerals and is leached at higher temperature (375°C; Seyfried Jr et al., 1984).

The reaction zone

The reaction zone is the area where the fluid reaches its “maturity”, i.e. becomes a black smoker-type fluid. Its lowest temperature limit is 350°C or above. Theoretical models predict that this temperature is reached at 1.5 to 2 km depth. The fluid chemistry will be conditioned by mineral equilibria phases such as plagioclase and epidote (Berndt et al., 1989; Seyfried Jr et al., 1991).

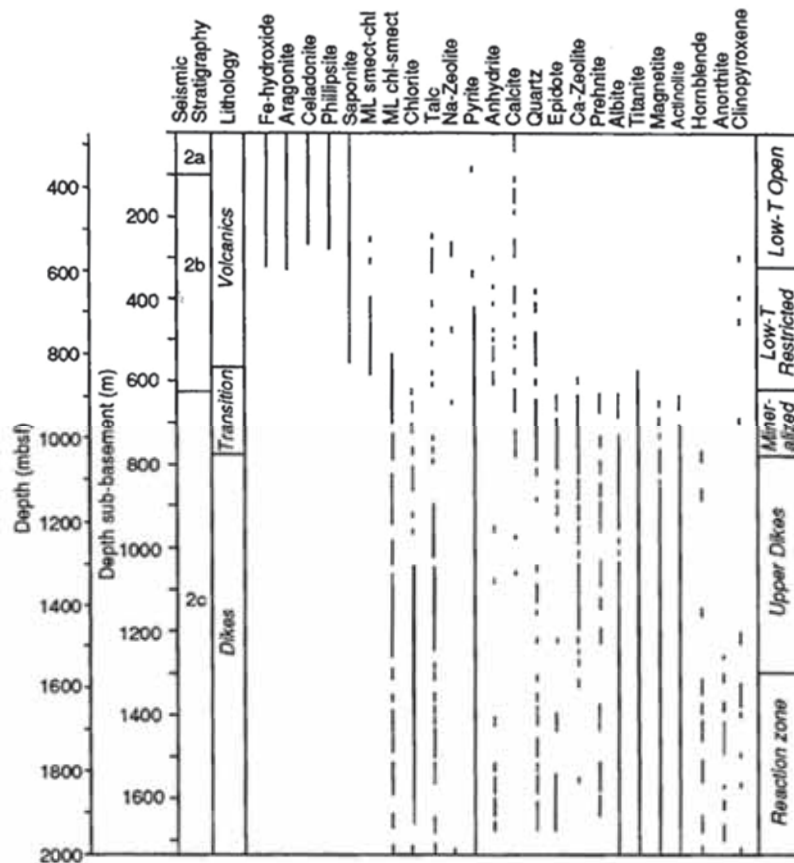


Figure 1 - 10 Diagram showing the mineral assemblage found as a function of depth in the basaltic substratum of the 504B Hole from IODP leg. This is thought to represent a good example of a recharge zone in a basaltic substratum in general (Alt, 1995).

The rocks from the base of the sheeted dike complex do not show Mg enrichment (Alt et al., 1989). This can be attained either by low W/R ratio leading to restricted exchange with seawater, or by interaction with an Mg-depleted fluid caused by secondary mineral precipitation in the shallower stages of alteration.

Upflow zone

The upflow zone is defined as the area where the matured hydrothermal fluids are transported upward, due to their lower buoyancy, to reach shallower conditions and eventually the discharge at the seafloor. The fluid is supposed to preserve most of its chemical signature inherited from the reaction zone thanks to rapid and focused fluid flow, the main cause of contamination being mixing with seawater in the subsurface (Edmond et al., 1979; Ravizza et al., 2001). The maximum buoyancy is acquired at conditions generally close to the critical point of seawater as the density of the fluids drops (Bischoff, 1991; Fontaine et al., 2008; Norton, 1984). The residence time in the upflow zone is unknown but

supposing that the fluid velocity within the seafloor is equivalent to the one of the outflow within black smokers ($0.7\text{-}5\text{m}\cdot\text{s}^{-1}$), the residence time for a 2 kmbsf reaction zone would be in the order of one hour (Alt, 1995; Delaney et al., 1987; Lowell et al., 1995). However this assumption is excessive and really should compose the lower limit of residence time evaluation. Moreover, others evaluated the residence time to be less than 3 years, based on Ra isotopes (Kadko and Butterfield, 1998).

The Stockwork formation

The stockwork is the shallowest part of the upflow zone and therefore the last place where water-rock interaction occurs before fluid discharge. Studies of stockworks from black smokers were conducted by submarine observations and through the study of ophiolitic analogs. Stockwork knowledge has greatly benefited from an IODP program that aimed at drilling into the hydrothermal field of TAG (Trans-Atlantic Geotraverse) to study the stockwork underneath. This successful operation drilled as deep as 125mbsf into the subsurface underneath the black smoker field. Their results revealed the hydrothermal stratigraphy and mineralogy (Fig I -11). This stockwork showed a typical Volcanogenic Massive Sulfide (VMS) deposits structure comparable to deposits from Oman or Cyprus ophiolites (Hannington et al., 1998). The stockwork is mostly composed of clastic breccias (sulfide debris from collapsed hydrothermal chimneys, pyrite clasts) in variable matrix (silica and anhydrite). The clasts are composed of former deposited minerals that have been reworked to form this consolidated breccia. The reworking is probably due to episodic seawater entrainment and relative discharge intensity variations. Intense discharge of high temperature black smoker fluid will entrain seawater into the mound. If the entrained seawater is sufficiently hot (above $\sim 150^{\circ}\text{C}$, Bischoff and Seyfried, 1978), anhydrite will precipitate and form an anhydrite cemented breccia (with pyritic clasts). This anhydrite matrix will act as an impermeable cap and concur in focusing the high temperature fluid (Campbell et al., 1984). Along with anhydrite, pyrite and chalcopyrite are found to precipitate as well (Petersen et al., 2000). During lower intensity episodes of high temperature fluid discharge, the anhydrite cap is not sustained and interaction with cold oxidizing seawater will dissolve the anhydrite framework (by retrograde destruction of anhydrite) which will lead to the collapse of the hydrothermal mound (Petersen et al., 2000). In the deepest part of the stockwork, at 125mbsf, the mineralogy corresponds to the greenschist facies with chloritized basalt breccias forming the quartz and chlorite stockwork (Fig I -11; Petersen et al., 2000).

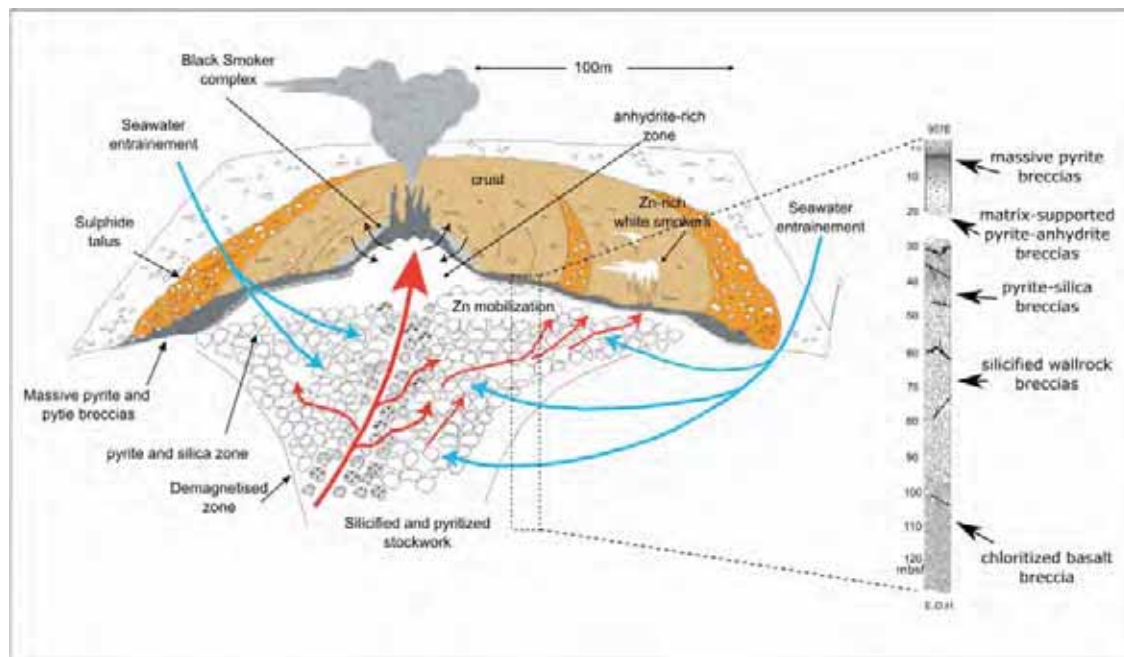


Figure I - 11 Cartoon of the TAG hydrothermal field and hydrothermal circulation and mineralogy in the subsurface inferred from 4 drilled hole (modified from Hannington et al., 1998 and Tivey, 2007).

The discharge

At the discharge, the hot acidic and reducing fluid mixes with the cold slightly basic and oxidizing seawater. This process provokes the precipitation of particles that constitute the black smoke. These particles are composed of pyrrhothite, Fe-rich sphalerite, pyrite, chalcopyrite, amorphous silica, Fe-oxyhydroxides, anhydrite and an undefined Fe-S ±Si and Fe-Si ±S phases, and trace quantities of barite, isocunbanite, wurtzite, covellite and marcasite (Mottl and McConachy, 1990). When discharging, these particles are further dispersed within the plume and sediments. These particles were long thought to consume massively the metals concentrated in the hydrothermal fluid. Mottl et al., 1990 demonstrated that within the first 22m of the plume, only ~35% (±25%) of Fe injected to the ocean are found in the dissolved form. But recent studies have shown that the hydrothermal fluids may have a broader effect on ocean chemical budget than previously thought (German et al., 2016; Resing et al., 2015). Especially, a plume of dissolved iron from the EPR was followed up to 4300 km to the west of the ridge in the Pacific Ocean (Resing et al., 2015).

Furthermore, the precipitation of minerals occurs at the first contact between seawater and hydrothermal fluid. This contributes to the formation of hydrothermal chimneys that can be tens of meters tall. Figure I - 12 presents the growth of hydrothermal chimney from the

juvenile stage to a more mature stage, and the associated mineral composition from the inner wall to the outer walls.

When hydrothermal fluids meet seawater, a thin ring of anhydrite will form, precluding extensive early mixing (stage 1, Fig I -12). The Cu-Fe sulphides will then grow into the inner wall of the chimney and initiate a more complex sulphide mineralogy (Haymon, 1983). This is illustrated in the stage 2 in figure I - 12. The chimney growth occurs at three locations, outwards and upwards by anhydrite precipitation, and inward by Cu-Fe sulphide precipitation.

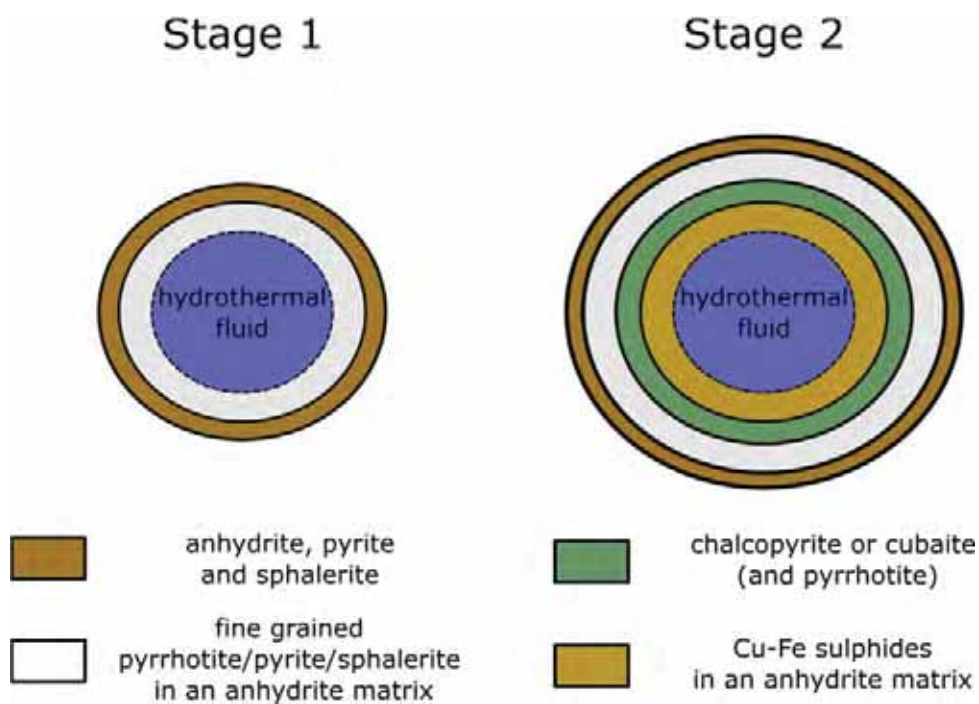


Figure I - 12 Modified from Haymon, (1983). Schematic growth of hydrothermal chimney in 2 stages (1: juvenile stage; 2: mature stage).

2.2.1 Control on fluid chemistry of black smokers

Physical parameter

The chemistry of the fluids is determined by many variables among which temperature is a major one. Two temperatures are of importance in a hydrothermal system: (1) the temperature measured at the vent at the seafloor during the dives and (2) the temperature inferred for the reaction zone which is deduced based on the fluid chemistry. In the absence of such chemical data the minimum temperature in the reaction zone is given by the highest temperature measured in the vent, as processes during the upflow such as conductive

cooling and mixing with seawater (or hydrothermal seawater) will systematically lead to lower temperature at the seafloor relative to reaction zone temperature. The exit temperature can reach 407°C which is the highest temperature ever measured at the discharge (Haase et al., 2007). Temperature is an important parameter that can fluctuate with time in response to tectonic/magmatic activity (Von Damm 1995, Tivey 1990, EPR) but also in response to tidal pressure change and to variability of the permeable system (Barreyre et al., 2014). Some temperature variations such as abrupt drops (from 3 to 160°C from initial temperature) or increases (10°C increase) at short time scale (from few hours to few days) are observed but remain unexplained (Barreyre et al., 2014).

The second important physical parameter is the pressure which governs the thermodynamic equilibria and determines the occurrence of the phase separation. The same distinction as temperature is made for pressure with the dichotomy of seafloor pressure, which is the pressure evaluated at the discharge, and the reaction zone pressure. The seafloor pressure can be approached using a simple water column depth relation.

$$P_{sf} = \rho \times g \times h$$

P_{sf} is Pressure at the seafloor in Pascal; ρ is the volumic mass ($\sim 1000\text{g/cm}^3$); g (9.8m.s^{-2}) is the gravitational acceleration and h is the length of the water column considered in meters.

To evaluate the depth below the seafloor based on pressure, we account for the different volumic masses of the water masses (water column seawater vs. below seafloor hydrostatic pressure). We therefore use a global volumetric mass representative of the hydrothermal cell: $\rho_{cold}=800\text{g/cm}^3$ (Fontaine et al., 2007).

The reaction zone pressure is determined from chemical indicators for fluid-rock reaction or phase separation. Because the hydrothermal cell is limited by the brittle/ductile boundary at the “cracking front zone”, seismic data can provide information on the maximum depth of water circulation. The maximum epicenter depth of seismic activity can also be interpreted as imaging the cracking front produced by cold seawater. This maximum depth can be determined by chemistry when the estimated pressure is converted to depth. This is supported by recent publications comparing depth of the hydrothermal system estimated by seismic data and depth estimated by geochemical geothermobarometer (Fontaine et al., 2009).

Phase separation

The hydrothermal upflow is triggered by changes in density when approaching conditions of phase separation (Bischoff, 1991; Norton, 1984).

Phase separation is a process during which the NaCl-rich solution will form a “vapor” phase depleted in NaCl and a “brine” phase enriched in NaCl. The conditions required to have phase separation are P and T above the two-phase boundary (experimentally determined; Fig I -13). These conditions depend on the initial NaCl concentration. Once phases are separated, the extent of NaCl enrichment is dependent on P and T, independently from the initial NaCl concentration. Phase separation of NaCl solutions has motivated many experimental studies since the black smoker discovery (Bischoff, 1991; Bischoff and Pitzer, 1985; Bischoff and Rosenbauer, 1988, 1984, 1985). Therefore, the two-phase boundary and critical point for seawater equivalent solution are well known nowadays (Fig I -13). When seawater penetrates the oceanic crust and heats gradually, the solution will eventually cross the two-phase boundary. If the solution crosses the curve at conditions below the critical point (sub-critical conditions), a low salinity vapor is produced and segregated from a high salinity solution. This is called “boiling”. The gases contained in the initial solution will tend to concentrate within the vapor phase while salts and metals will be present also but at lower concentration.

If the solution crosses the two-phase curve at conditions above the critical point (super-critical conditions), a salt-enriched liquid phase will “condense”. During this process, small droplets of high salinity will form, and the conjugate vapor phase will remain mostly identical. Phase separation is therefore an efficient process occurring within the oceanic crust to modify the NaCl concentrations of circulating fluids. If a two-phase fluid is brought to single phase conditions and no segregation of either phases has occurred, vapor and brine phases will mix to the initial composition. Therefore, for phase separation to efficiently change the chemistry of the fluid, a physical segregation of both phases needs to be operant. Many studies have focused on the physical process explaining the segregation of both phases (Fontaine et al., 2007; Fox, 1990; Goldfarb and Delaney, 1988; Fig I -14).

Chemically, the Na and Cl concentrations will be modified principally through this process. The P and T conditions beyond the two-phase curve will dictate the relative abundance of the two phases. The final composition of the fluid at the discharge will reflect more or less

the P-T conditions of the phase separation depending on the efficiency of the phase segregation (Fig I -14). As presented in Figure I - 14, the brine and vapor phases will have different flow dynamic, due to the wetting effect of the liquid phase, or brine. The latter will condensate on the inner wall and fill the backwater porosity leading to its storage (Fontaine et al., 2007). The vapor phase will preferentially flow through bigger channels.

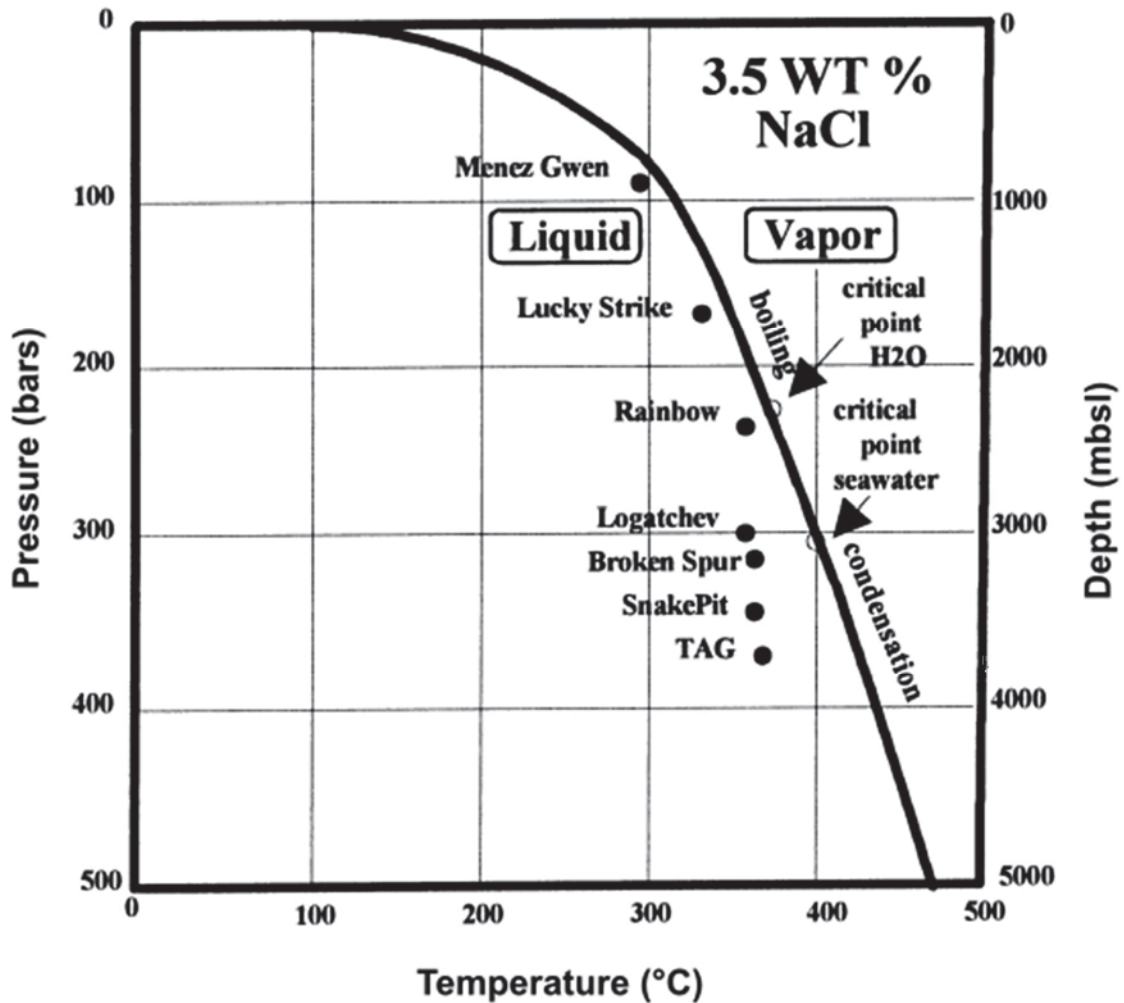


Figure I - 13 Pressure vs. Temperature diagram showing the two-phase boundary curve for seawater equivalent (from Charlou et al., 2000). Sites from the MAR are represented at discharge conditions.

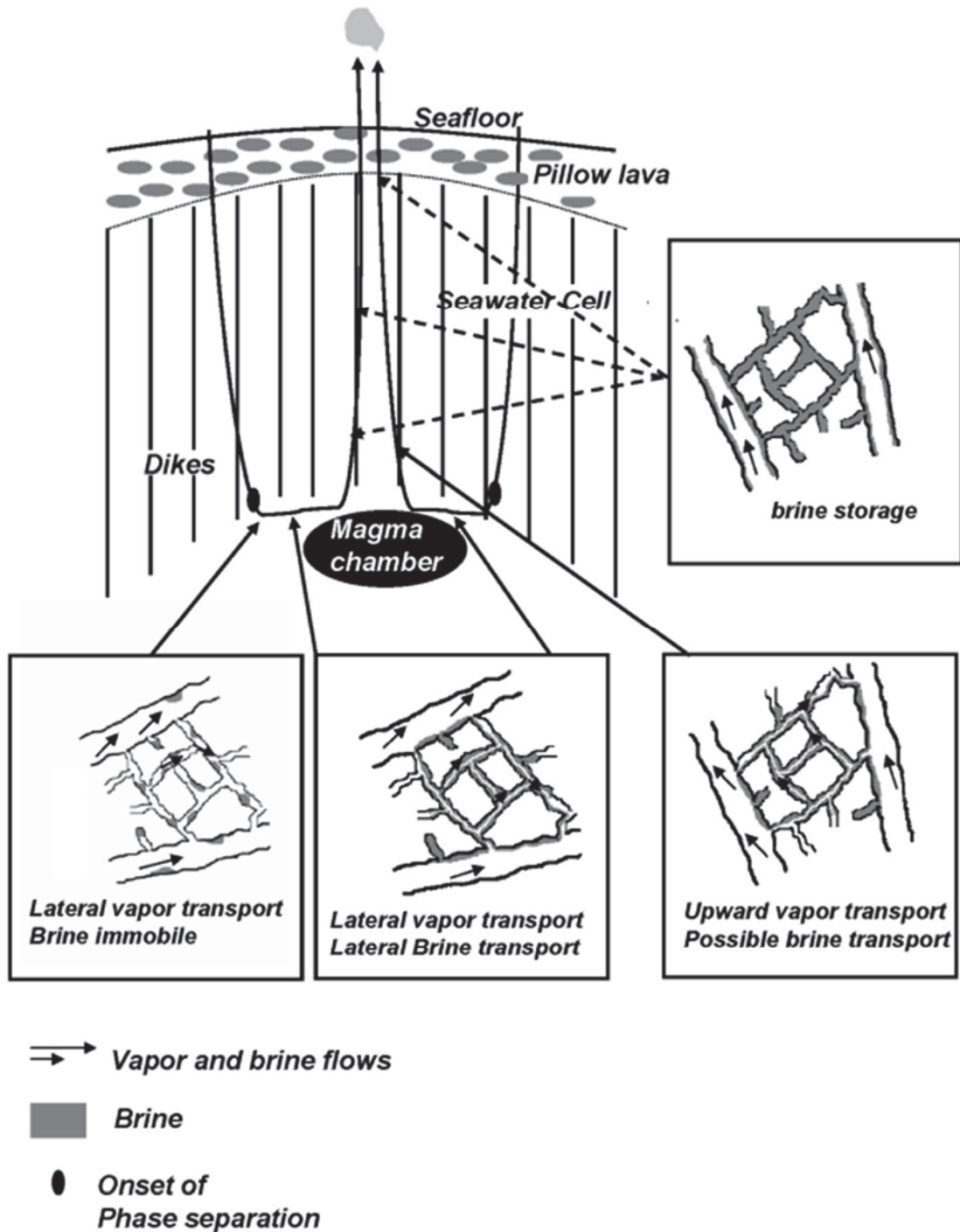


Figure I - 14 From Fontaine and Wilcock, (2006), cartoon showing the brine and vapor segregation at depth.

For the other elements, partition coefficients have been determined by several experimental studies near critical point conditions. The elements will partition into one phase or another independently of the initial concentration of the fluid (Berndt and Seyfried Jr, 1997; Pester et al., 2015; Pokrovski et al., 2005, Fig I -15). All the element will be enriched in the brine phase but the extent of that enrichment will be controlled by element affinity to the brine

or vapor phase. The partition coefficients can be derived in several manners. Figure I - 15 shows the partition of several elements (Cu, Fe, Zn, Mn, Ca and Sr) as element normalized to Cl ratios as a function of Cl concentration on log-log diagram. These ratios display a linear correlation with Cl depicting partitioning during phase separation. At low Cl concentration, halite precipitates, and the concentrations of all the elements increase drastically due to a “volatility” effect. This is related to change in Na/Cl ratios during halite precipitation. Figure I - 15b and c show the partitioning of Ca and Zn respectively for different initial concentrations. Partitioning is defined as the slope S_v between the initial Cl concentration and the point of halite precipitation. These diagrams show that the partitioning doesn't depend on initial concentration as S_v is constant at a value of ~ 0.66 for Ca and ~ 0.36 for Zn.

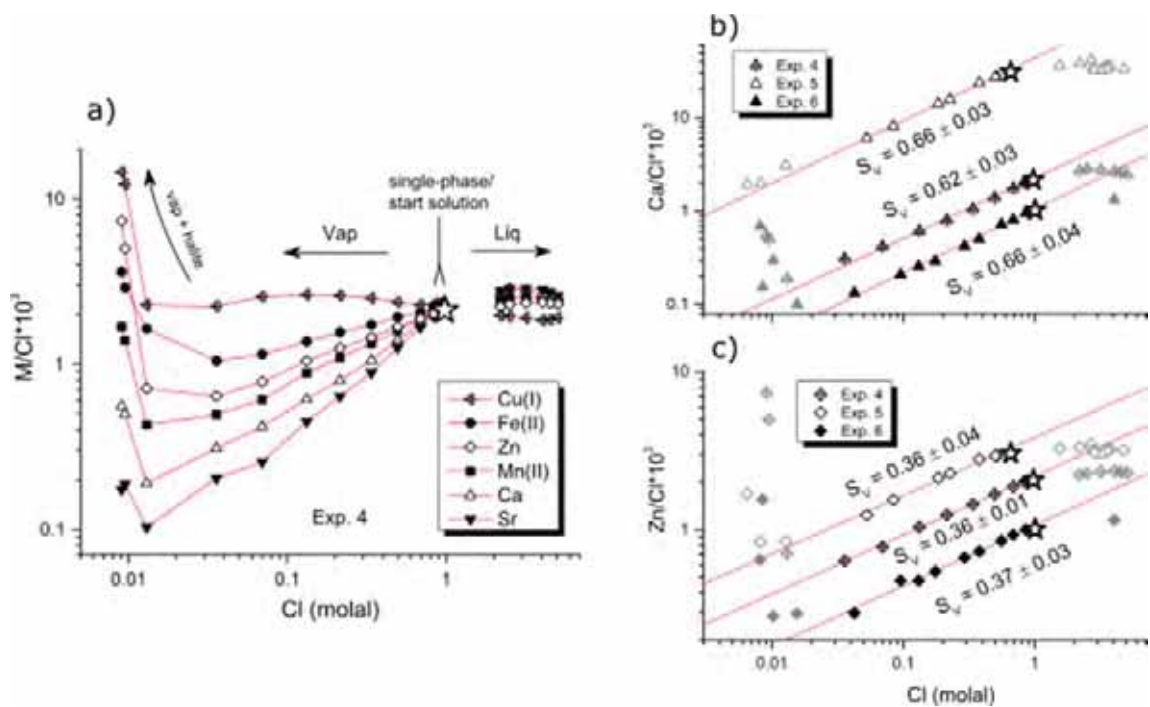


Figure I - 15 From Pester et al., (2015), (a) shows the partitioning of elements M measured for different experiments in the vapor phase. (b) and (c) show the partitioning for Ca and Zn with different starting fluid concentrations.

Water Rock interaction

Much of the chemical difference between initial fluid (seawater) and black smoker fluid can be attributed to water/rock interaction. In a first approximation, MORB is considered to be chemically homogeneous, although some local differences can appear, as at Lucky Strike where basalts are composed of enriched MORB due to the Azores hot spot proximity. The W/R ratio evaluates the amount of water in contact with a certain amount of rock,

which is required to explain the chemical composition of the fluid (Berndt et al., 1988; Edmond et al., 1979; Magenheim et al., 1995). Usually this is determined using “soluble” elements, which are quantitatively leached from the basalt. B and Li are generally good candidates as they are leached from the rock and not quantitatively removed from the solution through secondary mineral precipitation (Berndt et al., 1988; K. L. Von Damm et al., 1985). If an element is taken up into such mineral (e.g. hydrothermal plagioclase, chlorite, epidote, clay-like minerals), the W/R needs to be considered as a proxy of ongoing alteration because it is then not representative of the leaching of the host rock. Isotopic composition of solutions have also been used to infer the W/R ratio (Albarède et al., 1981; Chan et al., 1993; Foustoukos et al., 2004; Magenheim et al., 1995; Mottl et al., 2011; Shanks, 2001) and provide extra information because processes such as mass fractionation could modify the isotopic composition of a solution without noticeable or significant change in elemental concentration. This is the case for Lithium isotopic composition, that is influenced by clay minerals precipitation (Chan et al., 1993).

The residence time of the fluid within the hydrothermal circulation cell is still unknown. It is estimated to be of the order of the hour within the upflow zones (Alt, 1995). These are based on flow rates of 0.7-5 m/s measured at the hydrothermal fluids discharge for a 2 km-deep reaction zone and consistent with flow rates estimated by breccia analysis (Delaney et al., 1987). A residence time of less than three years was estimated based on radionuclides ($^{228}\text{Ra}/^{226}\text{Ra}$ ratio) but is not representative of the upflow zone only, but rather of the onset of water-rock reaction temperature of 200°C (Kadko and Butterfield, 1998). The residence time is important because it determines the completion of chemical equilibria, steady state reaction. As reaction rates are temperature dependent, both temperature and residence time are key parameters in the control of the final fluid composition.

A lot of information about fluid chemistry is provided by experimental studies that have been conducted even before the actual discovery of seafloor hot spring (Bischoff and Dickson, 1975; Bischoff and Seyfried, 1978; Hajash, 1975; Mottl et al., 1979; Mottl and Holland, 1978). These experiments aimed at understanding what changes occur when seawater is heated with basalt, and also when seawater is heated alone (Bischoff and Seyfried, 1978).

Heating of seawater alone allowed the discovery of the formation of a new mineral capable of efficiently remove Mg from the solution, the Mg-hydroxysulfate-hydrate (MHS₂H₂O; Bischoff and Seyfried, 1978). Precipitation of this mineral with anhydrite by heating

seawater alone already leads to considerable changes in the solution chemistry. Furthermore, the formation of MgSi hydroxide leads to a quantitative depletion of Mg from seawater and to a decrease of pH due to the relatively high proton concentration.

Anions

The sulfate is removed through two processes, precipitation of anhydrite and reduction into sulfide. Therefore there's supposedly no sulfate left in a pure hydrothermal fluid. S is reduced as H₂S and found in variable concentration in the fluids. The final sulfide concentration has two sources, which are the reduced sulfate as mentioned above but also basaltic sulphide leached from the rocks (Shanks, 2001).

The chloride concentrations of the fluid can be found both increased and decreased compared to seawater, and are mostly if not completely conservative during water-rock reactions (except for halite precipitation). Therefore the factor controlling the Cl concentrations in fluids is the phase separation and segregation. Therefore, Cl concentrations are to a first order an indication of the occurrence of phase separation at depth and to a second order a way to estimate the P-T conditions of this phase separation.

Bromide follows the same trend as chloride, as the large ionic radius is incompatible with most mineral lattices (Berndt and Seyfried Jr, 1997; Oosting and Von Damm, 1996; Von Damm et al., 1995). Therefore Br/Cl should not change during the processes involved in seafloor hydrothermal systems. Br will not be incorporated in the halite lattice. This allows checking on the halite precipitation/dissolution processes occurring at depth. The Br/Cl value of seawater are constant throughout the oceans, and so is the Br/Cl ratios of black smoker fluids. If Br/Cl of black smokers is lower or higher than for seawater, then halite is dissolving or precipitating at depth.

Fluoride is present in seawater but its content decreases in the final hydrothermal fluid. It is more reactive than chloride and can be incorporated in the hydrated minerals.

Cations

The alkali metals

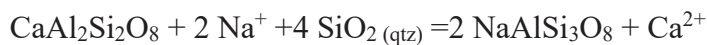
Alkali metals in basalts are not particularly enriched compared to other rocks but these elements are preferentially leached by the fluids. Therefore, the hydrothermal fluids are enriched in Li, Rb, Cs and K. At low temperatures (up to 100°C), these elements are incorporated into the secondary minerals forming in the first step of seafloor alteration. Na is the most abundant cation in the hydrothermal fluids because it is closely related to

chloride concentration of the fluid and because they are both highly enriched in seawater. Na doesn't behave conservatively and is taken up by the albitisation process. Therefore, the Na concentration in hydrothermal fluids is always lower than in seawater, especially when using the Cl normalized values.

The alkaline earth

Mg, Ca, Sr, Ba have different behaviors between each other. Mg is present in seawater as a major cation and decreases to zero in the final hydrothermal fluids due to secondary minerals precipitating along the hydrothermal cell (Bischoff and Dickson, 1975; Saccoccia and Seyfried Jr, 1994). Usually the presence of Mg in the fluid is considered as a result from contamination by ambient seawater. Nevertheless, some studies have shown that hydrothermal fluid might mix in the upflow with altered/hydrothermal seawater, intermediate between seawater and mature hydrothermal fluid (black-smoker like; Ravizza et al., 2001).

Calcium concentration values are found commonly enriched compared to seawater. Their variation are closely linked to the Na variations as while the latter is incorporated in the hydrothermal albite, Ca is leached from the magmatic anorthite as shown in the following equation (Berndt et al., 1989; Berndt and Seyfried Jr, 1993b).



Based on this reaction, the Ca/Na ratio of the hydrothermal fluid can provide qualitative information concerning the albitisation at depth.

Sr has variable behavior as both enrichment and depletion compared to seawater are observed. The observed Sr concentrations are not strictly related to Cl concentrations (Palmer, 1992). Most of the Initial Sr from seawater has been removed by anhydrite precipitation in the recharge zone at $T > 150^\circ\text{C}$, the extent of the remaining Sr is not well constrained yet. Ba concentrations are difficult to measure as BaSO_4 might precipitate during discharge. Generally Ba is enriched in hydrothermal fluids compared to seawater.

Transition metals

These elements are strongly controlled by the redox state and temperature of the fluids. Several experiments showed their relation to temperature (Janecky and Seyfried Jr, 1987; Mottl et al., 1979; Mottl and Holland, 1978; Pester et al., 2011; Seyfried Jr and Mottl, 1982). The Fe/Mn ratios have proved to be a valuable proxy for the temperature of

equilibrium and allowed the development of a geothermometer consistent with greenschist mineral facies (Pester et al., 2011).

Iron is enriched in hydrothermal fluids compared to seawater, with concentrations as high as 20mM (Douville et al., 2002). It is closely linked to Mn which is the second most abundant trace metals. Zn is also important and can attain a few mM. Cu is less concentrated and its solubility decreases drastically below 300°C. Concentrations of tens of micromoles are reported in hydrothermal fluids (Von Damm 1995).

Silica

Si concentration in hydrothermal fluids is usually 100 times that of seawater. It is a major element and has become important to determine P and T conditions of the reaction zone assuming control by quartz precipitation (Foustoukos and Seyfried, 2007; Von Damm et al., 1991). The quartz solubility has been empirically determine in several study (Fournier, 1983; Fournier et al., 1982; Foustoukos and Seyfried, 2007; Von Damm et al., 1991). The quartz solubility expression is shown as follow (Von Damm et al., 1991):

$$\ln(mSiO_2 \cdot nH_2O) = a + b \times \ln(\rho) + \left(c + \frac{d}{T}\right) + e \times P/T \quad (1)$$

Where P is in bars and T is in K, mSiO₂ is in molality, and n is the hydration number of the dissolved silica, and the other coefficient are empirically determined (a=-2.32888; b=1.79547; c=-2263.62; d=0.00407350; e=0.0398808). Because density is dependent on NaCl concentrations, this expression is also dependent on Cl concentrations.

Gazes

Hydrothermal fluids contain different dissolved gazes (Charlou et al., 2002; Douville et al., 2002). They define several groups, such as the noble gases (³He degassed from the mantle), the carbon based gases that are principally CO₂ and CH₄ (Charlou et al., 2002; Pester et al., 2012), the hydrogen (Klein et al., 2009) and hydrogen sulfide originating from host rocks and reduced sulfate from seawater (Ono et al., 2007; Shanks, 2001) in addition to N₂.

In ultramafic environments, the CH₄ can be abundant due to intense serpentinization occurring in subsurface. The highly reducing conditions favor the production of H₂ and CH₄. H₂ is produced by olivine hydration reaction and CH₄ is produced abiotically by the Fischer Tropsch reaction, like the Sabatier reaction (Boulart et al., 2013; Charlou et al., 2002).

2.3 Low temperature hydrothermal systems

Ultramafic hosted low temperature hydrothermal systems: example of Lost City and a the continental analog at hyper-alkaline springs of Oman

In December 2000, the Lost City Hydrothermal vent field was discovered on the Atlantis massif (30°N, Früh-Green et al., 2003; Kelley et al., 2002). The field is composed of several 10's of meters tall white chimneys composed of carbonate. The Atlantis massif is a former Ocean Core Complex where ultramafic material is found at the seafloor. On-going serpentinization of the peridotites produce these fluids at 40°C to 75°C. These fluids are very different from the other ultramafic hosted sites found on the MAR because the hydrothermal circulation is not driven by magmatic heat but rather by fracturation and exothermic reactions (Kelley et al., 2002). For example, the ultramafic-hosted Rainbow vent field has low pH and high H₂S, H₂ and CH₄ which show that the fluid interacts with peridotite, gabbros and basaltic substratum at high temperature. In comparison, the Lost City hydrothermal fluids have high pH, low H₂S and are enriched with H₂ and CH₄. They also have Ca concentrations enriched compared to those of seawater, but the K concentrations are equivalent to those of seawater. When hydrothermal fluid mixes with seawater, precipitation of Mg-hydroxide (brucite) and Ca-carbonate (calcite/aragonite) occurs and forms the chimneys. Recent studies of the fluids' chemistry have suggested that the relatively high level of Si and trace elements such as Rb and Cs measured (Seyfried et al., 2015) was related to a plagioclase component in the hydrothermal circulation cell which is coherent with previous observations of "plagioclase peridotite" at the Atlantis massif (Tamura et al., 2008).

This type of hydrothermal system is not exclusively observed in submarine environments. Ophiolites are pieces of ocean crust found on continents through tectonic movements termed obduction. One of the most famous and best preserved ophiolites is found in the Sultanate of Oman. Low temperature hydrothermalism also occurs in these environments through meteoric water percolation into the oceanic substratum and down into the ultramafic parts. In the Oman ophiolite, the hydrothermalism is manifested by hyperalkaline spring resurgence at lithological discontinuities (Barnes et al., 1978; Chavagnac et al., 2013b; Neal and Stanger, 1983). These fluids display clear similarities with the one from Lost City, the major difference being the salinity. They have high pH, up to 12, and are enriched in Ca and depleted in Mg and dissolved Inorganic Carbon (DIC).

At the hyperalkaline spring discharges, the contact between the Ca–OH type fluid depleted in DIC and atmospheric CO₂ triggers the precipitation of carbonates. Another mechanism is found when hyperalkaline spring waters mix with run-off water (Mg and DIC enriched). The precipitates formed are the same as in Lost city (Aragonite/ calcite, Brucite and minor hydrotalcite; Chavagnac et al., 2013a). The carbonate precipitation leads to the formation carbonate concretion called travertines, which display a large geographical extent. They constitutes a potential analog for the carbonated chimneys of Lost City hydrothermal fields.

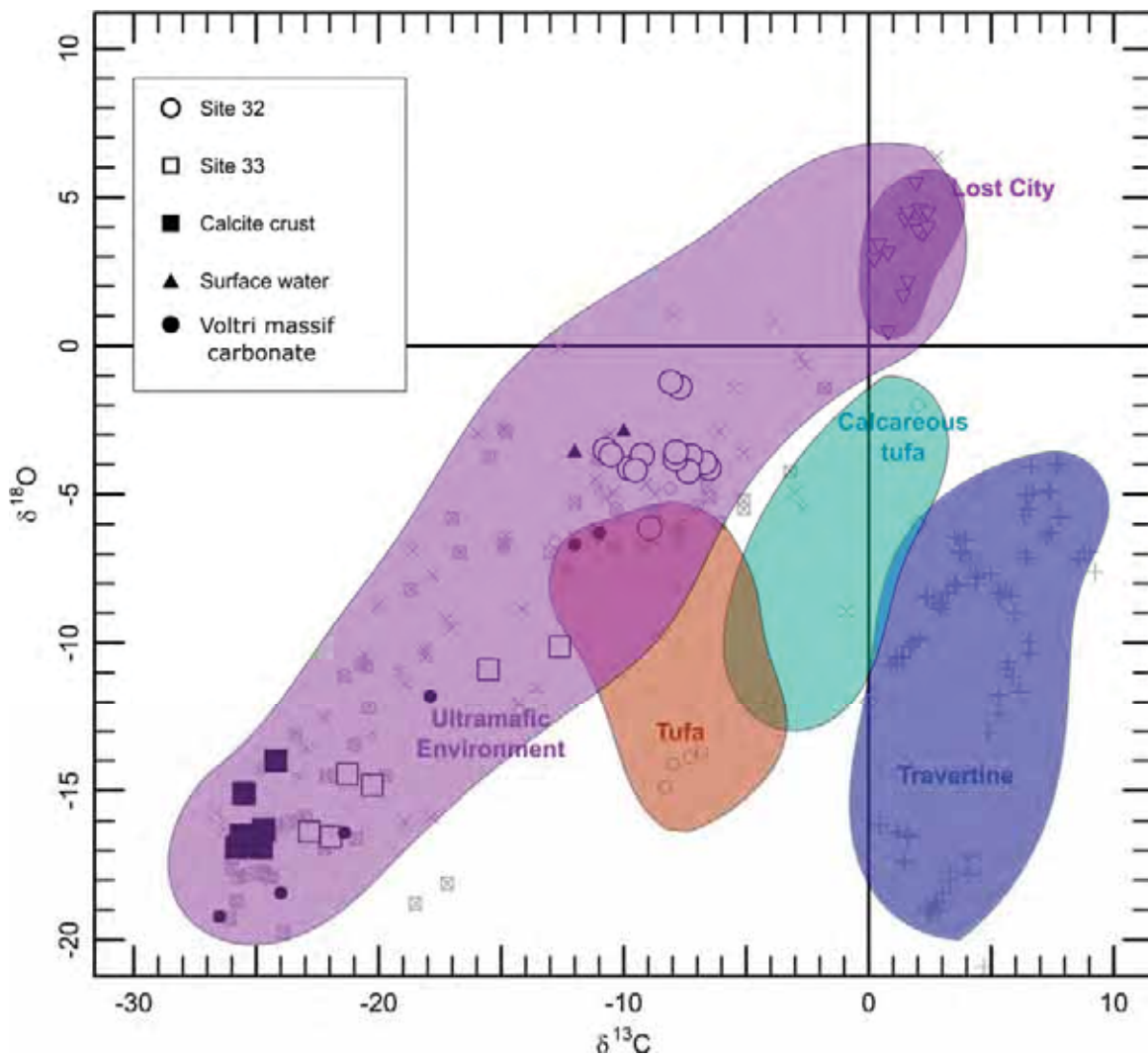


Figure I - 16 Carbon and oxygen stable isotope of carbonate concretion from different settings. From Leleu et al. (2016) in Annexe 1, it shows the diversity of carbonate precipitation through stable isotope signatures.

The study of these travertines are of major importance in domains such as biology of extreme environment (pH=12); paleo–chronology as it records environmental conditions at the time of the deposition and CO₂ storage as it forms by consuming directly (hyperalkaline

spring alone) or indirectly (when precipitation occurs by mixing with the surface waters) the atmospheric CO₂ (Clark and Fontes, 1990; Mervine et al. 2014). These travertines have been the object of a published study in which we conducted a multidisciplinary investigation involving petrographic observations combined with geochemical measurements (Mg and Sr for the trace element, and stable isotopes of C and O as well as Sr isotopes) and modelling of porosity and precipitation of calcite (Leleu et al., 2016). This publication is included as Annexe 1.

References

- Abrajano, T. A., Sturchio, N. C., Bohlke, J.K., Lyon, G. L., Poreda, R. J., Stevens C. M., 1998. Methane-hydrogen gas seeps, Zambales Ophiolite, Philippines: deep or shallow origin?: *Chemical Geology*, v. 71, p. 211–222.
- Albarède, F., Michard, A., Minster, J.-F., Michard, G., 1981. ⁸⁷Sr/⁸⁶Sr ratios in hydrothermal waters and deposits from the East Pacific Rise at 21°N. *Earth Planet. Sci. Lett.* 55, 229–236.
- Alt, J.C., 1995. Subseafloor Processes in Mid-Ocean Ridge Hydrothermal Systems. *Seafloor Hydrothermal Syst. Phys. Chem. Biol. Geol. Interact.* 85–114.
- Alt, J.C., Anderson, T.F., Bonnell, L., Muehlenbachs, K., 1989. 3. Mineralogy, chemistry, and stable isotopic compositions of hydrothermally altered sheeted dikes: ODP Hole 504B, Leg 1111 *Proc. Ocean Drill. Program Sci. Results* 11.
- Alt, J.C., Teagle, D.A.H., 2003. Hydrothermal alteration of upper oceanic crust formed at a fast-spreading ridge: mineral, chemical, and isotopic evidence from ODP Site 801. *Chem. Geol.* 201, 191–211. doi:10.1016/S0009-2541(03)00201-8
- Arrhenius, G., Bonatti, E., 1965. Neptunium and volcanism in the ocean, in: *Progress in Oceanography*. Sears M., London.
- Bach, W., Paulick, H., Garrido, C.J., Ildefonse, B., Meurer, W.P., Humphris, S.E., 2006. Unraveling the sequence of serpentinization reactions: petrography, mineral chemistry, and petrophysics of serpentinites from MAR 15 degree N (ODP Leg 209, Site 1274). *Geophys. Res. Lett.* 33. doi:10.1029/2006GL025681
- Barnes, I., O’neil, J.R., Trescases, J.-J., 1978. Present day serpentinization in New Caledonia, Oman and Yugoslavia. *Geochim. Cosmochim. Acta* 42, 144–145.
- Barreyre, T., Escartín, J., Sohn, R.A., Cannat, M., Ballu, V., Crawford, W.C., 2014. Temporal variability and tidal modulation of hydrothermal exit-fluid temperatures at the Lucky Strike deep-sea vent field, Mid-Atlantic Ridge: MAR vent-field temperature monitoring. *J. Geophys. Res. Solid Earth* 119, 2543–2566. doi:10.1002/2013JB010478
- Berndt, M.E., Seyfried Jr, W.E., 1997. Calibration of Br/Cl fractionation during subcritical phase separation of seawater: Possible halite at 9 to 10° N East Pacific Rise. *Geochim. Cosmochim. Acta* 61, 2849–2854.

Berndt, M.E., Seyfried Jr, W.E., 1993. Calcium and sodium exchange during hydrothermal alteration of calcic plagioclase at 400° C and 400 bars. *Geochim. Cosmochim. Acta* 57, 4445–4451.

Berndt, M.E., Seyfried Jr, W.E., Beck, J., 1988. Hydrothermal alteration processes at mid-ocean ridges_ experimental and theoretical constraints from Ca and Sr exchange-reactions and Sr isotopic-ratios. *J. Geophys. Res. - Solid Earth* 93, 4573–4583. doi:10.1029/JB093iB05p04573

Berndt, M.E., Seyfried Jr, W.E., Janecky, D.R., 1989. Plagioclase and epidote buffering of cation ratios in mid-ocean ridge hydrothermal fluids: Experimental results in and near the supercritical region. *Geochim. Cosmochim. Acta* 53, 2283–2300.

Bischoff, J., 1991. Densities of liquids and vapors in boiling NaCl-H₂O solutions: A PVTX summary from 300° to 500°C. *Am. J. Sciecn* 291, 309–338.

Bischoff, J.L., Dickson, F.W., 1975. Seawater-basalt interaction at 200°C and 500 bars: implications for origin of sea-floor heavy-metal deposits and regulation of seawater chemistry. *Earth Planet. Sci. Lett.* 25, 385–397.

Bischoff, J.L., Pitzer, K.S., 1985. Phase relations and adiabats in boiling seafloor geothermal systems. *Earth Planet. Sci. Lett.* 75, 327–338.

Bischoff, J.L., Rosenbauer, R.J., 1988. Liquid-vapor relations in the critical region of the system NaCl-H₂O from 380 to 415 C: A refined determination of the critical point and two-phase boundary of seawater. *Geochim. Cosmochim. Acta* 52, 2121–2126.

Bischoff, J.L., Rosenbauer, R.J., 1984. The critical point and two-phase boundary of seawater, 200-500°C. *Earth Planet. Sci. Lett.* 68, 172–180.

Bischoff, J., Rosenbauer, R.J., 1985. An empirical equation of state for hydrothermal seawater (3.2 percent NaCl). *Am. J. Sciecn* 285, 725–763.

Bischoff, J., Seyfried, W.E., 1978. Hydrothermal chemistry of seawater from 25° to 350°C. *Am. J. Sciecn* 278, 838–860.

Bostrom, K., Peterson, A., 1966. Precipitates from hydrothermal exhalations on the East Pacific Rise. *Econ. Geol.* 61, 1258–1265.

Boulart, C., Chavagnac, V., Monnin, C., Delacour, A., Ceuleneer, G., Hoareau, G., 2013. Differences in gas venting from ultramafic-hosted warm springs: the example of Oman and voltri ophiolites. *Ophioliti* 38, 143–156. doi:10.4454/ofioliti.v38i2.423

Bowers, T.S., Von Damm, K.L., Edmond, J.M., 1985. Chemical evolution of mid-ocean ridge hot springs. *Geochim. Cosmochim. Acta* 49, 2239–2252.

Campbell, I.H., McDougall, T.J., Turner, J.P., 1984. A note on fluid dynamic processes which can influence the deposition of massive sulfides. *Econ. Geol.* 79, 1905–1913.

Carlson, R.L., 2011. The effect of hydrothermal alteration on the seismic structure of the upper oceanic crust: Evidence from Holes 504B and 1256D: alteration and seismic structure. *Geochem. Geophys. Geosystems* 12. doi:10.1029/2011GC003624

Chan, L.-H., Edmond, J.M., Thompson, G., 1993. A Lithium Isotope Study of Hot Springs and Metabasalts From Mid-Ocean Ridge Hydrothermal Systems. *J. Geophys. Res.* 98, 9653–9659.

Charlou, J.L., Donval, J.P., Fouquet, Y., Jean-Baptiste, P., Holm, N., 2002. Geochemistry of high H₂ and CH₄ vent fluids issuing from ultramafic rocks at the Rainbow hydrothermal field (36° 14' N, MAR). *Chem. Geol.* 191, 345–359.

Charlou, J.L., Donval, J.P., Douville, E., Jean-Baptiste, P., Radford-Knoery, Fouquet, Y., Dapigny, A., Stievenard, M., 2000. Compared geochemical signatures and the evolution of Menez Gwen (37°50'N) and Lucky Strike (37°17'N) hydrothermal fluids, south of the Azores Triple Junction on the Mid-Atlantic Ridge. *Chem. Geol.* 171, 49–75.

Chavagnac, V., Ceuleneer, G., Monnin, C., Lansac, B., Hoareau, G., Boulart, C., 2013a. Mineralogical assemblages forming at hyperalkaline warm springs hosted on ultramafic rocks: A case study of Oman and Ligurian ophiolites: Mineral Precipitate at Alkaline Springs. *Geochem. Geophys. Geosystems* 14, 2474–2495. doi:10.1002/ggge.20146

Chavagnac, V., Monnin, C., Ceuleneer, G., Boulart, C., Hoareau, G., 2013b. Characterization of hyperalkaline fluids produced by low-temperature serpentinization of mantle peridotites in the Oman and Ligurian ophiolites: Hyperalkaline Waters in Oman and Liguria. *Geochem. Geophys. Geosystems* 14, 2496–2522. doi:10.1002/ggge.20147

Clark, I.D., Fontes, J.-C., 1990. Paleoclimatic Reconstruction in Northern Oman Based on Carbonates from Hyperalkaline Groundwaters. *Quat. Res.* 320–336. doi:0033-5894/90

Corliss, J.B., Dymond, J., Gondon, L.I., Edmond, J.M., Von Herzen, R.P., Ballard, R.D., Green, K., Williams, D., Brainbridge, A., Crane, K., van Andel, T.H., 1979. Submarine Thermal Springs on the Galapagos Rift. *Science* 203, 1073–1083.

Davis, E.E., Chapman, D.S., Wang, K., Villinger, H., Fisher, A.T., Robinson, S.W., Grigel, J., Pribnow, D., Stein, J., Becker, K., 1999. Regional heat flow variations across the sedimented Juan de Fuca Ridge eastern flank: Constrain on lithospheric cooling and lateral hydrothermal heat transport. *J. Geophys. Res.* 104, 17,675–17,688.

Davis, E., Elderfield, H., 2004. *Hydrogeology of the Oceanic Lithosphere*, Cambridge University press. ed.

Delacour, A., Früh-Green, G.L., Bernasconi, S.M., Schaeffer, P., Kelley, D.S., 2008. Carbon geochemistry of serpentinites in the Lost City Hydrothermal System (30°N, MAR). *Geochim. Cosmochim. Acta* 72, 3681–3702. doi:10.1016/j.gca.2008.04.039

Delaney, J.R., Mogk, D.W., Mottl, M.J., 1987. Quartz-cemented Breccias From the Mid-Atlantic Ridge: Samples of a High-Salinity Hydrothermal Upflow Zone. *J. Geophys. Res.* 92, 9175–9192.

Douville, E., Charlou, J.L., Oelkers, E.H., Bienvenu, P., Jove Colon, C.F., Donval, J.P., Fouquet, Y., Prieur, D., Appriou, P., 2002. The rainbow vent fluids (36 14' N, MAR): the influence of ultramafic rocks and phase separation on trace metal content in Mid-Atlantic Ridge hydrothermal fluids. *Chem. Geol.* 184, 37–48.

Dymond, J., Corliss, J.B., Heath, G.R., Field, C.W., Dasch, E.J., Veeh, H.H., 1973. Origin of metalliferous sediments from the Pacific Ocean. *Geol. Soc. Am. Bull.* 84, 3355–3372.

Edmond, J.M., Measures, C., McDuff, R.E., Chan, L.H., Collier, R., Grant, B., Gordon, L.I., Corliss, J.B., 1979. Ridge crest hydrothermal activity and the balances of the major and minor elements in the ocean: The Galapagos data. *Earth Planet. Sci. Lett.* 46, 1–18.

Edmonds, H.N., 2008. Chemical Signatures From Hydrothermal Venting on Slow Spreading Ridges, in: Rona, P.A., Devey, C.W., Dymont, J., Murton, B.J. (Eds.), Diversity of Hydrothermal Systems on Slow Spreading Ocean Ridges, AGU Monograph.

Elderfield, H., Schultz, A., 1996. Mid-ocean ridge hydrothermal fluxes and the chemical composition of the ocean. *Annu. Rev. Earth Planet. Sci.* 24, 191–224.

Fontaine, F.J., Cannat, M., Escartin, J., 2008. Hydrothermal circulation at slow-spreading mid-ocean ridges: The role of along-axis variations in axial lithospheric thickness. *Geology* 36, 759. doi:10.1130/G24885A.1

Fontaine, F.J., Wilcock, W.S.D., 2006. Dynamics and storage of brine in mid-ocean ridge hydrothermal systems. *J. Geophys. Res.* 111. doi:10.1029/2005JB003866

Fontaine, F.J., Wilcock, W.S.D., Butterfield, D.A., 2007. Physical controls on the salinity of mid-ocean ridge hydrothermal vent fluids. *Earth Planet. Sci. Lett.* 257, 132–145. doi:10.1016/j.epsl.2007.02.027

Fontaine, F.J., Wilcock, W.S.D., Foustoukos, D.E., Butterfield, D.A., 2009. A Si-Cl geothermobarometer for the reaction zone of high-temperature, basaltic-hosted mid-ocean ridge hydrothermal systems: Si/Cl-inferred P–T in MOR hydrothermal systems. *Geochem. Geophys. Geosystems* 10. doi:10.1029/2009GC002407

Fournier, R.O., 1983. A method of calculating Quartz solubilities in aqueous sodium chloride solutions. *Geochim. Cosmochim. ACTA* 47, 579–586.

Fournier, R.O., Rosenbauer, R.J., Bischoff, J., 1982. The solubility of quartz in aqueous sodium chloride solution at 350C and 180 to 500 bars. *Geochim. Cosmochim. Acta* 46, 1975–1978.

Foustoukos, D.I., James, R.H., Berndt, M.E., Seyfried, W.E., 2004. Lithium isotopic systematics of hydrothermal vent fluids at the Main Endeavour Field, Northern Juan de Fuca Ridge. *Chem. Geol.* 212, 17–26. doi:10.1016/j.chemgeo.2004.08.003

Foustoukos, D.I., Seyfried, W.E., 2007. Quartz solubility in the two-phase and critical region of the NaCl–KCl–H₂O system: Implications for submarine hydrothermal vent systems at 9°50'N East Pacific Rise. *Geochim. Cosmochim. Acta* 71, 186–201. doi:10.1016/j.gca.2006.08.038

Fox, C., 1990. Consequences of Phase-Separation on the Distribution of Hydrothermal Fluids as Ashes Vent Field, Axial Volcano, Juan-De-Fuca Ridge. *J. Geophys. Res.-Solid Earth Planets* 95, 12923–12926. doi:10.1029/JB095iB08p12923

Früh-Green, G., Kelley, D.S., Bernasconi, S.M., Karson, J.A., Ludwig, K.A., Butterfield, D.A., Boschi, C., Proskurowski, G., 2003. 30,000 Years of Hydrothermal Activity at the Lost City Vent Field. *Science* 301, 495–498.

German, C.R., Petersen, S., Hannington, M.D., 2016. Hydrothermal exploration of mid-ocean ridges: Where might the largest sulfide deposits be forming? *Chem. Geol.* 420, 114–126. doi:10.1016/j.chemgeo.2015.11.006

Goldfarb, M.S., Delaney, J.R., 1988. Response of Two-Phase Fluids to Fracture Configurations Within Submarine Hydrothermal Systems. *J. Geophys. Res. - Solid Earth* 93, 4585–4894. doi:10.1029/88JB07701

Haase, K.M., Petersen, S., Koschinsky, A., Seifert, R., Devey, C.W., Keir, R., Lackschewitz, K.S., Melchert, B., Perner, M., Schmale, O., Söling, J., Dübiller, N., Zielinski, F., Fretzdorff, S., Garbe-Schönberg, D., Westernströer, U., German, C.R., Shank,

T.M., Yoerger, D., Giere, O., Kuever, J., Marbler, H., Mawick, J., Mertens, C., Stöber, U., Walter, M., Ostertag-Henning, C., Paulick, H., Peters, M., Strauss, H., Sander, S., Stecher, J., Warmuth, M., Weber, S., 2007. Young volcanism and related hydrothermal activity at 5°S on the slow-spreading southern Mid-Atlantic Ridge: young volcanism and hydrothermal activity. *Geochem. Geophys. Geosystems* 8. doi:10.1029/2006GC001509

Hajash, A., 1975. Hydrothermal processes along mid-ocean ridges: an experimental investigation. *Contrib. Mineral. Petrol.* 53, 205–226.

Hannington, M.D., Galley, A.G., Herzig, P.M., Petersen, S., 1998. 28. Comparison of the TAG mound and stockwork complex with Cyprus-type massive sulfide deposits, in: *Proc Ocean Drill Program Sci Results*. pp. 389–415.

Hannington, M.D., de Ronde, C.D., Petersen, S., 2005. Sea-floor tectonics and submarine hydrothermal systems.

Haymon, R., 1983. Growth history of hydrothermal black smoker chimneys. *Nature* 301.

James, R.H., Elderfield, H., Palmer, M.R., 1995. The chemistry of hydrothermal fluids from the Broken Spur site, 29°N Mid-Atlantic Ridge. *Geochim. Cosmochim. Acta* 59, 651–659.

Janecky, D.R., Seyfried Jr, W.E., 1987. Transition metal mobility in oceanic ridge crest hydrothermal systems at 350° C–425° C, in: *Chemical Transport in Metasomatic Processes*. Springer, pp. 657–668.

Kadko, D., Butterfield, D.A., 1998. The relationship of hydrothermal fluid composition and crustal residence time to maturity of vent fields on the Juan de Fuca Ridge. *Geochim. Cosmochim. Acta* 62, 1521–1533.

Kawahata, H., Nohara, M., Ishizuka, H., Hasebe, S., Chiba, H., 2001. Sr isotope geochemistry and hydrothermal alteration of the Oman ophiolite. *J. Geophys. Res. - Solid Earth* 106, 11083–11099. doi:10.1029/2000JB900456

Kelley, D.S., Baross, J.A., Delaney, J.R., 2002. Volcanoes, Fluids, and Life at Mid-Ocean Ridge Spreading Centers. *Annu. Rev. Earth Planet. Sci.* 30, 385–491. doi:10.1146/annurev.earth.30.091201.141331

Klein, F., Bach, W., Jöns, N., McCollom, T., Moskowitz, B., Berquó, T., 2009. Iron partitioning and hydrogen generation during serpentinization of abyssal peridotites from 15°N on the Mid-Atlantic Ridge. *Geochim. Cosmochim. Acta* 73, 6868 – 6893.

Koschinsky, A., Garbe-Schönberg, D., Sander, S., Schmidt, K., Gennerich, H.-H., Strauss, H., 2008. Hydrothermal venting at pressure-temperature conditions above the critical point of seawater, 5 S on the Mid-Atlantic Ridge. *Geology* 36, 615–618.

Launay, J., Fontes, J. C., 1985. Les sources thermales de Prony (Nouvelle Calédonie) et leurs précipités chimiques, exemple de formation de brucite primaire. *Géologie de France* v.1, p83–100.

Leleu, T., Chavagnac, V., Delacour, A., Noiriél, C., Ceuleneer, G., Rommevaux, C., Ventalon, S., 2016. Travertines associated with hyperalkaline springs: evaluation as a proxy for paleoenvironmental conditions and sequestration of atmospheric CO₂. *J. Sediment. Res.*

Lister, C.R.B., 1972. On the thermal balance of a mid-ocean ridge. *Geophys. J. Int.* 26, 515–535.

Lowell, R., Rona, P., Vonherzen, R., 1995. Sea-Floor Hydrothermal Systems. *J. Geophys. Res.-Solid Earth* 100, 327–352. doi:10.1029/94JB02222

Macdonald, K.C., 2001. Mid-ocean Ridge Tectonics, Volcanism And Geomorphology, in: *Encyclopedia of Ocean Sciences*. Elsevier, pp. 1798–1813.

Magenheim, A.J., Spivack, A.J., Alt, J.C., Bayhurst, G., Chan, L.H., Zuleger, E., Gieskes, J.M., 1995. 13. Borehole fluid chemistry in Hole 504B, Leg 137: formation water or in situ reaction?, in: *Proceedings of the Ocean Drilling Program, Scientific Results*. pp. 141–52.

McKenzie, D.P., 1967. Some remarks on heat flow and gravity anomalies. *J. Geophys. Res.* 72, 6261–6273.

Mervine, E.M., Humphris, S.E., Sims, K.W.W., Kelemen, P.B., Jenkins, W.J., 2014. Carbonation rates of peridotite in the Samail Ophiolite, Sultanate of Oman, constrained through ¹⁴C dating and stable isotopes. *Geochim. Cosmochim. Acta* 126, 371 – 397.

Monnin, C., Chavagnac, V., Boulart, C., Ménez, B., Gérard, M., Gérard, E., Pisapia, C., Quémener, M., Erauso, G., Poestec, A., Quantas-Dombrowski, L., Payri, C., Pelletier, B. 2014. Fluid chemistry of the low temperature hyperalkaline hydrothermal system of Prony Bay (New Caledonia). *Biogeosciences*, v.11, p. 5687–5706.

Mottl, M.J., Holland, H.D., 1978. Chemical exchange during hydrothermal alteration of basalt by seawater—I. Experimental results for major and minor components of seawater. *Geochim. Cosmochim. Acta* 42, 1103–1115.

Mottl, M.J., Holland, H.D., Corr, R.F., 1979. Chemical exchange during hydrothermal alteration of basalt by seawater—II. Experimental results for Fe, Mn, and sulfur species. *Geochim. Cosmochim. Acta* 43, 869–884.

Mottl, M.J., McConachy, T.F., 1990. Chemical processes in buoyant hydrothermal plumes on the East Pacific Rise near 21°N. *Geochim. Cosmochim. Acta* 54, 1911–1927.

Mottl, M.J., Seewald, J.S., Wheat, C.G., Tivey, M.K., Michael, P.J., Proskurowski, G., McCollom, T.M., Reeves, E., Sharkey, J., You, C.-F., Chan, L.-H., Pichler, T., 2011. Chemistry of hot springs along the Eastern Lau Spreading Center. *Geochim. Cosmochim. Acta* 75, 1013–1038. doi:10.1016/j.gca.2010.12.008

Murray, J., Renard, A.F., 1891. Deep Sea Deposits, Report "Challenger3 Expedition (1873-1876).

Neal, C., Stanger, G., 1983. Hydrogen generation from mantle source rocks in Oman. *Earth Planet. Sci. Lett.* 66, 315 – 320.

1984. Theory of hydrothermal systems. *Annu. Rev. Earth Planet. Sci.* 12, 155–177.

Ono, S., Shanks, W.C., Rouxel, O.J., Rumble, D., 2007. S-33 constraints on the seawater sulfate contribution in modern seafloor hydrothermal vent sulfides. *Geochim. Cosmochim. Acta* 71, 1170–1182. doi:10.1016/j.gca.2006.11.017

Oosting, S.E., Von Damm, K.L., 1996. Bromide/chloride fractionation in seafloor hydrothermal fluxes from 9-10°N East Pacific Rise. *Earth Planet. Sci. Lett.* 144, 133–145.

Palmer, M.R., 1992. Controls over the chloride concentration of submarine hydrothermal vent fluids: evidence from Sr/Ca and ⁸⁷Sr/⁸⁶Sr ratios. *Earth Planet. Sci. Lett.* 109, 37–46.

Pester, N.J., Ding, K., Seyfried, W.E., 2015. Vapor–liquid partitioning of alkaline earth and transition metals in NaCl-dominated hydrothermal fluids: An experimental study from 360 to 465°C, near-critical to halite saturated conditions. *Geochim. Cosmochim. Acta* 168, 111–132. doi:10.1016/j.gca.2015.07.028

Pester, N.J., Reeves, E.P., Rough, M.E., Ding, K., Seewald, J.S., Seyfried, W.E., 2012. Subseafloor phase equilibria in high-temperature hydrothermal fluids of the Lucky Strike Seamount (Mid-Atlantic Ridge, 37°17'N). *Geochim. Cosmochim. Acta* 90, 303–322. doi:10.1016/j.gca.2012.05.018

Pester, N.J., Rough, M., Ding, K., Seyfried, W.E., 2011. A new Fe/Mn geothermometer for hydrothermal systems: Implications for high-salinity fluids at 13°N on the East Pacific Rise. *Geochim. Cosmochim. Acta* 75, 7881–7892. doi:10.1016/j.gca.2011.08.043

Petersen, S., Herzig, P.M., Hannington, M.D., 2000. Third dimension of a presently forming VMS deposit: TAG hydrothermal mound, Mid-Atlantic Ridge, 26 N. *Miner. Deposita* 35, 233–259.

Pokrovski, G.S., Roux, J., Harrichoury, J.-C., 2005. Fluid density control on vapor-liquid partitioning of metals in hydrothermal systems. *Geology* 33, 657–660.

Pomerol, C., Lagabrielle, Y., Renard, M., 2006. Structure et dynamique des fonds océaniques, in: *Eléments de Géologie*. Dunod, Paris, p. 762.

Ravizza, G., Blusztajn, J., Von Damm, K.L., Bray, A.M., Bach, W., Hart, S.R., 2001. Sr isotope variations in vent fluids from 9° 46'–9° 54' N East Pacific Rise: evidence of a non-zero-Mg fluid component. *Geochim. Cosmochim. Acta* 65, 729–739.

Resing, J.A., Sedwick, P.N., German, C.R., Jenkins, W.J., Moffett, J.W., Sohst, B.M., Tagliabue, A., 2015. Basin-scale transport of hydrothermal dissolved metals across the South Pacific Ocean. *Nature* 523, 200–203. doi:10.1038/nature14577

Saccocia, P.J., Seyfried Jr, W.E., 1994. The solubility of chlorite solid solutions in 3.2 wt% NaCl fluids from 300–400 C, 500 bars. *Geochim. Cosmochim. Acta* 58, 567–585.

Schmidt, K., Koschinsky, A., Garbe-Schönberg, D., de Carvalho, L.M., Seifert, R., 2007. Geochemistry of hydrothermal fluids from the ultramafic-hosted Logatchev hydrothermal field, 15°N on the Mid-Atlantic Ridge: Temporal and spatial investigation. *Chem. Geol.* 242, 1–21. doi:10.1016/j.chemgeo.2007.01.023

Seyfried Jr, W.E., Ding, K., Berndt, M.E., 1991. Phase equilibria constraints on the chemistry of hot fluids at mid-ocean ridges. *Geochim. Cosmochim. Acta* 55, 3559–3580.

Seyfried Jr, W.E., Janecky, D.R., Mottl, M.J., 1984. Alteration of the oceanic crust: Implications for geochemical cycles of lithium and boron. *Geochim. Cosmochim. Acta* 48, 557–569.

Seyfried Jr, W.E., Mottl, M.J., 1982. Hydrothermal alteration of basalt by seawater under seawater-dominated condition. *Geochim. Cosmochim. Acta* 46, 985–1002.

Seyfried, W.E., Pester, N.J., Tutolo, B.M., Ding, K., 2015. The Lost City hydrothermal system: Constraints imposed by vent fluid chemistry and reaction path models on subseafloor heat and mass transfer processes. *Geochim. Cosmochim. Acta* 163, 59–79. doi:10.1016/j.gca.2015.04.040

Shanks, W.C., 2001. Stable isotopes in seafloor hydrothermal systems: vent fluids, hydrothermal deposits, hydrothermal alteration, and microbial processes. *Rev. Mineral. Geochem.* 43, 469–525.

Skornyakova, I.S., 1965. Dispersed iron and manganese in Pacific Ocean sediments. *Int. Geol. Rev.* 7, 2161–2174.

Stein, C.A., Stein, S., 1994. Constraints on hydrothermal heat flux through the oceanic lithosphere from global heat flow. *J. Geophys. Res.* 99, 3081–3095.

Tamura, A., Arai, S., Ishimaru, S., Andal, E.S., 2008. Petrology and geochemistry of peridotites from IODP Site U1309 at Atlantis Massif, MAR 30°N: micro- and macro-scale melt penetrations into peridotites. *Contrib. Mineral. Petrol.* 155, 491–509. doi:10.1007/s00410-007-0254-0

Teagle, D.A., Alt, J.C., Chiba, H., Humphris, S.E., Halliday, A.N., 1998. Strontium and oxygen isotopic constraints on fluid mixing, alteration and mineralization in the TAG hydrothermal deposit. *Chem. Geol.* 149, 1–24.

Teagle, D.A.H., Bickle, M.J., Alt, J.C., 2003. Recharge flux to ocean-ridge black smoker systems: a geochemical estimate from ODP Hole 504B. *Earth Planet. Sci. Lett.* 210, 81–89. doi:10.1016/S0012-821X(03)00126-2

Tivey, M.K., 2007. Generation of seafloor hydrothermal vent fluids and associated mineral deposits.

Tivey, M.K. and R.E. McDuff, 1990. Mineral precipitation in the walls of black smoker chimneys: a quantitative model of transport and chemical reaction. *Journal of Geophysical Research*, 95, 12617-12637

Von Damm, K.L., Bischoff, J., Rosenbauer, R.J., 1991. Quartz solubility in hydrothermal seawater: an experimental study and equation describing quartz solubility for up to 0.5M NaCl solutions. *Am. J. Sci.* 291, 997–1007.

Von Damm, K.L., Edmond, J.M., Grant, B., Measures, C.I., Walden, B., Weiss, R.F., 1985. Chemistry of submarine hydrothermal solutions at 21°N, East Pacific Rise. *Geochim. Cosmochim. Acta* 49, 2197–2220.

Von Damm, K.L., Oosting, S.E., Kozłowski, R., Buttermore, L.G., Colodner, D., Edmonds, H.N., Edmond, J.M., Grebmeier, J.M., 1995. Evolution of East Pacific Rise hydrothermal vent fluids following a volcanic eruption. *Nature* 375, 47–51.

Von Damm, K., Edmond, J. t, Measures, C.I., Grant, B., 1985. Chemistry of submarine hydrothermal solutions at Guaymas Basin, Gulf of California. *Geochim. Cosmochim. Acta* 49, 2221–2237.

Von der Borsch, C.C., Rex, R.W., 1970. Amorphous iron oxide precipitates in sediments cored during Leg 5. *Deep Sea Drill. Proj.* 5, 541–544.

Wheat, C.G., Jannasch, H.W., Fisher, A.T., Becker, K., Sharkey, J., Hulme, S., 2010. Subseafloor seawater-basalt-microbe reactions: Continuous sampling of borehole fluids in a ridge flank environment: subseafloor borehole fluids. *Geochem. Geophys. Geosystems* 11. doi:10.1029/2010GC003057

Wheat, C.G., Mottl, M.J., Rudnicki, M., 2002. Trace element and REE composition of a low-temperature ridge-flank hydrothermal spring. *Geochim. Cosmochim. Acta* 66, 3693–3705.

CHAPITRE 2

THE LUCKY STRIKE HYDROTHERMAL FIELD

1 Discovery and geological context

The Lucky Strike hydrothermal field was discovered “accidentally” during the FAZAR cruise (French American Zaps and Rocks) in 1992, 400 km South West of the Azores islands ($37^{\circ}18'N$, $32^{\circ}16'W$; Langmuir et al., 1992). The cruise was devoted to a multidisciplinary survey of the ridge segment of the Mid Atlantic Ridge affected by the Azores hot spot. The cruise span from the Hayes Fracture zone at $32^{\circ}N$ to the Kurchatov fracture zone at $40^{\circ}30'N$ (Fig II -1). The scientific targets included: 1) an investigation of the petrological composition of the basalts, the presence of hydrothermal activity, bathymetry and characterization of the geophysical parameter of this part of the ridge; 2) a preparation of the FARA project (French American Ridge Atlantic), which intended to study active hydrothermal activity and petrological characteristic of recent volcanism along the MAR.

During a dredge on the first leg of the cruise, large fragments of sulfide chimney covered with mussels, shrimps and other organisms were brought back on board. The rock fragments contained typical minerals that compose hydrothermal chimneys (pyrite, chalcopyrite and sphalerite). The dredge also contained fresh basaltic rocks.

2 Geological setting

The Lucky Strike segment displays a central volcano in the rift valley (Fig II -2). It forms a broad platform extending on the ~ 11 km wide valley in the segment center. The platform depth is usually between 2000 and 1800 mbsl. The volcano rises 250 to 300m above the valley floor and extends over 50 km^2 (Humphris et al., 2002; Langmuir et al., 1997; Von Damm et al., 1998). Two prominent rises can be found as shallow as 1550mbsl. The hydrothermal site is located on a 5 km wide edifice at the center of the platform. Upon this edifice, bathymetric map reveals 3 volcanic cones rising 150m above a central depression. The Eastern cone consists of a N-S trending pillow ridge creating a rugged terrain which scale is out of the multibeam resolution but is readily observable on photo-mosaics and micro-bathymetry (Humphris et al., 2002). The lavas are highly vesicular and older than the lava recovered during the FAZAR dredge. The Southern cone displays younger glassy lava, relatively fresh and aphyric. Nautilé dives in 1994 during the FARA cruise revealed that the central depression forms a fossil lava lake (Fouquet et al., 1995). This fossil lava lake extends 320 m from West to East and 350m from North to South for a total surface of $\sim 1 \text{ km}^2$. The contour corresponds exactly to the 1734 mbsl isobaths (Ondréas et al., 2009).

The relationships between volcanic constructions and faults imply multiple episodes of volcanic and tectonic activity (Humphris et al., 2002). The faults observed on the volcanic cones clearly imply that they were affected by extensive tectonics postdating their formation. The faults are not observed on the fossil lava lake which suggests that the lava lake is younger than the last faulting events. Further evidences show that the freshest lava are shaped as lobate lava and are observed on the lava lake. These lobate lava do not occur on the volcanic cones (Ondréas et al., 2009).

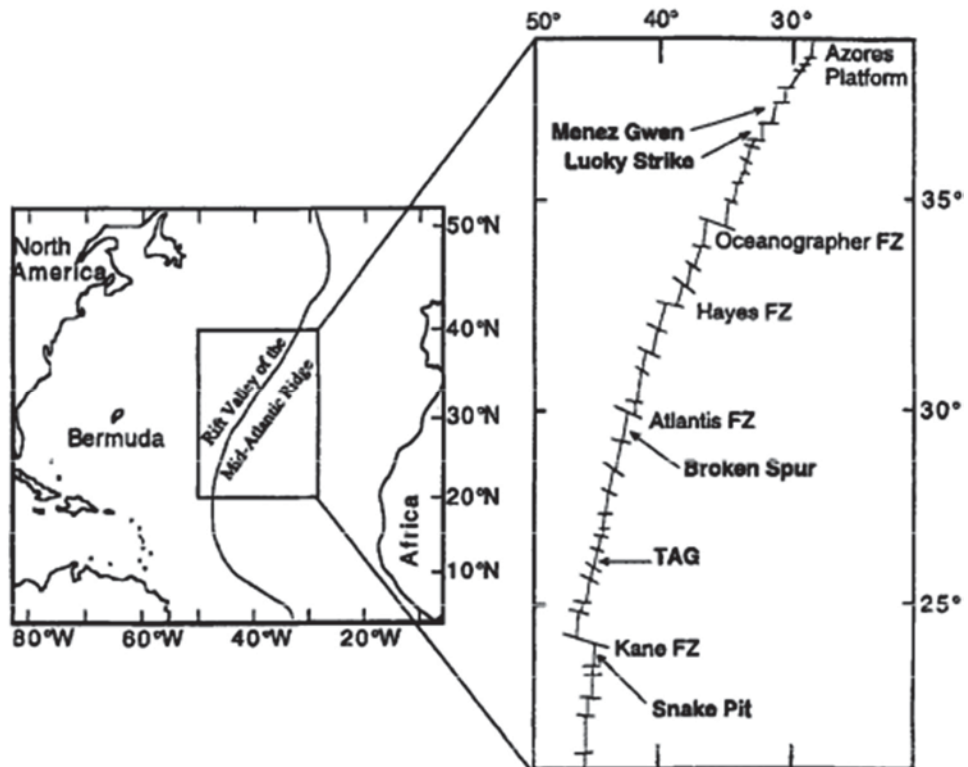


Figure II - 1 Map of the Northern Mid Atlantic ridge showing the major segments from Langmuir et al. (1997)

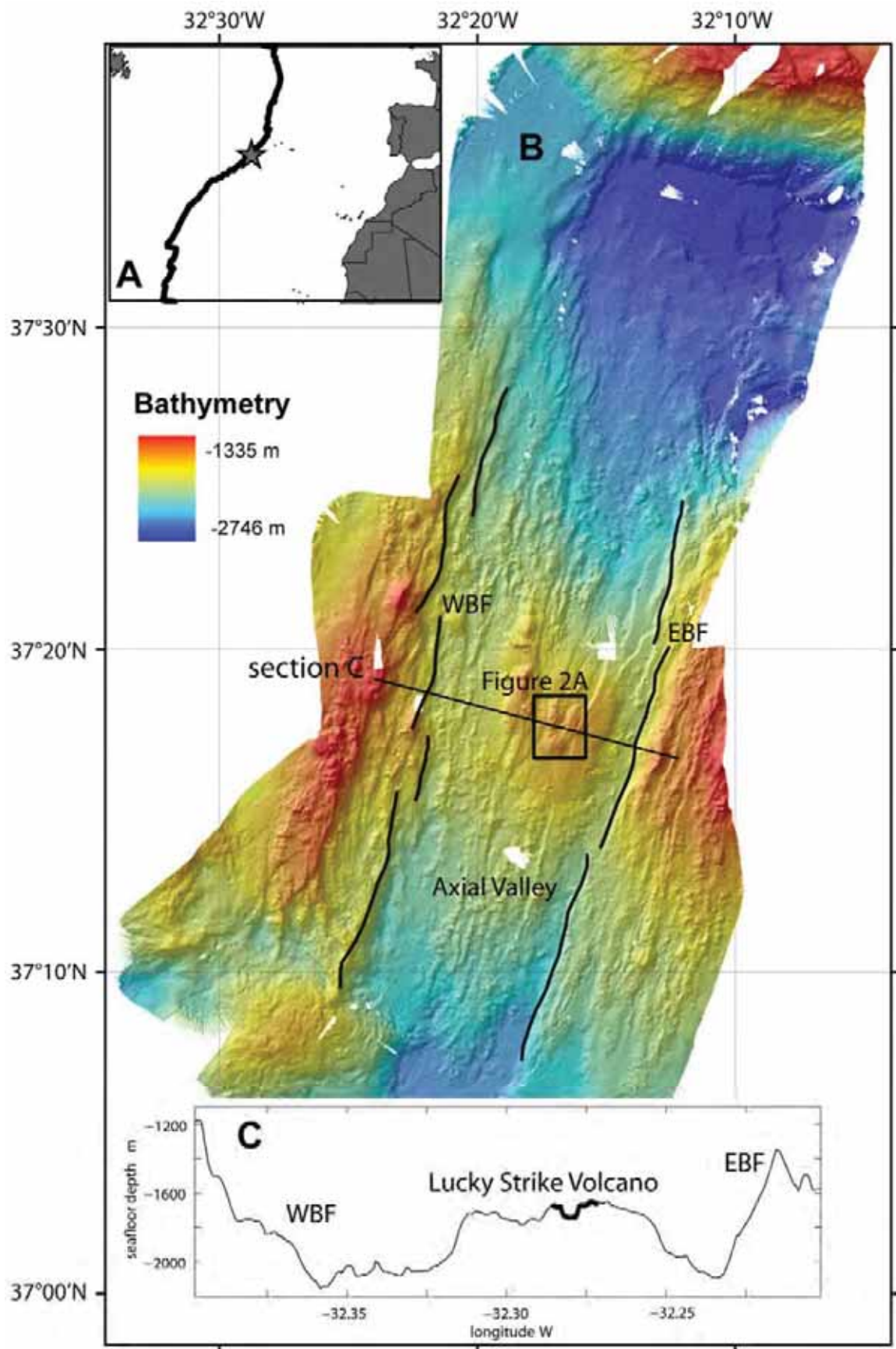


Figure II - 2 Bathymetric map of the Lucky Strike segment from Ondréas et al. (2009). The lines show the location of the main axial valley bounding faults. The black square indicate the location of the central volcano.

3 Basalt chemistry at Lucky Strike

The basalt samples show an enrichment in incompatible elements (K, Rb, Cs, Ba, La and Pb) compared to N-MORB. The seamount is built upon a hybrid basaltic substratum including 2 distinct endmembers of E and T MORB (Langmuir et al., 1997; Gale et al., 2011; Hamelin et al., 2013; Wanssen et al., 2015).

- Old and vesicular lavas on the top of the summit cones are particularly enriched in incompatible elements with Ba content up to 300ppm and Sr=300ppm. This enrichment is likely related to contamination by melts from the nearby Azores hot spot and are found at the segment centers (Gale et al., 2011)

- The central depression, composed of fresh and glassy lavas, shows a more moderate enrichment in such elements compared to N-MORB (60ppm and 110ppm of Ba and Sr respectively). These moderately enriched lavas are found all along the segment.

4 Subseafloor

Seismic reflexion data reveal the presence of a magmatic lens (AMC) and large faults (Singh et al., 2006). The top of the AMC has been imaged as a 3-4 km and 7 km long axial melt lens at 3.5 km below the seafloor (Fig II -3; Combier et al., 2015; Singh et al., 2006). The East Bounding Fault (EBF) could go down to what is supposed to be the AMC.

An array of 6 hydrophones was installed along the MAR 15 to 35°N and recorded an earthquake swarm in 2001 interpreted as a possible dike injection (Dziak, 2004). Active tectonics have an important role in this “magmatic” period and faults parallel to the ridge-axis are prevalent. The volcano is currently being rifted and the hydrothermal field has been active for 100s to 1000s of years (Seher et al., 2010).

In 2009, another swarm was observed by five ocean bottom sismometers (OBS) positioned at the summit of the Lucky Strike volcano. During this swarm, most of the seismic events formed 2 clusters located north and south of the hydrothermal field at depth between 1800 and 2500 mbsf. Both of them are aligned with the axial spreading direction and cracks orientation. Shallower events are aligned along axis and are interpreted as “cold” seawater penetration and development of the cracking front (Crawford et al., 2013).

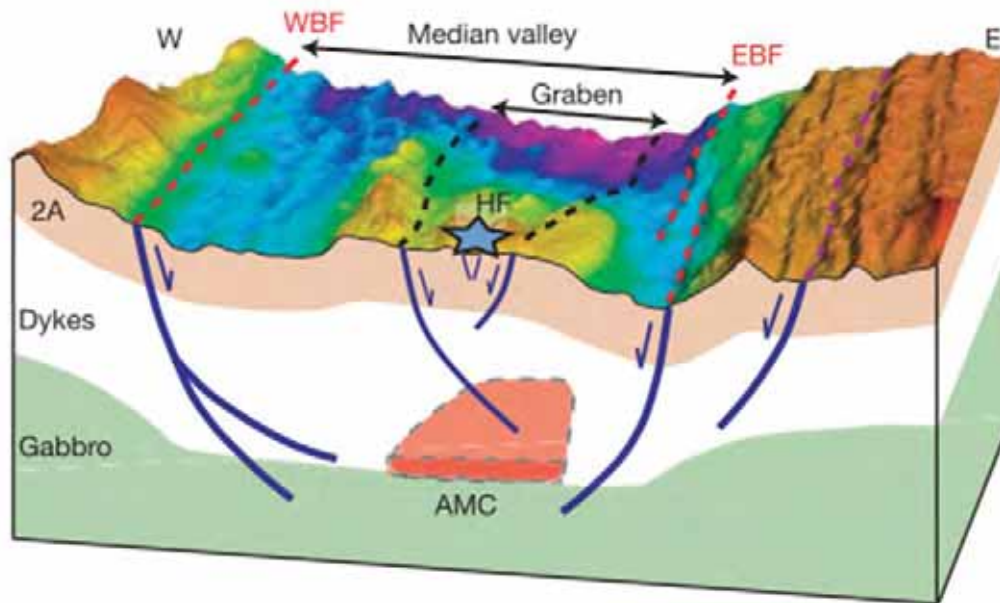


Figure II - 3 From Singh et al. (2006). Bloc diagram showing the Lucky Strike Hydrothermal Field bathymetry with the structure of the oceanic crust beneath.

5 Hydrothermal deposits

Humphris et al. (2002) report on the surface distribution of volcanic, hydrothermal deposits and sediments on the summit volcano depression (Fig II -4). The North East and North West sides of the fossil lava lake are dominated by sulfide rubbles, which are composed of massive sulfide talus, disaggregated sulfide structures and inactive/active chimneys.

At the south eastern area, hydrothermal deposits seems to be underlined by hydrothermally cemented breccias called slab (Humphris et al., 2002; Langmuir et al., 1997). This slab consists of an assemblage of basaltic glass, plagioclase crystals rimmed by amorphous silica as well as sulfides and barite grains.

Humphris et al. (2002) report on hydrothermal activity as an episodic event as indicated by different ages of sulfide deposits and inactive chimneys. Also there is a small number of active sites compared to the spatial extent of the deposits suggesting that hydrothermal activity used to be more intense and dispersed in the past. The fossil lava lake does not show any evidence of hydrothermal activity on its surface probably due to its low permeability.

The relation between hydrothermal activity and volcanic-tectonic processes on LS seamount are inter-related. At present, the LSHF would represent a volcanically controlled

phase of hydrothermal activity as the last magmatic event (i.e. the fossil lava lake) is not fractured by rifting yet.

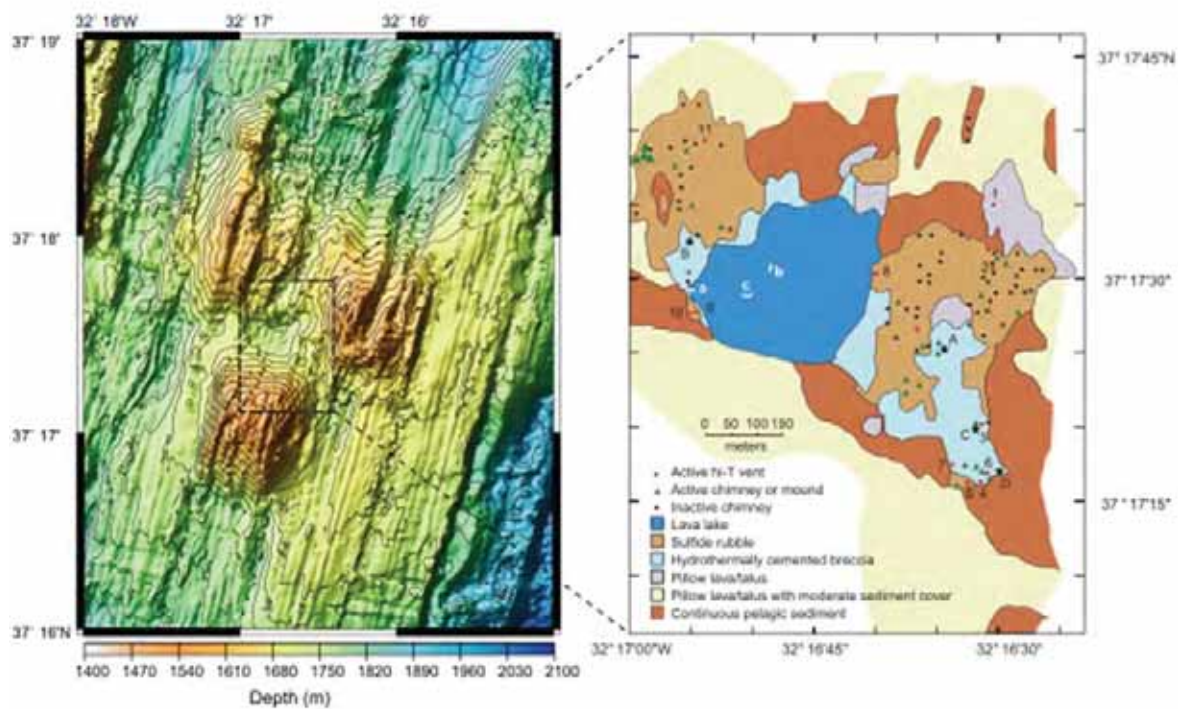


Figure II - 4 Modified from Humphris et al. (2002). Left: bathymetric map of the LSHF showing the 3 tectonised volcanic cones and the central depression where is situated the fossil lava lake. Right: Geological seafloor map showing the nature of the rocks at the surface surrounding the fossil lava lake.

6 Hydrothermal fluid venting at Lucky Strike

The hydrothermal fluids from the LSHF have been studied since their discovery at several time intervals. The first samples have been collected in 1993 during an Alvin program, scheduled after the evidence of active hydrothermal venting from the FAZAR discovery. Fluid sampling campaigns were organized over several years (1993, 1994, 1996, 1997, and 2008) and by different institutions (Charlou et al., 2000; Pester et al., 2012; Von Damm et al., 1998). This first study revealed a wide hydrothermal field of over $\sim 1 \text{ km}^2$ of surface.

All the sites discovered are located around the lava lake on specific areas (Fig II – 5), two groups of sites are situated at the northern talus, west (Jason, Helen and Bairo Alto) and east (Y3, Sintra and Statue of liberty). On the south-eastern side of the lava lake, numerous sites are situated on the fractured hydrothermal slab (Tour Eiffel, Montsegur, Petit Chimiste, etc). The south-western sites are situated on a fractured end of the lava lake. Among them, Crystal has been named for its crystal clear water.

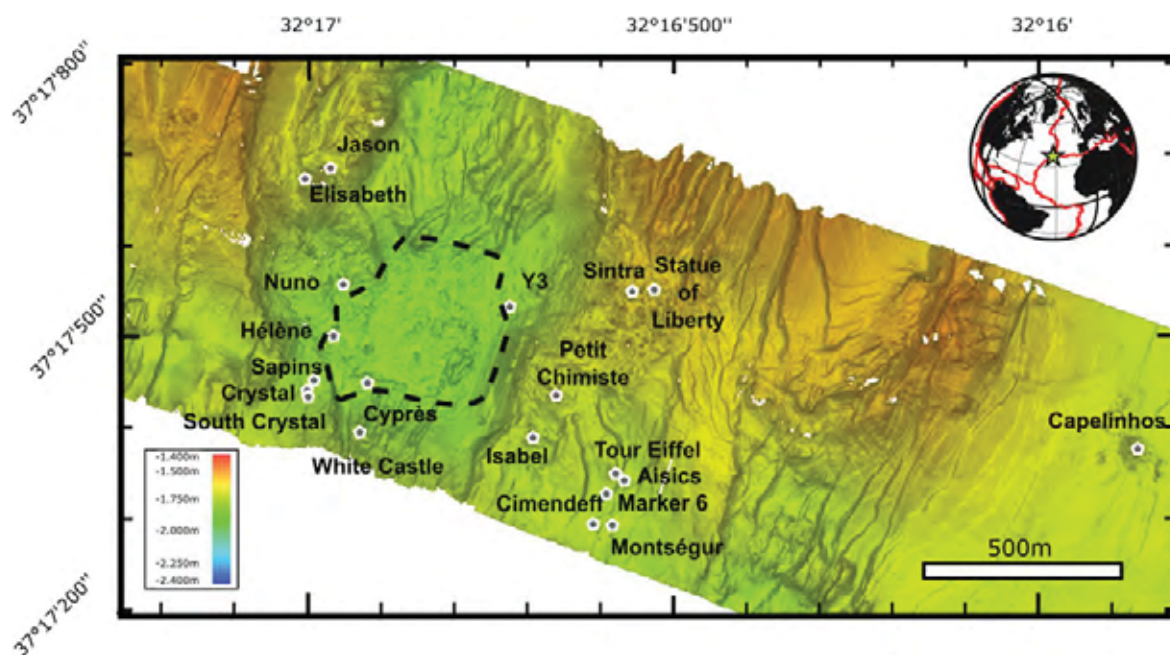


Figure II - 5: Microbathymetry map of the Uucky Strike Hydrothermal field. The dashed area represent the central fossil lava lake. The grey dots are the sites from where chemical data are available in the literature or in this study..

The fluid chemistry study revealed temperature of venting as high as 333°C for 2608 vent (also called Y3; Von Damm et al., 1998). The fluids were all depleted in Cl compared to seawater excepted for Sintra, Statue of Liberty and Jason (sampled in 1996) that have Cl concentration almost equal to that of seawater. Charlou et al. (2000) suggested that differences in Cl concentrations could be explained by hydrothermal seawater entrainment in the subsurface. These assumptions were based on a geographical control of Cl concentration and two different Sr isotope signatures. Nevertheless, Pester et al. (2012) showed that the seawater entrainment was unlikely, based on trace element distribution from site to site. They proposed that the fluid source originates from a unique, deep phase separation zone and that chemical differences are mostly due to slightly different phase separation conditions, subsequently modified by conductive cooling. The latter is consistent with the first hypothesis from Von Damm et al. (1998) who suggested a deep seated reaction zone ($P > 300$ bars based on silica concentrations and quartz solubility) feeding the whole hydrothermal field (Fig II -5).

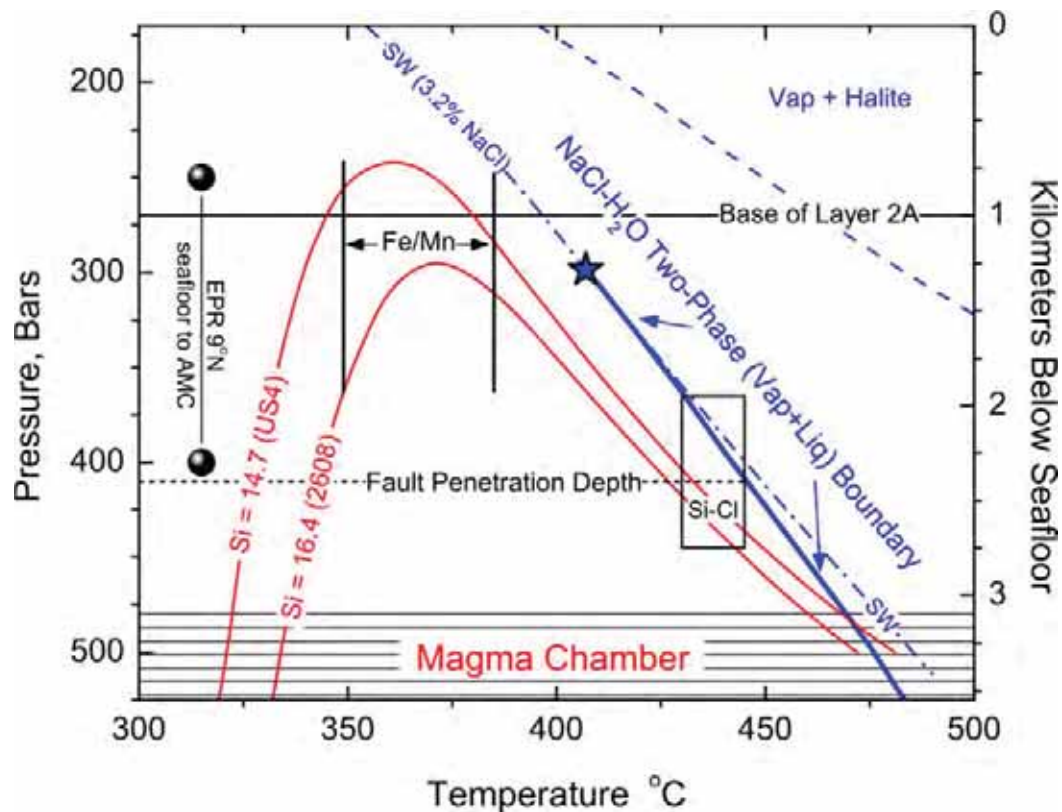


Figure II - 6 From Pester et al. (2012). P and T diagram that summarize the geophysical and geochemical constraint on the deep hydrothermal processes. Blue lines represent the 2 phase boundaries, the Si-Cl box represent the P and T conditions inferred for the phase separation zone (Fontaine et al., 2009). Si isopleth are calculated for quartz solubility using the model of Foustoukos and Seyfried (2007). Fe/Mn ratios represent the range of temperature inferred from the Fe-Mn geothermometer developed by Pester et al. (2011).

Later, the Si concentrations were used together with the Cl concentrations of the most depleted fluids of the LSHF to assess the P-T conditions taking place during phase separation (Fontaine et al., 2009; Fig II -5). These estimations, together with others obtained from different worldwide hydrothermal fields, were compared to the depth of the axial magma chamber, determined by geophysical methods, and gave results of 2500–2800 mbsf, that are consistent to a first order with a magma chamber at 3 kmbsf (Singh et al., 2006).

Lower-temperature fluids (8°C – 130°C) venting from cracks on the seafloor, termed diffuse venting, were also investigated to better characterize the heat and chemical exchange as they represent the most part of heat extraction from the crust (Barreyre et al., 2012; Mittelstaedt et al., 2012). These types of fluid are commonly regarded as high-temperature hydrothermal fluid mixed with seawater in the close subsurface of the seafloor. However, Cooper et al. (2000) studied the chemical composition of fluid samples collected at cracks from the hydrothermal slab. Based on temperature and both Mg and Li

concentrations measurements, these authors show that the chemical features of these fluids cannot be explained by mixing with a high-temperature fluid but are coherent with seawater that is conductively heated by the underlying high temperature fluid (Fig II -6).

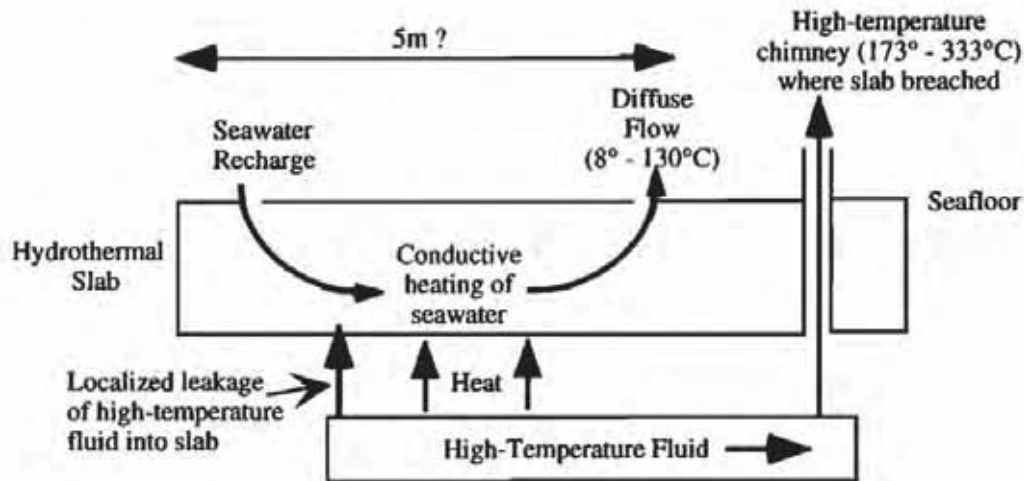


Figure II - 7 From Cooper et al. (2000), conceptual model for the diffuse flow system at Lucky Strike.

7 Hydrothermal fauna at the LSHF

The hydrothermal fluids discharging at the LSHF are key elements in the development of deep-sea hydrothermal ecosystems. The presence in the fluids of element in a reduced form are used in the metabolic chains of microorganisms and therefore influence the chemolithotroph organisms and their associated macrofauna (Henri, 2015). At the LSHF, the dominant species is *Bathymodiolus azoricus*, a mussel species found at every active site (Cuvelier et al., 2011, 2009; Lee Van Dover et al., 1996; Sarrazin et al., 2015). These mussels are associated with shrimps (*Mirocaris fortunate* and *chorocaris chacei*) and crabs (*Segonzacia mesatlantica*) communities with few polychaetes, gastropods, amphipods pycnogonides and copepods (Cuvelier et al., 2009; Lee Van Dover et al., 1996; Matabos et al., 2015; Sarrazin et al., 2015). The fauna assemblages are identified as a protected biogeographic province (Lee Van Dover et al., 1996).

Microbial mats are also present at LSHF (Sarradin et al., 1999; Desbruyeres et al., 2001) and cover mussel communities, diffuse vents, and chimneys. They are mostly composed of white filamentous bacteria that use the seawater oxygen to oxidize the hydrothermal sulfides (Bernard and Fenchel, 1995; Fenchel and Bernard, 1995; Gilhooly et al., 2007;

Nelson and Castenholz, 1981). These bacterial mats are dominated by Proteobacteria and bacteroidetes (Henri, 2015).

8 The EMSO Azores node: a multidisciplinary deep sea observatory

The EMSO Azores node (also mentioned as MoMARSat for monitoring the Mid Atlantic Ridge) is a non-cabled multidisciplinary observatory deployed in 2010 (Colaço et al., 2011) whose aims is to study the dynamic of hydrothermal systems on a long term (several years) at the Lucky Strike hydrothermal field. The scientific objectives are (1) to constrain hydrothermal heat and chemical fluxes to the ocean in relation with seismicity, volcanic activity and ground (seafloor) deformation at the ridge; (2) to evaluate the impact of environmental changes (deep seafloor, climatic and anthropogenic) on the deep seafloor ecosystems and hydrothermal communities; (3) to study the dynamics of water masses in a context of steep axial valley topography and the hydrothermal particles transport.

To investigate these scientific targets, a 3 components infrastructure has been installed in September 2010 (Fig II -7). The surface buoy named Borel, links the underwater instruments to shore through acoustic and satellite transmissions. Borel is equipped with GPS devices and sensors (e.g. air/wind speed sensors; Colaço et al., 2011).



Figure II - 8 Cartoon of the Emso Azores node infrastructure (www.fixO3.eu). At the seafloor, the two stations send data to the buoy BOREL. The Buoy then sends the data to the Ifremer center on shore.

The underwater part of the infrastructure is composed of two seafloor monitoring nodes (SEAMON) positioned at the West and the East of the hydrothermal field. SeaMon West is moored on the lava lake and is dedicated to the geophysical sensors. It is linked to OBS (Ocean Bottom Seismometer) and pressure gauges which allows the real-time transmission of seismic activity (Ballu et al., 2009; Crawford et al., 2013). The SeaMon East is dedicated to study of the ecosystems through an array of sensors constraining the chemical, biological and microbiological environment of the Tour Eiffel edifice (South East of the fossil lava lake). The station is wired to several devices including colonizer samples CISICs and an ecological module called TEMPO (Sarrazin et al., 2007). The latter is composed of Chemini Fe oxygen optode and a video camera system called SMOOVE. Chemini Fe and the oxygen optode are measuring the dissolved iron and O₂ in real time on a mussel bed which is filmed by SMOOVE at the base of the Tour Eiffel edifice during 2 minutes every 6 hours.

This infrastructure is recovered every year during a 15–20 days maintenance cruise. In between recovery and redeployment of the instruments, ROV dives are conducted for sampling and exploration purposes. Decoupled from the infrastructure, autonomous temperature sensors are left in hot vent orifices, diffuse venting zone and cracks to monitor

the temperature variation between vents (Barreyre et al., 2014), and recovered on the next maintenance cruise.

9 First results from the observatory

The installation of the observatory, 6 years ago, have improved the knowledge on hydrothermal field in general.

Especially, analysis of photomosaic and temperature sensors have allowed fine characterization of the discharge regime. The photomosaic images done on the same areas for several years have brought evidence of the decline of diffuse venting at the LSHF (Barreyre et al., 2012). Although temperature sensors have shown to be overall constant within a 3 years survey, but episodic (day scale) drops (10 to 160°C lower than initial temperature) have been observed. Comparison could be made with microseismic events but were not correlated (Barreyre et al., 2014). These episode of temperature drop and/or increase are the results of the subsurface. Small variations in temperature were related to a tidal change of hydrostatic pressure. The high permeability of the extrusive layer (seismic layer 2A) induce a tidal effect on the fluid discharge. Using the time response to tidal pressure of the temperature of the discharging fluid (diffused and focused); Barreyre and Sohn, (2016) were able to estimate the thickness of the extrusive volcanic layer 2A or at least the first limit to a major permeability gradient. They concluded that the layer 2A is 300m thick to the West of the lava lake while to the East, the layer 2A is twice as thick (600m; Fig II -8).

Escartin et al., (2015) have reviewed the visual information available on the Lucky Strike central volcano. This study produced a map that summarizes the state of the knowledge now available at this hydrothermal field (Fig II -9). This figure is a microbathymetric map on which are reported the known active hydrothermal sites and associated deposits. Apart from the main LSHF, three sites have been identified. At the south the main LSHF at the center of the axial graben is the Ewan site that presents active hydrothermal activity at temperature up to 20°C (Escartin et al., 2015). Based on microbathymetry data, the Grunnus site is located at ~2 km east of the fossil lava lake but is inferred to be inactive now as neither in situ observation nor hydrothermal plumes have been detected above it (Escartin et al., 2015). The Capelinhos vent sites is located ~1.5 km east of the main LSHF and has been discovered in 2013. This site presents almost no diffuse venting but focused venting at temperature as high as 328°C from numerous ten meter tall chimneys.

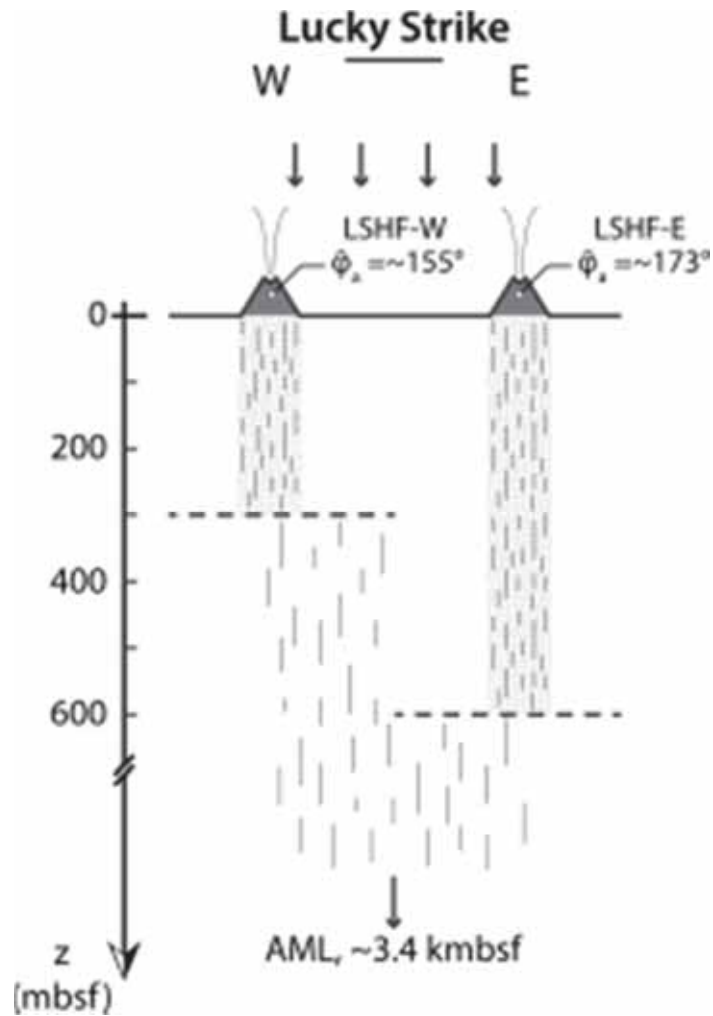


Figure II - 9 Subsurface depth of a permeability change inferred from phase lag response to tidal change in the T sensor from Barreyre and Sohn (2016). AML: Axial Magmatic Lens.

Also the limits of the seismically imaged AMC is reported together with the area of microseismicity activity during the 2009 seismic swarm (Combiere et al., 2015; Crawford et al., 2013; Singh et al., 2006). The main hydrothermal activity, which occurs at the volcano, is sustained by the heat provided by a shallow AMC, leading to a long-lived hydrothermal activity in this area.

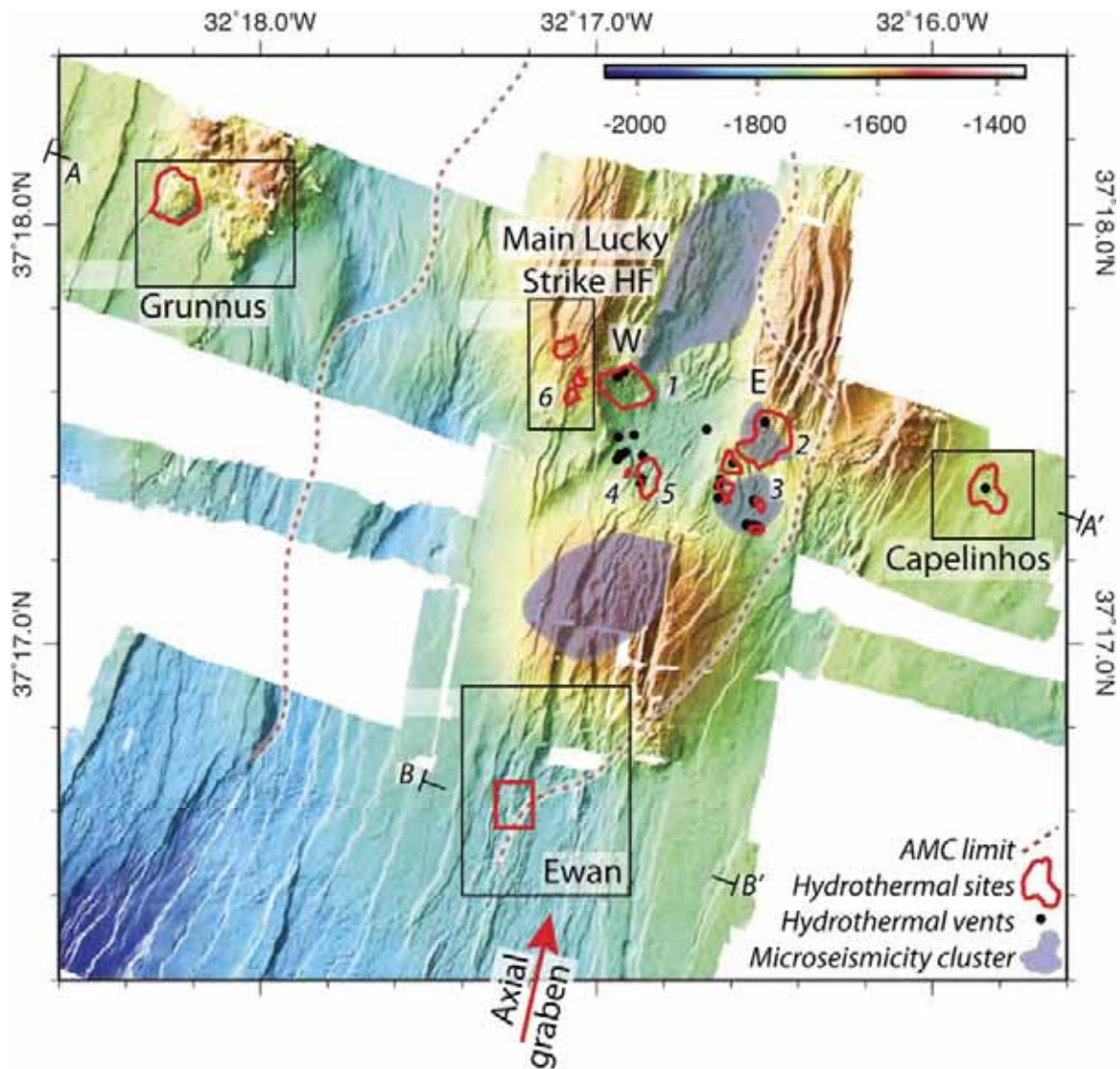


Figure II - 10 From Escartin et al. (2015), microbathymetry map of the central volcano of the Lucky Strike segment. Red contours represent hydrothermal deposits identified in the microbathymetry, and numbered following the classification from Barreyre et al. (2012). Black dots represent active vents. Brown dashed lines represent the limits of the AMC (Combiere et al., 2015; Singh et al., 2006). Blue areas represent the location of seismic clusters in the crusts (Crawford et al., 2013).

A lot of work has been produced at the LSHF since the observatory installation. Many results from geophysical studies have set the perfect conditions for an accurate characterization of the fluid chemistry. Therefore, the present work has focused on high temperature fluids for a large number of sites, each representative and defining groups based on their chemical and geographical characteristics. The chapters 4, 5 and 6 will focus on the fluid chemistry on the ground of the solid geophysical data acquired and 1) define a hydrothermal circulation model that includes the newly discovered vent site; 2) investigate the time series data acquired since the installation of the observatory infrastructure; and 3) use the opportunity of a well-known hydrothermal field which displays a wide variety of

fluid chemistry to explore the behavior of rare earth elements within the subsurface and at the early stage of hydrothermal fluid mixing with deep seawater at the discharge.

References

Ballu, V., Ammann, J., Pot, O., de Viron, O., Sasagawa, G.S., Reverdin, G., Bouin, M.-N., Cannat, M., Deplus, C., Deroussi, S., Maia, M., Diament, M., 2009. A seafloor experiment to monitor vertical deformation at the Lucky Strike volcano, Mid-Atlantic Ridge. *J. Geod.* 83, 147–159. doi:10.1007/s00190-008-0248-3

Barreyre, T., Escartín, J., Garcia, R., Cannat, M., Mittelstaedt, E., Prados, R., 2012. Structure, temporal evolution, and heat flux estimates from the Lucky Strike deep-sea hydrothermal field derived from seafloor image mosaics: hydrothermal outflow and image mosaics. *Geochem. Geophys. Geosystems* 13, doi:10.1029/2011GC003990

Barreyre, T., Escartin, J., Sohn, R., Cannat, M., Ballu, V., Crawford, W.C., 2014. Temporal variability and tidal modulation of hydrothermal exit-fluid temperatures at the Lucky Strike deep-sea vent field, Mid-Atlantic Ridge. *J. Geophys. Res.-Solid Earth* 119, 2543–2566.

Barreyre, T., Sohn, R.A., 2016. Poroelastic response of mid-ocean ridge hydrothermal systems to ocean tidal loading: Implications for shallow permeability structure: Shallow Upflow Zone Permeability. *Geophys. Res. Lett.* 43, 1660–1668. doi:10.1002/2015GL066479

Bernard, C., Fenchel, T., 1995. Mats of colourless sulphur bacteria. 2. Structure, composition of biota and successional patterns. *Mar. Ecol. Prog. Ser.*

Charlou, J.L., Donval, J.P., Douville, E., Jean-Baptiste, P., Radford-Knoery, Fouquet, Y., Dapoigny, A., Stievenard, M., 2000. Compared geochemical signatures and the evolution of Menez Gwen (37°50'N) and Lucky Strike (37°17'N) hydrothermal fluids, south of the Azores Triple Junction on the Mid-Atlantic Ridge. *Chem. Geol.* 171, 49–75.

Colaço, A., Blandin, J., Cannat, M., Carval, T., Chavagnac, V., Connelly, D., Fabian, M., Ghibon, S., Goslin, J., Miranda, J.M., Reverdin, G., Sarrazin, J., Waldmann, C., Sarradin, P.M., 2011. MoMAR-D: a technological challenge to monitor the dynamics of the Lucky Strike vent ecosystem. *ICES J. Mar. Sci.* 68, 416–424. doi:10.1093/icesjms/fsq075

Combiér, V., Seher, T., Singh, S.C., Crawford, W.C., Cannat, M., Escartín, J., Dusunur, D., 2015. Three-dimensional geometry of axial magma chamber roof and faults at Lucky Strike volcano on the Mid-Atlantic Ridge: magma chamber and faulting at Lucky Strike. *J. Geophys. Res. Solid Earth* 120, 5379–5400. doi:10.1002/2015JB012365

Cooper, M.J., Elderfield, H., Schultz, A., 2000. Diffuse hydrothermal fluids from Lucky Strike hydrothermal vent field: Evidence for a shallow conductively heated system. *Journal Geophys. Res.* 105, 19369–19375.

Crawford, W.C., Rai, A., Singh, S.C., Cannat, M., Escartin, J., Wang, H., Daniel, R., Combiér, V., 2013. Hydrothermal seismicity beneath the summit of Lucky Strike volcano, Mid-Atlantic Ridge. *Earth Planet. Sci. Lett.* 373, 118–128. doi:10.1016/j.epsl.2013.04.028

Cuvelier, D., Sarradin, P.-M., Sarrazin, J., Colaço, A., Copley, J.T., Desbruyères, D., Glover, A.G., Santos, R.S., Tyler, P.A., 2011. Hydrothermal faunal assemblages and

habitat characterisation at the Eiffel Tower edifice (Lucky Strike, Mid-Atlantic Ridge): Hydrothermal faunal assemblages and habitat characterisation of the Eiffel Tower. *Mar. Ecol.* 32, 243–255. doi:10.1111/j.1439-0485.2010.00431.x

Cuvelier, D., Sarrazin, J., Colaço, A., Copley, J., Desbruyères, D., Glover, A.G., Tyler, P., Serrão Santos, R., 2009. Distribution and spatial variation of hydrothermal faunal assemblages at Lucky Strike (Mid-Atlantic Ridge) revealed by high-resolution video image analysis. *Deep Sea Res. Part Oceanogr. Res. Pap.* 56, 2026–2040. doi:10.1016/j.dsr.2009.06.006

Desbruyères D., Almeida A., Biscoito M., Comtet T., Khripounoff A., Le Bris N., Sarradin P.-M., Segonzac M. (2001) Distribution of hydrothermal vent communities along the Northern Mid-Atlantic Ridge. Dispersal vs. environmental control: a review. *Hydrobiologia*, 440, 201–216

Dziak, R.P., 2004. Evidence of a recent magma dike intrusion at the slow spreading Lucky Strike segment, Mid-Atlantic Ridge. *J. Geophys. Res.* 109. doi:10.1029/2004JB003141

Escartin, J., Barreyre, T., Cannat, M., Garcia, R., Gracias, N., Deschamps, A., Salocchi, A., Sarradin, P.-M., Ballu, V., 2015. Hydrothermal activity along the slow-spreading Lucky Strike ridge segment (Mid-Atlantic Ridge): Distribution, heatflux, and geological controls. *Earth Planet. Sci. Lett.* 431, 173–185. doi:10.1016/j.epsl.2015.09.025

Fenchel, T., Bernard, C., 1995. Mats of colourless sulphur bacteria. I. Major microbial processes. *Mar. Ecol. Prog. Ser.* 128, 161–170.

Fontaine, F.J., Wilcock, W.S.D., Foustoukos, D.E., Butterfield, D.A., 2009. A Si-Cl geothermobarometer for the reaction zone of high-temperature, basaltic-hosted mid-ocean ridge hydrothermal systems: Si/Cl-inferred P–T in MOR hydrothermal systems. *Geochem. Geophys. Geosystems* 10. doi:10.1029/2009GC002407

Fouquet, Y., Ondréas, H., Charlou, J.L., Donval, J.P., Radford-Knoery, 1995. Atlantic lava lakes and hot vents. *Nature* 377, 201.

Foustoukos, D.I., Seyfried, W.E., 2007. Quartz solubility in the two-phase and critical region of the NaCl–KCl–H₂O system: Implications for submarine hydrothermal vent systems at 9°50'N East Pacific Rise. *Geochim. Cosmochim. Acta* 71, 186–201. doi:10.1016/j.gca.2006.08.038

Gale, A., Escrig, S., Gier, E.J., Langmuir, C.H., Goldstein, S.L., 2011. Enriched basalts at segment centers: The Lucky Strike (37°17'N) and Menez Gwen (37°50'N) segments of the Mid-Atlantic Ridge: enriched basalts at segment centers. *Geochem. Geophys. Geosystems* 12, doi:10.1029/2010GC003446

Gilhooly, W.P., Carney, R.S., Macko, S.A., 2007. Relationships between sulfide-oxidizing bacterial mats and their carbon sources in northern Gulf of Mexico cold seeps. *Org. Geochem.* 38, 380–393. doi:10.1016/j.orggeochem.2006.06.005

Hamelin C., Bezou A., Dosso L., Escartin J., Cannat M., Mevel C. (2013) Atypically depleted upper mantle component revealed by Hf isotopes at Lucky Strike segment. *Chem. Geol.* 341, 128–139. doi:10.1016/j.chemgeo.2013.01.013

Henri, P., 2015. Etude de l'altération précoce des verres basaltiques par les microorganismes en contexte hydrothermal océanique: Exemple du site de Lucky Strike (dorsale Médio-Atlantique, 37°N). Institut de Physique du Globe de Paris, Paris.

Humphris, S.E., Fornari, D.J., Scheirer, D.S., German, C.R., Parson, L.M., 2002. Geotectonic setting of hydrothermal activity on the summit of Lucky Strike Seamount (37°17'N, Mid-Atlantic Ridge): geotectonic setting. *Geochem. Geophys. Geosystems* 3, 1–25. doi:10.1029/2001GC000284

Langmuir, C.H., Klinkhammer, G.P., Bougault, H., 1992. Evaluation of the relationships among segmentation, hydrothermal activity and petrological diversity on the mid-Atlantic ridge: FAZAR (French American Zaps and Rocks) (Cruise report). Lamont-Doherty Earth Observatory of Columbia University, R/V Atlantis II.

Langmuir, C., Humphris, S.E., Fornari, D.J., Van Dover, C., Von Damm, K.L., Tivey, M.K., Colodner, D., Charlou, J.L., Desonie, D., Wilson, C., Fouquet, Y., Klinkhammer, G.P., Bougault, H., 1997. Hydrothermal vents near a mantle hot spot: the Lucky Strike vent field at 37°N on the Mid-Atlantic Ridge. *Earth Planet. Sci. Lett.* 148, 69–91.

Lee Van Dover, C., Desbruyères, D., Segonzac, M., Comtet, T., Saldanha, L., Fiala-Medioni, A., Langmuir, C., 1996. Biology of the Lucky Strike hydrothermal field. *Deep Sea Res. Part Oceanogr. Res. Pap.* 43, 1509–1529.

Lister, C.R.B., 1974. On the penetration of water into hot rock. *Geophys. J. Int.* 39, 465–509.

Matabos, M., Cuvelier, D., Brouard, J., Shillito, B., Ravaux, J., Zbinden, M., Barthelemy, D., Sarradin, P.M., Sarrazin, J., 2015. Behaviour study of two hydrothermal crustacean decapods: *Mirocaris fortunata* and *Segonzacia mesatlantica*, from the Lucky Strike vent field (Mid-Atlantic Ridge). *Deep Sea Res. Part II Top. Stud. Oceanogr.* 121, 146–158. doi:10.1016/j.dsr2.2015.04.008

Mittelstaedt, E., Escartín, J., Gracias, N., Olive, J.-A., Barreyre, T., Davaille, A., Cannat, M., Garcia, R., 2012. Quantifying diffuse and discrete venting at the Tour Eiffel vent site, Lucky Strike hydrothermal field: HEAT FLUX TOUR EIFFEL. *Geochem. Geophys. Geosystems* 13. doi:10.1029/2011GC003991

Nelson, D.C., Castenholz, R.W., 1981. Use of reduced sulfur compounds by *Beggiatoa* sp. *J. Bacteriol.* 147, 140–154.

Ondréas, H., Cannat, M., Fouquet, Y., Normand, A., Sarradin, P.M., Sarrazin, J., 2009. Recent volcanic events and the distribution of hydrothermal venting at the Lucky Strike hydrothermal field, Mid-Atlantic Ridge: LUCKY STRIKE VOLCANISM AND VENTING. *Geochem. Geophys. Geosystems* 10. doi:10.1029/2008GC002171

Pester, N.J., Reeves, E.P., Rough, M.E., Ding, K., Seewald, J.S., Seyfried, W.E., 2012. Subseafloor phase equilibria in high-temperature hydrothermal fluids of the Lucky Strike Seamount (Mid-Atlantic Ridge, 37°17'N). *Geochim. Cosmochim. Acta* 90, 303–322. doi:10.1016/j.gca.2012.05.018

Pester, N.J., Rough, M., Ding, K., Seyfried, W.E., 2011. A new Fe/Mn geothermometer for hydrothermal systems: Implications for high-salinity fluids at 13°N on the East Pacific Rise. *Geochim. Cosmochim. Acta* 75, 7881–7892. doi:10.1016/j.gca.2011.08.043

Sarradin, P.-M.; Caprais, J.-C.; Riso, R.; Kerouel, R.; Aminot, A., 1999. Chemical environment of the hydrothermal mussel communities in the Lucky Strike and Menez Gwen vent fields, Mid Atlantic Ridge; *Cahiers de Biologie Marine*, Volume 40, Issue 1, Pages 93-104

Sarrazin, J., Blandin, J., Delauney, L., Dentrecolas, S., Dorval, P., Dupont, J., Legrand, J., Leroux, D., Leon, P., Lévêque, J.P., others, 2007. TEMPO: a new ecological module for studying deep-sea community dynamics at hydrothermal vents, in: *Oceans 2007-Europe*. Ieee, pp. 1–4.

Sarrazin, J., Legendre, P., de Busserolles, F., Fabri, M.-C., Guilini, K., Ivanenko, V.N., Morineaux, M., Vanreusel, A., Sarradin, P.-M., 2015. Biodiversity patterns, environmental drivers and indicator species on a high-temperature hydrothermal edifice, Mid-Atlantic Ridge. *Deep Sea Res. Part II Top. Stud. Oceanogr.* 121, 177–192. doi:10.1016/j.dsr2.2015.04.013

Seher, T., Crawford, W.C., Singh, S.C., Cannat, M., 2010. Seismic layer 2A variations in the Lucky Strike segment at the Mid-Atlantic Ridge from reflection measurements. *J. Geophys. Res.* 115. doi:10.1029/2009JB006783

Singh, S.C., Crawford, W.C., Carton, H., Seher, T., Combier, V., Cannat, M., Pablo Canales, J., Düsünür, D., Escartin, J., Miguel Miranda, J., 2006. Discovery of a magma chamber and faults beneath a Mid-Atlantic Ridge hydrothermal field. *Nature* 442, 1029–1032. doi:10.1038/nature05105

Von Damm, K.L., Bray, A.M., Buttermore, L.G., Oosting, S.E., 1998. The geochemical controls on vent fluids from the Lucky Strike vent field, Mid-Atlantic Ridge. *Earth Planet. Sci. Lett.* 160, 521–536.

Wanssen, V. D., Shaw, A. M., Behn M. D., Soule, S. A., Escartin, J., Hamelin, C., 2015. Magmatic plumbing at Lucky Strike volcano based on olivine-hosted melt inclusion compositions. *Geochemistry, Geophysics, Geosystems*, 16, 126–147.

CHAPITRE 3

MATERIALS AND METHODS

1 Hydrothermal fluid sampling and processing

The fluids analyzed during this thesis were collected during 3 research cruises on board the R.V. “Pourquoi Pas?” in 2013, 2014 and 2015 (with corresponding PI: Jérôme Blandin, 2013 and Pierre Marie Sarradin, 2014 and 2015). The R.V. “Pourquoi Pas?” has the capacity of hosting and deploying the ROV Victor6000 (Remotely Operated Vehicle). On board, 35 scientists of different scientific expertise work together day and night to optimize the ship time, on 24h/24h working hours.

The French Vessel “Pourquoi pas?” (Fig III -1) is funded by both FOF (French Oceanographic Fleet; 55%) and French Ministry of Defense (45%), therefore these institutions share ship time (180 days and 150 days per year respectively). The ship is 107m long and 20m wide and is operated by Genavir. It is equipped on board with 1200m² scientific laboratories. It also has with 2 multibeam system capable of high quality bathymetric mapping, among other instruments.



Figure III - 1 Photographs of the R/V Pourquoi pas? on the Horta port (Faial island, Azores, A and B), C: photograph of the “Pourquoi pas?” and the buoy Borel (Ifremer/CNRS) on top of the Lucky Strike hydrothermal field, on the North Atlantic Ocean (37°N).

The ROV Victor 6000 (Fig III -2) is a cabled submersible vehicle capable of diving as deep as 6000m below sea-level. During a research cruise, a team of 8 mechanics and electronic engineers are on board to maintain and pilot the ROV scientific dives. The ROV maintenance can be performed day or night but generally daylight is preferred and dives are based on 12h short dives and 36h long dives. The ROV is equipped with HD cameras,

such as on both arms and at the front (principal), and several measuring devices such as high temperature probes, liquid sampler connected to a T probe, and a biological sampling devices. The ROV is capable of handling samples and tools at depth with two articulated arms, Sherpa and Maestro. The ROV may be equipped with a sampling module and a mapping module. These modules concern the lower part of the ROV Victor6000, and can be switched from dive to dive depending on the research objectives. The sampling module is equipped with a large retractable basket (Fig III - 2a). This basket can contain the collected samples (e.g. rocks, biobox, fluid sampler, etc...) and autonomous temperature probe to be used and placed at depth during the dive. The module is equipped with a high temperature probe for real time measurement. Another temperature probe is associated to a fluid sampling device called PEPITO (Sarradin et al., 2009). The mapping module has been used to map the LSHF by generating a mosaic from images in addition to high resolution bathymetry (Barreyre et al., 2012; Escartín et al., 2008, 2015). The pilots have a dedicated container installed on board as a control room of the ROV Victor6000. From there, and during each dive, two scientists who are in charge of fulfilling the operations objective, are assisted by two ROV team members who will manipulate the ROV. Both scientists and ROV team members have dedicated screens (Fig. III - 3) which enables them to pilot, guide, and manipulate independently at selected areas on the bottom seafloor (Fig III - 3).

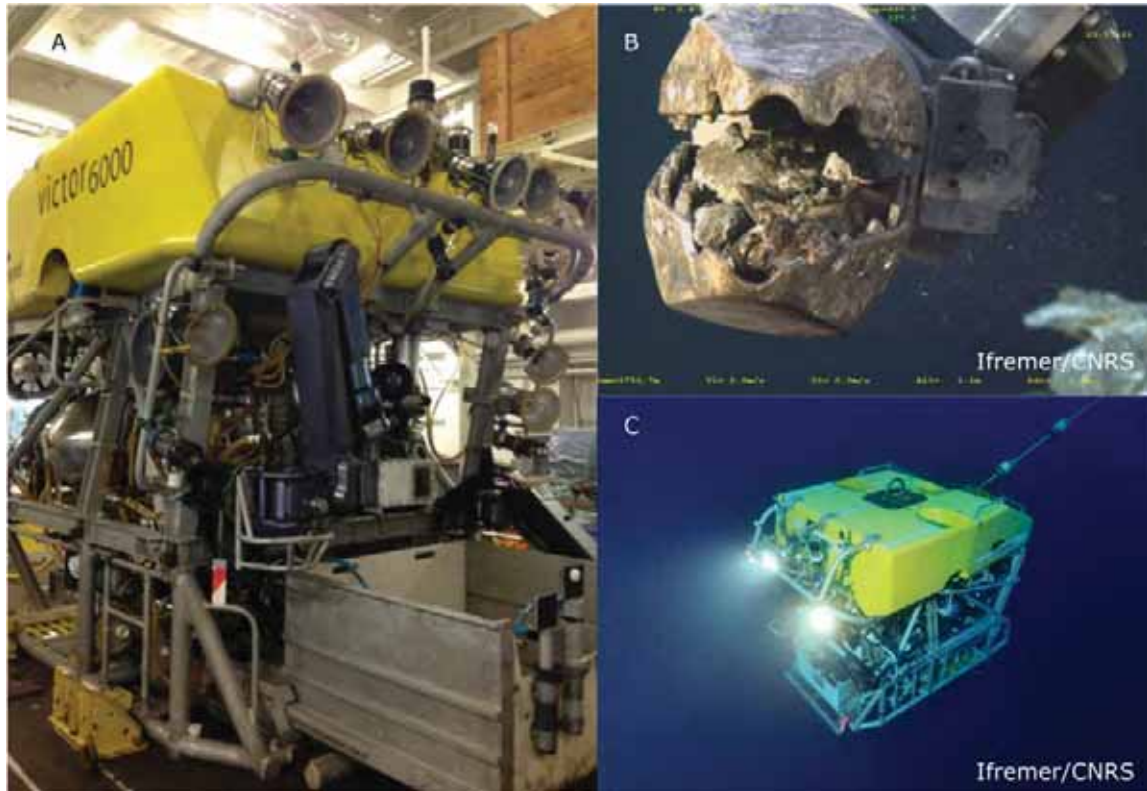


Figure III - 2 Photographs of the ROV on board the ship during maintenance (on the left), while sampling rocks with maestro (top right), and under water photograph of the oceanographic robot (bottom right).

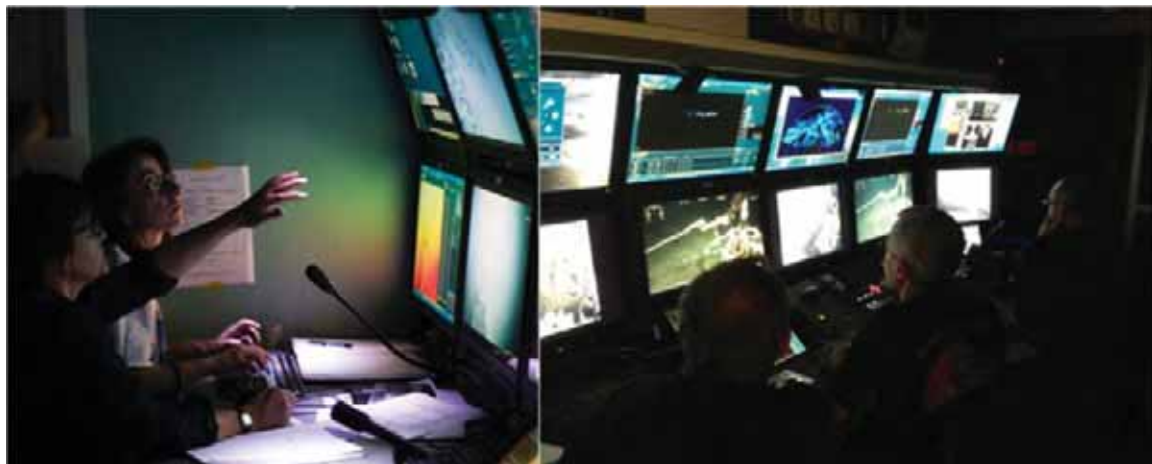


Figure III - 3 Photographs of the ROV container. On the left, the two scientist in charge of the dive program. On the right, ROV pilots, one is in charge of the Maestro arms and the other control the whole ROV mobility.

The sampler used for HT fluids is a titanium gas-tight syringe capable of resisting a temperature above 400°C and corrosion (Fig III - 4). Titanium material is used because of its chemical inertia and its pressure and temperature resistance. These samplers were borrowed from Ifremer biogeochemical department (P.M. Sarradin, Laboratoire des

Environnements Profonds). Handles were made at the GET mechanical workshop by Pascal Gisquet and Alain Castillo to allow ROV manipulation. On board, conditioning of high temperature fluid sampler consists in using a primary vacuum pump to ensure an internal pressure lower than 10^{-1} mbars. At depth, each fluid sampler is mechanically triggered by the ROV arm (Maestro) which will push on the syringe's spring. Because of the differential pressure between the deep sea (at Lucky Strike, ~ 170 bars) and the internal pressure of the sampler (10^{-1} mbars), the fluid is sucked in the device in 2-3s.

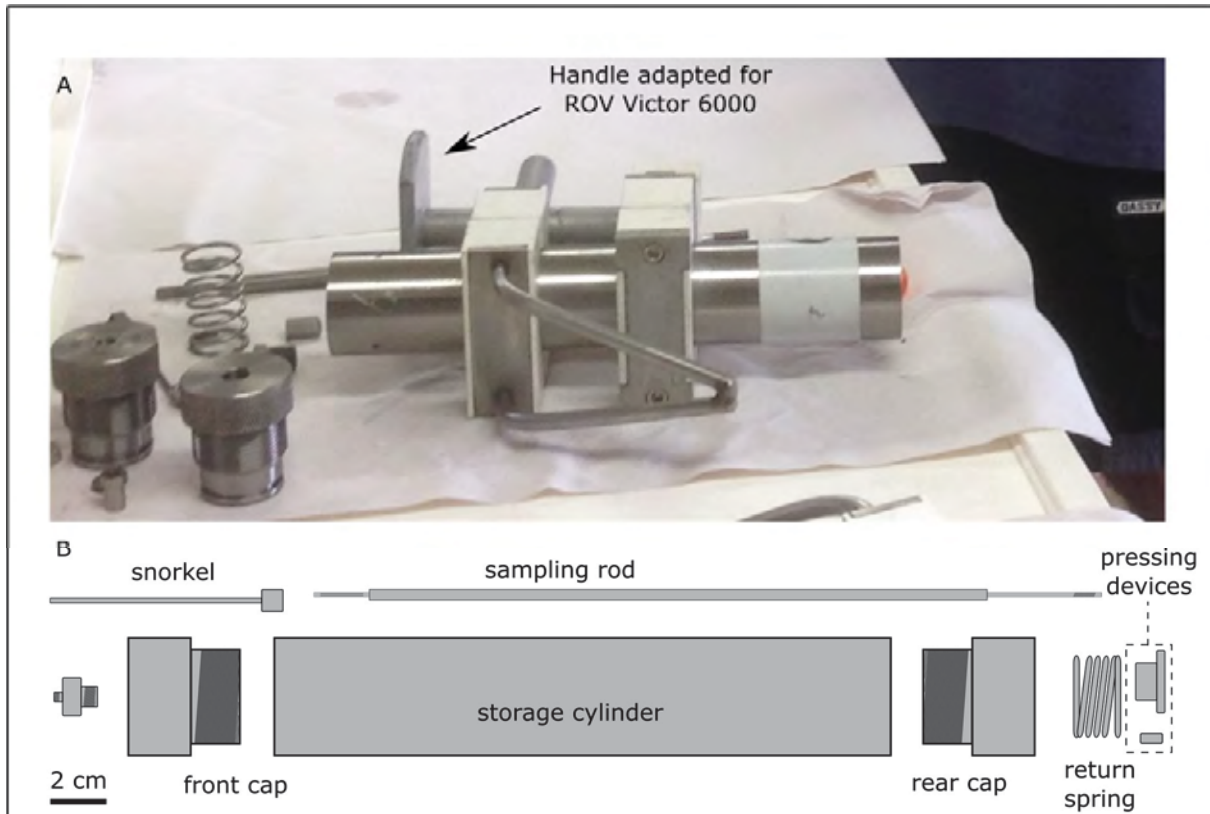


Figure III - 4 Photograph of a Titanium syringe with its handler during the cleaning process (top) and a cartoon showing the different part composing the sampler.

The collection of pure high temperature hydrothermal fluid is a difficult task to achieve because of the extreme environmental conditions at the seafloor.

This thesis has greatly benefited from earlier fluid sampling campaigns conducted by Valerie Chavagnac, Alain Castillo and Cédric Boulart. Since 2009, with the Bathyluck campaign and the deep-sea observatory program (EMSO Azores, which started in 2010) they developed an efficient sampling strategy. The aim is to secure, whatever the conditions are, a number of sampled sites which are representative of the chemical fluid diversity observed within the field. Therefore, specific sites are targeted each year and labelled as

Priority 1, (P1). The other sites are sampled when ROV operations and dive schedules allow it. The P1 sites are sampled each year to ensure a spatial and temporal coverage of the fluids diversity of Lucky Strike hydrothermal field. Before sampling, the ROV temperature probe is used to measure in situ the maximum temperature of the fluids but also to take marks at the position of the probe that give the highest temperature (purest fluid; Fig III - 5). Sampling is then a matter of replacing the titanium snorkel of the fluid sampler at the exact position of the temperature probe. If well positioned and if the fluid is hot enough, a white coloration of the snorkel indicates that the syringe is heated. At this moment, sampling can be done without taking risk of having much surrounding seawater entrained. This operation is, always, repeated 4 times per venting site in order to achieve a perfect determination of pure hydrothermal endmember (Fig III - 5). ROV dives generally last up to 36h with a full and diversified schedule. For practical reason (i.e. to avoid triggering of the fluid sampler in the ROV basket), collection of fluid samples is done preferentially at the beginning of each dive. Each fluid sampler is numbered (from 1 to 9), to record where each sampler was used and also to trace any mechanical malfunction from time to time.

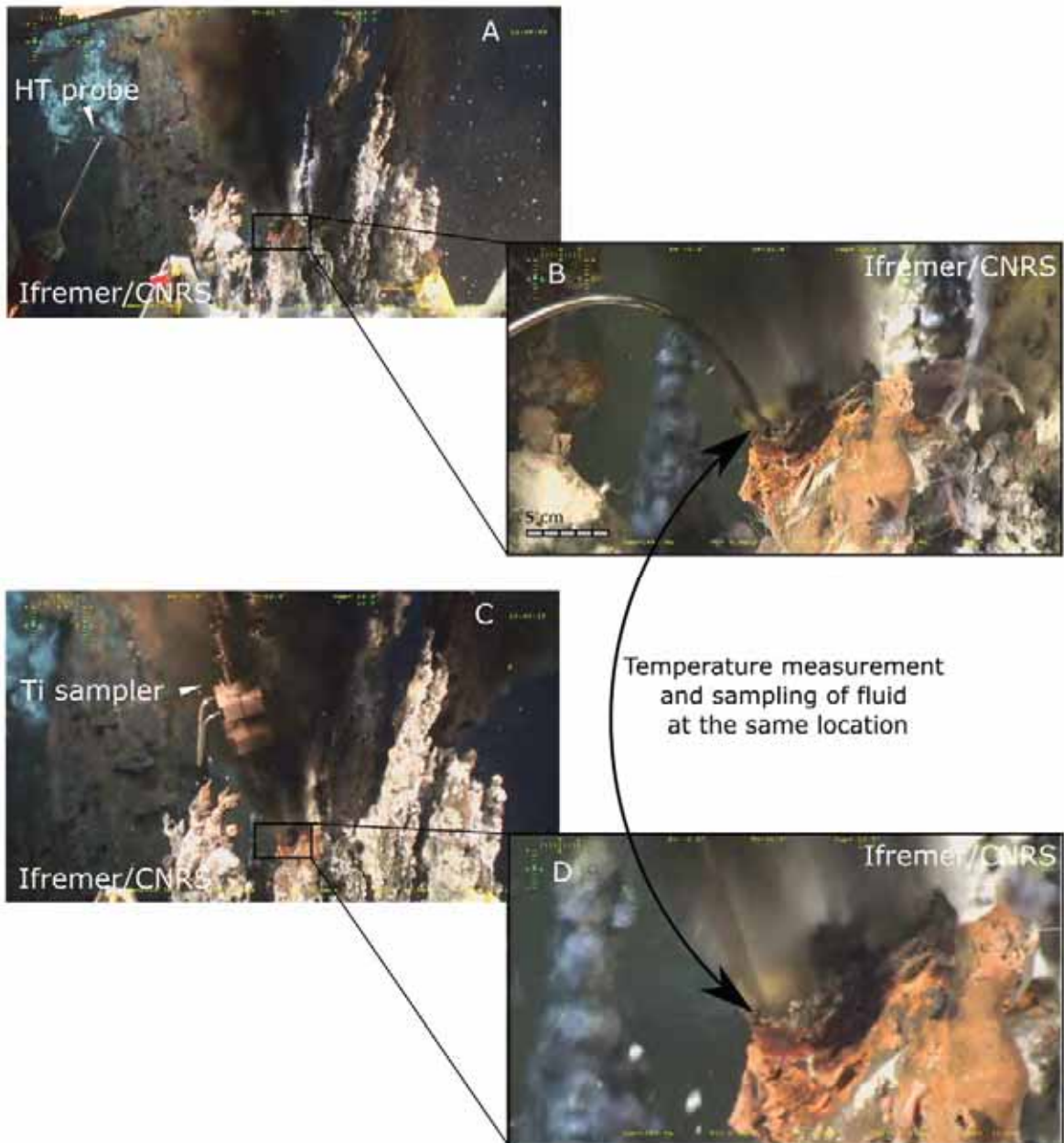


Figure III - 5 High temperature venting site Capelinhos. A and B show the temperature measurement using the HT temperature probe of the ROV Victor6000, B is a close up of the vent orifice where the temperature probe is inserted for real-time temperature measurement. It shows the position to take for fluid sampling. C and D pictures illustrates high temperature fluid sampling using gas-tight Ti syringe. A direct comparison between pictures B and D shows that snorkel of gas-tight Ti syringe is positioned at the same location as the temperature probe of ROV Victor6000, ensuring sample collection at the hottest hydrothermal fluid discharge.

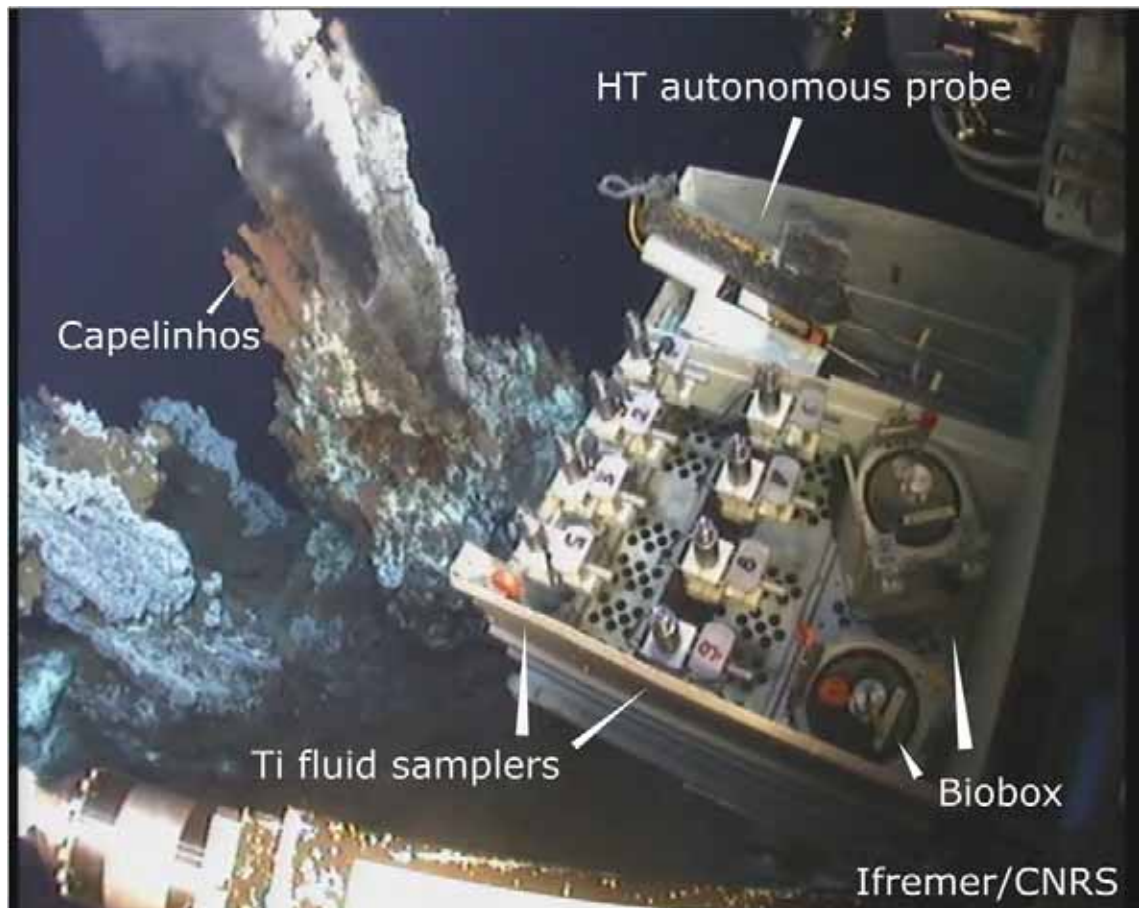


Figure III - 6 ROV basket facing the Capelinhos vent site during the 2015 cruise. The ROV basket contains 8 Ti samplers, 2 Biobox (Sterile boxes for biologic sampling purposes), and 2 HT autonomous probe, positioned in vent after fluid sampling at the same location. The photofragh is taken from the cemra placed on the ROV arm Sherpa.

As far as possible, the sampling strategy is always the same. In the frame of the deep sea observatory, sampling of biological material, geophysical measurement and hydrothermal fluid sampling are all accounted for to optimize the duration of the operations, the coherence of the acquired data/samples and the efficiency of dive schedule. Therefore, at each site, the sampling begins with biological material (e.g. hydrothermal chimney) in a Biobox (sterilized box only opened right before the sample is collected). The autonomous HT probe, which was installed in the previous year, is recovered. Then, the temperature is measured by the HT probe of the ROV. The real time observation of fluid temperature helps positioning the fluid sampler to obtain the purest fluids (Fig III -5). Four fluids volumes are sampled one after the other at the same orifice (Fig. III - 5). A new autonomous HT probe is installed at the same orifice, and left on site for an additional year.

When the ROV Victor 6000 is recovered on board of the research vessel, fluid samplers are immediately rinsed with clean tap water to wash away any seasalts, dried with an air

compressor and then transported to the wet laboratory (Fig III -7 and 8). First of all, the gases are extracted and stored into a stainless steel canister (Fig III -7). Fluids are then extracted, filtered (0.45µm Millipore HPAP) and dispatched into different aliquots (for major and trace cations/anions for Sr and Li isotopes analysis), each of them for specific analysis (Table 1).

Table III - 1 Presentation of bottle type and volume dispatched in different aliquots.

	Analyte	type of bottle	volume in the aliquots		instrument
On board	H ₂ S	LDPE bottle	30	unfiltered	H ₂ S electrodes
	Salinity/pH/Eh conductivity/TDS	LDPE bottle	30	filtered	pHmeter electrodes
On shore	Sr isotope	glass bottle	2	filtered	TIMS
	Li isotope	glass bottle	2	filtered	MC-ICP-MS
	Cations	LDPE bottle	100-125	filtered	ICP-OES/MS
	DIC	glass bottle	18	filtered	Carbon Analyzer
	Anions	polypropilene centrifugation tube	2	filtered	Ion Chromatography
total volume (ml)				~200	

By using different aliquots, we limit the risks of pollution of the whole sample. A 30mL LDPE bottle is kept for on-board analyses for pH, Eh, salinity, H₂S, and conductivity measurements. We also measure Fe concentration in fluids using a photometric instrument that provides a first indication of the Fe concentration in the fluid.

After fluid extraction, each part of the samplers is acid washed, rinsed with ultrapure MQ H₂O and dried. The parts are reassembled and the Ti gas-tight syringe is put to a pressure <0.1mbars by a primary vacuum pump.

Table III - 2 Summary of fluids samples collected during the three MoMAR cruises

Year of collection	number of sites covered	number of samples	% of pure fluid samples	Boxplots of Mg concentration (mM) for all the samples of each year
2013	12	37	71	
2014	13	49	87	
2015	13	57	84	

In total, for three scientists, it takes up to 1h30 to process entirely one sample from recovery at the ROV basket to the end of sampler conditioning. It means that each site sampled requires ~7h working hours from sampling at depth till on-board chemical analyses. 12 different hydrothermal sites have been sampled in 2013 (Table 2), which represent 91h. From 2013 to 2015, the number of collected samples increased significantly from 37 to 57, which is mostly due to upgrading the gas extraction system and adapting the handler by the GET mechanical workshop for improved ROV operations.



Figure III - 7 Photographs taken during the process of sample extraction in MoMARsat 2013. A: Mounting of a stainless steel canister to extract the gases; B: Extracting the fluid with a plastic syringe to be filtered through a 0.45 μ m Millipore filter and dispatched in several aliquots (C) Labelled aliquots of fluids and gazes dispatched on the working table.

2 On board analyses

pH measurements are conducted with an electrode calibrated at the beginning of the cruise with pH 4 and 7 buffer solutions. Most fluids have low $\text{pH}_{25^\circ\text{C}}$ comprised between 2.5 and 5. Eh, conductivity and salinity are calibrated using an adapted, commercialized and certified standard solution. Salinity is also measured by a refractometry at 20°C . Dissolved H_2S has been measured since the 2014 campaign using an electrochemical probe (MS08 from AquaMS) which allows continuous H_2S measurement. The dissolved H_2S react with a redox catalyzer. Oxidation of H_2S on the electrode produce an electric current that is proportional to the H_2S concentration. The current is then converted to a concentration. The electrode is coupled to a pH electrode, the coupled H_2S concentration and pH are used to determine the concentration of total dissolved sulfide. The precision is 2% and the calibration has been performed by the manufacturer.

3 On shore analyses

3.1 Anions

The major anions present in the hydrothermal fluid are chloride Cl^- , sulfate SO_4^{2-} , and bromine Br^- . They are measured using a technique called High Precision Ion Chromatography (HP-IC). This is a method based on differential retention time of these anions while flowing through a column containing anionic exchange resin. The results are displayed as peak areas identified by specific retention time for each element of interest. A calibration to convert peak area and concentration has been performed using a IAPSO standard solution (OSIL Ltd., UK) which contains Cl, SO_4 and Br. The concentrations of IAPSO are calculated from relations between salinity and major element in seawater (Millero et al., 2008). The maximum charge accepted by HP-IC is 500ppm, which implies that all fluid samples are diluted to different proportions.

Prior to each analyses session, four IAPSO standards were prepared by dilution factors of 400, 200, 150 and 100, while all fluid samples are diluted at 180 times. IAPSO seawater standard corresponds to Cl, SO_4 and Br concentrations of 19370 ppm, 2712 ppm and 67 ppm, respectively. Br is closely related to Cl concentration and less abundant by 3 orders of magnitude.

Peak area determination and derived concentration of samples were conducted using the Chromoleon software.

A IAPSO standard of known Cl, SO₄ and Br concentration, is analyzed as a sample every 8 samples to monitor the instrumental drift during the course of the analysis as shown for Br in Fig III - 8. The deviation is always below 5%, corresponding to a maximum Br concentration correction of ~7 μmol/l.

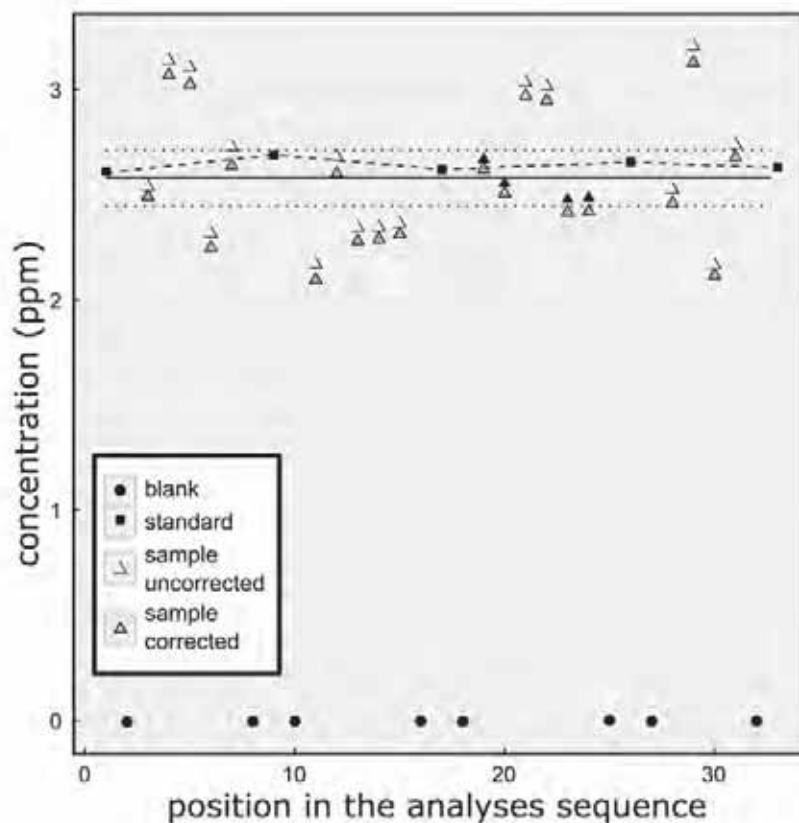


Figure III - 8 Drift correction of samples framed by standards and blanks. Drift is extrapolated from a standard to the following standard in the sequence. Correction is applied to measured value of a sample according to the extrapolation of the standard measurement deviation. Solid line is the “true” concentration of the standard and dashed lines and 95% confidence interval.

3.2 Major cations

Major cations were measured using Inductively Coupled Plasma- Atomic Emission Spectrometer (ICP-AES). This method allows simultaneous analyses of a broad range of elements. The ICP-AES is analogue to Flame Atomic Absorption Spectrometer (FAAS) and Flame Atomic Emission Spectrometer (FAES) but has a “flame” temperature of 6000 to 10000 K. The sample is ionized into an argon plasma as an aerosol after passing through a nebulizer. When the sample dissociates in the plasma, atomic and ionic spectral lines are excited and detected by photomultipliers. The signals are compared to calibration lines and converted from intensities to concentrations (Rollinson, 1994).

For Mg, Na, Ca and K analyses, a IAPSO standard solution is used as a calibration standard. Because they are abundant in seawater and because NaCl-rich solution tends to clog the introduction system by precipitating halite, samples and standard are diluted at different factors depending on the element. The methodology has been described in a publication (Besson et al., 2014).

Measurements of Na, K, and Ca required a dilution factor of 30, while Mg, which is close to zero in the purest samples, only needed a dilution factor of 10.

Si is enriched in black smoker fluid but not in seawater, so Si standard were prepared with a mono-elemental solution provided by Horiba and diluted to cover the expected concentration of the samples. To avoid NaCl effect of the matrix, samples were diluted 10 times. Drift correction was conducted as illustrated in Fig III - 8.

Fe and Mn are virtually absent in seawater but enriched in black smoker fluids. The concentrations of these elements in our samples were analyzed on pure samples, except for sample from the Capelinhos site (see Fluid chemistry section) which is highly concentrated compared to the other fluids. In 2013, the standard was prepared using a multi-elemental solution provided by Horiba (Mix21). In 2014 and 2015, the standards were prepared with a multi-elemental solution in a 35g/kg NaCl matrix to match the expected concentration of the samples. Some samples from 2013 have been measured again to confirm the validity of the measurement and indicated similar concentrations. The heavy charged solution of the pure sample has shown to affect significantly the sensitivity of the analysis over 20 samples. Rinsing the entire system has been done systematically after each 20 samples with HNO₃ 5% for at least 4h before a new analysis sequences can be run.

3.3 Trace elements

Trace element concentrations were determined using an Inductively Coupled Plasma Mass Spectrometer (ICP-MS) quadrupole instrument. The introduction and ionization system is the same as for ICP-AES. Ions are extracted from the plasma into a pumped-vacuum system and focused through an ion lens into a mass spectrometer (Rollinson, 1994). The quadrupole consist of 4 metal rods parallel to the ion beam and pair-connected. Voltages applied to the rods, cause the ions to oscillate. Oscillation magnitude is controlled by mass and charge of the ion. The ion can then be ejected from the stable ion beam depending on the oscillation magnitude applied. So depending on voltage, the rods filter the selected ions (Linge and Jarvis, 2009).

Sr, Rb and Cs (among others: Cu, Zn, and Al, etc...) were measured on a quadrupole ICP-MS Agilent at GET laboratory for 2013 samples and at Hydrosience Montpellier for samples from 2014 and 2015 surveys.

For 2013 samples, fluids have been diluted 180 times to allow passage analysis without clogging the sample introduction system. Before analysis, each individual samples was weighted and doped with an In/Re solution to serve as an internal standard. This allows drift correction with a close look on instrumental sensitivity. Fluids analyzed at Hydrosience Montpellier allowed less dilution, each samples was diluted to attain 500ppm of charge corresponding to dilution between 80 and 60 times.

3.4 Rare Earth Elements (REE)

REE concentrations were determined by Sector Field-Inductively Coupled Plasma- Mass Spectrometer (SF-ICP-MS) element XR coupled with Aridus2 Desolvator introduction system. In this type of ICP-MS, a magnetic field is applied perpendicular to the ion beam. This drives the ions to a circular motion whose radius depends on the magnetic field and the ion velocity. Ion travelling a particular arc will pass through narrow slit and reach the detector. Mass resolution is controlled by the width of the slit (Linge et al., 2009). At the beginning of an analysis sequence, a spiked SLRS-5 solution (international standard for river water, certified for all the REE) has been ran and gave the certified value for REE concentrations. REE measurements are highly sensitive to oxide interference caused by species that bond with oxygen. Then a Ce mono-elemental solution has been ran to evaluate the oxide formation percentage. CeO (mass 140+16) interferes with the Gd mass of 156. So the Gd analyzed for this sample is only due to oxide formation with Ce, then the calculated percentage of oxide will be corrected as well as the blank to the signals. The use of the Aridus 2 desolvation system lowers drastically the oxide formation (~0.05% on CeO).

Isotopic Dilution (ID)

Isotopic dilution is a method consisting in measuring an isotopic ratio to constrain an unknown concentration. To do so, an artificial solution, called “spike” with unnatural isotope abundances of the concerned element, will be added to the sample (natural abundances). The result is a mixed isotopic abundance between the spike and the sample. The measured isotopic ratio will depend on the weights and concentrations of both sample and spike. This is described by the ID equation:

$$[REE]_{spl} = [REE]_{spk} \times \frac{W_{spk}}{W_{spl}} \times \frac{M_{nat}}{M_{spk}} \times \frac{A_{spk}^2}{A_{nat}^2} \times \frac{(Rs-Rm)}{(Rm-R)} \quad (1)$$

X: spike=spk; sample=spl.

$[REE]_X$: REE concentration in spike/sample.

W_X : Weight of spike/sample.

M_X : Molar weight spike/natural.

A_X^n : #1 or #2 isotope abundance spike/natural.

R_X : #1/#2 isotope ratio for the spike/natural/mix (Rm; what we measure).

The error M on the ID equation is defined as follow:

$$M = \frac{(Re-Rs) \times Rm}{(Rm-Re) \times (Rs-R)} \quad (2)$$

From this relation, an ideal Rm can be calculated for the minimum M. Rm_{ideal} is derived from the following equation:

$$Rm_{ideal} = \sqrt{Rs * Rm} \quad (3)$$

In order to characterize the fourteen REE, we chose ^{150}Nd and ^{172}Yb spikes as representative of the light REE and the heavy REE respectively. Furthermore, a third spike of ^{153}Eu is used to ensure its concentration measurement because Eu behaves differently than the other REE in reduced solution such as hydrothermal black smoker fluids. The trispike solution has been tuned to hydrothermal fluid based on data from Douville et al., (1999), and prepared to reach as close as possible the Rm_{ideal} of each element when samples are spiked.

Sensitivity of the measurement during the analysis sequence may influence an external standard calibration, but such variations will affect both isotope in the same way. As a consequence, variations in sensitivity will not affect the measured ratio (Rm) of the spiked

elements. Furthermore, once spiked, (partial) sample loss will not change the Rm value and the concentration can be measured correctly.

Separation protocol

REE are present in seawater at low concentrations (few ppt). Hydrothermal fluids are enriched in REE compared to seawater by 10 to 100 times. To measure such low concentrations in a NaCl rich fluid, REE need to be separated/preconcentrated from the matrix. The chemical protocol used in this study is adapted from a seawater protocol used at the LEGOS laboratory which uses co-precipitation of REE with Fe oxyhydroxide. The LEGOS protocol consists in the addition of iron solution to an already spiked seawater and then co-precipitation of REE with Fe oxyhydroxide.

The trispike was added to the samples in an amount dependent on the estimated REE concentrations. Because black smokers already contain iron in a reduced form, no iron was added to the purest hydrothermal samples but some of it was added to hydrothermal plume samples (Saleban Ali, 2016). Furthermore, as black smokers' fluid are reducing, a droplet of clean H₂O₂ was added to the solution to oxidize and put the iron on the ferric form. Then the pH is risen up to 8 to induce the REE co-precipitation with iron oxy-hydroxide. After co-precipitation in 50ml Falcon centrifugation tube, 24h are needed to allow sedimentation of iron particles, after which supernatant is removed and the aliquots are refilled with ultrapure water (H₂O MQ) and centrifuged. This operation is repeated 3 times to ensure that a maximum NaCl is removed from the matrix. When rinsed, the iron precipitates are dissolved in HCl 6N to be transferred in Teflon Beaker Savillex, then evaporated and dissolved in the appropriate acid for resin exchange separation. The figure III - 9 shows the resin exchange protocols for 1) iron separation and 2) residual Ba separation. This last part is especially important for hydrothermal fluids as these solutions are enriched in Ba compared to seawater. Ba needs to be removed because it may interfere with Nd masses when forming oxides or hydroxides during HR-ICP-MS analyses. As Nd is in the tri-spike, it is crucial to separate well Ba. We use a trispike solution (¹⁵⁰Nd, ¹⁵³Eu, and ¹⁷²Yb) to spike the samples. The elements are determined by external calibration by a multi-elemental solution containing all the REE and prepared at 10, 50 and 100 ppt. The measured external concentration is compared to the ID calculated concentration to determine the recovery % (recovery in % = 100*[c]_{ext.} / [c]_{di}). The recovery is used to extrapolate to the non-spiked REE concentration assuming linearity of recovery between Light-REE Nd, to Heavy-REE Yb. This method has proved to be efficient by comparing a double spike (Nd, Yb), to a

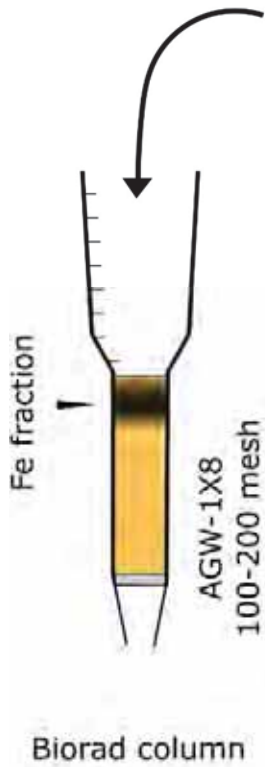
multispike method (Rousseau et al., 2013). The trispike characteristics used are indicated in Table III – 3:

Table III - 3 Trispike characteristics used in REE measurement protocol.

	Nd	Eu	Yb
[c] ppb	8,021	9,302	0,533
isotope #1	150	151	172
isotope #2	146	153	174
A¹_{nat}	0,056	0,478	0,218
A²_{nat}	0,172	0,522	0,318
A¹_s	0,978	0,977	0,949
A²_s	0,004	0,023	0,012
Me	144,237	151,964	173,038
Ms	149,806	150,966	171,968
Re	0,327	0,916	0,686
Rs	222,364	42,503	79,083
Rm_{ideal}	8,533	6,240	7,365

Samples have been dissolved in a same batch of HNO₃ 0.3N doped with In/Re solution to ~0.1ppb. They all have the same In and Re concentration, which allows a very close look on sensitivity monitoring.

1st purification



	acid	volume
cleaning	HCl 0.1N	5
	HCl 6N	5
conditioning		5
sample introduction	HCl 6N	1
		0.5
REE recovery		4
Fe elution	HCl 0.1N	8
cleaning	HCl 0.1N	8
	HCl 6N	10
	HCl 1N	5
storage	HCl 1N	

2nd purification

	acide	volume
cleaning	HNO ₃ 2.5N	10
	mQ H ₂ O	1
	HCl 6N	10
conditioning	HCl 2N	2
sample introduction		0.5
élution Sr	HCl 2N	0.5
		3
élution Ba	mQ H ₂ O	1
	HNO ₃ 2.5N	8.2
REE recovery	mQ H ₂ O	1
	HCl 6N	15
cleaning		10
	mQ H ₂ O	2
	HNO ₃ 2.5N	10
	mQ H ₂ O	2
storage	HCl 1N	2

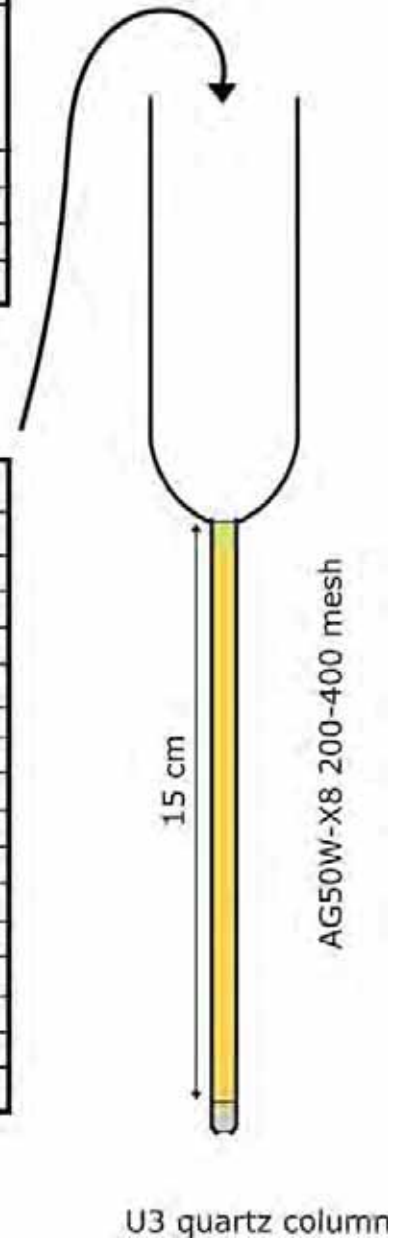


Figure III - 9 Description of REE separation through resin exchange protocol

3.5 Sr isotopes

Sr isotopes have been measured using a Thermal Ionized Mass Spectrometer (TIMS) Mat Finnigan261. Samples are purified chemically and deposited on a high melting point metal filament. When heated, elements are ionized and guided to a curved tube through a powerful electromagnet which splits the atoms according to their mass. The obtained mass spectrum allows calculation of isotopic ratios (Rollinson, 1994).

For our samples, Sr is separated by passage through ion exchange resin, Sr-spec provided by Eichrom. 1.6ml of resin were rinsed and introduced into Teflon column. Samples have been weighted and evaporated in Savillex beaker in order to obtain 300 to 500 ng of strontium. The residu was dissolved into 0.5ml of HNO₃ 2N. Sr is eluted from the matrix with H₂O MQ. The Sr fraction is evaporated on a tungsten filament (previously degassed) using a H₃PO₄ solution (150μl). Before each run of analysis, an international standard is measured to check on the accuracy of the measurements. The standard used is NBS-987 and was measured at ⁸⁷Sr/⁸⁶Sr value of 0.710250 (2σE=0.000011; n=14). The accepted value for NBS-987 is ⁸⁷Sr/⁸⁶Sr=0.710248 (2σE=0.000011; Thirlwall, 1991).

3.6 Li concentration analysis

As Li concentration measurement was not a classic type of analyzes at the GET laboratory before this thesis, a special treatment was necessary to assess the reliability and accuracy of the measurements. We conducted several sequences of analysis to check on the effect of salinity on Li measurement. The results of this investigation are presented in an article that was submitted to Geostandard and Geoanalytical Research.

Measurements of Lithium in Seawater by Inductively Coupled Plasma-Atomic Emission Spectrometry: IAPSO Seawater reference material measurement and applications to Black Smoker Hydrothermal Fluids

Thomas Leleu^{1,*}, Valérie Chavagnac¹, Philippe Besson¹

1 : Géosciences Environnement Toulouse, GET UMR5563, Observatoire Midi-Pyrénées, Université de Toulouse, 14 Avenue Edouard Belin, 31400 Toulouse, France

*: corresponding author: thomas.leleu@get.obs-mip.fr (05 61 33 26 63)

Keywords: ICP-AES, IAPSO, seawater, lithium, hydrothermal fluids

Submitted at Geostandard and Geoanalytical Research in February 2015 (GGR-0353).

Abstract

We report on a analytical procedure to determine Li concentration in seawater and seawater derived hydrothermal fluid using inductively coupled plasma-atomic emission spectrometry (ICP-AES) with no sample preparation prior to analysis and validation by measurement on their matrix-match standard IAPSO reference material. Several matrixes have been used to test their effect on measurement accuracy. No significant biases were observed. The best results for IAPSO measurement of Li concentration were obtained when direct analysis were conducted with no other preparation. A value of 0.171 ± 0.002 (1s) $\mu\text{g g}^{-1}$ ($24.6 \pm 0.3 \mu\text{mol l}^{-1}$) is obtained for IAPSO which is really close to published values of $0.187 \mu\text{g g}^{-1}$ ($27 \mu\text{mol l}^{-1}$; Gieskes et al. 1991). The method has been successfully applied on hydrothermal fluid samples as testified by a good Li vs Mg correlation ($R^2 > 0.99$).

Introduction

Lithium element and its stable isotopes are becoming a key element to characterize silicate erosion budget and palaeoclimatic reconstruction (Vigier and Godderis, 2014). Li content in hydrothermal fluid has been used to assess water/rock ratio and residence time of

seawater in hydrothermal systems (Foustoukos et al. 2004; Von Damm et al. 1985). The fractionation of Li stable isotopes entrained by basalt/gabbro dissolution and secondary mineral formation provides precious indicators of subsurface conditions in oceanic hydrothermal systems (Chan and Edmond, 1988; Foustoukos et al., 2004). In previous studies, different measurement procedures have been used to determine Li concentration in highly-charged solution, either with ICP-MS coupled with online isotope dilution technique (Foustoukos et al. 2004), FAAS (Riley and Tongudai, 1964; Angino and Billings, 1966; Burrell, 1967; Fabricand et al. 1967; Chester, 2009), FAES (Gieskes et al. 1991), and ICP-AES (Pester et al. 2011). Most of these studies provide neither the Li concentration measured in their matrix-match standard nor which standard they have used to validate their measurement. In the present study, we propose a detailed analytical and instrumental protocol using ICP-AES and IAPSO seawater as a reference material to determine precisely and accurately the Li concentration of seawater and seawater derived hydrothermal fluid.

Instrumentation

Analytical development was carried out at the Geosciences Environment Toulouse (GET, UMR5563 CNRS/UPS/IRD/CNES) on a ULTIMA 2 inductively coupled plasma-atomic emission spectrometer from Horiba Jobin Yvon Technology. Besson et al. (2014) presented a measurement protocol to determine major element concentration of seawater. Our instrumental and analytical procedure has therefore been based on this study. To enable analyses of heavily charged solutions, a specific nebulizer (PTFE Mira Nebulizer, supplied by Horiba Jobin Yvon Technology) was used to introduce the solution into the ICP-AES. The nebulizer was inserted into a glass cyclonic chamber and operated at a maximum sample flow rate of 1 ml min^{-1} and with a maximum total dissolved solute of 300 g l^{-1} . Li is a minor element in seawater and hydrothermal fluids, it is thus necessary to use pure samples to determine its concentration, while measurement of major species (Na, K, Ca) needed a 30-times dilution to be determined (Besson et al. 2014).

In order to counteract clogging, after each batch of analyses (approximately twenty samples), the sample introduction system (torch/nebulizer/cyclonic glass chamber) was rinsed online with HNO_3 5 wt% for 45 min with a high flow rate of 5 ml min^{-1} and dismantled after 4 runs of analyses of 20 samples each for further cleaning. All parts were immersed in a bath of HNO_3 5 wt% for 24hr at room temperature under a fume hood, then rinsed with Milli-Q water and dried in an oven at 50°C for several hours. The limits of quantification (LOQ) were determined by analyzing ten blank solutions of Milli-Q water

and were calculated as ten times the standard deviation. The value of LOQ presented in table1 is an average value of all LOQ values determined after each run (n=7).

Li concentrations in seawater and IAPSO standard seawater

Literature on Li concentration in seawater provides various data reported in figure III - 10. The Li concentrations are comprised between 0.170 and 0.194 $\mu\text{g kg}^{-1}$. Li in seawater is considered to be a conservative element closely related to salinity (Fabricand et al. 1966; Burrell, 1967; Wright and Colling, 1995). Several studies have investigated the Li-chlorinity ratio for various oceans. Riley and Tongudai (1964) compared 30 samples from different locations and found a covariance between Li and salinity regardless of the ocean with Li ($\mu\text{g g}^{-1}$)/Cl (‰) ($\times 10^3$) ratio of $9.39 \pm 0.17 \mu\text{g g}^{-1} \text{‰} (\times 10^3)$. Fabricand et al. (1966, 1967) studied the variation of Li with depth in three locations in the Atlantic ocean ($10^{\circ}59'N$, $49^{\circ}36'W$, n=21, $18^{\circ}59'N$, $22^{\circ}30.54'W$, n=16 and $10^{\circ}56'N$, $49^{\circ}30'W$, n=22, respectively) and found average correlation of Li/Cl(‰) values of 8.71 ± 0.14 , 9.03 ± 0.16 and $9.17 \pm 0.10 \mu\text{g g}^{-1} \text{‰} (\times 10^3)$ respectively. Burrell (1967) found a correlation of $9.0 \pm 0.2 \mu\text{g g}^{-1} \text{‰} (\times 10^3)$ in South Atlantic Ocean. This range of Li-chlorinity ratio applied to IAPSO salinity of 34.991 g l^{-1} (Batch P150, 22/08/2008) leads to a range of $0.169 \pm 0.003 \mu\text{g g}^{-1}$ to $0.183 \pm 0.003 \mu\text{g g}^{-1}$ based on the relation $S(\text{‰})=1.80655 \cdot \text{Cl}(\text{‰})$; Millero et al. 2008).

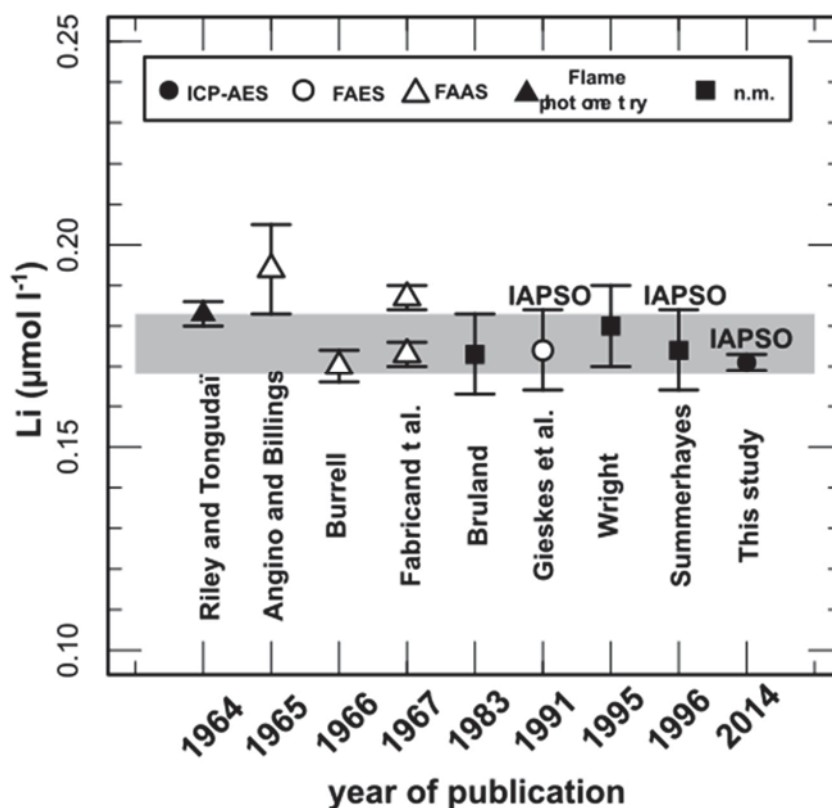


Figure III - 10 Reported seawater Li concentration in literature. Question mark corresponds to methods not mentioned within reference. The grey area corresponds to lower and upper limits of calculated IAPSO Li concentration value based on $S(\%)=34.991 \text{ g l}^{-1}$ and Li-chlorinity ratio from Fabricand et al. (1966) and Riley and Tongudai, (1964), respectively.

Data acquisition and processing

ICP-AES instrument was calibrated with a mono-elemental Li 2 wt% HNO₃ solution of 1000 μg g⁻¹ concentration supplied by Horiba Jobin Yvon (catalogue number: JYICP-LI, Lot No. LI1050711). The solution was diluted at different level in 5 wt% HNO₃ so as to obtain a calibration range between 0.2 μg g⁻¹ and 5 μg g⁻¹. The calibration curve obtained had squared fit regression coefficient better than 0.999 for each run. A first set of solution of Li doped at 1 μg g⁻¹ in Milli-Q ultrapure water was performed to check on the best set of parameters for the ICP-AES analyses at the beginning of the project. A memory effect has been observed in blank analyses after calibration, as evidenced by a residual 0.01 μg g⁻¹ in a blank solution. This issue was corrected by increasing rinsing time from 30 to 240 seconds. A second set of the same solution has been run to check on drift through analyses. The drift has been evaluated by ten consecutive measurements of the 1 μg g⁻¹ solution

which give an average concentration of $1.029 \pm 0.004 \mu\text{g g}^{-1}$ (1s). Matrix effects have been tested using different certified solutions and concentrations are reported in Table 3. Mix21 standard is a multi-elemental solution of $100 \mu\text{g g}^{-1}$ provided by Horiba Jobin Yvon (catalogue number: JYICP-MIX21, Lot No. M260110) and the Spex standard is a SPEXertificate® multi-elemental solution with 35 g l^{-1} NaCl solution in 5 wt% HNO₃ (catalogue number: XSPEXF-2782, Lot No. 24-123CR). The different solutions do not contain any Li and are used to observe the effect of other elements and/or salt on Li determination. They were prepared by dilution and addition of mono-elemental Li solution to attain the range of interest for Li concentration and matrix. For low Li concentration (0.7 and $1.5 \mu\text{g g}^{-1}$) there is no obvious salinity effect. For higher concentration, a small decrease of measured Li compared to theoretical Li is observed at increasing salinity content. Nevertheless, measurements at salinity of 35 g l^{-1} NaCl are in agreement with theoretical concentration. Linear regression performed on the different matrix gives intercept lower than $0.01 \mu\text{g g}^{-1}$ (similar to our limit of quantification) indicating that the method is reliable and the salinity effect is not significant. Only one intercept for the highest salinity had a value of $0.12 \mu\text{g g}^{-1}$, due to a bias in the $3 \mu\text{g g}^{-1}$ Li solution. Based on the behavior of the other measurements at this salinity, a reasonable explanation is an error during manipulation and preparation of this solution. Limits of quantification and detection have been calculated for each run ($n = 7$) based on the standard deviation of 10 successive analytical blanks for each run. The mean limits of quantification and detection are $0.002 \mu\text{g g}^{-1}$ and $0.0006 \mu\text{g g}^{-1}$, respectively.

IAPSO as a reference material for measurements

Lithium concentration measurements of the IAPSO seawater reference material are shown in Figure III - 11. Both direct measurement and standard addition technique have been applied. The standard addition techniques give a range of Li concentration between 0.162 ± 0.010 and $0.190 \pm 0.010 \mu\text{g g}^{-1}$ (23.3 ± 1.4 and $27.9 \pm 1.4 \mu\text{mol l}^{-1}$) consistent with Li concentrations reported in the literature. The variation of Li concentration is nevertheless too large for reliable quantification (Figure III- 11). The discrepancy between our two standard addition tests can be explained by uncertainty subsequent to doping the IAPSO. The preferred method is the direct measurement of Li in IAPSO seawater reference material with no sample preparation which gives an average concentration of $0.171 \pm 0.002 \mu\text{g g}^{-1}$ ($24.6 \pm 0.3 \mu\text{mol l}^{-1}$; $n=4$). Direct measurements are within range error to what is accepted to be Li content in IAPSO and generally in seawater (Angino and Billings, 1966; Burrell,

1967; Gieskes et al. 1991; Riley and Tongudai, 1964; Summerhayes and Thorpe, 1996) as presented in Figure III - 11.

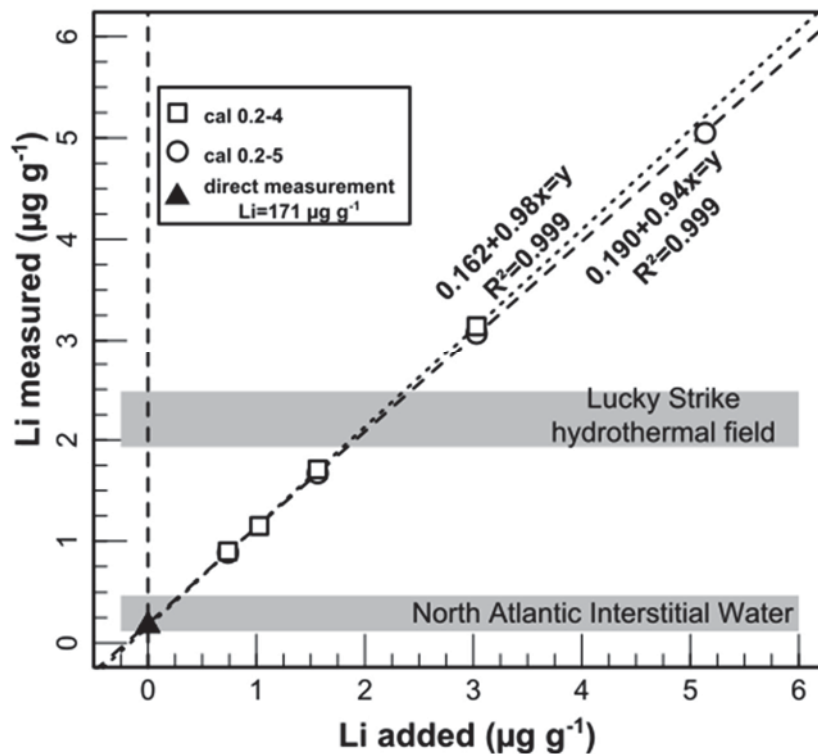


Figure III - 11 IAPSO seawater Li concentration determination. Full triangles are standard addition technique applied with calibration from 0.2 to 4 µg g⁻¹. Triangles are standard addition technique applied with calibration from 0.2 to 5 µg g⁻¹. Full square is the direct measurement of IAPSO. Grey areas corresponds to published values of Lucky Strike hydrothermal fluids and North Atlantic interstitial waters (Charlou et al. 2000; Gieskes et al. 1985).

A measurement method to precisely analyze Li concentration of a charged matrix such as seawater derived hydrothermal fluids has been developed with no need of sample preparation. Measurements on both synthetic seawater-like solution and IAPSO reference material show reliable data. Li concentration of IAPSO seawater reference material has been measured four times with a mean value of 0.171 ± 0.002 µg g⁻¹. Application to hydrothermal fluids shows really good correlation with measured Mg concentration ($R^2 > 0.99$) leading to Li end-member hydrothermal composition to be precisely and accurately determined.

3.7 Li isotopes determination

Instrument:

Li isotope measurements are conducted using TIMS or MC-ICP-MS. To use these instruments, it is necessary to first separate the Li element from the matrix.

Li isotopes separation

Li elution and separation from NaCl-rich matrix was carried out by ion exchange column. The protocol was developed by Jonathan Prunier based on the chemical protocol presented in James and Palmer (2000) and adapted to NaCl solution. The protocol uses a 2 column separation approach at the GET laboratory, Teflon column made on size and proposed by Millipore. The first passage separates Li from the other elements. However, because Li and Na have close elution peaks, we use a second column to remove any residual Na, because Na can affect Li isotopes measurement (Fig III -12B; Jeffcoate et al., 2004).

Li isotope composition

Li isotope measurements are performed by TIMS or MC-ICP-MS. The analysis of Li isotope ratio are biased by mass fractionation. To avoid biased measurement ratios a standard is run before and after the sample analysis. The Li isotope ratio obtained for the standard is biased on the same manner as for the sample. Therefore, by comparing the measurement on the sample with the neighboring standards, at the same conditions and concentrations, we can overcome the mass fractionation issue. This method is called “standard bracketing”. The standards used in Li isotopes are usually L-SVEC (provided by NIST) or IRMM-16. Both are in the form of lithium carbonate (Li_2CO_3) powders and have the same $^7\text{Li}/^6\text{Li}$ ratio which make them directly comparable (Abundances: $^6\text{Li}=7.5889\%$; $^7\text{Li}=92.4111\%$; $^7\text{Li}/^6\text{Li}=12.17714$; (Taylor and Wellum, 2003).

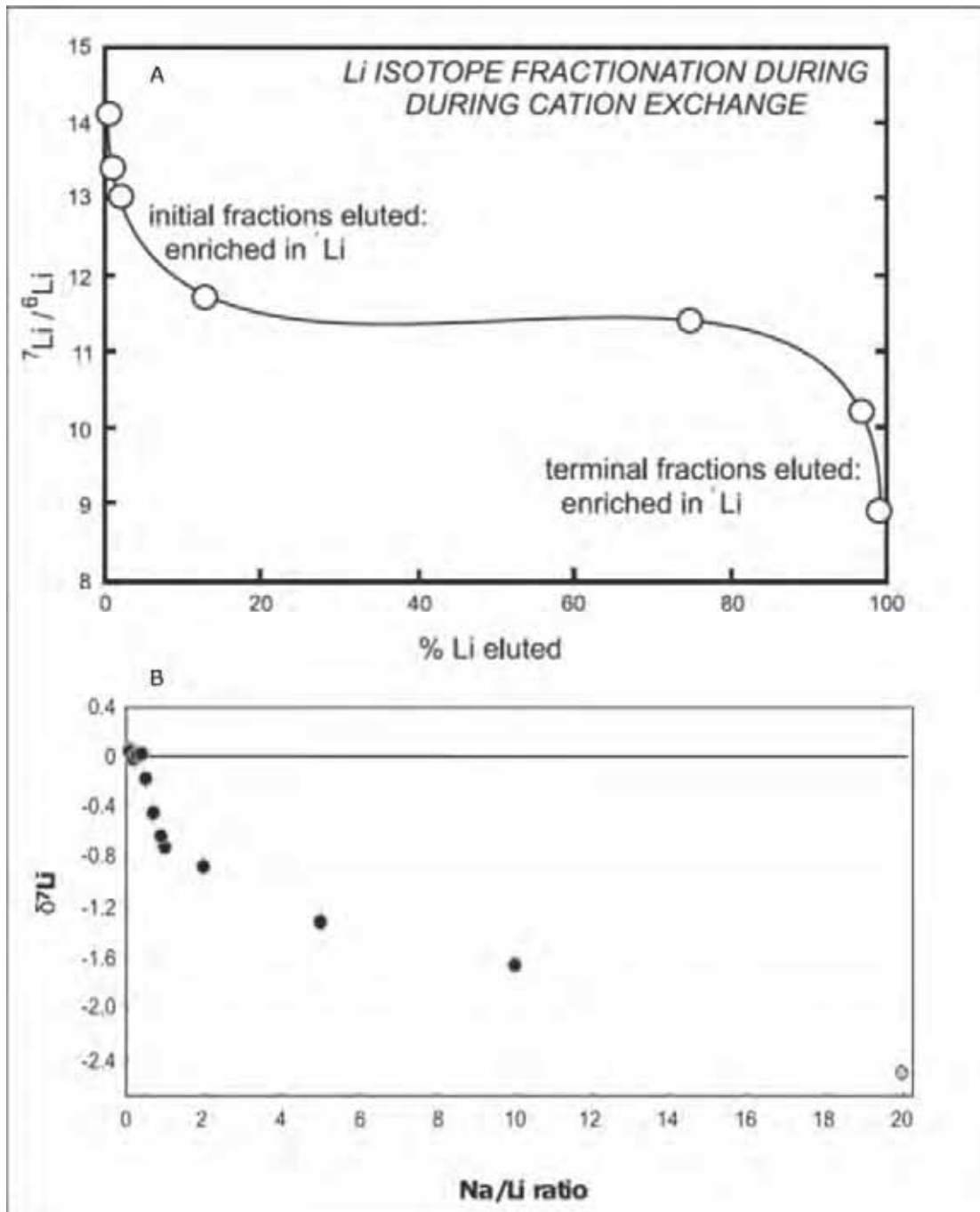


Figure III - 12 From Tomascak (2004), Ratio of ${}^7\text{Li}$ as a function of percentage of elution. It shows that the first fraction of Li eluted is significantly heavier until ~10% Li eluted then stable. At ~90% of elution, ${}^6\text{Li}$ increase and the ${}^7\text{Li}$ ratio is lower. B: From Jeffcoate et al. (2004), the figure show $\delta^7\text{Li}$ as a function of Na/Li ratio in solution. Addition of Na in solution tends to lower the measured value of $\delta^7\text{Li}$.

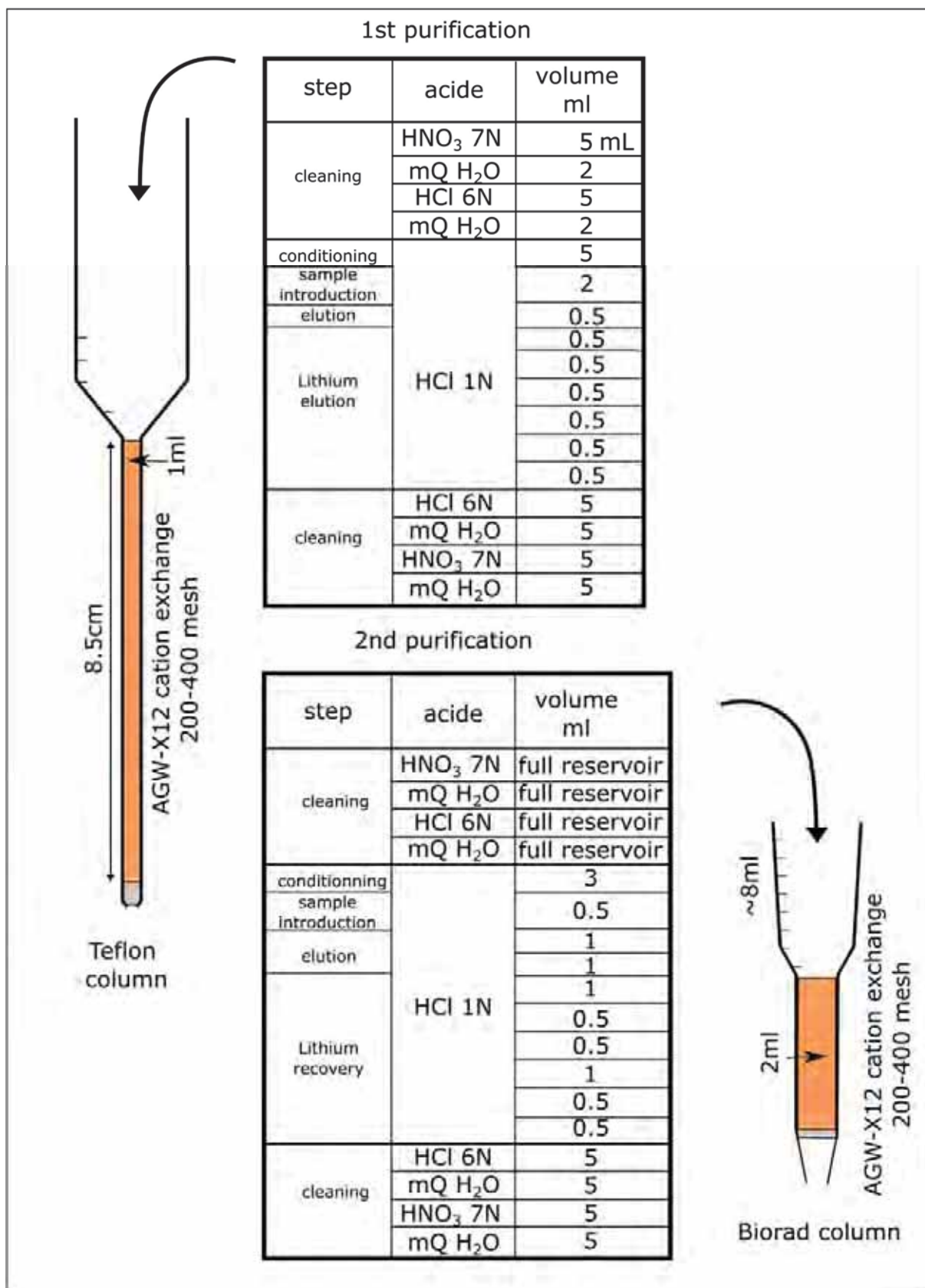


Figure III - 13 Description of the Li separation protocol through resin exchange column. All the acids used are prepared by dilution of bi-distilled acid.

As samples are compared to standard, Li isotope uses the delta notation terminology. This notation simplify interpretations by using more comprehensible number as the differences between the samples and standards are found after the 3rd decimal. The delta notation is derived following the equation:

$$\delta ^7Li = \left[\frac{\left(\frac{^7Li}{^6Li}\right)_{spl}}{\left(\frac{^7Li}{^6Li}\right)_{std}} - 1 \right] * 1000 \quad (4)$$

The Li isotope measurement presented in Fig III - 12B, varies depending on the Na/Li ratio of the analyte. A 1:1 ratio leads to a δ^7Li value of $\sim -0.8\%$ and as low as -2.4% for a ratio of 20:1. Furthermore, it is important to achieve a complete recovery of Li. As shown in Fig III -12A, Li fractionate during elution through columns (Fig III - 13), the first 10% of the Li eluted show a $^7Li/^6Li$ ratio between 12 and 14, enriched in Li^7 , while the last 10% show Li^7/Li^6 ratio between 9 and 10. This means that if a fraction of the Li is lost, it might greatly affect the measured ratio. The whole separation protocol is illustrated in Fig III -13.

Li isotopes have been analyzed by MC-ICP-MS Neptune at the GET laboratory in 2014 and at Ifremer Laboratory in Brest for 2015 and 2016. Prior to Li isotope measurements, it is necessary to determine the Li concentration of the studied sample so as to adjust the Li concentration of the standard to that of the samples. We determined that the concentration of the analyzed solution as well as the standard was optimal at ~ 350 ppb of Li in HNO_3 0.27-0.32N.

Different analysis sequences have been performed to determine this concentration and evaluate the charge effect on the Li measurement. To do so, a mono-elemental solution have been used to act both as a sample and a standard. Three concentrations have been prepared for the bracketing standard, 75, 175 and 350ppb. “Samples” were prepared at concentrations between 50 and 350ppb. The goal is to evaluate the effect on the measured delta notation of the sample Li concentration, for each of the three prepared standards. The results are shown in Fig III -14. First, the isotopic composition varies from -10 to 7% . The standard and samples have the same isotopic composition so the δ^7Li should be zero. The zero values for the samples are obtained when the concentration is equivalent to that of the standard. This highlights the charge effect which tends to bias the measured ratio in

response to the concentration difference between the sample and the standard. For the 75 ppb standard sequence, a small change in Li concentration of the analyte (compared to that of the standard at 75 ppb) leads to an important variation in $\delta^7\text{Li}$. For the sequence with a 350 ppb standard, the changes are tighter and no significant variations in $\delta^7\text{Li}$ is observed when the Li concentration is higher than ~ 280 ppb (80% of the Li concentration of the standard). This observation leads to the conclusion that samples and standards should be prepared so as to have a concentration of 350ppb.

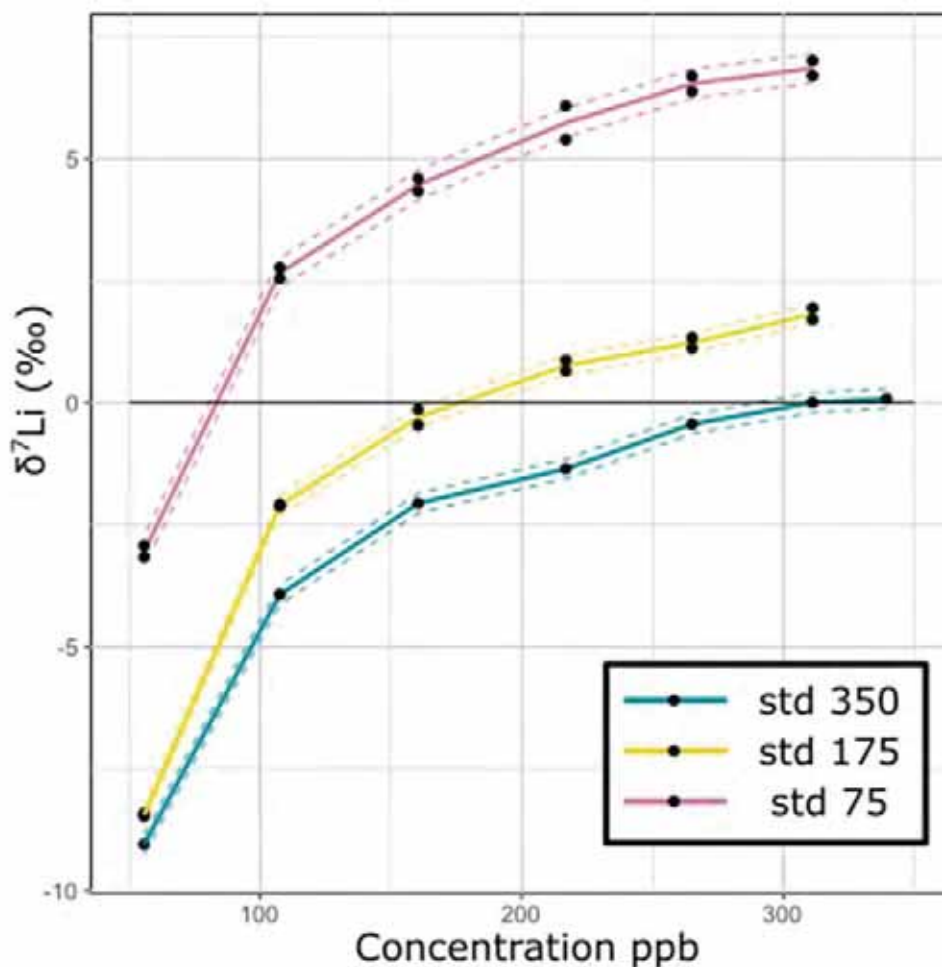


Figure III - 14 $\delta^7\text{Li}$ as function of Li concentration at 3 different bracketing standard concentrations. The figure shows the effect of the difference between sample and standard concentration on the $\delta^7\text{Li}$ measurement.

Two IAPSO samples have been processed through chemical elution protocol to assess the accuracy of our method. Due to low Li concentration in seawater (171 ppb) and high NaCl content (~ 35000 ppm), seven separations of 100ng of Li from IAPSO have been performed and reunified at the end of the elution in order to have a 2ml of solution with $[\text{Li}] = 350$ ppb.

When measuring the IAPSO bracketed by IRMM-16 standard solution, we obtained a $\delta^7\text{Li}$ of 30.3 ‰ (± 0.3) and 30.5 ‰ (± 0.3), consistent with expected values for seawater ($\delta^7\text{Li}=31\text{‰} \pm 0.5$).

3.8 Nd isotopes

Nd isotope determination were conducted by Hassan SALEBAN ALI during his Master thesis in the GET laboratory.

The isotopic composition of Nd was obtained by Nd separation through the same chemical protocol as described for REE concentrations with one additional step. The un-spiked samples were processed through the previous steps of co-precipitation, and double column exchange with an additional column to isolate Nd from the other REE. Nd is eluted from a Ln-spec resin with HCl 0.25M. Nd isotopic composition measurements were conducted at the IUEM laboratory in Brest on a Thermo-Ionized Mass Spectrometer (Thermo Finnigan Triton). The $^{143}\text{Nd}/^{144}\text{Nd}$ ratio was defined as the average of 100 measurements of ion intensities following the static collection mode. The $^{143}\text{Nd}/^{144}\text{Nd}$ ratios were normalized to $^{146}\text{Nd}/^{144}\text{Nd} = 0,7219$. Measured $^{143}\text{Nd}/^{144}\text{Nd}$ values for La Jolla standard of 1-5 ng Nd (recommended values of 0,511860) was $0,511850 \pm 12$ ($1\sigma\text{E}$, $n = 13$). The Nd isotopic composition uses a ϵNd notation to reflect the $^{143}\text{Nd}/^{144}\text{Nd}$ ratio compared to Chondrite Uniform Reservoir (CHUR) as follow:

$$\epsilon\text{Nd} = \left\{ \frac{\left(\frac{^{143}\text{Nd}}{^{144}\text{Nd}} \right)_{\text{sample}}}{\left(\frac{^{143}\text{Nd}}{^{144}\text{Nd}} \right)_{\text{CHUR}}} - 1 \right\} \times 10^4$$

References

- Angino, E.E., Billings, G.K., 1966. Lithium content of sea water by atomic absorption spectrometry. *Geochim. Cosmochim. Acta* 30, 153–158.
- Barreyre, T., Escartín, J., Garcia, R., Cannat, M., Mittelstaedt, E., Prados, R., 2012. Structure, temporal evolution, and heat flux estimates from the Lucky Strike deep-sea

hydrothermal field derived from seafloor image mosaics: hydrothermal outflow and image mosaics. *Geochem. Geophys. Geosystems* 13. doi:10.1029/2011GC003990

Besson, P., Degboe, J., Berge, B., Chavagnac, V., Fabre, S., Berger, G., 2014. Calcium, Na, K and Mg Concentrations in Seawater by Inductively Coupled Plasma-Atomic Emission Spectrometry: Applications to IAPSO Seawater Reference Material, Hydrothermal Fluids and Synthetic Seawater Solutions. *Geostand. Geoanalytical Res.* 38, 355–362. doi:10.1111/j.1751-908X.2013.00269.x

Burrell, D.C., 1967. Trace elements in marine waters by atomic absorption spectrophotometry. *Anal. Chim. Acta* 38, 447–455.

Chan, L.-H., Edmond, J.M., 1988. Variation of lithium isotope composition in the marine environment: A preliminary report. *Geochim. Cosmochim. Acta* 52, 1711–1717.

Charlou, J.L., Donval, J.P., Douville, E., Jean-Baptiste, P., Radford-Knoery, Fouquet, Y., Dapoigny, A., Stievenard, M., 2000. Compared geochemical signatures and the evolution of Menez Gwen (37°50'N) and Lucky Strike (37°17'N) hydrothermal fluids, south of the Azores Triple Junction on the Mid-Atlantic Ridge. *Chem. Geol.* 171, 49–75.

Chester, R., 2009. Trace elements in the oceans, in: *Marine Geochemistry*. Wiley-Blackwell, p. 520.

Douville, E., Bienvenu, P., Charlou, J.L., Donval, J.P., Fouquet, Y., Appriou, P., Gamo, T., 1999. Yttrium and rare earth elements in fluids from various deep-sea hydrothermal systems. *Geochim. Cosmochim. Acta* 63, 627–643.

Escartín, J., García, R., Delaunoy, O., Ferrer, J., Gracias, N., Elibol, A., Cufi, X., Neumann, L., Fornari, D.J., Humphris, S.E., Renard, J., 2008. Globally aligned photomosaic of the Lucky Strike hydrothermal vent field (Mid-Atlantic Ridge, 37°18.5'N): Release of georeferenced data, mosaic construction, and viewing software: Lucky Strike vent field georeferenced image mosaic. *Geochem. Geophys. Geosystems* 9, doi:10.1029/2008GC002204

Escartin J., Barreyre T., Cannat M., Garcia R., Gracias N., Deschamps A., Salocchi A., Sarradin P.-M., Ballu V. (2015) Hydrothermal activity along the slow-spreading Lucky Strike ridge segment (Mid-Atlantic Ridge): Distribution, heatflux, and geological controls. *Earth Planet. Sci. Lett.* **431**, 173–185. doi:10.1016/j.epsl.2015.09.025

Fabricand, B.P., Imbimbo, E.S., Brey, M.E., 1967. Atomic Absorption analyses for Ca, Li, Mg, K, Rb, and Sr at two Atlantic Ocean stations. *Deep-Sea Res.* 14, 785–789.

Fabricand, B.P., Imbimbo, E.S., Brey, M.E., Weston, J.A., 1966. Atomic Absorption Analyses for Li, Mg, K, Rb, and Sr in Ocean Waters. *J. Geophys. Res.* 71, 3917–3921.

Foustoukos, D.I., James, R.H., Berndt, M.E., Seyfried, W.E., 2004. Lithium isotopic systematics of hydrothermal vent fluids at the Main Endeavour Field, Northern Juan de Fuca Ridge. *Chem. Geol.* 212, 17–26. doi:10.1016/j.chemgeo.2004.08.003

Gieskes, J.M., Gamo, T., Brumsack, H., others, 1991. Chemical methods for interstitial water analysis aboard JOIDES Resolution. Ocean Drilling Program, Texas A & M University.

Gieskes, J.M., Johnston, K., Boehm, Ma., 1985. Interstitial water chemistry at DSDP Leg 82 Holes. Initial Rep. Deep Sea Drill. Proj. 82, 539–542. doi:doi:10.1594/PANGAEA.806527

James, R.H., Palmer, M.R., 2000. The lithium isotope composition of international rock standards. *Chem. Geol.* 166, 319–326.

Jeffcoate, A.B., Elliott, T., Thomas, A., Bouman, C., 2004. Precise/Small Sample Size Determinations of Lithium Isotopic Compositions of Geological Reference Materials and Modern Seawater by MC-ICP-MS. *Geostand. Geoanalytical Res.* 28, 161–172.

Linge, K.L., Jarvis, K.E., 2009. Quadrupole ICP-MS: Introduction to Instrumentation, Measurement Techniques and Analytical Capabilities. *Geostand. Geoanalytical Res.* 33, 445–467.

Millero, F.J., Feistel, R., Wright, D.G., McDougall, T.J., 2008. The composition of Standard Seawater and the definition of the Reference-Composition Salinity Scale. *Deep Sea Res. Part Oceanogr. Res. Pap.* 55, 50–72. doi:10.1016/j.dsr.2007.10.001

Pester, N.J., Rough, M., Ding, K., Seyfried, W.E., 2011. A new Fe/Mn geothermometer for hydrothermal systems: Implications for high-salinity fluids at 13°N on the East Pacific Rise. *Geochim. Cosmochim. Acta* 75, 7881–7892. doi:10.1016/j.gca.2011.08.043

Riley, J.P., Tongudai, M., 1964. The lithium content of sea water, in: *Deep Sea Research and Oceanographic Abstracts*. Elsevier, pp. 563–568.

Rollinson, H.R., 1994. Using geochemical data: evaluation, presentation, interpretation. Longman Singapore Publishers, Singapore.

Saleban Ali, H., 2016. Impact du fluide hydrothermal de haute température sur la composition isotopique de l'eau de mer profonde. Université Paul Sabatier, Toulouse.

Sarradin, P.-M., Waeles, M., Bernagout, S., Le Gall, C., Sarrazin, J., Riso, R., 2009. Speciation of dissolved copper within an active hydrothermal edifice on the Lucky Strike vent field (MAR, 37°N). *Sci. Total Environ.* 407, 869–878. doi:10.1016/j.scitotenv.2008.09.056

Summerhayes, C.P., Thorpe, S.A., 1996. Chapter 11, in: *Oceanography An Illustrated Guide*. pp. 165–181.

Taylor, P., Wellum, R., 2003. Isotopic Reference Materials Certified by IRMM.

Thirlwall, M.F., 1991. Long-term reproducibility of multicollector Sr and Nd isotope ratio analysis. *Chem. Geol. Isot. Geosci. Sect.* 94, 85–104.

Tomascak, T., 2004. Developments in the understanding and application of lithium isotopes in the earth and planetary sciences. *Rev. Mineral. Geochem.* 55, 153–195.

Vigier, N., Godderis, Y., 2014. A new approach for modeling the Cenozoic oceanic lithium isotope paleo-variations: the key role of climate. *Clim. Past Discuss.* 10, 3027–3051. doi:10.5194/cpd-10-3027-2014

Von Damm, K.L., Edmond, J.M., Grant, B., Measures, C.I., Walden, B., Weiss, R.F., 1985. Chemistry of submarine hydrothermal solutions at 21°N, East Pacific Rise. *Geochim. Cosmochim. Acta* 49, 2197–2220.

Wright, J., Colling, A., 1995. Chapter 6 - The seawater solution, in: Wright, J., Colling, A. (Eds.), *Seawater: Its Composition, Properties and Behaviour (Second Edition)*. Pergamon, Singapore, pp. 85 – 127.

CHAPITRE 4

SPATIAL VARIATIONS IN VENT CHEMISTRY AT THE LUCKY STRIKE HYDROTHERMAL FIELD, MID ATLANTIC RIDGE (37°N): IMPLICATIONS FOR SUBSEAFLOOR FLOW GEOMETRY.

Leleu Th., Chavagnac V., Cannat M., Fontaine F., Ceuleneer G. Castillo A.

Submitted to *Geochimica et Cosmochimica Acta* (Ref: GCA-D-16-00566)

Abstract

The Lucky Strike Hydrothermal Field, located at the center of a magmatically-robust segment of the Mid-Atlantic Ridge, is a key target to understand geophysical, geological and biological processes in Mid Ocean Ridge axial domains (<1My). As such, the field hosts since 2010, a deep sea observatory (EMSO-Azores) dedicated to the survey of the interrelations between volcanic, seismic and hydrothermal processes together with seafloor ecosystem evolution. During the MoMAR 13 maintenance cruise of this observatory, a new active site, named Capelinhos, venting high temperature black smoker fluid (324°C) was discovered approximately 1.5 km east of the long known historical active sites. We report on its first chemical analysis and its implication for the global hydrothermal circulation cell at this field. With an end-member at 262 mM, Capelinhos fluids are the most chloride depleted fluids of all LSHF. Both major cations (Ca, Na, and K) and trace elements (Li, Cs, Rb, and Sr) concentrations display a linear correlation when compared to Cl concentration which implies a unique deep source fluid. Fe, Mn, Cl and Si allow characterization of both phase separation and reaction zone in terms of the pressure and temperature conditions of water-rock interactions. The Si-Cl geothermobarometry, at Capelinhos indicates phase separation conditions at 435–440°C, and 370–390 bars (2500–2800 mbsf) consistent with former estimations for LSHF vapor-dominated fluids. However, Capelinhos fluids show Fe and Mn concentrations (~2800µM and ~640µM) 3–4 times higher than all other LSHF fluids. These chemical features imply a higher temperature of equilibrium with greenschist facies minerals in the reaction zone estimated at ~400°C at Capelinhos and between 350 and 375°C for the other LSHF sites based on the Fe/Mn geothermometer (Pester et al., 2011). Interpreting P–T discrepancies between the Fe–Mn, Si and Cl geothermobarometry in terms of residence time beneath individual vent sites, we infer that up flowing fluids beneath Capelinhos stop reacting shortly after phase separation compared to other LSHF sites. We propose that the measured Cl–Si–Fe–Mn variability at LSHF sites is related to permeability variations in the hydrothermal upflow zone. The dense and complex fracture network due to the Lucky Strike axial graben which hosts the historical LSHF sites likely enhances conductive heat exchange between the up flowing hydrothermal fluids and seawater modifying fluid chemistry to lower P–T conditions beneath these sites. This participates to the stockwork formation underneath these vent sites. Conversely, emerging 1.5 km away from this axial fractured zone, Capelinhos fluids are more representative of the deeper part of the hydrothermal upflow.

Résumé

Le champs hydrothermal de Lucky Strike, situé sur la dorsale médio-atlantique est très intéressant pour comprendre les différents processus ayant lieu dans les zones axiales des rides océaniques (<1Ma), à savoir les processus géophysique, géologique et biologique. Ainsi, depuis 2010 ce champs hydrothermal accueille un observatoire fond de mer (EMSO-Açores) qui est dédié à l'étude des relations existant entre les processus magmatic, sismique et hydrothermaux avec l'évolution de l'écosystème du plancher océanique. Durant la campagne de maintenance MoMAR 13, un nouveau site de décharge de fluide à haute température a été découvert. Ce site, nommé Capelinhos, émet des fluides de type fumeur noir à 324°C et est situé à 1,5 km à l'Est des sites connus depuis 1993. Les fluides de Capelinhos sont les plus appauvris en Cl, parmi les sites observés, avec un end-member à Cl=262mM. Les concentrations des cations majeurs (Na, Ca, K) et mineurs (Li, Cs, Rb, Sr) montrent une relation linéaire avec les concentrations en Cl qui impliquent une même source profonde et homogène qui alimente le champs hydrothermal. Les éléments tels que le Fe, Mn, Cl et Si permettent de caractériser les conditions de pression et de température de la zone de séparation de phase et de la zone de réaction. Le géothermomètre Si-Cl, appliqué au fluide de Capelinhos, suggèrent une zone de séparation de phase à une température de 335-440°C et une pression de 370-390 bars, équivalent à 2500-2800 m sous le plancher océanique. Ceci est cohérent avec les estimations précédentes basées sur les fluides à dominante vapeur des sites historiques. De plus, les fluides de Capelinhos montrent des concentrations en Fe et Mn (~2800µM et ~640µM) trois à quatre fois supérieures à celles mesurées pour les autres sites. Ceci indique des conditions dans la zone de réaction des minéraux du faciès schiste vert à une température de 400°C, estimée à partir du géothermomètre Fe/Mn (Pester et al., 2011), alors que les autres sites suggèrent plutôt une température de 350 à 375°C. Les différences de conditions de pression et de température estimées pour la zone de séparation de phase et la zone de réaction peuvent être interprétées en terme de temps de résidence dans la zone de remontée. Ainsi, les fluides de Capelinhos semblent avoir peu évolué depuis la zone de séparation de phase par comparaison avec les autres sites. Ainsi les différences mesurées en Cl, Si, Fe, Mn sont liées à la perméabilité du substratum. Le réseau complexe de fracture à l'axe facilite les échanges de chaleurs et vont conduire les fluides vers des températures d'équilibre différentes de celles de la séparation de phase. Les fluides de Capelinhos représentent le mieux les fluides profonds de la zone de remontée.

1. Introduction

Hydrothermal fluid circulation at mid-ocean ridges (MOR) is one of the major processes controlling the out-going heat fluxes of the oceanic lithosphere (Chen and Morgan, 1990; Stein and Stein, 1994), the geochemical composition of the crust (Kelley and Delaney, 1987; Kelley and Robinson, 1990; Alt and Teagle, 2003; Barker et al., 2008; Brant et al., 2012), the chemical composition of the ocean (Elderfield and Schultz, 1996; Resing et al., 2015) and the development of peculiar chemo-synthetic ecosystems (Martin et al., 2008 and references therein). Increasing attention has been drawn to the study of black smokers since their discovery along the East Pacific Rise off the Galapagos Islands in 1977. They have shown an unexpected diversity in geological setting, hydrothermal ecosystems and fluid chemistry (Campbell et al., 1988; Von Damm, 1988, 2000; Douville et al., 2002; Ludwig et al., 2006; Schmidt et al., 2007, 2011). From the recharge zone to the discharge area, seawater is transformed into high temperature hydrothermal fluid, acquiring its chemical composition in the reaction zone, which is likely located on top of the axial magmatic chamber (AMC) where the temperature are the highest. High temperature fluids can be further modified by interactions with the rocks along with the upflow pathway to the seafloor and also by the precipitation of secondary minerals, depending on the fluid velocity (Saccocia and Seyfried, 1994; Lowell, 2003; Coogan, 2008; Steele-MacInnis et al., 2012). These interactions occur over a wide range of pressure and temperature conditions (from the deepest part of the hydrothermal cell to the discharge, ΔP and ΔT can be a few hundred bars and °C, respectively). Variations can be observed depending on the nature of the host rocks (i.e. extrusive basaltic and/or mantellic substrate). The chemical composition of focused vent hydrothermal fluids can, therefore, be used as a tracer of deep crustal processes, constraining the pressure and temperature conditions at which water-rock interactions took place in the crust (Seyfried et al., 1998; Seyfried, 2003; Von Damm et al., 2003; Mottl et al., 2011; Reeves et al., 2011).

The Lucky Strike Hydrothermal Field (LSHF) was discovered at 37°N along the slow-spreading Mid-Atlantic Ridge (MAR) in 1992 during the FAZAR cruise (Langmuir et al., 1997). The discovery motivated several subsequent research cruises with the objective of better characterizing the geological, geochemical, geophysical and biological context of the vents (Fouquet et al., 1995; Langmuir et al., 1997; Von Damm et al., 1998; Charlou et al., 2000; Ondréas et al., 2009; Barreyre et al., 2012; Pester et al., 2012; Escartin et al., 2015). The first comprehensive study on the Lucky Strike vent chemistry (Von Damm et al., 1998)

indicated that the discharge of focused fluids (sampled in 1993 and 1996) originated from deep rooted fluids that underwent near-surface processes in the upflow (Von Damm et al., 1998). Charlou et al. (2000) analyzed fluids from ten active sites of the LSHF. All samples were depleted in chloride relative to seawater (3.2% NaCl) and were spatially correlated with Cl variability from ~420mM at the South Eastern sites, to ~520mM at the North Western sites. These authors proposed that a relatively shallow reaction zone provided vapor-like fluids (i.e., $Cl < Cl_{sw}$) to the upflow zone at subcritical conditions (lower temperature and pressure than 407°C and 298bars, equivalent to ~1300 mbsf; Bischoff, 1991). Chemical data presented by Charlou et al. (2000) also suggested that sampled vapor-dominated fluids underwent substantial subsurface mixing with seawater prior to venting.

Pester et al. (2012) used trace element and chloride co-variation in fluids at five active vents, sampled eleven years later, to infer P–T equilibrium conditions during upflow (chloride ranged then from 414mM to 588mM). The analyzed fluids display both chloride depletion and enrichment relative to seawater, which lead to the proposal that a unique, deep source (or reaction zone) feeds the hydrothermal field (Pester et al. 2012). Converse to Charlou et al. (2000), Pester et al. (2012) proposed that the fluids underwent phase separation at 430–450°C and pressure at about 400 bars, and that subtle changes in pressure and/or temperature can explain the diversity observed in chlorinity. These authors argue that the hot fluid equilibrates with the greenschist facies of basaltic host rocks at temperatures lower than those of the phase separation (i.e. 350–380 °C), i.e. the result of conductive cooling prior to discharge.

Comparing these different perspectives of the plumbing circulation system below the LSHF highlights the difficulties that arise when interpreting the chemical composition of vent fluids. This is compounded by the lack of spatial (e.g. LSHF) and temporal (e.g. yearly-basis) continuity between the studies.

The EMSO-AZORES program started in 2010, following the installation of the long-term, deep sea observatory (FP6-ESONET; Person et al., 2009; Colaço et al., 2011). This instrumental infrastructure is dedicated to continuous monitoring of hydrothermal system dynamics. Yearly maintenance cruises allowed the collection of hydrothermal fluids complementary to the continuous data of the observatory (www.emso-fr.org/fr/EMSO-Azores). A new, high-temperature venting site, named Capelinhos (T=324°C, Table 1) was discovered during the MoMARsat 13 (2013) maintenance cruise (Escartin et al., 2015; Fig IV - 1). Capelinhos lies approximately 1.5 km east of the main LSHF, while all other

active/inactive venting sites are located around a fossil lava lake (Humphris et al., 2002; Ondréas et al., 2009; Barreyre et al., 2012; Fig IV - 1). The discovery of this new site argues for subsurface fluid circulation at the LSHF over a much larger spatial scale than previously thought.

In this study, we report on the first chemical data acquired for the Capelinhos vent site and we compare its chemical characteristics with data from 12 other active LSHF vents sampled during the same cruise. Using this dataset, we show that Capelinhos is a key site to assess the role of subsurface mixing, phase separation, and conductive cooling processes on the chemistry of the LSHF fluids.

2. Geological setting

The ~65 km long Lucky Strike segment is located south of the Azores islands along the MAR between 37°03'N and 37°37'N (Detrick et al., 1995). The spreading rate is ~22 mm/yr (Cannat et al., 1999; Miranda et al., 2005). The LSHF is situated on top of a central volcano that includes a fossil lava lake (300m of diameter) framed by three ancient volcanic cones and truncated by N010°–N030° faults and fissures (Fouquet et al., 1995; Fig IV - 1). The fossil lava lake is significantly less fissured than its surroundings, indicating a relatively recent formation (Humphris et al., 2002; Ondréas et al., 2009). Seismic data have constrained the occurrence of a magmatic lens (or AMC), at a depth of about 3500 m below the summit of the volcano (Singh et al., 2006). Microseismic events recorded between 2007 to 2009 are located above the AMC at depths between 1800 and 2500m below seafloor (bsf), and interpreted as the product of fracturing induced by penetration of colder down-flowing fluids into the hot rocks (Crawford et al., 2013). If this interpretation is correct, these microseismic events document the existence of two predominantly along-axis hydrothermal cells, with a central upflow zone centered beneath the LSHF.

The LSHF vents display various structures from small hydrothermal mounds to tens of meters high sulfide towers sitting on large mounds, as well as thin towers, several meters high (Fig IV - 2). Close to the focused fluid chimneys, diffuse venting occurs through cracks at temperatures below 100°C and flanges with pool temperatures higher than 200°C (Cooper et al., 2000; Barreyre et al., 2014). The long-term history of hydrothermal activity at Lucky Strike is evidenced by metalliferous deposits and the presence of dead mussel shells in inactive sites (Langmuir et al., 1997; Humphris et al., 2002). The last volcanic event, that formed the fossil lava lake, has buried most of the “old” hydrothermal field

leaving only relicts of past hydrothermal activity (Humphris et al., 2002; Ondréas et al., 2009). The spatial distribution of old inactive hydrothermal deposits compared to those associated with active hydrothermal ones indicates that the northeastern part of the hydrothermal field is largely extinct (near the Sintra site; Fig IV – 1; Ondréas et al., 2009; Barreyre et al., 2012). There are other indications that suggest a relatively recent decline of the hydrothermal activity, based on images mosaic, observations and temperature measurements of diffuse and focused fluids (Ondréas et al., 2009; Barreyre et al., 2012). Approximately 20 to 30 active vents are currently known and investigated at Lucky Strike, distributed around the fossil lava lake (Barreyre et al., 2012; Fig IV - 1).

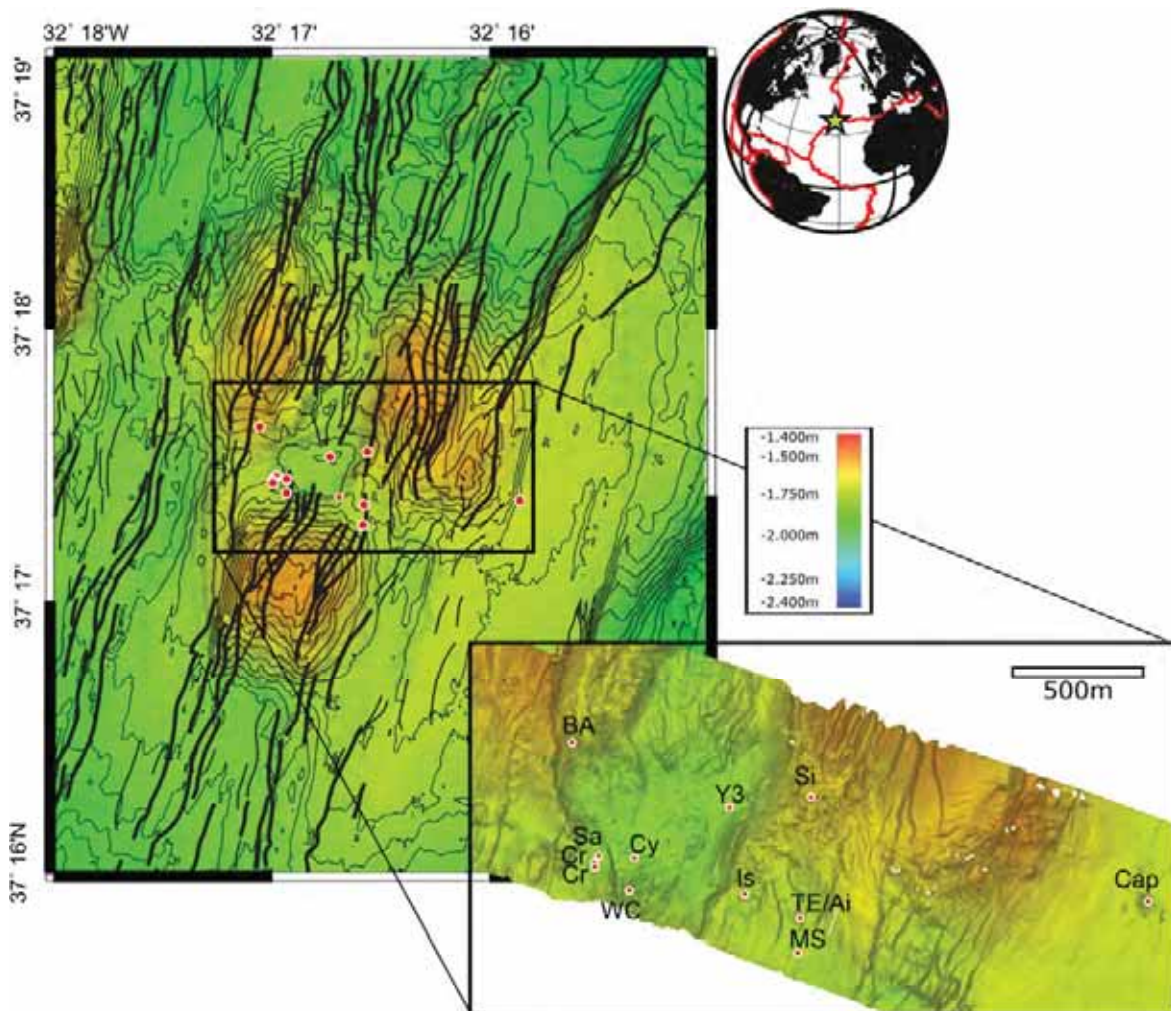


Figure IV - 1 Bathymetric map of the Lucky Strike central volcano. Active hydrothermal vents are represented. Sapins=Sap. Crystal=Cr.; South Crystal=Sth Cr.; White Castle=WC; Isabel=Is.; Tour Eiffel=TE; Aisics= ASC; Montsegur= Mr, Capelinhos=Cap. Modified from Humphris et al., 2002.

The northwestern area hosts several active sites with high temperature vents (Bairo Alto, Nuno, Helene and Jason) on a curvilinear scarp formed by mass wasting and partly comprised of massive sulfides (Ondréas et al., 2009; Escartin et al., 2015). This area has been chosen as an exclusion zone to preserve the original hydrothermal habitat, in respect with the Lucky Strike Marine Protected area (Mullineaux, 1998). As a consequence, this area is off limits for sampling.

The northeastern hydrothermal area is situated on a bench comprising surficial hydrothermal deposits. Despite its geographical extension, the hydrothermal activity in this area is declining as illustrated by lower temperature venting sites (at 196°C for Sintra, Statue of Liberty now extinct; Table VI - 1). Proximal to this area, the 18m high Y3 active site (probably collapsed on its own weight between 2012 and 2013) is isolated in the north east part of the fossil lava lake.

The southeastern area, between the northeastern and southern volcanic cones, is a highly tectonised terrain. The vents are set upon hydrothermally cemented volcanoclastic breccias called “slab” (Cooper et al., 2000; Humphris et al., 2002). This slab is thought to have sealed the permeability of the seafloor in this area which lead to fluid discharge through faults (Isabel, Montsegur, Tour Eiffel, Aisics; Humphris et al., 2002; Ondréas et al., 2009).

The southwestern area at the end of the fossil lava lake is truncated by a 20m scarp, caused by the movement along a normal fault that post-dates the last eruptions (Ondréas et al., 2009). The absence of large hydrothermal deposits in this area implies that hydrothermal fluid venting is nascent, despite observation of inactive oxidized chimneys partially buried by lavas. The active venting occurs along the fault scarp (South Crystal, Crystal, Sapins and White Castle) or on the lava lake itself (Cyprés).

The Capelinhos site is situated approximately 1.5 km eastward of the LSHF on the western flank of the axial volcano (Escartin et al., 2015). It is set on pillow lava and comprises several chimneys forming a “candelabra-like structure” on top of a 10 meter high sulfide mound (Fig IV - 2). Extinct chimneys are characterized by orange colored oxidizing material while active chimneys are dark grey and covered by a white filamentous bacterial mat. Diffuse venting at Capelinhos is limited to the close vicinity of the black smokers that expel fluids at temperatures up to 324°C (Escartin et al., 2015; Table IV - 1).

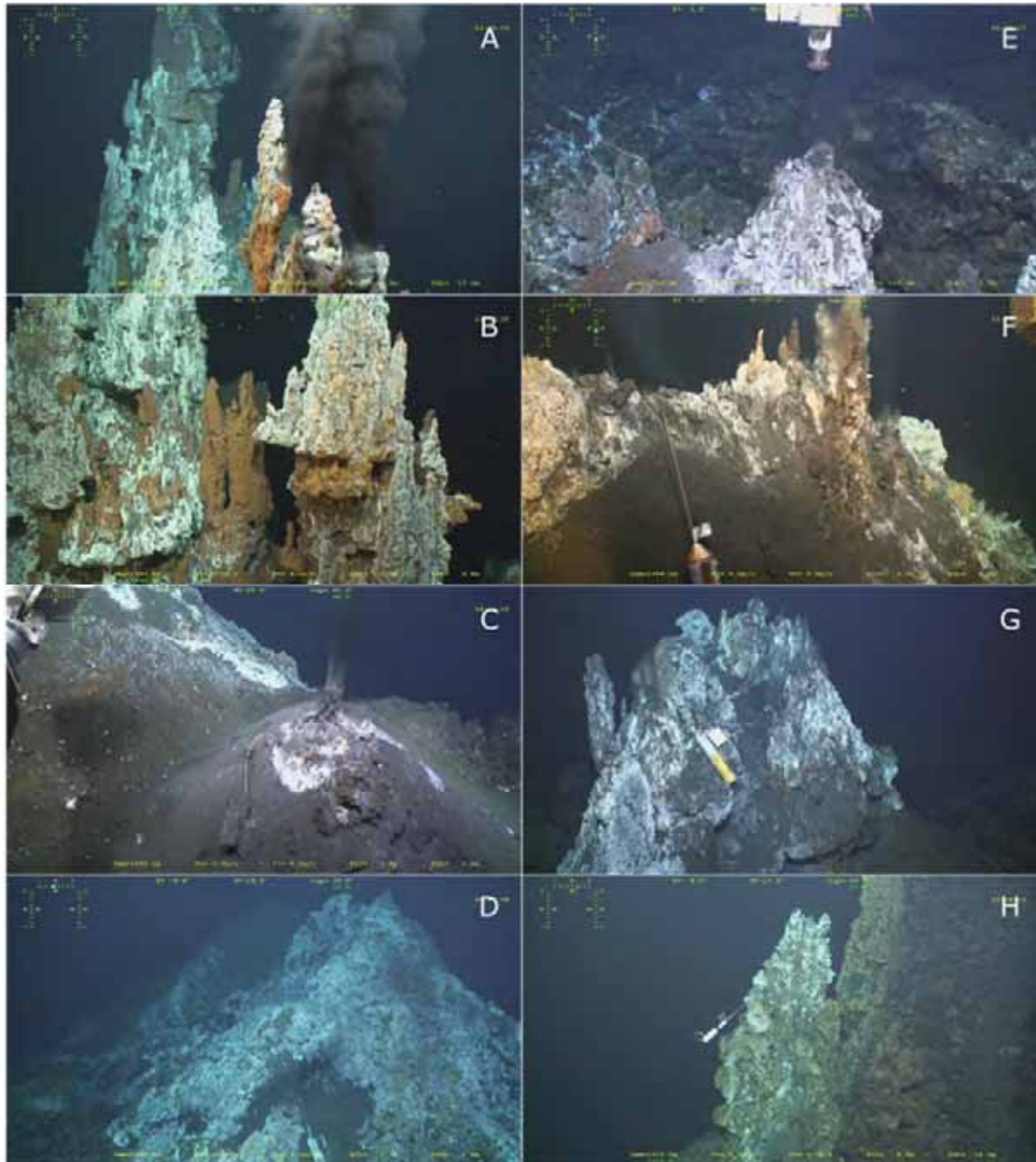


Figure IV - 2 Overview of vent sites diversity. Snapshots of ROV photographs (Ifremer-CNRS, MoMARsat 13), A, B: Capelinhos; C: aisics; D: Montsegur; E: Cyprès; F: White Castle; G: Crystal; H: Sintra. A and B shows candelabra like structure of capelinhos vent site that discharge several focused high T fluid. C and D shows hydrothermal mound at two sites in the South Eastern area. Aisics mound is not as developed as Montsegur but both lack of tall enduring chimneys. E, F and G are situated in the North Western area. High T vents display an elongated wall-like structure closely related to underlying faults. H is situated in the declining North Eastern area and have tall enduring chimneys which are probably inherited from past intense activity.

3. Sampling and analytical method

3.1 Sampling

The fluid samples studied in this paper were collected during the MoMARsat'13 EMSO-AZORES maintenance cruise on the French Research vessel "Pourquoi Pas?" in September 2013. The 13 sampling sites (12 sites in the main LSHF, and Capelinhos) were chosen to document the fluid diversity identified at Lucky Strike by previous studies (Von Damm et al., 1998; Charlou et al., 2000; Pester et al., 2012; Chavagnac et al., 2015). Each vent site was sampled four times in succession (total duration of sampling <1 hour) to allow a better characterization of the end-member fluid. In-situ temperatures were measured in the vents prior to sampling using the ROV Victor 6000 high temperature probe. High-temperature fluids were collected with 200ml titanium gas-tight samplers handled and triggered by the hydraulic arm of the ROV. The time delay between each fluid sampling at a given vent did not exceed 20 minutes. The samples were processed immediately on board after the ROV recovery. First, gases were extracted from sampler and transferred into vacuumed stainless steel canisters, by direct connection, or ultra-clean water sealed glass bottles for further analysis. The fluid samples were then extracted, filtered through 0.45 μ m Millipore filters as pore size of filterable elements (Raiswell and Canfield, 2012) and split into different aliquots for onshore analysis and stored at 4°C in a cold room. pH, Eh, salinity and conductivity were measured on-board immediately after processing.

Table IV - 1 Summary of fluid sampling. The table present location, depth and details on fluid sampling for each site (minimum pH, minimum Mg measured and corresponding seawater entrainment, and maximum temperature measured).

site	depth (mbsl)	Longitude	Latitude	area	pH ^a	Mg ^b (mM)	n sample	%SW ^c	T in situ (°C)
Capelinhos	1665	32°15.830'	37°17.350'	Capelinhos	2.56	1.63	4	3.02	324
Aisics	1689.3	32°16.530'	37°17.338'	South East	3.1	1.11	7	2.06	295
Tour Eiffel	1684	32°16.532'	37°17.343'	South East	3.26	0.89	3	1.65	325
Mont Ségur	1701	32°16.534	37°17.284'	South East	3.33	1.63	2	3.02	316
Cyrpès	1738.7	32°16.863'	37°17.450'	South West	2.84	1.53	3	2.84	304
Isabel	1683.7	32°16.638'	37°17.377'	South East	2.93	1.55	3	2.87	224
White Castle	1708.9	32°16.869'	37°17.383'	South West	2.9	1.16	3	2.16	317
Crystal	1723.3	32°16.921'	37°17.453'	South West	3.17	1.61	2	2.98	335
Sapins	1718.6	32°16.888'	37°17.439'	South West	3.56	3.6	3	6.67	280
South Crystal	1720.5	32°16.935'	37°17.445'	South West	2.93	0.75	3	1.39	341
Sintra	1614.7	32°16.498'	32°17.529'	North East	3.89	12.99	1	24.06	196
Y3	1727.3	32°16.671'	37°17.512'	North East	2.92	1.06	3	1.97	325

3.2 Analytical methods

All the chemical analyses were conducted at the Geosciences Environment Toulouse (GET) laboratory. Ca, Na, K, Mg, Si, Fe, Mn and Li concentrations were determined with an inductively coupled plasma atomic emission spectrometer (ICP-AES) Horiba Ultima2 instrument. Errors on analyses are indicated in Table IV - 2. The instrument is calibrated using mono elemental solutions, multi elemental solutions, and IAPSO standard solution (Besson et al., 2014). The latter is a seawater standard solution provided by OSIL and certified for its salinity. Salinity controls major element concentrations in seawater (Millero et al., 2008). Li concentration measurements of IAPSO give an average concentration of $24.6 \pm 0.3 \mu\text{M}$ (rsd=1%; n=4). The analytical drift is quantified by the standard bracketing after every 8 samples. Analytical precision is better than 2%. Sr, Rb and Cs concentrations were measured using an inductively coupled plasma mass spectrometer ICP-MS Agilent7000. The standard used was a NASS 6 solution (international seawater standard certified for some trace metals) and give values of $79.1\mu\text{M}$, $1.17\mu\text{M}$, 1.19 nM for Sr, Rb and Cs respectively (n=3). Drift corrections are made using an in-house multi-elementary standard doped with In and Re before analysis. Anions were determined by anionic chromatography (Cl, SO₄, Br) calibrated with a IAPSO standard seawater solution.

Table IV - 2 Analytical method and precision. The table presents the instruments used to measure the major and trace elements in the sampled hydrothermal fluids, and the associated error (residual standard deviation).

element	instrument	rsd
Ca	ICP AES ^a	2%
K	ICP AES	2%
Na	ICP AES	4%
Fe	ICP AES	3%
Mn	ICP AES	3%
Si	ICP AES	2%
Li	ICP AES	2%
Rb	ICP MS ^b	3%
Sr	ICP MS	2%
Cs	ICP MS	10%
Cl	IC ^c	3%
SO₄	IC	2%
Br	IC	4%

a: Inductively Coupled Plasma Atomic Emission Spectrometer

b: Inductively Coupled Plasma Mass Spectrometer

c: Ion Chromatography

Sr isotopic composition was measured at the GET laboratory using a MAT FINIGAN 261 thermal ionization mass spectrometer. Analyses were performed on the samples which contain the lowest Mg concentrations. Sr was isolated from the matrix using Sr-Spec resin (Eichrom, USA). The $^{87}\text{Sr}/^{86}\text{Sr}$ ratio was defined as the average of 100 measurements of ion intensities following the static collection mode. The $^{87}\text{Sr}/^{86}\text{Sr}$ ratios were normalized to $^{86}\text{Sr}/^{88}\text{Sr} = 0.1194$. Measured values for NBS 987 standard (recommended values of 0.710250) was $^{87}\text{Sr}/^{86}\text{Sr} = 0.710250 \pm 0.000011$ ($2\sigma\text{E}$, $n = 14$).

Table IV - 3 End-member composition of fluids from the Lucky Strike Hydrothermal Field. The concentration of end-member fluids for each sites calculated based on least-square regression of elt vs. Mg , at $\text{Mg}=0$.

	Ca	K	Na	Fe	Mn	Si	Cl	SO ₄	Br	Rb	Sr	Li	Cs	⁸⁷ Sr/ ⁸⁶ Sr	T**	P**
units	mM	mM	mM	μM	μM	mM	mM	mM	mM	μM	μM	μM	nM		°C	bars
Capelinhos	18	12.1	205	2789	639	14.1	262	-0.4	0.4	18.7	35.9	197.3	129	0.70384	403	350
SE area																
Aisics	35.4	19.59	310	417	195	14.9	420	0.11	0.65	28.5	80.1	272.9	184	0.70422	368	225
Aisics	37.2	18.97	317	452	226	15.7	418	0.02	0.66	28.5	80.5	266.3	180	0.70428	365	n.d.
MontSégur	36.1	19.6	325	284	179	15.2	422	-0.06	0.65	28.2	80.3	265	178	0.70423	354	225
TourEiffel	39	19.66	334	574	229	16	416	0.9	0.64	27.7	81.2	262.6	179	0.70448	376	300
central area																
Cypès	43.2	23.37	399	411	309	18.6	520	-0.48	0.84	36.4	112.5	319	222	0.70403	345	n.d.
Isabel	39.6	22.32	373	250	147	14.1	470	-0.2	0.73	32.5	105	276.8	199	0.7043	357	n.d.
White Castle	38.3	23.24	381	313	254	16.3	481	-0.2	0.75	35.9	111.2	301.6	221	0.70502	341	n.d.
SW area																
Crystal	53.5	28.35	446	507	260	17.3	569	2.56	0.88	50	180	367.9	231	0.70414	364	300
Sapins	48.3	26.6	442	201	245	17.5	568	-0.28	0.87	39.6	118.1	332.9	243	0.70429	322	n.d.
South Crystal	49.3	28.3	445	593	232	17	570	-0.1	0.89	42.5	125	346.1	260	0.704	377	300
NE area																
Sintra	53.7	27.1	433	185	164	12.8	537	0.35	0.85	39.3	115.5	343.5	244	0.70423	337	n.d.
Y3	52.9	25.5	432	686	323	17.1	574	0.03	0.9	42.3	144.7	323.3	253	0.70401	368	300
SW*	10.3	10.2	469	0	0	0.17	546	28.2	0.841	1.3	90.6	25.6	2.3	0.70916	n.d.	n.d.

* Seawater data from Millero et al. 2008 and Charlou et al. 2010

** Temperature calculated by Fe/Mn geothermometer and Pressure estimated from Fe/Mn and Si (see details in text)

4. Results

The temperature of the focused fluid discharge at the 13 sampled vents ranges from 196°C to 340°C (Table IV - 1). It is difficult to sample the venting hydrothermal fluid without entraining small amounts of the surrounding seawater into the sampler. Consequently, the composition of the end-member hydrothermal fluids is calculated by linear extrapolation to zero-Mg of the least-square regression method (Von Damm, 1988). Only hydrothermal end-members will be considered in the discussion section. Although the Mg extrapolation is sometimes debatable (Gamo et al., 1996; Ravizza et al., 2001), most end-member calculated values of sulfate in our samples are close to zero which supports the Mg extrapolation approach. Seawater entrainment, estimated from Mg content of the purest fluids, is usually lower than 3% (Table IV - 1). Only the purest fluid, based on the pH values have been analyzed for their chemical composition. The calculated end-member chemical compositions are reported in Table IV - 3. The compositions of all analyzed samples are given in the Supplementary Materials (Fig IV - S1).

Chloride, Sulfate, Bromide

Hydrothermal fluids of the LSHF exhibit chloride concentrations between 420 mM (SE sites: Montsegur, Aisics, and Tour Eiffel sites; Fig IV - 1) and 580 mM (NE sites: Y3 and Sintra; and South Crystal, Crystal and Sapins for the SW group). White Castle, Isabel and Cyprès display Cl concentration closer to seawater at values ranging between 480 mM and 520mM. Capelinhos presents the lowest chloride concentration ever measured at LSHF at 262 mM.

Sulfate is removed from heated seawater through anhydrite precipitation and/or sulfate reduction (producing H₂S). As a consequence, the sulfate concentrations recalculated at Mg=0 in the end-member hydrothermal fluids should be close to 0 mM. However some vents display non-zero calculated concentrations for SO₄ (Crystal and Tour Eiffel) while other display slightly negative calculated concentration (e.g. Capelinhos, Aisics, Cyprès), in line with previous studies (Von Damm et al., 1998, Table IV - 3). Br concentrations display variations similar to Cl concentrations, whereby maximum Br concentrations are found in Y3 fluids at 885µM close to the seawater value of 838 µM while minimum values are found for Capelinhos fluids at 379µM.

Iron and Manganese

Capelinhos end-member vent fluids show very high Fe and Mn concentrations: 2800 μM for Fe and 640 μM for Mn. At the other sites, Fe and Mn concentrations in end-member fluids vary between 200 μM (Sintra) and 700 μM (South Crystal) for iron (Fig IV - 3a) and between 150 (Sintra) and 330 μM (South Crystal) for manganese (Fig IV - 3b).

Silica

Silica concentrations of the hydrothermal end-members vary from 12.8 mM at Sintra (NE group of sites) to 18.7 mM at Cyprès. The Si concentration at Capelinhos is 14.1 mM. High chlorinity fluids tend to have high Silica concentrations, but Si and Cl do not correlate beyond this: the silica concentration at Capelinhos is of the same order as for the TE group of sites, despite distinct chlorinities (Fig IV - 3c).

Sodium, Calcium and Potassium

Na, Ca and K constitute the major cations and are closely linked to Cl concentration due to charge balance. Maximum Na concentrations (445mM) are found in Crystal and South Crystal fluids (SW group of sites), while the minimum Na concentration (205 mM) is obtained for Capelinhos.

Maximum Ca concentration are found in Sintra, Y3, Crystal and South Crystal fluids with values around 53 mM while at Capelinhos the Ca concentration does not exceed 18mM.

Maximum K concentrations (~28 mM) are found in South Crystal and Crystal (SW group of sites) and the minimum concentration (12.1 mM) is measured at Capelinhos.

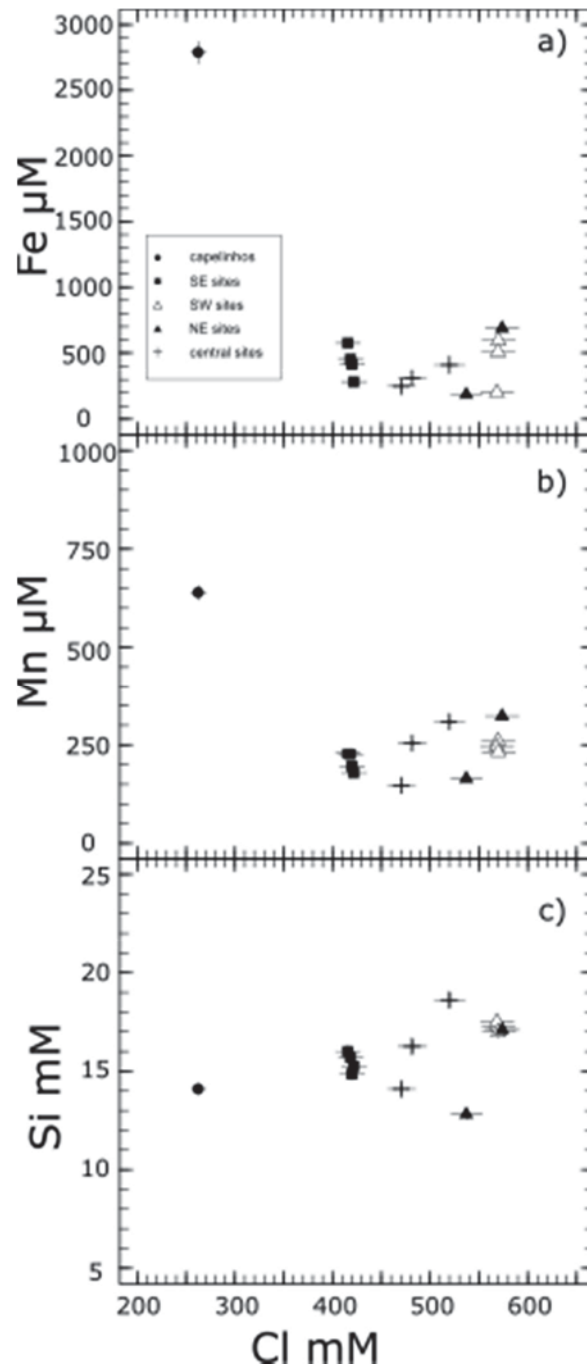


Figure IV - 3 Fe, Mn and Si vs. Cl. Diagram a) Fe versus Cl; b) Mn and versus Cl and c) Si versus Cl. These diagram shows non-correlation of these element compared to Cl.

Rubidium, Strontium, Cesium and Lithium

Rb, Cs and Li are highly enriched in the LSHF fluids compared to seawater (from 10 to 20 times seawater concentration). Concentrations in Rb, Li, Cs and Sr are correlated to the fluid's chlorinity (Fig IV - 3). Minimum and maximum Rb concentrations are 19 μ M and 50 μ M for Capelinhos and Crystal, respectively. Minimum and maximum Li concentrations are 197 μ M and 368 μ M, also for Capelinhos and Crystal, respectively. Sr follows the same

pattern with a maximum concentration of 180 μ M for Crystal and a minimum concentration of 36 μ M at Capelinhos.

Sr isotopes

Strontium isotopes ($^{87}\text{Sr}/^{86}\text{Sr}$) show variations due to mixing of end-member fluids with seawater during sampling. Plotting Sr isotope ratios against the Mg/Sr ratios distinguishes seawater entrainment from Sr variations in the end-member fluid (Albarède et al., 1981; Ravizza et al., 2001; Fig IV - S1). The less radiogenic end-member fluid compositions (0.7038 to 0.7040; Table IV - 3) were calculated for Capelinhos, Y3 (of the NE group of sites), Crystal and South Crystal (for the SE group of sites). The SE sites (Aisics, Tour Eiffel, and Montsegur) have a more radiogenic signature (0.7042-0.7043; Table IV - 3). Cyprès (0.7042) and White Castle (0.7045), of the central group, display variable signatures.

5. Origin of the end-member hydrothermal fluids diversity

Due to a serious lack of constraints on the extent of recharge zones, and circulation pathways of a deep hydrothermal cell, it is hard to testify to the “source” or “sources” of a hydrothermal field as, in the end, the two primary sources are the oceanic crust and seawater. The hydrothermal fluid represents the product of the interaction between the two of them. As a matter of simplification, however we propose to define the source fluid of the hydrothermal system as the fluid that can be found in the deepest region of the hydrothermal cell(s), where it reaches the low density and viscosity values that facilitate its upflow to the discharge zone. It is well known that phase separation allows for maximum buoyancy of “hot” source fluid relative to surrounding colder fluid (Fontaine and Wilcock, 2006; Coumou et al., 2008). Therefore, discussing the unicity or multiplicity of the source fluid comes down to evaluating whether or not the fluids sampled at the vents could originate from a chemically identical hydrothermal fluid in the phase separation region.

Cl is the major anion present in hydrothermal fluids, and is also the main control on cation abundances due to charge balance. We define 5 groups of sites with increasing Cl concentrations: Capelinhos (Cl: 262mM), the SE group of sites (Tour Eiffel, Montsegur, Aisics; Cl_{average}: ~420mM), the Central group of sites (Isabel, White Castle, Cyprès; Cl_{average}: ~495mM) and the SW group of sites (Crystal, South Crystal, Sapins; Cl_{average}:

~580mM). The NE group of sites (Y3 and Sintra; Cl_{average} : 580mM) also has high chlorinity but is in a different area and so define its own group.

In previous studies, Charlou et al. (2000) propose that Cl variability could be due to seawater mixing at subsurface conditions prior to fluid venting. To confirm or infirm the occurrence of seawater mixing, we use the Sr isotope compositions of the purest fluids as a tracer of sources and mixing. Indeed, pure hydrothermal fluid acquire the Sr isotopic signature of the rocks with which it interacts, i.e basalt at LSHF (Albarède et al., 1981). Moreover, basalt and seawater have different and distinctive strontium isotope composition, and therefore mixing of pure hydrothermal fluid with surrounding seawater will be testified by a Sr isotopic signature that departs from that of the basaltic one.

Although the extent of Sr uptake from the fluid through anhydrite precipitation in the recharge zone is not known, complete equilibrium between basaltic Sr and fluid Sr is rarely observed (Albarède et al., 1981; Michard et al., 1984; Ravizza et al., 2001). Therefore, the more radiogenic Sr isotope signature in the fluids is explained by initial Sr of seawater origin, which remains and mixes with basaltic Sr to form the end-member fluid and/or by subsurface mixing with surrounding hydrothermal seawater (Berndt et al., 1988; Palmer, 1992; Ravizza et al., 2001). The $^{87}\text{Sr}/^{86}\text{Sr}$ ratios of fluid end-members at the LSHF do vary between 0.7038 and 0.7045 but they do not follow the east-west chlorinity gradient, nor do they show a geographical trend. Capelinhos, two of the SW sites (South Crystal and Crystal), and one of the NE sites (Y3) have similar $^{87}\text{Sr}/^{86}\text{Sr}$ ratio at 0.7038-0.7040. The SE sites (Tour Eiffel, Aisics, Montsegur) have slightly more radiogenic Sr isotopic ratio (0.7042-0.7043; Table 3) and the most radiogenic fluids come from one of the central sites (White Castle with 0.7045). For comparison, basalts from the Lucky Strike area have been analyzed for $^{87}\text{Sr}/^{86}\text{Sr}$ and gave values at 0.70298 (0.00007, n=13, including T- and E-MORB, Hamelin et al., 2013). The observed range in Sr isotope signature of the fluids, therefore, cannot be explained by local differences in the substratum. The tight but significant differences in Sr isotopic signature between the highest chlorinity and lowest chlorinity fluids means that Capelinhos fluid, compared to LSHF, has less interaction with radiogenic Sr-rich material such as extensively altered rocks and/or with hydrothermal seawater. In contrast, the SE sites with vapor dominated chlorinity values have more radiogenic Sr isotope ratio. This contradicts the mixing model invoked by Charlou et al. (2000), which explained Cl variation by subsurface mixing. These results rule out a

hydrothermal seawater component that would bring more radiogenic material but they suggest more complicated processes to account for Cl variability at LSHF.

Apart from seawater mixing, Cl concentration variations in end-member fluids can result from two processes: phase separation or formation of a mineral phase significantly enriched in chloride, e.g. halite (Edmond et al., 1979; Seyfried et al., 1986; Von Damm, 1988; Bischoff and Rosenbauer, 1989; Berndt and Seyfried, 1990). Formation of halite at depth can be assessed through the Br/Cl ratios because Br doesn't substitute in the halite lattice. Precipitation of halite would increase the Br/Cl ratio of hydrothermal fluids compared to the seawater value of 1.54×10^3 (mM/mM) whereas halite dissolution would produce the opposite effect, i.e. decreasing the Br/Cl ratio (Oosting and Von Damm, 1998; Foustoukos and Seyfried, 2007). The most chloride-depleted end-member fluid of the LSHF, i.e. Capelinhos, exhibits a Br/Cl ratio of 1.53×10^3 , at the lower end of the Br/Cl range of the LSHF (between 1.53×10^3 for Sapins and 1.561×10^3 for Cyprès; Table 3) but all are equivalent to the seawater ratio. This is also illustrated in Figure 4 with no variation of $\log(\text{Br/Cl})$ with $\log(\text{Cl})$. Consequently, the variability of Cl concentrations cannot be explained by halite formation but must be due to a phase separation process occurring at depth.

Previous studies have explained Cl concentrations of the LSHF end-member fluids as a response to subsurface mixing between a shallow phase-separated hydrothermal fluid and evolved seawater (Charlou et al., 2000), or to phase separation at high P and T conditions to induce primary vapors having up to or even higher chlorinity than seawater prior to phase separation (Pester et al., 2012).

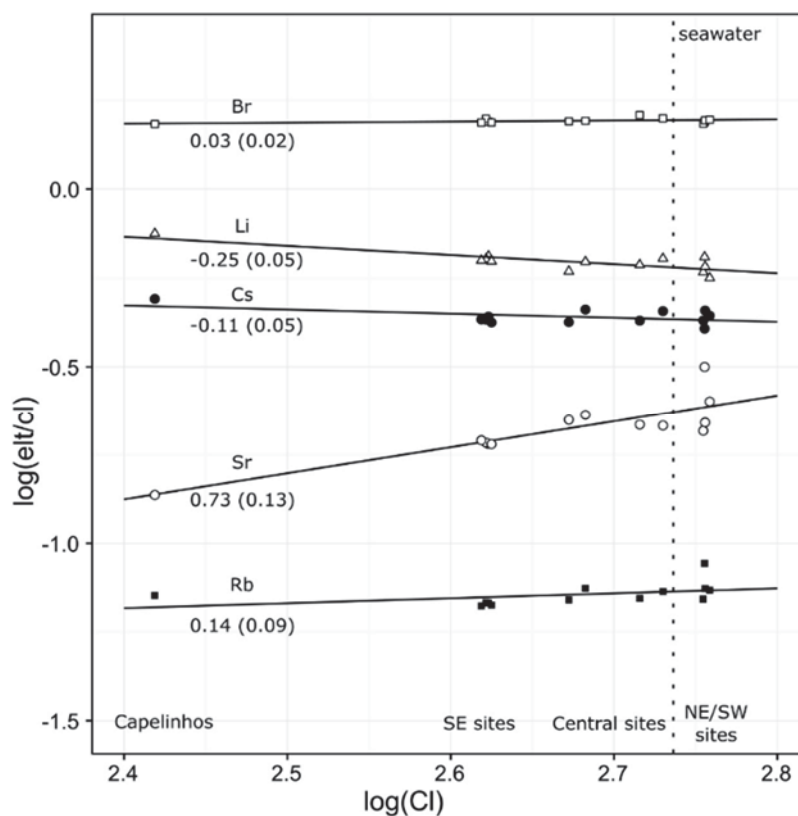


Figure IV - 4 $\log(Elt/Cl)$ vs $\log(Cl)$ diagram. Diagram of elt/Cl versus Cl showing the linear relationship between trace element and chlorinity, a proxy for the effect of phase separation.

In our study, we address this issue by investigating the distribution of trace element concentrations (Br, Li, Sr, Rb and Cs) over the extended chlorinity range provided by the Capelinhos site, as these elements are controlled by vapor/brine partition coefficients during phase separation. Vapor/brine element partitioning has been the subject of several experimental studies which showed that the considered elements of interest may be enriched in the brine phase at different affinities (Pester et al., 2015; Foustoukos and Seyfried, 2007; Foustoukos et al., 2004; Berndt and Seyfried, 1997; among others). For example, Br has a partition coefficient close to 1 between vapor and brine, leading to conservative Br/Cl ratios during phase separation (Pester et al., 2015; Oosting and Von Damm, 1996). This is clearly illustrated in Fig IV - 4 which shows a linear slope close to 0 in the $\log(Br/Cl)$ versus $\log(Cl)$ diagram. In contrast, Li and Cs distributions exhibit a positive linear trend while Rb and Sr show the opposite way, indicating a preferential partitioning to the vapor and brine phases, respectively. This is in line with previous studies (Berndt and Seyfried, 1990; Pokrovski et al., 2005; Foustoukos and Seyfried, 2007a; Pester et al., 2015). This is also coherent with the LSHF study of Pester et al. (2012), apart for Rb

which shows less brine affinity due to the extended Cl range brought by Capelinhos fluid. Note, however, that without Capelinhos fluid, Rb presents a steeper linear slope at +0.38, identical that one at +0.35 reported in Pester et al. (2012). Element vapor/brine partitioning can be summarized as follow $Sr < Rb < Br < Cs < Li$ with increasing affinities for the vapor phase. Therefore, the linear correlation of each of these elements over the Cl range (from 262mM to 580mM; Fig IV - 3) supports a phase separation process controlling overall trace element abundances as proposed by Pester et al. (2012).

Nevertheless, very local variations can be observed, as both Crystal and South Crystal fluids display high Sr/Cl, high Rb/Cl, and low Li/Cl compared to Sapins, which belongs to the SW group and is located a few meter apart (Fig IV - 1). These differences are unlikely to be explained by phase separation processes in the reaction zone but rather by local, shallow differences in the hydrothermal pathways. Crystal appears to be a relatively young vent site, earning its name from the former discharge of “crystal” clear water (Von Damm et al., 1998; Pester et al., 2012). Anhydrite dissolution in the upflowzone could potentially explain the observed excess Ca, SO₄ and Sr of fluids at this site, compared to the fluids at nearby South Crystal (Fig IV - S1). Higher Li, Rb and Cs concentrations, regarded as highly mobile elements in basalts, could be due to alteration of fresh basalt at depth. Although some differences are explained between these two sites (e.g. anhydrite implication), the trace element differences between them remains problematic.

To sum-up, the distribution of trace element as a function of the extended Cl content of hydrothermal fluid brought by the Capelinhos fluids, is controlled by phase separation process, and therefore suggests that a unique fluid source feeds the hydrothermal circulation cell(s) at the LSHF

6. Pressure and temperature of the reaction zone

While Li, Rb, Sr and Cs variations are indicators of phase separation occurring at depth, other elements such as Fe, Mn and Si are sensitive to processes other than phase separation (Fig IV - 3). The mentioned elements provide information about hydrothermal circulation from the phase separation zone to the seafloor (e.g. upflow zone) and therefore the extent of the reaction zone. Phase separation represents the starting point of up flowing fluid, and represents the deepest part of the reaction zone that can be chemically recorded. In contrast, the up-flow zone records all the interactions between the fluid and the rock starting from the separation phase zone till the seafloor, whereby the last chemical equilibration point of

fluids with the greenschist facies mineral assemblages marks the roof of the reaction zone, i.e. the shallowest part at which fluid-rock interactions will cease.

We will now use chemical tracers to infer P and T conditions tracing the fluid pathway from the deepest part, i.e. phase separation zone/base of the reaction zone, to the shallowest part, i.e. roof of the reaction zone in the up-flow zone. This is based on two independent hypotheses: 1) phase separation and quartz equilibrium are concomitant and the fluid up-flows fast enough to avoid modification (Fontaine et al., 2009); here P and T conditions are constrained by Cl concentration (conservative element) and Si concentrations (PTX sensitive element), and 2) since quartz equilibrium and greenschist minerals facies equilibrium occurs concomitantly at the roof of the reaction zone, T will be constrained by Fe and Mn concentrations ratios (Pester et al., 2011) while P will be deduced from estimated T and quartz solubility relations (Von Damm et al., 1991; Foustoukos and Seyfried, 2007b).

6.1 *P–T conditions of phase separation*

Since the late 1960's, geochemical tools have been developed to assess the P and T conditions of the reaction zone of hydrothermal systems, in particular at submarine hydrothermal systems, using quartz solubility (Fournier and Rowe, 1966; Fournier, 1983; Von Damm et al., 1991; Foustoukos and Seyfried, 2007b). Von Damm et al. (1991) derived a semi-empirical relation for geothermobarometry of silica that takes into account the effect of salinity on quartz solubility based on seawater/quartz reaction experiment and data from literature. These authors derived the following equation:

$$\ln(mSiO_2 \cdot nH_2O) = a + b \times \ln(\rho) + \left(c + \frac{d}{T}\right) + e \times P/T \quad (1)$$

With P in bars and T in K, $mSiO_2$ in molality, and n is the hydration number of the dissolved silica ($a=-2.32888$; $b=1.79547$; $c=-2263.62$; $d=0.00407350$; $e=0.0398808$) (Von Damm et al., 1991). Later, Foustoukos and Seyfried (2007b) investigated quartz equilibria close to the two phase boundary conditions and adapted equation (1) (applied to pure water) with a Setchenow term which accounts for deviation from ideality. Quartz solubility has a retrograde behavior meaning that for a constant pressure, it will increase with temperature until a maximum value is attained, above which quartz solubility decreases (Fournier et al., 1982; Von Damm et al., 1991; Foustoukos and Seyfried 2007b; Fig IV - 5b). Therefore,

interpretation of Si concentrations in fluids as related to quartz solubility is not straightforward and requires careful considerations.

Si and Cl end-member fluid concentrations have been used as a geothermobarometer to determine the depth at which phase separation occurs for several hydrothermal systems worldwide (Fontaine et al., 2009). This is based on the assumption that Cl and Si content of hydrothermal fluids vary according to P and T conditions, independently from one another and that the silica concentration corresponds to equilibrium with quartz in the domain of phase separation (Fournier, 1983; Bischoff and Rosenbauer, 1985; Bischoff, 1991; Von Damm et al., 1991; Driesner, 2007; Driesner and Heinrich, 2007; Foustoukos and Seyfried, 2007b; Fontaine et al., 2009). This geothermobarometer is adapted to vapor-like fluids because they are more likely to exit the phase separation zone and therefore more likely to record the P–T conditions of phase separation. The intercept between Cl and Si theoretical isopleths provides unique set of P and T conditions at which equilibrium of both elements is achieved. This geothermobarometer is highly sensitive to subsurface processes such as altered seawater entrainment, which would modify both Si and Cl concentrations of the discharging fluid, but also to conductive cooling which would impact only Si concentrations. As an example, if mixing of low Cl and high Si hydrothermal fluid with seawater or silica precipitation occurs prior to fluid discharge, the Cl and Si concentrations of end-member hydrothermal fluid will produce biased estimates of P and T conditions for the phase separation zone. These limitations are partly addressed here by choosing the most vapor-like fluid of the LSHF. When applying this Si-Cl geothermobarometer to the Capelinhos fluids, we obtain a temperature of 438°C and a pressure of 375 bars for the phase separation zone, that corresponds to a depth of 2600 mbsf (using a cold hydrostatic pressure gradient of $\rho=800\text{kg/m}^3$ for pressure to depth beyond seafloor conversion, Fontaine et al., 2009). Fontaine et al. (2009) determined similar P and T conditions at 390 bars and 440°C for the LSHF phase separation zone using the Tour Eiffel chemical data for fluids collected in 1993 (Charlou et al., 2000).

To sum-up, the Si-Cl geothermobarometer applied on the most-vapor dominated hydrothermal fluid of the LSHF infers that phase separation zone occurs at a depth of 2600mbsf at 438°C, less than a kilometer above the AMC. These P-T conditions for phase separation are in line with previous estimate of Fontaine et al. (2009).

6.2 *P–T conditions in the upflow zone*

We infer from the previous section that phase separation takes place at about 2600mbsf, depth at which hydrothermal fluids upflow towards the seafloor. However, recent geophysical data acquired through the EMSO-Azores observatory infrastructure indicate that micro-seismic clusters between 1800 and 2500 mbsf as a consequence of thermal cracking of the rocks at and near the base of the Lucky Strike hydrothermal circulation cell(s) (Crawford et al., 2013). Such event may imply modifications of the P-T conditions along the upflow zone, even though such events are not essential to produce variable P-T conditions if we consider that Quartz re-equilibration may occur in the upflow zone rather than solely in the separation phase zone. In such case, the Si-Cl geothermobarometer will produce underestimation of P-T conditions at the separation zone.

We will now consider the eventuality that Si concentrations of hydrothermal fluids reflect Quartz re-equilibration along the upflow zone, i.e. the roof of the reaction zone. In this case, quartz equilibrium and fluid-greenschist minerals facies equilibrium occurs concomitantly. The working hypothesis is that most fluid-rock interactions occur in greenschist facies T conditions as evidenced by the Fe and Mn concentrations of hot vent fluids which are consistent with greenschist facies alteration minerals such as chlorite, magnetite and sodium-bearing plagioclase (Pester et al., 2011). Moreover, Quartz veins in the ocean crust are often associated to greenschist facies minerals such as pyrite, chlorite, amphibole and epidosite (Delaney et al., 1987; Honnorez 2003; Heft et al., 2008; Alt et al., 2010). The reaction zone is often described as the epidosite zone, on top of AMC, but quartz and sulfide veins are also associated with amphibole and chlorite at shallower depth in the greenschist conditions (Delaney et al., 1987; Heft et al., 2008; Alt et al., 2010). The P-T conditions of the roof of the reaction zone will be deduced from quartz solubility relations (Von Damm et al., 1991; Foustoukos and Seyfried, 2007b) at T constrained by the Fe and Mn concentrations of hydrothermal fluids (Pester et al., 2011).

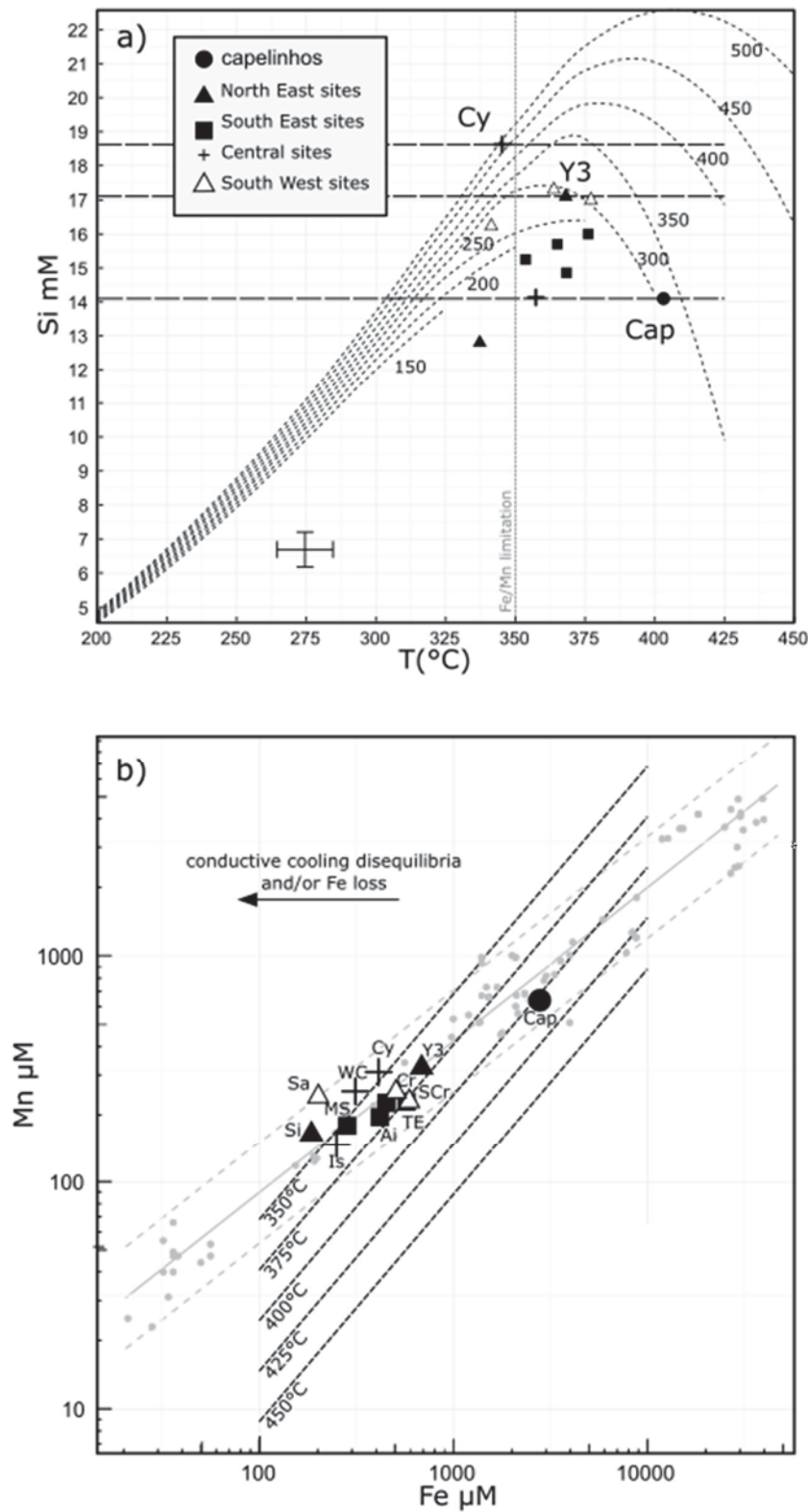


Figure IV - 5 Geochemical information for P and T. a) Quartz geothermometer based on Foustoukos and Seyfried (2007b). Points represent Si measured in fluids with calculated temperature from Fe and Mn geothermometer. Grey dashed lines represent the "classical" approach to evaluate P and T (see text for details). b) Fe and Mn concentration on a logarithm scale (Modified from Pester et al., 2011). Grey line represent basalt alteration line and black dashed lines are isotherms calculated from the Fe/Mn geothermometer.

The Fe–Mn geothermometer developed by Pester et al. (2011) is based on the experimental results of basalt alteration by seawater over a wide range of P and T conditions, i.e. from 500 to 1000 bars and 200 to 500°C (Mottl et al., 1979). They show that transition metal concentrations such as Fe and Mn of hydrothermal fluids are strongly controlled by temperature while pressure has a minimal effect (Pester et al., 2011 and references therein). They derived the following equation:

$$T = 331.24 + 112.41 \times \log(Fe/Mn) \quad (2)$$

With T in °C and Fe and Mn are concentrations in µM. This geothermometer is best suited for 350-450°C temperatures whereby below and above these limits, uncertainties are too high to provide further information than the Si geobarometer (Pester et al., 2011). Capelinhos end-member fluid, as the most-vapor dominated one, exhibits the highest Fe and Mn concentrations of all the LSHF fluids, equivalent to Fe concentration found at Broken Spur (29°N) or MARK (23°N) on the MAR (Campbell et al., 1988; James et al., 1995). These high concentrations suggest a minimum temperature of greenschist facies equilibrium at 400°C, which when combined to a Si content at 14,1 mM, reveals P-T conditions at 300 bars and 400°C, respectively, for the Capelinhos fluids, i.e. close to the critical point of seawater (Fig IV - 5a). Applying the same approach to our 2013 survey of LSHF fluid chemistry, the most brine-dominated hydrothermal fluids, i.e. the SW group and Y3 of the NE group, are also coherent with 300 bars for the roof of the reaction zone but at temperature lower than 375°C. By comparison, the classical approach is based on the assumption that hydrothermal fluids exhibiting the highest Si concentrations will best estimate the minimum P condition over a range of temperatures at which quartz solubility is maximal (Von Damm, 2000; Von Damm et al., 1998; Foustoukos and Seyfried, 2007b; Fig IV - 5a). Previously, the reaction zone conditions were first determined for the site Y3/2608, that had the highest Si concentration at that time of sampling, revealing equilibration at P=300 bars and T=360-380°C (Si=17.5 mM; Von Damm et al., 1998).

These P and T conditions at 300 bars and <400°C are significantly lower than 375 bars and 438°C conditions estimated from the Si-Cl thermobarometer of Fontaine et al. (2009). The P-T discrepancy between Von Damm et al. (1998) and Fontaine et al. (2009) results is partly due to the choice of quartz solubility relation. Fontaine et al. (2009) used quartz solubility relation from Foustoukos and Seyfried (2007b) which predict, for relatively low temperature range, higher pressure and temperature necessary to reach the same Si

concentrations obtained in the model of Von Damm et al. (1991). In contrast, at higher temperature range, the relation is reversed whereby the lowest pressure are predicted for Von Damm's model. Temperature is a key parameter impacting significantly the P-T estimates of the reaction zone based on Quartz solubility relations. The temperature difference between this minimum temperature of greenschist facies reaction as seen from Fe and Mn concentrations and that of phase separation deduced from the Si-Cl co-variations can be produced by other process acting along the upflow zone, such as conductive cooling. Fe is more sensitive to environmental changes (e.g. pH and redox conditions) than Mn does. Any temperature changes will be readily reflected by changes in Fe, while Mn changes more slowly (Pester et al., 2011; Seyfried, 1995). Rapid conductive cooling in the subsurface and/or Fe loss at discharge would therefore be indicated by an apparent enrichment in Mn (Fig IV - 5b). The LSHF fluids sampled in 2013 does not show the deviation in Mn but they do exhibit both depletion in Fe and Mn compared to Capelinhos fluid which exhibits the highest Fe and Mn concentrations of all LSHF fluids. These high concentrations suggests a minimum temperature of greenschist facies equilibrium at 400°C (Fig IV - 5a) while other sites of LSHF, calculations indicate temperatures comprised between 350 and 375°C (Table 3), coherent with the range of temperature suggested by quartz solubility (Von Damm et al., 1998; Pester et al., 2012).

To sum-up, the P-T conditions of the separation phase zone till the last conditions of fluid-greenschist facie mineral assemblage equilibrium, i.e the base and roof of the reaction zone, respectively, greatly depend on the models considered for the quartz solubility relation, the geothermometer as the most representative of the greenschist facie mineral assemblage and the environmental changes that may occur. This is evidenced by P-T conditions that vary between 300 - 375 bars and 350 - 438°C deduced for this area.

6.3 P-T fluid pathway at LSHF

A parameter that is barely taken into account between chemical experimental studies and natural hydrothermal fluids, is time-scale. For example, Quartz solubility experiments show equilibration on a timescale of several days (Von Damm et al., 1991; Foustoukos and Seyfried 2007b) while fluid discharge from the base of the upflow to the seafloor is thought to be of few hours (Delaney et al., 1987; Alt, 1995). Furthermore, Seewald and Seyfried (1990) showed that Si concentration response to temperature change was slow compared to Fe and Mn. So, all depends on the geological hypothesis considered at the start, i.e.

permeability, which greatly influence pressure estimates. What we propose to do is to carry out calculations that are based on quartz solubility relation from Foustoukos and Seyfried (2007b), Fe–Mn geothermometer from Pester et al. (2011) and NaCl–H₂O properties from Driesner and Heinrich (2007) but for which P estimates are acquired by injection of calculated temperature and fluid density that best matches the measured concentrations of hydrothermal fluids (our 2013 LSHF chemistry survey). The errors in pressure (± 25 bars) are based on the error on temperature from Fe–Mn thermometer ($\pm 11^\circ\text{C}$) applied to the model of quartz solubility. Therefore, the estimated pressure acquired for the roof of the reaction zone should not be taken as “true” pressure of equilibration (or depth estimation) but rather as a proxy of residence time in the reaction zone due to incomplete Si equilibrium. The results as a P and T path of the fluids are shown in Figure 6.

We estimate the P and T conditions of Capelinhos fluids at 350 bars and 404°C , corresponding to a depth of ~ 2300 mbsf ($\rho=800\text{kg/m}^3$), while results for the NE, SW and SE sites would suggest lower P–T conditions (~ 300 bars and $\sim 370^\circ\text{C}$), i.e. shallower depth ~ 1600 mbsf. The shallower and colder P and T conditions at the sites situated near the lava lake depict a higher residence time in the upflow zone compared to Capelinhos and therefore indicate conditions closer to the seafloor conditions. We anticipate that rapid fluid extraction at Capelinhos leads to relatively low residence time in the upflow zone and consequently limited changes in chemistry after phase separation. This fast extraction might be triggered by enhanced permeability associated with the system of normal faults that bound the axial graben to the east. Capelinhos is located near a minor west-facing fault that belongs to this system, ~ 1.5 km to the east of the larger offset fault that was labelled F2 by Combier et al. (2015; Fig IV - 6). It is clear that fluids from Capelinhos have cooled from reaction zone ($\sim 400^\circ\text{C}$) to the discharge (324°C), nevertheless they record little evidence of further interactions with the substratum along the upflow. We believe that Capelinhos fluids have cooled conductively but exited the seafloor fast enough to maintain a chemical composition close to that at phase separation condition until they reached the surface.

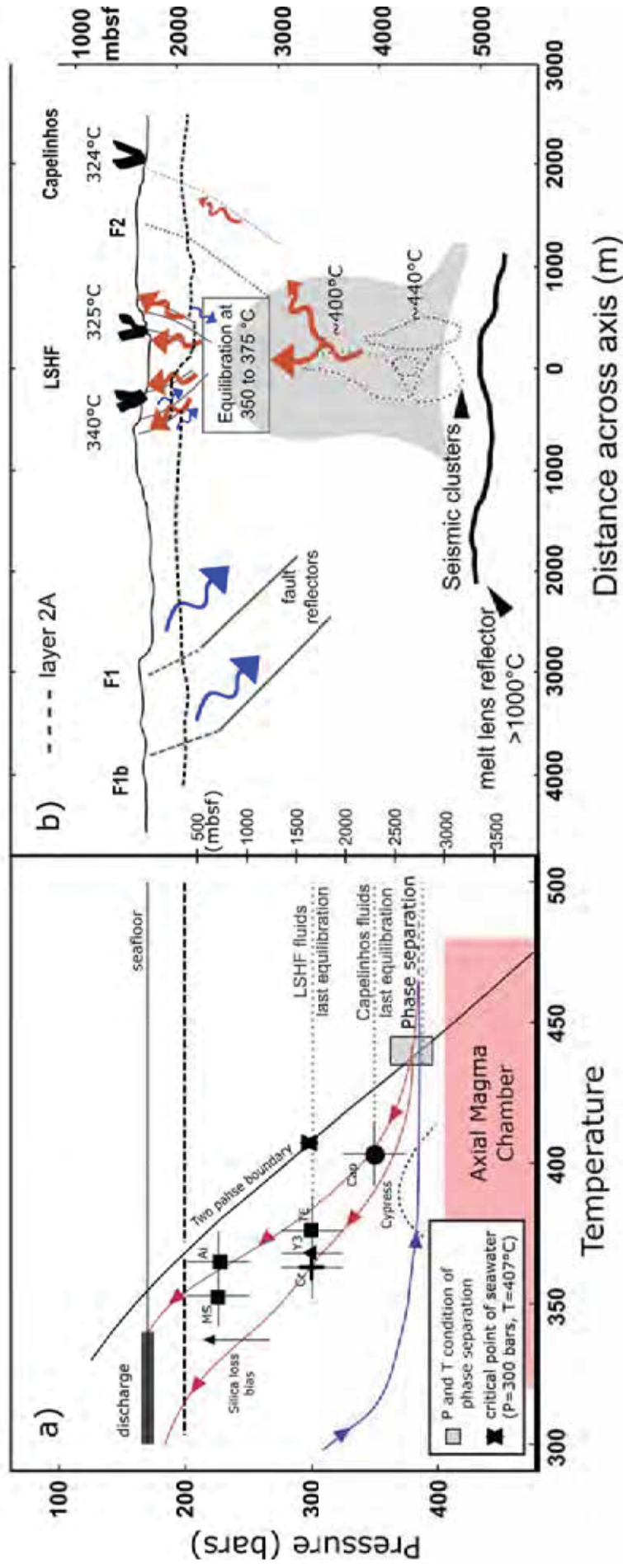


Figure IV - 6 Fluid circulation. a) Calculated P and T of some vents at equilibria with quartz are presented. P and T were calculated using the Fe/Mn geothermometer of Pester et al. (2011), quartz geothermobarometer (Foustoukos and Seyfried, 2007b) and NaCl-H₂O solution properties (Driesner et al., 2007) (See details in text). Dotted lines represent the depth of the base of layer 2A for western and eastern sites (Arnulf et al., 2011). The red shaded domain represents the range of depth to the top of the axial magma chamber as identified by Singh et al. (2006) and Combier et al. (2015). Grey lines represent fault labeled F1, F1b in Combier et al. (2015), dotted grey line correspond to F2. The blue line represents the inferred P - T path in the recharge zone where cold seawater percolate through oceanic crusts and gradually interacts with rocks. Red lines represents the inferred P - T path in the upflow zone, based on the conditions estimated from fluid chemistry. The grey rectangle represents the phase separation zone estimated from the Si and Cl concentrations in the low salinity fluids (Capelinhos, TE) using the geothermobarometer proposed by Fontaine et al. (2009). b) Modified from Escartin et al. (2015). Cartoon representing the hydrothermal cell under the LSHF. Blue arrows represent downward flow of seawater; red arrows are focused hot fluid moving upward through cracks and faults. Black star represents the hypothetical position of Capelinhos fluid extraction through a high angle fault. Seismic clusters are from Crawford et al. (2013). F1, F1b and F2 from Combier et al. (2015).

At the lava lake spatial scale, the SE sites (Tour Eiffel, Aisics and Montsegur) show similar Cl end-members as well as major and trace element end-member concentrations (Ca, Na, K, Li, Br, Cs, Rb, Sr; Table IV - 3). However, Si content is lower at Aisics and Montségur than at Tour Eiffel. This difference leads to an apparent shallow equilibration of Aisics and Montségur (Fig IV - 6), but this is probably an artifact due to Si loss along the upflow through amorphous silica precipitation induced by conductive cooling (Fig IV - 5 and 6). Also, the “shallow” equilibration could be a locally enhanced residence time of the fluid discharging at Montsegur and Aisics compared to TE, but since Aisics and TE are just a few meters apart (Fig IV - 1), it seems unlikely.

The consistency of P and T inferred from Y3, Crystal, South Crystal and Tour Eiffel makes it clear that most fluids have the same residence time in the upflow zone. However, end-member fluids of Capelinhos and Cyprès sites clearly suggest a higher pressure and/or temperature conditions and therefore extraction from a deeper part of the reaction zone through a complex channeling network to the seafloor.

Information about channeling pathway of hydrothermal fluid to the surface can be obtained by studies of fossil hydrothermal system, such as the sulfides formations in the Troodos ophiolite (Keith et al., 2016). Although this study is not directly comparable to our fluid data, an analog phenomenon might be happening at the LSHF. These authors discussed the formation of sulfides of a fossil hydrothermal system in the Troodos ophiolite based on the variation of Fe/Zn ratio in sphalerite. They concluded that the massive sulphides were formed by a 400°C fluid, whilst the stockwork sulphide indicate cooler fluid temperature. Cooler temperatures were accompanied by mineralogical and isotopic evidence of seawater mixing. At LSHF, the lower temperature recorded by some fluid end-members could be related to intense cooling of the substratum due to the along-axis recharge zone and enhanced cold seawater saturated environment as the upflow zone becomes shallower. The lack of iron in the main LSHF fluids compared to Capelinhos is then explained by loss through sulfide precipitation following conductive cooling. By comparison, the fluids of the fossil lava lake LSHF sites, which originate from the same deep rooted source, display lower Fe–Mn concentrations leading to calculated temperature indicative of conductive cooling (Fig IV - 5). Fractures observed on the axial graben allows local seawater recharge (Humphris et al., 2002; Ondréas et al., 2009), which enhances conductive cooling of the sealed upflow zone and leads to Si and/or Fe and Mn losses within the stockwork (Fig IV - 6). This faulting allows seawater to percolate down to the brittle ductile front as deep as

2800 mbsf (Crawford et al., 2013). By conductive cooling of the upflow zone, the down-flowing seawater feeds an actively forming stockwork

7. Chloride variability within the LSHF.

Several studies investigate discharge of brine phases to explain worldwide salinity variation in submarine hydrothermal fluids. With the use of numerical modelling, Schoofs and Hansen (2000) conclude that high chlorinity fluids could be due to slow brine entrainment leading to depletion of the brine layer at depth. This process could produce fluid venting with salinity up to two-time higher than that of seawater, accompanied by a cooler exit temperature (Schoofs and Hansen, 2000). At LSHF, Crystal, South Crystal, Sapins, and Y3 end-member fluids are characterized by salinities just slightly above that of seawater while discharging within the highest temperature recorded at the LSHF, i.e. up to 340°C. These features contradict numerical modelling predictions that argue for cooler fluid discharge when brine is entrained (Schoofs and Hansen, 2000).

Using numerical modelling, Fontaine and Wilcock (2006) investigated the buoyancy of a brine and its capacity to flow upward. They showed that brine produced under supercritical conditions with salinity lower than 20-25wt% NaCl could flow towards the surface while being stored within the rock backwater porosity in the reaction zone. Meanwhile, vapor phase flows preferentially through wider cracks (Goldfarb and Delaney, 1988; Fontaine and Wilcock, 2006). These authors further developed the hypothesis that permeability gradients could act as a barrier for brine upflow and tend to concentrate brine at the base of the layer 2A (Fontaine et al., 2007). When the upflow zone is saturated with brine, or during cooling of the system, brine can be entrained, and mixed with vapor or seawater salinity hydrothermal fluid, which leads to fluid discharge with higher salinity than seawater.

Coumou et al. (2009) conducted numerical modelling to investigate salinity variations at discharge zones for different heat flux and pressure. For a pressure of 150 bars at the seafloor and ~250 bars at the bottom of the system, i.e. phase separation zone ~1000mbsf, these simulations show temporal variations in vent fluid salinity with several spikes at salinity higher than seawater over periods of several years. These salinity spikes are also associated with little temperature spikes of a few degree (<10°C). However, these salinity and temperature spikes were not observed for simulations at higher pressures (250 and 350 bars at the seafloor) while assuming the same heat flux. Coumou et al. (2009) explain these salinity pulses as due to brine mobilization as the porosity of the upflow zone gets saturated.

Deep phase separation leads to vapor and brine formation but due to different physical behavior and the wetting effect of the liquid (brine) phase, brines will segregate and be stored in backwater porosity or will coat the walls of larger channels (Fontaine and Wilcock, 2006). As long as brine saturation is lower than a threshold value (10-20%), the brines do not form a continuous medium and remain immobile. However, when this threshold is reached, and provided that the vertical pressure gradients in the upflow is high enough compared to brine density (Fontaine and Wilcock, 2006; Fontaine et al., 2007), then the brine phase is ready to be flushed (Coumou et al., 2009). Further mixing of this brine with vapors and/or seawater during the upflow produces a transient spike in salinity. Salinity then returns to the initial vapor-like one, while the brine layer builds up again and reduce saturation of the backwater porosity.

In the natural hydrothermal environment, flushing of the brine backwater porosity is illustrated over a 12-15 months period by in-situ monitoring of Cl concentrations at the Main Endeavour Field (Larson et al., 2009). These authors showed evidence of Cl variability related to brine entrainment and were able to reconstruct the brine salinity and temperature. They explained brine entrainments by changes in the layer 2A permeability and brine storage up to the base of layer 2A. Considering the LSHF, chlorinity contents of the Y3 end-member fluid increased from 436 mM in 1993 (Von Damm et al. 1998) to 586 mM in 2013 (this study, Table 3). Furthermore, the increase in Cl content is found with a decrease in Si end-member (corresponding to ~30 bars, close to the error), which argue for a higher residence time in the upflow zone. Although the physical conditions at LSHF (170 bar at seafloor, ~400 bars at phase separation zone) are different from the numerical models of Coumou et al. (2009), we propose that Cl spikes, i.e. salinity variations, could be caused by fluid circulation dynamics rather than mixing in subsurface or phase separation conditions. This is based on the recent study of Barreyre and Sohn (2016) who assessed the thickness of layer 2A based on the tidal response of temperature sensors positioned at LSHF. They pointed out that the base of layer 2A was not homogeneously deep over the LSHF, showing a difference of 300m between the west and east of the fossil lava lake area, with the deepest base of layer 2A on the eastern site at 600 mbsf (Fig IV - 6). From our 2013 LSHF chemical survey, we propose that the decreasing Cl contents from west to east of the fossil lava lake (SW group at ~580 mM to Capelinhos at ~260 mM) are affected by the increasing thickness of the layer 2A from west to east, whereby modifying the dynamic of the hydrothermal fluid circulation cell. Nonetheless, the effect of shallow permeability

on the variability of discharging fluid salinity needs then to be further addressed by numerical modelling as permeability is a crucial parameter for the residence time of the fluid in the upflow zone.

Conclusion

A new active site, named Capelinhos, was discovered at LSHF in 2013. The site is situated approximately 1.5 km east of the main Lucky Strike axial graben and fossil lava lake, where the well-known LSHF vents are located. Capelinhos vents high temperature black smoker fluids at 324°C. Its fluid chemistry has two distinct characteristics compared to the other LSHF vent sites: 1) the lowest Cl concentration ever measured at LSHF and 2) the highest Fe and Mn concentration (2800 μM and 640 μM respectively). By combining geothermobarometer based on end-member fluid chemistry, we show that Capelinhos fluids were formed at supercritical conditions, as are the other vapor-dominated fluids from LSHF. The temperature of the phase separation zone, estimated from Si-Cl geothermobarometry is 438°C and its depth is 2600mbsf. These results are in agreement with the maximum depth of microseismic events reported in Crawford et al. (2013) which are interpreted as due to rapid heat exchange between hot rocks and down-going hydrothermal fluids.

Equilibrium temperatures calculated using the Fe–Mn geothermometer of Pester et al (2011) range between ~370°C for LSHF fluids and ~400°C for Capelinhos. By combining quartz solubility with these calculated temperatures, the minimum equilibration temperature and pressure in the reaction zone appears to be deeper for Capelinhos fluids (350 bars) than for LSHF (300 bars). Because the fluids vent at temperatures that are still well within the greenschist facies realm, these conditions are not thought to be representative of the top of the reaction zone. More accurately, they are indicative of significant differences in the residence time of the fluid in the upflow zone between Capelinhos and the other LSHF vents.

We propose a new model of the hydrothermal path based on data from Capelinhos. When crossing the 2-phase boundary, the recharging fluid undergoes phase separation at ~2600 mbsf. The fluid starts flowing upward and differentiate by entrainment of brine in subsurface. Fluids (vapor and brines) moving upwards beneath the lava lake undergo intense conductive cooling due to high residence time in the upflow zone related to the heterogeneous thickness of the layer 2A and complex porous/fractured media.. These brine

mixing and cooling processes likely participates to the formation of an extensive stockwork beneath the lava lake. Fluids (vapors) discharging at Capelinhos, diverted from the vertical upflow zone by a high angle fault zone, undergo significant cooling but limited chemical changes.

Acknowledgements

We are grateful to the chemistry facility of the Géoscience Environment Toulouse laboratory (GET). Th. Leleu acknowledges the French Ministry of Education and Research for the financial support of his Ph.D. fellowship. We also acknowledge financial support from the French ANR Lucky scales project (ANR-14-CE02-0008-03) and the EU project EMSO (<http://www.emso-eu.org/>).

References

- Albarède F., Michard A., Minster J.-F., Michard G. (1981) $^{87}\text{Sr}/^{86}\text{Sr}$ ratios in hydrothermal waters and deposits from the East Pacific Rise at 21°N. *Earth Planet. Sci. Lett.* 55, 229–236.
- Alt J. C. (1995) Seafloor processes in mid-ocean ridge hydrothermal systems. In: *Seafloor Hydrothermal Systems: Physical, Chemical, Biological, and Geological Interactions*. (eds. S. E. Humphris, R. A. Zierenberg, L. S. Mullineaux and R. E. Thomson). *Geophys. Mon. 91*. Am. Geophys. Un., Washington, DC. Pp 85-114.
- Alt J. C., Teagle D. A. H. (2003) Hydrothermal alteration of upper oceanic crust formed at a fast-spreading ridge: mineral, chemical, and isotopic evidence from ODP Site 801. *Chem. Geol.* 201, 191–211. doi:10.1016/S0009-2541(03)00201-8
- Alt J. C., Laverne C., Coggon R. M., Teagle D. A. H., Banerjee N. R., Morgan S., Smith-Duque C., Harris M., Galli L. (2010) Subsurface structure of a submarine hydrothermal system in ocean crust formed at the East Pacific Rise, ODP/IODP Site 1256. *Geochem. Geophys. Geosystems* 10, 1-28. doi: 10.10292010GC003144
- Arnulf A. F., Singh S. C., Harding A. J., Kent G. M., Crawford W. (2011) Strong seismic heterogeneity in layer 2A near hydrothermal vents at the Mid-Atlantic Ridge: Seismic heterogeneity in Layer 2A. *Geophys. Res. Lett.* 38. doi:10.1029/2011GL047753
- Barker A. K., Coogan L. A., Gillis K. M., Weis D. (2008) Strontium isotope constraints on fluid flow in the sheeted dike complex of fast spreading crust: Pervasive fluid flow at Pito Deep: Strontium isotope constraints, 1. *Geochem. Geophys. Geosystems* 9. doi:10.1029/2007GC001901
- Barreyre T., Escartín J., Garcia R., Canna, M., Mittelstaedt E., Prados R. (2012) Structure, temporal evolution, and heat flux estimates from the Lucky Strike deep-sea hydrothermal field derived from seafloor image mosaics: Hydrothermal outflow and image mosaics. *Geochem. Geophys. Geosystems* 13. doi:10.1029/2011GC003990
- Barreyre T., Sohn R. A. (2016) Poroelastic response of mid-ocean ridge hydrothermal systems to ocean tidal loading: Implications for shallow permeability

structure: Shallow Upflow Zone Permeability. *Geophys. Res. Lett.* 43, 1660–1668. doi:10.1002/2015GL066479

Berndt M. E., Seyfried Jr W. E., Beck W.J. (1988) Hydrothermal Alteration Processes at Mid-Ocean Ridges: Experimental and Theoretical Constraints From Ca and Sr Exchange Reactions and Sr Isotopic Ratios. *J. Geophys. Res.* 93, 4573–4583.

Berndt M. E., Seyfried, Jr., W. E., Janecky, D. R. (1989) Plagioclase and epidote buffering of cation ratios in mid-ocean ridge hydrothermal fluids: Experimental results in and near the supercritical region. *Geochim. Cosmochim. Acta* 53, 2283–2300.

Berndt M. E., Seyfried, Jr., W. E. (1990) Boron, bromine, and other trace elements as clues to the fate of chlorine in mid-ocean ridge vent fluids. *Geochim. Cosmochim. Acta* 54, 2235–2245.

Besson P., Degboe J., Berge B., Chavagnac V., Fabre S., Berger G. (2014) Calcium, Na, K and Mg Concentrations in Seawater by Inductively Coupled Plasma-Atomic Emission Spectrometry: Applications to IAPSO Seawater Reference Material, Hydrothermal Fluids and Synthetic Seawater Solutions. *Geostand. Geoanalytical Res.* 38, 355–362. doi:10.1111/j.1751-908X.2013.00269.x

Bischoff J. (1991) Densities of liquids and vapors in boiling NaCl-H₂O solutions: A PVTX summary from 300° to 500°C. *Am. J. Sciecn* 291, 309–338.

Bischoff J., Rosenbauer R. J. (1985) An empirical equation of state for hydrothermal seawater (3.2 percent NaCl). *Am. J. Sciecn* 285, 725–763.

Bischoff J., Rosenbauer R. J. (1989) Salinity variations in Submarine Hydrothermal Systems by Layered Double-Diffusive Convection. *J. Geol.* 97, 613–623.

Brant C., Coogan L. A., Gillis K. M., Seyfried, Jr., W. E., Pester N. J., Spence J. (2012) Lithium and Li-isotopes in young altered upper oceanic crust from the East Pacific Rise. *Geochim. Cosmochim. Acta* 96, 272–293. doi:10.1016/j.gca.2012.08.025

Buck W. R., Lavier L. L., Poliakov A. N. (2005) Modes of faulting at mid-ocean ridges. *Nature* 434, 719–723.

Campbell A. C., Bowers T. S., Measures C. I., Falkner K. K., Khadem M., Edmond J. (1988) A time series of vent fluid compositions from 21°N, East Pacific Rise (1979, 1981, 1985), and the Guaymas Basin, Gulf of California (1982, 1985). *J. Geophys. Res. - Solid Earth* 93, 4537–4549.

Cannat M., Briais A., Deplus C., Escartin J., Georgen J., Lin J., Mercouriev S., Meyzen C., Muller M., Pouliquen G., Rabain A., da Silva P. (1999) Mid-Atlantic-Azores hotspot interactions: along-axis migration of a hotspot-derived event of enhanced magmatism 10 to 4 Ma ago. *Earth Planet. Sci. Lett.* 173, 257–269.

Charlou J. L., Donval J. P., Douville E., Jean-Baptiste P., Radford-Knoery J., Fouquet Y., Dapoigny A., Stievenard M. (2000) Compared geochemical signatures and the evolution of Menez Gwen (37°50'N) and Lucky Strike (37°17'N) hydrothermal fluids, south of the Azores Triple Junction on the Mid-Atlantic Ridge. *Chem. Geol.* 171, 49–75.

Charlou J. L., Donval J. P., Konn C., Ondréas H., Fouquet Y., Jean-Baptiste P., Fourré E. (2010) High Production and Fluxes of H₂ and CH₄ and Evidence of Abiotic Hydrocarbon Synthesis by Serpentinization in Ultramafic-Hosted Hydrothermal Systems on the Mid-Atlantic Ridge. In: *Diversity of Hydrothermal Systems on Slow Spreading*

Ocean Ridges (eds. Rona P. A., Devey C., Dymont J., Murton, B). *Geophys. Mon.* 188. Am. Geophys. Un., Washington, DC. pp 265-296.

Chavagnac V., Leleu T., Boulart C., Barreyre T., Castillo A., Menjot L., Cannat M., Escartín J., Sarradin P.-M. (2015) Deep-Sea Observatory EMSO-Azores (Lucky Strike, 37°17'N MAR): Impact of Fluid Circulation Pathway on Chemical Hydrothermal Fluxes, in: *Follow the Fluids: Integrating Multidisciplinary Observations of Deep-Sea Hydrothermal Systems II*. Presented at the AGU Fall Meeting, San Francisco.

Chen Y., Morgan W. J. (1990) A Nonlinear Rheology Model for Mid-Ocean Ridge Axis Topography. *J. Geophys. Res.* 95, 17583–17604.

Colaço A., Blandin J., Cannat M., Carval T., Chavagnac V., Connelly D., Fabian M., Ghiron S., Goslin J., Miranda J. M., Reverdin G., Sarrazin J., Waldmann C., Sarradin P. M. (2011) MoMAR-D: a technological challenge to monitor the dynamics of the Lucky Strike vent ecosystem. *ICES J. Mar. Sci.* 68, 416–424. doi:10.1093/icesjms/fsq075

Comber V., Seher T., Singh S. C., Crawford W. C., Cannat M., Escartín J., Dusunur D. (2015) Three-dimensional geometry of axial magma chamber roof and faults at Lucky Strike volcano on the Mid-Atlantic Ridge: Magma chamber and faulting at Lucky Strike. *J. Geophys. Res. Solid Earth* 120, 5379–5400. doi:10.1002/2015JB012365

Cooper M. J., Elderfield H., Schultz A. (2000) Diffuse hydrothermal fluids from Lucky Strike hydrothermal vent field: Evidence for a shallow conductively heated system. *Journal Geophys. Res.* 105, 19369–19375.

Coumou D., Matthäi S., Geiger S., Driesner T. (2008) A parallel FE-FV scheme to solve fluid flow in complex geologic media. *Computers & Geosciences*, 34, 1697-1707. Doi: 10.1016/j.cageo.2007.11.010

Coumou D., Driesner T., Weis P., Heinrich C. A. (2009) Phase separation, brine formation, and salinity variation at Black Smoker hydrothermal systems. *J. Geophys. Res.* 114. doi:10.1029/2008JB005764

Crawford W. C., Rai A., Singh S. C., Cannat M., Escartín J., Wang H., Daniel R., Comber V. (2013) Hydrothermal seismicity beneath the summit of Lucky Strike volcano, Mid-Atlantic Ridge. *Earth Planet. Sci. Lett.* 373, 118–128. doi:10.1016/j.epsl.2013.04.028

Delaney J. R., Mogk D. W., Mottl M. J. (1987) Quartz-Cemented Breccias From the Mid-Atlantic Ridge: Samples of a High-Salinity Hydrothermal Upflow Zone. *J. Geophys. Res.* 92, 3767-3787.

Detrick R. S., Needham D., Renard V. (1995) Gravity-Anomalies and Crustal thickness variations along the Mid-Atlantic Ridge between 33°N and 40°N. *J. Geophys. Res.* 100, 3767–3787. doi:10.1029/94JB02649

Douville E., Charlou J. L., Oelkers E. H., Bienvu P., Jove Colon, C. F., Donval J. P., Fouquet Y., Prieur D., Appriou P. (2002) The rainbow vent fluids (36 14' N, MAR): the influence of ultramafic rocks and phase separation on trace metal content in Mid-Atlantic Ridge hydrothermal fluids. *Chem. Geol.* 184, 37–48.

Driesner T. (2007) The system H₂O–NaCl. Part II: Correlations for molar volume, enthalpy, and isobaric heat capacity from 0 to 1000°C, 1 to 5000bar, and 0 to 1 XNaCl. *Geochim. Cosmochim. Acta* 71, 4902–4919. doi:10.1016/j.gca.2007.05.026

Driesner T., Heinrich C. A. (2007) The system H₂O–NaCl. Part I: Correlation formulae for phase relations in temperature–pressure–composition space from 0 to 1000°C,

0 to 5000bar, and 0 to 1 XNaCl. *Geochim. Cosmochim. Acta* 71, 4880–4901. doi:10.1016/j.gca.2006.01.033

Edmond J. M., Measures C., McDuff R. E., Chan L. H., Collier R., Grant B., Gordon L. I., Corliss J. B. (1979) Ridge crest hydrothermal activity and the balances of the major and minor elements in the ocean: The Galapagos data. *Earth Planet. Sci. Lett.* 46, 1–18.

Elderfield H., Schultz A. (1996) Mid-ocean ridge hydrothermal fluxes and the chemical composition of the ocean. *Annu. Rev. Earth Planet. Sci.* 24, 191–224.

EMSO-Azores - EMSO France. URL <http://www.emso-fr.org/fr/EMSO-Azores> (accessed 5.15.16).

Escartin J., Barreyre T., Cannat M., Garcia R., Gracias N., Deschamps A., Salocchi A., Sarradin P.-M., Ballu V. (2015) Hydrothermal activity along the slow-spreading Lucky Strike ridge segment (Mid-Atlantic Ridge): Distribution, heatflux, and geological controls. *Earth Planet. Sci. Lett.* 431, 173–185. doi:10.1016/j.epsl.2015.09.025

Fontaine F. J., Wilcock W. S. D. (2006) Dynamics and storage of brine in mid-ocean ridge hydrothermal systems. *J. Geophys. Res.* 111. doi:10.1029/2005JB003866

Fontaine F. J., Wilcock W. S. D., Butterfield D. A. (2007) Physical controls on the salinity of mid-ocean ridge hydrothermal vent fluids. *Earth Planet. Sci. Lett.* 257, 132–145. doi:10.1016/j.epsl.2007.02.027

Fontaine F. J., Wilcock W. S. D., Foustoukos D. I., Butterfield D. A. (2009) A Si-Cl geothermobarometer for the reaction zone of high-temperature, basaltic-hosted mid-ocean ridge hydrothermal systems: Si/Cl-inferred P–T in MOR hydrothermal systems. *Geochem. Geophys. Geosystems* 10. doi:10.1029/2009GC002407

Fontaine F. J., Cannat M., Escartin J., Crawford W. C. (2014) Along-axis hydrothermal flow at the axis of slow spreading Mid-Ocean Ridges: Insights from numerical models of the Lucky Strike vent field (MAR). *Geochem. Geophys. Geosystems* 15, 2918–2931. doi:10.1002/2014GC005372

Fouquet Y., Ondréas H., Charlou J. L., Donval J. P., Radford-Knoery J. (1995) Atlantic lava lakes and hot vents. *Nature* 377, 201.

Fournier R. O., Rowe P. J. (1966) Estimation of underground temperatures from the silica content of water from hot springs and wet-steam wells. *Am. J. Sci.* 264, 685–697.

Fournier R. O., Rosenbauer R. J., Bischoff J. (1982) The solubility of quartz in aqueous sodium chloride solution at 350°C and 180 to 500 bars. *Geochim. Cosmochim. Acta* 46, 1975–1978.

Fournier R. O. (1983) A method of calculating Quartz solubilities in aqueous sodium chloride solutions. *Geochim. Cosmochim. Acta* 47, 579–586.

Foustoukos D. I., Seyfried, Jr., W. E. (2007a) Trace element partitioning between vapor, brine and halite under extreme phase separation conditions. *Geochim. Cosmochim. Acta* 71, 2056–2071. doi:10.1016/j.gca.2007.01.024

Foustoukos D. I., Seyfried, Jr., W. E. (2007b) Quartz solubility in the two-phase and critical region of the NaCl–KCl–H₂O system: Implications for submarine hydrothermal vent systems at 9°50'N East Pacific Rise. *Geochim. Cosmochim. Acta* 71, 186–201. doi:10.1016/j.gca.2006.08.038

Gamo T., Chiba H., Masuda H., Edmonds H. N., Fujioka K., Kodama Y., Namba H., Sano Y. (1996) Chemical characteristics of hydrothermal fluids from the TAG mound of the mid-Atlantic Ridge in August 1994: implications for spatial and temporal variability of hydrothermal activity. *Geophys. Res. Lett.* 23, 3483–3486.

German C. R., Petersen S., Hannington M. D. (2016) Hydrothermal exploration of mid-ocean ridges: Where might the largest sulfide deposits be forming? *Chem. Geol.* 420, 114–126. doi:10.1016/j.chemgeo.2015.11.006

Goldfarb M. S., Delaney J. R. (1998) Response of Two-Phase Fluids to Fracture Configurations Within Submarine Hydrothermal Systems. *J. Geophys. Res.* 93, B5, 4585–4594.

Hamelin C., Bezos A., Dosso L., Escartin J., Cannat M., Mevel C. (2013) Atypically depleted upper mantle component revealed by Hf isotopes at Lucky Strike segment. *Chem. Geol.* 341, 128–139. doi:10.1016/j.chemgeo.2013.01.013

Hasenclever J., Theissen-Krah S., Rüpke L. H., Morgan J. P., Iyer K., Petersen S., Devey C.W. (2014) Hybrid shallow on-axis and deep off-axis hydrothermal circulation at fast-spreading ridges. *Nature* 508, 508–512. doi:10.1038/nature13174

Heft K. L., Gillis K. M., Pollock M. A., Karson J. A., Klein E. M. (2008) Role of upwelling hydrothermal fluids in the development of alteration patterns at fast spreading ridges: Evidence from the sheeted dike complex at Pito Deep. *Geochem. Geophys. Geosystems* 9, 1–21.

Honnorez J. (2003) Hydrothermal alteration vs. ocean-floor metamorphism. A comparison between two case histories: the TAG hydrothermal mound (Mid-Atlantic Ridge) vs. DSDP/ODP Hole 504B (Equatorial East Pacific). *C.R. Géoscience* 335, 781–824. doi: 10.1016/j.crte.2003.08.009

Humphris S. E., Fornari D. J., Scheirer D. S., German C. R., Parson L. M. (2002) Geotectonic setting of hydrothermal activity on the summit of Lucky Strike Seamount (37°17'N, Mid-Atlantic Ridge): Geotectonic setting. *Geochem. Geophys. Geosystems* 3, 1–25. doi:10.1029/2001GC000284

James R. H., Elderfield H., Palmer M. R. (1995) The chemistry of hydrothermal fluids from the Broken Spur site, 29°N Mid-Atlantic Ridge. *Geochim. Cosmochim. Acta* 59, 651–659.

Keith M., Haase K. M., Klemd R., Krumm S., Strauss H. (2016) Systematic variations of trace element and sulfur isotope compositions in pyrite with stratigraphic depth in the Skouriotissa volcanic-hosted massive sulfide deposit, Troodos ophiolite, Cyprus. *Chem. Geol.* 423, 7–18. doi:10.1016/j.chemgeo.2015.12.012

Kelley D. S., Delaney J. R. (1987) Two-phase separation and fracturing in mid-ocean ridge gabbros at temperatures greater than 700°C. *Earth Planet. Sci. Lett.* 83, 53–66.

Kelley D. S., Robinson P. T. (1990) Development of a brine-dominated hydrothermal system at temperatures of 400–500 C in the upper level plutonic sequence, Troodos ophiolite, Cyprus. *Geochim. Cosmochim. Acta* 54, 653–661.

Langmuir C., Humphris S. E., Fornari D. J., Van Dover C., Von Damm K. L., Tivey M. K., Colodner D., Charlou J. L., Desonie D., Wilson C., Fouquet Y., Klinkhammer G. P., Bougault H. (1997). Hydrothermal vents near a mantle hot spot: the Lucky Strike vent field at 37°N on the Mid-Atlantic Ridge. *Earth Planet. Sci. Lett.* 148, 69–91.

Larson B. I., Lilley M. D., Olson E. J. (2009) Parameters of subsurface brines and hydrothermal processes 12-15 months after 1999 magmatic event at the Main Endeavor Field as inferred from in situ time series measurements of Chloride and Temperature. *J. Geophys. Res.*, 114, B01207, p1-18. doi: 10.1029/2008JB005627

Lowell R. P. (2003) Anhydrite precipitation and the relationship between focused and diffuse flow in seafloor hydrothermal systems. *J. Geophys. Res.* 108. doi:10.1029/2002JB002371

Ludwig K. A., Kelley D. S., Butterfield D. A., Nelson B. K., Früh-Green G. (2006) Formation and evolution of carbonate chimneys at the Lost City Hydrothermal Field. *Geochim. Cosmochim. Acta* 70, 3625–3645. doi:10.1016/j.gca.2006.04.016

Martin W., Baross J., Kelley D., Russell M. J. (2008) Hydrothermal vents and the origin of life. *Nat. Rev. Microbiol.* doi:10.1038/nrmicro1991

Michard G., Albarède F., Michard A., Minster J.-F., Charlou J. L., Tan N. (1984) Chemistry of solutions from the 13°N East Pacific Rise hydrothermal site. *Earth Planet. Sci. Lett.* 67, 297–307.

Millero F. J., Feistel R., Wright D. G., McDougall T. J. (2008) The composition of Standard Seawater and the definition of the Reference-Composition Salinity Scale. *Deep Sea Res. Part Oceanogr. Res. Pap.* 55, 50–72. doi:10.1016/j.dsr.2007.10.001

Miranda J. M., Luis J. F., Lourenço N., Santos F. M. (2005) Identification of the magnetization low of the Lucky Strike hydrothermal vent using surface magnetic data: magnetization low of Lucky Strike. *J. Geophys. Res. Solid Earth* 110. doi:10.1029/2004JB003085

Mottl M. J., Holland H. D., Corr R. F. (1979) Chemical exchange during hydrothermal alteration of basalt by seawater—II. Experimental results for Fe, Mn, and sulfur species. *Geochim. Cosmochim. Acta* 43, 869–884.

Mottl M. J., Seewald J. S., Wheat C. G., Tivey M. K., Michael P. J., Proskurowski G., McCollom T. M., Reeves E., Sharkey J., You C.-F., Chan L.-H., Pichler T. (2011) Chemistry of hot springs along the Eastern Lau Spreading Center. *Geochim. Cosmochim. Acta* 75, 1013–1038. doi:10.1016/j.gca.2010.12.008

Mullineaux L. (1998). Deep-sea hydrothermal vents sanctuaries: a position paper. *InterRidge News* 8, 45–50.

Ondréas H., Cannat M., Fouquet Y., Normand A., Sarradin P. M., Sarrazin J. (2009) Recent volcanic events and the distribution of hydrothermal venting at the Lucky Strike hydrothermal field, Mid-Atlantic Ridge: Lucky Strike volcanism and venting. *Geochem. Geophys. Geosystems* 10. doi:10.1029/2008GC002171

Palmer M. R. (1992) Controls over the chloride concentration of submarine hydrothermal vent fluids: evidence from Sr/Ca and ⁸⁷Sr/⁸⁶Sr ratios. *Earth Planet. Sci. Lett.* 109, 37–46.

Person R., Miranda J. M., Puillat I. (2009) ESONEWS-MoMAR/DA demonstration mission to establish a multidisciplinary observatory at hydrothermal vents on the Mid-Atlantic Ridge. *Esonews* 3, 1–8.

Pester N. J., Rough M., Ding K., Seyfried, Jr., W. E. (2011) A new Fe/Mn geothermometer for hydrothermal systems: Implications for high-salinity fluids at 13°N on

the East Pacific Rise. *Geochim. Cosmochim. Acta* 75, 7881–7892. doi:10.1016/j.gca.2011.08.043

Pester N. J., Ding K., Seyfried, Jr., W. E. (2014) Magmatic eruptions and iron volatility in deep-sea hydrothermal fluids. *Geology* 42, 255–258. doi:10.1130/G35079.1

Pester N. J., Reeves E. P., Rough M. E., Ding K., Seewald J. S., Seyfried, Jr., W. E. (2012) Subseafloor phase equilibria in high-temperature hydrothermal fluids of the Lucky Strike Seamount (Mid-Atlantic Ridge, 37°17'N). *Geochim. Cosmochim. Acta* 90, 303–322. doi:10.1016/j.gca.2012.05.018

Pester N. J., Ding K., Seyfried, Jr., W. E. (2015) Vapor–liquid partitioning of alkaline earth and transition metals in NaCl-dominated hydrothermal fluids: An experimental study from 360 to 465°C, near-critical to halite saturated conditions. *Geochim. Cosmochim. Acta* 168, 111–132. doi:10.1016/j.gca.2015.07.028

Pokrovski G. S., Roux J., Harrichoury J.-C. (2005) Fluid density control on vapor-liquid partitioning of metals in hydrothermal systems. *Geology* 33, 657–660.

Ravizza G., Blusztajn J., Von Damm K. L., Bray A. M., Bach W., Hart S. R. (2001) Sr isotope variations in vent fluids from 9° 46'–9° 54' N East Pacific Rise: evidence of a non-zero-Mg fluid component. *Geochim. Cosmochim. Acta* 65, 729–739.

Reeves E. P., Seewald J. S., Saccocia P., Bach W., Craddock P. R., Shanks W. C., Sylva S. P., Walsh E., Pichler T., Rosner M. (2011) Geochemistry of hydrothermal fluids from the PACMANUS, Northeast Pual and Vienna Woods hydrothermal fields, Manus Basin, Papua New Guinea. *Geochim. Cosmochim. Acta* 75, 1088–1123. doi:10.1016/j.gca.2010.11.008

Resing J. A., Sedwick P. N., German C. R., Jenkins W. J., Moffett J. W., Sohst B. M., Tagliabue A. (2015) Basin-scale transport of hydrothermal dissolved metals across the South Pacific Ocean. *Nature* 523, 200–203. doi:10.1038/nature14577

Saccocia P. J., Seyfried, Jr., W. E. (1994). The solubility of chlorite solid solutions in 3.2 wt% NaCl fluids from 300–400 °C, 500 bars. *Geochim. Cosmochim. Acta* 58, 567–585.

Schmidt K., Koschinsky A., Garbeschönberg D., Decarvalho L., Seifert R. (2007) Geochemistry of hydrothermal fluids from the ultramafic-hosted Logatchev hydrothermal field, 15°N on the Mid-Atlantic Ridge: Temporal and spatial investigation. *Chem. Geol.* 242, 1–21. doi:10.1016/j.chemgeo.2007.01.023

Schmidt K., Garbe-Schönberg D., Koschinsky A., Strauss H., Jost C. L., Klevenz V., Königer P. (2011) Fluid elemental and stable isotope composition of the Nibelungen hydrothermal field (8°18'S, Mid-Atlantic Ridge): Constraints on fluid–rock interaction in heterogeneous lithosphere. *Chem. Geol.* 280, 1–18. doi:10.1016/j.chemgeo.2010.07.008

Schoofs S., Hansen U. (2000) Depletion of a brine layer at the base of ridge-crest hydrothermal systems. *Earth Planet. Sci. Lett.* 180, 341–353.

Seewald J. S., Seyfried, Jr., W. E. (1990) The effect of temperature on metal mobility in subseafloor hydrothermal systems: constraints from basalt alteration experiments. *Earth Planet. Sci. Lett.* 101, 388–403.

Seyfried, Jr., W. E. (2003) Chemistry of hydrothermal vent fluids from the Main Endeavour Field, northern Juan de Fuca Ridge: Geochemical controls in the aftermath of June 1999 seismic events. *J. Geophys. Res.* 108. doi:10.1029/2002JB001957

Seyfried, Jr., W. E., Berndt M. E., Janecky D. R. (1986) Chloride depletions and enrichments in seafloor hydrothermal fluids: Constraints from experimental basalt alteration studies. *Geochim. Cosmochim. Acta* 50, 469–475.

Seyfried, Jr., W. E., Chen X., Chan L.-H. (1998) Trace element mobility and lithium isotope exchange during hydrothermal alteration of seafloor weathered basalt: an experimental study at 350 C, 500 bars. *Geochim. Cosmochim. Acta* 62, 949–960.

Singh S. C., Crawford W. C., Carton H., Seher T., Combier V., Cannat M., Pablo Canales J., Dusunur D., Escartin J., Miguel Miranda J. (2006) Discovery of a magma chamber and faults beneath a Mid-Atlantic Ridge hydrothermal field. *Nature* 442, 1029–1032. doi:10.1038/nature05105

Steele-MacInnis M., Han L., Lowell R. P., Rimstidt J. D., Bodnar R. J. (2012) The role of fluid phase immiscibility in quartz dissolution and precipitation in sub-seafloor hydrothermal systems. *Earth Planet. Sci. Lett.* 321-322, 139–151. doi:10.1016/j.epsl.2011.12.037

Stein C. A., Stein S. (1994) Constraints on hydrothermal heat flux through the oceanic lithosphere from global heat flow. *J. Geophys. Res.* 99, 3081–3095.

Von Damm K. L. (1988) Systematics and postulated controls on submarine hydrothermal solution chemistry. *J. Geophys. Res.-Solid Earth* 93, 4551–4561.

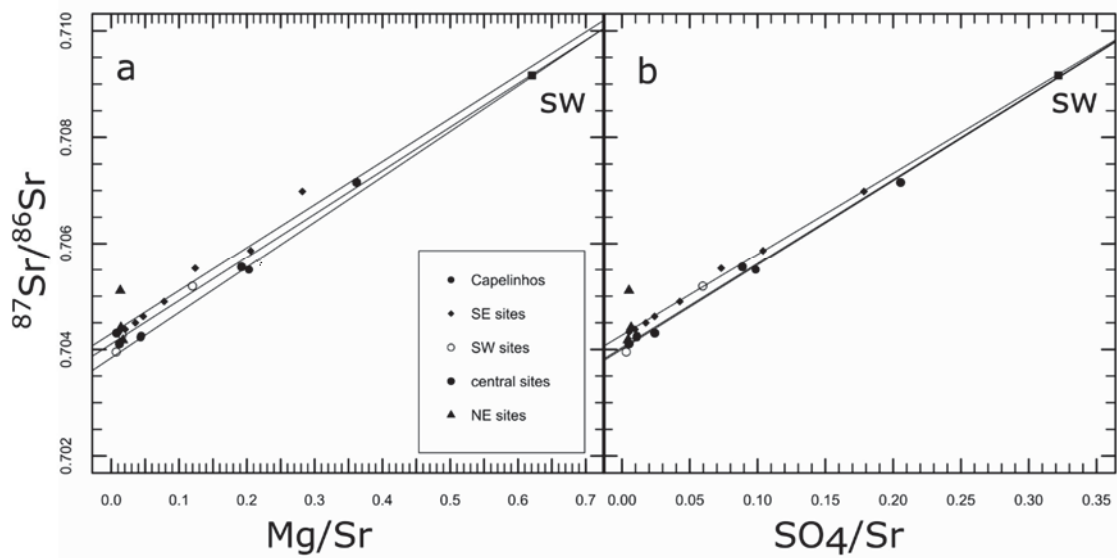
Von Damm K. L. (2000) Chemistry of hydrothermal vent fluids from 9–10 N, East Pacific Rise: “Time zero,” the immediate post-eruptive period. *J. Geophys. Res. Solid Earth* 1978–2012 105, 11203–11222.

Von Damm K. L., Edmond J., Measures C. I., Grant B. (1985) Chemistry of submarine hydrothermal solutions at Guaymas Basin, Gulf of California. *Geochim. Cosmochim. Acta* 49, 2221–2237.

Von Damm K. L., Bischoff J., Rosenbauer R. J. (1991) Quartz solubility in hydrothermal seawater: an experimental study and equation describing quartz solubility for up to 0.5M NaCl solutions. *Am. J. Sci.* 291, 997–1007.

Von Damm K. L., Bray A. M., Buttermore L. G., Oosting S. E. (1998) The geochemical controls on vent fluids from the Lucky Strike vent field, Mid-Atlantic Ridge. *Earth Planet. Sci. Lett.* 160, 521–536.

Von Damm K. L., Lilley M.D., Shanks III W. C., Brockington M., Bray A. M., O’Grady K. M., Olson E., Graham A., Proskurowski G. (2003) Extraordinary phase separation and segregation in vent fluids from the southern East Pacific Rise. *Earth Planet. Sci. Lett.* 206, 365–378.



regression	site	$^{87}\text{Sr}/^{86}\text{Sr}$	r^2
Mg/Sr	capelinhos	0.70384	0.999
	SE	0.70423	0.986
	SW	0.70410	0.996
SO ₄ /Sr	capelinhos	0.70403	0.998
	SE	0.70426	0.998
	SW	0.70400	0.997

Figure IV- S 1 Diagram of $^{87}\text{Sr}/^{86}\text{Sr}$ as a function of Mg/Sr (a) and SO₄/Sr (b). a) shows the usual way of determining the Sr isotope end-member of fluids. b) is a method for determining Sr isotope end-member of fluid by using sulfate. Sulfate in fluids will be dependent on seawater entrained during sampling, as SO₄ is enriched in SW compared to pure hydrothermal fluid. Sulfate will also be dependent on anhydrite. Dissolution of anhydrite could contribute to Ca, SO₄ and Sr concentration measured in the fluid and consequently, Sr isotope signature. Assuming Sr isotope signatures of SW and hydrothermal fluid, dissolution of anhydrite dissolution bias can be corrected as in Fig IV- S1b. Consequently, endmember determined for SW sites are better determined by SO₄/Sr least square regression. When no suspicion of anhydrite dissolution, Mg/Sr should be preferred for slightly negative end-member values of SO₄ would overcorrect Sr isotope determination (e.g. Capelinhos).

CHAPITRE 5

TIME-SERIE STUDY OF HOT VENT CHEMISTRY FROM THE
LUCKY STRIKE HYDROTHERMAL FIELD (37°N):
CONTRIBUTION FROM THE EMSO-AZORES DEEP SEA
OBSERVATORY.

Abstract

The Lucky Strike hydrothermal field located at 37°N on the Mid Atlantic Ridge is one of the most studied hydrothermal field on a slow spreading ridge. This hydrothermal field has been chosen to host a deep sea observatory equipped with geophysical and biological modules that communicate through satellite with the on-shore laboratory at Ifremer in near real-time. In this context of long-term study of the Lucky strike hydrothermal field, high temperature fluids have been collected each year since 2009 during maintenance cruises of the infrastructure of the observatory. This study presents the fluid chemistry of end-members from 2009 to 2015 determined for 13 hydrothermal vents. First, we show that at least two time scales are at play with (1) the sampling time scale of ~1 hour; (2) the yearly variations.

Sampling of more than 300 high temperature fluid since 2009 displayed 5% of samples with anomalously low Si concentration (2–3 mM), inconsistent with mixing with seawater at the discharge. From this observation we propose that a subsurface aquifer of conductively cooled hydrothermal fluid surrounds the focused conduit of high temperature fluid. This fluid is episodically flushed within the chimney in line with temperature data from autonomous probe (Barreyre et al. 2014).

On the year-scale, together with the literature data, we analyze the changes that have occurred at this field since its discovery and first fluid samples from 1993. Based on the Si and Cl data from the newly discovered Capelinhos site, which vents the most vapor dominated fluid, we infer the P and T conditions of the phase separation and confirm that, although a little difference is noticed, the longer known Tour Eiffel and Montségur sites (also vapor dominated) are suitable to estimate accurately the P and T conditions of the phase separation zone. Therefore, we estimate these conditions for the complete time series of these sites (12 years). We show that along the 12 year study represented (6 years from literature and 6 years from this work), the P–T are mostly stable with P between 380 and 390 bars and T between 430 and 440 °C. Some excursions toward shallower and cooler conditions (P~360 and T~425°C) coincide with seismic events observed by geophysical data. Furthermore, Ca/Na ratios, which are a proxy of albitisation, from 1993 to 2015 have fluctuated following a “boom and bust” behavior related to the seismic events. The time span between two peaks of the “boom and bust” pattern is of ~7 years. Intersite variations can be explained by phase separation and preferential uptake of Ca into the brine phase for

all but the South Eastern sites. This suggests that the substratum underneath the SE sites are more altered than for the other sites (i.e. North Eastern, South Western, Central and Capelinhos).

The Fe and Mn are proxies of the reaction zone temperature but no variations are observed for the fluids. Capelinhos fluids display an apparent Fe–Mn calculated temperature of ~403°C while the other sites display temperatures between 350 and 380°C. This difference is interpreted to be due to metal trapping in the reaction zone, therefore if we consider Capelinhos fluids as representative of the metal mobilized, then we can estimate the Fe trapped in subsurface to be ~65% that of the total Fe mobilized.

Furthermore, isotopic data for Li and Sr indicate contrasting W/R ratios. The Li data shows W/R ratio close to 1 attesting for a relatively fresh basalt underneath. The Sr based W/R ratio indicates a higher value (7–8) due to residual strontium.

Résumé

Le champ hydrothermal de Lucky Strike, situé à 37°N sur la ride médio-atlantique est un des sites les plus étudié sur une dorsale à faible taux d'accrétion. Ce champ hydrothermal a été choisi pour accueillir un observatoire fond de mer équipé de modules dédié à la géophysique et à la biologie du système hydrothermal qui communique les données par satellite en temps réel avec le centre Ifremer à Brest. Dans ce contexte d'étude en série temporelle, les fluides de haute température ont été échantillonnés depuis 2009 à l'occasion de campagne annuelle de maintenance de l'observatoire. Cette étude présente les compositions chimiques des fluides end-member calculées pour les années 2009 et 2015 pour 13 sites actifs. Dans un premier temps, nous mettons en évidence l'existence de plusieurs échelles de variabilité temporelle. La première étant une variabilité à l'échelle de l'heure. La seconde est la variation temporelle.

Depuis 2009, le prélèvement de plus de 300 fluides de haute température montré pour 5% d'entre eux des valeurs étonnamment faible en Si (2–3mM), qui ne s'expliquent pas par un mélange entre un fluide pure et l'eau de mer. A partir de cette observation, nous proposons un modèle de circulation hydrothermal en subsurface. Dans ce modèle un fluide hydrothermal refroidi à l'équilibre avec le quartz à des conditions de pressions et de température de 1170 (plancher océanique de cette zone) et 150 °C est stocké en subsurface, à proximité des événements hydrothermaux de haute température, et parfois ressort de manière

épisode, ce qui fait écho aux profils de température montrant des variations du même ordre (Barreyre et al., 2014).

Sur l'échelle de temps pluri-annuelle, à partir de nos données et de celles de la littérature, nous étudions les changements chimiques des fluides depuis la découverte du champ hydrothermal en 1993. En nous basant sur le géothermobaromètre Si-Cl, nous déterminons que les conditions de pression et de température de séparation de phase estimées à partir des fluides de Capelinhos sont sensiblement les mêmes que celles estimées par les fluides des sites Tour Eiffel et Montsegur. Ainsi, nous pouvons estimer ces conditions en couvrant l'intégralité de la période de temps de la base de données chimiques dont nous disposons. Nous montrons que sur les 12 années représentées, les estimations sont stables avec des pressions entre 380 et 390 bars et des températures entre 430 et 440°C. Quelques événements vers des conditions moins profondes sont observables (P=360 bars et T~425°C) semblent coïncider avec des événements sismiques observés avec l'instrumentation de l'observatoire. De plus, le rapport Ca/Na est un indicateur d'albitisation, de 1993 à 2015 ce rapport a fluctué suivant un profil en dent de scie pour tous les sites. Les variations du rapport entre les sites s'expliquent par la séparation de phase et par le partitionnement préférentiel du Ca dans la phase saumure, sauf pour les sites du Sud Est qui montrent un rapport plus élevé. Cela suggère un substratum plus altéré dans la zone de remontée de ces sites (Tour Eiffel, Montsegur, Aisics, Cimendeff).

Le Fe et le Mn sont des indicateurs de la température de la zone de réaction et ne montrent pas de variations temporelles. Les fluides de Capelinhos montrent une température d'équilibre apparente d'environ 40°C tandis que les sites situés autour du lac de lave indiquent des températures entre 350 et 380°C. Cette différence peut être interprétée en termes de piégeage de métaux dans la zone de remontée. Ainsi en se basant sur le rapport Fe/Mn de Capelinhos est le rapport des fluides au départ de la zone de remontée, et que les teneurs en Mn sont conservées. On peut évaluer que 65% du Fe mobilisé dans la zone de réaction est stocké dans la zone de remontée, ainsi les faibles concentrations en Fe et Mn des sites autour du lac de lave ne sont pas dues à un substratum altéré mais plutôt à la formation du stockwork.

De plus, les données isotopiques de Li et Sr suggèrent des rapports eau-roche (W/R) différents. Pour le Li, les valeurs du W/R montrent des rapports proches de 1, ce qui atteste de la relative fraîcheur du substratum. En revanche, pour le Sr, les valeurs de W/R sont plus

élevées (entre 7 et 8) et s'expliquent par des relations plus complexes avec des minéraux secondaires et d'altération.

1. Introduction

Mid Ocean Ridges (MOR) spread both magmatically by sill injection (Henstock et al., 1993; Phipps Morgan et al., 1987), and tectonically through long-lived detachment faults eventually forming oceanic core complexes (Cannat et al., 2006; Escartín et al., 2008; Ildefonse et al., 2007). These mechanisms allow seawater to flow through the oceanic crust and discharge above the anomalous heat formed by the Axial Magma Chamber beneath the ridge. Therefore, the chemistry of the discharging hydrothermal fluid is highly dependent on the deep geological processes acting at ridge axis. Many studies have investigated the chemical response of hydrothermal fluids to volcanic eruption during replenishment of the axial magmatic chamber (Butterfield et al., 1997; Pester et al., 2014; Von Damm, 2004, 2000). Time series studies were essentially carried out at fast-spreading ridge, e.g. the East Pacific Rise (EPR), where magmatic activity is intense (Campbell et al., 1988). But most of them were based on little time span which ones up to a couple of years (Campbell et al., 1988; Von Damm, 2004). In particular, the longest time series of black smoker fluids span over a 17 years time period at the EPR with fluid samples collected at two-year's time interval. Between 1990 and 2009, two sill intrusion events occurred in 1992 and 2007 (Pester et al., 2014; Von Damm, 2004). Pester et al. (2014) were able to link magmatic activity to differences in fluid chemistry expressed as higher H_2 and H_2S , lower Chloride concentrations. Furthermore, the increasing transition metal variations, i.e. Fe and Mn in particular, have shown to be correlated to these events, with stable concentrations in between these two events (Pester et al., 2014).

To date, most of the long term study on hydrothermal fluid chemistry focused on fast spreading ridges but little has been studied in a slow-spreading ridge (Pester et al., 2014; Von Damm et al., 1995). Despite the continuous discovery of hydrothermal vents on ultra-slow to slow spreading ridges and the wide variety observed in fluid chemistry, the time dependent processes of these systems has not been assessed thus far (Edmonds, 2008) and reference therein). In recent years, the European Multidisciplinary Seafloor and water-column Observatory (EMSO program) enabled the set-up of 15 deep-sea observatories at key locations of the European Seas. Among them, the EMSO-Azores node was installed in

2010 at the Lucky Strike hydrothermal field (LSHF) located at 37°N on the Mid-Atlantic Ridge (MAR), whereby the instrumental infrastructure is dedicated to yearly monitoring of hydrothermal system dynamics (Colaço et al., 2011; Person et al., 2009). The geographical location of the LSHF in vicinity of the Azores Islands made it an accessible target in less than a sailing day. The LSHF constitutes one of the largest hydrothermal field known to date on slow-spreading ridge, i.e. 1 km² (Humphris et al., 2002), and since its discovery in 1992, several research cruises characterized the geological, geochemical, geophysical and biological context of the vents (Barreyre et al., 2012; Charlou et al., 2000; Fouquet et al., 1995; Langmuir et al., 1997; Leleu et al., submitted; Ondréas et al., 2009; Pester et al., 2012; Von Damm et al., 1998; Escartin et al., 2015). Since 2009, hot vents have been sampled on yearly-basis at this location, providing a 7 year time-series in the frame of the EMSO-Azores. Together with the previous published chemistry data (Charlou et al., 2000; Langmuir et al., 1997; Leleu et al., submitted; Pester et al., 2012; Von Damm et al., 1998), this dataset constitutes the longest time series, i.e. 12 years (1993 - 2015), of fluid chemistry on slow-spreading ridge.

In this study, we report on the chemical variations observed in hot hydrothermal vents along the 12 years long time series and we interpret them as indicative of processes occurring at depth (reaction zone and/or subsurface). We also discuss the reliability of end-member interpretations when not related to a solid background in terms of sample collection and geophysical, geological information. Within this comprehensive study of vent interrelation and hydrothermal circulation, we assess the amounts of iron stored at depth in these systems as massive sulfides. Elemental concentrations are further completed by Sr and Li isotopic composition of the most recent fluids to constrain precipitation/dissolution and/or mixing processes operating at the subsurface.

2. Geological context

The Lucky Strike segment is ~65 km long and is situated south of the Azores islands along the MAR between 37°03'N and 37°37'N (Detrick et al., 1995). The recent spreading rate is ~2.2 cm/yr (Cannat et al., 1999; Miranda et al., 2005). A fossil lava lake (300m in diameter) framed by three ancient volcanic cones constitutes the central volcanic edifice, tectonised by N010°–N030° faults and fissures, where the LSHF is hosted (Fig. V – 1; Fouquet et al., 1995). The fossil lava lake was formed during the last volcanic event and is poorly tectonised, indicating a relatively recent setting compared to the volcanic cones (Humphris

et al., 2002; Ondréas et al., 2009). A magmatic lens (or AMC) was identified by seismic study at a depth of about 3500 m below the summit of the volcano (Singh et al., 2006). Micro-seismic events recorded by ocean bottom seismometers between 2007 and 2009 cluster at depths between 1800 and 2500m below seafloor (mbsf) just above the AMC. They are interpreted as the product of hydraulic fracturing induced by penetration of cold down-going fluids into hot rocks (Crawford et al., 2013). Furthermore, intense seismic swarms were also identified since then within the deep-sea observatory infrastructure, in August-September 2011 and October 2012 (Crawford et al., 2015).

Table V - 1 Summary of hydrothermal sites presenting different parameter.

site	depth (mbsl)	longitude (W)	latitude (N)	area*	sources	number of years represented	discovery	T _{discovery} (°C)	T ₂₀₁₅ (°C)
Capelinhos	1665	32°15.830'	37°17.350'	East	a	3	2013	324	319
Sintra	1614	32°16.498'	32°17.529'	North East	a, b, c	8	1993	212	207
Y3	1727	32°16.671'	37°17.512'	North East	b, c	9	1994	324	326
Statue of Liberty	1628	32°16.670'	37°17.560'	North East	b, c	2	1993	202	extinct
Aisics	1689	32°16.530'	37°17.338'	South East	a	8	2009	298	307
Tour Eiffel	1684	32°16.532'	37°17.343'	South East	a, b, c	11	1993	325	324
Montségur	1701	32°16.534'	37°17.284'	South East	a, b, c, d	12	1993	297	320
Marker 6	1703	32°16.553'	37°17.282'	South East	b, c	2	1993	303	-
Cimendeff	1700	32°16.553'	37°17.286'	South East	a, b, c	5	1993	302	308
Petit Chimiste	1648	32°16.631'	37°17.392'	South East	c	1	1994	1648	-
Isabel	1683	32°16.638'	37°17.377'	South East	a, d	7	2008	292	294
Cyprès	1738	32°16.863'	37°17.450'	South West	a	5	2009	188	302
White Castle	1708	32°16.869'	37°17.383'	South West	a	6	2009	310	311
Crystal	1723	32°16.921'	37°17.453'	South West	a, b, c	7	1996	281	329
Sapins	1718	32°16.888'	37°17.439'	South West	a	3	2013	280	236
South Crystal	1720	32°16.935'	37°17.445'	South West	a	6	2009	340	336
Helene	1722	32°16.888'	32°17.499'	South West	c	1	1994	284	-
nuno	1727	32°16.933'	37°17.494'	South West	a, c	2	1994	172	-
Jason	1644	32°16.936'	37°17.637'	North West	b	1	1996	308	-
Elisabeth	1680	32°16.917'	37°17.647'	North West	d	1	2008	270	-

a: this study; b: Von damm et al., 1996; c: Charlou et al., 2000; d: Pester et al., 2012

* compared to the fossil lava lake

The LSHF vents display several types of structures and chemistry (Barreyre et al., 2012; Leleu et al., submitted). These hydrothermal vents are distributed around the central fossil lava lake in 5 different areas that are characterized by specific chemical venting fluids (Leleu et al., submitted). We will summarize underneath the main features of each area and associated fluids.

The northwestern (NW) area hosts several active sites with high temperature vents (Bairo Alto, Nuno, Helene and Jason) on a curvilinear scarp formed by mass wasting and partly comprised of massive sulfides (Escartin et al., 2015; Ondréas et al., 2009). The fluid chemistry showed a chlorinity equivalent to that of seawater but fluid sampling is poor with

only two sites sampled, i.e. Jason in 1996 and Elisabeth in 2008. This area was chosen as an exclusion zone to preserve the original hydrothermal habitat, in respect with the Lucky Strike Marine Protected area (Mullineaux, 1998). As a consequence, this area is off limits for sampling and no further samples were acquired.

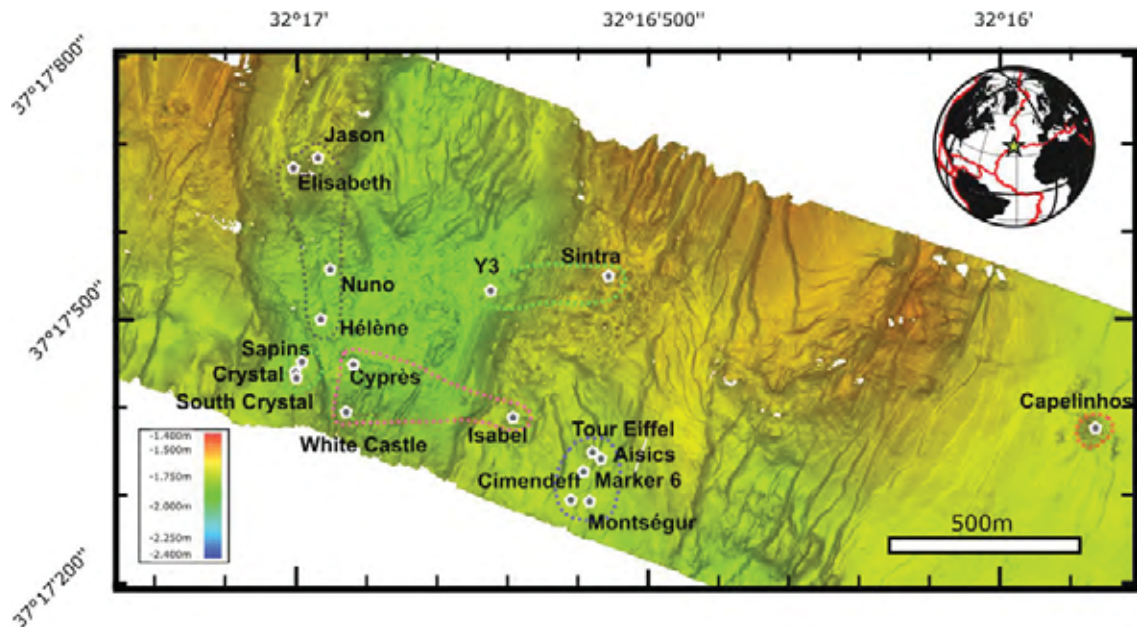


Figure V - 1 Micro-bathymetric map of the Lucky Strike Hydrothermal Field. The dashed area represent the different salinity observed from this study. Red dashed area represent the most Cl depleted fluid of Capelinhos. Blue dashed area represent the vapor dominated fluids from the SE of the lava lake. Light purple area represents the Intermediary salinity group in the vicinity of the lava lake limit. The green dashed areas represent the high salinity fluids that are found at the SW and NE of the lava lake. The grey dashed area represent the fluids of the NW areas which are not part of this study.

The northeastern (NE) hydrothermal area is constituted of surficial hydrothermal deposits hosting numerous inactive structures and 2 active venting sites named Sintra and Y3 (Table V - 1). Y3 site (also named 2608 vent, Barreyre et al., 2012) is isolated in the north eastern part of the fossil lava lake and was sampled regularly since 1996. At present, these fluids discharging as black smoker at 326°C are rich in Si, Fe and Mn have higher salinity than seawater. In contrast, fluids at Sintra site have relatively clear and low exit temperature at 196-209°C and low amount of trace metal concentrations, displaying evidence of conductive cooling (Table V - 1; Leleu et al., submitted). Y3 is a well-known site due to its 18m high chimney, but it was found collapsed in 2013 and stands since then as a gathering of 1-2 m high chimneys sitting on top of a 2-3m diameter pedestal.

The southwestern (SW) area is situated at the southwestern end of the fossil lava lake, which is truncated by a 20m high scarp. This scarp is caused by movement along a normal fault that post-dates the last eruption (Ondr eas et al., 2009). The absence of large

hydrothermal deposits in this area implies that there has been venting since recent times, however, inactive oxidizing chimneys were observed partially buried by lavas. The active venting occurs along the fault scarp (South Crystal, Crystal, Sapins and White Castle) or on the lava lake itself (Cyprès) (Fig V - 1). Among these active vent sites, fluid chemistry is variable in terms of chlorinity concentrations whereby South Crystal, Crystal and Sapins exhibit Cl concentrations equivalent or slightly higher than that of seawater whereas White Castle and Cyprès present lower chlorinity ones (Leleu et al., submitted). Furthermore, major and trace element concentrations do vary from site to site without any specific trend, e.g. Ca content ranges between 44.9 and 37.9 mM among them (Leleu et al., submitted).

The southeastern (SE) area is composed of hydrothermally cemented volcanoclastic breccias. This impermeable substrate was called “slab” (Cooper et al., 2000; Humphris et al., 2002). Cooper et al. (2000) investigated the chemical composition of fluid issued from the slab. These authors suggested that the slab hosted and drove conductively heated seawater. This slab is thought to have sealed the permeability of the seafloor in this area, which lead to fluid discharge through faults. Active vent sites are numerous in this area as reported by Charlou et al. (2000) and Von Damm et al. (1998). The lack of clear marking and photo-mosaic of the seafloor did not permit a clear follow up of some of these vents through the years, e.g. Petit Chimiste, Hélène (Barreyre et al., 2012). The most well-known sites are Tour Eiffel, Aisics, Montsegur, Cimendeff and Isabel (Humphris et al., 2002; Ondréas et al., 2009). Apart from Isabel site which shows almost clear venting, all of them are black smokers discharging fluids at temperature above 300°C with high concentrations in metals. Nonetheless, all of them display lower chlorinity than seawater and Tour Eiffel has been the most vapor-dominated site identified at LSHF until the discovery of Capelinhos in 2013 (Escartin et al., 2015; Leleu et al., submitted).

The Capelinhos site is situated approximately 1.5 km eastward of the main LSHF on the western flank of the axial volcano (Escartin et al., 2015). It is set on pillow lava and comprises several chimneys forming a “candelabra-like structure” on top of a 10 meters high sulfide mound. Extinct chimneys are characterized by orange colored oxidizing material while active chimneys are dark grey and covered by a white filamentous bacterial mat. Diffuse venting at Capelinhos is limited to the close vicinity of the black smokers at the base of the edifice. Capelinhos expels black smoker fluids at temperatures up to 324°C and is the most vapor-dominated fluid together with the most-enriched metal concentrations of all the LSHF (Leleu et al., submitted).

3. Materials and methods

3.1 Sampling

The fluid samples studied in this paper were collected during the Bathyluck cruise in 2009, and within the MoMAR program (EMSO-Azores) from 2010 to 2015 maintenance cruises on the French Research vessels *Pourquoi Pas?* and *La Thalassa*. The 13 sampling sites (12 sites in the main LSHF, and Capelinhos) were chosen to spatially document the fluid diversity identified at Lucky Strike by previous studies (Von Damm et al., 1998; Charlou et al., 2000; Pester et al., 2012; Chavagnac et al., 2015; Leleu et al., submitted). From 2009 to 2015, each vent site was sampled four times in succession (total duration of sampling <1 hour) to allow a better characterization of the end-member fluid. In-situ temperatures were measured in the vents prior to sampling using the ROV Victor 6000 high temperature probe that was inserted inside the chimney with immediate temperature reading in the ROV control room. High-temperature fluids were collected with 200ml titanium gas-tight samplers handled and triggered by the hydraulic arm of the ROV. In 2009, further fluid sampling was carried out using 750ml capacity titanium bottles, which are not gas-tight. The time delay between each fluid sampling at a given vent did not exceed 20 minutes. The samples were processed immediately on board of the research vessel after the ROV recovery. First, gases were extracted from sampler and stored in stainless steel canisters or glass bottles for further on-shore analysis. The fluid samples were then extracted, filtered through 0.45µm Millipore filters and split into different aliquots stored at 4°C in a cold room for onshore analysis. pH, Eh, salinity and conductivity were measured on-board immediately after processing.

3.2. Elemental concentration measurement

All the chemical analyses were conducted at the Geosciences Environment Toulouse (GET) laboratory, the IUEM laboratory and the Ifremer Brest center. Ca, Na, K, Mg, Si, Fe, Mn and Li concentrations were determined with an inductively coupled plasma absorption emission spectrometer (ICP-AES; Horiba Ultima2). Error on analysis are indicated in Table 2. The instrument is calibrated using mono elemental solutions, multi elemental solution and IAPSO standard solution (Besson et al., 2014). The latter is a seawater standard solution provided by OSIL (UK) and certified for its salinity. Salinity controls major elements concentrations in seawater (Millero et al., 2008). Li concentration measurements of IAPSO give an average concentration of $24.6 \pm 0.3 \mu\text{M}$ (rsd=1%; n=4). The analytical

drift is quantified by the standard bracketing method after every 8 samples. Analytical precision is better than 2%. Sr, Rb and Cs concentrations were measured using an inductively coupled plasma mass spectrometer ICP-MS Agilent5000. The standard used is the NASS 6 solution (international seawater standard certified for some trace metals) and gives values of 79.1µM, 1.17µM, 1.19 nM for Sr, Rb and Cs respectively (n=3). Drift corrections are made using an in-house multi-elementary standard doped with In and Re before analysis. Anions (Cl, SO₄, and Br) were determined by anionic chromatography calibrated with a IAPSO standard seawater solution that was diluted at different proportion with MQ-H₂O to the cover the entire range of anion concentrations.

3.3. Sr and Li isotopic compositions

Sr isotopic composition of individual fluid sample was measured at the GET laboratory using a MAT FINIGAN 261 thermal ionization mass spectrometer. Analyses were performed on the purest samples, i.e. the lowest pH and Mg values. Sr was isolated from the matrix using Sr-Spec resin (Eichrom, USA). The ⁸⁷Sr/⁸⁶Sr ratio was determined as the average of 100 measurements of ion intensities following the static collection mode. The ⁸⁷Sr/⁸⁶Sr ratios were normalized to ⁸⁶Sr/⁸⁸Sr = 0.1194. Measured values for NBS 987 standard (recommended values of 0.710250) was ⁸⁷Sr/⁸⁶Sr = 0.710250 ± 0.000011 (2σE, n = 14).

The sample chosen for Sr isotope composition were also analyzed for their Li isotopic composition. Li was separated and isolated from the matrix using a two cationic exchange column eluted with HCl 1N. Li isotopes were determined using a MC-ICP-MS Neptune at the GET laboratory and Ifremer laboratory. Li analysis were done by standard bracketing using a IRMM-16 Li standard of the same concentration. Analytical uncertainty was 0.2 ‰ (1sd). IRMM-16 is equivalent within error to the widely used standard L-SVEC. Therefore, the δ⁷Li values determined by IRMM-16 are directly comparable to those determined relative to L-SVEC. Li isotopes are expressed with a δ notation as follow:

$$\delta^7Li = \left(\frac{\left(\frac{{}^7Li}{{}^6Li} \right)_{sample}}{\left(\frac{{}^7Li}{{}^6Li} \right)_{IRMM-16}} - 1 \right) \times 1000$$

In addition, IASPO seawater solution was also processed as the sample protocol and its Li isotopic composition was measured at δ⁷Li=30.5 ± 0,2 ‰, in line with literature values at 30.7±0.4 ‰ (Rosner et al., 2007)

Table V - 2 Analytical method

element	instrument	rsd
Ca	ICP AES ^a	2%
K	ICP AES	2%
Na	ICP AES	4%
Fe	ICP AES	3%
Mn	ICP AES	3%
Si	ICP AES	2%
Li	ICP AES	2%
Rb	ICP MS ^b	3%
Sr	ICP MS	2%
Cs	ICP MS	10%
Cl	IC ^c	3%
SO₄	IC	2%
Br	IC	4%
⁸⁷ Sr/ ⁸⁶ Sr	TIMS ^d	0,000010
$\delta^7\text{Li}$	MC-ICP-MS ^e	0,2 ‰

a: Inductively Coupled Plasma Atomic Emission Spectrometer

b: Inductively Coupled Plasma Mass Spectrometer

c: Ion Chromatography

d: Thermo Ionized Mass Spectrometer

e: Multi Collector Inductively Coupled Plasma Mass Spectrometer

4. Results

During percolation of seawater in the oceanic crust, water/rock interactions allow precipitation of secondary phases such as smectite and chlorite. As a result, the hydrothermally modified seawater becomes increasingly depleted in Mg toward a zero Mg hydrothermal fluid. It is difficult to sample hydrothermal fluid without entraining small amounts of surrounding seawater into the fluid sampler. Consequently, the composition of the end-member hydrothermal fluids are calculated by linear extrapolation to zero-Mg of the least-square regression method (Von Damm et al., 1985). Only hydrothermal end-members will be considered in the discussion section. Although the Mg extrapolation is sometimes debatable (Gamo et al., 1996; Ravizza et al., 2001), most end-member calculated values of sulfate in our samples are close to zero which supports the Mg extrapolation approach.

For each year and each site since 2009, chemical analyses were carried out on fluid samples. We acquired the most extensive chemical and isotopic dataset for 2013, 2014 and 2015 samples, for which the results are presented in Fig V – 2 and 3 as the concentration variation

of eight elements (Cl, Si, Ca, Na, Fe, Mn, Sr, and Li) against Mg concentration. We then calculated the chemical composition of hydrothermal fluid end-members for the period comprised between 2009 and 2015, whose results are reported in table 3. We present the results in two distinct sections: 1) the definition of site groups between 2013 and 2015 based on individual chemical analyses, and 2) elemental variation of end-members for each site groups since 1993 till 2015.

4.1. Group of sites between 2013 and 2015

Chloride in hydrothermal fluid is the major ion in solution. Vent fluids from the LSHF display both enrichment and depletion in that element compared to Cl seawater concentration at 545 mM. In addition, geological observations indicate that hydrothermal vents exhibit different morphologies (see section 2.1). In order to simplify the interpretation over the 30 sites that have been sampled and studied since 1992, several groups of sites were identified based on their chemical similarities and on site location in comparison to the vent-free fossil lava lake. Leleu et al. (submitted) defined 5 groups of sites for which we summarize underneath the main features over the period 2013 to 2015.

The NE sites are Y3 at the very limit of the lava lake (Fig V - 1) and Sintra on the hydrothermal talus. Both of them have Cl concentrations equivalent or slightly above seawater (Table V - 3).

The SW group is composed of sites (South Crystal, Crystal and Sapins) aligned along a minor fault close to South Western scarp of the fossil lava lake. They display the highest temperature measured at the LSHF, i.e. 340°C at South Crystal (Table V - 1). Between 2013 and 2015, only South Crystal, Crystal and Sapins were sampled and all of them show Cl concentrations slightly higher than that of seawater but equivalent values to those of the NE sites.

The SE group correspond to the sites situated on the highly faulted and hydrothermal slab covered area between the North Eastern and Southern volcanic cones. It comprises the active vent sites named Tour Eiffel, Aisics, Montsegur and Cimendeff. They have Cl concentrations being ~20–25% lower than that of seawater.

The central group represents an intermediary group both spatially and chemically between the SW/NE and SE sites as evidenced by Cl concentration. It comprises Cyprès and White Castle, located on the western side of the fossil lava lake, that have Cl concentrations

slightly lower than seawater (~5 – 10%) as well as Isabel, located on the eastern side of the fossil lava lake, exhibiting Cl concentration at 10% lower than seawater.

The last group is composed only of 1 active site, i.e. Capelinhos, which has Cl concentration at 60% lower than seawater. This site is situated well away from the fossil lava lake (Leleu et al., submitted). This is the most-vapor dominated site of all LSHF ones and has remained as such since its discovery in 2013.

The Cl dispersion is further observed among these site groups showing variable major and trace element concentrations in Na, K, Ca and Li whereby the later increases in concentration for increasing Cl ones. However, this is not systematically the case for other elements such as Si, Fe, Mn, Br, Cs and Rb, for example the central group may exhibit higher concentrations of Si and Mn than the SW and NE groups.

4.2. Time-series of hot vent chemistry since 1993

In this section, we will consider the concentrations of hydrothermal end-members calculated from the measured samples over the period 2009 till 2015. The results are reported in Table V - 3 together with previous literature datasets according to the group of sites previously defined. Within this framework and based on the literature, we will add Statue of Liberty to the NE group, Helene and Nuno to the SW group and Petit Chimiste and Marker 6 to the SE group.

4.2.1. Chloride, sulfate and bromine

The lowest and stable Cl concentrations found at LSHF are the fluids from the Capelinhos site at 262 mM. Prior to 2013, i.e. year of Capelinhos discovery, the SE group was the most vapor-dominated fluid known at LSHF with Cl concentrations that vary from 400 to 450 mM but mostly around ~430 mM, with the lowest value between 2008 and 2011. Over the period spanning from 1993 and present, the NE group presents the highest Cl content of all LSHF groups with a maximum value at 588mM. The 2008 fluids mark the transition from Cl-depleted fluids compared to seawater to Cl-enriched fluids from the NE and SW groups. The SW sites have shown over the years chlorinities very close to those of the NE group. Note, however, that prior to 2011, the SW group displayed a rather vapor-dominated Cl concentration at 515-535 mM while rising up abruptly at ~580mM in 2011 (TableV – 3).

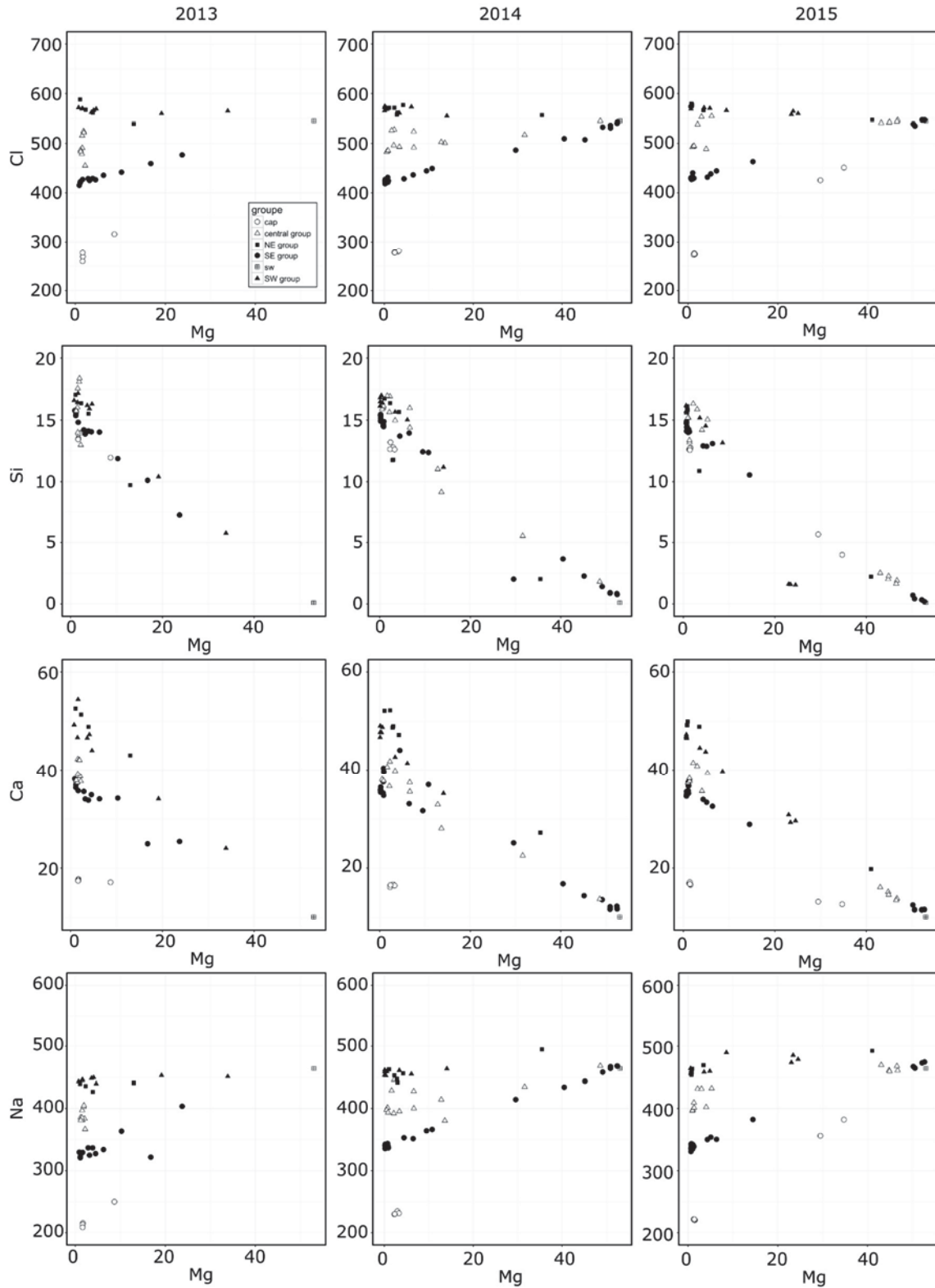


Figure V - 2 Cl, Si, Na, Ca vs Mg diagrams showing the dilution effect of hot fluids by local deep seawater entrainment. Concentrations are in mM. These diagrams are used to determine the endmembers concentration by extrapolation of the least square regression to Mg=0. Groups of sites are presented as explained in Leleu et al., sub. Open circle: capelinhos; Open triangle: central group (Isabel, White Castle, Cyprès); Full square: North Eastern group (Y3 and Sintra); Full circle: South Eastern sites (Aisics, Tour Eiffel, Montsegur Cimendeff); Full triangle: South West group (Crystal, South Crystal, Sapins).

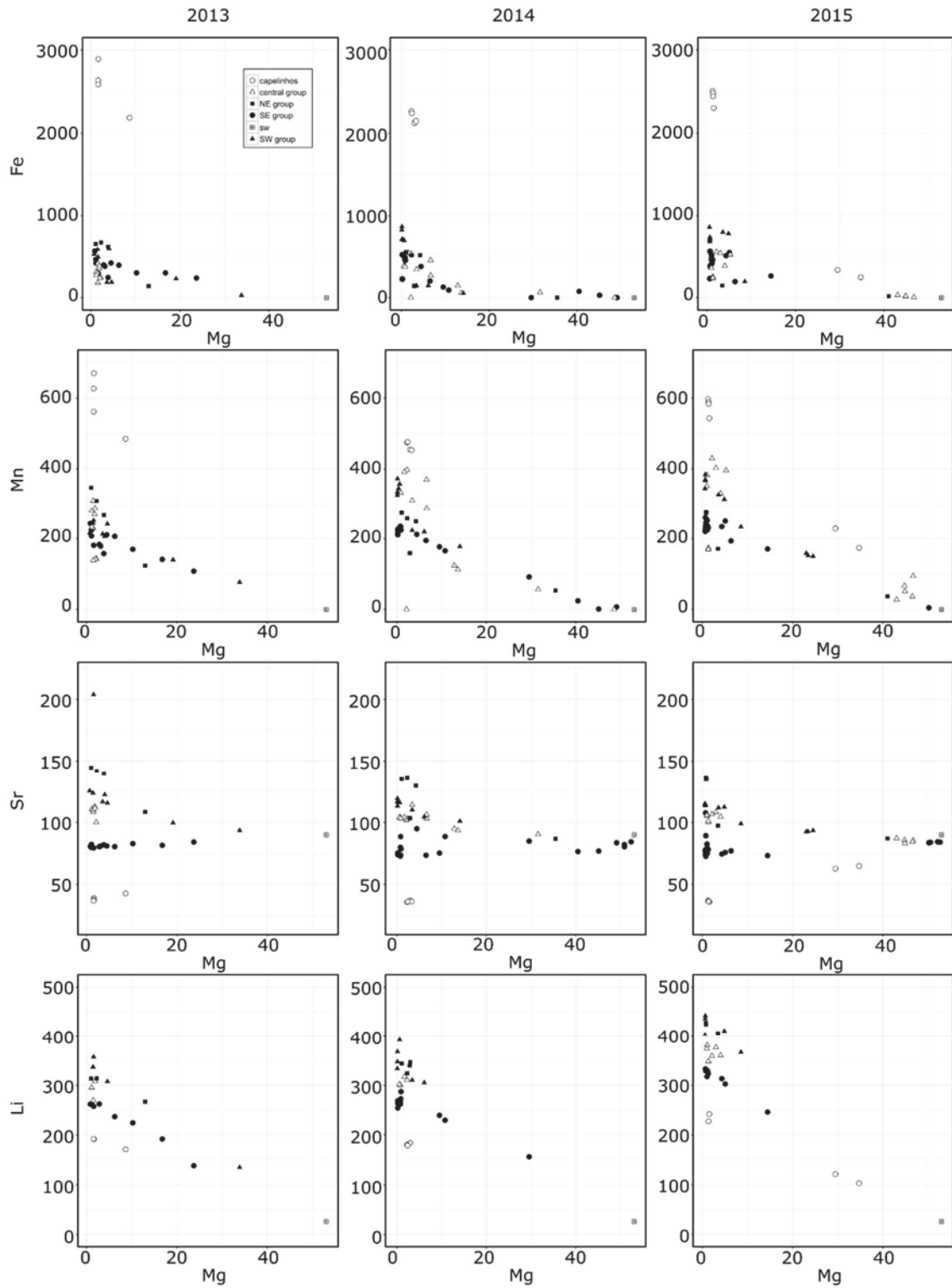


Figure V - 3 Fe, Mn, Sr, Li vs Mg diagrams showing the dilution effect of hot fluids by local deep seawater entrainment. Mg concentrations are in mM, Fe, Mn, Sr and Li concentrations are in μM . Symbols are the same as used in Fig V - 2.

The Cl concentration of the central group shows two different and distinctive behaviors whereby Isabel and White Castle sites display limited Cl concentration variations between 464 and 505 mM over the years while Cyprès site exhibits increasing chlorinity starting at 489mM in 2009 to 548mM at present time.

Sulfate (SO_4) is removed from the initial seawater by anhydrite precipitation and reduction to H_2S . Therefore, the SO_4 content of the hydrothermal end-members reflect the seawater entrainment in the same manner as does Mg. Generally, calculated end-member display negative values of SO_4 . On the contrary, some end-members display positive concentrations, for example in 2010, 2012 and 2014 for the SE group (Table 3).

Bromide (Br) content generally shows the same variations as for Cl ones, from year to year and from site group to site group. Br is considered as a conservative element in submarine hydrothermal system. Accordingly, the lowest concentrations are found at $394\mu\text{M}$ for Capelinhos and the highest ones at $1037\mu\text{M}$ for the SW sites close to the seawater value at $838\mu\text{M}$.

4.2.2 Na, K and Ca

Na, K and Ca are the major cations in solution. They are dependent on the Cl concentration and water-rock interaction equilibrium but all of them are enriched in hydrothermal fluids compared to seawater concentrations.

Na concentrations are correlated to Cl ones as it is the major cation that counter balance the charge of the solution to maintain electro-neutrality. As a result, Na concentrations vary from 205 mM for the most Cl-depleted fluids at Capelinhos to 493 mM for the most Cl-enriched ones at the SW group. The SE group shows progressive decreasing Na concentration from 400 mM in 1993 until 310 mM in 2009, from when it increases gradually till its present concentration at about 341 mM. The NE group exhibits seawater value in 1993, decreasing abruptly to 400 mM in 1994 from when Na concentrations increase with little variations from year to year until seawater value at present time. The SW and NE group shows the highest Na concentrations of all the LSHF groups through the years. The central group for which we have an annual survey since 2008, exhibits Na concentrations fluctuating between those of the NE and SE groups.

Ca and K concentrations vary according to Cl concentrations as the lowest concentrations are at 16.8 and 12.1 mM for Capelinhos fluids and the highest ones at 53.7 and 29.8 mM for NE/SW groups, respectively. The Ca concentrations show two principal features: 1) a

“general” increase since 1993 for all the LSHF groups, and 2) a sharp decrease since 2013 for all LSHF groups. In contrast, the K concentrations have varied significantly from year to year and from group to group. Two general trends affecting all LSHF groups can be observed with 1) a general increase between 1993 and 1997 and 2) a V-shape distribution between 2008 and 2015 with the lowest concentrations in 2011.

4.2.3 Silica

The silica concentrations of hydrothermal end-members are comprised generally between 10.2 and 18.6mM any year between 1993 and 2015, apart from two outsiders for the central group in 2009 and the SE group in 2012. Capelinhos has Si concentrations slightly decreasing from 14.1 to 13 mM since 2013. The SE group has values ranging between 13 and 15 mM, however some vents display very low Si concentration down to 1.7mM between 2009 and 2012. The NE group displays a wide range of Si concentrations because Sintra and Statue of Liberty have a rather stable Si concentration at 11.3 - 13.2 mM while Y3 vent has Si concentrations which vary between 13.9 and 17.5 mM. The SW group displays increasing Si concentrations from 1996 to 2013 (14.8 to 17.5 mM) and decreasing concentrations from 2013 to 2105. The central group displays different ranges in concentrations from site to site but each of them exhibit their lowest value in 2009.

4.2.4 Iron and Manganese

All groups display enriched concentrations of both Fe and Mn compared to seawater ones whereby the highest concentrations are obtained for Capelinhos site at 2.7 mM and ~600 μ M, respectively. For the Fe concentrations and in the 1990's, the NE and SE groups were the most-enriched ones whereas the SW group was the most-depleted one. Since 2008, all groups display, overall, a V-shape trend of Fe concentrations mimicking the trend observed for K ones. Within this trend, the SW group is now the most enriched ones compared to the NE group, which is the most-depleted one. The Mn concentrations display similar variation as those obtained for Fe concentrations apart from the Y3 site of the NE group, which shows systematically Mn concentrations equivalent to those of the SW group. For the central group, the Mn concentrations tend to increase progressively since 2009 while the Fe concentrations do vary from site to site but still within the Fe range define by the SW and NE groups.

4.2.5 Rubidium, Strontium, Cesium and Lithium

The dataset of Rb, Cs and Li concentrations is quite limited compared to the Sr one, for which systematic measurements on all groups of the LSHF were carried out since 1993.

Rb, Sr, Cs and Li concentrations vary accordingly to Cl concentration, whereby the most Cl-depleted group, i.e. Capelinhos, exhibits the lowest concentrations at 16.8 μ M, 33.4 μ M, 128 μ M, and 188.5 μ M, respectively whereas the SW and NE groups as the most Cl-enriched ones show the highest concentrations at 50.1 μ M, 179.3 μ M, 277 μ M, and 444.1 μ M, respectively (Table V - 3). Since 2010, the Cs concentrations have continuously increased from year to year and for all groups of sites. There is limited amount of Li concentrations with an annual survey between 2013 and 2015, exhibiting a sudden increase by up to 40% of the Li concentrations in 2015. This is observed for all groups without exception. In comparison, the Rb concentrations of all LSHF groups exhibit a sharp increase in 2008 and 2013. Finally, the Sr concentrations display similar fluctuations through the years as it is observed for K, Fe and Ca ones for the period comprised between 2008 and 2013. Since 2013, the Sr concentrations have slightly decreased. Note that in 2013, the SE group do not show a sharp increase in concentration compared to all other ones.

4.2.6 Strontium and Lithium isotopic compositions

The strontium isotopic compositions of end-members are determined based on selected samples of each group by linear extrapolation of Mg/Sr to 0. The less radiogenic $^{87}\text{Sr}/^{86}\text{Sr}$ end-member is determined at 0.7038 for Capelinhos in 2013 whereas the most radiogenic one is determined at 0.7045 for White Castle site belonging to the central group.

The Li isotopic compositions are reported in Table 3 as delta notation referring to the $^7\text{Li}/^6\text{Li}$ of the IRMM-16 (NIST) international standard. The $\delta^7\text{Li}$ end-member values range between +4.1‰ and +6.4‰. No differences appear between groups.

Table V - 3: calculated end member values of the fluids sampled at Lucky Strike. End-member values for fluids from 1933 to 2008 are from the literature (Charlou et al., 2000; Pester et al., 2012; Von Damm et al., 1998).

group	site	year	number of sample	T in situ (°C)	Cl (mM)	SO ₄ (mM)	Br (µM)	Si (mM)	Ca (mM)	K (mM)	Na (mM)	Fe (µM)	Mn (µM)	Sr (µM)	Rb (µM)	Cs (µM)	Li (µM)	⁸⁷ Sr/ ⁸⁶ Sr	δ ⁷ Li (‰)*	
Capelinhos		2013	4	324	262	-0,5	394	14,1	18,0	12,1	205	2754	628	35,7	18,7	129	198	0,70380	5,2	
		2014	4	318,5	264	-0,4	395	13,5	16,8	12,7	219	2309	490	33,4	16,8	128	189	0,70394	4,7	
		2015	4	319	267	-0,3	414	13,0	17,1	12,6	215	2425	591	34,6	16,8	131	241	0,70392	4,1	
Sintra		1993	6	212	530	0,1	n.d	13,2	37,3	24,3	469	169	219	98,1	n.d	n.d	n.d	0,70399	n.d	
		1994	1	215	496	n.d	869	11,5	38,2	25,3	400	260	228	93,0	33,2	225	356	n.d	n.d	
		1996	5	222	532	-0,5	n.d	13,3	42,1	27,2	401	191	217	93,3	n.d	n.d	n.d	0,70403	n.d	
		2009	5	196	536	-0,6	n.d	11,3	52,7	25,0	414	162	156	105,7	n.d	n.d	n.d	n.d	n.d	
		2011	3	207	565	-0,8	n.d	12,3	48,6	22,2	456	228	254	93,8	31,2	217	n.d	n.d	n.d	
		2013	1	196	537	-0,5	850	12,9	53,7	27,0	433	185	164	114,5	39,3	245	345	0,70418	6,4	
		2014	3	208	561	-0,9	901	12,2	51,4	28,6	447	145	168	103,5	35,2	245	362	0,70410	5,5	
		2015	2	207	567	22,0	891	11,6	51,6	29,0	473	155	183	97,4	34,6	255	433	0,70404	5,8	
	North Eastern sites	Statue of Liberty	1993	8	202	546	2,0	n.d	12,8	34,3	24,4	483	184	254	105,0	n.d	n.d	n.d	0,70386	n.d
			1994	2	185	513	n.d	911	12,1	37,7	24,7	428	225	272	101,0	32,9	n.d	341	n.d	n.d
		1994	2	324	472	n.d	922	15,4	36,7	24,8	402	863	446	119,0	39,1	235	357	n.d	n.d	
		1996	5	328	526	0,3	n.d	17,5	42,1	27,4	406	749	389	118,0	n.d	n.d	n.d	0,70420	n.d	
		2008	3	324	588	n.d	935	16,4	49,0	28,7	467	808	337	150,0	53,0	n.d	371	n.d	n.d	
		2009	6	286	554	2,4	n.d	14,2	53,1	25,5	440	396	266	144,7	n.d	n.d	n.d	n.d	n.d	
		2011	4	325	574	-0,2	n.d	13,9	47,0	22,6	470	387	201	121,8	34,8	228	n.d	n.d	n.d	
		2012	2	326	592	1,6	n.d	16,0	48,2	26,0	466	257	199	118,9	0,7	216	n.d	n.d	n.d	
		2013	3	325	574	0,0	932	17,1	52,9	25,5	433	687	323	144,6	42,3	253	323	0,70401	5,9	
		2014	3	323	574	0,7	895	17,1	52,5	27,9	457	554	273	135,8	39,0	265	344	0,70397	5,6	
	2015	4	326	578	-0,2	982	16,3	50,0	28,0	457	563	280	136,2	39,5	269	433	0,70388	5,5		

group	site	year	number of T in situ sample	number of T in situ (°C)	Cl (mM)	SO ₄ (mM)	Br (µM)	Si (mM)	Ca (mM)	K (mM)	Na (mM)	Fe (µM)	Mn (µM)	Sr (µM)	Rb (µM)	Cs (µM)	Li (µM)	⁸⁷ Sr/ ⁸⁶ Sr	δ ⁷ Li (‰)*
		1996	4	281	535	0,6	n.d	14,8	35,3	28,8	431	56	73	91,3	n.d	n.d	n.d	0,70428	n.d
		2008	2	308	538	n.d	843	15,6	43,0	27,8	443	746	295	126,0	47,0	n.d	359	n.d	n.d
		2009	8	327	528	0,9	n.d	14,2	45,6	25,4	414	487	299	113,4	n.d	n.d	n.d	n.d	n.d
	Crystal	2010	1	558	558	-0,1	n.d	14,0	47,3	27,4	447	497	180	108,8	37,4	259	n.d	n.d	n.d
		2011	3	335	551	-0,2	n.d	14,7	42,6	23,0	455	428	240	101,4	32,8	238	n.d	n.d	n.d
		2013	2	340	570	2,5	886	17,3	51,1*	28,3	446	467	249	179,3	50,1	233	368	0,704*	5,4
		2014	3	336	571	1,1	880	16,7	48,7	29,2	457	716	360	115,2	38,2	257	383	0,70415	4,7
		2015	4	329	573	0,0	1037	15,9	47,3	29,3	457	726	377	114,5	38,8	266	444	0,70403	4,4
South Western sites		2013	3	280	568	-0,4	873	17,5	48,3	26,6	442	197	245	117,6	39,6	244	334	0,70394	4,5
	Sapins	2014	3	279	566	-0,5	866	16,5	44,9	29,1	459	140	243	108,2	36,8	253	336	0,70917	n.d
		2015	4	236	571	-0,6	907	9,8	45,6	29,6	493	121	279	98,2	37,1	254	433	0,70404	6,0
		2009	5	340	520	0,1	n.d	14,9	44,8	25,4	410	673	321	110,4	n.d	n.d	n.d	n.d	n.d
		2011	7	341	556	0,1	n.d	15,3	44,3	22,8	457	599	262	101,5	33,4	229	n.d	n.d	n.d
		2012	2	340	575	0,7	n.d	16,7	48,3	27,2	444	397	213	106,4	29,9	241	n.d	n.d	n.d
	South Crystal	2013	3	340	570	-0,1	901	17,0	49,3	28,3	445	593	232	125,3	42,5	260	346	0,70400	5,4
		2014	2	339	568	0,3	880	16,5	47,3	29,8	457	852	330	118,1	38,7	259	342	0,70404	5,4
		2015	3	336	575	-0,2	924	16,2	47,1	29,4	461	867	348	114,6	39,2	277	427	0,70430	5,5
	Helene	1994	1	284	514	n.d	874	15,9	38,1	24,7	426	129	84	94,0	32,9	n.d	323	n.d	n.d
		1994	1	172	533	n.d	924	14,9	35,6	26,7	446	31	126	67,0	34,4	n.d	302	n.d	n.d
	Nuro	2009	2	526	526	0,6	n.d	12,4	41,8	23,7	402	54	112	102,8	n.d	n.d	n.d	n.d	n.d
North Western sites	Jason	1996	4	308	542	0,1	n.d	14,8	41,7	27,6	420	770	262	103,0	n.d	n.d	n.d	0,70383	n.d
	Elisabeth	2008	3	270	554	n.d	874	13,8	44,0	27,5	438	660	220	120,0	47,0	n.d	338	n.d	n.d
	Marker 6	1993	4	303	437	1,9	n.d	17,1	30,8	20,4	406	202	271	80,9	n.d	n.d	n.d	n.d	n.d
		1994	3	308	428	n.d	821	14,4	33,2	21,1	366	33	279	78,0	19,4	n.d	278	n.d	n.d
	Pettit Chimiste	1994	1	230	424	n.d	827	14,2	31,3	21,1	363	273	175	99,0	23,0	158	267	n.d	n.d
South Eastern sites		1993	2	302	439	1,2	n.d	16,3	29,8	20,5	382	275	271	79,9	n.d	n.d	n.d	n.d	n.d
		1994	1	310	422	n.d	743	15,8	33,6	22,1	364	363	289	79,0	22,7	n.d	280	n.d	n.d
	Cimendeff /Marker 7	2011	4	418	418	-0,1	n.d	14,5	33,7	16,6	344	191	192	68,0	22,9	173	n.d	n.d	n.d
		2014	4	423	423	3,3	658	15,5	36,2	20,9	338	227	215	74,3	25,6	181	267	n.d	n.d
		2015	4	428	428	0,0	702	14,9	35,2	20,7	333	230	225	76,5	26,2	184	n.d	n.d	n.d

group	site	year	number of T in situ sample	temperature (°C)	Cl (mM)	SO ₄ (mM)	Br (µM)	Si (mM)	Ca (mM)	K (mM)	Na (mM)	Fe (µM)	Mn (µM)	Sr (µM)	Rb (µM)	Cs (µM)	Li (µM)	⁸⁷ Sr/ ⁸⁶ Sr	δ ⁷ Li (‰)*	
Aicis		2009	3	298	403	0,5	n.d.	13,5	34,2	18,5	321	341	186	71,3	n.d.	n.d.	n.d.	n.d.	n.d.	
		2010	3	296	435	7,0	n.d.	13,7	41,9	19,4	329	317	176	81,2	23,4	151	n.d.	n.d.	n.d.	
		2011	13	300	424	0,1	n.d.	14,6	34,4	19,1	322	336	181	65,8	25,4	163	n.d.	n.d.	n.d.	
		2012	2	305	443	3,2	n.d.	1,7	38,5	19,1	329	81	222	76,3	2,8	n.d.	n.d.	n.d.	n.d.	
		2013	7	303	419	0,0	661	15,4	36,6	19,2	315	439	214	80,1	28,5	180	270	0,70422	5,3	
		2014	6	304	422	3,3	658	14,9	39,3	21,1	338	465	232	80,9	25,4	182	276	0,70420	5,3	
		2015	7	307	428	1,3	702	14,3	37,1	21,1	336	486	245	77,3	26,3	190	333	0,70427	5,4	
	South Eastern sites		1993	2	297	440	1,5	n.d.	16,0	30,0	20,6	385	252	261	77,1	n.d.	n.d.	n.d.	0,70421	n.d.
			1993*		319	436	1,2	n.d.	16,3	30,0	20,7	382	280	272	78,7	n.d.	n.d.	n.d.	n.d.	n.d.
			1994	2*	310	433	n.d.	781	16,1	33,2	21,9	357	282	303	77,0	22,7	n.d.	287	0,70422	n.d.
			1996	4	318	441	0,5	n.d.	15,2	33,4	22,7	339	467	256	72,1	n.d.	n.d.	n.d.	n.d.	n.d.
			1997	-	294	427	n.d.	n.d.	15,2	34,0	24,0	348	704	303	83,0	33,1	n.d.	306	n.d.	n.d.
			2008	1	299	414	n.d.	661	14,7	33,0	20,1	332	321	223	78,0	33,0	n.d.	288	n.d.	n.d.
			2009	5	296	403	0,2	n.d.	12,1	34,0	18,2	309	267	179	71,5	n.d.	n.d.	n.d.	n.d.	n.d.
			2011	3	316	399	0,0	n.d.	14,6	31,6	15,0	324	303	181	61,6	21,2	162	n.d.	n.d.	n.d.
		2012	2	322	439	2,4	n.d.	14,9	38,0	18,6	335	244	180	70,1	23,1	n.d.	n.d.	n.d.	n.d.	
		2013	2	316	422	-0,1	668	15,3	36,1	19,6	325	284	179	80,2	28,3	178	265	0,70421	5,2	
		2014	2	288	423	2,9	641	14,0	40,1	21,2	341	132	215	81,2	26,0	185	287	0,70454	5,1	
		2015	4	320	428	0,0	655	14,6	35,6	20,9	341	388	241	86,6	30,7	201	332	0,70413	4,8	
Tour Eiffel			1993	6	325	438	1,2	n.d.	15,7	29,8	20,7	386	623	267	77,3	n.d.	n.d.	n.d.	0,70419	n.d.
			1994	4	324	417	n.d.	735	13,3	32,3	21,6	347	624	289	76,0	22,7	167	286	n.d.	n.d.
			1996	7	323	441	0,9	n.d.	15,4	33,0	22,2	346	595	257	74,9	n.d.	n.d.	n.d.	0,70420	n.d.
		1997	-	324	431	n.d.	n.d.	15,7	34,0	23,0	349	269	300	83,0	33,5	n.d.	297	n.d.	n.d.	
		2009	7	316	408	0,4	n.d.	12,7	35,2	18,9	321	386	193	73,3	n.d.	n.d.	n.d.	n.d.	n.d.	
		2010	2	296	433	0,4	n.d.	14,6	35,1	20,2	329	346	165	68,4	23,6	166	n.d.	n.d.	n.d.	
		2011	5	325	416	0,1	n.d.	11,2	32,3	17,6	344	336	162	66,8	23,6	176	n.d.	n.d.	n.d.	
		2012	2	322	447	3,3	n.d.	14,0	38,1	18,7	340	318	176	70,1	22,7	150	n.d.	n.d.	n.d.	
		2013	3	325	415	0,8	638	15,2	39,0	19,6	334	489	229	80,6	27,8	180	263	0,70428	5,1	
		2014	4	323	420	0,2	638	15,1	35,8	21,1	337	522	226	74,2	26,1	186	262	0,70427	5,4	
	2015	2	324	427	0,1	681	14,3	35,8	21,0	341	585	270	74,1	26,4	192	335	0,70421	5,2		

group	site	year	number of T in situ sample	Cl (mM)	SO ₄ (mM)	Br (µM)	Si (mM)	Ca (mM)	K (mM)	Na (mM)	Fe (µM)	Mn (µM)	Sr (µM)	Rb (µM)	Cs (µM)	Li (µM)	⁸⁷ Sr/ ⁸⁶ Sr	δ ⁷ Li (‰)*
		2008	3	487	n.d	771	13,7	37,0	23,5	394	352	187	107,0	39,0	n.d	308	n.d	n.d
		2009	2	496	1,5	n.d	10,2	36,4	21,1	385	190	146	100,9	n.d	n.d	n.d	n.d	n.d
		2011	4	475	0,0	n.d	12,1	35,4	18,5	396	172	128	86,2	26,4	192	n.d	n.d	n.d
	Isabel	2012	2	505	0,0	n.d	14,3	39,9	21,7	390	199	141	89,3	27,5	184	n.d	n.d	n.d
		2013	3	470	-0,2	937	14,2	39,6	22,3	374	229	147	104,9	32,6	199	277	0,70429	4,9
		2014	3	486	0,6	775	13,4	37,5	22,7	376	136	157	95,4	29,8	198	n.d	n.d	n.d
		2015	3	493	-0,4	779	13,6	38,8	24,4	405	251	176	100,6	30,9	204	357	0,70425	6,1
		2009	7	464	2,3	n.d	12,8	38,3	21,8	373	264	305	112,1	n.d	n.d	n.d	n.d	n.d
		2011	4	476	0,2	n.d	14,9	34,8	18,7	400	451	428	88,1	28,3	193	n.d	n.d	n.d
	White Castle	2012	2	492	-0,2	n.d	16,6	38,2	22,6	381	308	284	96,5	30,3	200	n.d	n.d	n.d
		2013	3	481	-0,2	829	16,3	38,4	23,2	382	302	254	111,1	36,0	221	302	0,70501	5,6
		2014	6	486	0,8	780	16,2	38,9	24,6	394	307	279	106,2	32,7	225	305	0,70406	5,0
		2015	3	489	-0,1	788	15,5	37,9	24,4	396	407	369	105,8	33,4	225	386	0,70400	4,8
		2009	2	489	4,6	n.d	4,0	37,1	20,9	356	n.d	n.d	91,3	n.d	n.d	n.d	n.d	n.d
		2010	2	512	-0,6	n.d	19,5	41,5	22,9	404	378,1	204,6	97,0	32,5	234,0	n.d	n.d	n.d
		2011	3	505	-0,3	n.d	17,6	37,1	19,3	418	425	364	88,4	28,5	200	n.d	n.d	n.d
	Cyprès	2013	3	520	-0,5	750	18,6	43,2	23,4	399	397	299	112,4	36,4	222	319	0,70402	5,7
		2014	3	525	-0,5	821	17,8	42,1	26,4	432	546	414	104,3	33,7	231	325	0,70405	5,1
		2015	3	548	9,1	882	16,9	42,7	25,8	430	576	438	108,4	33,5	227	386	0,70417	5,4

5 Discussion

5.1 Time-series of hot vent chemistry: a matter of time-scale

Time series study of hydrothermal vent chemistry require special attention due to the temporal scale at which fluids are collected compared to the time scale at which seismic/tectonic/magmatic processes are taking place. From the discharge to geological processes, time scale variation of 10 orders of magnitude are at play (Lowell et al., 1995) and reference there in). The duration of a hydrothermal field is thought to be in the order of 10^3 – 10^6 years while the residence time of the fluid within the oceanic crust is constrained between 1 to 10 years (Lowell et al., 1995). At the discharge, precipitation of sulfide particles takes place within 0.3 to 3s of the turbulent mixing between hot hydrothermal fluid and cold deep-seawater. So the time scale at which samples are collected are complex parameters.

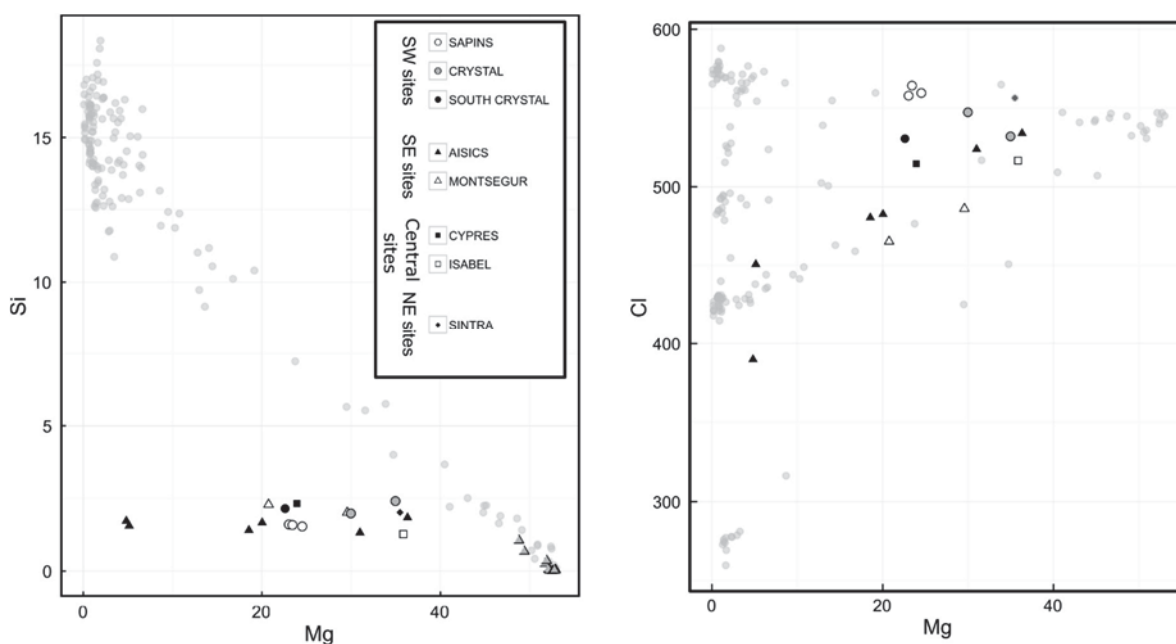


Figure V - 4 Mixing diagram between hydrothermal fluids and seawater based on Mg concentration. They focus on the low dissolved Si samples. Grey dots are measured black smoker samples. All data presented regroup sample measurements from 2009 to 2015.

Focusing on one vent at the LSHF seems unlikely representative of the dynamic of hydrothermal fluid circulation due to the geographic extension and complex inter-relation between vents (Barreyre et al., 2012; Escartin et al., 2015; Leleu et al., submitted). It is also important to identify and distinguish short time scale processes acting on several minutes to day range as shown by temperature records (Barreyre et al., 2014) over longtime processes taking place on months as evidenced by seismic swarms (Crawford et al., 2013).

In other words, any geophysical variations depicted at any hydrothermal field and at different time-scale should also be transferred and/or recorded in the chemical composition of hydrothermal end-members. Fluid sampling is carried out during research oceanic cruises most of the time on a yearly basis, implying punctual sample collection as a snapshot of hydrothermal fluid circulation. Taking the LSHF as an example, over the 348 fluid samples collected since 2009, 17 of them (5% of total sample collection) shows a systematic depletion in dissolved Si with values comprised between 1.5 and 2mM (Fig V - 4). This is significant and cannot be disregarded or rejected. In addition, this depletion cannot be accounted by direct dilution with surrounding deep seawater based on the following evidences: 1) the occurrence of this type of fluids is not associated to any specific sites or years (Table V - 3; Fig V - 4), 2) these low silica samples are collected during the same dives and within 10-20 minutes to other samples that display expected black smoker Si concentrations (Table V - 3), 3) they don't show any dilution evidence for other elements, i.e. low Si samples located on the south eastern side of the fossil lava lake have chlorinity typical of the SE group, and 4) Si depleted fluids can be found as well as at low Mg concentrations, close to the pure hydrothermal end-members. Furthermore, in 2015, sampling of Sapins hydrothermal vents, i.e. SW group, leads to complete extinction of the discharging vents (in situ T_{measured} at 302°C, Table 1), indicating that the fluid sampler inflow (~200ml in 2–3s) was higher than the vent fluid outflow (MoMARSat 2015 Cruise report). At this site, 3 samples out of the 4 collected ones exhibit this Si concentration depletion. We argue that these fluids, that have lost ~85% of their dissolved Si concentrations compared to normal black smoker fluids, are the results of Si precipitation from “normal” hydrothermal fluid.

Using Si geothermometer for seawater-like solution at 170 bar (depth of LSHF at 1700mbsl, Von Damm et al., 1991), we find that a temperature of 100 to 150°C is necessary to obtain a dissolved Si concentrations at 1.5 to 2.3 mM respectively. This is further sustained by experimental study of basalt-water alteration which shows Si concentrations between 2.3 and 3 mM at 150°C (James et al., 2003). Alternatively, heating of seawater in contact with basalt induces Si-Mg precipitates to form at temperature starting at 250°C (Bischoff and Seyfried, 1978). Such process may produce the observed low Si concentration but cannot account for the measured Mg and Cl concentrations of our samples compared to seawater (Bischoff and Seyfried, 1978; Von Damm et al., 1991). Furthermore, the linear trend between Cl and Mg concentrations including these low Si

fluids do not allow to decipher them from “normal” black smoker fluids (Fig V - 4). We propose that a shallow aquifer composed of conductively cooled hydrothermal fluid is actively forming the hydrothermal slab that is composed of silicified basaltic breccias (Fig V - 4). Cooper et al. (2000) proposed that seawater could be conductively heated within the subsurface by the up-flowing high temperature hydrothermal fluid. This hydrothermal seawater would participate to the formation of the hydrothermal slab largely found around the SE sites (Humphris et al., 2002). We propose that in a manner similar to what is proposed by Cooper et al. (2000), high temperature fluids can be conductively cooled at the subsurface edges of the upflow zone and form a shallow aquifer, in filling local porosity, close to the main discharge (Fig V - 5).

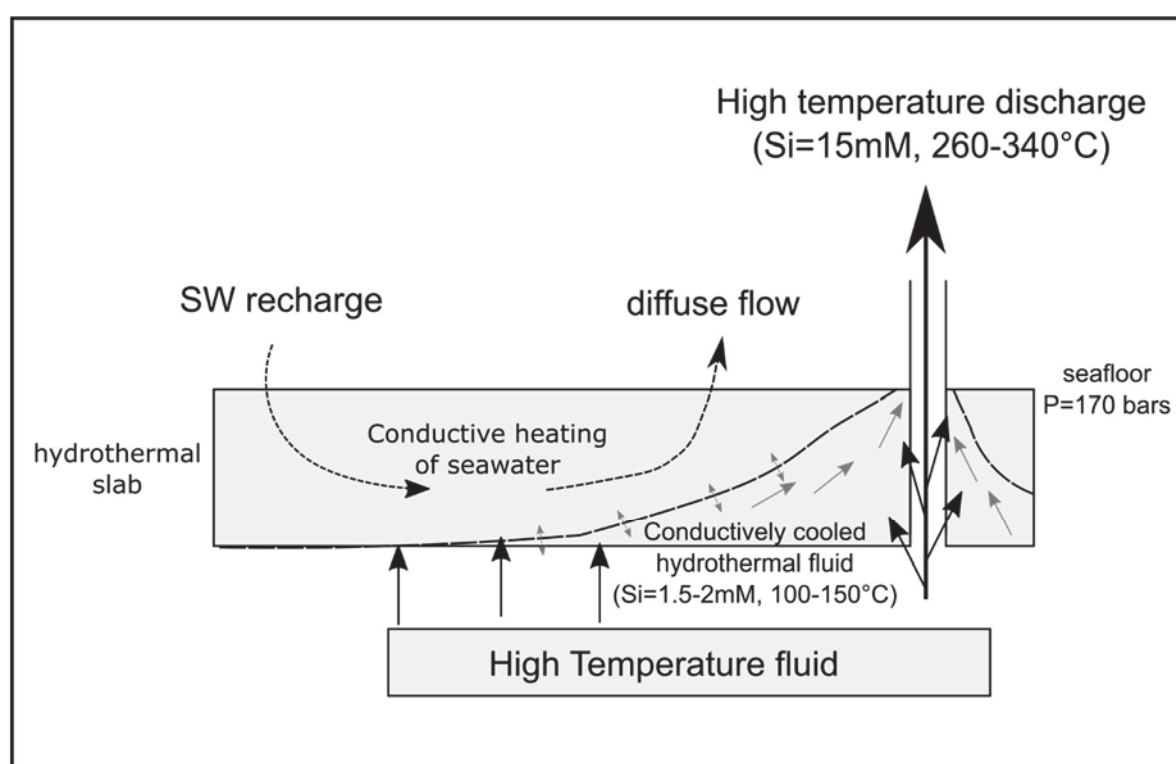


Figure V - 5 Cartoon of shallow hydrothermal circulation beneath the hydrothermal vents. Modified from Cooper et al. (2000). The silica cemented breccias or slab form an impermeable cap where conductively heated seawater and conductively cooled hydrothermal fluid can mix and sometimes be entrained in the focused fluids. Black arrows represent the high temperature fluids, the grey arrows are the proposed conductively cooled hydrothermal fluid. Dashed arrows represent the conductively heated seawater.

The dynamic of such a cooled hydrothermal fluid is probably related to subsurface/seafloor processes such as tidal pressure change. In situ autonomous temperature sensors recorded not only the tidal signal but also episodic temperature excursion (Barreyre et al., 2014). This is evidenced as either a temperature drop of 4°C to 160°C from the initial temperature over a few hours, or a temperature increase up to 10°C for several days (Barreyre et al.,

2014). These temperature surveys of focused fluids highlight the high temporal variability of discharging fluid temperature and therefore the potential for contrasted and variable fluid chemistry. We anticipate that the fluid collections at Sapins may represent one example of low temperature fluid excursion. In summary, interpreting time-series of hot fluid chemistry is not as strait forward as anticipated and call upon caution for apparent chemical variability of focused hydrothermal end-members from one year to the other. Furthermore, we suggest that a pool of hydrothermal fluid, conductively cooled and more or less mixed with deep seawater, is located in the subsurface vicinity of focused fluids (Fig V - 5). Only extensive fluid sampling over long-term time series allow to reveal the occurrence of peculiar fluid.

5.2 Proxy of phase separation conditions and its reliability: Application to SE group from 1993 to 2015.

To study the fluid elemental variations over long-term time series, we chose a global approach by using exclusively fluid end-members but excluding the low Si samples presented in the previous section. Differences in fluid salinity compared to seawater are widely observed in hydrothermal fluids of submarine environments that are most likely related to phase separation. Therefore, studies have been conducted to better understand this process and the effect of P and T on the solution salinity (Bischoff, 1991; Bischoff and Rosenbauer, 1985; Driesner, 2007; Foustoukos and Seyfried, 2007b, c). The fluid flow properties that depends on substrate permeability, impact the chemical response to P–T conditions and variations, which in turn may produce chloride variability in the discharging fluids (Fontaine et al., 2007; Fox, 1990; Goldfarb and Delaney, 1988; Leleu et al., submitted). Previous fluid chemistry studies argue for a unique phase separating source feeding the LSHF and flowing towards the seafloor, despite a fairly high chemical diversity (Leleu et al., submitted; Pester et al., 2012; Von Damm et al., 1998).

Fontaine et al., (2009) developed a geothermobarometer based on the Cl and Si concentrations with the hypothesis that these two element concentrations are fixed at phase separation conditions without any further modification along the up-flow pathway to the seafloor. On one hand, Cl depends on the phase separation condition as vapor and brine phases will form above the two-phase boundary of seawater. The vapor phase being less dense than the brine one, will flow up-wards more efficiently than the brine one. Physical properties of brine and vapor phases are radically different from one another as the brine

wetting effect enables its condensation on the fracture walls and the backwater porosity (Fontaine et al., 2007; Goldfarb and Delaney, 1988). Therefore, the brine phase is quantitatively stored at depth during this process (Fontaine et al., 2007). Nevertheless, venting of brine phase by entrainment during the upflow is punctually observed and might be related to uncomplete brine/vapor segregation (Larson et al., 2009). This entrainment may occur when the phase separation conditions change and are insufficient to sustain the same fluxes of brine and vapor (Schoofs and Hansen, 2000). Alternatively, brine segregation may lead to the saturation of the backwater porosity, provoking brine flushing effect on punctual time-scales (Coumou et al., 2009; Fontaine et al., 2007).

On the other hand, Si is widely used in submarine system as a chemical proxy of quartz equilibrium at depth, whose concentrations reflect specific P–T conditions (Fournier, 1983; Foustoukos and Seyfried, 2007a; Von Damm et al., 1991). Si is systematically enriched in black smoker fluids compared to seawater due to alteration process of basaltic glass and silicate minerals at depth. However, the occurrence of quartz veins in the reaction zone and upflow zones in both ophiolites and oceanic crust suggest that dissolved Silica is controlled by quartz precipitation conditions at depth (Alt et al., 1989; Delaney et al., 1987). Therefore, the solubility of quartz has been investigated in the NaCl–H₂O system to be used as a geothermobarometer in hydrothermal system (Fournier, 1983; Von Damm et al., 1991; Foustoukos and Seyfried, 2007a). Numerical modeling studies suggest that quartz maximum precipitation will occur concomitantly to phase separation condition (Steele-MacInnis et al., 2012). This is confirmed by occurrence of high salinity fluid inclusions in quartz forming in the reaction zone (Kelley and Robinson, 1990). Note that quartz occurrence with greenschist facies mineral assemblages as well as hydrothermal fluids that are conductively cooled and/or mixed with seawater, may bias the P–T condition estimates due to quartz/amorphous silica precipitation along the up-flow pathway to the seafloor (Steele-MacInnis et al., 2012; Von Damm et al., 1998).

Si–Cl geothermobarometer is applicable to vapor-dominated fluids, which are most likely to flow fast enough to avoid any substantial changes in element concentrations on the way up to the seafloor. Capelinhos site is the most vapor-dominated fluid venting at the LSHF and was sampled yearly since 2013 (Leleu et al., submitted). Prior to 2013, the most vapor-dominated vents at LSHF were Tour Eiffel and Montségur sites, both of them belonging to the SE group. Figure V - 6a and 6b show the application of the Si–Cl geothermobarometer to these two sites over the period 1993 to 2015 in comparison to Capelinhos group for 2013

till 2015, respectively. At Capelinhos group, the separation phase occurs at 380-370 bars and 437-442°C, with little variation over three years arguing for a maximum depth of the reaction zone at 2800-2500 mbsf (Leleu et al., submitted). In comparison and for the same time period at Tour Eiffel and Montségur sites, the separation phase is determined to take place at 390–370 bars and 437 – 442 °C, which are equivalent to P and T estimates of Capelinhos. Despite higher chlorinity in Tour Eiffel and Montségur fluids compared to Capelinhos, the three of them reflect the same P–T conditions at depth for separation phase between 2013 and 2015. Within this framework, Tour Eiffel and Montségur sites can be used as a proxy of P–T estimates of the separation phase prior to 2013.

Overall, P–T estimates of separation phase cluster for all two sites at 380 ± 10 bars and $435 \pm 5^\circ\text{C}$, over the period spanning between 1993 and 2015, in line with P–T conditions determined for Capelinhos site (Fig V - 6c). These estimates indicate that phase separation is located at $\sim 2650 \pm 200$ mbsf, approximately 700 m above the roof of the AMC. Note that since 2013, the phase separation zone seems to “move” toward the surface, by ~ 200 meters (Fig V - 6c). However, departure from these general estimates are nevertheless observed on punctual years, whereby temperature remains essentially constant for concomitant for larger pressure range, e.g. isothermal decompression. For example, pressure drops to 355 bars for both Tour Eiffel and Montsegur sites in 2009, while in 2011 and 1994 only Tour Eiffel site indicates lower P estimate at 345 and 365 bars, respectively. These punctual lower pressure estimates may provide valuable information about fluid modification during the upflow to the seafloor as a response to magmatic and/or tectonic events that may control ultimately silica precipitation and/or brine entrainment/segregation.

For instance in 2009, a seismic swarm has been recorded by the seismometer array of the EMSO observatory infrastructure (Crawford et al., 2013). The depth of the intense seismic activity has been evaluated to occur between 2500 and 3000 mbsf, in the depth range of phase separation predicted by Si-Cl geothermobarometer (Crawford et al., 2013; Leleu et al., submitted). Crawford et al. (2013) argue that the 3 month-long event swarm in April–June 2009, results from a thermal cracking of the rocks due to down-flowing cold seawater. Note that fluid sampling in September 2009, occurred a couple of months after the timing of these seismic events which are observed less than a year later than the 2008 AMC replenishment, i.e. evidenced by high CO₂ concentrations in fluids collected in July 2008 (Pester et al., 2012).

Similarly, lower P excursion inferred from July 2011 fluid chemical composition takes place before the occurrence of seismic swarm detected in August-September 2011 (Crawford et al., 2015) but still less than a year after the AMC replenishment, evidenced by high dissolved CO₂ concentrations in October 2010 fluids (Chavagnac, pers. comm.) . The magmatic activity in 2010 is sustained by a drastic change of micro-organism diversity preserved in in-situ microbial-colonisers which display enhanced occurrence of thermophile archaea (Rommevaux et al., submitted).

Although the shallower P - T estimates should be taken with caution, they at least provide information about a perturbation of the upflow zone, either by temperature and/or pressure changes associated with a displacement of the cracking front. Depth changes of the cracking front are a likely place for phase separation but it remains to elucidate the time-scale at which the impact of seismic swarm is preserved and recorded by the chemical features of hot vents. At least from these two particular examples, we may suggest that a two month delay between seismic swarm and fluid sampling allows to detect any depth variability of the thermal cracking front.

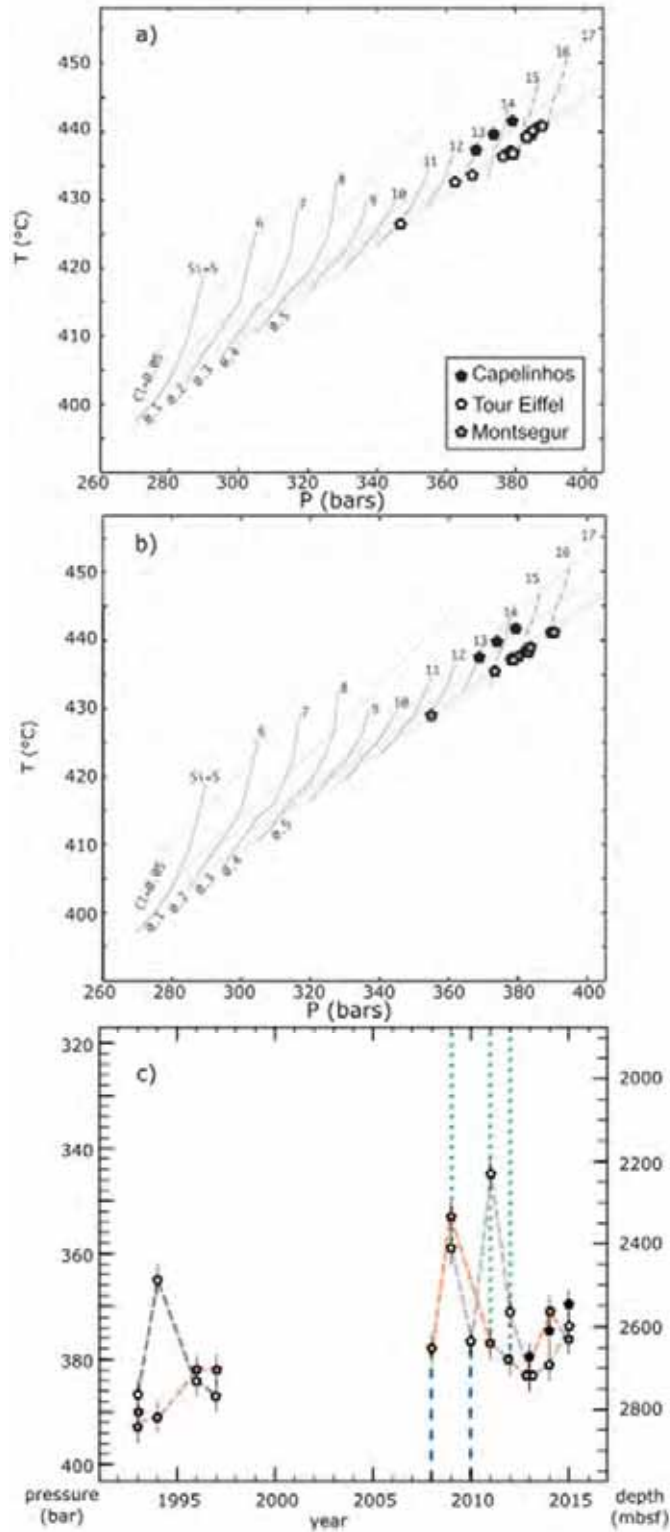


Figure V - 6 Si-Cl chart for P and T determinations in the separation phase. Modified from Fontaine et al. (2009). Si and Cl variations are representative of specific P and T conditions. Tour Eiffel endmembers from 1993 to 2015 are represented in a); Montségur endmembers from 1993 to 2015 are represented in b). Both are represented with Capelinhos endmembers from 2013, 2014 and 2015. C) presents the evolution of the P and T estimated based on a and b. Blue dashed line are the observed magmatic CO₂ degassing (Pester et al., 2012; Chavagnac et al., unpublished data). Green dotted line mark the seismic swarms recorded by the OBS network (Crawford et al., 2013, 2015).

5.3 Alteration state of the substratum

Despite the discrete chemical variability between each group of vents, and more locally between each vents, a general trend can be drawn by using boxplots of all the data available for each year. We believe that this approach is best suited to describe the temporal chemical variability at the hydrothermal system over a long-term time scale.

In hydrothermal vent fluids, Na and Ca concentrations are found respectively depleted and enriched compared to seawater ones. This is due to the alteration degree of calcic plagioclase (anorthite) to more stable sodic plagioclase (albite; Berndt and Seyfried Jr, 1993; Von Damm, 1988). The Ca/Na ratios constitutes a proxy of plagioclase equilibria by means of anorthite percentage in equilibrium with the fluids, i.e. the extent of albitisation process (Berndt and Seyfried Jr, 1993; Pester et al., 2012). Keep in mind that during phase separation, Ca is preferentially partitioned into the brine phase while Na will remain in the vapor phase (Pester et al., 2015). This means that Ca/Na ratios will not only depend on plagioclase alteration in the reaction zone but also to phase separation process.

Focusing on the 2013-2015 fluids which are the most representative of the diversity identified at LSHF, we observe the effect of phase separation on the Ca/Na ratios as shown on Figure V - 7. The lowest Ca/Na values at 0.08, are found for Capelinhos vent site while the highest Ca/Na ones at 0.105 are obtained for the most brine-dominated fluids of the SW group. This trend is coherent with phase separation process for Capelinhos, central and SW groups but do not explain the very Ca/Na ratios obtained on the NE and SE groups (Fig V - 7). The NE sites have markedly higher Ca/Na ratios than the SW sites by up to 20% although both of them exhibit similar Cl content above seawater values. We interpret these variations as being due to the intense alteration of the substratum as evidenced by surficial hydrothermal deposits and lower temperature of discharging fluid, e.g. ~200°C (Humphris et al., 2002; Ondréas et al., 2009). This area probably encountered already a high degree of albitisation at depth. In contrast, the SW group sits on an area which doesn't display such deposits but merely post-dating lava lake fractures and fresh lava, e.g. probably reflecting a much less altered substrate at depth. The SE group displays high Ca/Na ratios equivalent to the NE ones, although the fluid venting is vapor-dominated at this location. We showed earlier that the SE group, among which Tour Eiffel belongs, may be used as a proxy of Capelinhos site for determining the P-T conditions taking during phase separation. The

large variation of Ca/Na ratios between Capelinhos and the NE group towards higher values clearly illustrates higher degree of albitisation of the substratum in the SE area.

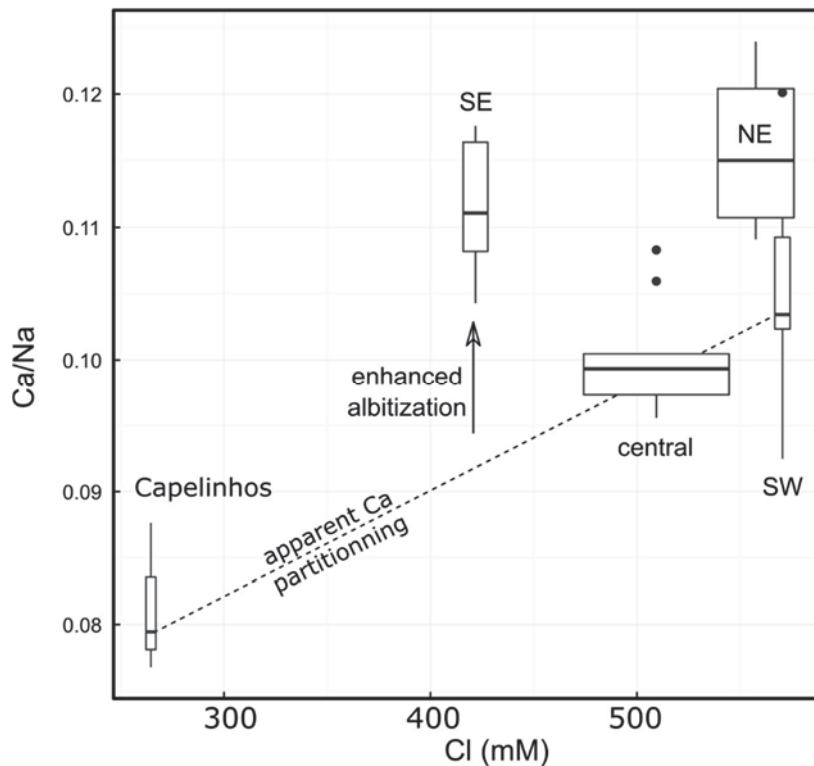


Figure V - 7 Boxplot diagram presenting the fluid Ca/Na ratios per group of site groups for 2013, 2014, 2015 as a function of the Cl concentration.

Using boxplots of all the Ca/Na ratios for each year and group of sites, we may assess the temporal variability of the albitisation process over time, as shown in Figure V - 8. On a global temporal point of view, the albitisation process seems to increase progressively between 1993 and 1997, whereby the 1993 SE and NE groups are characterized by Ca/Na ratios at 0.008 identical to those of Capelinhos at present time and increasing up to 0.1 in 1997. Since 2008, each group of sites display higher Ca/Na values than in 1993, in line with on-going albitization of the substrate. Over the 2008 till 2015 period, two magmatic events took place in 2008 and 2010 together with three month-long seismic swarms in April-June 2009, August-September 2011 and October 2012 (Crawford et al., 2015). All of them probably influenced the hydrothermal circulation by changing the brittle/ductile boundary and emplacing new materials and/or allowing access to fresher rocks. The latter would provide a comprehensive explanation to the sudden increase of Ca/Na ratios taking place in 2009 and 2010. Further evidence on the extent of the oceanic crust alteration can be extracted from the temporal variability of K/Cl ratios, even though K as an alkali element is as sensitive to phase separation as Ca (Berndt and Seyfried, 1990) displaying

concomitant increasing K/Cl ratios and Cl concentrations. While this is clearly observed on the temporal variability of site groups (Table V - 2), the simultaneous co-variation of the each group K/Cl curves (Fig V - 9) and from year to year, may point out the oxidizing conditions of the oceanic crust alteration. Between 2008 and 2015, the K/Cl ratios have systematically decreased from 0.052 in 2008 to 0.038 in 2011 while systematically increasing back to 0.052 in 2015.

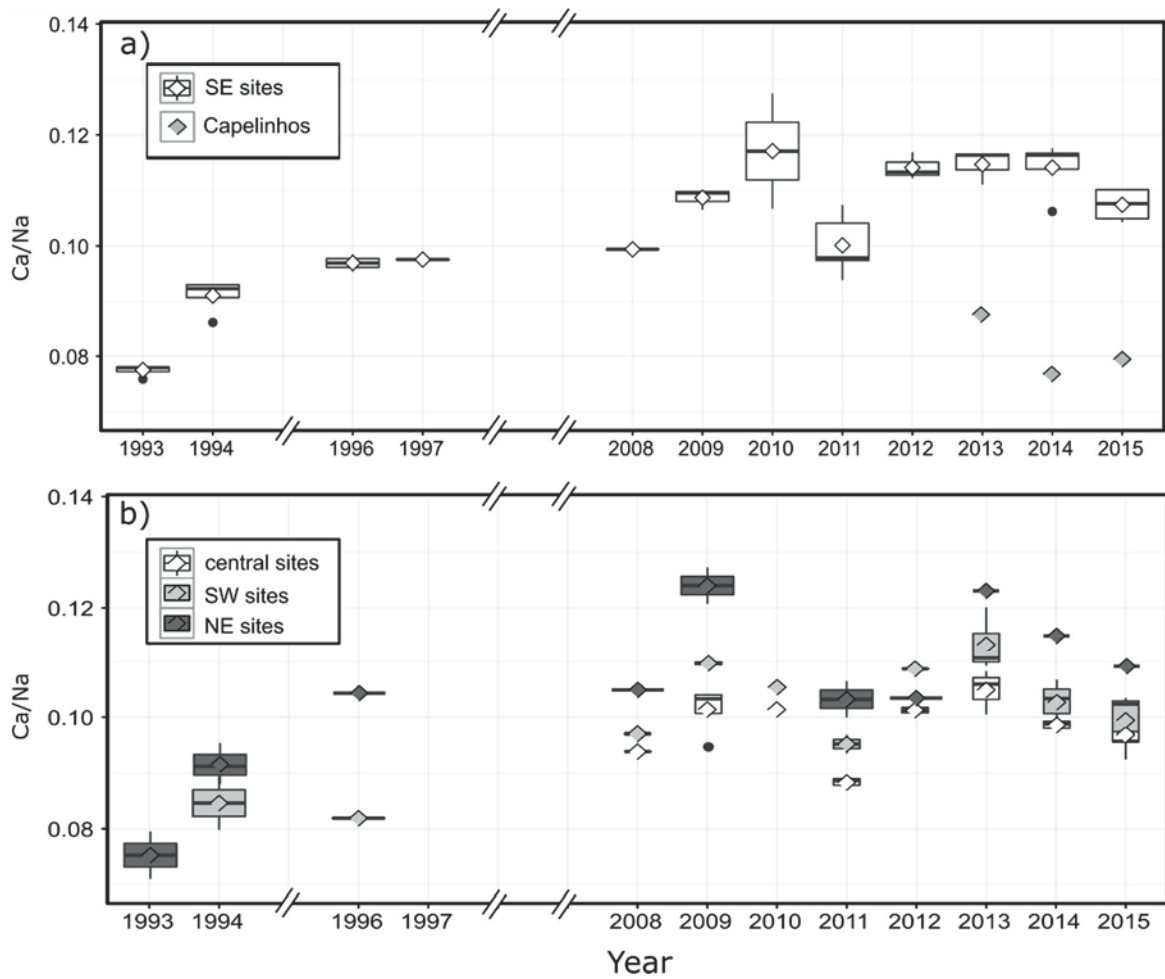


Figure V - 8 Time series of Ca/Na boxplots of end-members selected for different groups (see text for details).

In summary, the relative Ca/Na ratios of the fluids within the same area are representative of alteration process occurring at depth, but for inter-comparison, it is necessary to take into account the partitioning of these elements during phase separation.

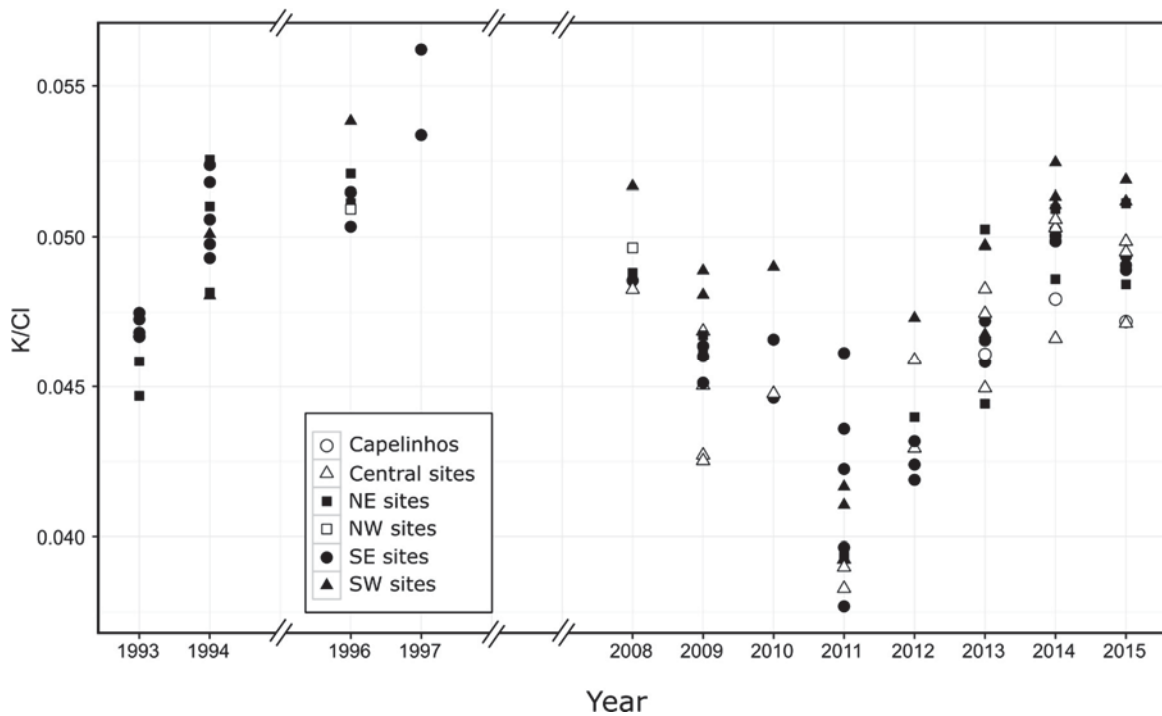


Figure V - 9: Time serie of K/Cl values of the endmember from table V – 2.

5.4 Apparent temperature of greenschist mineral equilibration (Fe-Mn variations per sites).

Pester et al. (2011) used basalt alteration with seawater experiment and compiled data from the literature to investigate the response of Fe and Mn concentration to temperature change. These elements are highly dependent on temperature and environmental conditions as well as pH and redox. These authors were able to develop a geothermometer based on the ratio of Fe and Mn. Fig V - 10 display Fe and Mn on a logarithmic scale for different groups. The highest temperature recorded by this geothermometer is 400°C for Capelinhos vent site. Conductive cooling in such diagram is marked by an apparent enrichment in Mn compared to Fe. This is due to a faster response to temperature change of Fe, while Mn behaves more conservatively. The SE area displays also a trend typical of conductive cooling. Again, caution need to be taken because Fe precipitate as it mixes with seawater at the seafloor discharge. Poor quality samples, with significant amount of seawater entrained, will display a similar trend as a conductive cooling in the subsurface.

The SE sites display a maximum temperature of equilibrium with greenschist facies minerals at 375°C, especially for Tour Eiffel, which show almost no variations through the years (Table V - 3). Some of the fluids in the SE area display a trend toward conductive

cooling out of the range of equilibrium with basalt. Some have been discussed already by Pester et al. (2012), especially the 1993 and 1996 group. Montsegur fluids seem to follow this conductive cooling trend in 2014, but rather than a subsurface process affecting reaction temperatures, it is more likely due to the poor quality data sampled this year which had at best ~10mM of Mg, i.e. ~20% of seawater entrained. That much seawater entrainment likely resulted in loss of Fe.

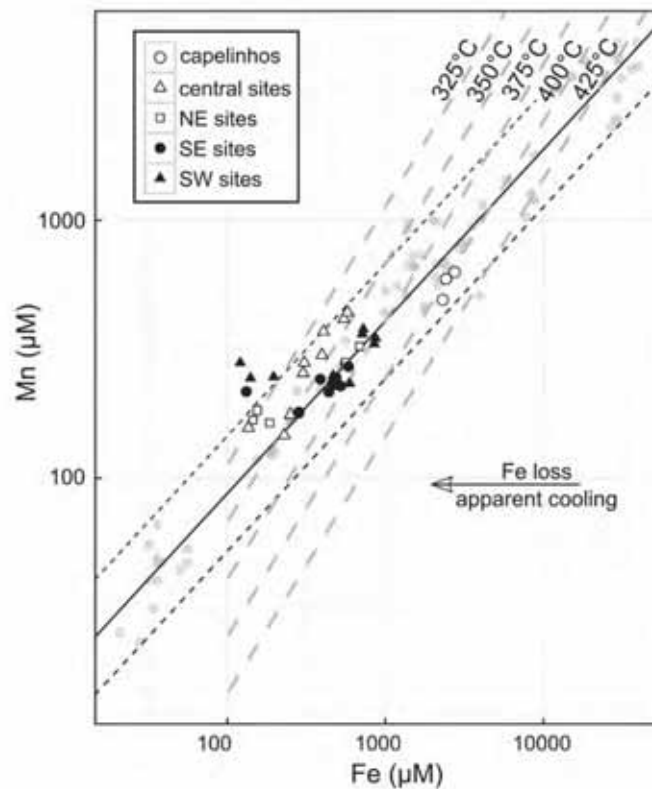


Figure V - 10 Fe and Mn diagram on logarithmic scales. Grey dots are experimental data from literature. Solid line represent the basalt alteration experiment with a 95% confidence interval (dashed black line). Dotted grey lines are isotherm for basalt experiments at different temperatures.

In the South West area, Crystal site is interesting in that it shows a gradual increase in temperature. Crystal earned its name from the crystal clear discharging fluid at $T=281^{\circ}\text{C}$ (Von Damm et al., 1998). Since then, Crystal site has evolved and show now the highest temperature of the LSHF with the close-by South Crystal site, venting fluid at temperature of $\sim 340^{\circ}\text{C}$. In 1996, Crystal was well within the basalt alteration experiment range, at lower temperature than 325°C , and progressively attained higher temperature close to 380°C . Sapins, which is situated close by the Crystal and South Crystal sites, vents at lower

temperature, and accordingly display lower temperature of equilibration (i.e. $<350^{\circ}\text{C}$). The fluids from Sapins lies on the conductive cooling trend, and from 2013 to 2015 seems to cool in subsurface. Alike Montsegur fluid in 2014, samples of Sapins in 2015 display the low Si fluids. Although it is clear that samples for Sapins in 2015 have an apparent poor quality, regarding the Mg concentration, we believe that the apparent cooling observed from Fe and Mn concentrations is significant and indicate that Sapins is currently clogging due to silica precipitation of a cold hydrothermal fluid. Sapins expels clear fluid at $\sim 300^{\circ}\text{C}$ which indicates high temperature at depth but also that seawater entrainment will not modify drastically the Fe and Mn concentrations. This suggest that unlike fluids from Montsegur sampled in 2014, the seawater entrained is not the cause of the apparent low temperature but the conductive cooling during upflow.

The North East area has been well studied in former fluid studies (Charlou et al., 2000; Von Damm et al., 1998), the Fe and Mn concentrations of the sites situated at the old deposits area with many inactive sites (Statue of Liberty) are consistent with a low temperature of fluids conductively cooled. They display a temperature of equilibration around 325°C , that is stable through the years for a discharge temperature of 210°C . Statue of Liberty is now extinct but Sintra shows constant temperatures of $\sim 207 \pm 10^{\circ}\text{C}$ since 1993. Y3 is situated on the edge of the fossil lava lake and displays higher temperature of equilibration at $\sim 375^{\circ}\text{C}$ and stable through the years. The lowest apparent temperature at Y3 is attained in 2012 ($\sim 340^{\circ}\text{C}$), which also coincides with the collapse of the 18 meters high chimney of Y3.

The central sites, that include White Castle, Isabel and Cyprès, all display temperatures equilibrated between 325 and 350°C . The Fe and Mn concentrations are coherent with the basalt experiment (Fig V - 10). This group is characterized by a cooler temperature of equilibrium, despite high dissolved Si concentration for Cyprès (Leleu et al., submitted).

Capelinhos' temperature of equilibration is 400°C , and is stable for 2013, 2014 and 2015.

To sum up, we observe 3 temperatures of apparent equilibrium with greenschist mineral facies. The most active vent is the Capelinhos site with several chimneys venting $\sim 324^{\circ}\text{C}$ fluid and indicating 400°C in subsurface. Next comes fluids equilibrated at $T \sim 370^{\circ}\text{C}$, and discharging at $T > 300^{\circ}\text{C}$ (SW sites: South Crystal, Crystal; SE: Tour Eiffel, Aisics, Montsegur; NE: Y3). Other vents that discharge fluids at temperature between 200 and 300 indicate lower temperatures of equilibration. Leleu et al. (submitted) discussed that a unique source fluid was feeding the whole hydrothermal system. Capelinhos fluids are

channeled shortly after phase separation likely through a deep reaching fault transporting fluid to the discharge zone fast enough to limit the chemical reaction with the host rock. The low chlorinity also is important concurring with the fast extraction of these fluids. Therefore, Capelinhos fluids best represent the fluid after phase separation. This means that the apparent lower temperature of equilibrium with greenschist facies minerals are related to cooling processes and storage of both Fe and Mn. We cannot account for the Mn storage but we can calculate a “missing Fe” amount that would represent Fe sequestered in the stockwork beneath the LSHF. Therefore, normalization to Fe/Mn ratio equivalent to that of Capelinhos (~4.4) provides a minimum estimate of the Fe sequestered within the subsurface. As it is difficult to evaluate the subsurface storage of Fe in terms of volume without too many unconstrained assumptions, we can nevertheless provide a relative storage range of 65% ($\pm 14\%$) for the sites around the lava lake. In other words, only ~35% of Fe mobilized in the reaction zone is discharged into the seawater at the main LSHF.

5.5 Three years isotopic variations

Major elements in records last mineral equilibria encountered during upflow. They provide valuable indications of fluid-rock interaction in the upflow zone. But phase separation effects on fluid chemistry might alter or reset the fluid chemistry and lead to biased conclusions. Therefore the need of indicators that would not be affected by phase separation is important. Isotopes of Strontium and Lithium are perfectly suited for this as they both have a different signature in sources (i.e, basalt and seawater) and neither of them will be fractionated during phase separation. The conjunction of both isotopes is valuable because they are not controlled by the same minerals. Sr isotope are mainly controlled by plagioclase dissolution, and anhydrite precipitation (Berndt et al., 1988), while elemental Li is quantitatively extracted from basalt (Seyfried Jr et al., 1998) and incorporated by Mg-bearing secondary phases such as chlorite and smectite (Millot, 2013; Seyfried Jr et al., 1998).

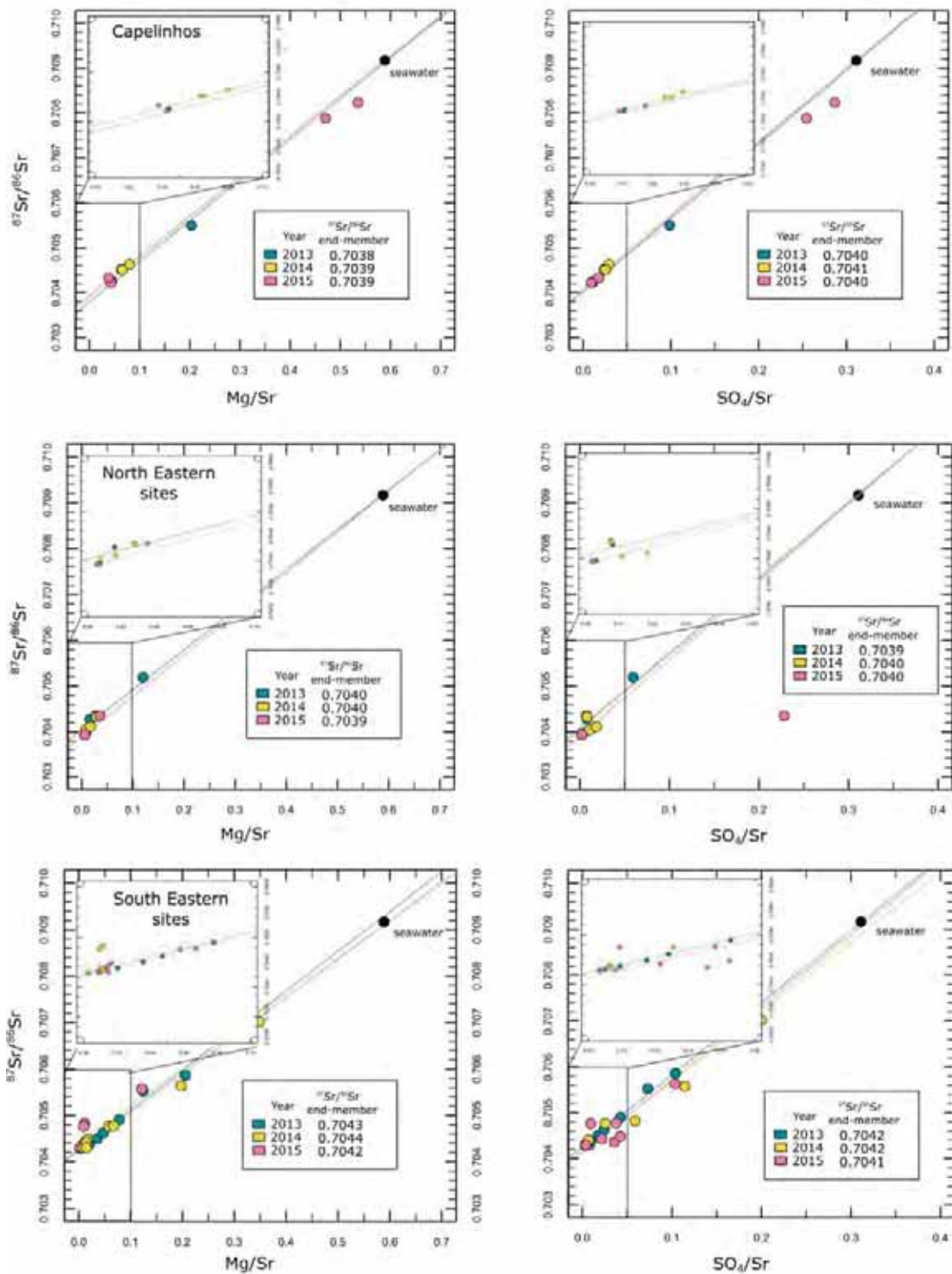
Sr isotopes variations: from yearly stable signature to sampling time-scale variations.

Some samples display a typical Sr isotope enrichment toward more radiogenic value. These samples also show enrichment in Ca, SO₄ and Sr, which is coherent with anhydrite dissolution in subsurface. Comparison of Strontium isotope end-members determinations has been done by Mg/Sr and SO₄/Sr extrapolation. Usually end-members are determined by Mg/Sr end-members but in the case of anhydrite dissolution prior sampling, a significant

amount of Strontium might be added to the solution, and will bias the determined end-member toward more radiogenic values. A way to treat this issue is to investigate the relations between Sr isotope and SO_4/Sr . As Mg, SO_4 is supposed to be completely removed from the hydrothermal vents, through anhydrite precipitation and sulphur reduction in the H_2S form. If the SO_4 end-member is different from zero, this means that anhydrite is intervening somehow. Usually, Mg extrapolation yields to SO_4 endmember value lower than zero. This is due to limited anhydrite precipitation at the discharge because the 300°C fluid, rich in calcium mixes with a 2°C seawater, rich in SO_4 . If the SO_4 endmember is higher than 0, this means that anhydrite has been dissolved shortly before sampling and/or within the sampler. This provides extra sulfate to the solution compared to what would be expected from simple hydrothermal fluid/seawater mixing. This entrainment might explain some high Sr isotope value for the fluid, therefore $^{87}\text{Sr}/^{86}\text{Sr}$ isotope end-member are corrected by extrapolation through $\text{SO}_4/\text{Sr}=0$ when needed (Fig V - 11). Despite correction, some samples still display anomalously high Sr isotope ratio. Equivalent variations have been observed at EPR (Ravizza et al., 2001). These authors observed at Biovent a systematic deviations toward higher Sr isotope ratio and suggested that an intermediary fluid (IF) was at play within the subsurface for this vent. This IF is supposed to have lost ~50% of Mg from seawater with unchanged Sr concentration nor isotopic signature, which corresponds to fluids sampled in the 504B borehole (Magenheim et al., 1995). They estimate this IF to account for 3 to 10% of the volume sampled. Although the implication of an identical IF in some samples from Lucky Strike fluids would not account for the observed variations, another type of fluid depleted in Mg and enriched in radiogenic strontium could explain this discrepancy. This enrichment is not observed at one specific site but in several sites and years. Again these observations seems to be in the order of a really short timescale (within several minutes) at the field scale but they are decoupled from the shallow cooled hydrothermal fluid discussed previously.

Nevertheless, on a time scale of a few years, general observations can be done. The first observation is the apparent stable Sr signature over 3 years for fluid samples targeted for analysis. The second observation is the difference between groups and especially between vents. Capelinhos shows the lowest Sr isotope ratios of the groups together with Crystal, South Crystal and Y3, that show $^{87}\text{Sr}/^{86}\text{Sr}=0.7039-0.7040$. The highest end-member is found for the vents of the South Eastern area with $^{87}\text{Sr}/^{86}\text{Sr}=0.7042-0.7043$. The vents of

the central area have Sr isotope ratio in between these two values ($^{87}\text{Sr}/^{86}\text{Sr} \sim 0.7041$; Table V – 3).



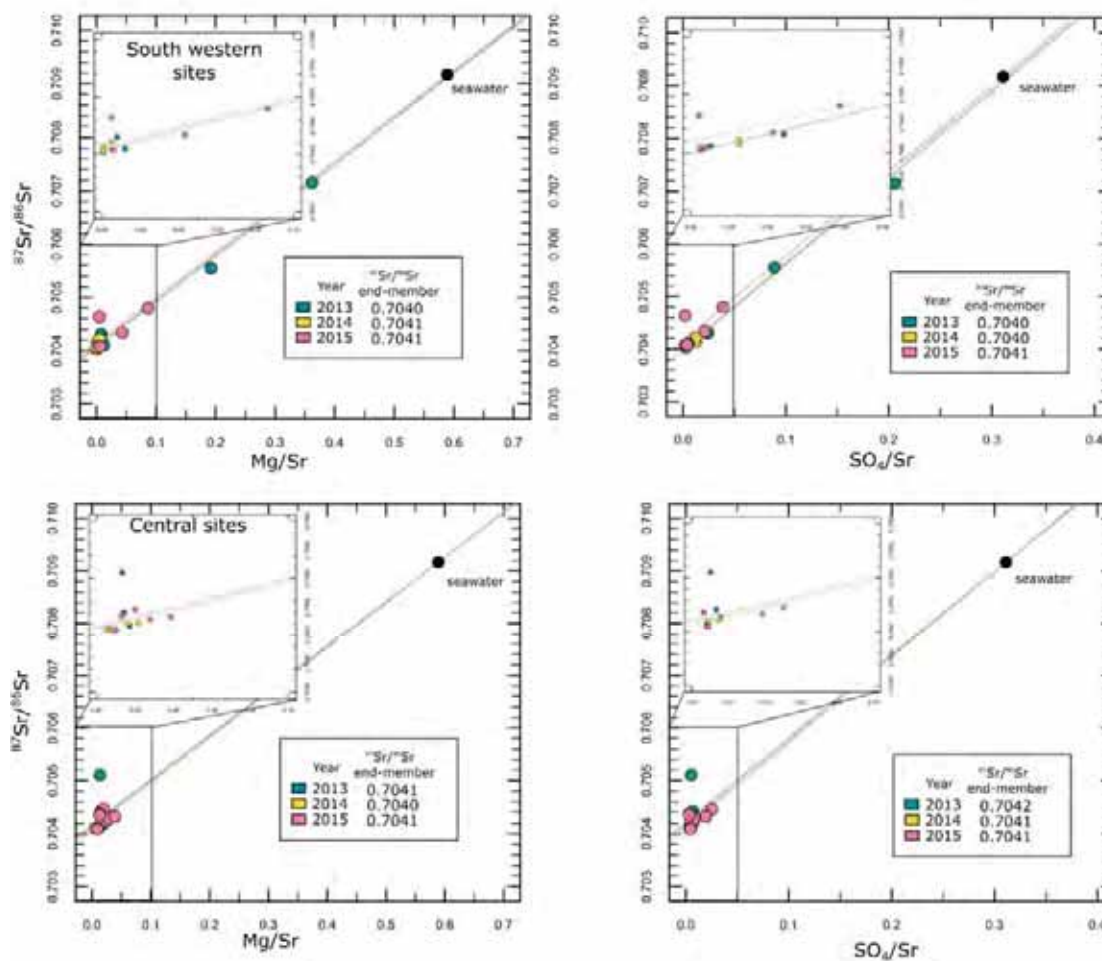


Figure V - $^{87}\text{Sr}/^{86}\text{Sr}$ of fluid samples presented as a function of Mg/Sr and Mg/SO_4 . The color code indicate the year of samples collection. Each graph presents the determination of Sr isotope end-member determination.

Other samples display typical enrichment in sulfate. These samples also show enrichment in Ca and Sr which is coherent with anhydrite dissolution in subsurface. These samples will be discussed in the isotope section. Nevertheless, anhydrite dissolution and quartz precipitation in close-subsurface clearly indicates that dynamic processes occurs within the close vicinity of vents and are hardly observable on yearly sample basis.

Li isotopes: signature of fresh basaltic Li vs. secondary mineral fractionation.

Lithium isotopes are difficult to interpret as they vary between sites. No systematic differences in $\delta^7\text{Li}$ is found with Cl (Fig V - 12). This is coherent with the studies from Seyfried Jr et al. (1998) that found no fractionation of Li isotope during phase separation. For individual sites, different pattern are observed from 2013 to 2015. Most of the sites are constant throughout the years (Tour Eiffel, Aisics, Montségur, Cyprès, South Crystal,

Sintra and Y3) except Capelinhos, crystal and White Castle have significant lower $\delta^7\text{Li}$ in 2015 (Table V - 3). This is opposed to sapins and Isabel sites which display an increase toward heavier values. This is accompanied by a general increase in Li isotope for all the sites.

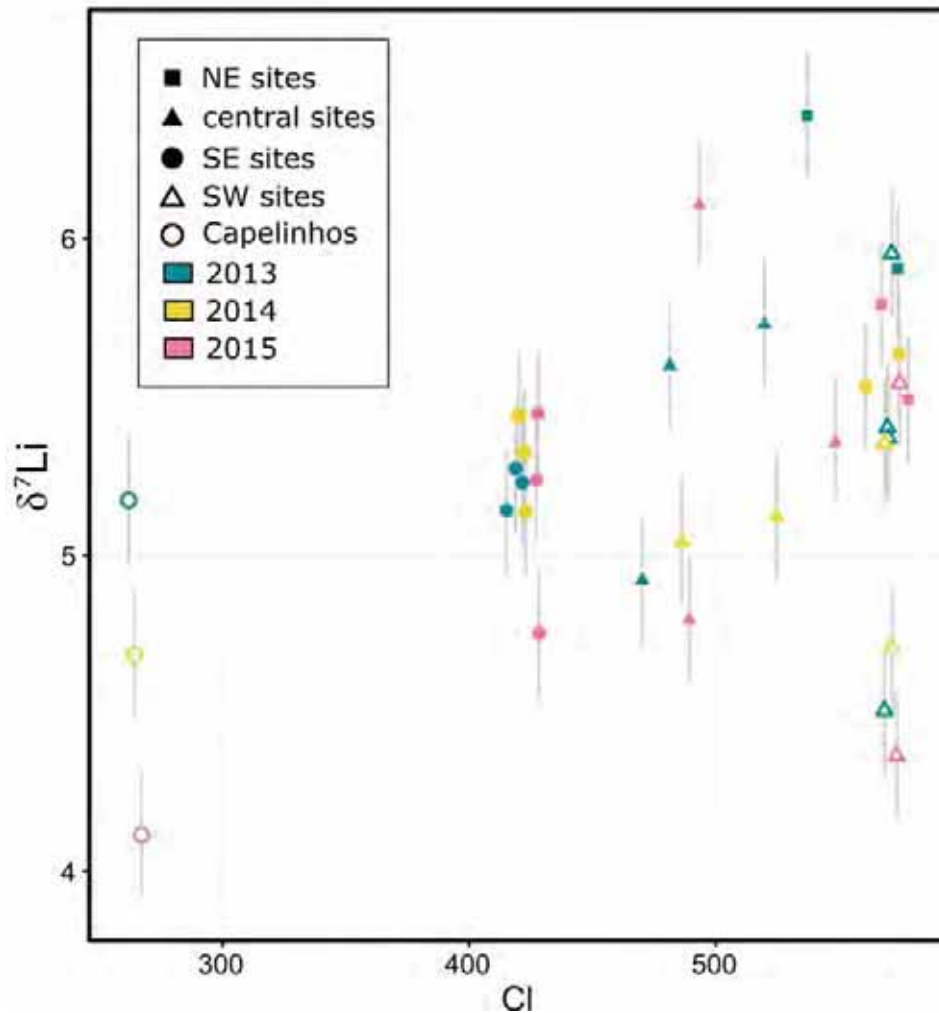


Figure V - 12 $\delta^7\text{Li}$ vs Cl diagram showing that Li isotopes are not affected by phase separation.

Li and Sr isotope suggest a residual seawater component of 15 to 20% (Fig V - 13). From 2013 to 2015, no significant changes in the end-members are observable. Still a significant change has occurred when comparing to the data from 1997 samples (Bray, 2001). The Tour Eiffel sample display Li isotope slightly heavier than the samples from 2013, 2014 and 2015. ^7Li enrichment can happen relative to ^6Li incorporation into secondary minerals (Chan et al., 1993, 1992). If we consider quantitative leaching of Li from the basalt, this would imply that basalt from the ridge at lucky strike have already supported intensive alteration leading to heavier signature than standard MORB and consistent with the fresh basalt value from Bray (2001). Otherwise, the slight department from the accepted MORB

value would be due to secondary minerals precipitation with uptake of ^6Li . Our preferred hypothesis is the quantitative leaching of Li with almost no fractionation. This hypothesis is supported by the analysis of fresh basalt at 5 ‰ from Lucky Strike (Bray, 2001).

The Li signature of LSHF fluid indicate also that Li is leached from basalt at high temperature without significant fractionation. Therefore Li is a good indicator of the water–rock ratios for the global circulation cell leading to the changes observed from the seawater to the hydrothermal fluid.

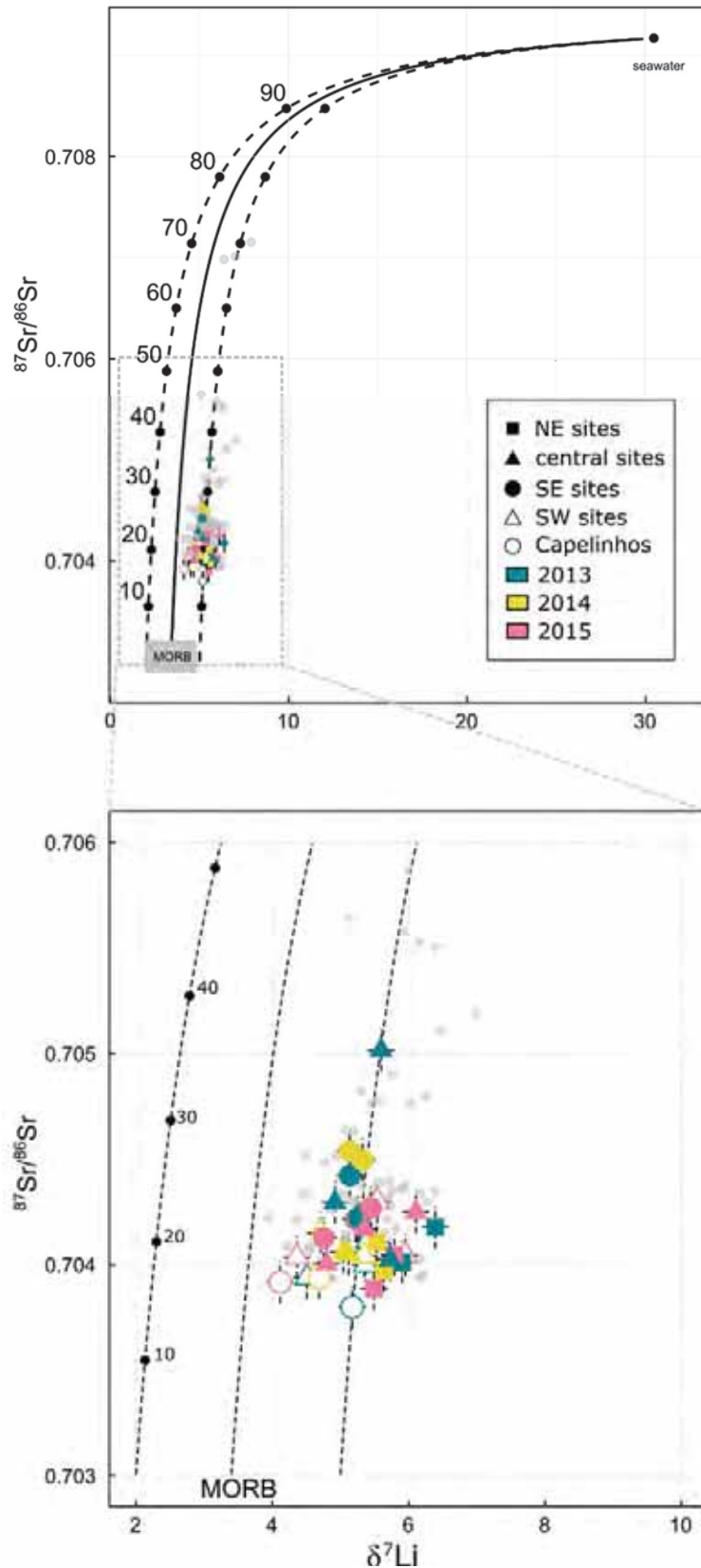


Figure V - 13 $\delta^7\text{Li}$ vs $^{87}\text{Sr}/^{86}\text{Sr}$ diagram showing the sources for basalt and seawater with mixing curves. MORB values are $\delta^7\text{Li}_{\text{MORB}} = 3.4 \pm 1.4$, $\text{Li}_{\text{MORB}} = 4\text{ppm}$; $\delta^7\text{Li}_{\text{SW}} = 30.5$, $\text{Li}_{\text{SW}} = 0.17\text{ppm}$. Grey dots are the measured samples, coloured dots represents calculated endmembers.

5.6 Water–Rock determination

The water–rock ratio (W/R) is a parameter that provides an idea of the amount of water that has interacted with a rock to produce the observed concentration of the element of interest in the fluid. Calculation of W/R needs parameters such as fresh rock concentrations and isotopic signatures and starting fluid concentrations and isotopic signature. Several studies investigate the W/R ratio of hydrothermal fluids (Berndt et al., 1989; Chan et al., 2002; Foustoukos et al., 2004; Verney-Carron et al., 2015; Von Damm et al., 1985). They use Li and Sr to evaluate W/R of fluids through different methods. Li is quantitatively removed from basalt which means that the fluid will be highly enriched in Li and that the W/R will be small (close to 1). If higher W/R are found for an element this would mean that this element is not easily extractable and/or incorporated into secondary phases. Furthermore phase separation partitions trace elements preferentially in the brine phase (Sr, Rb, and Cs) or in the vapor phase (Li). This means that element concentrations not only depend on rock interaction but might be concentrated or diluted by the effect of phase separation. This process could lead to a biased W/R ratio if changes in chlorinity are not accounted for (Berndt et al., 1989; Foustoukos et al., 2004). For example, low Li and Cl fluids with high Li/Cl ratios display a higher enrichment in Li than the high Li and Cl fluids with lower Li/Cl values.

Trace element partitioning has been investigated by several authors and found that on a $\log(\text{elt}/\text{Cl})-\log(\text{Cl})$, the slope provided by least square regression was the same for several phase separation experiments and independent of the starting fluid concentration. Using this value of slope, extracted from our data of trace elements, it is possible to apply a correction to the W/R calculation.

The strontium cycle in the ocean crust is mainly controlled by plagioclase dissolution and recrystallization and anhydrite precipitation. Berndt et al. (1988) developed a model for W/R determination that accounts both Sr uptake by anhydrite precipitation and Sr release by plagioclase dissolution using the following equations:

$$W/R = Sr_r \times \frac{\left[\frac{1}{Sr_i} - \frac{1}{Fr} \left(\frac{1}{Sr_i} - \frac{1}{Sr_f} \right) \right]}{\ln\left(\frac{Sr_i}{Sr_f}\right) - \ln(Fi)} \quad (1)$$

$$Fi = \frac{{}^{87}\text{Sr}/{}^{86}\text{Sr}_f - {}^{87}\text{Sr}/{}^{86}\text{Sr}_r}{{}^{87}\text{Sr}/{}^{86}\text{Sr}_i - {}^{87}\text{Sr}/{}^{86}\text{Sr}_r} \quad (2)$$

$$F_f = \frac{{}^{87}\text{Sr}/{}^{86}\text{Sr}_i - {}^{87}\text{Sr}/{}^{86}\text{Sr}_f}{{}^{87}\text{Sr}/{}^{86}\text{Sr}_i - {}^{87}\text{Sr}/{}^{86}\text{Sr}_r} \quad (3)$$

Sr are concentration in ppm, with the subscript as: i: initial in solution, r: rock, f: final in solution.

As these equations uses the Sr concentration of the final fluids, it is important to correct it for phase separation. Partitioning between vapor and brine has been established by experimental studies (Foustoukos and Seyfried, 2007b; Pester et al., 2015; Pokrovski et al., 2005). Confrontation to natural samples of brine and vapor from the LSHF suggests that similar partitioning is occurring at depth (Leleu et al., submitted; Pester et al., 2012). Therefore, correction of phase separation can be done by extrapolation of log (elt/Cl) to log (Cl) value of seawater (starting fluid). This provides a good approximation of the concentration of the element (Sr or Li) without phase separation.

Li based W/R ratios have been calculated using the model of Magenheim et al. (1995). This model accounts that an incrementally altered rock and partitioned Li into the fluid and alteration phases. The relationship between W/R ratio with both isotope X and Y in solution is described as follows (Chan et al., 2002; Foustoukos et al., 2004; Magenheim et al., 1995; Millot et al., 2010):

$$R/W = -\frac{1}{D} \times \ln \left[\frac{X_r - DX}{X_r - DX_0} \right] \quad (4)$$

$$R/W = -\frac{1}{\alpha D} \times \ln \left[\frac{Y_r - \alpha DY}{Y_r - \alpha DY_0} \right] \quad (5)$$

X and Y are Li⁶ and Li⁷ respectively, r and 0 subscripts stand for rock and initial fluid (seawater). D is the elemental partitioning between the Li in solution and the coexisting minerals. The fractionation factor α for Lithium at between fluid and minerals has been determined empirically. As the reaction zone temperature is probably around 400°C as indicated by Fe/Mn geothermometer for Capelinhos vent site, a value of D=0.23 and $\alpha=0.997$ were used for W/R calculation (Berger et al., 1988; Chan et al., 2002; Millot et al., 2010). Interestingly, Li in 2015 increase in every group of sites. Therefore the calculated W/R ratio for Li in 2015 moves toward values lower than one. This increase in Lithium

imply that fresh basaltic material is available. This is also consistent with the observations of Rb and K, also considered as extractable elements.

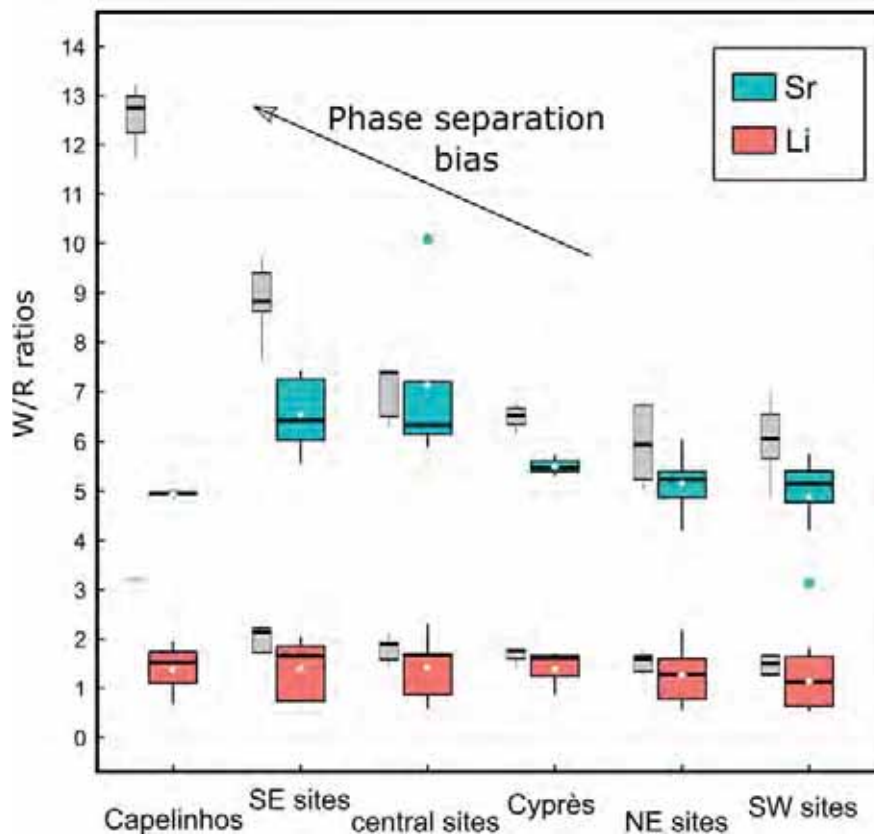


Figure V - 14 W/R ratio presented for different group and calculated from Sr and Li. Uncorrected from phase separation are indicated in grey. Boxplots regroup the year 2013, 2014 and 2015 for each groups.

Figure V - 14 shows the results of the W/R calculated for Li and Sr with corrected and uncorrected concentrations. W/R are similar for the Li which means that Li is leached quantitatively from the rocks as expected. W/R ratios calculated for Sr are generally higher because Sr is comprised in precipitation and dissolution processes of albitisation (Berndt et al., 1988). The W/R ratio for the SE sites are higher than for the other groups. This is coherent with an increased albitisation as suggested in the previous section.

Conclusion

The yearly monitoring of a slow spreading ridge hydrothermal system provides valuable information on the dynamics of fluid circulation, conditions, and W/R reactions. Repetitive sampling allowed to identify a shallow pool of cooled hydrothermal fluid which complements a pre-existing model of shallow seawater circulation. This fluid contributes to the formation of a hydrothermal slab by quartz precipitation. This hydrothermal fluid

dynamics is related to minute/day scale, opposite to year scale differences in end-member chemistry.

Geothermobarometry such as Si-Cl has been shown to be sensitive to deep processes of cracking, responding to seismic events. Following a seismic swarm beneath the fossil lava lake, the Si-Cl indicate relatively cooler and shallower T and P than maximum inferred conditions. But it is difficult to assess the meaning of this indicator and decipher if seismic activity induced a perturbation in the chemistry, or if the equilibrium of Quartz is reached after a seismic activity at different condition. For these reasons, Si and Cl are useful to indicate a perturbation in chemistry, but fail to conclude on small variations in P and T conditions.

From the 1993 to 2015, a relative increase in the Ca/Na of the fluids seems to indicate that albitisation occurs in the subsurface. But since “continuous”, yearly sampling from 2008 to 2015, the Ca/Na ratio display a boom and bust pattern which suggest a more complicated process is governing Ca and Na chemistry in time. Moreover further interpretations on chemistry change are limited due to the lack of information during the 9 year gap between 1997 and 2008.

Li isotopes argue for a quantitative leaching from the host rock with W/R calculated at ~2 for all the groups. Sr isotope ratios allows the calculation of W/R which indicate a higher value for the South Eastern sites which is coherent with the high Ca/Na ratio at these sites. This suggest that the substratum of SE area is highly altered relatively to the fluids found in the other areas.

This study highlights the importance of repetitive sampling and time serie follow up of a hydrothermal field such as Lucky Strike, whose size and vents location likely result in a complex pattern of fluid circulation. Nevertheless, despite one of the largest dataset on fluid chemistry, temporal constraints are only to be interpreted on the sampling scale or of the cruise scale (e.g. 20 minutes and 1 year respectively). Such deep-sea observatory need a more comprehensive and continuous sampling strategy that integrate the infrastructure already in place.

References

- Alt, J.C., Anderson, T.F., Bonnell, L., Muehlenbachs, K., 1989. 3. Mineralogy, chemistry, and stable isotopic compositions of hydrothermally altered sheeted dikes: ODP Hole 504B, LEG 1111. *Proc. Ocean Drill. Program Sci. Results* 11.
- Barreyre, T., Escartín, J., Garcia, R., Cannat, M., Mittelstaedt, E., Prados, R., 2012. Structure, temporal evolution, and heat flux estimates from the Lucky Strike deep-sea hydrothermal field derived from seafloor image mosaics: hydrothermal outflow and image mosaics. *Geochem. Geophys. Geosystems* 13, doi:10.1029/2011GC003990
- Barreyre, T., Escartín, J., Sohn, R., Cannat, M., Ballu, V., Crawford, W.C., 2014. Temporal variability and tidal modulation of hydrothermal exit-fluid temperatures at the Lucky Strike deep-sea vent field, Mid-Atlantic Ridge. *J. Geophys. Res.-Solid Earth* 119, 2543–2566.
- Berger, G., Schott, J., Guy, C., 1988. Behavior of Li, Rb, and Cs during basalt glass and olivine dissolution and chlorite, smectite and zeolite precipitation from seawater: experimental investigations and modelization between 50° and 300°C. *Chem. Geol.* 71, 297–312.
- Berndt, M.E., Seyfried Jr, W.E., 1993. Calcium and sodium exchange during hydrothermal alteration of calcic plagioclase at 400°C and 400 bars. *Geochim. Cosmochim. Acta* 57, 4445–4451.
- Berndt, M.E., Seyfried Jr, W.E., Beck, J., 1988. Hydrothermal alteration processes at mid-ocean ridges: experimental and theoretical constraints from Ca and Sr exchange-reactions and Sr isotopic-ratios. *J. Geophys. Res. – Solid Earth* 93, 4573–4583. doi:10.1029/JB093iB05p04573
- Berndt, M.E., Seyfried Jr, W.E., Janecky, D.R., 1989. Plagioclase and epidote buffering of cation ratios in mid-ocean ridge hydrothermal fluids: Experimental results in and near the supercritical region. *Geochim. Cosmochim. Acta* 53, 2283–2300.
- Besson, P., Degboe, J., Berge, B., Chavagnac, V., Fabre, S., Berger, G., 2014. Calcium, Na, K and Mg Concentrations in Seawater by Inductively Coupled Plasma-Atomic Emission Spectrometry: Applications to IAPSO Seawater Reference Material, Hydrothermal Fluids and Synthetic Seawater Solutions. *Geostand. Geoanalytical Res.* 38, 355–362. doi:10.1111/j.1751-908X.2013.00269.x
- Bischoff, J., 1991. Densities of liquids and vapors in boiling NaCl-H₂O solutions: A PVTX summary from 300° to 500°C. *Am. J. Sciecn* 291, 309–338.
- Bischoff, J., Rosenbauer, R.J., 1985. An empirical equation of state for hydrothermal seawater (3.2 percent NaCl). *Am. J. Sciecn* 285, 725–763.
- Bischoff, J., Seyfried, W.E., 1978. Hydrothermal chemistry of seawater from 25° to 350°C. *Am. J. Sciecn* 278, 838–860.
- Bray, A.M., 2001. The geochemistry of boron and lithium in mid-ocean ridge hydrothermal fluids. University of New Hampshire.
- Butterfield, D.A., Jonasson, I.R., Massoth, G.J., Feely, R.A., Roe, K.K., Embley, R.E., Holden, J.F., McDuff, R.E., Lilley, M.D., Delaney, J.R., 1997. Seafloor eruptions and evolution of hydrothermal fluid chemistry. *Philos. Trans. R. Soc. Lond. Math. Phys. Eng. Sci.* 355, 369–386. doi:10.1098/rsta.1997.0013

Campbell, A.C., Bowers, T.S., Measures, C.I., Falkner, K.K., Khadem, M., Edmond, J.M., 1998. A Times Series of Vent Fluid Compositions From 21°N, East Pacific Rise (1979, 1981, 1985), and the Guaymas Basin, Gulf of California (1982, 1985). *J. Geophys. Res.-Solid Earth* 93, 4537–4549.

Cannat, M., Briais, A., Deplus, C., Escartin, J., Georgen, J., Lin, J., Mercouriev, S., Meyzen, C., Muller, M., Pouliquen, G., Rabain, A., da Silva, P., 1999. Mid-Atlantic-Azores hotspot interactions: along-axis migration of a hotspot-derived event of enhanced magmatism 10 to 4 Ma ago. *Earth Planet. Sci. Lett.* 173, 257–269.

Chan, L.H., Alt, J.C., Teagle, D.A.H., 2002. Lithium and lithium isotope profiles through the upper oceanic crust: a study of seawater-basalt exchange at ODP Sites 504B and 896A. *Earth Planet. Sci. Lett.* 201, 187–201.

Chan, L.-H., Edmond, J.M., Thompson, G., 1993. A Lithium Isotope Study of Hot Springs and Metabasalts From Mid-Ocean Ridge Hydrothermal Systems. *J. Geophys. Res.* 98, 9653–9659.

Chan, L.H., Edmond, J.M., Thompson, G., Gillis, K., 1992. Lithium isotopic composition of submarine basalts: implications for the lithium cycle in the oceans. *Earth Planet. Sci. Lett.* 108, 151–160.

Charlou, J.L., Donval, J.P., Douville, E., Jean-Baptiste, P., Radford-Knoery, Fouquet, Y., Dapigny, A., Stievenard, M., 2000. Compared geochemical signatures and the evolution of Menez Gwen (37°50'N) and Lucky Strike (37°17'N) hydrothermal fluids, south of the Azores Triple Junction on the Mid-Atlantic Ridge. *Chem. Geol.* 171, 49–75.

Chavagnac, V., Leleu, T., Boulart, C., Barreyre, T., Castillo, A., Menjot, L., Cannat, M., Escartín, J., Sarradin, P.-M., 2015. Deep-Sea Observatory EMSO-Azores (Lucky Strike, 37°17'N MAR): Impact of Fluid Circulation Pathway on Chemical Hydrothermal Fluxes, in: *Follow the Fluids: Integrating Multidisciplinary Observations of Deep-Sea Hydrothermal Systems II*. Presented at the AGU Fall Meeting, San Francisco.

Colaço, A., Blandin, J., Cannat, M., Carval, T., Chavagnac, V., Connelly, D., Fabian, M., Ghiro, S., Goslin, J., Miranda, J.M., Reverdin, G., Sarrazin, J., Waldmann, C., Sarradin, P.M., 2011. MoMAR-D: a technological challenge to monitor the dynamics of the Lucky Strike vent ecosystem. *ICES J. Mar. Sci.* 68, 416–424. doi:10.1093/icesjms/fsq075

Cooper, M.J., Elderfield, H., Schultz, A., 2000. Diffuse hydrothermal fluids from Lucky Strike hydrothermal vent field: Evidence for a shallow conductively heated system. *Journal Geophys. Res.* 105, 19369–19375.

Coumou, D., Driesner, T., Weis, P., Heinrich, C.A., 2009. Phase separation, brine formation, and salinity variation at Black Smoker hydrothermal systems. *J. Geophys. Res.* 114. doi:10.1029/2008JB005764

Crawford, W.C., Cannat, M., Escartin, J., Baillard, C., Daniel, R., 2015. Variations in seismicity within Lucky Strike volcano (37°17'N MAR) from 2007-2015, from a seafloor seismometer network. Presented at the AGU Fall Meeting, San Francisco.

Crawford, W.C., Rai, A., Singh, S.C., Cannat, M., Escartin, J., Wang, H., Daniel, R., Combier, V., 2013. Hydrothermal seismicity beneath the summit of Lucky Strike volcano, Mid-Atlantic Ridge. *Earth Planet. Sci. Lett.* 373, 118–128. doi:10.1016/j.epsl.2013.04.028

Delaney, J.R., Mogk, D.W., Mottl, M.J., 1987. Quartz-cemented Breccias From the Mid-Atlantic Ridge: Samples of a High-Salinity Hydrothermal Upflow Zone. *J. Geophys. Res.* 92, 9175–9192.

Detrick, R.S., Needham, D., Renard, V., 1995. Gravity-Anomalies and Crustal thickness variations along the Mid-Atlantic Ridge between 33°N and 40°N. *J. Geophys. Res.* 100, 3767–3787. doi:10.1029/94JB02649

Driesner, T., 2007. The system H₂O–NaCl. Part II: Correlations for molar volume, enthalpy, and isobaric heat capacity from 0 to 1000°C, 1 to 5000bar, and 0 to 1 XNaCl. *Geochim. Cosmochim. Acta* 71, 4902–4919. doi:10.1016/j.gca.2007.05.026

Edmonds, H.N., 2008. Chemical Signatures From Hydrothermal Venting on Slow Spreading Ridges, in: Rona, P.A., Devey, C.W., Dymont, J., Murton, B.J. (Eds.), *Diversity of Hydrothermal Systems on Slow Spreading Ocean Ridges*, AGU Monograph.

EMSO-Azores - EMSO France [WWW Document], n.d. URL <http://www.emso-fr.org/fr/EMSO-Azores> (accessed 5.15.16).

Escartin, J., Barreyre, T., Cannat, M., Garcia, R., Gracias, N., Deschamps, A., Salocchi, A., Sarradin, P.-M., Ballu, V., 2015. Hydrothermal activity along the slow-spreading Lucky Strike ridge segment (Mid-Atlantic Ridge): Distribution, heatflux, and geological controls. *Earth Planet. Sci. Lett.* 431, 173–185. doi:10.1016/j.epsl.2015.09.025

Escartín, J., García, R., Delaunoy, O., Ferrer, J., Gracias, N., Elibol, A., Cufí, X., Neumann, L., Fornari, D.J., Humphris, S.E., Renard, J., 2008. Globally aligned photomosaic of the Lucky Strike hydrothermal vent field (Mid-Atlantic Ridge, 37°18.5'N): Release of georeferenced data, mosaic construction, and viewing software: Lucky Strike vent field georeferenced image mosaic. *Geochem. Geophys. Geosystems* 9. doi:10.1029/2008GC002204

Fontaine, F.J., Wilcock, W.S.D., Butterfield, D.A., 2007. Physical controls on the salinity of mid-ocean ridge hydrothermal vent fluids. *Earth Planet. Sci. Lett.* 257, 132–145. doi:10.1016/j.epsl.2007.02.027

Fontaine, F.J., Wilcock, W.S.D., Foustoukos, D.E., Butterfield, D.A., 2009. A Si-Cl geothermobarometer for the reaction zone of high-temperature, basaltic-hosted mid-ocean ridge hydrothermal systems: Si/Cl-inferred P–T in MOR hydrothermal systems. *Geochem. Geophys. Geosystems* 10. doi:10.1029/2009GC002407

Fouquet, Y., Ondréas, H., Charlou, J.L., Donval, J.P., Radford-Knoery, 1995. Atlantic lava lakes and hot vents. *Nature* 377, 201.

Fournier, R.O., 1983. A method of calculating Quartz solubilities in aqueous sodium chloride solutions. *Geochim. Cosmochim. ACTA* 47, 579–586.

Foustoukos, D.I., James, R.H., Berndt, M.E., Seyfried, W.E., 2004. Lithium isotopic systematics of hydrothermal vent fluids at the Main Endeavour Field, Northern Juan de Fuca Ridge. *Chem. Geol.* 212, 17–26. doi:10.1016/j.chemgeo.2004.08.003

Foustoukos, D.I., Seyfried, W.E., 2007a. Quartz solubility in the two-phase and critical region of the NaCl–KCl–H₂O system: Implications for submarine hydrothermal vent systems at 9°50'N East Pacific Rise. *Geochim. Cosmochim. Acta* 71, 186–201. doi:10.1016/j.gca.2006.08.038

Foustoukos, D.I., Seyfried, W.E., 2007b. Trace element partitioning between vapor, brine and halite under extreme phase separation conditions. *Geochim. Cosmochim. Acta* 71, 2056–2071. doi:10.1016/j.gca.2007.01.024

Foustoukos, D.I., Seyfried, W.E., 2007c. Fluid Phase Separation Processes in Submarine Hydrothermal Systems. *Rev. Mineral. Geochem.* 65, 213–239. doi:10.2138/rmg.2007.65.7

Fox, C., 1990. Consequences of Phase-Separation on the Distribution of Hydrothermal Fluids as Ashes Vent Field, Axial Volcano, Juan-De-Fuca Ridge. *J. Geophys. Res.-Solid Earth Planets* 95, 12923–12926. doi:10.1029/JB095iB08p12923

Gamo, T., Chiba, H., Masuda, H., Edmonds, H.N., Fujioka, K., Kodama, Y., Namba, H., Sano, Y., 1996. Chemical characteristics of hydrothermal fluids from the TAG mound of the mid-Atlantic Ridge in August 1994: implications for spatial and temporal variability of hydrothermal activity. *Geophys. Res. Lett.* 23, 3483–3486.

Goldfarb, M.S., Delaney, J.R., 1988. Response of Two-phase fluids fracture configurations within submarine hydrothermal systems. *J. Geophys. Res.-Solid Earth* 93, 4585–4594.

Henstock, T.J., Woods, A.W., White, R.S., 1993. The Accretion of Oceanic Crust by Episodic Sill Intrusion. *J. Geophys. Res.* 98, 4143–4161.

Humphris, S.E., Fornari, D.J., Scheirer, D.S., German, C.R., Parson, L.M., 2002. Geotectonic setting of hydrothermal activity on the summit of Lucky Strike Seamount (37°17'N, Mid-Atlantic Ridge): geotectonic setting. *Geochem. Geophys. Geosystems* 3, 1–25. doi:10.1029/2001GC000284

Ildefonse, B., Blackman, D.K., John, B.E., Ohara, Y., Miller, D.J., MacLeod, C.J., others, 2007. Oceanic core complexes and crustal accretion at slow-spreading ridges. *Geology* 35, 623–626.

James, R.H., Allen, D.E., Seyfried Jr, W.E., 2003. An experimental study of alteration of oceanic crust and terrigenous sediments at moderate temperatures (51 to 350 C): Insights as to chemical processes in near-shore ridge-flank hydrothermal systems. *Geochim. Cosmochim. Acta* 67, 681–691.

Kelley, D., Robinson, P.T., 1990. Development of a brine-dominated hydrothermal system at temperatures of 400-500°C in the upper level plutonic sequence, Troodos ophiolite, Cyprus. *Geochim. Cosmochim. Acta* 54, 653–661.

Langmuir, C., Humphris, S.E., Fornari, D.J., Van Dover, C., Von Damm, K.L., Tivey, M.K., Colodner, D., Charlou, J.L., Desonie, D., Wilson, C., Fouquet, Y., Klinkhammer, G.P., Bougault, H., 1997. Hydrothermal vents near a mantle hot spot: the Lucky Strike vent field at 37°N on the Mid-Atlantic Ridge. *Earth Planet. Sci. Lett.* 148, 69–91.

Larson, B.I., Lilley, M.D., Olson, E.J., 2009. Parameters of subsurface brines and hydrothermal processes 12–15 months after the 1999 magmatic event at the Main Endeavor Field as inferred from in situ time series measurements of chloride and temperature. *J. Geophys. Res.* 114. doi:10.1029/2008JB005627

Leleu, T., Chavagnac, V., Cannat, M., Fontaine, F.J., Ceuleneer, G., Castillo, A., submitted. Spatial variations in vent chemistry at the Lucky Strike Hydrothermal Field, Mid-Atlantic Ridge (37°N): Implications for seafloor flow geometry and stockwork formation. *Geochim. Cosmochim. Acta* submitted.

Lowell, R.P., Rona, P., Von Herzen, R.P., 1995. Seafloor hydrothermal systems. *J. Geophys. Res.* 100, 327–352.

Magenheim, A.J., Spivack, A.J., Alt, J.C., Bayhurst, G., Chan, L.H., Zuleger, E., Gieskes, J.M., 1995. 13. Borehole fluid chemistry in Hole 504B, leg 137: formation water or in-situ reaction?, in: *Proceedings of the Ocean Drilling Program, Scientific Results*. pp. 141–52.

Millero, F.J., Feistel, R., Wright, D.G., McDougall, T.J., 2008. The composition of Standard Seawater and the definition of the Reference-Composition Salinity Scale. *Deep Sea Res. Part Oceanogr. Res. Pap.* 55, 50–72. doi:10.1016/j.dsr.2007.10.001

Millot, R., 2013. *Les isotopes du lithium: exemples d'applications en géochimie*. Université d'Orléans.

Millot, R., Scaillet, B., Sanjuan, B., 2010. Lithium isotopes in island arc geothermal systems: Guadeloupe, Martinique (French West Indies) and experimental approach. *Geochim. Cosmochim. Acta* 74, 1852–1871. doi:10.1016/j.gca.2009.12.007

Miranda, J.M., Luis, J.F., Lourenço, N., Santos, F.M., 2005. Identification of the magnetization low of the Lucky Strike hydrothermal vent using surface magnetic data: magnetization low of Lucky Strike. *J. Geophys. Res. Solid Earth* 110. doi:10.1029/2004JB003085

Mullineaux, L., 1998. Deep-sea hydrothermal vents sanctuaries: a position paper. *InterRidge News* 8, 45–50.

Ondréas, H., Cannat, M., Fouquet, Y., Normand, A., Sarradin, P.M., Sarrazin, J., 2009. Recent volcanic events and the distribution of hydrothermal venting at the Lucky Strike hydrothermal field, Mid-Atlantic Ridge: Lucky Strike volcanism and venting. *Geochem. Geophys. Geosystems* 10. doi:10.1029/2008GC002171

Person, R., Miranda, J.M., Puillat, I., 2009. ESONEWS-MoMAR/DA demonstration mission to establish a multidisciplinary observatory at hydrothermal vents on the Mid-Atlantic Ridge. *Esonews* 3, 1–8.

Pester, N.J., Ding, K., Seyfried, W.E., 2015. Vapor–liquid partitioning of alkaline earth and transition metals in NaCl-dominated hydrothermal fluids: An experimental study from 360 to 465°C, near-critical to halite saturated conditions. *Geochim. Cosmochim. Acta* 168, 111–132. doi:10.1016/j.gca.2015.07.028

Pester, N.J., Ding, K., Seyfried, W.E., 2014. Magmatic eruptions and iron volatility in deep-sea hydrothermal fluids. *Geology* 42, 255–258. doi:10.1130/G35079.1

Pester, N.J., Reeves, E.P., Rough, M.E., Ding, K., Seewald, J.S., Seyfried, W.E., 2012. Subseafloor phase equilibria in high-temperature hydrothermal fluids of the Lucky Strike Seamount (Mid-Atlantic Ridge, 37°17'N). *Geochim. Cosmochim. Acta* 90, 303–322. doi:10.1016/j.gca.2012.05.018

Pester, N.J., Rough, M., Ding, K., Seyfried, W.E., 2011. A new Fe/Mn geothermometer for hydrothermal systems: Implications for high-salinity fluids at 13°N on the East Pacific Rise. *Geochim. Cosmochim. Acta* 75, 7881–7892. doi:10.1016/j.gca.2011.08.043

Phipps Morgan, J., Parmentier, E.M., Lin, J., 1987. Mechanisms for the origin of mid-ocean ridge axial topography: Implications for the thermal and mechanical structure of accreting plate boundaries. *J. Geophys. Res. Solid Earth* 92, 12823–12836.

Pokrovski, G.S., Roux, J., Harrichoury, J.-C., 2005. Fluid density control on vapor-liquid partitioning of metals in hydrothermal systems. *Geology* 33, 657–660.

Ravizza, G., Blusztajn, J., Von Damm, K.L., Bray, A.M., Bach, W., Hart, S.R., 2001. Sr isotope variations in vent fluids from 9° 46'-9° 54' N East Pacific Rise: evidence of a non-zero-Mg fluid component. *Geochim. Cosmochim. Acta* 65, 729–739.

Rosner, M., Ball, L., Peucker-Ehrenbrink, B., Blusztajn, J., Bach, W., Erzinger, J., 2007. A simplified, accurate and fast method for lithium isotope analysis of rocks and fluids, and $\delta^7\text{Li}$ values of seawater and rock reference materials. *Geostand. Geoanalytical Res.* 31, 77–88.

Schoofs, S., Hansen, U., 2000. Depletion of a brine layer at the base of ridge-crest hydrothermal systems. *Earth Planet. Sci. Lett.* 180, 341–353.

Seyfried Jr, W.E., Chen, X., Chan, L.-H., 1998. Trace element mobility and lithium isotope exchange during hydrothermal alteration of seafloor weathered basalt: an experimental study at 350 C, 500 bars. *Geochim. Cosmochim. Acta* 62, 949–960.

Singh, S.C., Crawford, W.C., Carton, H., Seher, T., Combier, V., Cannat, M., Pablo Canales, J., Düsünür, D., Escartin, J., Miguel Miranda, J., 2006. Discovery of a magma chamber and faults beneath a Mid-Atlantic Ridge hydrothermal field. *Nature* 442, 1029–1032. doi:10.1038/nature05105

Steele-MacInnis, M., Han, L., Lowell, R.P., Rimstidt, J.D., Bodnar, R.J., 2012. The role of fluid phase immiscibility in quartz dissolution and precipitation in sub-seafloor hydrothermal systems. *Earth Planet. Sci. Lett.* 321-322, 139–151. doi:10.1016/j.epsl.2011.12.037

Verney-Carron, A., Vigier, N., Millot, R., Hardarson, B.S., 2015. Lithium isotopes in hydrothermally altered basalts from Hengill (SW Iceland). *Earth Planet. Sci. Lett.* 411, 62–71. doi:10.1016/j.epsl.2014.11.047

Von Damm, K.L., 2004. Evolution of the Hydrothermal System at East Pacific Rise 9°50'N: Geochemical Evidence for Changes in The Upper Oceanic Crust, in: German, C.R., Lin, J., Parson, L.M. (Eds.), *Geophysical Monograph Series*. American Geophysical Union, Washington, D. C., pp. 285–304.

Von Damm, K.L., 2000. Chemistry of hydrothermal vent fluids from 9–10 N, East Pacific Rise: “Time zero,” the immediate posteruptive period. *J. Geophys. Res. Solid Earth* 1978–2012 105, 11203–11222.

Von Damm, K.L., 1988. Systematics and postulated controls on submarine hydrothermal solution chemistry. *J. Geophys. Res.-Solid Earth* 93, 4551–4561.

Von Damm, K.L., Bischoff, J., Rosenbauer, R.J., 1991. Quartz solubility in hydrothermal seawater: an experimental study and equation describing quartz solubility for up to 0.5M NaCl solutions. *Am. J. Sci.* 291, 997–1007.

Von Damm, K.L., Bray, A.M., Buttermore, L.G., Oosting, S.E., 1998. The geochemical controls on vent fluids from the Lucky Strike vent field, Mid-Atlantic Ridge. *Earth Planet. Sci. Lett.* 160, 521–536.

Von Damm, K.L., Edmond, J.M., Grant, B., Measures, C.I., Walden, B., Weiss, R.F., 1985. Chemistry of submarine hydrothermal solutions at 21°N, East Pacific Rise. *Geochim. Cosmochim. Acta* 49, 2197–2220.

Von Damm, K.L., Oosting, S.E., Kozlowski, R., Buttermore, L.G., Colodner, D., Edmonds, H.N., Edmond, J.M., Grebmeier, J.M., 1995. Evolution of East Pacific Rise hydrothermal vent fluids following a volcanic eruption. *Nature* 375, 47–51.

CHAPITRE 6

REE AND Nd ISOTOPE SIGNATURES OF HYDROTHERMAL
FLUIDS AND THEIR IMPACT ON THE NORTH ATLANTIC DEEP
WATER: A CASE STUDY OF THE LUCKY STRIKE
HYDROTHERMAL FIELD (37°N, MID-ATLANTIC RIDGE)

Abstract

This study presents data of REE in hydrothermal fluids from the Lucky Strike hydrothermal field. The fluids were sampled during 3 maintenance cruises of the Emso Azores deep sea observatory onboard the French R/V “Pourquoi pas?” in 2013, 2014 and 2015. They were analyzed for major and trace elements, and isotopes ($^{87}\text{Sr}/^{86}\text{Sr}$ and $\delta^7\text{Li}$). The present study focus on 1) the behavior of REE within the mixing zone in the proximal hydrothermal plume and 2) the information from REE chondrite normalized patterns of the end-member fluids.

On the proximal plume, we show that Eu behaves conservatively while the other REE clearly display early scavenging. This affects the REE chondrite normalized pattern by enhancing the positive Eu anomaly typical of submarine hydrothermal fluids.

The study of end-member fluid concentration does not reveal any apparent relation between total REE concentration and salinity of the fluid, the latter being a controlled by phase separation processes. However, the relative abundance of LREE and HREE, characterized by the general slope of the chondrite normalized REE pattern, increases with Cl concentration. This suggests that phase separation fractionates the REE with LREE enrichment in the brine phase. Furthermore, the calculated Eu anomaly of the endmember fluid suggests a control by the alteration phases in subsurface, such as albite.

Résumé

Cette étude présente des données de terres rares contenues dans des fluides hydrothermaux provenant du champ hydrothermal de Lucky Strike. Ces fluides ont été échantillonnés au cours de 3 campagne océanographique dans le cadre du projet d’observatoire fond de mer EMSO–Açores, à bord du navire « Pourquoi pas ? » en 2013, 2014 et 2015. Ils ont été analysés pour les éléments majeurs, mineurs et trace ainsi que pour les isotopes du Sr et du Li. La présente étude se concentre sur 1) les concentrations en terre rare des fluides hydrothermaux purs normalisés au chondrite, puis en 2) sur le comportement des terres rares dans les premiers mètres de mélange eau de mer et fluide hydrothermal.

L’étude des fluides purs ne révèle pas de corrélation entre la concentration totale en terre rare et la chlorinité des fluides. En revanche, l’enrichissement en terre rare légère, avec l’indicateur Nd/Yb, semble corrélér au Cl, ce qui est cohérent avec le partitionnement des

terres rares entre les phases vapeur et saumure lors de la séparation de phase. De plus, les anomalies en Eu calculées suggèrent un contrôle minéralogique dans la zone de remontée, liée à l'albitisation.

Concernant les fluides de la zone de mélange, nous montrons un fort piégeage des terres rares par les particules précipités. Ce piégeage n'est pas dépendant de la spéciation, comme en atteste les calculs d'anomalie en Eu. Les mesures effectuées sur les isotopes du Nd mettent en évidence des phénomènes de dissolution de matériel porche des compositions de l'eau de mer et invisible via les concentrations mesurées. Ce phénomène peut donner lieu à des échanges à plus grande échelle spatiale pouvant potentiellement modifier le rapport isotopique du Nd dans l'océan à proximité des rides océanique, sans en modifier la concentration.

1 Introduction

Among the periodic table of chemical elements, the “rare earth elements” (REE) represent a unique group of 15 elements whose atomic numbers range from 57 (Lanthanum) to 71 Lutetium). From La to Lu, the atomic mass increases while the radius of the atom decreases, resulting in variable fractionations between the different REE during different processes, i.e. igneous, metamorphic, hydrothermal and sedimentary. Accordingly, REEs are useful geological tracers (Haas et al., 1995). Within the global biogeochemical cycles, the hydrothermal submarine vents are a major source of numerous elements to the ocean (Elderfield and Schultz, 1996). Recently, Resing et al., (2015) showed that the Iron originating from the East Pacific Rise could be traced up to 4,300 km away from the mid-ocean ridge (MOR). However, hydrothermal vents have been considered as a sink of REEs rather than a source to the ocean, due to co-precipitation process occurring in the buoyant to non-buoyant hydrothermal plumes, i.e. REE scavenging by mineral surface charge (German et al., 1990; Jeandel et al., 2013).

Fluids originated from various hydrothermal fields located at MORs, backarc basins and subduction zones display similar REE patterns when normalized to chondrite (Allen and Seyfried, 2003; Douville et al., 2002, 1999; Klinkhammer et al., 1994; Michard, 1989; Cole et al., 2014; Craddock et al., 2010). Over all, they are characterized by various light REE enrichment over heavy REE together with positive Europium anomalies (Michard, 1989; Craddock et al., 2010). However, none of these studies have investigated the variability of

REE distribution within a hydrothermal field displaying a broad spectrum of chlorine concentrations.

Alternatively, the fate of hydrothermal REE once expelled into deep seawater was investigated solely through the REE signatures of particulate matters while the dissolved phase has been poorly examined (German et al., 2002). As a result, the REE record of hydrothermal venting has largely been studied from a sedimentary perspective (Chavagnac et al., 2008, 2005; German et al., 2002, 1990). Recent studies highlighted mechanisms of elemental exchange only detectable through isotopic studies, i.e. Nd isotopic composition (Lacan and Jeandel, 2005, 2001). This process taking place at the interface between the continental margin and the ocean and is called “boundary exchange”. Moreover, Jeandel et al. (2013) introduced the hypothesis that a “ridge exchange” process, similar to the “boundary exchange” one, may occur and modify the Nd isotopic composition of deep seawater. This hypothesis was based on Nd isotope signatures of deep Pacific seawater being much more radiogenic than the accepted values at depth where Mn concentration were maxima.

To address this hypothesis of “ridge exchange”, this study reports on the dissolved REE concentrations and the Nd isotopic compositions of black smoker end-members and buoyant hydrothermal fluids collected within the first seconds of end-member fluids mixing with seawater. We chose the Lucky Strike hydrothermal field at 37°N along the Mid Atlantic Ridge because the dynamic of hydrothermal activity at this location was monitored continuously since 2010 via the set-up of the deep-sea observatory (EMSO-Azores), providing a well detailed geological, mineralogical, geochemical, and biological framework. We investigate, first, the effect of end-member chemical compositions on the REE distributions of each selected hydrothermal sites before assessing the fate of hydrothermal REE in the early phase of mixing above the vents.

2 Geological and hydrothermal setting

2.1. Geological context

The Lucky Strike hydrothermal field (LSHF) is located on the Lucky Strike Segment of the Mid Atlantic Ridge (MAR) at 37°N, 400 km to the Southwest of the Azores island (Langmuir et al., 1997). The LSHF is situated at a depth of 1700mbsl on top of a central volcano whose central flat depression constituted by a fossil lava lake, is surrounded by three old and fractured volcanic cones (Fouquet et al., 1995). Since the discovery of the

LSHF in 1992, most of the observed hydrothermal activity (20 to 30 active vents) was described close by and around the fossil lava lake boundaries as well as between the north east and south east cones, which is an area heavily faulted (Humphris et al., 2002; Von Damm et al., 1998; Barreyre et al., 2012; Escartin et al., 2015; Leleu et al., submitted; Figure VI - 1). The LSHF vents display various structures from small hydrothermal mounds to tens of meters high sulfide towers sitting on large mounds. Temperatures of focused hydrothermal fluids vary between 196 and 340°C, while diffuse venting occurs through cracks at temperatures below 100°C and flanges with pool temperatures higher than 200°C (Cooper et al., 2000; Barreyre et al., 2012). In recent years, hydrothermal activity was investigated up to several km away from the main LSHF via ROV dives, during which the active Capelinhos site (324°C) was discovered in 2013 on top of pillow lavas approximately 1.5 km eastwards of the Tour Eiffel site (Escartin et al., 2015; Leleu et al., submitted).

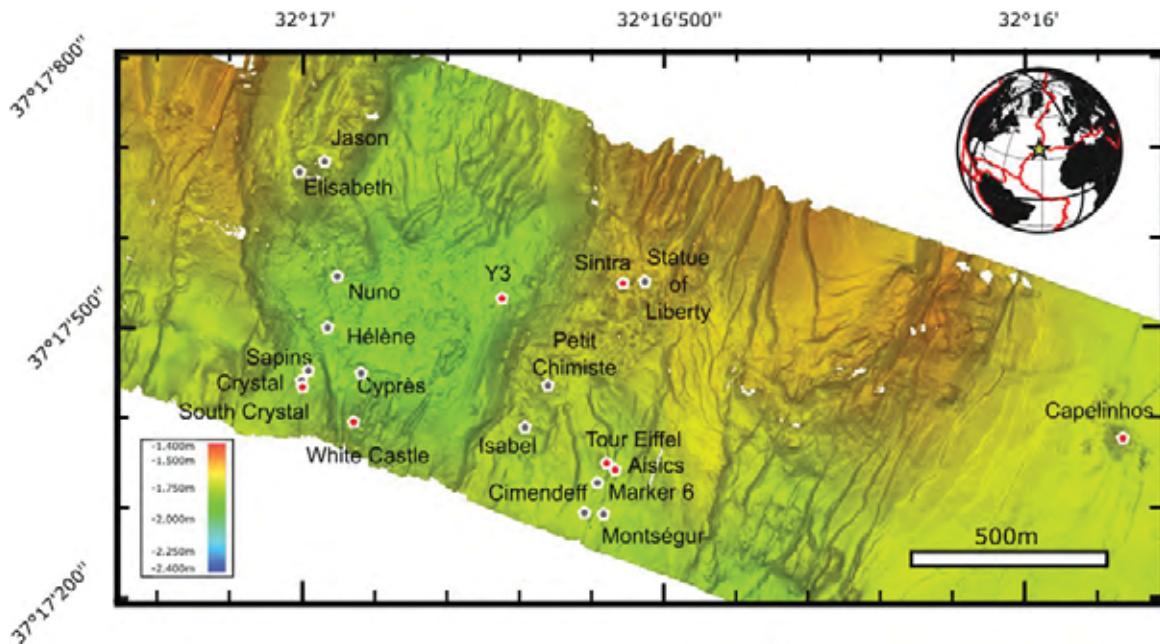


Figure VI - 1 Micro-bathymetric map of the Lucky Strike Hydrothermal Field. Red dots represent sites sampled in this study. Gray dots represent sites sampled in previous studies.

The substratum at Lucky Strike segment is a complex basaltic assemblage of E-MORB (Enriched -Mid Ocean Ridge Basalt) and T-MORB (Transitional-MORB between E-MORB and Normal MORB; Dosso et al., 1999; Gale et al., 2011; Hamelin et al., 2013). These rocks reflect the geochemical gradient observed south of the Azores triple junction between the plume and mantle sources (Dosso et al., 1999; Gale et al., 2011; Hamelin et al., 2013).

The Lucky Strike hydrothermal field has been the object of several studies since its discovery in 1992 (Charlou et al., 2000; Dziak, 2004; Langmuir et al., 1997; Pester et al., 2012; Singh et al., 2006; Von Damm et al., 1998). Since 2010, it is the selected place to set up a multidisciplinary deep sea observatory (Colaço et al., 2011). This deep sea observatory constitutes the EMSO-Azores node and comprises a continuous biological, geophysical and geochemical investigation (Colaço et al., 2011). Especially, the fluids from Lucky Strike are the most documented at the MAR in terms of spatial variation within a single field and in terms of temporal variations (Charlou et al., 2000; Leleu et al., 2015, submitted, in prep.; Pester et al., 2012; Von Damm et al., 1998).

2.2. Focused hydrothermal fluids

Repeated fluid sampling shows persistent inter-site differences in the chloride composition of end-member hot fluids, resulting from distinct fluid pathways and distinct rock compositions in the reaction zone and/or in the upflow zone (Langmuir et al., 1997; Von Damm et al., 1998; Charlou et al., 2000; Pester et al., 2012; Chavagnac et al., 2015; Leleu et al., submitted). These studies set up the perfect conditions to investigate the control on REE geochemical behavior, as primary rock vs. complexation and Chlorine distribution. The fluid chemistry variability at LSHF can be classified into 5 groups based on salinity and location within the hydrothermal field compared to the fossil lava lake locations (Leleu et al., submitted), which are, from low to high Cl concentrations: Capelinhos, the South Eastern sites (Tour Eiffel, Aisics, Montsegur), the central sites (White Castle, Cyprès), the North Eastern sites (Sintra, Y3) and the South Western sites (South Crystal). All the details on the spatial and temporal chemical variability of hydrothermal fluids are reported in Leleu et al. (submitted, in prep). We will summarize underneath the major features:

- The distribution of major cations (Ca, Na, and K) and trace elements (Br, Li, Cs, Rb, and Sr) concentrations when compared to chloride concentrations (260-580 mM) argue for a unique source that undergoes phase separation and feeds the LSHF (Leleu et al., submitted).
- The phase separation zone at the LSHF is estimated at 2500-2800 mbsf at temperature of 430-440°C, based on Si and Cl values of the most vapor dominated fluids (Fontaine et al., 2009; Leleu et al., submitted).
- The temperature of the roof of the reaction zone is estimated at 400°C for Capelinhos but clusters around 370°C for the other sites at the LSHF. The salinity

differences between sites originate from permeability gradient within the subsurface, whereby vapor-dominated fluids preferentially flow through large pipe and fissure while the brine-dominated phase will tend to fill backwater porosity and smaller scale fissures (Fontaine et al., 2007; Leleu et al., submitted).

- Capelinhos, as the most vapor-dominated fluid, probably follows an almost direct upflow to the discharge area at the seafloor, limiting further interaction with the host rock and/or subsurface mixing, prior to discharge (Leleu et al., submitted). By comparison, the fluids issued from other sites of the main LSHF, remain in a lower permeability zone, enhancing water-rock interaction with host-rock, i.e. chemical interactions between the up flowing hydrothermal fluids and unaltered seawater through cooling/mixing processes.
- Chemical variability expressed in terms of metal concentrations, e.g. Fe and Mn, is controlled by upflow zone, brine saturation state in subsurface, permeability and faulting (Leleu et al., submitted).

3 Method

3.1 Sample collection

The focused and buoyant hydrothermal fluids were collected during three maintenance cruises, MoMARsat 2013, 2014 and 2015, of the EMSO-azores deep sea observatory on board the *R.V. Pourquoi Pas?*. In-situ temperatures were measured in vents prior to sampling using the ROV Victor 6000 high temperature probe. 14 focused fluids were sampled with 200 ml gas tight titanium syringe manipulated and triggered via the hydraulic arm of the ROV Victor6000. These samples were selected over the vent chemical diversity of the LSHF based on Cl concentrations as defined in Leleu et al., (submitted). The samples were processed immediately on board after the ROV recovery. First, gases were extracted from sampler and stored in canisters for future on-shore analysis. The fluid samples were then extracted with a clean and sterile plastic syringe, filtered through 0.45 μ m Millipore filters and split into different aliquots for onshore analysis and stored at 4°C in a cold room. pH, Eh, salinity and conductivity were measured on-board immediately after processing. The studied sample characteristic are listed in table VI - 1.

Fluid sampling in the buoyant hydrothermal plume at temperatures below 150°C was carried out using the PEPITO sampler equipped on the ROV Victor 6000 (Cotte et al., 2015; Sarradin et al., 2009). The snorkel of the PEPITO device which is manipulated by

the hydraulic arm of the ROV Victor 6000, was placed within the buoyant hydrothermal plume. In-situ temperature sensor attached to the PEPITO snorkel allowed real-time monitoring of temperature, enabling fluid collection at selected temperatures. This sampling device permits in situ 0.45 μ m filtration of fluids as described in Cotte et al. (2015). 17 buoyant hydrothermal fluids were collected at Aisics, White Castle, Y3 and Capelinhos within the same ROV dive as focused hydrothermal fluids collection. The samples were processed immediately on board after the ROV recovery and split into different aliquots for on-shore analyses. The general information of each studied sample is reported in table VI - 1.

Table VI - 1 Summary of fluid samples used for the REE measurement. The Ti syringe samples are pure hydrothermal fluid while the PEPITO samples are buoyant plume samples.

area	site	longitude (W)	latitude (N)	Depth (mbsf)	year sampled	instrument	sample ID	Temperature (in-situ °C)
South East	Aisics	32°16.530'	37°17.338'	1689	2013	Ti syringe	M13FLU03	303
					2014	Ti syringe	M14FLU08	304
					2015	Ti syringe	M15FLU03	307
					2015	Ti syringe	M15FLU01	307
					2015	PEPITO	PL2-598-D2	97
					2015	PEPITO	PL2-598-D3	108
					2015	PEPITO	PL2-598-E1	121
					2015	PEPITO	PL2-598-E2	133
					2015	PEPITO	PL2-598-E3	154
						Tour Eiffel	32°16.532'	37°17.343'
Capelinhos		32°15.830'	37°17.350'	1665	2013	Ti syringe	M13FLU30	324
					2013	Ti syringe	M13FLU31	324
					2015	Ti syringe	M15FLU37	319
					2015	PEPITO	PL6-602-D1	89
					2015	PEPITO	PL6-602-D2	101
					2015	PEPITO	PL6-602-D3	112
					2015	PEPITO	PL6-602-E1	121
					2015	PEPITO	PL6-602-E3	139
Central sites	White Castle	32°16.869'	37°17.383'	1708	2013	Ti syringe	M13FLU14	308
					2015	Ti syringe	M15FLU27	311
					2015	PEPITO	PL5-601-C1	93
					2015	PEPITO	PL5-601-C2	100
					2015	PEPITO	PL5-601-C3	117
					2015	PEPITO	PL5-601-D1	113
						Cypress	32°16.863'	37°17.450'
North East	Y3	32°16.671'	37°17.512'	1727	2014	Ti syringe	M14FLU16	323
					2014	PEPITO	PL7-582-B1	45
					2014	PEPITO	PL7-582-B3	70
					2014	PEPITO	PL7-582-C2	127
						Sintra	32°16.498'	32°17.529'

3.2 Sample processing and determination of REE concentrations

The analytical methods used for major and trace element concentrations in focused and buoyant hydrothermal fluids were described in detail in previous publications (Leleu et al., submitted; Cotte et al., 2015).

Sample processing was carried out at the LEGOS laboratory of the Observatoire Midi-Pyrénées. We used 10 ml of high temperature hydrothermal fluid and 15-30ml of buoyant hydrothermal plume fluids for REE concentration determinations. The REE pre-concentration and purification technic developed at the LEGOS laboratory for seawater (Lacan et al., 2001, 2005), had to be modified and adapted to the peculiar chemical composition of hydrothermal fluid. Before any chemical treatment, a solution of tri-spikes i.e. ^{146}Nd , ^{153}Eu and ^{174}Yb isotopes, was added to all samples together with a droplet of ultrapure H_2O_2 to ensure all the conversion of dissolved Fe present as Fe^{2+} in reducing hydrothermal fluids, to its oxidized Fe^{3+} form. After homogenization during 24 h at room

temperature, the pH of the solution was risen up to 8 to promote the precipitation of Fe oxyhydroxide particles $\text{Fe}(\text{OH})_3$ which scavenge by adsorption all dissolved REE. The solutions were left to sediment for another 24 h at room temperature before centrifugation and removal of supernatant. The precipitate was rinsed three times with MQ- H_2O to ensure the removal of all major ions, e.g. Na and Ba in particular. The precipitate was then evaporated and dissolved in bi-distilled HCl 6M prior to liquid chromatography with a AG1-X8 anionic column to isolate the REE fraction from the remaining major elements, i.e. the Fe used for precipitation. After elution of the REE, the solution is then evaporated on a hotplate till dryness and dissolved into HCl 2N for elution through AG50W-X8 cationic column. This last step allows removal of Ba, which is crucial for isobaric interferences with the spiked Nd. The details of the procedure are described in Saleban Ali (2016).

REE concentration analyses were performed with a High-Resolution Inductively Coupled Mass Spectrometer (HR-ICP-MS) Element XR at the Observatoire Midi-Pyrénées. Sample introduction was done by an Aridus desolvating nebulizer to reduce oxide formation, which was controlled by analyzing a Ce solution, measured at <0.05%. Samples were dissolved in a HNO_3 0.3N solution doped with Indium and Rhenium to follow the plasma fluctuation through the course of the analyses. Calibration of the instrument was performed with an in-house multiple REE standard at 10, 50 and 100ppt. Measured background intensities of ultrapure HNO_3 0.3N in between samples were subtracted to the sample intensity, which corresponds to 0.01-0.2% for the LREE and 0.2-0.6% for the HREE. Instrumental errors are usually less than 3% for the LREE and for the HREE.

3.3 Nd isotopic compositions

The un-spiked fluid samples were treated through the previous steps of co-precipitation, and double column exchange with an additional column to isolate Nd from the other REEs. Nd is eluted with HCl 0.25M from a Ln-spec resin. Nd isotopic composition measurements were conducted at the IUEM laboratory in Brest on a Thermo-Ionized Mass Spectrometer (Thermo Finnigan Triton). The $^{143}\text{Nd}/^{144}\text{Nd}$ ratio was defined as the average of 100 measurements of ion intensities following the static collection mode. The $^{143}\text{Nd}/^{144}\text{Nd}$ ratios were normalized to $^{146}\text{Nd}/^{144}\text{Nd} = 0.7219$. Measured $^{143}\text{Nd}/^{144}\text{Nd}$ values for La Jolla standard of 1-5 ng Nd (recommended values of 0.511860) was 0.511850 ± 12 (1σ E, n =

13). The Nd isotopic composition uses a ϵNd notation to reflect the $^{143}\text{Nd}/^{144}\text{Nd}$ ratio compared to CHUR (Chondrite Uniform Reservoir) as follows:

$$\epsilon\text{Nd} = \left\{ \frac{\left(\frac{^{143}\text{Nd}}{^{144}\text{Nd}} \right)_{\text{sample}}}{\left(\frac{^{143}\text{Nd}}{^{144}\text{Nd}} \right)_{\text{CHUR}}} - 1 \right\} \times 10^4$$

3.4 REE End-member calculation and Normalization

Pure hydrothermal fluids often highlight small amounts of seawater entrainment during fluid sampling. It is now widely accepted that hydrothermal fluids are Mg free due to Mg uptake by secondary mineral taking place during the hydrothermal circulation within the host rock (Campbell et al., 1988; Von Damm, 1988). As Mg is a major element of seawater, it is used to calculate the concentrations in pure hydrothermal fluids by extrapolating the measured Mg concentration to nil.

Two normalization values are used to visualize the REE concentrations obtained in pure and buoyant hydrothermal fluids: 1) chondrite abundances in order to compare their REE patterns to that of the substratum (Craddock et al., 2010; Douville et al., 1999; Klinkhammer et al., 1994; Michard, 1989) and 2) North Atlantic Deep Water values (NADW, Zheng et al., 2016) to investigate the REE distribution within a couple of meters of the proximal hydrothermal plume. The anomalous behaviors of Eu, La and Ce are quantified as Eu/Eu^* , La/La^* , and Ce/Ce^* of normalized values following the equations:

$$\frac{\text{Eu}_N}{\text{Eu}_N^*} = \frac{\text{Eu}_N}{\frac{\text{Sm}_N + \text{Gd}_N}{2}} \quad (1)$$

$$\frac{\text{La}_N}{\text{La}_N^*} = \frac{\text{La}_N}{\frac{3 \times (\text{Ce}_N + \text{Nd}_N)}{2}} \quad (2)$$

$$\frac{\text{Ce}_N}{\text{Ce}_N^*} = \frac{\text{Ce}_N}{2\text{Pr}_N - \text{Nd}_N} \quad (3)$$

The anomalies are calculated by extrapolation of the neighboring elements (e.g. Sm and Gd) to the expected value of an element (e.g. Eu). They depend on the normalization values

used to describe the REE patterns. The La anomaly is calculated by extrapolation of the Ce and Nd.

Depending on the normalization, we will index the different anomalies with SW for NADW, and Ch for chondrite normalization. Fractionation among the REE distribution is reported as Nd/Yb for M-REE over HREE and La/Yb for LREE over HREE.

4 Results

4.1 REE concentrations of pure hydrothermal end-member fluids

The REE concentrations of individual pure hydrothermal fluids are reported together with the calculated end-member values in Table VI - 2 and 3. The results report to the dissolved REE concentrations. Hydrothermal fluids used for this study chlorinity range between 260 mM and 580 mM, which cover the chemical variation observed in the LSHF (Leleu et al., submitted). The total REE concentrations expressed as $\Sigma[\text{REE}]$ vary from 5,1 nM (White Castle in 2013) up to 24,5 nM (Capelinhos in 2013), i.e. corresponding to 50-200 times more enriched values than seawater ones at 0,12 nM (Zheng et al., 2016). In addition, the $\Sigma[\text{REE}]$ do not correlate with any fluid groups or year of sampling, but do vary within a single vent. For example, the $\Sigma[\text{REE}]$ has been evaluated on two samples of the Capelinhos site in 2013 which have been collected within 20 minutes from each other. These two samples have $\Sigma[\text{REE}]$ at 24,5 and 17,7 nM. The Eu concentration accounts for 20% of $\Sigma[\text{REE}]$ in M13FLU30, and ~10% of $\Sigma[\text{REE}]$ in M13FLU31. This highlights that absolute concentrations have to be treated with caution due to apparent small-scale temporal variability of fluid REE concentrations. Therefore, we will focus on ratio and normalized concentrations rather than absolute concentrations to avoid any over-interpretation. Figure VI - 3 presents the chondrite-normalized REE patterns of all end-member compared to previous REE datasets acquired on hydrothermal fluids collected at LSHF, local T- and N-MORB at Lucky Strike segment and NADW. All the end-member fluids exhibit the typical light-REE (LREE) enrichment over the heavy-REE (HREE) together with a strong positive $\text{Eu}/\text{Eu}_{\text{Ch}}^*$ anomaly at 5,3 - 55,2 (Table VI - 2), in line with previous findings (Douville et al., 1999). Moreover, among the LREE distribution, samples display either positive or negative $\text{La}/\text{La}_{\text{Ch}}^*$ anomalies, ranging between 0,4 and 9.1 (Table VI - 2).

4.2 REE concentrations of the buoyant hydrothermal plume fluids

The REE concentrations of 17 buoyant hydrothermal fluids are reported together with those of their associated hydrothermal end-member values in Table VI - 3, and inform about the dissolved REE concentrations. All hydrothermal plume fluids have REE concentrations lower than their respective end-member fluid concentrations, but still significantly higher than those of the NADW. At the Aisics site, they have the highest $\Sigma[\text{REE}]$ values at 3,4 - 6 nM while the Capelinhos plume samples show the lowest $\Sigma[\text{REE}]$ at 1 – 1.5 nM. Figure 4 presents the NADW normalized REE patterns of all buoyant hydrothermal fluids alongside their respective hydrothermal end-members. Furthermore, the REE patterns of buoyant hydrothermal plume fluids mimic those of pure end-members, indicating that the REE source is of hydrothermal origin but diluted to different degrees with NADW. Overall, all samples display a strong enrichment in LREE over HREE together with strong positive $\text{Eu}/\text{Eu}_{\text{sw}}^*$ and $\text{Ce}/\text{Ce}_{\text{sw}}^*$ anomalies. Note, however, that some discrepancies are highlighted from site to site in terms of $\text{La}/\text{La}_{\text{sw}}^*$ anomalies as it is the case for the Aisics site, and the MREE enrichment over LREE and HREE as it is the case for the Capelinhos site.

4.3 Nd Isotopic composition of hydrothermal fluids

The Nd isotopic compositions were measured on four pure and eleven buoyant ones, and are reported in Table 3. The ϵNd values of pure hydrothermal fluids range between +8,9 and +9 at Aisics and White Castle, and are +7,8 at Capelinhos and Y3 sites. In comparison, the ϵNd values of buoyant hydrothermal plumes vary between +6,6 and +8,9, the latter being identical within error to the Nd isotope signature of the pure hydrothermal fluids.

5 Discussion

5.1 Subsurface controls

5.1.1 State of the art

The first studies of REE concentrations in submarine hydrothermal fluids suggested that their REE patterns when normalized to chondrite reflect the primary control by the mineralogical and chemical composition of the host rocks (Douville et al., 1999; Michard, 1989). In particular, plagioclase was considered as the main source of REE, while albitisation was the process responsible for their dispersion in the fluid phase, a scenario a priori consistent with the parallelism between REE_{CH} patterns of fluid and plagioclase

phenocrysts (from Lucky Strike basalts, Fig VI - 2). Recent studies on REE complexation highlight the role of chemical conditions (i.e. redox) and secondary mineral alteration state rather than a primary host rock control on REE distribution (Allen and Seyfried, 2005; Bach et al., 2003; Haas et al., 1995). Especially, the pronounced positive Eu anomaly observed in hydrothermal fluids was interpreted as being controlled by plagioclase phenocryst dissolution owing to the similarities between chondrite-normalized REE patterns of plagioclase and of the hydrothermal fluid. (Douville et al., 1999; Klinkhammer et al., 1994). However, this simple and attractive scenario has been undermined by theoretical considerations on the thermodynamic properties of each REE and water/rock experiments (Allen and Seyfried, 2005). Especially, experiments on plagioclase-free ultramafic rocks have revealed the same positive Eu anomaly in the reacted fluids, leading to a speciation control of REE behavior rather than a mineralogical control. This speciation did not affect the distribution of the other REE.

Table VI - 2 Measured and calculated end-member (bold) of the fluid samples.

Sample ID	year	Mg mM	Cl mM	La pM	Ce pM	Pr pM	Nd pM	Sm pM	Eu pM	Gd pM	Tb pM	Dy pM	Ho pM	Er pM	Tm pM	Yb pM	Lu pM	ΣREE nM	Eu/EuCh* La/LaCh*	
seawater		53,1	545	38,7	4,0	5,1	23,8	4,5	1,2	6,8	1,1	8,4	2,3	7,9	1,2	8,7	1,5	0,1		
M13FLU30	2013	1,6	277,2	10888,2	4959,5	506,2	1759,2	250,1	4734,7	266,4	31,2	178,3	31,7	77,3	8,7	46,5	6,3	23,7	55,0	2,5
capelinhos			262	11233,1	5117,1	522,2	1814,4	257,9	4885,2	274,7	32,1	183,7	32,6	79,5	9,0	47,7	6,4	24,5	55,0	2,5
M13FLU31	2013	1,6	259,6	12738,2	1519,9	135,8	652,0	206,5	1572,8	182,7	19,7	85,0	11,7	27,6	2,9	19,2	2,2	17,2	24,0	9,0
capelinhos			262	13141,1	1568,0	140,0	671,9	212,9	1622,6	188,3	20,3	87,4	12,0	28,3	2,9	19,5	2,2	17,7	24,0	9,0
M15FLU38	2015	1,5	273,9	1234,0	2340,1	238,2	1072,1	271,0	1656,0	289,6	33,1	161,6	32,8	74,9	12,0	70,7	11,1	7,5	17,7	0,6
capelinhos			267,3	1269,8	2410,1	245,2	1103,6	279,0	1705,6	298,1	34,1	166,2	33,7	76,9	12,3	72,5	11,4	7,7	17,7	0,6
M13FLU03	2013	2,9	428,6	2584,1	3379,5	407,2	1579,3	267,6	712,2	274,8	31,9	168,9	28,0	60,4	6,1	46,9	3,9	9,6	7,9	0,8
aisics			428,8	2729,5	3572,3	430,2	1668,1	282,6	752,8	290,1	33,7	178,1	29,4	63,4	6,4	49,1	4,0	10,1	7,9	0,8
M14FLU08	2014	0,8	431	5809,5	8969,7	1053,5	4124,0	633,4	1125,2	641,3	86,6	464,3	70,8	152,1	14,8	71,3	7,5	23,2	5,3	0,7
aisics			422,4	5895,0	9102,5	1069,0	4184,7	642,7	1141,9	650,7	87,9	471,1	71,8	154,3	15,0	72,2	7,6	23,6	5,3	0,7
M15FLU03	2015	1,0	440,1	2575,1	6849,2	705,3	2756,6	448,8	994,3	399,4	57,7	309,7	46,8	99,4	10,7	51,5	5,4	15,3	7,0	0,4
aisics			427,8	2626,3	6987,3	719,5	2811,8	457,7	1014,4	407,3	58,9	315,8	47,7	101,2	10,9	52,4	5,5	15,6	7,0	0,4
M13FLU44	2013	0,9	425,1	3217,1	3824,3	427,8	1726,4	274,0	852,3	276,7	36,0	193,5	31,5	75,9	8,0	40,0	5,1	11,0	9,3	0,9
tour eiffel			425,2	3271,6	3889,8	435,0	1755,6	278,6	866,9	281,3	36,6	196,7	32,0	77,1	8,1	40,5	5,2	11,2	9,3	0,9
M14FLU10	2014	0,2	422,4	6403,6	8532,6	397,4	1471,4	198,6	863,7	209,9	28,9	162,7	26,4	60,9	6,3	32,4	3,6	18,4	12,7	1,0
tour eiffel			420,2	6428,8	8566,4	399,0	1477,2	199,4	867,1	210,7	29,1	163,4	26,5	61,1	6,3	32,5	3,6	18,5	12,7	1,0
M15FLU27	2015	1,0	486,6	3701,0	5325,6	563,7	2010,0	255,4	1205,9	229,1	30,7	152,8	23,6	49,3	5,3	26,0	3,0	13,6	14,8	0,8
white castle			481,4	3770,2	5426,1	574,3	2047,5	260,2	1228,7	233,3	31,2	155,5	24,0	50,1	5,4	26,4	3,0	13,8	14,8	0,8
M13FLU14	2013	1,2	492,2	853,5	1345,5	118,0	585,9	203,8	1556,0	192,2	20,6	86,2	13,1	27,8	4,0	18,3	3,0	5,0	23,4	0,7
white castle			489,3	872,0	1376,0	120,5	598,7	208,3	1591,3	196,4	21,1	87,9	13,4	28,2	4,1	18,5	3,0	5,1	23,4	0,7
M13FLU39	2013	1,9	521,5	3379,1	3100,8	267,7	913,3	127,3	895,8	125,0	15,7	84,3	15,7	38,1	4,9	26,4	3,6	9,0	21,2	1,3
cypres			519,7	3505,1	3217,6	277,6	946,9	131,9	929,6	129,4	16,3	87,2	16,2	39,2	5,1	27,0	3,7	9,3	21,2	1,3
M13FLU17	2013	1,5	569,1	10910,7	4047,1	390,6	1238,3	157,5	1148,1	151,8	17,8	86,6	15,1	31,4	3,6	19,0	2,3	18,2	22,1	3,2
south crystal sites			570	11224,4	4163,7	401,7	1273,3	161,9	1181,2	155,9	18,3	88,9	15,5	32,1	3,7	19,3	2,4	18,7	22,2	3,2
M13FLU27	2013	13,0	539	947,4	1286,9	158,5	772,3	195,0	1075,0	182,3	20,3	91,8	12,7	26,5	2,3	10,5	1,3	4,8	17,5	0,7
sintra			537	1242,5	1703,4	208,3	1015,4	243,7	1423,6	239,3	26,6	118,9	16,1	32,5	2,7	11,1	1,3	6,3	17,6	0,7
M14FLU16	2014	1,0	570,9	5512,0	6451,1	485,6	1710,4	207,9	709,8	182,2	23,7	125,5	21,1	47,9	5,1	25,1	3,1	15,5	10,8	1,1
Y3			574,2	5622,5	6581,2	495,3	1744,5	212,0	724,1	185,7	24,2	127,9	21,5	48,7	5,2	25,4	3,1	15,8	10,8	1,1

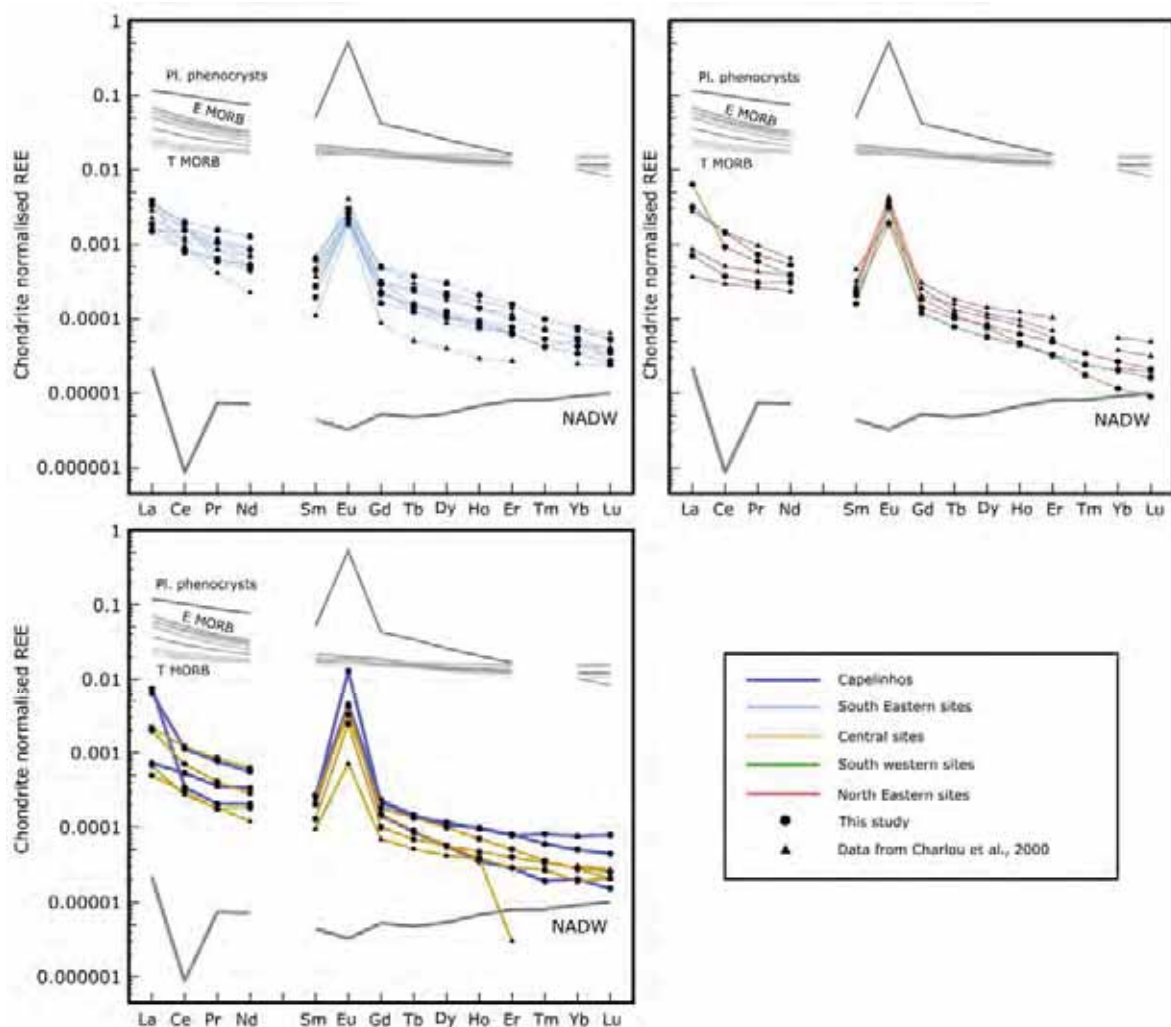


Figure VI - 2 Hydrothermal fluid REE pattern normalized to Chondrite (Evensen et al., 1978). Grey solid lines represent the potential source of REE, NADW (Zheng et al., 2016), T-MORB and E-MORB (Hamelin et al., 2013) and plagioclase phenocrysts (Douville et al., 1999).

REE might form strong complexes with Cl, F, SO₄ (Migdisov et al., 2016, and references therein). F and SO₄ concentrations of seawater are mostly lost in the first stage of the recharge zone because F is incorporated into clay-like minerals and SO₄ is consumed by anhydrite precipitation, and/or reduced to H₂S (Von Damm, 1988). Cl is the only inorganic ligand left to the fluid and is highly concentrated compared to any other element. Under highly reducing conditions such as in hydrothermal fluids, the Eu is in the bivalent form while the other REEs remain in trivalent state (Migdisov et al., 2016). Bivalent Eu behaves as Sr at such conditions, due to similar ionic radii (Shannon, 1976, fig VI - 4), and is incorporated into the same secondary minerals.

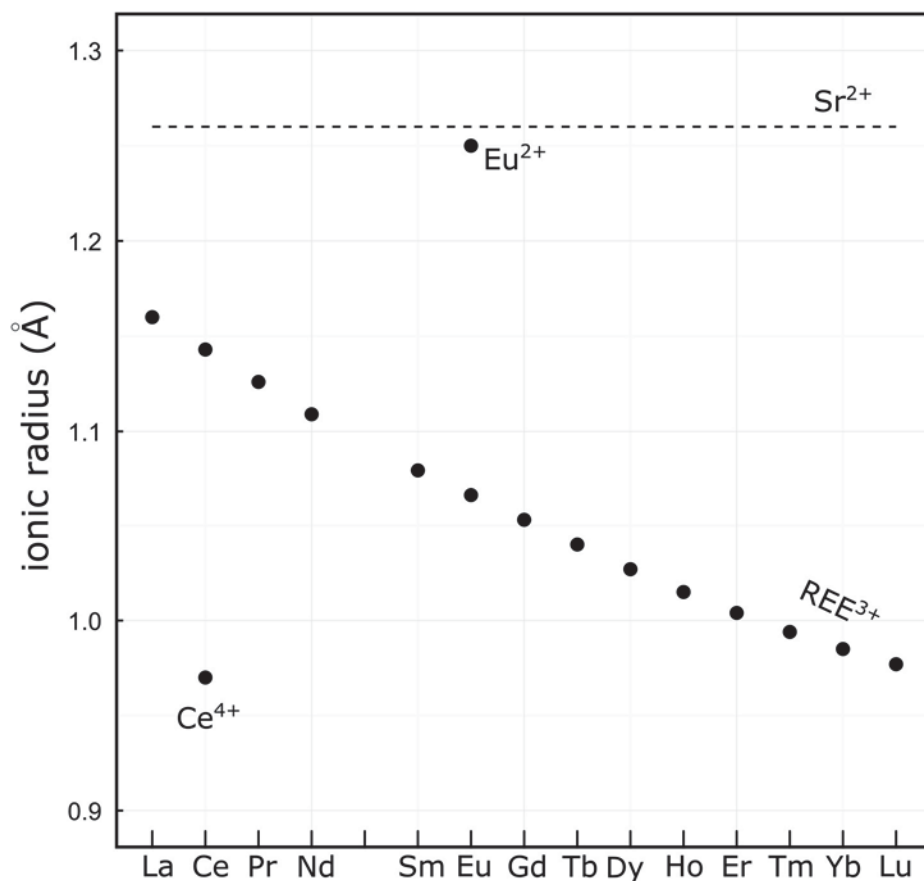


Figure VI - 3 Ionic radii (8 coordination number) for each trivalent REE element and Ce⁴⁺, Eu²⁺ and Sr²⁺ based on Shannon (1976).

5.1.2 The effect of phase separation

Phase separation partitioning of major and trace element has been broadly investigated both experimentally and from natural systems (Berndt and Seyfried Jr, 1997; Bischoff and Rosenbauer, 1989; Foustoukos and Seyfried, 2007; Pester et al., 2015; Pokrovski et al., 2005). These studies have shown different partitioning behavior into brine or vapor depending on the element for example, Sr will partition into the brine preferentially while Li will partition into the vapor phase (Leleu et al., submitted). However little is known about partitioning of REE elements during phase separation. Shmulovich et al. (2002) investigated experimentally the REE partitioning at conditions relevant to subseafloor systems, such as black smoker fields, and showed that HREE were preferentially concentrated into the vapor phase, while LREE were concentrated into the brine.

Although LSHF fluids display a wide range of chlorinity (i.e. 260 - 580 mM), Leleu et al. (submitted) showed that major and trace element distribution is controlled by phase separation of a unique deep-rooted fluid. This provides a unique opportunity to test

experimental results of phase separation on a natural system at the scale of a hydrothermal field.

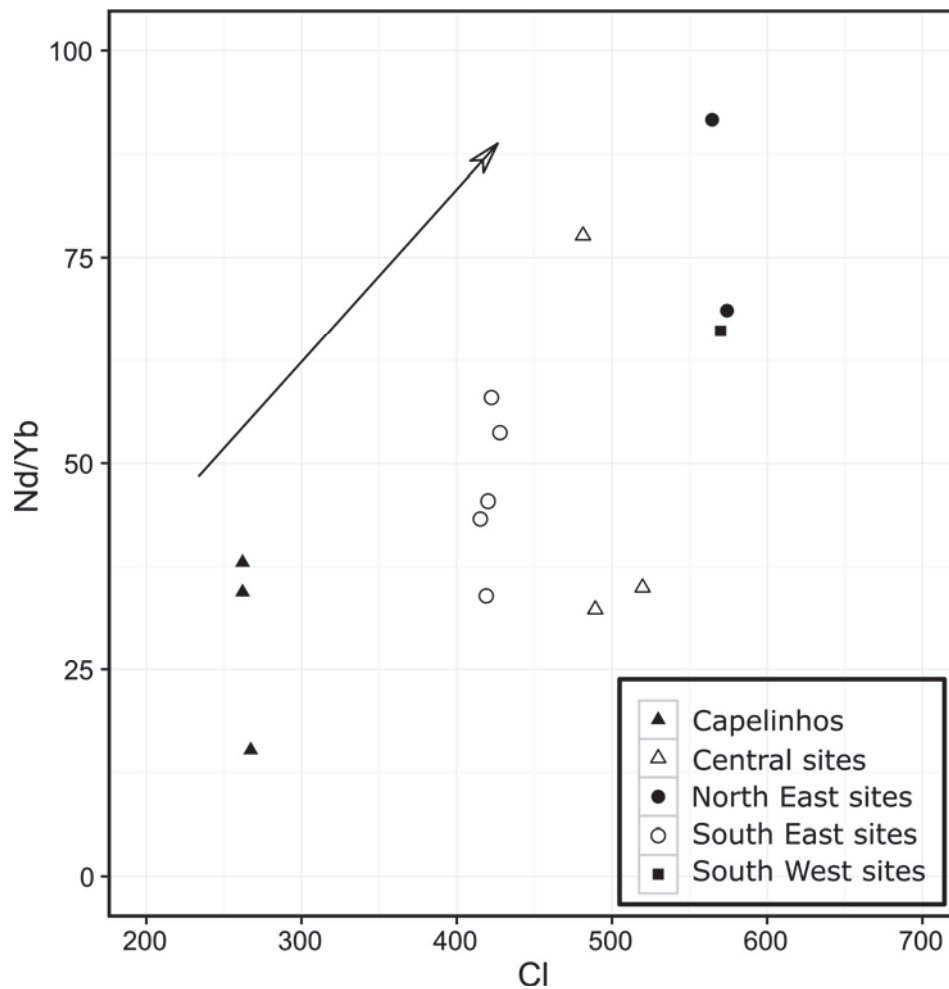


Figure VI - 4 Nd/Yb ratios compared to Cl concentration in mM.

The concentrations of Σ REEs or each REEs of the Lucky Strike fluids don't show any clear correlation with chloride concentrations (Table VI - 2). However, taking Nd and Yb as representative of L-REE and H-REE respectively, we can use the Nd/Yb ratio to assess the effect of phase separation on the L-REE and H-REE partitioning between vapor and brine. As hydrothermal fluids may display at different degrees both La and Ce anomalies (Table VI - 2 and 3), we chose Nd for the L-REE. The Nd/Yb ratios display some scattering within a single group but in general do show a general increase with Cl concentrations, e.g. the high salinity fluid from the SW and NE area display a Nd/Yb ratio ranging from ~60 to ~90 while the most vapor dominated fluid from Capelinhos has Nd/Yb ratios ranging between ~15 and ~40. This suggests that L-REE is preferentially partitioned into the brine phase, marking the effect of phase separation (Fig VI - 4). The sites venting fluids with an

intermediate chlorinity (i.e. the Central and SE groups) all have Nd/Yb ratios between the lowest and highest salinity fluids. Our results clearly show that phase separation leads to an L-REE enrichment of the brine phase while the vapor one is enriched in H-REEs, in line with experimental results (Shmulovich et al., 2002).

5.1.3 Mineralogical controls on REE distribution of hydrothermal fluids

When normalized to chondrite, REE distribution displays, at first order, similar patterns (fig VI - 2) characterized by a large Eu anomaly and enrichment in L-REE over H-REE. As black smoker fluids result from the interaction between seawater and basalt, the chondrite-normalized REE patterns of MORBs and North Atlantic Deep waters are represented for comparison. First of all, hydrothermal fluids are significantly more enriched in REEs than seawater: three order of magnitude for the LREEs, and one order of magnitude for the HREEs. The general slope indicates enrichment of LREE over HREE, which highlights the REE partitioning due to phase separation (see previous section). The second feature that can be observed is an Eu enrichment of all the fluids, as evidenced by the positive Eu anomalies as high as 55.

Although REE_{Ch} patterns at Lucky Strike hydrothermal fluids seem uniform from group to group, the Eu anomalies do vary between 5 and 55, which may be indicative of subsurface processes, i.e. secondary mineral formation such as anhydrite, and/or primary host rock influences, i.e. albitisation of magmatic feldspars (Douville et al., 1999; Klinkhammer et al., 1994).

The Eu anomaly is minimum at 5 for the SE sites which exhibit ~Cl=420mM while the Eu anomalies scatter within the same range, between 9.8 and 55 for other sites which are characterized by low and high Cl contents (260 - 580 mM; fig VI - 2). This clearly shows that the magnitude of the Eu anomalies is independent from the phase separation process. In reduced hydrothermal fluids, Eu is in the bivalent form, while the other REEs remain in trivalent state (Migdisov et al., 2016). As the Eu and Sr elements have similar ionic radii (Shannon, 1976), the Eu element should be incorporated into the same Sr-bearing secondary minerals. Leleu et al. (in prep) showed that the SE sites are marked by higher Ca/Na ratio (~0.12) and more radiogenic Sr isotopic composition (~0.7043) compared to the other sites (Ca/Na = and $^{87}\text{Sr}/^{86}\text{Sr}=0.7038-0.7040$). These features indicate that the SE sites are imprinted by a more pronounced stage of albitisation compared to the other sites (Fig VI – 5b). These observations confirm that the extent of Eu anomaly is controlled by

secondary mineral processes and not only by the reducing conditions, even though these conditions are necessary.

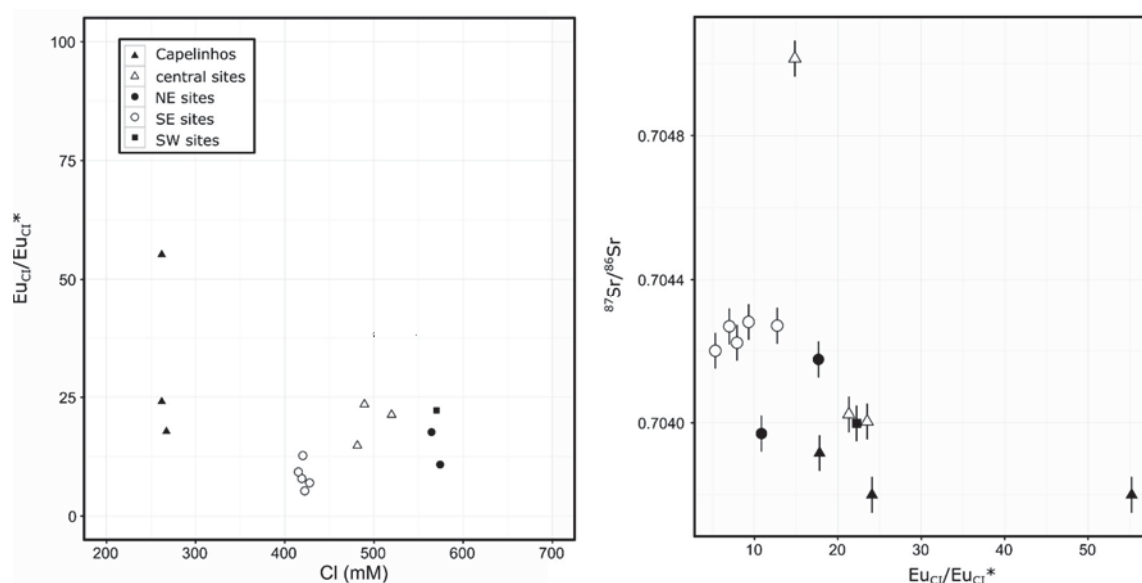


Figure VI - 5 a: Diagram of Eu anomaly (chondrite normalized) against Cl concentration in mM. b: Strontium isotope ratios against Eu anomaly (chondrite normalized).

Finally, three samples (2 at Capelinhos and 1 at South Crystal) display strong positive La/La_{Ch}* anomalies at 2.5 - 9 (table VI - 2). As Capelinhos is Cl depleted and South Crystal is Cl-enriched, the La/La_{Ch}* anomalies do not result from phase separation process. Such La anomaly has already been observed at other submarine hydrothermal systems, such as the Snake Pit's hydrothermal field on the MAR at 23°N (Douville et al., 1999) and the Sister's Peak, Two Boats, and Mephisto sites on the MAR at 5°S (Schmidt et al., 2010). Allen and Seyfried (2005) obtained similar La anomalies during water-rock experiments on ultramafic rock.

Douville et al. (1999) suggested that such La anomaly may result from different La complexation behavior with chloride consecutively to an increase in seafloor temperature. However, at LSHF, Leleu et al. (in prep) argue that the P-T conditions of the reaction zone have remained stable between 2013 and 2015, suggesting that a temperature increase cannot account for the La anomalies. Moreover, Douville et al. (1999) suggested that the La anomaly may be representative of the primary rocks as some feldspar crystals display similar La enrichment. At LSHF, the Eu/Eu_{Ch}* anomalies do not show any difference in feldspars for the two sites which exhibit positive La/La_{Ch}* anomalies. Based on experimental datasets, Allen and Seyfried (2005) also suggested a Cl complexation

influence on La concentration. However at LSHF, the three concerned samples have different Cl concentrations.

Alternatively, water-column studies have also detected La anomalies in the dissolved and particulate phases of different waters masses in the Polar Frontal zone. Garcia-Solsona et al. (2014) proposed that the La anomalies result from the partial dissolution of barite crystals, as La has similar size as barium ion (Piper, 1974). In our case study, the La anomaly can be explained by similar process as barite commonly forms as a secondary mineral at hydrothermal system.

To sum-up, chondrite-normalized REE patterns of end-member fluids provide crucial information about phase separation process (L-REE enrichment over H-REE), degree of alteration ($\text{Eu}/\text{Eu}_{\text{Ch}}^*$ and $^{87}\text{Sr}/^{86}\text{Sr}$), and partial dissolution of hydrothermal mineral ($\text{La}/\text{La}_{\text{Ch}}^*$).

5.2 Fate of REE within the proximal buoyant hydrothermal plume:

Current knowledge of trace element behavior in hydrothermal plume

In hydrothermal plumes, most of the dissolved trace elements present in high quantities in hot and reducing hydrothermal fluid, do not stay in a dissolved form once they are discharged into the alkaline and oxygenated environment of the deep seawater (see for review German and Seyfried, 2014; and reference therein). This is due to co-precipitation and oxy-hydroxide scavenging processes that take place along the mixing continuum from the proximal buoyant plume till dispersion of non-buoyant hydrothermal plume within the water column. These processes have been identified based on the variation of element concentrations measured in particulate matter collected within the non-buoyant hydrothermal plume (German et al., 1991, 1990; Rudnicki and Elderfield, 1993; Sherrell et al., 1999; Trocine and Trefry, 1988) These studies have shown that dissolved metals such as Cu, Zn, Fe and Pb precipitate within seconds of fluids mixing as polymetallic sulfide minerals, settling down immediately at the hydrothermal site. Note that additional sulfate minerals, e.g. anhydrite and barite, together with amorphous silica may form as well, leading to systematic depletion in Cu, Pb, Zn, Fe, Ba, Ca and Si concentrations of the non-buoyant hydrothermal particles (Lilley et al., 1995). In contrast, oxyanions behave as stable dissolved species controlled by a fixed ratio of their concentration over dissolved Fe ones. These ratios of particulate matter are distinctive but homogeneous from one ocean to the other, reflecting chemical composition of the water mass at the sampling site rather than

hydrothermal input (Feely et al., 1996). Finally, other trace elements such as REE, Th and Pa, are particle-reactive and are enriched according to the Fe content in the particulate phase (German et al., 1991, 1990). This is due to the formation of Fe oxy-hydroxides that dominates in young non-buoyant hydrothermal plume, and that scavenge by mineral surface charge seawater-derived dissolved elements.

Overall, the distribution of any hydrothermally-sourced element to the water column have been explained by inorganic and/or organic geochemical processes, arguing that a hydrothermal plume acts as a sink rather than a source of trace elements to the water column (German and Seyfried, 2014; Klinkhammer et al., 1983). However, the detection of high dissolved Fe anomalies in the deep water column starting from the ridge axis till several hundreds of km away from the discharge area (Nishioka et al., 2013; Resing et al., 2015), clearly challenges this conclusion, and in particular the REE whose behavior have been identified as being iron-dependent.

Table VI - 3 Measured concentrations of samples from the hydrothermal plume and associated pure fluid concentrations.

site	Sample	year	% of hydrothermal fluid	La	Ce	Pr	Nd	Sm	Eu	Gd	Tb	Dy	Ho	Er	Tm	Yb	Lu	ΣREE	Eu/Eu ^{tot} *	Ce/Ce ^{tot} *	¹⁴³ Nd/ ¹⁴⁴ Nd (10 ⁻⁵)	εNd(2σ)
	NADW		0,0	23,07	5,87	3,8	16,61	3,25	0,94	4,52	0,72	5,65	1,49	5,08	0,78	5,28	0,89	0,08			n.d.	-12,0
	PL2-598-D2	2015	30,5	1041,7	992,4	126,1	478,7	72,6	138,3	73,5	10,6	57,5	9,4	22,4	2,5	12,3	1,6	3,0	7,6	4,5	n.d.	n.d.
	PL2-598-D3	2015	34,4	2072,9	1363,0	179,0	672,5	100,2	188,2	98,3	13,9	76,1	12,7	29,0	3,1	15,3	1,8	4,8	7,6	4,3	0,512974(13)	6,6(0,4)
Aisics	PL2-598-E1	2015	38,6	67,2	218,0	34,9	152,4	29,2	47,2	19,2	2,7	14,5	2,3	5,5	0,7	3,7	0,5	0,6	7,6	4,0	0,513096(10)	8,9(0,4)
	PL2-598-E2	2015	42,5	1196,6	1882,6	239,7	948,6	187,2	368,5	180,9	21,7	114,1	18,3	42,4	4,5	22,5	2,8	5,2	8,0	4,6	n.d.	n.d.
	PL2-598-E3	2015	49,3	1269,4	2005,3	252,0	1004,5	196,3	392,3	191,1	23,0	119,8	19,2	44,5	4,9	24,2	3,0	5,5	8,1	4,7	0,513027(8)	7,6(0,4)
	M15FLU01	2015	100,0	2575,1	6849,2	705,3	2756,6	448,8	994,3	399,4	57,7	309,7	46,8	99,4	10,7	51,5	5,4	15,3	9,3	5,7	0,513097(13)	8,9(0,4)
	PL5-601-C1	2015	28,9	522,5	712,9	78,6	273,6	44,0	208,5	39,4	4,5	23,9	4,1	10,9	1,3	6,7	1,0	1,9	19,9	4,9	0,512986(100)	6,8(2)
	PL5-601-C2	2015	31,4	861,7	1115,4	124,0	437,9	61,8	283,8	57,3	7,1	37,4	6,3	15,6	1,9	9,5	1,3	3,0	19,1	4,9	0,513081(7)	8,6(0,4)
White Castle	PL5-601-C3	2015	36,7	687,6	866,6	96,2	327,0	42,7	206,2	40,9	5,0	27,4	4,7	11,5	1,4	7,4	1,1	2,3	19,8	4,8	0,513059(4)	8,2(0,4)
	PL5-601-D1	2015	35,5	683,2	851,2	93,8	314,2	38,9	186,1	36,3	4,7	25,5	4,3	11,0	1,3	6,6	1,1	2,3	19,8	4,8	0,513056(13)	8,1(0,4)
	M15FLU27	2015	100,0	3701,0	5325,6	563,7	2010,0	255,4	1205,9	229,1	30,7	152,8	23,6	49,3	5,3	26,0	3,0	13,6	19,8	5,2	0,513099(86)	9(0,4)
	PL6-602-D1	2015	27,0	76,4	137,3	28,1	152,9	70,0	372,7	60,9	6,2	26,3	4,3	9,9	1,4	6,5	1,2	1,0	22,6	4,2	n.d.	n.d.
	PL6-602-D2	2015	30,7	80,9	155,3	30,3	173,1	77,8	427,2	68,0	6,8	28,4	4,0	9,2	1,0	5,3	0,8	1,1	23,3	4,8	n.d.	n.d.
	PL6-602-D3	2015	34,2	102,6	201,7	28,5	100,6	19,2	87,2	14,6	2,0	7,1	0,8	1,3	0,1	0,4	0,0	0,6	20,3	3,8	n.d.	n.d.
Capelinhos	PL6-602-E1	2015	37,20	97,8	196,3	37,8	210,0	78,6	426,3	70,8	8,0	34,3	5,0	11,7	1,4	7,3	1,2	1,2	22,8	4,6	n.d.	n.d.
	PL6-602-E3	2015	42,9	88,9	190,0	37,6	213,0	80,4	437,7	73,0	8,3	36,0	5,0	11,3	1,4	7,0	1,0	1,2	22,8	4,6	n.d.	n.d.
	M15FLU37	2015	100,0	1234,0	2340,1	238,2	1072,1	271,0	1648,0	289,6	33,1	161,6	32,8	74,9	12,0	70,7	11,1	7,5	23,8	6,6	0,513037(9)	7,8(0,4)
	PL7-582-B1	2014	12,9	454,6	513,9	54,4	185,5	27,9	92,6	26,5	3,3	19,0	3,6	10,0	1,2	6,6	1,0	1,4	13,6	5,0	n.d.	n.d.
	PL7-582-B3	2014	20,8	681,0	765,0	80,5	262,4	29,9	88,8	27,8	3,8	22,2	4,4	11,7	1,4	7,4	1,1	2,0	12,3	4,9	n.d.	n.d.
Y3	PL7-582-C2	2014	38,6	1044,0	1207,3	127,0	426,5	51,7	154,7	47,1	6,2	34,9	6,5	16,5	2,1	10,7	1,5	3,1	12,5	5,0	0,513031(10)	7,7(0,4)
	M14FLU16	2014	100,0	5512,0	6451,1	485,6	1710,4	207,9	709,7	182,2	23,7	125,5	21,1	47,9	5,1	25,1	3,1	15,5	14,5	7,2	0,513038(5)	7,8(0,4)

The present study provides the unique opportunity to assess the fate of REE within the buoyant hydrothermal plume, i.e. at a maximum of height of 2m above the discharge area, by measuring the REE concentration of the dissolved hydrothermal fraction and to identify the impact of hydrothermal fluid onto the Nd isotopic signature of the NADW. REE concentrations and Nd isotopic compositions have never been measured on the dissolved fraction of any buoyant hydrothermal plume thus far.

Table VI - 4 Major and trace element concentrations associated to REE concentrations of the hydrothermal plume fluid samples.

Site	sample ID	Type of sample	Mg	Temperature	Fe	Mn	Fe/Mn	Eu _{Cl} /Eu _{Cl} *	Ce _{Cl} /Ce _{Cl} *
aisics	PL2-598-D2	plume	37,7	96,7	146,00	64,30	2,27	7,62	4,50
	PL2-598-D3	plume	35,3	108,5	165,70	72,90	2,27	7,61	4,32
	PL2-598-E1	plume	33,1	121,0	194,60	83,40	2,33	7,58	4,04
	PL2-598-E2	plume	30,4	132,9	220,70	96,00	2,30	8,03	4,65
	PL2-598-E3	plume	29,8	153,8	230,00	102,20	2,25	8,13	4,74
	M15FLU01	pure	1,1	307,0	512,3	251,60	2,04	9,34	5,68
white castle	PL5-601-C1	plume	41,5	92,7	87,70	68,80	1,27	19,94	4,88
	PL5-601-C2	plume	33,9	100,4	147,80	122,30	1,21	19,05	4,88
	PL5-601-C3	plume	38,6	116,7	110,60	91,10	1,21	19,77	4,77
	PL5-601-D1	plume	38,2	112,9	107,80	91,70	1,18	19,80	4,76
	M15FLU27	pure	1,0	311,0	360,7	351,40	1,03	19,85	5,16
capelinhos	PL6-602-D1	plume	38,3	89,1	512,20	107,60	4,76	22,65	4,19
	PL6-602-D2	plume	35,7	100,9	585,60	122,20	4,79	23,32	4,80
	PL6-602-D3	plume	34,7	111,8	741,40	159,90	4,64	20,28	3,85
	PL6-602-E1	plume	30,8	121,2	768,40	158,20	4,86	22,77	4,61
	PL6-602-E3	plume	30,9	139,1	857,30	197,10	4,35	22,77	4,65
	M15FLU37	pure	1,3	319,0	2503,7	597,60	4,19	23,78	6,55
Y3	PL7-582-B1	plume	35,8	45,2	50,50	28,50	1,77	13,63	5,01
	PL7-582-B3	plume	37,0	70,4	99,00	50,60	1,96	12,31	4,90
	PL7-582-C2	plume	33,5	127,2	172,70	88,90	1,94	12,51	5,00
	M14FLU16	pure	1,0	323,0	552,5	273,70	2,02	14,48	7,20

Quantification of pure end-member and NADW contributions in the buoyant hydrothermal plume

To evaluate the fate of REE within the proximal buoyant plume, it is primordial to quantify the relative proportion of pure hydrothermal fluid compared to NADW. This can be done using two independent parameters: in-situ temperature measurements based on an adiabatic mixing hypothesis and Mg concentrations of the solution, i.e. conservative behavior of Mg within the buoyant hydrothermal plume, as illustrated in figure VI - 6. Apart from two exceptions at Y3 site, all fluid samples plot on or within error bars onto the mixing trend, indicating coherent calculated proportions of pure end-member and NADW components in the fluid mixture. Moreover, individual pure hydrothermal fluids that were analyzed, are very close to the calculated end-member (i.e. >97% of pure end-member). In comparison,

the samples of buoyant hydrothermal plume fluids are composed of 14-50% of pure end-member. In summary, by combining two independent parameters, i.e. temperature and dissolved Mg concentration, the buoyant hydrothermal fluid corresponds to a dilution factor by NADW entrainment comprised between 2,5 and 9,6 of pure end-members.

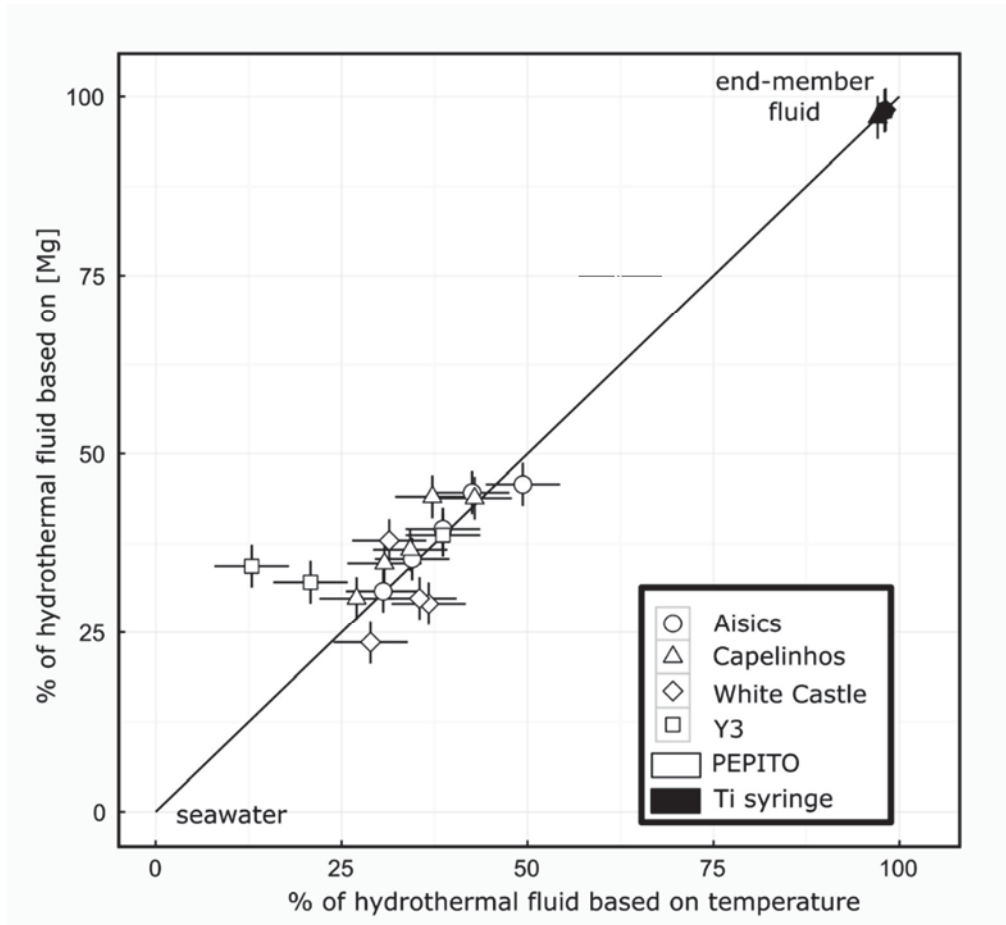


Figure VI - 6 comparison of the proportion of hydrothermal fluid in percent based on magnesium concentration and in situ temperature recorded during sample collection.

REE distribution within the buoyant hydrothermal plume

The deep seawater normalization is better than chondrite normalization to investigate the mixing process of seawater and hydrothermal fluid. The NADW-normalized REE patterns of all buoyant plume fluids mimic those of the pure end-member as well as strong positive Ce/Ce_{sw}^* and Eu/Eu_{sw}^* anomalies but at intermediate REE concentrations between those of the pure end-member and the NADW (Fig VI - 6). These features clearly evidence the diluting effect of NADW, which contains 10^3 less REE than pure end-member (Zheng et al., 2016). Finally, the dissolved Fe/Mn ratios of each buoyant hydrothermal fluid exhibit

rather homogeneous values for each sites (Aisics: 2,25-2,33; White Castle: 1,18-1,27, Capelinhos: 4,35-4,76, and Y3: 1,77-1,94). As suggested by Cotte et al. (personal communication), these values are similar to Fe/Mn ratios calculated on dissolved phase of pure end-members (Aisics: 2,03; White Castle: 1,18; Capelinhos: 4,20; Y3: 2,02).

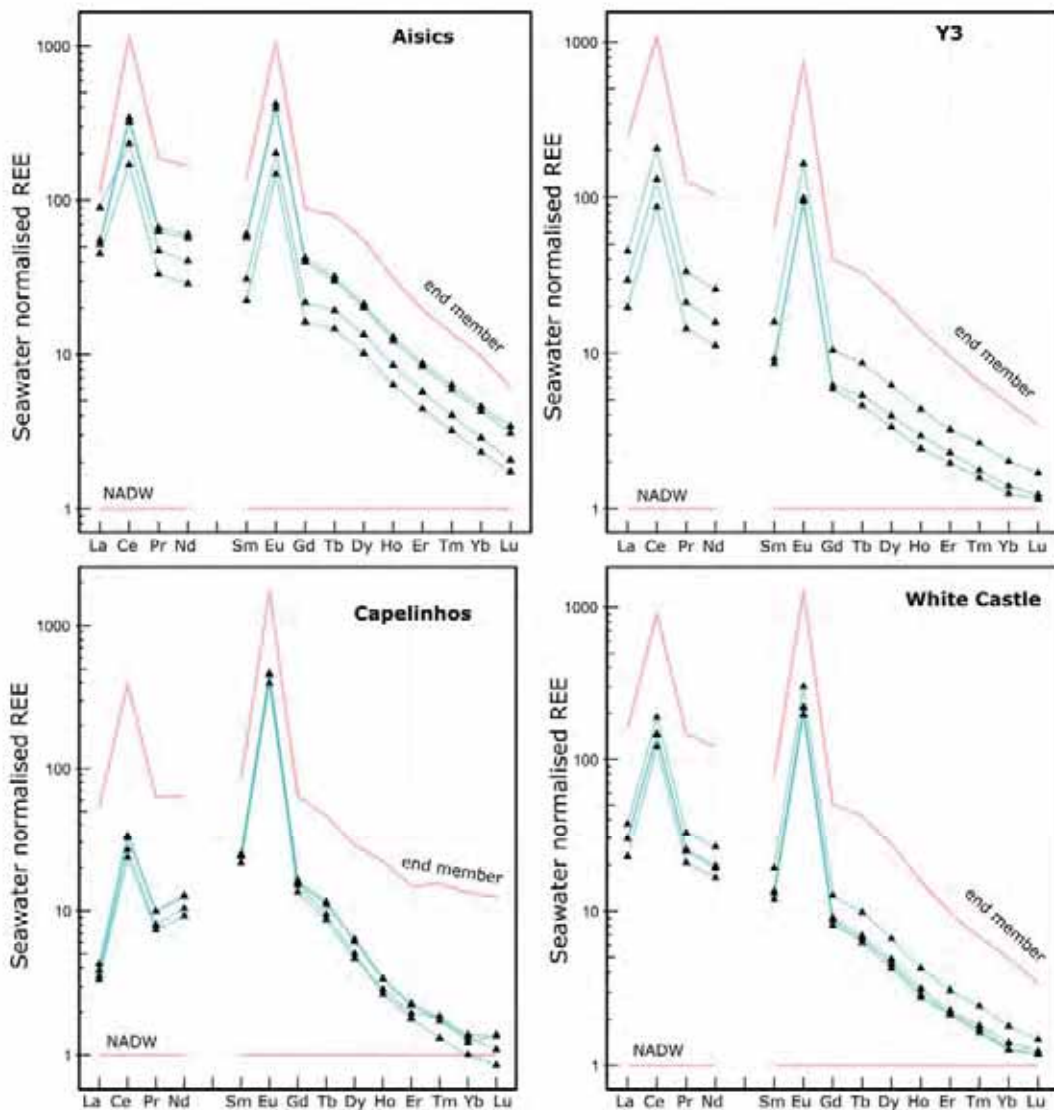


Figure VI - 7 NADW normalized REE patterns of hydrothermal fluids from MoMAR 2014, 2015. Red lines indicate the two mixing poles (pure fluid and deep seawater). Blue line represents the measured plume fluid samples.

All the REE_w patterns display high enrichment in LREE compared to HREE apart from the fluids of the Capelinhos site whose REE_w patterns display a concave shape with a maximum reached at Sm (Fig VI - 7). Such concave shape has been described for pure fluid

on the MAR at the 5°S (Schmidt et al., 2010). These fluids are inferred to originate from anhydrite precipitation in the subsurface, a process that would tend to preferentially uptake LREE and that could account for the bell shaped REE_{SW} observed at Capelinhos.

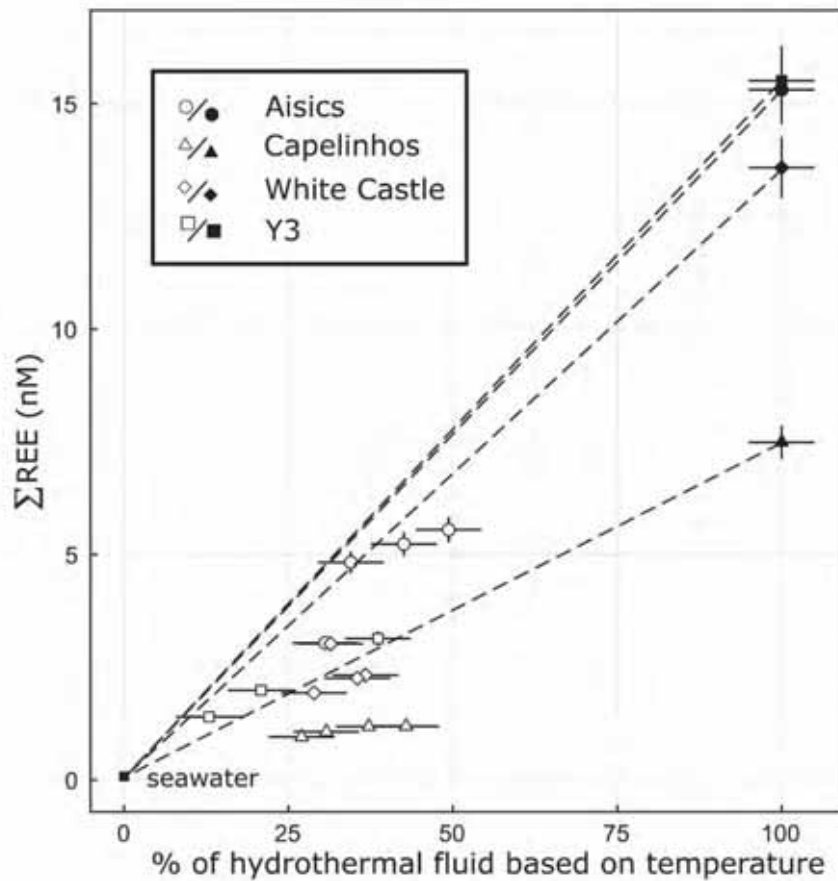


Figure VI - 8 Total REE concentration compared to theoretical concentration (dashed line) as a function of the hydrothermal fluid proportions. Open symbols represent the plume samples, full symbols represent the pure fluid samples.

Based on the relative proportions of pure end-member and NADW presented in the previous section, we can determine the evolution of REE concentrations in the mixture with increasing contribution of the NADW, as shown in figure VI - 8. When compared to the theoretical dilution, assuming a conservative mixing trend, between NADW waters and pure hydrothermal fluid end-members, nearly all the analyzed plumes samples are lower than the predicted values (excepted two samples at Aisics and Y3 which are within error). Such deviations from theoretical values argue for REE scavenging due to surface charge process during mineral precipitation in the early stages of discharge (German et al., 1991, 1990).

Figure VI - 9 displays the detailed mixing behavior for three elements, Ce, Eu, and Yb. Ce and Yb are representative of the LREE and HREE respectively. Furthermore, Ce has a peculiar behavior in seawater (Migdisov et al., 2016). Eu is also known to behave peculiarly in hydrothermal fluid (Migdisov et al., 2016). Even accounting for the error on hydrothermal fluid proportion, scavenging can be observed for each of the three elements. Ce displays a systematic depletion compared to the expected concentration. Eu seems to behave more conservatively, as they are close to the theoretical mixing line than the other elements, but still display evidence of scavenging (Fig VI – 9). The systematic depletion of Ce could be explained by the oxidation and removal by Cerianite precipitation which is responsible for the negative Ce anomaly of the REE_{Ch} pattern of seawater (Migdisov et al., 2016). The concave patterns from Capelinhos are also visible on this diagram as compared to the other site, the extent of scavenging is higher. Measured concentrations of Ce and Yb in Capelinhos fluids display a dramatic scavenging but such loss is not observed for Eu, or not to such extent.

To further investigate the scavenging process, figure VI - 10 displays the Eu anomaly for NADW-normalized values of both samples and theoretical values, based on the conservative mixing of Eu, Gd and Sm. The theoretical lines are constructed by calculation of the Eu anomaly of a conservative mixture of the hydrothermal fluid end member and the NADW.

Scavenging might be different for Eu²⁺ and the other REE³⁺ due to speciation and ionic radii (Fig VI - 3). In this case the Eu anomaly should not behave conservatively through mixing. Fig VI - 10 shows that nearly all the calculated anomalies from the measured samples agree with a conservative mixing trends. This doesn't mean that scavenging is not occurring but rather that scavenging affects Eu²⁺ the same way it affects the other REE. Furthermore, this shows that the Eu anomaly values of hydrothermal fluid from the buoyant plume record that of the pure fluid till a high degree of mixing/dilution despite evidence of scavenging (Fig VI - 9). For Aisics, the Eu_{sw}/Eu_{sw}^* anomaly has a value of 9.3. The plume values for this site are situated between 7.6 and 8.1, which is slightly lower than expected by theoretical curve (Fig VI - 10). Lower than expected Eu anomaly might be due to a preferential uptake of Eu compared to its neighboring REE (Sm, Gd) or a mixed component from more diluted location from the plume.

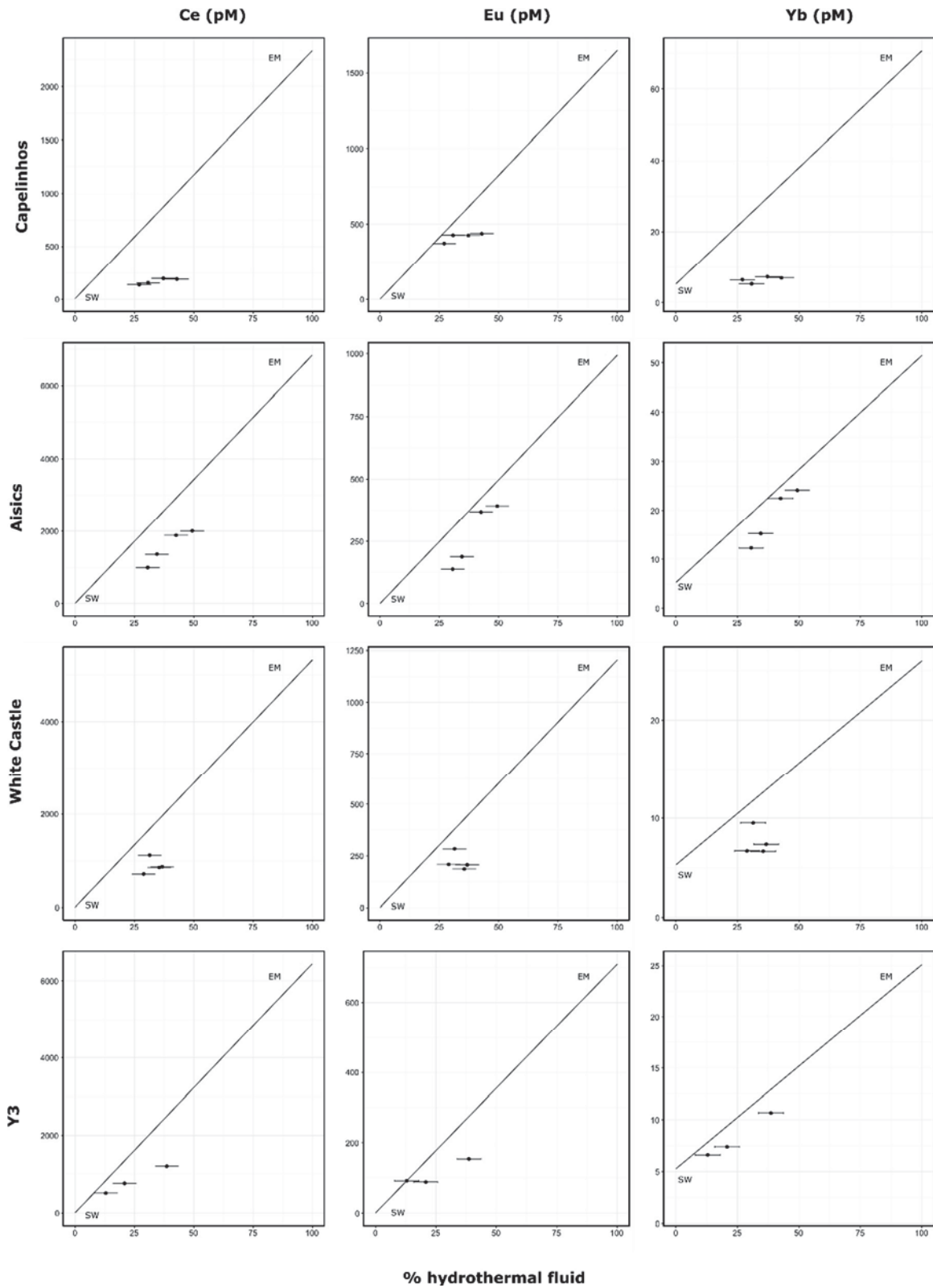


Figure VI - 9 Comparison of elemental concentration measured in the plume sample and the theoretical mixing line between NADW and end-member fluid (solid line) for Ce, Eu and Yb.

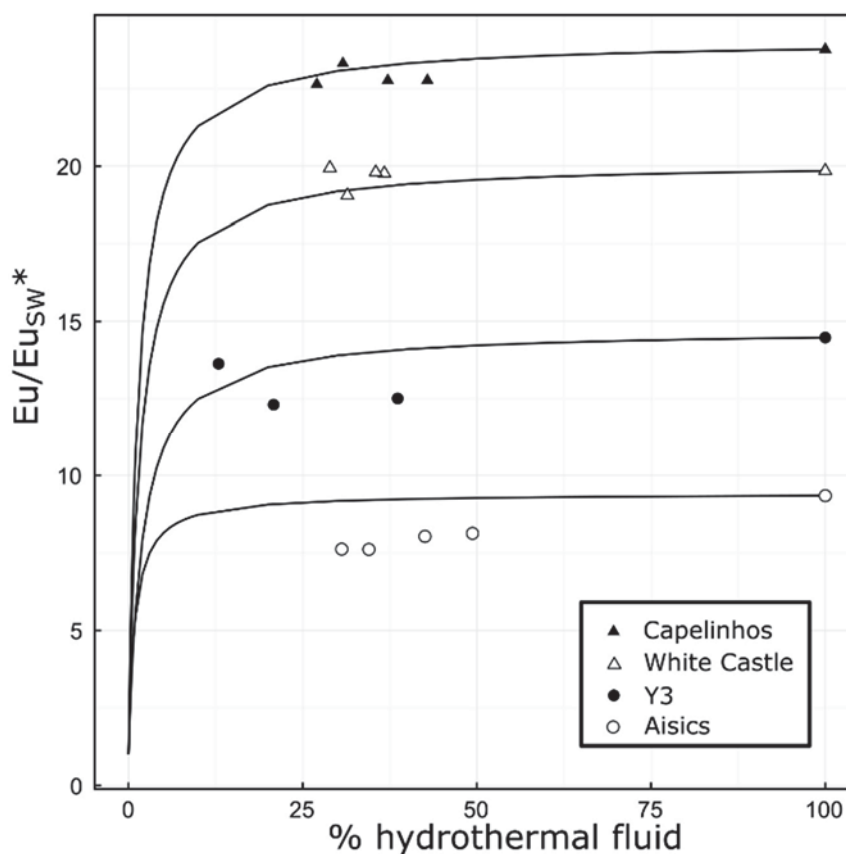


Figure VI - 10 Proportion of hydrothermal fluid compared to the normalized Eu anomaly. Solid lines are theoretical mixing line between measured endmember fluid and seawater.

5.3 Isotopic evolution within the plume

To investigate on the effect of scavenging within the plume, Nd isotopes have been measured both buoyant plume and pure fluid samples. The end-member fluids display contrasting values consistent with the basalt diversity observed in the basalt within and close to Lucky Strike ϵ Nd values between 6.1 and 9.1 (Hamelin et al., 2013).

When focusing on the plume samples from Aisics and White Castle, isotopic data provides an additional information about plume processes. Figure VI - 11 shows the isotopic composition expressed as ϵ Nd compared to the proportion of hydrothermal fluids. Theoretical mixing curves are shown for several scenario. Conservative mixing show an almost constant isotopic composition with decreasing proportion of hydrothermal fluid explained by the high difference in concentration in the sources. The dashed lines are scenarios of mixing with a scavenging of the initial fluid concentration for 50, 80 and 90% of initial concentration loss. The plume samples of White Castle display isotopic compositions close to the conservative mixing curve, and situated within error indicating

limited scavenging. This observation is consistent with the REE concentrations observed in the previous section.

On the contrary, the plume samples from Aisics seem to indicate a ~90% loss which is not observed on REE concentration measurement (Fig VI - 7) and not suggested by Eu anomalies (Fig VI - 9). The only viable explanation for such values of ϵ_{Nd} is entrainment and dissolution of small particles formed at lower mixing proportions of fluid. Because the sampling device uses in-situ filtration, those particles have to be less than $0.45\mu\text{m}$ long. This model of scavenging by precipitation and dissolution is a step forward into evidence for the ridge exchange processes that could affect the Nd isotopic balance of water masses in the oceans (Jeandel et al., 2013).

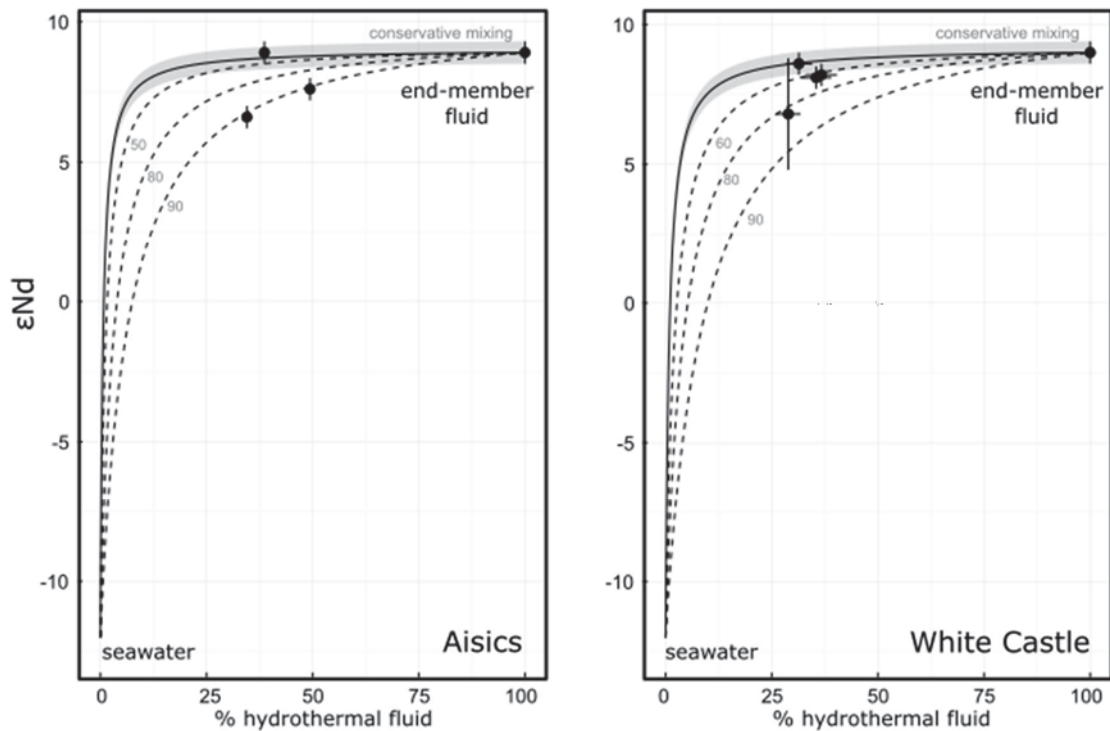


Figure VI - 11 Nd isotope ratios for plume and end-member fluids against their hydrothermal fluid proportion based on temperature. Dashed line mimic an initial loss of Nd of 50, 60, and 90 percent. Grey area represent the error of the model based on the error of the end-member.

Conclusion

The REE investigation of REE concentration of hydrothermal fluids from the Lucky Strike hydrothermal fluids provides useful indicators of both subsurface and discharge processes. This study also questions the relative importance of mineral phases versus complexation control.

During the first moments of discharge of the hydrothermal fluid and the first stages of mixing with seawater, trivalent REE are scavenged by mineral precipitation while divalent Eu tend to act more conservatively. This peculiar behavior tends to produce a large Eu_N anomaly observable at high dilution of hydrothermal fluid in seawater.

However, the scavenging indicators might be obscured by redissolution of particles formed in a more evolved fluid-seawater mix, especially changing the isotopic composition without significantly changing the concentrations. This process is a first step into characterizing a ridge exchange .

Furthermore, the data presented in this study suggest that Cl-complexes and phase separation influence the relative abundance of LREE over the HREE. The slope of REE_{Ch} pattern therefore depends on Cl concentration. The reduced form of Eu is responsible for the observed anomaly but the extent of Eu anomaly seems to depend on the nature of the host rock, and especially the alteration stage through albitisation.

References

Allen, D.E., Seyfried, W.E., 2005. REE controls in ultramafic hosted MOR hydrothermal systems: An experimental study at elevated temperature and pressure. *Geochim. Cosmochim. Acta* 69, 675–683. doi:10.1016/j.gca.2004.07.016

Allen, D.E., Seyfried, W.E., 2003. Compositional controls on vent fluids from ultramafic-hosted hydrothermal systems at mid-ocean ridges: An experimental study at 400°C, 500 bars. *Geochim. Cosmochim. Acta* 67, 1531–1542. doi:10.1016/S0016-7037(02)01173-0

Bach, W., Roberts, S., Vanko, D.A., Binns, R.A., Yeats, C.J., Craddock, P.R., Humphris, S.E., 2003. Controls of fluid chemistry and complexation on rare-earth element contents of anhydrite from the Pacmanus seafloor hydrothermal system, Manus Basin, Papua New Guinea. *Miner. Deposita* 38, 916–935. doi:10.1007/s00126-002-0325-0

Barreyre, T., Escartín, J., Garcia, R., Cannat, M., Mittelstaedt, E., Prados, R., 2012. Structure, temporal evolution, and heat flux estimates from the Lucky Strike deep-sea hydrothermal field derived from seafloor image mosaics: hydrothermal outflow and image mosaics. *Geochem. Geophys. Geosystems* 13. doi:10.1029/2011GC003990

Barreyre, T., Escartin, J., Sohn, R., Cannat, M., Ballu, V., Crawford, W.C., 2014. Temporal variability and tidal modulation of hydrothermal exit-fluid temperatures at the Lucky Strike deep-sea vent field, Mid-Atlantic Ridge. *J. Geophys. Res.-Solid Earth* 119, 2543–2566.

Berndt, M.E., Seyfried Jr, W.E., 1997. Calibration of BrCl fractionation during subcritical phase separation of seawater: Possible halite at 9 to 10° N East Pacific Rise. *Geochim. Cosmochim. Acta* 61, 2849–2854.

Berndt, M.E., Seyfried Jr, W.E., Janecky, D.R., 1989. Plagioclase and epidote buffering of cation ratios in mid-ocean ridge hydrothermal fluids: Experimental results in and near the supercritical region. *Geochim. Cosmochim. Acta* 53, 2283–2300.

Bischoff, J., Rosenbauer, R.J., 1989. Salinity variations in Submarine Hydrothermal Systems by Layered Double-Diffusive Convection. *J. Geol.* 97, 613–623.

Campbell, A.C., Palmer, M.R., Klinkhammer, G.P., Bowers, T.S., Edmond, J.M., Lawrence, J.R., Thompson, G., Humphris, S.E., Rona, P.A., Karson, J.A., 1988. Chemistry of hot springs on the Mid-Atlantic Ridge. *Nature* 335, 514–519.

Charlou, J.L., Donval, J.P., Douville, E., Jean-Baptiste, P., Radford-Knoery, Fouquet, Y., Dapoigny, A., Stievenard, M., 2000. Compared geochemical signatures and the evolution of Menez Gwen (37°50'N) and Lucky Strike (37°17'N) hydrothermal fluids, south of the Azores Triple Junction on the Mid-Atlantic Ridge. *Chem. Geol.* 171, 49–75.

Chavagnac, V., German, C., Milton, J., Palmer, M., 2005. Sources of REE in sediment cores from the Rainbow vent site (36°14'N, MAR). *Chem. Geol.* 216, 329–352. doi:10.1016/j.chemgeo.2004.11.015

Chavagnac, V., Lair, M., Milton, J.A., Lloyd, A., Croudace, I.W., Palmer, M.R., Green, D.R.H., Cherkashev, G.A., 2008. Tracing dust input to the Mid-Atlantic Ridge between 14°45'N and 36°14'N: Geochemical and Sr isotope study. *Mar. Geol.* 247, 208–225. doi:10.1016/j.margeo.2007.09.003

Colaço, A., Blandin, J., Cannat, M., Carval, T., Chavagnac, V., Connelly, D., Fabian, M., Ghiron, S., Goslin, J., Miranda, J.M., Reverdin, G., Sarradin, J., Waldmann, C., Sarradin, P.M., 2011. MoMAR-D: a technological challenge to monitor the dynamics of the Lucky Strike vent ecosystem. *ICES J. Mar. Sci.* 68, 416–424. doi:10.1093/icesjms/fsq075

Cole, C.S., James, R.H., Connelly, D.P., Hathorne, E.C., 2014. Rare earth elements as indicators of hydrothermal processes within the East Scotia subduction zone system. *Geochim. Cosmochim. Acta* 140, 20–38. doi:10.1016/j.gca.2014.05.018

Cotte, L., Waeles, M., Pernet-Coudrier, B., Sarradin, P.-M., Cathalot, C., Riso, R.D., 2015. A comparison of in situ vs. ex situ filtration methods on the assessment of dissolved and particulate metals at hydrothermal vents. *Deep Sea Res. Part Oceanogr. Res. Pap.* 105, 186–194. doi:10.1016/j.dsr.2015.09.005

Craddock, P.R., Bach, W., Seewald, J.S., Rouxel, O.J., Reeves, E., Tivey, M.K., 2010. Rare earth element abundances in hydrothermal fluids from the Manus Basin, Papua New Guinea: Indicators of sub-seafloor hydrothermal processes in back-arc basins. *Geochim. Cosmochim. Acta* 74, 5494–5513. doi:10.1016/j.gca.2010.07.003

Crawford, W.C., Rai, A., Singh, S.C., Cannat, M., Escartin, J., Wang, H., Daniel, R., Combier, V., 2013. Hydrothermal seismicity beneath the summit of Lucky Strike volcano, Mid-Atlantic Ridge. *Earth Planet. Sci. Lett.* 373, 118–128. doi:10.1016/j.epsl.2013.04.028

Douville, E., Bienvenu, P., Charlou, J.L., Donval, J.P., Fouquet, Y., Appriou, P., Gamo, T., 1999. Yttrium and rare earth elements in fluids from various deep-sea hydrothermal systems. *Geochim. Cosmochim. Acta* 63, 627–643.

Douville, E., Charlou, J.L., Oelkers, E.H., Bienvenu, P., Jove Colon, C.F., Donval, J.P., Fouquet, Y., Prieur, D., Appriou, P., 2002. The rainbow vent fluids (36°14' N, MAR):

the influence of ultramafic rocks and phase separation on trace metal content in Mid-Atlantic Ridge hydrothermal fluids. *Chem. Geol.* 184, 37–48.

Dziak, R.P., 2004. Evidence of a recent magma dike intrusion at the slow spreading Lucky Strike segment, Mid-Atlantic Ridge. *J. Geophys. Res.* 109. doi:10.1029/2004JB003141

Elderfield, H., Schultz, A., 1996. Mid-ocean ridge hydrothermal fluxes and the chemical composition of the ocean. *Annu. Rev. Earth Planet. Sci.* 24, 191–224.

Escartin, J., Barreyre, T., Cannat, M., Garcia, R., Gracías, N., Deschamps, A., Salocchi, A., Sarradin, P.-M., Ballu, V., 2015. Hydrothermal activity along the slow-spreading Lucky Strike ridge segment (Mid-Atlantic Ridge): Distribution, heatflux, and geological controls. *Earth Planet. Sci. Lett.* 431, 173–185. doi:10.1016/j.epsl.2015.09.025

Evensen, N., Hamilton, P.J., O’nions, R.K., 1978. Rare-earth abundances in chondritic meteorites. *Geochim. Cosmochim. Acta* 42, 1199–1212.

Feely, R.A., Baker, E.T., Marumo, K., Urabe, T., Ishibashi, J., Gendron, J., Lebon, G.T., Okamura, K., 1996. Hydrothermal plume particles and dissolved phosphate over the superfast-spreading southern East Pacific Rise. *Geochim. Cosmochim. Acta* 60, 2297–2323.

Fontaine, F.J., Wilcock, W.S.D., Butterfield, D.A., 2007. Physical controls on the salinity of mid-ocean ridge hydrothermal vent fluids. *Earth Planet. Sci. Lett.* 257, 132–145. doi:10.1016/j.epsl.2007.02.027

Fontaine, F.J., Wilcock, W.S.D., Foustoukos, D.E., Butterfield, D.A., 2009. A Si-Cl geothermobarometer for the reaction zone of high-temperature, basaltic-hosted mid-ocean ridge hydrothermal systems: Si/Cl-inferred P–T in MOR hydrothermal systems. *Geochem. Geophys. Geosystems* 10. doi:10.1029/2009GC002407

Fouquet, Y., Ondréas, H., Charlou, J.L., Donval, J.P., Radford-Knoery, 1995. Atlantic lava lakes and hot vents. *Nature* 377, 201.

Foustoukos, D.I., Seyfried, W.E., 2007. Trace element partitioning between vapor, brine and halite under extreme phase separation conditions. *Geochim. Cosmochim. Acta* 71, 2056–2071. doi:10.1016/j.gca.2007.01.024

Gale, A., Escrig, S., Gier, E.J., Langmuir, C.H., Goldstein, S.L., 2011. Enriched basalts at segment centers: The Lucky Strike (37°17’N) and Menez Gwen (37°50’N) segments of the Mid-Atlantic Ridge: enriched basalts at segment centers. *Geochem. Geophys. Geosystems* 12. doi:10.1029/2010GC003446

García-Solsona E., Jeandel C., Labatut M., Lacan F., Vance D., Chavagnac, V., Pradoux C., 2014. Rare earth elements and Nd isotopes tracing water mass mixing and particle-seawater interactions in the SE Atlantic. *Geochim. Cosmochim. Acta*, 125, 351–372

German, C.R., Colley, S., Palmer, M.R., Khripounoff, A., Klinkhammer, G.P., 2002. Hydrothermal plume-particle fluxes at 13 N on the East Pacific Rise. *Deep Sea Res. Part Oceanogr. Res. Pap.* 49, 1921–1940.

German, C.R., Fler, A.P., Bacon, M.P., Edmond, J.M., 1991. Hydrothermal scavenging at the Mid-Atlantic Ridge: radionuclide distributions. *Earth Planet. Sci. Lett.* 170–181.

German, C.R., Klinkhammer, G.P., Edmond, J.M., Mitra, A., Elderfield, H., 1990. Hydrothermal scavenging of rare-earth elements in ocean. *Nature* 345.

German, C.R., Seyfried, W.E., 2014. Hydrothermal Processes, in: *Treatise on Geochemistry*. Elsevier, pp. 191–233.

Haas, J.R., Shock, E.L., Sassani, D.C., 1995. Rare Earth Elements in hydrothermal systems: Estimates of standard partial molal thermodynamic properties of aqueous complexes of the rare earth elements at high pressures and temperatures. *Geochim. Cosmochim. Acta* 59, 4329–4350.

Hamelin, C., Bezos, A., Dosso, L., Escartin, J., Cannat, M., Mevel, C., 2013. Atypically depleted upper mantle component revealed by Hf isotopes at Lucky Strike segment. *Chem. Geol.* 341, 128–139. doi:10.1016/j.chemgeo.2013.01.013

Humphris, S.E., Fornari, D.J., Scheirer, D.S., German, C.R., Parson, L.M., 2002. Geotectonic setting of hydrothermal activity on the summit of Lucky Strike Seamount (37°17'N, Mid-Atlantic Ridge): GEOTECTONIC SETTING. *Geochem. Geophys. Geosystems* 3, 1–25. doi:10.1029/2001GC000284

Jeandel, C., Delattre, H., Grenier, M., Pradoux, C., Lacan, F., 2013. Rare earth element concentrations and Nd isotopes in the Southeast Pacific Ocean: REE and Nd isotopes in the south east pacific. *Geochem. Geophys. Geosystems* 14, 328–341. doi:10.1029/2012GC004309

Klinkhammer, G.P., Elderfield, H., Edmond, J.M., Mitra, A., 1994. Geochemical implications of rare earth element patterns in hydrothermal fluids from mid-ocean ridges. *Geochim. Cosmochim. Acta* 58, 5105–5113.

Klinkhammer, G.P., Elderfield, H., Hudson, A., 1983. Rare earth elements in seawater near hydrothermal vents. *Nature* 305.

Lacan, F., Jeandel, C., 2005. Neodymium isotopes as a new tool for quantifying exchange fluxes at the continent–ocean interface. *Earth Planet. Sci. Lett.* 232, 245–257. doi:10.1016/j.epsl.2005.01.004

Lacan, F., Jeandel, C., 2001. Tracing Papua New Guinea imprint on the central Equatorial Pacific Ocean using neodymium isotopic compositions and Rare Earth Element patterns. *Earth Planet. Sci. Lett.* 186, 497–512.

Langmuir, C., Humphris, S.E., Fornari, D.J., Van Dover, C., Von Damm, K.L., Tivey, M.K., Colodner, D., Charlou, J.L., Desonie, D., Wilson, C., Fouquet, Y., Klinkhammer, G.P., Bougault, H., 1997. Hydrothermal vents near a mantle hot spot: the Lucky Strike vent field at 37°N on the Mid-Atlantic Ridge. *Earth Planet. Sci. Lett.* 148, 69–91.

Leleu, T., Chavagnac, V., Cannat, M., Fontaine, F.J., Ceuleneer, G., Castillo, A., submitted. Spatial variations in vent chemistry at the Lucky Strike Hydrothermal Field, Mid-Atlantic Ridge (37°N): Implications for subseafloor flow geometry and stockwork formation. *Geochim. Cosmochim. Acta* submitted.

Leleu, T., Chavagnac, V., Ceuleneer, G., in prep. Temporal evolution of fluid from Lucky Strike hydrothermal field.

Lilley, M.D., Feely, R.A., Trefry, J.H., 1995. Chemical and Biochemical Transformations in Hydrothermal Plumes, in: *Seafloor Hydrothermal Systems: Physical,*

Chemical, Biological, and Geological Interactions. American Geophysical Union, pp. 369–391.

Michard, A., 1989. Rare earth element systematics in hydrothermal fluids. *Geochim. Cosmochim. Acta* 53, 745–750.

Migdisov, A., Williams-Jones, A.E., Brugger, J., Caporuscio, F.A., 2016. Hydrothermal transport, deposition, and fractionation of the REE: Experimental data and thermodynamic calculations. *Chem. Geol.* 439, 13–42. doi:10.1016/j.chemgeo.2016.06.005

Nishioka, J., Nakatsuka, T., Watanabe, Y.W., Yasuda, I., Kuma, K., Ogawa, H., Ebuchi, N., Scherbinin, A., Volkov, Y.N., Shiraiwa, T., Wakatsuchi, M., 2013. Intensive mixing along an island chain controls oceanic biogeochemical cycles: mixing controls biogeochemical cycles. *Glob. Biogeochem. Cycles* 27, 920–929. doi:10.1002/gbc.20088

Pester, N.J., Ding, K., Seyfried, W.E., 2015. Vapor–liquid partitioning of alkaline earth and transition metals in NaCl-dominated hydrothermal fluids: An experimental study from 360 to 465°C, near-critical to halite saturated conditions. *Geochim. Cosmochim. Acta* 168, 111–132. doi:10.1016/j.gca.2015.07.028

Pester, N.J., Reeves, E.P., Rough, M.E., Ding, K., Seewald, J.S., Seyfried, W.E., 2012. Subseafloor phase equilibria in high-temperature hydrothermal fluids of the Lucky Strike Seamount (Mid-Atlantic Ridge, 37°17'N). *Geochim. Cosmochim. Acta* 90, 303–322. doi:10.1016/j.gca.2012.05.018

Piper D. Z., 1974, Rare Earth Elements in the sedimentary cycle: a summary. *Chem. Geol.* 14, 285–304.

Pokrovski, G.S., Roux, J., Harrichoury, J.-C., 2005. Fluid density control on vapor-liquid partitioning of metals in hydrothermal systems. *Geology* 33, 657–660.

Resing, J.A., Sedwick, P.N., German, C.R., Jenkins, W.J., Moffett, J.W., Sohst, B.M., Tagliabue, A., 2015. Basin-scale transport of hydrothermal dissolved metals across the South Pacific Ocean. *Nature* 523, 200–203. Doi:10.1038/nature14577

Rudnicki, M.D., Elderfield, H., 1993. A chemical model of the buoyant and neutrally buoyant plume above the TAG vent field, 26 degree N, Mid-Atlantic Ridge. *Geochim. Cosmochim. Acta* 57, 2939–2957.

Saleban Ali, H., 2016. Impact du fluide hydrothermal de haute température sur la composition isotopique de l'eau de mer profonde. Université Paul Sabatier, Toulouse.

Sarradin, P.-M., Waeles, M., Bernagout, S., Le Gall, C., Sarrazin, J., Riso, R., 2009. Speciation of dissolved copper within an active hydrothermal edifice on the Lucky Strike vent field (MAR, 37°N). *Sci. Total Environ.* 407, 869–878. doi:10.1016/j.scitotenv.2008.09.056

Schmidt, K., Garbe-Schönberg, D., Bau, M., Koschinsky, A., 2010a. Rare earth element distribution in 400°C hot hydrothermal fluids from 5°S, MAR: The role of anhydrite in controlling highly variable distribution patterns. *Geochim. Cosmochim. Acta* 74, 4058–4077. doi:10.1016/j.gca.2010.04.007

Shannon, R. t, 1976. Revised effective ionic radii and systematic studies of interatomic distances in halides and chalcogenides. *Acta Crystallogr. A* 32, 751–767.

Sherrell, R.M., Field, M.P., Ravizza, G., 1999. Uptake and fractionation of rare earth elements on hydrothermal plume particles at 9 45' N, East Pacific Rise. *Geochim. Cosmochim. Acta* 63, 1709–1722.

Shmulovich, K., Heinrich, W., Möller, P., Dulski, P., 2002. Experimental determination of REE fractionation between liquid and vapor in the systems NaCl–H₂O and CaCl₂–H₂O up to 450 °C. *Contrib. Mineral. Petrol.* 144, 257–273. doi:10.1007/s00410-002-0397-y

Singh, S.C., Crawford, W.C., Carton, H., Seher, T., Combier, V., Cannat, M., Pablo Canales, J., Düsünür, D., Escartin, J., Miguel Miranda, J., 2006. Discovery of a magma chamber and faults beneath a Mid-Atlantic Ridge hydrothermal field. *Nature* 442, 1029–1032. doi:10.1038/nature05105

Trocine, R.P., Trefry, J.H., 1988. Distribution and chemistry of suspended particles from an active hydrothermal vent site on the Mid-Atlantic Ridge at 26°N. *Earth Planet. Sci. Lett.* 1–15.

Von Damm, K.L., 1988. Systematics and postulated controls on submarine hydrothermal solution chemistry. *J. Geophys. Res.-Solid Earth* 93, 4551–4561.

Von Damm, K.L., Bray, A.M., Buttermore, L.G., Oosting, S.E., 1998. The geochemical controls on vent fluids from the Lucky Strike vent field, Mid-Atlantic Ridge. *Earth Planet. Sci. Lett.* 160, 521–536.

Zheng, X.-Y., Plancherel, Y., Saito, M.A., Scott, P.M., Henderson, G.M., 2016. Rare earth elements (REE) in the tropical South Atlantic and quantitative deconvolution of their non-conservative behavior. *Geochim. Cosmochim. Acta* 177, 217–237. doi:10.1016/j.gca.2016.01.018

CONCLUSION ET PERSPECTIVES

Ce travail de thèse s'est déroulé dans un contexte d'observatoire fond de mer. Un effort important a été apporté à l'échantillonnage systématique des fluides hydrothermaux lors des trois campagnes MoMARsat (2013, 2014, 2015) auxquelles j'ai eu la chance de participer. L'analyse chimique très complète réalisée à terre a permis d'apporter un jeu de données complémentaire de celles effectuées par les instruments déployés chaque année. Cela m'a permis de construire une base de données chimique inédite en contexte de dorsale lente. L'élaboration de cette base de données a également nécessité du développement analytique notamment pour la mesure de la concentration en terres rares et en Li dont la composition isotopique n'était pas mesurée auparavant au GET pour ce type d'échantillons.

Les fluides hydrothermaux ont la particularité d'être chargés en sels. Mais à l'instar de l'eau de mer, il n'existe pas de solution standard internationalement reconnue et utilisée dans la communauté scientifique pour certifier de la qualité des mesures effectuées et de confirmer leur inter comparabilité entre différentes équipes. Plus particulièrement, la mesure de la concentration du Li dans une matrice de type eau de mer a fait l'objet d'une étude fine car celle-ci était primordiale pour la bonne détermination de la composition isotopique de Li, et de son application comme traceur de processus. La problématique autour du Li élémentaire comme pour beaucoup d'éléments est qu'il n'existe pas de standard international tout à fait adapté aux fluides hydrothermaux de type fumeur noir. En effet, des standards d'eau de mer existent pour quelques éléments traces (par exemple le NASS 6 est une solution d'eau de mer de référence certifié pour les éléments suivant : As, Cd, Cr, Co, Cu, Fe, Pb, Mn, Mo, Ni, U, V, et Zn avec des concentrations variant de 0.01 à 10 ppb); il n'y a pas d'équivalent pour les éléments ultra-traces. Nous avons utilisé le IAPSO qui est un standard de salinité de l'eau de mer, parce que les éléments dissous dans nos fluides sont

liés à la concentration en Cl en solution. Ainsi nous avons obtenu d'excellents résultats sur la mesure du Li élémentaire dans une solution chargée en sel (i.e. le IAPSO), nous donnant une entière confiance dans les concentrations mesurées dans les fluides hydrothermaux. Les mesures qui ont pu ainsi être acquises pour la détermination des isotopes du Lithium ont une qualité que nous avons pu tester *a posteriori* par comparaison avec ce qui est connu par ailleurs sur la composition isotopique en Li de l'eau de mer.

Au cours de cette thèse, la découverte du site hydrothermal de Capelinhos à l'écart du lac de lave fossile a donné accès à une autre échelle spatiale de la circulation hydrothermale à Lucky Strike. Il est alors apparu nécessaire de réinterpréter les données chimiques en tenant compte de ce nouveau site pour proposer un chemin de circulation de fluide au sein de la lithosphère. Ainsi, les sites hydrothermaux ont été classifiés par groupe en fonction de leur salinité et de leur position géographique par rapport au lac de lave fossile. Cette réinterprétation a été faite en ne prenant en compte que les fluides échantillonnés en 2013 qui offraient la meilleure couverture spatiale à ce moment. Elle s'appuie aussi sur des données géophysiques, acquises au sein de l'observatoire, telles que celles apportées par les capteurs de température autonome. La distribution des éléments traces selon la chlorinité de chaque groupe de sites met en exergue une source unique en profondeur, alimentant l'ensemble de la cellule hydrothermale à Lucky Strike. Par ailleurs, l'application de plusieurs outils géochimiques (géothermomètre Si-Cl, solubilité du quartz et géothermomètre Fe-Mn) a permis d'estimer les conditions de pression et température lors des interactions eau-roche en profondeur. Ces estimations sont différentes pour les fluides de Capelinhos et pour les fluides hydrothermaux « historiquement » connus autour du lac de lave fossile. Ces estimations concernent deux aspects : l'une porte sur les conditions de séparation de phase tandis que l'autre fixe les conditions atteintes par les minéraux du faciès schiste vert. Ces estimations de P et T dépendent en grande partie du (des) postulat(s) de départ, c'est-à-dire des hypothèses qui sont faites pour l'utilisation de ces outils. Ainsi, la zone de séparation de phase a été évaluée à des conditions de pression et de température de 390 bars et 438°C. Ceci correspond à une profondeur de 2600 m sous le plancher océanique. Cette estimation est équivalente à celles proposées par Fontaine et al. (2009) pour des fluides du site Tour Eiffel collectés en 1994 et 1997. Toutefois, en choisissant d'autres hypothèses telles que la concordance des courbes de solubilité du quartz avec les températures données par les rapports Fe/Mn (contrôlé par les minéraux du faciès schiste vert), il est possible de « localiser » l'endroit où se font les dernières interactions eau/roche

en utilisant à la fois la solubilité du quartz pour estimer la pression et le rapport Fe/Mn pour contraindre la température. Cette dernière estimation décrit donc la fin des interactions eau–roche que nous définissons comme étant le toit de la zone de réaction. Ceci indique une pression de 340 bars pour Capelinhos et une température de 400°C alors que les autres sites ont une température calculée plus faible comprise entre 350 et 380°C pour une pression de l'ordre de 300 bars. Ces deux estimations ne sont pas indépendantes l'une de l'autre, car toutes deux se basent sur la solubilité du quartz. Pourtant, si nous considérons que la zone de séparation de phase marque le début de la remontée de fluide tandis que le toit de la zone de réaction marque la fin de l'enregistrement des conditions P et T par les compositions des fluides, alors l'écart de P et T entre l'estimation de la zone de séparation de phase (qui est la même d'un groupe de sites à l'autre) et le toit de la zone de réaction (qui diffère selon le groupe de sites) donne une idée qualitative des temps de résidence dans la zone de remontée du fluide. Ainsi, Capelinhos, avec un toit de zone de réaction plus chaud et plus profond que les autres groupes, montre un temps de résidence relativement court, en cohérence avec sa plus faible densité (plus forte flottabilité). Par contre, les autres groupes, qui sont enrichis en Cl par rapport à Capelinhos, ont un temps de résidence dans la zone de remontée relativement plus long, donc une interaction avec le substratum potentiellement plus marquée.

De plus, la diversité des concentrations en Cl observées et en particulier leur variabilité temporelle (les sites de Y3 et Crystal passent d'une concentration en Cl à dominance vapeur en 1993 à celle à dominance saumure en 2013) semble liée à la structure de la croûte. Autrement dit, la composition de ces fluides est contrôlée par des paramètres physiques et structuraux du plancher océanique comme la présence de failles F2 pour Capelinhos et la perméabilité et l'épaisseur de la couche sismique 2A (plus épaisse à l'ouest qu'à l'est du lac de lave fossile (Arnulf et al., 2011)). Ainsi, nous avons discuté de l'effet de la structure de la croûte sur la composition des fluides hydrothermaux à la décharge.

Pour résumer, une zone de séparation de phase provoque la remontée d'un fluide initialement homogène. La ségrégation plus ou moins efficace selon la structure de la croûte et la perméabilité va être responsable de la diversité des concentrations en Cl observée au niveau du plancher océanique. Les fluides de Capelinhos, bien qu'éloignés de la source de chaleur (~1.5 km du lac de lave surplombant la lentille magmatique axiale), vont enregistrer les conditions les plus profondes. Par conséquent, les autres fluides vont dériver des fluides de Capelinhos en passant plus de temps dans la zone de remontée.

A partir de ce modèle de circulation hydrothermale, nous avons réinterprété les variations temporelles entre 1993 et 2015 de la composition chimique des fluides à deux échelles de temps : 1) L'échelle de l'échantillonnage, de ~10 min entre chaque échantillon d'un même site, et 2) L'échelle annuelle de la campagne d'échantillonnage.

A l'échelle de l'échantillonnage entre 2009 et 2015, le prélèvement de 350 échantillons de fluides hydrothermaux a permis de mettre en évidence l'existence d'un fluide hydrothermal refroidi (~100–150°C) dans la roche encaissante poreuse et qui est proche du fluide hydrothermal focalisé chaud. Ce fluide hydrothermal refroidi conductivement est complémentaire de celui envisagé dans le modèle de réchauffement conductif de l'eau de mer par la proximité du fluide chaud. Nous aurions ainsi deux compartiments isolés qui échangent de la chaleur en subsurface depuis la zone de décharge des fluides hydrothermaux de haute température qui sont, quant à eux, focalisés. Ce fluide montre une origine commune avec le fluide chaud focalisé, de par sa concentration en Cl qui est similaire à celle du fluide de haute température, mais qui est caractérisée par une concentration systématiquement plus faible en Si (~2mM). Les occurrences de ce type de fluides interviennent à une échelle de temps inférieure à l'heure. Ces observations impliquent que cet emmagasinement de fluide est très localisé au site de décharge. Une telle dynamique est à rapprocher aux observations de saut ou de chute épisodique des températures enregistrées par les sondes de température autonome (Barreyre et al., 2014). Ce fluide local qui a perdu du Silicium par précipitation de quartz et/ou de silice amorphe, participe probablement intensément à la formation du stockwork. Ainsi, des processus très locaux de subsurface sont à l'œuvre et ne sont détectables qu'en échantillonnant abondamment et à un pas de temps resserré.

A l'échelle pluriannuelle, nous ajoutons une base de données de 6 ans d'échantillonnage des mêmes sites répartis partout sur le champ hydrothermal, à laquelle j'ai participé pendant 3 ans. A partir des données de la littérature et ce malgré un gap d'échantillonnage de 9 ans entre 1997 et 2008, les fluides de Lucky Strike sont étudiés depuis 22 ans, ce qui forme la plus grande série temporelle de composition de fluides pour une dorsale lente. Entre 2013 et 2015, les fluides de Tour Eiffel et de Montségur en comparaison avec ceux de Capelinhos montrent des estimations de pression et de température de la zone de séparation de phase cohérentes entre elles. Les fluides de Montségur et de Tour Eiffel étaient les plus appauvris en Cl dans les années 1990 et ont une couverture temporelle qui s'étale sur 12 ans. Nous pouvons donc utiliser le géothermobaromètre Si-Cl sur ces 2 sites pour suivre la variabilité

des conditions P et T de la zone de séparation de phase à l'échelle annuelle. L'étude de ces variations depuis 1993 montre une tendance qui reste stable à une température autour de 425–440°C et à une pression comprise entre 390 et 380 bars, équivalente à 2800 à 2600 m de profondeur. Quelques évènements ou excursions vers des profondeurs/pressions moins élevées (P entre 360–340 bars, équivalent à 2200-2400 m sous le plancher océanique) sont toutefois à noter à la suite d'évènements sismiques enregistrés par les OBS en Avril-Juin 2009, Août-Septembre 2011 et Octobre 2012 (Crawford et al., 2015) ou par des données géochimiques avec des concentrations élevées en CO₂ en 2008 et 2010 (Pester et al., 2012; Rommevaux et al., soumis). Ces variabilités suggèrent que la zone de remontée des fluides depuis la zone de séparation de phase peut être perturbée par des évènements profonds et se répercuter sur la chimie du fluide à la décharge. Ce genre d'observations n'a jamais été fait jusque-là sur un champ hydrothermal de dorsale lente.

Par ailleurs, le rapport élémentaire Ca/Na est un bon indicateur des processus d'altération, en particulier de l'albitisation. Dans les années 1990, le rapport Ca/Na a augmenté globalement, ce qui est cohérent avec une augmentation de degré d'altération du substratum. Cependant depuis 2008, tous les groupes de sites semblent indiquer des variations en « dents de scie », la valeur la plus basse ayant été atteinte en 2011. Ces rapports bien qu'inégaux selon les groupes étudiés, ne montrent pas forcément les mêmes degrés d'altération. La séparation de phase va avoir tendance à appauvrir préférentiellement le Ca dans la phase vapeur, comme l'atteste le très faible rapport Ca/Na à Capelinhos par rapport aux autres groupes. Seuls les sites du sud-est montrent un fort rapport Ca/Na qui ne peut pas être attribué à la séparation de phase. Cela suggère une altération accrue par rapport aux autres sites.

Les temps de résidence différents entre Capelinhos et les autres groupes autour du lac de lave fossile, sont marqués par des différences de température calculée dans la zone de réaction. Le temps de résidence dans la zone de remontée est relativement long autour du lac de lave fossile et se traduit par un refroidissement conductif marqué. Ce processus provoque une perte significative des éléments tels que le Fe et le Mn, puisque les fluides issus du champ de Lucky Strike sont 3-4 fois plus appauvris en Fe que ceux de Capelinhos. Cette perte de Fe peut s'expliquer par la formation de pyrite ou d'autres minéraux du facies schiste vert, correspondant à un stockage de ~60% de la quantité de Fe mobilisée dans la zone de réaction. Nous proposons que les plus faibles flux de métaux à Lucky Strike ne

sont pas dus à un substrat très altéré, mais sont plutôt les conséquences d'un refroidissement conductif accru en subsurface dans la zone autour du lac de lave fossile.

Dans la zone de remontée, l'impact des processus affectant la composition des fluides peut être appréhendé par le couplage des concentrations élémentaires en Sr et Li corrigées de l'effet de séparation de phase et des compositions isotopiques $^{87}\text{Sr}/^{86}\text{Sr}$ et $^7\text{Li}/^6\text{Li}$. Les mesures des isotopes du Li montrent une signature des fluides très proche de celle du basalte. Ainsi, en utilisant ces compositions isotopiques et les concentrations en Li corrigées, nous obtenons des valeurs du rapport eau-roche, i.e. W/R, comprises entre 1 et 2 pour tous les groupes de sites décrits. Cette valeur confirme l'hypothèse d'un substratum basaltique peu altéré. Par contre, la diversité des compositions isotopiques en Sr des fluides a révélé que 15–20% du Sr en solution étaient d'origine eau de mer résiduelle. Cette contribution résiduelle en Sr induit des rapports W/Rs calculés supérieurs à 5 mais qui se répartissent néanmoins en deux groupes distincts. Les groupes du NE et SW présentent des rapports W/Rs de 5 identiques à ceux de Capelinhos, alors que les groupes du SE et du centre montrent, quant à eux, des rapports W/Rs plus élevés à 6-7. Cette variabilité des rapports W/Rs retranscrit pour ces deux groupes de sites soit un stade d'altération plus élevé soit une influence de précipitation/dissolution de minéraux de type anhydrite sur le parcours de remontée de fluide.

L'effet de précipitation/dissolution de minéraux secondaires peut être évalué à partir de la distribution des terres rares dans les fluides hydrothermaux. En nous basant sur la diversité des spectres normalisés aux chondrites des fluides purs, nous pouvons observer l'effet de séparation de phase se traduisant par un enrichissement relatif en terres rares légères dans les phases les plus salées. L'anomalie en Eu qui est principalement due à une valence 2+, différente des autres terres rares qui ont une valence 3+, montre une affinité des terres rares avec le cycle géochimique du Sr, cohérent avec des rayons ioniques similaires dans ces conditions très réductrices. Ainsi l'étendue de l'anomalie en Eu va être contrôlée par le degré d'albitisation du substratum.

Les terres rares mesurées dans le panache proximal entre 150 et 50°C ont subi un piégeage important, par incorporation ou adsorption dans les particules précipitées, avec des concentrations mesurées systématiquement inférieures aux concentrations théorique de mélange entre les fluides purs et l'eau de mer environnante. Cependant les anomalies en Eu calculées pour le mélange théorique entre les 2 pôles et l'anomalie calculée pour les échantillons mesurés du panache sont cohérentes ce qui implique que la spéciation des

éléments n'influence pas le piégeage observé. L'étude des isotopes de Nd a montré, en plus du piégeage, que des phénomènes de re-dissolution de particules avaient lieu dans le panache. Ceci confirme l'existence d'un phénomène de « ridge exchange », équivalent à celui nommé « boundary exchange », et qui est observé aux interfaces océan–plateforme continentale et qui est capable de modifier la composition isotopique en Nd sans en changer la concentration. Etant donné la répartition des sites hydrothermaux sur les dorsales, il est clair que ce phénomène pourrait former une composante importante pour contraindre le bilan chimique de l'eau de mer.

Au cours de cette thèse, j'ai pu établir un classement cohérent des sites hydrothermaux selon leurs caractéristiques géochimiques et isotopiques et j'ai proposé un nouveau modèle de circulation de fluide hydrothermal basé sur des campagnes d'échantillonnage exhaustif. A travers une étude spatio-temporelle de composition des fluides hydrothermaux entre 1993 et 2015, j'ai pu mettre en relation la chimie des fluides et les phénomènes détectés par des mesures géophysiques (séismicité, température *in-situ*). D'une part, l'étude des terres rares dans les fluides purs apporte des informations du contrôle minéralogique sur l'Eu en subsurface. D'autre part, l'étude des concentrations en terres rares du panache hydrothermal est très prometteuse pour contraindre l'impact des flux hydrothermaux sur la composition chimique et isotopique de l'océan, en particulier le cycle biogéochimique du Nd dans l'océan.

Mises bout à bout, ces observations montrent la voie à suivre pour les années futures. Les variations chimiques, pour les fluides et physiques, pour la croûte océanique en subsurface, sont concomitantes. Cependant, les moyens d'avoir un suivi temporel de la composition des fluides ne sont pas aussi développés que pour l'équipement géophysique (sonde de température, OBS). Un lien doit être fait entre l'échelle de temps et le pas de l'échantillonnage des fluides et les mesures *in-situ* des paramètres physiques. En ce sens, un projet de préleveur *in-situ* autonome de fluides de haute température est développé au GET en collaboration avec TOP industrie et va répondre à cette problématique. Un tel système pourrait être couplé à des capteurs de température et prélever le fluide pur lors des événements épisodiques repérés par les actuelles sondes de température autonome (Barreyre et al., 2014). Ces événements montrent à la fois des chutes de température de l'ordre de 150°C, ou des hausses de température d'une dizaine de °C et s'étalent sur 1 à 10 jours. L'échantillonnage de telles périodes de temps pourrait donner des éléments de réponse aux hypothèses émises durant cette thèse.

D'autres projets de collaboration avec des équipes américaines ont lieu en ce moment au sein de l'observatoire pour mettre en place un capteur de Cl in-situ à Lucky Strike. Ce capteur de chlorinité *in-situ* a montré son efficacité pour lier des phénomènes physiques et les compositions chimiques des événements hydrothermaux dans un contexte de dorsale rapide. Une telle approche pourrait apporter des éléments complémentaires sur la diversité de salinité en contexte de dorsale lente. Notamment, couplée à de la modélisation de circulation de fluide bi-phasique, l'hypothèse du contrôle par la structure de la croûte et la répartition de la porosité sur la composition des fluides pourrait être plus amplement discutée. Ces 2 projets de préleveurs et capteurs pourront se baser sur le modèle de circulation proposé dans cette thèse.

De plus, le phénomène de dissolution de phases minéralogiques secondaires observé *via* les isotopes du Nd dans les fluides du panache hydrothermal pourrait être une source de modification isotopique du Nd dans l'océan à grande échelle, analogue à ce qu'on a déduit des mesures de Fe provenant du panache hydrothermale de l'EPR jusqu'à 4300 km de distance de la dorsale (Resing et al., 2015). Pour confirmer un tel effet, d'autres analyses pourraient être effectuées pour tester les effets des contextes magmatiques (EPR), tectonique (faille de détachement, 13°N MAR), en plus des informations fournies par Lucky Strike (à la fois en contexte tectonique et magmatique). Ainsi il serait possible d'améliorer l'évaluation de l'impact global de l'hydrothermalisme aux dorsales sur le bilan chimique du Nd dans l'océan.

CONCLUSION AND PERSPECTIVES

Black smoker fluids from the Lucky Strike hydrothermal field located at 37°N on the Mid Atlantic ridge have been studied during this PhD Thesis. This hydrothermal field is one of the largest on the seafloor and the vents display a chemical variety at the discharge that is yet to be explained. This thesis was carried out in the context of a deep sea observatory. Therefore, an important focus was brought on the systematic sampling of hydrothermal fluids during the three MoMAR cruises (in 2013, 2014, and 2015) I have been involved in. The chemical analysis performed on–shore allowed to build a complete dataset that complement the ones collected by the in–situ instruments deployed each year. This chemical dataset is unique in the context of a slow spreading ridge. Building this dataset needed some analytical or protocol developments in order to validate Rare Earth Element (REE) and Li elemental and isotopic composition measurements as the Li isotope measurement was not done at the GET laboratory for this kind of samples.

Hydrothermal fluids are charged in salts. Unlike seawater, standard solution with internationally recognized certified concentration for major and/or trace elements does not exist for this type of samples. Certified solutions are commonly used in the scientific community to validate the measurement of concentrations. A special care has been brought for Li concentration analysis to ensure reproducible and accurate measurements. The Li isotopic analyses need to be accurate and precise at specific Li concentration to optimize the standard bracketing method. The issue with Li measurements, as for many other elements, is that no international standard exist for such concentrations in a salted matrix of that of black smokers. Some standards do exist for trace elements in seawater (e.g. NASS 6 is a seawater standard solution certified for the following elements: As, Cd, Cr, Co, Cu, Fe, Pb, Mn, Mo, Ni, U, V, and Zn at concentration range between 0.1 to 10ppb) but there is no equivalent for hydrothermal fluids. Because dissolved elements are related to salinity, we used the IAPSO (seawater reference with a certified salinity) as a standard for calibration and control on major elements concentrations (Ca, K, Na, Br, Cl, SO₄, and Mg) and trace element (Sr, Cs, Rb, and Li). We obtained excellent results in Li concentration measurement in salted matrix (i.e. IAPSO), allowing us to be confident in the measured concentrations in the fluids. Therefore the Li isotope compositions are also of a good quality as confirmed by analysis of standard Li materials (IAPSO and IRMM-16).

During this thesis, the discovery of a new high temperature venting site named Capelinhos, and located out of the fossil lava lake vicinity, highlights that hydrothermal circulation underneath the Lucky Strike hydrothermal field is of broader scale. It was then necessary to propose a new hydrothermal circulation model by re-interpreting the chemical data of the fluids of Lucky Strike including fluids from Capelinhos. Hydrothermal sites have been classified in groups according to their geographical position referenced to the lava lake and based on their Cl concentrations. This re-interpretation only takes into account the fluids sampled in 2013 that cover most of the known active sites. It also takes into account geophysical constraints acquired through the deep-sea observatory such as autonomous temperature sensors and microseismicity. The trace element distribution compared to the Cl concentration of each group highlights that the whole hydrothermal field is fed by a unique deep rooted source. The application of several geochemical tools allows for the estimation of pressure and temperature conditions of water–rock interactions (Si–Cl geothermobarometer; quartz solubility and Fe/Mn geothermometer). These estimations differ for Capelinhos fluids when compared to the other groups. The first estimation based on Si–Cl geothermobarometer relates to the phase separation zone while the Fe/Mn and quartz solubility estimation relates to the reaction zone (in the greenschist facies conditions). These estimations highly depend on the hypothesis that are made. Phase separation has been estimated at 390 bars (~2600 mbsf) and 438°C. This estimation is equivalent to that proposed by Fontaine et al. (2009) for fluids of the Tour Eiffel site and collected in 1994 and 1997. Nevertheless, if we make the hypothesis that quartz and greenschist facies mineral reach equilibrium concomitantly, then the estimated P and T conditions depict the roof the reaction zone. This indicates a temperature and pressure of ~400°C and 340 bars respectively for Capelinhos, while estimations range from 350 to 380°C and ~300 bars for the other groups. These two estimations are not independent from each other because they are both based on the quartz solubility assumption. However, we can consider that the phase separation zone depicts the beginning of fluid upflow, so that we can determine relatively the residence time of the fluid within the upflow zone as being related to the difference between the estimated roof of reaction zone and the phase separation zone. Therefore, Capelinhos, with a deep and hot roof of reaction zone, has a short residence time compared to the other sites, which is coherent with its low density fluids (high buoyancy). The more Cl enriched groups exhibit relatively longer residence time in the upflow zone, and potentially a marked interaction with the substrate.

Moreover, the Cl concentration diversity at Lucky Strike, and particularly its variability with time (Y3 and Crystal show Cl concentrations lower than seawater in the 1990s but have higher concentrations at the present time), is linked to the crustal structure. The chemical diversity is controlled by physical and structural parameters such as large faults (F2 for Capelinhos) and the shallow permeability of the seismic layer 2A (thicker to the West of the lava lake; Arnulf et al. 2011).

To summarize, the phase separation zone triggers the upflow of a homogeneous fluid. Brine segregation is more or less efficient depending on physical controls and fracturing of the crust and is responsible for the chemical diversity observed at the discharge. Capelinhos fluids are relatively far from the axial magmatic lens but preserved a chemical composition that is representative of a deeper origin. However, the fluids located around the lava lake will evolve further by spending relatively more time in the upflow zone, and therefore by recording a chemical signature coherent with more pronounced water-rock interactions.

From this model, we reinterpreted the temporal variations between 1993 and 2015 of the chemical composition of hydrothermal fluids at two time scales: 1) the sampling time scale (~10min) and 2) the annual time scale.

At the sampling time scale, between 2009 and 2015, 350 samples were collected. The chemical dataset provided evidence of a conductively cooled hydrothermal fluid (~100–150°C) within the rock and closed to the focused fluid. This cooled fluid is complementary to the conductively heated sweater inferred from Cooper et al. (2000). So at the subsurface, two compartments exchange heat without (or limited) matter exchange. This cooled fluid originates from the focused hot fluid as shown by identical Cl concentrations, but is characterized by a systematic lower Si concentration (~2–3mM). The fact that these fluids are sampled in such a small time scale implies that their dynamics are controlled by localized subsurface process. This dynamics could be linked to the episodic temperature drops observed by the autonomous temperature probes (Barreyre et al., 2014). This hydrothermal fluid, although cooled probably participates to the stockwork formation by quartz and/or amorphous silica precipitation. These types of processes are only observed thanks to repeated and dense sampling and fluid collection at short time scale.

Regarding the long-term time-scale, the dataset covers 22 years of sampling (1993 to 2015) with a 11 years gap between 1997 and 2008. We added up to 6 years of chemical end-members at the same sites at the Lucky Strike hydrothermal field since the installation of

the observatory. This study constitutes the longest time series study of hydrothermal fluids on a slow spreading ridge. Between 2013 and 2015, Tour Eiffel and Montségur fluids show the same estimations of P and T conditions for the phase separation zone as Capelinhos does. This allows to infer the P and T variations for phase separation, through the Si-Cl geothermobarometer, for the complete time series for these two sites, each one having a 12-year long fluid records. Since 1993, the estimation seems stable between 425–440°C and 390–380 bars (2800–2600 mbsf). Some events are nevertheless noticeable indicating P and T conditions of equilibration toward shallower conditions (360–340 bars), which correspond to seismic activity recorded by OBS in 2009, 2011, 2012 (Crawford et al., 2015) or to CO₂ increase in the fluid in 2008 and 2010 (Pester et al 2012; Rommevaux et al., submitted). This indicates that the upflow zone may undergo some deep changes which are recorded somehow by the fluid. This cross-correlation between geophysical and geochemical observations has never been obtained at a slow spreading ridge, thus far.

Moreover, the Ca/Na ratio is a good indicator of substratum alteration through albitisation. Since the 1990s, the Ca/Na ratios of fluids have increased, which suggests that the substratum is albitized. Since 2008, the Ca/Na variations seem to behave as a boom and burst pattern with the lowest value attained in 2011. Comparison of groups shows different Ca/Na ratios, which are not necessarily linked to the alteration state, but rather to the partitioning of Ca during phase separation. However, the high Ca/Na ratio of fluids from the South Eastern group is not explained by Ca partitioning during phase separation which indicates that for this area, the substratum is highly albitized compared to the other.

The difference of residence time between Capelinhos and the other groups is marked by the temperature difference at the roof of the reaction zone. This indicates an enhanced conductive cooling for the fluids around the fossil lava lake by loss of elements such as Fe and Mn that are currently 3 to 4 time less concentrated than for Capelinhos fluids. This loss can be explained by the precipitation of pyrite for instance or other minerals belonging to the greenschist facies. If we consider that Capelinhos are representative of the fluid chemistry without Fe loss, then for the other groups, ~60% of Fe mobilized in the reaction zone is stored by mineral precipitation in the upflow zone. Therefore, the low Fe and Mn concentrations observed at Lucky Strike are due to mineral precipitation and stockwork formation rather than an altered substrate. In the upflow zone, fluid-rock interactions can be inferred by coupling the Sr and Li concentrations and isotopic compositions (⁸⁷Sr/⁸⁶Sr and ⁷Li/⁶Li). The Li isotopic composition measured in the fluid are very close to the basaltic

signature which indicates limited Li isotope fractionation by secondary mineral formation, and quantitative leaching of basaltic Li. Calculation of W/R ratios based on Li isotopic composition and concentration indicates values between 1 and 2, coherent with interactions and leakage of a relatively fresh basalt. However, the Sr isotopic compositions display a systematic diversity between groups with the SE groups displaying $^{87}\text{Sr}/^{86}\text{Sr}$ values at 0.7043 while the other groups display values at 0.7039-0.704. The coupling of Li and Sr isotopic signatures indicates that 15–20% of Sr residual originates from seawater. The W/R ratios determined by Sr concentrations and isotopic signatures argue that groups from the North East, South West and Capelinhos are around 5 but the South East and Central sites show W/R slightly higher (at ~7–8). Again, this could be related to enhanced albitisation and/or anhydrite dissolution that would affect the geochemical cycle of Sr.

The effect of precipitation/dissolution of minerals can be evaluated under the scope of REE concentrations in hydrothermal fluids. Based on the diversity observed for the chondrite normalized REE patterns we can infer the effect of phase separation on their distribution at the scale of the hydrothermal field. Also the Eu anomaly is found to be due to its speciation and valence in a reduced environment which behave differently than the other trivalent REE. As Eu is bivalent in such environment, it behaves like Sr and can be incorporated in Sr bearing minerals such as anhydrite/albite. Therefore, the magnitude of Eu anomaly is controlled by the alteration of the substratum, and particularly by albitisation.

Dissolved REE have also been measured in the buoyant plume at temperature between 150°C and 20°C. The measurements show that scavenging is occurring through adsorption/incorporation into precipitated particles. The measured REE are systematically lower than expected by conservative mixing but the calculated Eu anomaly is equivalent to that obtained for conservative mixing. This means that the speciation does not affect the efficiency of scavenging. The Nd isotopic compositions of buoyant plume fluids have also been measured and their mixing have been modeled. Some measured Nd isotopic compositions indicate that scavenging occurs which removes 90% of the initial Nd. This observation is not coherent with the magnitude of the scavenging observed from the measured concentrations. This can only be explained by redissolution of particles formed in a more seawater dominated part of the plume. This tends to confirm the process of “ridge exchange”, equivalent to the “boundary exchange” observed at the continent–ocean interface. These processes are able to change the Nd isotopic composition without changing its concentration. The hydrothermal activity is found everywhere on the mid-ocean ridge

and back arc basin, therefore this ridge exchange could have a real impact on the Nd budget of the ocean.

During this thesis, I was able to classify the hydrothermal sites based on their geochemical and geographical characteristics and to propose a new model for hydrothermal fluid circulation. Through our spatial and temporal study of the fluid composition between 1993 and 2015, I was able to link fluid chemical composition and process detected by geophysical measurements. REE study of pure fluid samples indicates that the magnitude of Eu anomaly is controlled by substratum mineralogy. The study of dissolved REE in a buoyant plume is of great interest to constrain the Nd isotopic budget of the ocean.

Chemical variations of the fluids are accompanied by geophysical events (temperature drops, seismic swarms...). However, the means of temporal survey of fluid composition are not as developed as for geophysical surveys. Therefore a link should be done between the time scale of fluid sampling and in-situ measurement of physical parameters. The GET is currently developing an automated pure fluid sample device in collaboration with TOP industry. This device will be able to be linked to the seafloor stations and be programmed to sample concomitantly to a geophysical event, as temperature drops recorded by HT probes. Sampling of pure fluid during this kind of event would greatly improve the comprehension of the system at the subsurface-chimney scale.

Other project of collaboration are actually taking place at Lucky Strike such as the installation of an in-situ Chlorinity sensor. This sensor has proved to be efficient to decipher tidal signals from episodic brine flush on a fast spreading ridge. Such approach would be of great interest to explain further the Cl diversity and dynamics of the fluids from the LSHF related to a slow spreading ridge and could provide broader advance to the hypothesis proposed for a structural control on the Cl concentrations though different brine segregation. These 2 projects of in-situ instruments probing the fluid chemistry will benefit from the proposed model of circulation.

Furthermore, the dissolution process observed through Nd isotopic compositions in the buoyant fluid are of great interest in the ocean chemical budget. The importance of hydrothermal activity in that domain has recently been restated by the study of Resing et al. (2015) who were able to trace an EPR hydrothermal plume to as far as 4300 km east of the ridge in the Pacific Ocean through Fe concentration. To confirm such an impact, the same kind of measurement could be performed under different setting such as magmatic

accretion context (EPR), tectonic accretion (Ocean Core Complex, 13°N, MAR) besides the information brought by Lucky Strike (tectonic and magmatic context). This would facilitate a global scale model for the ocean chemistry.

References

Arnulf A. F., Singh S. C., Harding A. J., Kent G. M., Crawford W. (2011) Strong seismic heterogeneity in layer 2A near hydrothermal vents at the Mid-Atlantic Ridge: Seismic heterogeneity in Layer 2A. *Geophys. Res. Lett.* **38**. doi:10.1029/2011GL047753

Barreyre, T., Escartin, J., Sohn, R., Cannat, M., Ballu, V., Crawford, W.C., 2014. Temporal variability and tidal modulation of hydrothermal exit-fluid temperatures at the Lucky Strike deep-sea vent field, Mid-Atlantic Ridge. *J. Geophys. Res.-Solid Earth* 119, 2543–2566.

Crawford, W.C., Cannat, M., Escartin, J., Baillard, C., Daniel, R., 2015. Variations in seismicity within Lucky Strike volcano (37°17'N MAR) from 2007-2015, from a seafloor seismometer network. Presented at the AGU Fall Meeting, San Francisco.

Fontaine, F.J., Wilcock, W.S.D., Foustoukos, D.E., Butterfield, D.A., 2009. A Si-Cl geothermobarometer for the reaction zone of high-temperature, basaltic-hosted mid-ocean ridge hydrothermal systems: Si/Cl-inferred P–T in MOR hydrothermal systems. *Geochem. Geophys. Geosystems* 10. doi:10.1029/2009GC002407

Pester, N.J., Reeves, E.P., Rough, M.E., Ding, K., Seewald, J.S., Seyfried, W.E., 2012. Subseafloor phase equilibria in high-temperature hydrothermal fluids of the Lucky Strike Seamount (Mid-Atlantic Ridge, 37°17'N). *Geochim. Cosmochim. Acta* 90, 303–322. doi:10.1016/j.gca.2012.05.018

Resing, J.A., Sedwick, P.N., German, C.R., Jenkins, W.J., Moffett, J.W., Sohst, B.M., Tagliabue, A., 2015. Basin-scale transport of hydrothermal dissolved metals across the South Pacific Ocean. *Nature* 523, 200–203. doi:10.1038/nature14577

LISTE DES FIGURES

Figure I - 1 From Beaulieu et al., 2015. The map shows the repartition of hydrothermal vents on the mid-ocean ridge at different spreading rates. 18

Figure I - 2 Cartoon of the ridge morphology dependent on the spreading rate. This show the fast, intermediary and slow spreading ridge type (modified from MacDonald 2001). 19

Figure I - 3 Classical representation of the oceanic structure associated to P wave's velocity. Modified from Pomerol et al., 2006. 20

Figure I - 4 Modified from Carlson (2011). Seismic and lithologic profile from 2 IODP core, 504B on the Nazca plate and 1256D on the Cocos plate. Tr: Transition zone; G: Gabbros section..... 21

Figure I - 5 Measured Heat Flux as a function of Age of the oceanic crust. From Elderfield and Schultz (1996). Dashed line is the predicted heat flux based on geophysical model based on (McKenzie, 1967). Solid line is average measurements of heat flux by thermistor. The discrepancy between observed and predicted heat fluxes is very low after 65 Ma and maximal for Age < 1Ma, at ridge axis. 23

Figure I - 6 Photograph of « Active Pot » black smoker in the Irinovskoe hydrothermal field (13°N) taken during the ODEMAR cruise in 2013 by ROV dive Ifremer/CNRS. 24

Figure I - 7 Cartoon of hydrothermal circulation illustrating the geographical extent of fluid (High or low temperature) within the crust..... 25

Figure I - 8 Cartoon of the general hydrothermal circulation cell (modified from Alt, 1995). This shows the general composition of the oceanic crust..... 26

Figure I - 9 Cartoon of the recharge zone of a hydrothermal system (modified from Alt, 1995) 27

Figure I - 10 Diagram showing the mineral assemblage found as a function of depth in the basaltic substratum of the 504B Hole from IODP leg. This is thought to represent a good example of a recharge zone in a basaltic substratum in general (Alt, 1995). 29

Figure I - 11 Cartoon of the TAG hydrothermal field and hydrothermal circulation and mineralogy in the subsurface inferred from 4 drilled hole (modified from Hannington et al., 1998 and Tivey, 2007). 31

Figure I - 12 Modified from Haymon, (1983). Schematic growth of hydrothermal chimney in 2 stages (1: juvenile stage; 2: mature stage). 32

Figure I - 13 Pressure vs. Temperature diagram showing the two-phase boundary curve for seawater equivalent (from Charlou et al., 2000). Sites from the MAR are represented at discharge conditions.....	35
Figure I - 14 From Fontaine and Wilcock, (2006), cartoon showing the brine and vapor segregation at depth.	36
Figure I - 15 From Pester et al., (2015), (a) shows the partitioning of elements M measured for different experimenst in the vapor phase. (b) and (c) show the partitioning for Ca and Zn with different starting fluid concentrations.	37
Figure I - 16 Carbon and oxygen stable isotope of carbonate concretion from different settings. From Leleu et al. (2016) in Annexe 1, it shows the diversity of carbonate precipitation through stable isotope signatures.....	43
Figure II - 1 Map of the Northern Mid Atlantic ridge showing the major segments from Langmuir et al. (1997).....	56
Figure II - 2 Bathymetric map of the Lucky Strike segment from Ondréas et al. (2009). The lines show the location of the main axial valley bounding faults. The black square indicate the central volcano.	57
Figure II - 3 From Singh et al. (2006). Bloc diagram showing the Lucky Strike Hydrothermal Field bathymetry with the structure of the oceanic crust beneath.	59
Figure II - 4 Modified from Humphris et al. (2002). Left: bathymetric map of the LSHF showing the 3 tectonised volcanic cones and the central depression where is situated the fossil lava lake. Right: Geological seafloor map showing the nature of the rocks at the surface surrounding the fossil lava lake.....	60
Figure II - 5: Microbathymetry map of the ucky Strike Hydrothermal field. The dashed area represent the central fossil lava lake. The grey dots are the sites from where chemical data are available in the literature or in this study.....	61
Figure II - 6 From Pester et al. (2012). P and T diagram that summarize the geophysical and geochemical constraint on the deep hydrothermal processes. Blue lines represent the 2 phase boundaries, the Si–Cl box represent the P and T conditions inferred for the phase separation zone (Fontaine et al., 2009). Si isopleth are calculated for quartz solubility using the model of Foustoukos and Seyfried (2007). Fe/Mn ratios represent the range of	

temperature inferred from the Fe–Mn geothermometer developed by Pester et al. (2011).
.....62

Figure II - 7 From Cooper et al. (2000), conceptual model for the diffuse flow system at Lucky Strike.....63

Figure II - 8 Cartoon of the Emso Azores node infrastructure (www.fixO3.eu). At the seafloor, the two stations sends data to the buoy BOREL. The Buoy then sends the data to the Ifremer center on shore.65

Figure II - 9 Subsurface depth of a permeability change inferred from phase lag response to tidal change in the T sensor from Barreyre and Sohn (2016). AML: Axial Magmatic Lens.....67

Figure II - 10 From Escartin et al. (2015), microbathymetry map of the central volcano of the Lucky Strike segment. Red contours represent hydrothermal deposits identified in the microbathymetry, and numbered following the classification from Barreyre et al. (2012). Black dots represent active vents. Brown dashed lines represent the limits of the AMC (Combiér et al., 2015; Singh et al., 2006).Blue areas represent the location of seismic clusters in the crusts (Crawford et al., 2013).68

Figure III - 1 Photographs of the R/V Pourquoi pas? on the Horta port (Faial island, Azores, A and B), C: photograph of the “Pourquoi pas?” and the buoy Borel (Ifremer/CNRS) on top of the Lucky Strike hydrothermal field, on the North Atlantic Ocean (37°N).....77

Figure III - 2 Photographs of the ROV on board the ship during maintenance (on the left), while sampling rocks with maestro (top right), and under water photograph of the oceanographic robot (bottom right).79

Figure III - 3 Photographs of the ROV container. On the left, the two scientist in charge of the dive program. On the right, ROV pilots, one is in charge of the Maestro arms and the other control the whole ROV mobility.79

Figure III - 4 Photograph of a Titanium syringe with its handler during the cleaning process (top) and a cartoon showing the different part composing the sampler.....80

Figure III - 5 High temperature venting site Capelinhos. A and B show the temperature measurement using the HT temperature probe of the ROV Victor6000, B is a close up of the vent orifice where the temperature probe is inserted for real-time temperature

measurement. It shows the position to take for fluid sampling. C and D pictures illustrates high temperature fluid sampling using gas-tight Ti syringe. A direct comparison between pictures B and D shows that snorkel of gas-tight Ti syringe is positioned at the same location as the temperature probe of ROV Victor6000, ensuring sample collection at the hottest hydrothermal fluid discharge.82

Figure III - 6 ROV basket facing the Capelinhos vent site during the 2015 cruise. The ROV basket contains 8 Ti samplers, 2 Biobox (Sterile boxes for biologic sampling purposes), and 2 HT autonomous probe, positioned in vent after fluid sampling at the same location. The photofragh is taken from the cemra placed on the ROV arm Sherpa.83

Figure III - 7 Photographs taken during the process of sample extraction in MoMARsat 2013. A: Mounting of a stainless steel canister to extract the gases; B: Extracting the fluid with a plastic syringe to be filtered through a 0.45µm Millipore filter and dispatched in several aliquots (C) Labelled aliquots of fluids and gazes dispatched on the working table.85

Figure III - 8 Drift correction of samples framed by standards and blanks. Drift is extrapolated from a standard to the following standard in the sequence. Correction is applied to measured value of a sample according to the extrapolation of the standard measurement deviation. Solid line is the “true” concentration of the standard and dashed lines and 95% confidence interval.87

Figure III - 9 Description of REE separation through resin exchange protocol93

Figure III - 10 Reported seawater Li concentration in literature. Question mark corresponds to methods not mentioned within reference. The grey area corresponds to lower and upper limits of calculated IAPSO Li concentration value based on S(‰)=34.991 g l⁻¹ and Li-chlorinity ratio from Fabricand et al. (1966) and Riley and Tongudai, (1964), respectively.98

Figure III - 11 IAPSO seawater Li concentration determination. Full triangles are standard addition technique applied with calibration from 0.2 to 4 µg g⁻¹. Triangles are standard addition technique applied with calibration from 0.2 to 5 µg g⁻¹. Full square is the direct measurement of IAPSO. Grey areas corresponds to published values of Lucky Strike hydrothermal fluids and North Atlantic interstitial waters (Charlou et al. 2000; Gieskes et al. 1985). 100

Figure III - 12 From Tomascak (2004), Ratio of $^{7/6}\text{Li}$ as a function of percentage of elution. It shows that the first fraction of Li eluted is significantly heavier until ~10% Li eluted then stable. At ~90% of elution, ^6Li increase and the $^{7/6}\text{Li}$ ratio is lower. B: From Jeffcoate et al. (2004), the figure show $\delta^7\text{Li}$ as a function of Na/Li ratio in solution. Addition of Na in solution tends to lower the measured value of $\delta^7\text{Li}$ 102

Figure III - 13 Description of the Li separation protocol through resin exchange column. All the acids used are prepared by dilution of bi-distilled acid. 103

Figure III - 14 $\delta^7\text{Li}$ as function of Li concentration at 3 different bracketing standard concentrations. The figure shows the effect of the difference between sample and standard concentration on the $\delta^7\text{Li}$ measurement. 105

Figure IV - 1 Bathymetric map of the Lucky Strike central volcano. Active hydrothermal vents are represented. Sapins=Sap. Crystal=Cr.; South Crystal= Sth Cr.; White Castle=WC; Isabel=Is.; Tour Eiffel=TE; Aisics= ASC; Montsegur= Mr, Capelinhos=Cap. Modified from Humphris et al., 2002. 118

Figure IV - 2 Overview of vent sites diversity. Snapshots of ROV photographs (Ifremer-CNRS, MoMARsat 13), A, B: Capelinhos; C: aisics; D: Montsegur; E: Cyprès; F: White Castle; G: Crystal; H: Sintra. A and B shows candelabra like structure of capelinhos vent site that discharge several focused high T fluid. C and D shows hydrothermal mound at two sites in the South Eastern area. Aisics mound is not as developed as Montsegur but both lack of tall endured chimneys. E, F and G are situated in the North Western area. High T vents display an elongated wall-like structure closely related to underlying faults. H is situated in the declining North Eastern area and have tall endured chimneys which are probably inherited from past intense activity..... 120

Figure IV - 3 Fe, Mn and Si vs. Cl. Diagram a) Fe versus Cl; b) Mn and versus Cl and c) Si versus Cl. These diagram shows non-correlation of these element compared to Cl. .. 127

Figure IV - 4 $\log(\text{Elt}/\text{Cl})$ vs $\log(\text{Cl})$ diagram. Diagram of elt/Cl versus Cl showing the linear relationship between trace element and chlorinity, a proxy for the effect of phase separation. 131

Figure IV - 5 Geochemical information for P and T. a) Quartz geothermobarometer based on Foustoukos and Seyfried (2007b). Points represent Si measured in fluids with calculated

temperature from Fe and Mn geothermometer. Grey dashed lines represent the “classical” approach to evaluate P and T (see text for details). b) Fe and Mn concentration on a logarithm scale (Modified from Pester et al., 2011). Grey line represent basalt alteration line and black dashed lines are isotherms calculated from the Fe/Mn geothermometer. . 136

Figure IV - 6 Fluid circulation. a) Calculated P and T of some vents at equilibria with quartz are presented. P and T were calculated using the Fe/Mn geothermometer of Pester et al. (2011), quartz geothermobarometer (Foustoukos and Seyfried, 2007b) and NaCl-H₂O solution properties (Driesner et al., 2007) (See details in text). Dotted lines represent the depth of the base of layer 2A for western and eastern sites (Arnulf et al., 2011). The red shaded domain represents the range of depth to the top of the axial magma chamber as identified by Singh et al. (2006) and Combier et al. (2015). Grey lines represent fault labeled F1, F1b in Combier et al. (2015), dotted grey line correspond to F2. The blue line represents the inferred P–T path in the recharge zone where cold seawater percolate through oceanic crusts and gradually interacts with rocks. Red lines represents the inferred P–T path in the upflow zone, based on the conditions estimated from fluid chemistry. The grey rectangle represents the phase separation zone estimated from the Si and Cl concentrations in the low salinity fluids (Capelinhos, TE) using the geothermobarometer proposed by Fontaine et al. (2009). b) Modified from Escartin et al. (2015). Cartoon representing the hydrothermal cell under the LSHF. Blue arrows represent downward flow of seawater; red arrows are focused hot fluid moving upward through cracks and faults. Black star represents the hypothetic position of Capelinhos fluid extraction through a high angle fault. Seismic clusters are from Crawford et al. (2013). F1, F1b and F2 from Combier et al. (2015). . . 140

Figure IV- S 1 Diagram of ⁸⁷Sr/⁸⁶Sr as a function of Mg/Sr (a) and SO₄/Sr (b). a) shows the usual way of determining the Sr isotope end-member of fluids. b) is a method for determining Si isotope end-member of fluid by using sulfate. Sulfate in fluids will be dependent on seawater entrained during sampling, as SO₄ is enriched in SW compared to pure hydrothermal fluid. Sulfate will also be dependent on anhydrite. Dissolution of anhydrite could contribute to Ca, SO₄ and Sr concentration measured in the fluid and consequently, Sr isotope signature. Assuming Sr isotope signatures of SW and hydrothermal fluid, dissolution of anhydrite dissolution bias can be corrected as in Fig IV-S1b. Consequently, endmember determined for SW sites are better determined by SO₄/Sr least square regression. When no suspicion of anhydrite dissolution, Mg/Sr should be prefer

d for slightly negative end-member values of SO_4 would overcorrect Sr isotope determination (e.g. Capelinhos)..... 153

Figure V - 1 Micro-bathymetric map of the Lucky Strike Hydrothermal Field. The dashed area represent the different salinity observed from this study. Red dashed area represent the most Cl depleted fluid of Capelinhos. Blue dashed area represent the vapor dominated fluids from the SE of the lava lake. Light purple area represents the Intermediary salinity group in the vicinity of the lava lake limit. The green dashed areas represent the high salinity fluids that are found at the SW and NE of the lava lake. The grey dashed area represent the fluids of the NW areas which are not part of this study. 163

Figure V - 2 Cl, Si, Na, Ca vs Mg diagrams showing the dilution effect of hot fluids by local deep seawater entrainment. Concentrations are in mM. These diagrams are used to determine the endmembers concentration by extrapolation of the least square regression to $\text{Mg}=0$. Groups of sites are presented as explained in Leleu et al., sub. Open circle: capelinhos; Open triangle: central group (Isabel, White Castle, Cyprès); Full square: North Eastern group (Y3 and Sintra); Full circle: South Eastern sites (Aisics, Tour Eiffel, Montsegur Cimendeff); Full triangle: South West group (Crystal, South Crystal, Sapins). 170

Figure V - 3 Fe, Mn, Sr, Li vs Mg diagrams showing the dilution effect of hot fluids by local deep seawater entrainment. Mg concentrations are in mM, Fe, Mn, Sr and Li concentrations are in μM . Symbols are the same as used in Fig V - 2. 171

Figure V - 4 Mixing diagram between hydrothermal fluids and seawater based on Mg concentration. They focus on the low dissolved Si samples. Grey dots are measured black smoker samples. All data presented regroup sample measurements from 2009 to 2015. 179

Figure V - 5 Cartoon of shallow hydrothermal circulation beneath the hydrothermal vents. Modified from Cooper et al. (2000). The silica cemented breccias or slab form an impermeable cap where conductively heated seawater and conductively cooled hydrothermal fluid can mix and sometimes be entrained in the focused fluids. Black arrows represent the high temperature fluids, the grey arrows are the proposed conductively cooled hydrothermal fluid. Dashed arrows represent the conductively heated seawater. 181

Figure V - 6 Si-Cl chart for P and T determinations in the separation phase. Modified from Fontaine et al. (2009). Si and Cl variations are representative of specific P and T conditions. Tour Eiffel endmembers from 1993 to 2015 are represented in a); Montségur endmembers from 1993 to 2015 are represented in b). Both are represented with Capelinhos endmembers from 2013, 2014 and 2015. C) presents the evolution of the P and T estimated based on a and b. Blue dashed line are the observed magmatic CO₂ degassing (Pester et al., 2012; Chavagnac et al., unpublished data). Green dotted line mark the seismic swarms recorded by the OBS network (Crawford et al., 2013, 2015). 186

Figure V - 7 Boxplot diagram presenting the fluid Ca/Na ratios per group of site groups for 2013, 2014, 2015 as a function of the Cl concentration. 188

Figure V - 8 Time series of Ca/Na boxplots of end-members selected for different groups (see text for details). 189

Figure V - 9: Time serie of K/Cl values of the endmember from table V – 2. 190

Figure V - 10 Fe and Mn diagram on logarithmic scales. Grey dots are experimental data from literature. Solid line represent the basalt alteration experiment with a 95% confidence interval (dashed black line). Dotted grey lines are isotherm for basalt experiments at different temperatures. 191

Figure V - 11 ⁸⁷Sr/⁸⁶Sr of fluid samples presented as a function of Mg/Sr and Mg/SO₄. The color code indicate the year of samples collection. Each graph presents the determination of Sr isotope end-member determination. 196

Figure V - 12 $\delta^7\text{Li}$ vs Cl diagram showing that Li isotopes are not affected by phase separation. 197

Figure V - 13 $\delta^7\text{Li}$ vs ⁸⁷Sr/⁸⁶Sr diagram showing the sources for basalt and seawater with mixing curves. MORB values are $\delta^7\text{Li}_{\text{MORB}}=3.4 \pm 1.4$, $\text{Li}_{\text{MORB}}=4\text{ppm}$; $\delta^7\text{Li}_{\text{SW}}=30.5$, $\text{Li}_{\text{SW}}=0.17\text{ppm}$. Grey dots are the measured samples, coloured dots represents calculated endmembers. 199

Figure V - 14 W/R ratio presented for different group and calculated from Sr and Li. Uncorrected from phase separation are indicated in grey. Boxplots regroup the year 2013, 2014 and 2015 for each groups. 202

Figure VI - 1 Micro-bathymetric map of the Lucky Strike Hydrothermal Field. Red dots represent sites sampled in this study. Gray dots represent sites sampled in previous studies.216

Figure VI - 2 Hydrothermal fluid REE pattern normalized to Chondrite (Evensen et al., 1978). Grey solid lines represent the potential source of REE, NADW (Zheng et al., 2016), T-MORB and E-MORB (Hamelin et al., 2013) and plagioclase phenocrysts (Douville et al., 1999).227

Figure VI - 3 Ionic radii (8 coordination number) for each trivalent REE element and Ce^{4+} , Eu^{2+} and Sr^{2+} based on Shannon (1976).228

Figure VI - 4 Nd/Yb ratios compared to Cl concentration in mM.....229

Figure VI - 5 a: Diagram of Eu anomaly (chondrite normalized) against Cl concentration in mM. b: Strontium isotope ratios against Eu anomaly (chondrite normalized).....231

Figure VI - 6 comparison of the proportion of hydrothermal fluid in percent based on magnesium concentration and in situ temperature recorded during sample collection. ..236

Figure VI - 7 NADW normalized REE patterns of hydrothermal fluids from MoMAR 2014, 2015. Red lines indicate the two mixing poles (pure fluid and deep seawater). Blue line represents the measured plume fluid samples.....237

Figure VI - 8 Total REE concentration compared to theoretical concentration (dashed line) as a function of the hydrothermal fluid proportions. Open symbols represent the plume samples, full symbols represent the pure fluid samples.....238

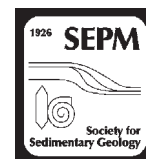
Figure VI - 9 Comparison of elemental concentration measured in the plume sample and the theoretical mixing line between NADW and end-member fluid (solid line) for Ce, Eu and Yb.....240

Figure VI - 10 Proportion of hydrothermal fluid compared to the normalized Eu anomaly. Solid lines are theoretical mixing line between measured endmember fluid and seawater.241

Figure VI - 11 Nd isotope ratios for plume and end-member fluids against their hydrothermal fluid proportion based on temperature. Dashed line mimic an initial loss of Nd of 50, 60, and 90 percent. Grey area represent the error of the model based on the error of the end-member.242

ANNEXE 1:

ACCEPTED ARTICLE IN JOURNAL OF SEDIMENTARY
RESEARCH



TRAVERTINES ASSOCIATED WITH HYPERALKALINE SPRINGS: EVALUATION AS A PROXY FOR PALEOENVIRONMENTAL CONDITIONS AND SEQUESTRATION OF ATMOSPHERIC CO₂

THOMAS LELEU,¹ VALERIE CHAVAGNAC,¹ ADELIE DELACOUR,^{1,2} CATHERINE NOIRIEL,¹ GEORGES CEULENEER,¹ MARKUS ARETZ,¹ CELINE ROMMEVAUX,³ AND SANDRA VENTALON⁴

¹ Géosciences Environnement Toulouse, Observatoire Midi-Pyrénées, Université de Toulouse, CNRS, IRD, Université Paul Sabatier, 14 Avenue Edouard Belin, 31400 Toulouse, France

² Université de Lyon, UJM-Saint-Etienne, Laboratoire Magmas et Volcans, UMR 6524, F-42023 Saint Etienne, France

³ Laboratoire Géomicrobiologie, CNRS, IPGP, Sorbonne Paris Cité, Université Paris Diderot, UMR 7154, Paris, France

⁴ Université de Lille 1, CNRS, UMR 8187 LOG, 59655 Villeneuve d'Ascq, France

e-mail: thomas.leleu@get.obs-mip.fr

ABSTRACT: Travertine are found in ophiolite massifs in association with bicarbonate-depleted hyperalkaline spring waters (pH up to 11.9), in contrast with most continental carbonates (e.g., travertine, tufa, speleothems) that precipitate from calcium bicarbonate-enriched waters. Here travertines formed from bicarbonate-depleted hyperalkaline spring water were subjected to a multidisciplinary and multi-scale approach to evaluate their potential as proxies of past climatic records and sequestration of atmospheric CO₂.

Two mechanisms of calcium carbonate precipitation were apparent: 1) hydration-hydroxylation reaction due to the mixing of hyperalkaline and surface runoff waters, or 2) dissolution of atmospheric CO_{2(g)} into hyperalkaline waters.

For two sites, the bulk chemical signature of travertines (Mg, Ca, and Sr wt%) are consistent with “prior calcite precipitation” (PCP) processes and thus likely records the environmental conditions at the time of their formation. However, for the third site, the trace-element concentrations in the various carbonate fabrics indicate some recrystallization. Constant δ¹⁸O values indicate that hydration and hydroxylation reactions completely buffer the oxygen isotope composition of the water (equilibrium state) from which a paleo-temperature can be estimated. In contrast, δ¹³C values reflect potential carbon sources, either from surface runoff waters or atmospheric CO₂.

Within the framework of continental carbonate, calcium carbonate formation in bicarbonate-depleted hyperalkaline environments results in a linear and positive co-variation of δ¹⁸O and δ¹³C values and defines a unique and distinctive stable-isotope field on a δ¹⁸O–δ¹³C plot, in contrast to carbonates formed in more typical bicarbonate-enriched environments. Moreover, the combined variations in δ¹⁸O, δ¹³C, and ⁸⁷Sr/⁸⁶Sr between laminae document the changes in the paleo-activity of hyperalkaline spring and surface runoff waters on the time scale of formation. The ⁸⁷Sr/⁸⁶Sr ratio represents a tracer for quantifying surface runoff water contribution. Furthermore, the amount of CO₂ sequestered in travertine has been estimated following different scenarios of formation. The calculated CO₂ sequestered for these deposits ranges from 9 kgCO₂ yr⁻¹ to 522 kgCO₂ yr⁻¹.

INTRODUCTION

Continental carbonates (e.g., speleothems, calcrete, lacustrine limestone, travertine, calcareous tufa, and tufa) are characterized by specific petrofacies resulting from a complex and dynamic interplay of physical, chemical, and biological activity (e.g., Pentecost 2005 and reference therein; Fouke 2011; Gandin and Capezzuoli 2014; Arenas et al. 2014; Capezzuoli et al. 2014). The characterization of continental carbonate is of growing interest because of their ability to preserve paleoenvironmental and paleoclimate information at the time of their formation.

Overall, continental carbonates form predominantly at ambient temperature from calcium bicarbonate-enriched (Ca-CO₃²⁻ type) waters. Alkalinity is derived either from dissolution of carbonate minerals, CO₂ present in the atmosphere and soils above water table, or CO₂ thermally generated in the deep Earth's crust (Pentecost and Viles 1994; Pentecost 2005).

Alternatively, continental carbonates can be associated with hyperalkaline thermal springs located in ophiolite massifs, where circulating groundwaters interact with deep crustal rock and are typically depleted in dissolved inorganic carbon (DIC, e.g., Oman: Neal and Stanger 1983, Chavagnac et al. 2013a; New Caledonia: Launay and Fontes 1985, Monnin et al. 2014; Philippines: Abrajano et al. 1988). In this case, the serpentinization process has led to the conversion of initial Mg-HCO₃ type waters into Ca-OH type hyperalkaline waters depleted both in DIC and Mg but enriched in Ca (Barnes et al. 1967; Barnes and O'Neil 1969; Barnes et al. 1978; Neal and Stanger 1984; Bruni et al. 2002; Cipolli et al. 2004; Sader et al. 2007; Kelemen and Matter 2008; Chavagnac et al. 2013b; Monnin et al. 2014). Precipitation of calcium carbonate from hyperalkaline spring waters is possible only if carbonate ions are available which is typically accomplished in two ways: 1) mixing between DIC-depleted hyperalkaline waters and DIC-rich surface runoff waters, and/or

2) via diffusion and dissolution of atmospheric $\text{CO}_{2(g)}$ into spring waters. As a result, the conditions leading to calcium carbonate formation in hyperalkaline springs is fundamentally different from carbonates that precipitate from bicarbonate-rich waters. However, thus far little is known on the reliability of these deposits as a proxy for past climatic records.

The purpose of this study is to provide a comprehensive and detailed study of three calcium carbonate deposits formed at DIC-depleted hyperalkaline springs in the Oman ophiolite. The objectives are 1) to assess the relationship between the petrologic features and fabrics and the geochemical and isotopic signatures, and 2) to discuss the potential of these deposits as proxies for the past climatic record and sequestration of atmospheric CO_2 .

BACKGROUND

General Spring Characteristics and Nomenclature

The general characteristics of carbonate deposits collected in Oman can be summarized as follows:

- 1) They are associated with warm-temperature (20–65°C) hyperalkaline springs (pH ranges from 10 to 11.9) extremely depleted in Mg and DIC; the springs are preferentially located near two major structural discontinuities, i.e., the basal thrust plane (the contact between the peridotitic mantle section and the underlying sedimentary and metamorphic rocks) and the “paleo-Moho” (the contact between the peridotite mantle section and the overlying gabbroic crustal section) (Neal and Stanger 1984; Pauckert et al. 2012; Chavagnac et al. 2013a).
- 2) Gas emissions at these springs are essentially composed of $\text{H}_{2(g)}$ and $\text{CH}_{4(g)}$ without any $\text{CO}_{2(g)}$ (Sano et al. 1993; Boulart et al. 2013).
- 3) Mineral assemblage forming at spring discharge is essentially composed of calcite and aragonite (Chavagnac et al. 2013b).
- 4) Climatic conditions, e.g., arid or wet seasons, influence the formation rates and the morphologies of the carbonate deposits (Clark and Fontes 1990; Clark et al. 1992).

Over the last 20 years, classification and definition of continental carbonates have evolved based on lithological, petrological, geochemical, and isotopic characteristics (e.g., Capezuoli et al. 2014; Gandin and Capezuoli 2008; Pentecost 2005; Ford and Pedley 1996; Pentecost and Viles 1994).

Based on the most recent classification of Capezuoli et al. (2014), the Oman carbonate deposits share characteristics that are indicative of both travertine and tufa deposits, i.e., “calcareous tufa” or “travertine tufa.” However, their formation is directly linked to the activity of hyperalkaline waters, which testifies to a hydrothermal origin, i.e., a closer link to travertine terminology. Therefore, we refer to these deposits as travertine in agreement with previous publications (Clark and Fontes 1990; Clark et al. 1992; Mervine et al. 2014).

Geological Context

The Oman ophiolite is one of the largest and best-preserved sections of oceanic lithosphere (30,000 km²) exposed on land (Coleman 1981), (Fig. 1). The ophiolite is composed of two major lithological units, the mantle section and the crustal section. The mantle section rests on top of a metamorphic, amphibolitic sole, itself resting on sedimentary rocks (carbonates, sandstones, and radiolarites) (e.g., Coleman 1981). It is formed mostly by variably serpentinized residual mantle harzburgites and dunites. Mafic to felsic intrusive lithologies (pyroxenites, wehrlites, troctolites, gabbros, tonalities) are a minor although ubiquitous constituent of the mantle section (Boudier and Coleman 1981; Ceuleneer et al. 1996; Amri et al. 1996; Python and Ceuleneer 2003). The crustal section, which overlies the mantle section, is more heterogeneous in terms of lithology, including ultramafic

and gabbroic cumulates (Juteau et al. 1988; Abily and Ceuleneer 2013), granitic differentiates, and extrusive rocks (diabase dikes and pillow lavas) (Pallister and Hopson 1981; Alabaster et al. 1982; Amri et al. 1996).

At present, alteration of the ultramafic rocks through serpentinization reactions is driven by percolation of ancient and/or modern meteoric waters through fractures (Chavagnac et al. 2013a). Serpentinization reactions lead to the formation of hyperalkaline springs (25 to 40°C, Chavagnac et al. 2013a), which are numerous over the entire ophiolite belt and associated with travertine deposits (Neal and Stanger 1984; Kelemen et al. 2011; Chavagnac et al. 2013a; Mervine et al. 2014) (Figs. 1, 2).

Climate of Oman

The ophiolite crops out in the Northern Oman Mountains, located at the southeastern horn of the Arabian Peninsula (22–24°N). The climatic conditions are typical of a dry tropical area, with maximum air temperature ranging between 20 and 35°C during winter and > 40°C in summer. The climate of the northeastern side of the mountain faces the Gulf of Oman and has some marine influence, whereas the southwestern side faces the Arabian Sands and is predominantly continental. The present-day average rainfall on the Northern Oman Mountains is on the order of 100 mm yr⁻¹ (Clark and Fontes 1990) and is influenced by two sources of precipitation: the Mediterranean Sea and the Indian Ocean. These two influences define a boundary called the Inter-Tropical Convergence Zone (ITCZ). The ITCZ varies seasonally along a north to south gradient. The Oman hydrology is highly variable because of the rainfall intensity variation and evaporation rates (Kwarteng et al. 2009).

Paleoclimate Records of Oman

Over longer timescales, paleoclimate studies on various materials (speleothems, lake sediments, and travertine) have revealed an alternation of humid and arid periods in Oman (Clark and Fontes 1990; Clark et al. 1992; Fleitmann et al. 2003; Fleitmann et al. 2004; Fleitmann et al. 2007; Fuchs and Buerkert 2008; Mervine et al. 2014). ¹⁴C dating methods, geochemistry, and stable-isotope (C and O) signatures were used to determine the timespan during which precipitation intensity had varied. For example, Fleitmann et al. (2003) linked the temporal $\delta^{18}\text{O}$ variations of the precipitation recorded in speleothems (between -12 and -4‰) from Hoti cave (Oman) to the ITCZ shifts. Typically, previous results concentrated their effort on either geochemical features or petrological ones, rather than a combination of the two. Such observations are, however, crucial to elucidate the causal-consequence link between climate change and travertine morphology.

SAMPLES AND METHODS

Among a large series of travertine sites visited during three field campaigns (December 2008, January 2010, and January 2011), three sites were selected from hyperalkaline springs for which geological setting, chemical composition of hyperalkaline spring waters, gas emissions, and mineralogical assemblages have been carefully studied (Neal and Stanger 1984; Weyhenmeyer et al. 2002; Pauckert et al. 2012; Chavagnac et al. 2013a; Chavagnac et al. 2013b; Boulart et al. 2013; Mervine et al. 2014) (Fig. 1, Table 1) and best elucidate the different styles of carbonate precipitation. The samples were sawn with a diamond blade perpendicular to the lamination for microscopic-scale description. In addition, we used a micro-dremel to powder each lamina of samples 32 and 33, which were first identified in microscopic observations (Fig. 3). To decipher whether travertine formed in a DIC-depleted environment constitutes a potential proxy of past climate variability, each sample was consequently characterized using various analytical techniques (details are reported in the Appendix Supplementary Material). We summarize their usefulness below:

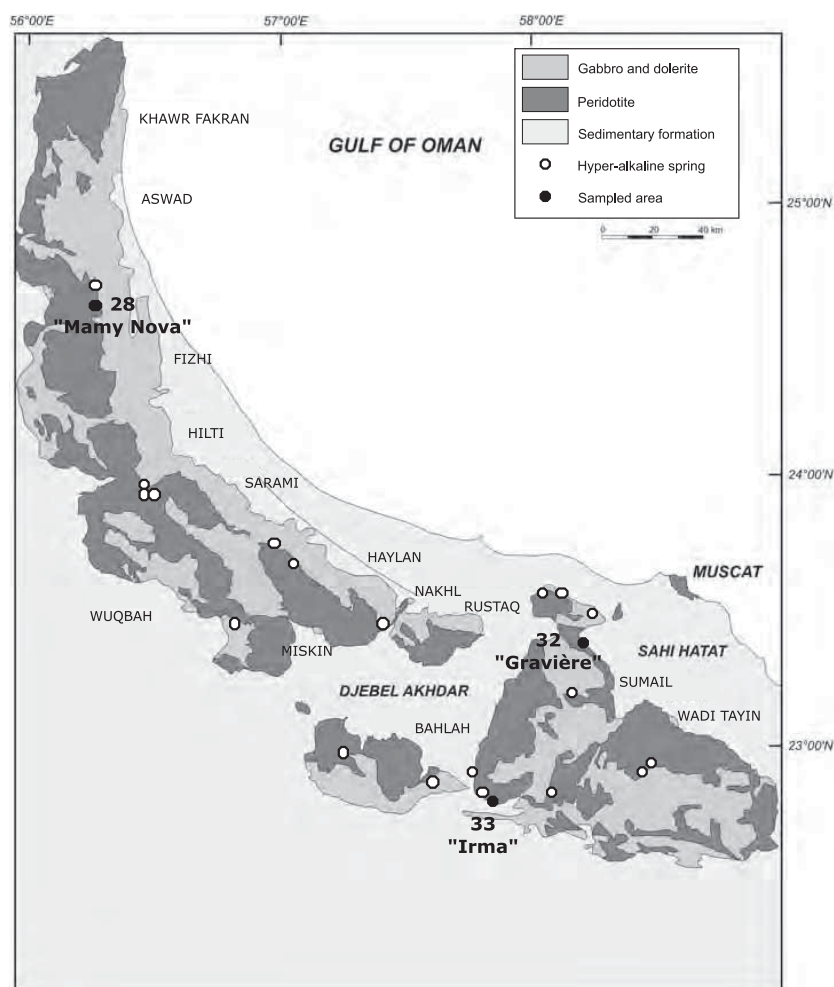


FIG. 1.—Simplified geological map of the Sultanate of Oman (modified from Chavagnac et al. 2013b).

- Scanning electron microscopy (SEM) coupled with energy-dispersive spectroscopy (EDS) to identify chemical changes in the sample, based on code color imaging of chemical elements on thin-section areas.
- Raman analysis and cathodoluminescence in order to determine calcium carbonate polymorphs from thin sections.
- Electron microprobe analyses to detect and observe the repartition of substituted elements into the carbonates, such as magnesium (Mg) and strontium (Sr).
- Oxygen and carbon isotope compositions were conducted to identify precipitation mechanisms and to characterize mixing processes.
- $^{87}\text{Sr}/^{86}\text{Sr}$ isotope composition in order to quantify the mixing proportion between surface runoff and hyperalkaline spring waters that control the formation of travertine.

RESULTS

Site Description and Petrographic Analysis

In the first section of this paper, we describe each sampling site following the concept of sedimentary depositional facies (Fouke et al. 2001; Veysey et al. 2008; Fouke 2011) together with the main microscopic

observations. In the following sections, we present the stable-isotope and radiogenic-isotope compositions from two of the sites.

“Mamy Nova” Site (Sample 28)

Site “Mamy Nova” is located in the wadi Zabyn, running through the Fizh massif (Fig. 1). The local topographic and geological setting corresponds to a mixing area between runoff and groundwaters that interacted with mantle peridotites on their way to the spring, although the main discharge itself lies on a gabbroic substratum. However, no sedimentary and metamorphic rocks are found in wadi Zabyn upstream from spring waters, which run exclusively in the mantle harzburgites. In the valley bottom, terrace deposits composed of cemented gravel bars are partially preserved, topping the gabbroic substratum. Both terrace and substratum are incised by the stream flow. The hyperalkaline spring discharge is located 1 to 2 m above the surface waters and emerges from a fractured zone running through the lower crustal section (Table 1; Fig. 2). Modern to ancient carbonate deposits occur from the spring discharge area over a distance of 1 km along the surface waters. Carbonate encrustation around gravels can be observed in the stream bottom. Small-scale (10 cm high) step-shaped micro-terracettes are present in the channel facies.

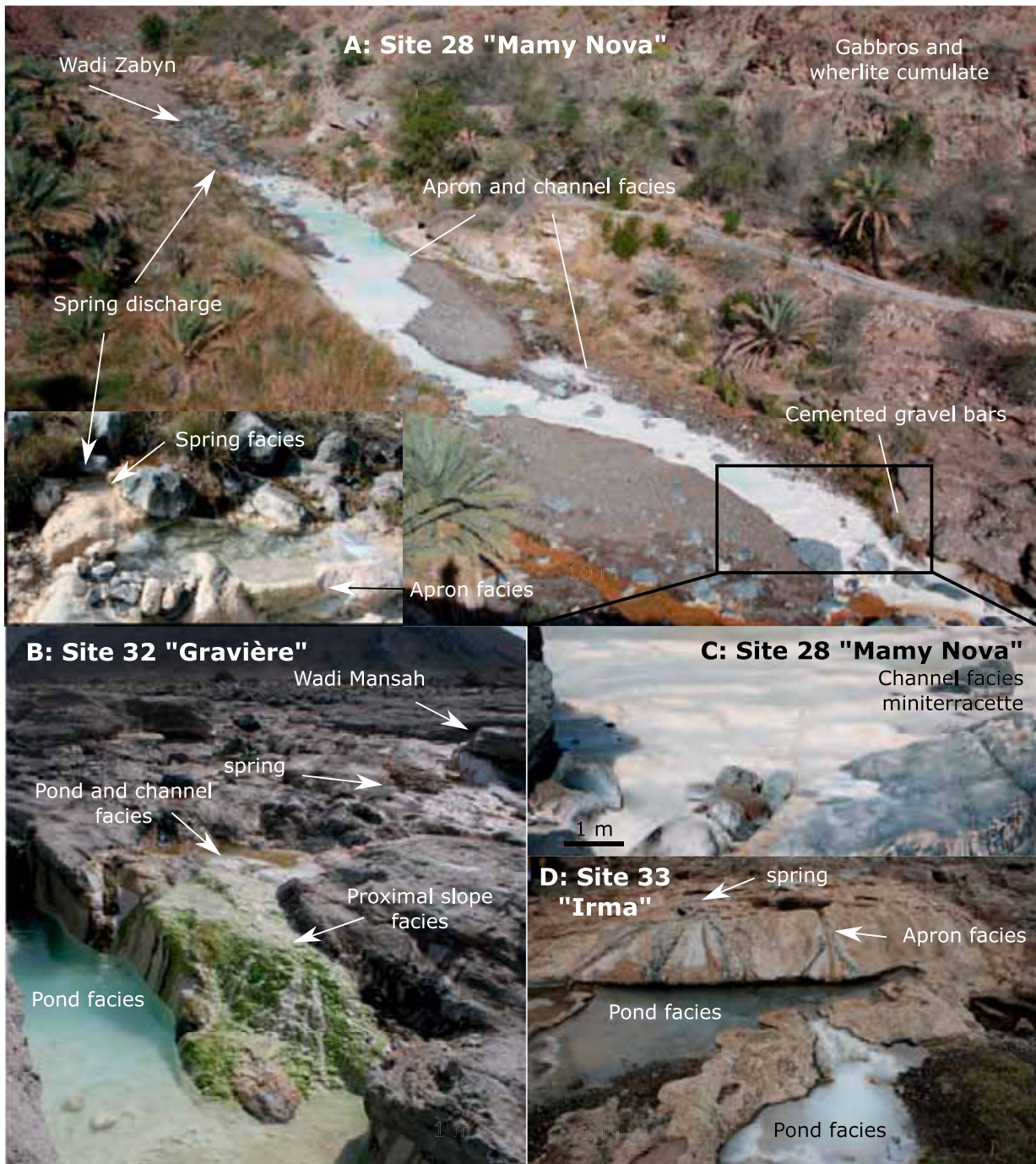


FIG. 2.—Photographs of the sampling sites presenting the carbonate depositional facies at the hyperalkaline springs.

Sample 28 was taken from a carbonate gravel bar, which consists of a conglomerate of ultramafic rocks partially cemented by calcium carbonate. Pores are partially filled with detrital material consisting of a mixture of micritic allochems (clotted peloids partially cemented or redissolved), micrite, clays, and ultramafic fragments (Fig. 4A). Precipitation of

carbonates occurred in the vadose zone, as suggested by the presence of aragonite microstalactic cement in some pores and discontinuous $\approx 100\text{-}\mu\text{m}$ -thick drusy calcite cement that precipitated around the pores (Fig. 4B, C, D). Si- and Mg-rich clavate ($10\text{--}25\ \mu\text{m}$ in diameter and rich in organic matter) that underline a growth stage of the drusy isopacheous sparite, as

TABLE 1.—Location and geological context of travertine samples. Chemical composition of hyperalkaline springs: Chavagnac et al. (2013b); Mineralogical precipitates™: Chavagnac et al. (2013a).

Site	Name	Latitude (N)	Longitude (E)	Altitude (masl)	Geological Context	T (°C)	pH	Surface Precipitate™	Stream-Bed Precipitate™	Consolidated Precipitate™
28	Mamy Nova	24°31'221	56°18'071	395	Within the crustal section, bedded gabbro and ultrabasic cumulates	38.6	11.0	Aragonite, brucite	Aragonite, brucite	Aragonite, calcite, hydrotalcite? Iowaité?
32	Gravière	23°19'211	58°13'421	367	Mixing peridotite gabbro, very altered	31.0	11.5	Calcite, aragonite	Aragonite, brucite, suolunite	Aragonite, calcite, hydrotalcite?
33	Irma	22°48'431	57°50'161	485	In serpentinite, just above the contact with Hawasinah	25.8	11.7	Calcite, aragonite	Calcite	Calcite

well as the presence of aragonite needle-like features topped by a Si- and Mg-rich film (Fig. 4B).

“Gravière” Site (Sample 32)

At this site, the substratum of the hyperalkaline spring is located close to the boundary between mantle peridotites and lower crustal gabbroic cumulates. Meteoric waters travel through a large drainage system originating in the sedimentary and metamorphic rocks of the Saih Hatat and running through mantle peridotites (Table 2; Fig. 1). The valley is partially filled with highly cemented gravel bars that are incised by stream flow and partially covered by uncemented modern gravels. The hyperalkaline spring emerges on cemented gravel bars, where it mixes with the surface runoff waters (Fig. 2). At the spring discharge area, a modern carbonate deposit can be observed covering the stream bottom. Sample 32 was taken in the channel facies where the wadi Mansah and the hyperalkaline spring mix (Fig. 2). A green algae and/or bacterial mat

covers the modern surface of the carbonate deposit in the channel facies (Fig. 2).

On a macroscopic scale, the sample is composed of a succession of 13 laminae exhibiting distinctive coloration, mineralogy, fabrics, and porosity (Fig. 5). The observations are summarized in Table 2. The sample displays a very complex spatial organization, with an alternation of light-, intermediate-, and dark-gray layers (Fig. 5). The laminae are composed of gothic-arch calcite, crystallized aragonite bushes, drusy calcite cement (Fig. 5, zones A and B), a Mg-, and Si-rich organic material (Fig. 5, zones A, B, D, and E) that contains also Al, dark-gray spheroids (Fig. 5, zone C), and micro-spheroids embedded in Mg-, Al-, and Si-rich organic material (Fig. 5, zone D). Large pores are also filled with drusy calcite cement (Fig. 5, zone C).

“Irma” Site (Sample 33)

The “Irma” site is located along the foothills of the Samail Massif in mantle peridotites overlying the sedimentary rocks of the Hawasina

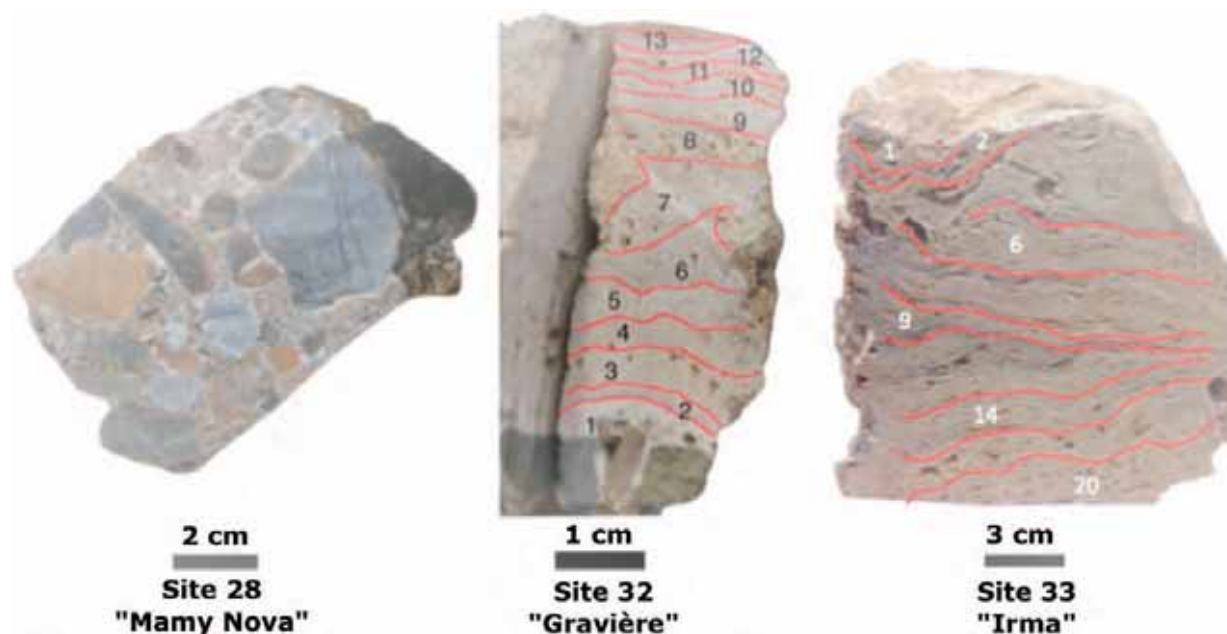


FIG. 3.—Macroscopic photographs of the three studied carbonate samples. On samples 32 and 33 hand specimens, we denote the laminae identified upon microscopic observation.

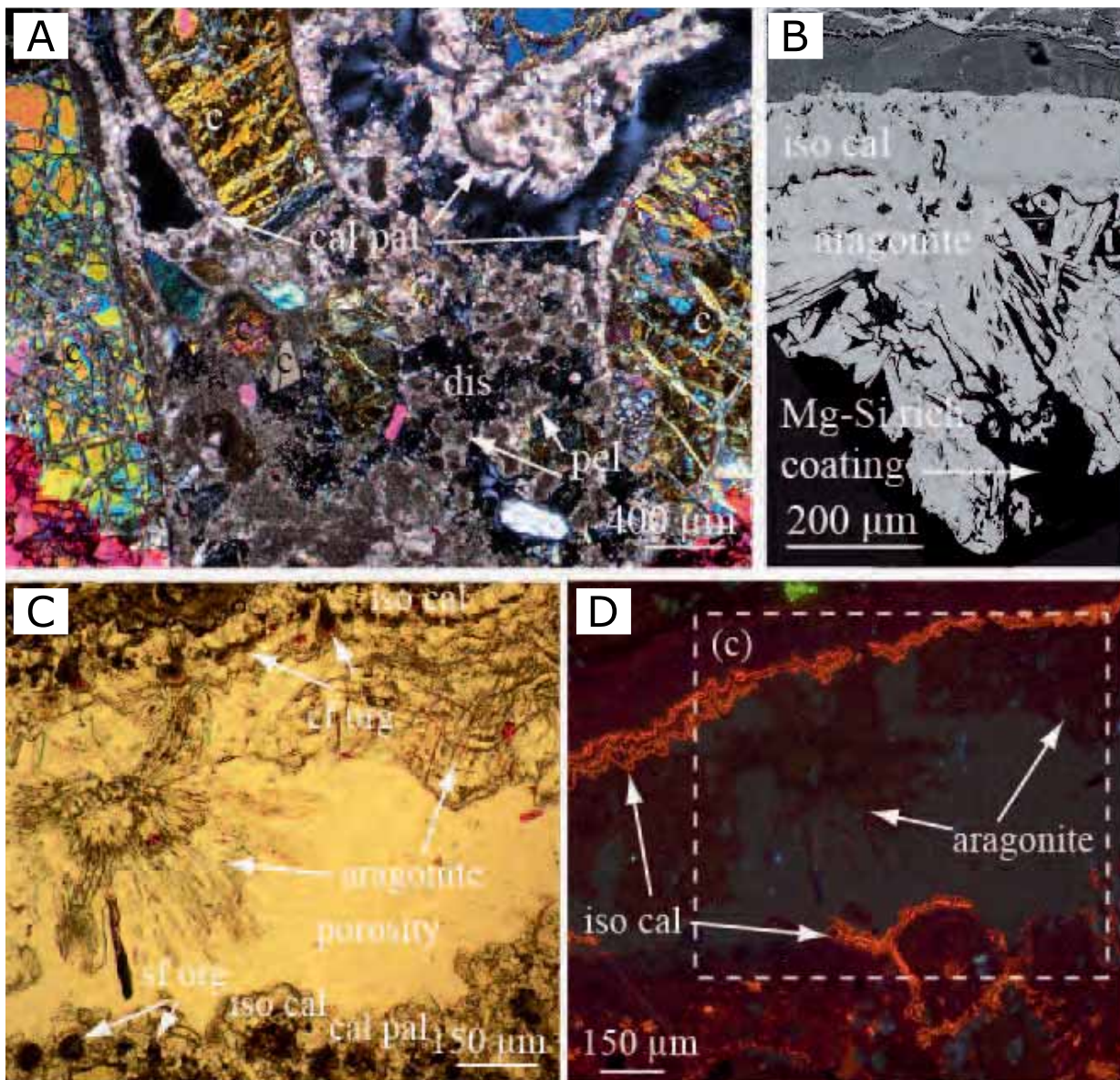


FIG. 4.—Microscopic observations of sample 28 in **A**) plane-polarized light; **B**) SEM-EDX; **C**) detail of a pore which depicts aragonite bush, and both aragonite and calcite cement in transmitted polarized-light microscopy; **D**) view of area **C**) in cathodoluminescence. Legend: pel, peloid; c, ultramafic element of the conglomerate; iso cal, isopachous calcite cement; dis, dissolution feature; sf org, spherical feature (organic material); cf org, clavate feature (organic material); dis, dissolution feature; cal pal, palisade calcite.

Formation and the greenschists and amphibolites of the metamorphic sole (Fig. 1). The local drainage system is located entirely within highly serpentinized mantle peridotites. The site itself is a large kilometer-wide terrace characterized by a layer of recent travertine several meters thick. There is no obvious surface runoff, implying that the precipitation of calcium carbonate takes up carbon from atmospheric CO_2 (Table 2; Fig. 2). Deposits form successive pools separated by aprons around and downstream of the hyperalkaline spring (Fig. 2).

Sample 33 was collected in the flowing hyperalkaline spring. It consists of calcite raft (sparite) deposits alternating with more organic-rich layers of

vuggy calcite (micrite) displaying a laminoid-fenestral fabric (type LF-A according to Flügel (2004); Fig. 6A, B). Sparite overgrowths are observed on both sides of the rafts (Fig. 6D). Ultramafic detrital particles may occur between rafts (Fig. 6C).

Chemical Composition of Carbonate Fabrics

Electron microprobe analyses were carried out on the various calcium carbonate fabrics. Chemical compositions of carbonate samples are reported in Table 3 and Figure 7 according to the sample and from

TABLE 2.—Microscopic description of samples based on petrographic fabrics and mineralogy.

Travertine Site/Name	Lamina	Petrographic Fabric
28/Mamy Nova	lamina 1: contact with substrate lamina 2: pore filling	Fibrous aragonite Needle-like aragonite
32/Gravière	lamina 1 and 2: contact with substrate lamina 3 to 13: contact with stream waters	Laminae of recrystallized aragonite bushes and drusy calcite cement Low-gray aragonite bushes and relatively darker spheroids to the top of thin section with a major structure at lamina 7/8 boundary made of thick dark organic matrix
33/Irma	lamina 1 to 26	Calcite rafts fabric (sparite) and mixed calcite and organic material (micrite) as laminoid-fenestral fabric

lamina to lamina. Carbonates exhibit different Mg and Sr content from one sample to another and from one lamina fabric to the other. For example, sparite calcite contains little Mg (≈ 0.05 wt%) and Sr (≈ 0.05 wt%). It contrasts with Mg-rich drusy calcite (Mg = 0.54 wt%, Sr = 0.05 wt%) and Sr-rich aragonite needles (Mg = 0.08 wt%; Sr = 0.58 wt%) (Table 3).

Carbon, Oxygen, and Strontium Isotope Compositions

Carbon (C) and oxygen (O) isotope compositions were determined on 13 laminae of sample 32 and 6 laminae from sample 33. The results are reported in Table 4 and Figure 8. Sample 32 displays variations in $\delta^{18}\text{O}$ values ranging between -1.22 and -6.13% VPDB and $\delta^{13}\text{C}$ values ranging between -10.75 and -6.52% VPDB. However, the central part of sample

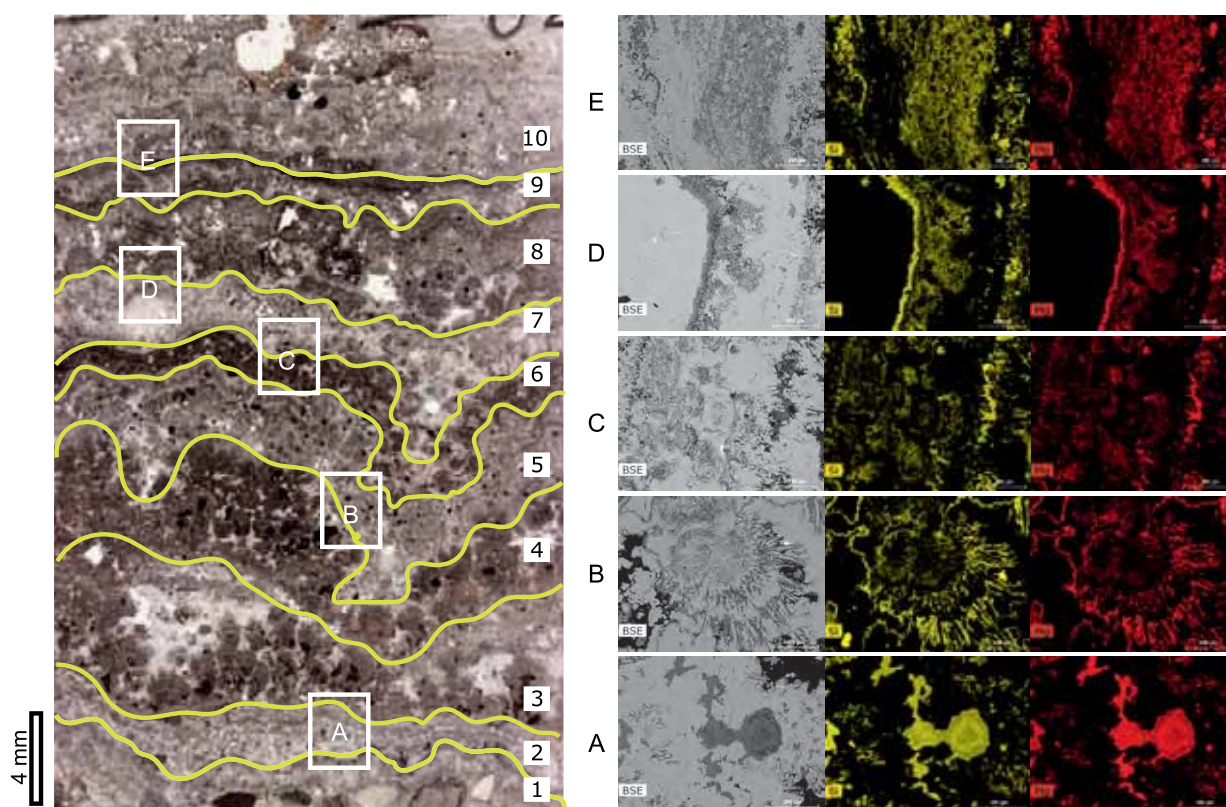


FIG. 5.—Detailed microscopic observations of sample 32 based on thin-section SEM chemical maps. **Zone A**) Pore spaces are filled with clays as shown by high concentration of Si, Mg, and Al elements at the transition between laminae 2 and 3. **Zone B**) Acicular calcium carbonate is approximately oriented toward the surface and grows from a micritic circular point. A thin film composed of Si, Al, Mg, and O overlies each generation of needle aragonite. **Zone C**) The transition between laminae 6 and 7 exhibits a variation from Si- and Mg-rich areas in the dark micritic lamina to Si, Mg, and Al-rich micro-oncoid, together with the occurrence of Si, Mg-rich $\mu\text{-size}$ grain (serpentine). **Zone D**) The sparry calcium carbonate in a pore in lamina 7 is haloed by Mg-Si-rich matrix. This lamina is irregularly thick. Some calcium carbonate crystals are contained in the matrix, the most remarkable example being the rectangular crystal in the dark matrix. A Ca carbonate layer formed over the matrix, first sparry calcite, then intergrown needle-like aragonite with the Si-Mg-rich matrix in contact with a pore. **Zone E**) The dark micritic lamina 9 appears to be composed of several rounded carbonates crystals in a Mg-Si-rich matrix.

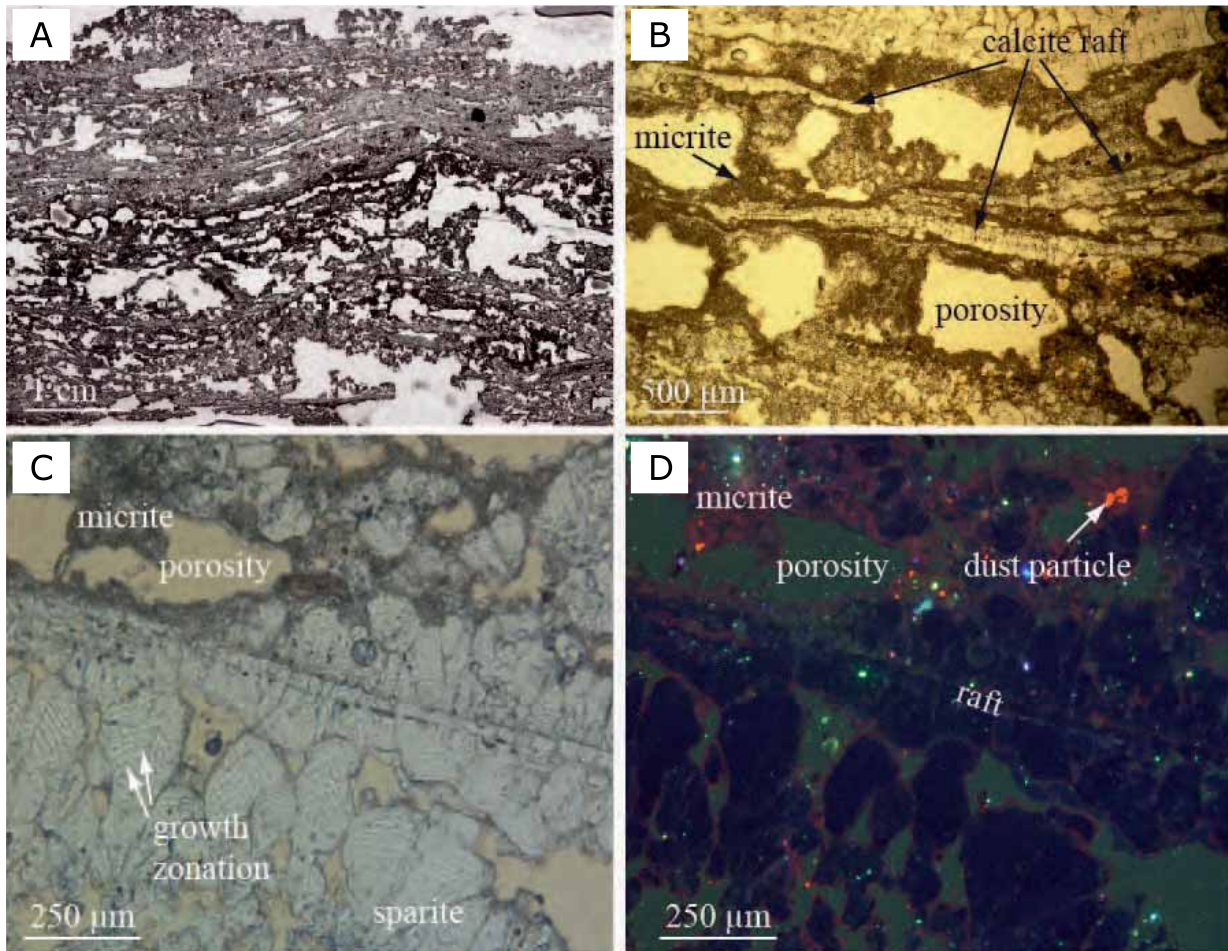


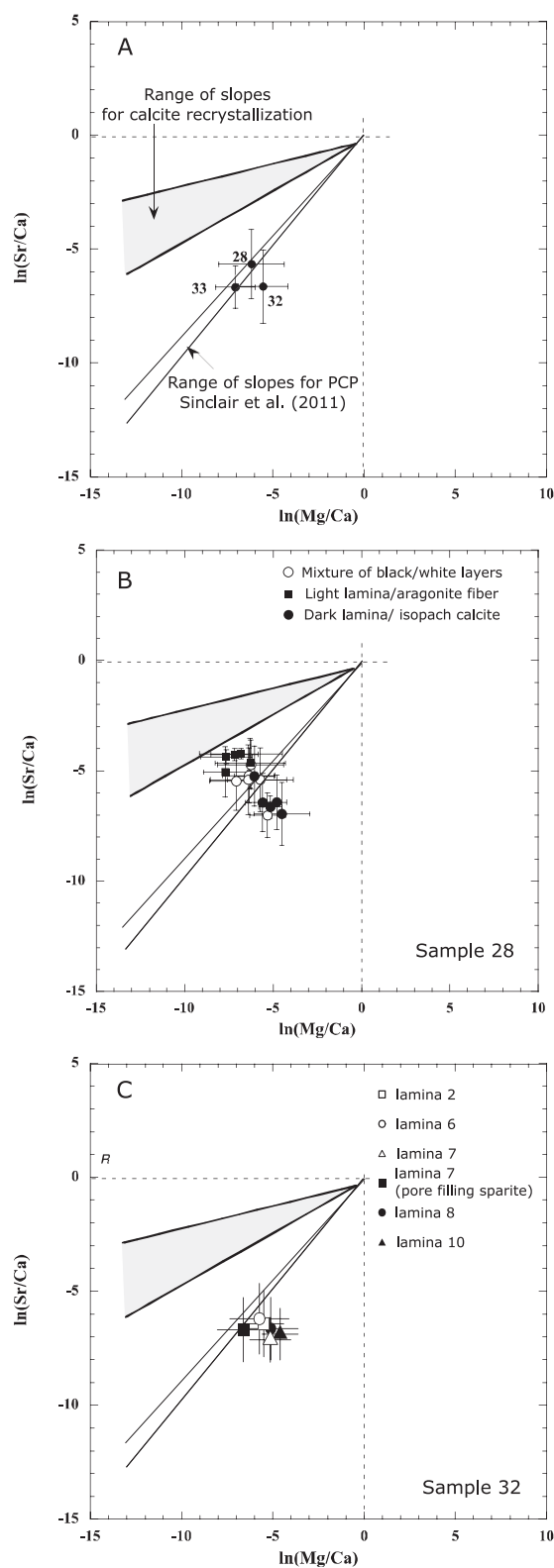
FIG. 6.—A, B) microscopy observations of sample 33 in transmitted polarized-light microscopy. C, D) Detail of a raft growth pattern in transmitted polarized-light microscopy and cathodoluminescence, respectively.

32 is characterized by a nearly constant $\delta^{18}\text{O}$ value with a mean value of -3.9% (VPDB). Some laminae of sample 33 show an extreme depletion in both ^{13}C and ^{18}O isotopes, with $\delta^{18}\text{O}$ values ranging from -16.54% to -10.12% (VPDB) and $\delta^{13}\text{C}$ values from -22.84% to -12.62% (VPDB).

While the $^{87}\text{Sr}/^{86}\text{Sr}$ ratio varies between 0.707282 and 0.707994 in sample 32, it is almost constant in sample 33 with a mean value of 0.70821, which is similar to that of hyperalkaline spring at this site (0.708164; Table 4). For sample 32, the most radiogenic Sr isotope ratio

TABLE 3.—Electron microprobe analyses of calcium carbonates.

Site	Lamina Petrofabric	Number of Analysis	Mg wt%	Sr wt%	Ca wt%	ln(Mg/Ca)	1 σ D	ln(Sr/Ca)	1 σ D
28	all	260	0.24	0.34	39.47	-6.0	1.8	-5.3	1.5
	dark lamina (isopach calcite)	120	0.44	0.05	39.49	-5.1	1.3	-6.8	1.3
	light lamina (aragonite fiber)	140	0.08	0.58	39.45	-7.2	1.8	-4.4	0.8
32	all	223	0.29	0.09	39.68	-5.5	1.4	-6.6	1.6
	lamina 2 (gothic arch calcite and aragonite bushes)	36	0.20	0.11	39.76	-5.5	1.1	-6.4	1.5
	lamina 6 (aragonite bush and calcite cement)	50	0.27	0.16	39.64	-5.7	1.6	-6.2	1.6
	lamina 7 (spheroid calcite)	30	0.39	0.03	39.60	-5.1	1.1	-7.1	1.0
	lamina 7 (in-filling sparite)	42	0.11	0.07	39.85	-6.6	1.4	-6.7	1.4
	lamina 8 (micro-spheroid calcite)	34	0.34	0.07	39.67	-5.1	1.5	-6.6	1.4
	lamina 10 (drusy calcite)	31	0.54	0.05	39.55	-4.6	1.0	-6.9	1.1
33	all (spar calcite)	29	0.05	0.05	39.90	-7.1	1.1	-6.7	0.9



(close to surface-water signature) is measured in lamina 1 at the contact with the substrate, while the least radiogenic Sr isotope ratio (close to hyperalkaline spring signature) is measured in lamina 8, located next to a μm -thick Si- and Mg-rich layer (Table 4).

DISCUSSION

Linking Fabrics and Chemical Composition of Travertines

The distinctive fabrics of aragonite and calcite crystals seem to support the primary formation of these minerals (Renaut and Jones 1997). Nevertheless, it is necessary to decipher whether their morphologies express the environmental conditions at which they formed, or if they result from post-formation recrystallization. Divalent cations in aqueous solution (e.g., Mg, Sr, Ba, Mn, and Fe) may substitute for Ca in the crystal lattice during precipitation and recrystallization of carbonate, and when compared to their lamina fabric, can help elucidate primary versus secondary mineral phases. Our approach is based on previous karst waters and speleothem studies which showed that a constant slope in a $\ln(\text{Sr}/\text{Ca})$ vs. $\ln(\text{Mg}/\text{Ca})$ plot is due to a low Sr and Mg partition coefficient in calcite (Huang et al. 2001; Fairchild et al. 2000; Fairchild et al. 2006; McMillan et al. 2005; Johnson et al. 2006; Matthey et al. 2009), where dissolved Mg and Sr ions preferentially remain in solution while Ca precipitates as calcium carbonate. This chemical trend applied to speleothems has been named “prior calcite precipitation” (PCP). Based on a worldwide study of speleothems, Sinclair (2011) and Sinclair et al. (2012) were able to distinguish co-variation of Mg, Ca, and Sr concentrations that truly reflect environmental conditions compared to those induced by post-formation recrystallization. When applied to our samples as shown in Figure 7, the average $\ln(\text{Mg}/\text{Ca})$ and $\ln(\text{Sr}/\text{Ca})$ ratios of carbonate, without any distinction between carbonate fabrics, plot on or in error bars of the PCP slope (Fig. 7A), suggesting early calcite–water interaction, and not recrystallization.

However, the situation is more complicated when this approach is applied locally to the various carbonate fabrics of a travertine sample. For instance, in sample 28 (Fig. 7B), the dark sparitic lamina plots underneath the PCP slope whereas the white needle-like aragonite fabric plots above the PCP trend towards the range of calcite recrystallization. The combination of fabric and chemical compositions suggests at least partial carbonate recrystallization. Therefore, the geochemical record for climatic reconstruction is less useful for the cemented gravels in sample 28. Alternatively, all of the various carbonate fabrics of sample 32 plot slightly underneath the PCP trend (Fig. 7C), due potentially to different mixing proportions between hyperalkaline springs and runoff waters, which supply significant amounts of Mg and bicarbonate ions in solution compared to lack of supply of Mg from the hyperalkaline waters (Chavagnac et al. 2013b). Here, higher Mg content in carbonates suggests either an increase in runoff water proportion or a reduction of hyperalkaline spring-water influence. Finally, sparitic calcite crystals of sample 33, which are formed at the air–water interface, show $\ln(\text{Mg}/\text{Ca})$ and $\ln(\text{Sr}/\text{Ca})$ ratios coherent with PCP processes, recording paleo-environmental conditions at the time of their precipitation.

Isotopic Records in Travertine

If well preserved, the carbon and oxygen isotopes can record environmental information in carbonate deposits (e.g., Darling et al. 2005; Lachniet 2009; Brady et al. 2010). The $\delta^{13}\text{C}$ values can be used to infer the origin of the carbon source, i.e., atmospheric CO_2 and/or DIC

FIG. 7.—Cross-plots of $\ln(\text{Sr}/\text{Ca})$ vs. $\ln(\text{Mg}/\text{Ca})$ according to Sinclair (2011) and Sinclair et al. (2012), (A) the average bulk calcium carbonate composition of samples 28, 32, and 33, (B) two fabrics average compositions of sample 28, and (C) average chemical composition of the laminae defined for sample 32 (including the different fabrics identified).

TABLE 4.—Thickness (cm), $\delta^{18}\text{O}$ (VPDB), $\delta^{13}\text{C}$ (VPDB) and $^{87}\text{Sr}/^{86}\text{Sr}$ ratios of individual laminae of samples 32 and 33. Calculated values of mixing contribution of hyperalkaline springs in % and paleotemperature are also reported (see text for details).

Site-Lamina Number	Thickness	$\delta^{13}\text{C}_{\text{PDB}} \text{‰}$	$\delta^{18}\text{O}_{\text{SMOW}} \text{‰}$	$\delta^{18}\text{O}_{\text{PDB}} \text{‰}$	$^{87}\text{Sr}/^{86}\text{Sr}$ ($2\sigma_{\text{E}}$)	% Hyperalkaline Water in the Mixing Area	Calculated Paleotemperature in °C
Site 32-1	0.4	-7.71	29.48	-1.39	0.707994 (11)	33.3	14.8
Site 32-2	0.2	-8.08	29.66	-1.22	0.707947 (6)	35.9	14.1
Site 32-3	0.4	-6.52	26.66	-4.12	0.707813 (7)	43.5	27.5
Site 32-4	0.5	-6.91	26.84	-3.96	0.707761 (9)	46.5	26.6
Site 32-4 duplicata		-6.69	26.86	-3.93			26.5
Site 32-5	0.5	-7.26	27.1	-3.7	0.707784 (8)	45.2	25.4
Site 32-5 duplicata		-7.36	26.56	-4.23			28.0
Site 32-6	0.7	-7.89	26.99	-3.81	0.707749 (10)	47.2	25.9
Site 32-7	0.8	-7.86	27.23	-3.57	0.707695 (12)	50.3	24.8
Site 32-8	0.7	-10.75	27.31	-3.49	0.707282 (12)	74.5	24.4
Site 32-9	0.3	-10.52	27.14	-3.67	0.707390 (9)	68	25.2
Site 32-10	0.2	-9.77	26.66	-4.13	0.707513 (8)	60.9	27.5
Site 32-11	0.2	-9.24	27.13	-3.68	0.707743 (10)	47.5	25.3
Site 32-12	0.2	-9.53	26.60	-4.18	0.707419 (8)	66.3	27.8
Site 32-13	0.6	-8.94	24.60	-6.13	0.707438 (8)	65.3	37.9
Site 33-1	1	-12.62	20.48	-10.12	0.708163 (11)	n.d.	n.d.
Site 33-2	1	-15.53	19.69	-10.89	0.708214 (7)	n.d.	n.d.
Site 33-6	1.7	-21.27	16.03	-14.44	0.708197 (6)	n.d.	n.d.
Site 33-9	0.5	-20.26	15.64	-14.81	0.708260 (9)	n.d.	n.d.
Site 33-14	1.2	-22.84	14.05	-16.36	0.708209 (8)	n.d.	n.d.
Site 33-20	2	-21.96	13.86	-16.54	0.708177 (9)	n.d.	n.d.
spring 33bW1		n.m.	n.m.	n.m.	0.708164 (8)	n.d.	n.d.
spring 32W1		n.m.	n.m.	n.m.	0.706686 (8)	n.d.	n.d.
spring 33W1 (pH = 9.8)		n.m.	n.m.	n.m.	0.708614 (48)	n.d.	n.d.
spring 33W1 (pH = 10.5)		n.m.	n.m.	n.m.	0.708522 (18)	n.d.	n.d.
Calcite rafts ^a		-25.5	n.m.	-15.1	n.m.	n.d.	n.d.
		-25.6		-16.5		n.d.	n.d.
		-25.8		-16.8		n.d.	n.d.
		-24.8		-16.9		n.d.	n.d.
Rain water ^b		-7	-0.55 to -2.95	n.d.	n.m.	n.d.	n.d.
Ophiolite aquifer ^c		-13.6 to -15.6	-1.0 to -1.4	n.d.	n.m.	n.d.	n.d.
Surface water from wadi samail catchment ^d		-11.9 to -13.8	-1.60 to -2.41	n.d.	0.70844 to 0.70870	n.d.	n.d.

^a Clark and Fontes (1992).

^b Matter et al. (2005) and Weyhenmeyer (2000).

^c Matter et al. (2005).

^d Weyhenmeyer et al. (2002).

n.d. not determined.

n.m. not measured.

from runoff waters. The $\delta^{18}\text{O}$ is commonly used as a proxy for temperature and rainfall which is controlled by evaporation, condensation, climate, altitude, latitude, and distance from seawater (Dansgaard 1964).

Figure 8 presents the variation in $\delta^{18}\text{O}$ values as a function of $\delta^{13}\text{C}$ values for all laminae, and depicts two different trends. For sample 32, the $\delta^{18}\text{O}$ values are almost constant, while the $\delta^{13}\text{C}$ values are variable. A positive correlation is observed between atmospheric signature and calcite crust values for sample 33. These two distinctive trends can be interpreted through two different mechanisms: (1) hydration-hydroxylation reactions ($\text{CO}_{2(\text{aq})} + \text{H}_2\text{O} \leftrightarrow \text{HCO}_3^- + \text{H}^+$, and $\text{CO}_{2(\text{aq})} + \text{OH}^- \leftrightarrow \text{HCO}_3^-$ (aq), respectively) or (2) a kinetic effect during diffusion and dissolution of atmospheric CO_2 at the air–water interface (Neal and Stanger 1984; Clark and Fontes 1990; Clark et al. 1992).

For sample 32, the $\delta^{18}\text{O}$ values remain nearly constant for all laminae, apart from three, with variable $\delta^{13}\text{C}$ values (Fig. 8). The low occurrence of aragonite (less than 10%; Chavagnac et al. 2013a) does not seem to affect the oxygen isotope composition significantly, as the latter has a nearly constant value throughout the laminae. Constant $\delta^{18}\text{O}$ values likely

indicate that hydration and hydroxylation reactions completely buffer the oxygen isotope composition of water (i.e., equilibrium state). Oxygen isotope equilibrium between HCO_3^- (aq) and H_2O is achieved, and therefore $\delta^{18}\text{O}$ values are not affected by kinetic effects (Mickler et al. 2006). Therefore, it is possible to calculate the equilibrium temperature using the following equation (Grossman 2012 and references therein):

$$T = 15.7 - 4.36 \times (\delta^{18}\text{O}_{\text{cal}} - \delta^{18}\text{O}_{\text{water}}) + 0.12 \times (\delta^{18}\text{O}_{\text{cal}} - \delta^{18}\text{O}_{\text{water}})^2 \quad (1)$$

Where T is temperature (°C), $\delta^{18}\text{O}_{\text{cal}}$ (carbonate) is given relative to the VPDB standard and $\delta^{18}\text{O}_{\text{water}}$ is the oxygen isotope composition of the water (in SMOW) (Table 4). A value of -1.6‰ (SMOW) was chosen for the $\delta^{18}\text{O}_{\text{water}}$ in line with water being a mixture between groundwater from the ophiolite aquifer at -1.0 to -1.4‰ (SMOW, Matter et al. 2005) and surface runoff waters at -1.6 to -2.41‰ (SMOW, Weyhenmeyer 2000). Sample 32 records wide temperature variations between 14.1 and 37.9°C (mean temperature of $25.4 \pm 11^\circ\text{C}$). The lowest temperature of 14.1°C is striking. Nevertheless, it is not completely inconsistent with a drastic

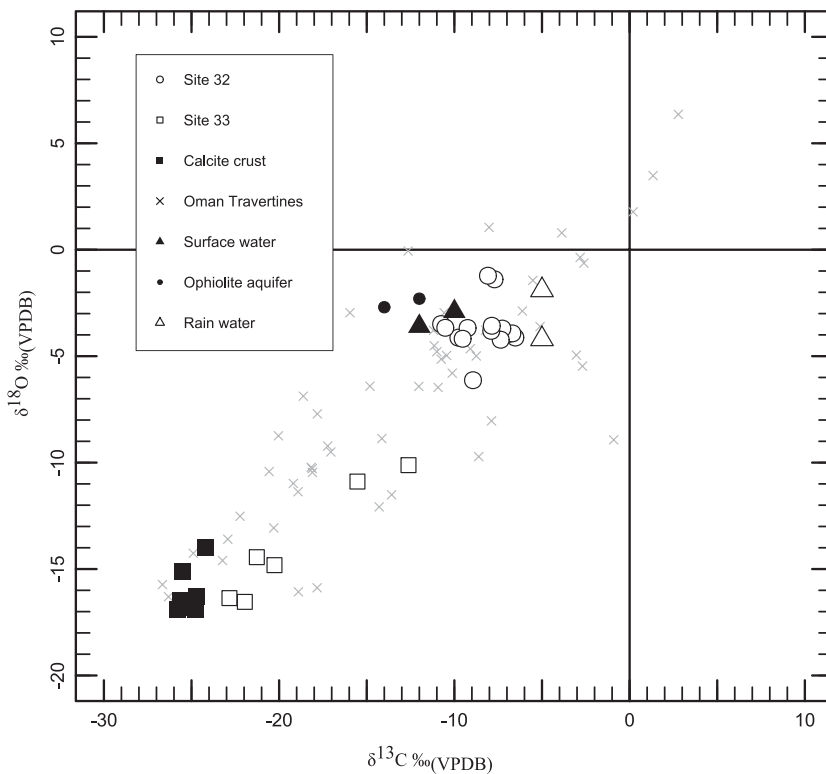


Fig. 8.—Plot of $\delta^{18}\text{O}$ values vs. $\delta^{13}\text{C}$ values of distinctive laminae of samples 32 and 33. Atmospheric CO_2 has a $\delta^{13}\text{C}$ value of -7‰ . Calcite crust (black square): Clark et al. 1992; Oman travertines (cross): Clark and Fontes 1990, Mervine et al. 2014; Surface runoff waters (black triangle): Weyhenmeyer 2000; Ophiolite aquifer (black dot) and rain water (white triangle): Matter et al. 2005.

cooling of $6.5 \pm 0.6^\circ\text{C}$ for late Pleistocene Oman groundwaters (Weyhenmeyer et al. 2000). Unfortunately, the lack of sample ages severely restricts the interpretation of these paleo-temperatures in terms of a temporal climatic record.

In contrast, $\delta^{18}\text{O}$ and $\delta^{13}\text{C}$ values in sample 33 are close to calcite crust (sparite) values reported in Clark et al. (1992) (Fig. 8). Calcite precipitation is induced by evaporation and atmospheric conversion of gaseous CO_2 into carbonated species at the air–water interface. In this context, the coupled depletions in ^{18}O and ^{13}C result from both hydroxylation reactions and kinetic effects based on the difference in diffusion rates of $^{13}\text{CO}_2$ and $^{12}\text{CO}_2$ (Dietzel et al. 1992; Clark et al. 1990).

As a result, stable-isotope compositions alone are seriously limited to assess past climatic conditions without additional information on carbonate fabric and chemical composition. However, $\delta^{13}\text{C}$ values may be useful to elucidate the sources of carbon supply in this particular DIC-depleted environmental context of travertine formation.

Hyperalkaline Spring vs. Surface Runoff Waters and the Climatic Record

Further information about the climatic record may be provided by strontium isotope composition because each geological formation and solution exhibits distinctive $^{87}\text{Sr}/^{86}\text{Sr}$ ratios in this region. To confirm a potential contribution of surface runoff waters in travertine formation, the mixing equation of Albarède (1995) was used:

$$\begin{aligned} \left(\frac{^{87}\text{Sr}}{^{86}\text{Sr}}\right)_M = & \left(\frac{f_A * \text{Sr}_A * \left(\frac{^{87}\text{Sr}}{^{86}\text{Sr}}\right)_A}{f_A * \text{Sr}_A + (1 - f_A) * \text{Sr}_B} \right) \\ & + \left(\frac{(1 - f_A) * \text{Sr}_B * \left(\frac{^{87}\text{Sr}}{^{86}\text{Sr}}\right)_B}{f_A * \text{Sr}_A + (1 - f_A) * \text{Sr}_B} \right) \end{aligned} \quad (2)$$

where A and B stand for two components, i.e., surface runoff and hyperalkaline waters, f_A the proportion of component A in the mixture, Sr_A and Sr_B are the Sr concentration of components A and B, respectively, and M is a mixture of these two components characterized by $\left(\frac{^{87}\text{Sr}}{^{86}\text{Sr}}\right)_M$ isotope composition. In our study, the measured $^{87}\text{Sr}/^{86}\text{Sr}$ from each laminae of travertine represents the mixture M. For the calculations, Sr concentrations of $5.7 \mu\text{mol l}^{-1}$ and $6.1 \mu\text{mol l}^{-1}$ and $^{87}\text{Sr}/^{86}\text{Sr}$ ratios of 0.70860 and 0.706686 were taken for surface runoff waters (Weyhenmeyer 2000) and hyperalkaline waters, respectively (Chavagnac et al. 2013b). Sr concentration and isotope composition of hyperalkaline waters are considered constant, as the springs are perennial. The results are presented in Table 4.

Figure 9A illustrates the variation in $^{87}\text{Sr}/^{86}\text{Sr}$ ratios, $\delta^{18}\text{O}$ and $\delta^{13}\text{C}$ values as a function of laminae thickness throughout sample 32. Strikingly, the Sr isotope signature co-varies with the $\delta^{13}\text{C}$ values throughout sample 32, whereby the contribution of surface runoff waters varied from 25 to 67%. While the contribution of each end member is almost constant (about 45–50%) in laminae 3 to 7, a 25% decrease is noted at the transition between laminae 7 and 8, where the $^{87}\text{Sr}/^{86}\text{Sr}$ ratios decrease from 0.707695 to 0.707282 (Fig. 9). This observation seems to indicate a significant change in the hydrological regime where the contribution from surface water becomes subsidiary to the spring water. This is also sustained by the strong accumulation of Si- and Mg-rich organic material observed in microscopic scale at this transition, suggesting less surface runoff water. In comparison, the co-variation in Sr and C isotope compositions from laminae 8 to 11 indicates an increasing contribution of surface runoff water from 25 to 34% (Fig. 9).

Additionally, the variation in $\delta^{18}\text{O}$ values of sample 32 are similar to what was obtained for a speleothem in Hoti cave (from -1.39‰ to -6.13‰ for sample 32, from -2 to -6‰ for the Hoti Cave’s speleothem; Burns et al. 2001; Fleitmann et al. 2007). For the speleothem with a constant

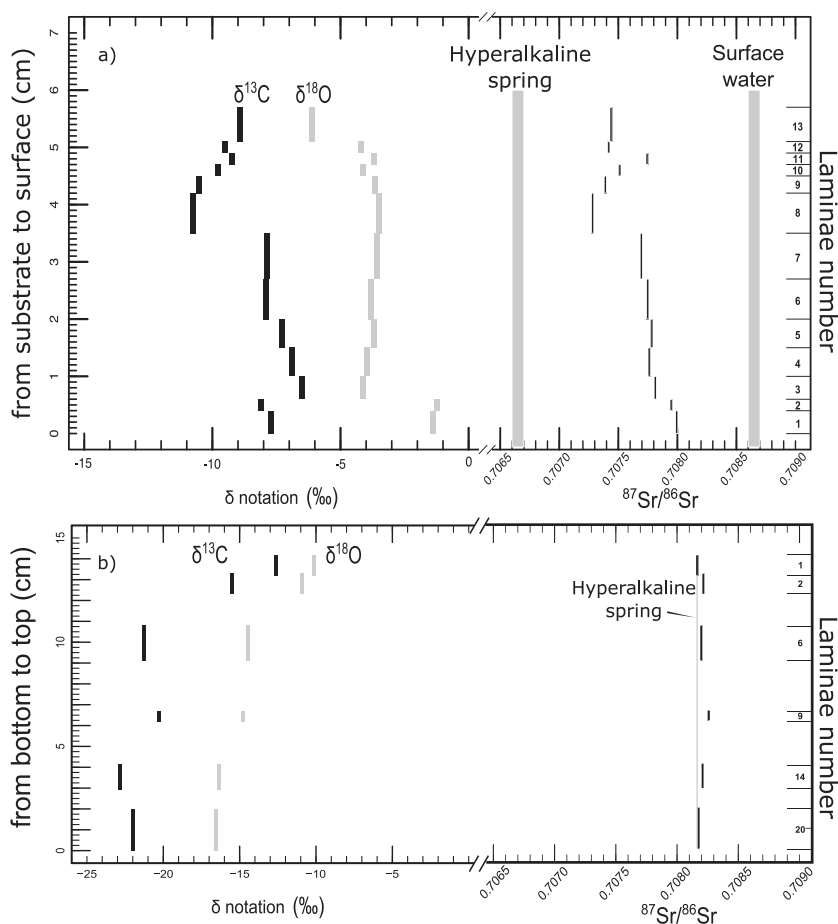


FIG. 9.—Variations of $\delta^{18}\text{O}$ and $\delta^{13}\text{C}$ values and $^{87}\text{Sr}/^{86}\text{Sr}$ ratio along the **A)** sample 32 and **B)** sample 33. Sr-isotope composition of surface runoff water are from Weyhenmeyer 2000.

temperature in the cave, the reason for such variations of the $\delta^{18}\text{O}$ values are interpreted as being due to the northward shift of the ITCZ (Burns et al. 2001; Fleitmann et al. 2007). However, in our study we do not have any temporal constraint of travertine formation; it is therefore difficult to infer with confidence the $\delta^{18}\text{O}$ signature of the dominating rain waters. So because neither temperature nor sources are well constrained, in terms of the past climatic record, we can conclude only that the contribution of surface waters in the mixing area has fluctuated through time.

For comparison, all laminae of sample 33 exhibit $^{87}\text{Sr}/^{86}\text{Sr}$ ratios very close to the signature of hyperalkaline spring water (i.e., 0.708164), indicating no evidence of mixing with surface waters (Fig. 9B). In contrast, large variations in $\delta^{13}\text{C}$ values are observed (between -12.6 and -22.8% VPDB, Fig. 9B). In this sample, the kinetic effect induced by the diffusion of $\text{CO}_2(\text{g})$ at the air–water interface is the major process modifying the C isotope compositions. The unique source of C in sample 33 is atmospheric $\text{CO}_2(\text{g})$, i.e., a potentially arid climate, as there is no evidence of surface runoff waters based on both $^{87}\text{Sr}/^{86}\text{Sr}$ ratios and the link between carbonate fabric and chemical composition.

In summary, the stable-isotope and radiogenic-isotope signatures of laminae document the paleo-activity of hyperalkaline spring waters through time, and contribute to a better understanding of the mechanisms leading to the formation of travertine in a DIC-depleted environment. $^{87}\text{Sr}/^{86}\text{Sr}$ ratios have shown to be a useful tracer for quantifying surface runoff water contribution in this setting.

DIC-Depleted vs. DIC-Enriched Environment for Continental Carbonate Formation

In Oman, the close relationship between the occurrence of travertine and the DIC-depleted hyperalkaline spring waters contrasts radically with most of continental travertines that precipitate from DIC-enriched waters (Capezzuoli et al. 2014). A fundamental question arises from this particular mode of formation: What do the stable-isotope compositions of carbonates record when they are formed in such contrasted DIC environments?

Figure 10 compares the variations in $\delta^{13}\text{C}$ and $\delta^{18}\text{O}$ values obtained in this study with data presented in the literature and obtained on both DIC-depleted and DIC-enriched environments. Each carbonate deposit defines different fields, although some data from Oman travertines overlap with tufa. All carbonates formed under continental DIC-depleted hyperalkaline conditions define a linear and positive trend between the negative values of $\delta^{13}\text{C}$ and $\delta^{18}\text{O}$ values. This is in line with the data acquired on carbonate deposits found at the Liguria hyperalkaline waters (Teboul et al. 2016). In addition, carbonates associated with submarine hyperalkaline springs (e.g., the Lost City hydrothermal field located at 30°N along the Mid-Atlantic Ridge, 800 m water depth; Kelley et al. 2001), exhibit positive $\delta^{13}\text{C}$ and $\delta^{18}\text{O}$ values, at the top end of the linear trend defined by carbonates found at continental DIC-depleted hyperalkaline conditions. Their stable-isotope signature is consistent with marine carbonates, for which the main source of carbon is provided by seawater bicarbonate ions. In general terms, the

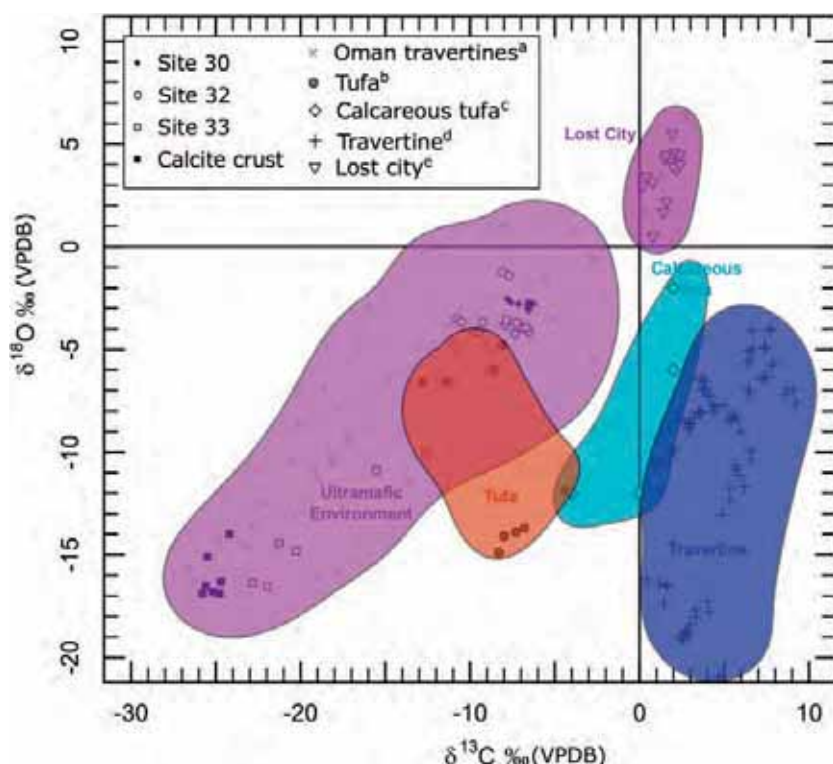


FIG. 10.—Plot of $\delta^{18}\text{O}$ values vs. $\delta^{13}\text{C}$ values of distinctive laminae (travertine 32 and 33). ^a Mervine et al. 2014; ^b Caton 2009, Janssen et al. 1999; ^c Cremaschi et al. 2010, Pola et al. 2014, Chafetz and Lawrence 1994, Guo et al. 1996, Kele et al. 2008, Fouke et al. 2001; ^d O'Neil and Barnes 1971, Schwarzenbach et al. 2013, Teboul et al. 2016; ^e Früh-Green et al. 2003, Dubinina et al. 2007.

variation of stable-isotope signatures reflects the source of carbon supply and the processes that led to carbonate formation, i.e., hydration and hydroxylation reactions and/or diffusion of $\text{CO}_{2(\text{g})}$ at the air–water interface, rather than climatic records.

For DIC-enriched environment, Gandin and Capezuoli (2008) demonstrated that calcareous tufa exhibits negative $\delta^{13}\text{C}$ and $\delta^{18}\text{O}$ values that represent outgassing of meteoric and soil derivation (Pentecost 2005) and cool temperature and saturation levels of spring water (Chafetz and Lawrence 1994), respectively. Photosynthetic effects associated with development of microorganisms remained very limited. The C and O stable-isotope compositions reflect the signature of the water from which the calcareous tufa derived, i.e., the local climatic regime. Tufas present negative but intermediate stable-isotope compositions between “DIC-depleted” travertine and calcareous tufa. This reflects the physicochemical signature of karstic water and microorganism activity (Capezuoli et al. 2014). Finally, “DIC-enriched” travertines are characterized by positive $\delta^{13}\text{C}$ but negative $\delta^{18}\text{O}$ values, which illustrate the complex interplay between the source of groundwater thermally heated and tectonic and volcanic activity. In the latter case, little information can be obtained for the past climatic record, but it provides an innovative way to monitor past volcanic carbon dioxide emissions (Capezuoli et al. 2014).

To summarize, carbonate deposits have a great potential for better defining the physicochemical environmental conditions and the processes that led to their formation. In their study of calcitic–aragonitic travertine–tufa deposits (DIC-enriched environment), Teboul et al. (2016) argue that combining geochemical tracers (Ba and Sr among others) with stable-isotope compositions provide valuable constraints on hydrogeological and paleo-hydrogeological circulation. Based on the present study (DIC-depleted environment), the combination of geochemical tracers with fabric description provides a crucial indicator of crystallization versus recrystallization at the time of carbonate formation, and thus a potential proxy of

past environmental conditions. When these observations are combined with isotopic tracers such as O, C, and Sr, then the environmental conditions can be better defined in terms of surface-runoff contribution and source of carbon supply.

Sequestration of Atmospheric CO_2 during Travertine Formation

Precipitation rate of travertine from hyperalkaline springs is variable, and will depend on the amount of calcium available, spring flow rate, and temperature, among other parameters (Pentecost 2005). The amount of atmospheric $\text{CO}_{2(\text{g})}$ uptake and calcium carbonate amount sequestered in travertine can be estimated either based on the volume and age of the travertine terraces (e.g., Mervine et al. 2014), or from the chemistry and flow rate of spring waters. In the latter case, the assumption is made that calcite precipitation occurs until thermodynamic equilibrium with atmospheric P_{CO_2} is reached, or evaporation is total. Calcite was taken as the reference for calculations as it is the main mineral found in travertine (it is also the more stable mineral versus aragonite over geologic time). Volume of calcite precipitate was estimated for sites 28, 32, and 33 based on average chemistry analyses (data from this study and Pentecost 2005) and flow rate at spring (unpublished data), according to the following equation:

$$V_{\text{travertine}} = \frac{V_{\text{cal}}}{1 - \phi} = \frac{Q \times v_{\text{cal}}}{1 - \phi} \int_t \Delta C_a dt \quad (3)$$

$V_{\text{travertine}}$ is the volume of precipitated travertine (which can also be expressed as a rate, i.e., $\text{m}^3 \text{yr}^{-1}$, when divided by time t), V_{cal} is the volume of precipitated calcite, ϕ is the porosity of travertine, v_{cal} is the molar volume of calcite ($\text{m}^3 \text{mol}^{-1}$), and ΔC_a is the difference in calcium concentration between the spring ($[\text{Ca}_s]$) and the calcium-depleted solution

TABLE 5.—Results of geochemical modeling with CHESS giving an estimate of CO₂ uptake and travertine deposits rate (per year). Input data: [CO₂] = 280 ppm, porosity = 0.35, data of [Ca_i] from Chavagnac et al. (2013b) and Q from (Chavagnac, unpublished data).

	Site 28	Site 32	Site 33	Average for 50 sites
Q (l s ⁻¹)	0.5	0.2	0.1	25
[Ca _i] spring (M)	1.18 10 ⁻³	1.88 10 ⁻³	1.09 10 ⁻⁴	1.67 10 ⁻³
pH _i (modelling result)	11.0	11.5	11.6	
SI calcite (log)	1.34	1.73	0.40	
SI aragonite (log)	1.19	1.58	0.25	
SI Monohydrocalcite (log)	0.46	0.87	-0.14	
[Ca _{eq}] (M)	2.18 10 ⁻⁴	1.24 10 ⁻⁴	4.53 10 ⁻⁵	1.29 10 ⁻⁴
Hypothesis 1: thermodynamic equilibrium is reached				
CO ₂ sequestred (kg yr ⁻¹)	666	487	9	5.4 10 ⁴
Vtravertine /t (m ³ yr ⁻¹)	8.6	6.3	0.1	692
Hypothesis 2: evaporation is total				
CO ₂ sequestred (kg yr ⁻¹)	817	522	15	5.8 10 ⁴
Vtravertine /t (m ³ yr ⁻¹)	10.5	6.7	0.2	749

(equal to [Ca_{eq}] when thermodynamic equilibrium is reached, or to [Ca_{ev}] = 0 M when evaporation is total). [Ca_{eq}] was calculated from geochemical modeling using CHESS (Van der Lee 1998). First, the chemical equilibrium of the solutions at the spring was calculated using the CHESS database and the Debye-Hückel model of activity correction. Charge balance was set on OH⁻ and DIC was imposed through a low fugacity of CO₂ (resulting in values from 10⁻¹² to 3 × 10⁻¹⁰ atm). Due to the low amount of DIC, all the discharge waters are undersaturated with respect to calcite. The calculated pH (pH_i) is in good agreement with values measured in the field (Table 5). Secondly, a fugacity of CO₂ of 2.8 × 10⁻⁴ atm was imposed to mimic equilibrium with Quaternary interglacial atmospheric P_{CO₂}. Dissolution of CO₂ from the atmosphere into the waters causes oversaturation with respect to calcite, aragonite, and monohydrocalcite (except for site 33, where water remains undersaturated with monohydrocalcite). The saturation index (SI) of calcite is higher than 1, enabling precipitation, but it is worth noting that SI for site 33 is smaller than the critical supersaturation of 4–10 reported in Pentecost (2005); there, precipitation must be triggered by evaporation, which is in agreement with the observation of calcite rafts. Given an average porosity of 35% (Noiriel, unpublished data), the volume of travertine deposit varies for site between ≈ 0.1 and ≈ 10 m³ yr⁻¹. Calculation assuming about 50 travertine deposits in Oman for a cumulative flow rate of 25 l s⁻¹ (i.e., Q = 0.5 l s⁻¹ in average), an average [Ca_i] = 1.67 mM, and an estimate of the total travertine area in the Samail Ophiolite of 10⁷ m² (Kelemen and Matter 2008; Mervine et al. 2014) gives a deposition rate of ≈ 0.05 mm yr⁻¹ sequestering ≈ 5 10⁴ kg CO₂ yr⁻¹. This value is three orders of magnitude smaller than the one estimated by Mervine et al. (2014) on the same number of travertine deposits. As [Ca_i] is generally between 1 and 2 mM for hyperalkaline springs (Chavagnac et al. 2013b), the flow rate represents the largest uncertainty in the calculation, which could have been higher in the past, leading to a higher deposition rate (regardless, it is not likely to be three orders of magnitude higher than actual). CO₂ can also be transformed into organic matter through biological processes (e.g., photosynthesis), although its content in travertine does not generally exceed a few percent (Pentecost 2005). On the other hand, a lower P_{CO₂} (e.g., during Quaternary glacial periods) or a saturation index higher than 0 (i.e., equilibrium not reached and Ca being exported through streams after mixing with runoff waters) will counterbalance the deposition rate.

From equilibrium calculations, it appears that the best conditions to store CO₂ as calcium carbonate depend on initial Ca concentration and surface waters mixing with hyperalkaline springs. It seems clear that the rate of sequestration of atmospheric CO₂ also depends on the mechanism of precipitation, which should be accounted for large-scale evaluation.

CONCLUSION

A detailed multi-disciplinary approach, from macroscopic to microscopic scale, has been accomplished on three travertine samples formed under DIC-depleted hyperalkaline environments in order to 1) assess the relationship between the petrologic features and fabrics and the geochemical and isotopic signatures, and 2) discuss the potential of these deposits as proxies for past climatic record and sequestration of atmospheric CO₂. The samples illustrate two distinct mechanisms of calcium carbonate formation, either from mixing of hyperalkaline and surface runoff waters (sample 28 and 32) or from dissolution of atmospheric CO_{2(g)} into hyperalkaline waters (sample 33).

We conclude:

- Travertines as a whole are characterized by chemical compositions, expressed in terms of Mg, Ca, and Sr contents, consistent with “prior calcite precipitation” (PCP) process, i.e., the record of environmental conditions at the time of their formation. However, by comparing trace-element concentrations from one fabric to the other (sparite, drusy, spheroid calcite or aragonite micro-stalactic and needle-like aragonite), it is possible to distinguish between recrystallization conditions (sample 28) and temporal variation of environmental conditions (samples 32 and 33).
- The linear and positive variations in δ¹⁸O and δ¹³C values between laminae reflects two different mechanisms: (1) hydration-hydroxylation reactions from which a paleo-temperature of water can be extracted (sample 32) and/or (2) kinetic effects induced by diffusion of CO₂ at the air–water interface (sample 33).
- The combined variations in O, C, and Sr isotope signatures between laminae document the paleo-activity of hyperalkaline spring and surface runoff waters through formation time scales. The ⁸⁷Sr/⁸⁶Sr ratio represents a useful tracer for quantifying surface runoff water contribution, and acts as an indicator of rainfall intensity.
- In the framework of continental carbonates, travertine formed in a DIC-depleted environment exhibit δ¹⁸O and δ¹³C values that contrast to those formed in a DIC-enriched environment. With the prospect of assessing the past climatic record, it appears necessary 1) to combine the detailed petrological observations with chemical compositions at the lamina to unravel crystallization versus recrystallization processes, and 2) to corroborate radiogenic and stable-isotope analyses for quantifying precipitation intensity.
- Finally, the influence of climate should be addressed when quantifying carbonation rates, as shown by the range of CO₂ sequestered in the different scenarios illustrated by our samples (from 9 kg CO₂ yr⁻¹ to 522 kg CO₂ yr⁻¹).

SUPPLEMENTAL MATERIAL

An Appendix is available from JSR’s Data Archive: <http://sepm.org/pages.aspx?pageid=229>.

ACKNOWLEDGMENTS

We acknowledge the technical help of Chantal Perrache (LMV Saint-Etienne) and Michel Thibault, Jonathan Prunier, and Pierre Brunet (GET, Toulouse) for the analyses of O and C isotopes, mineralogical, geochemical, and Sr isotopes, respectively. We also acknowledge the comments of two anonymous reviewers and the editors, which greatly improved the quality and presentation of the data reported in this study.

REFERENCES

- ABLY, B., AND CEULENEER, G., 2013, The dunitic mantle-crust transition in the Oman ophiolite: residue of melt-rock interaction, cumulates from high-MgO melts, or both? *Geology*, v. 41, p. 67–70.
- ABRAJANO, T.A., STURCHIO, N.C., BOHLKE, J.K., LYON, G.L., POREDA, R.J., AND STEVENS, C.M., 1988, Methane-hydrogen gas seeps, Zambales Ophiolite, Philippines: deep or shallow origin? *Chemical Geology*, v. 71, p. 211–222.
- ALABASTER, T., PEARCE, J., AND MALPAS, J., 1982, The volcanic stratigraphy and petrogenesis of the Oman ophiolite complex: *Contributions to Mineralogy and Petrology*, v. 81, p. 168–183.
- ALBARÈDE, F., 1995, *Introduction to Geochemical modelling*: Cambridge University Press, Cambridge, UK, 543 p.
- AMRI, I., BENOIT, M., AND CEULENEER, G., 1996, Tectonic setting for the genesis of oceanic plagiogranites: evidence from a paleo-spreading structure in the Oman ophiolite: *Earth and Planetary Science Letters*, v. 139, p. 177–194.
- ARENAS, C., VASQUEZ-URBEZ, M., AUQUÉ, L., SANCHO, C., OSACAR, C., AND PARDO, G., 2014, Intrinsic and extrinsic controls of spatial and temporal variations in modern fluvial tufa sedimentation: a thirteen-year record from a semi-arid environment: *Sedimentology*, v. 61, p. 90–132.
- BARNES, I., AND O'NEIL, J.R., 1969, Relationship between fluids in some fresh alpine-type ultramafics and possible modern serpentinization, western United States: *Geological Society of America, Bulletin*, v. 80, p. 1947–1960.
- BARNES, I., LAMARCHE, V., JR., AND HIMMELBERG, G., 1967, Geochemical evidence of present-day serpentinization: *Science*, v. 156, p. 830–832.
- BARNES, I., O'NEIL, J.R., AND TRESCASES, J.-J., 1978, Present day serpentinization in New Caledonia, Oman and Yugoslavia: *Geochimica et Cosmochimica Acta*, v. 42, p. 144–145.
- BOUDIER, F., AND COLEMAN, R.G., 1981, Cross-section through the peridotite in the Semail ophiolite, Southeastern Oman mountains: *Journal of Geophysical Research*, v. 86, p. 2573–2592.
- BOULART, C., CHAVAGNAC, V., MONNIN, C., DELACOUR, A., CEULENEER, G., AND HOAREAU, G., 2013, Differences in gas venting from ultramafic-hosted warm springs: the example of Oman and voltri ophiolites: *Ophiolite*, v. 38, p. 143–156.
- BRADY, A.L., SLATER, G.F., OMELOM, C.R., SOUTHAM, G., DRUSCHEL, G., ANDERSEN, D.T., HAWES, I., LAVAL, B., AND LIM, D.S.S., 2010, Photosynthetic isotope biosignatures in laminated micro-stromatolitic and non-laminated nodules associated with modern, freshwater microbialites in Pavilion Lake, B.C.: *Chemical Geology*, v. 274, p. 56–67.
- BRUNI, J., CANEPA, M., CHIODINI, G., CIONI, R., CIPOLLI, F., LONGINELLI, A., MARINI, L., OTTONELLO, G., AND VETUSCHI ZUCCOLINI, M., 2002, Irreversible water-rock mass transfer accompanying the generation of the neutral, Mg-HCO₃ and high-pH, Ca-OH spring waters of the Genova province, Italy: *Applied Geochemistry*, v. 17, p. 455–474.
- BURNS, S.J., FLEITMANN, D., MATTER, A., NEFF, U., AND MANGINI, A., 2001, Speleothem evidence from Oman for continental pluvial events during interglacial periods: *Geology*, v. 29, p. 623–626.
- CAPEZZUOLI, E., GANDIN, A., AND PEDLEY, M., 2014, Decoding tufa and travertine (fresh water carbonates) in the sedimentary record: The state of the art: *Sedimentology*, v. 61, p. 1–21.
- CATON, J.C., 2009, Environmental controls on the formation and isotopic composition of a laminated tufa in Red Butte canyon, Utah: University of Utah, 119 p.
- CEULENEER, G., MONNEREAU, M., AND AMRI, I., 1996, Thermal structure of a fossil mantle diaper inferred from the distribution of mafic cumulates: *Nature*, v. 379, p. 149–153.
- CHAFETZ, H., AND LAWRENCE, J., 1994, Stable isotopic variability within modern travertines: *Géographie Physique et Quaternaire*, v. 48, p. 257–273.
- CHAVAGNAC, V., CEULENEER, G., MONNIN, C., LANSAC, B., HOAREAU, G., AND BOULART, C., 2013a, Mineralogical assemblages forming at hyperalkaline warm springs hosted on ultramafic rocks: a case study of Oman and Ligurian ophiolites: *Geochemistry Geophysics Geosystems*, v. 14, p. 2474–2495.
- CHAVAGNAC, V., MONNIN, C., CEULENEER, G., BOULART, C., AND HOAREAU, G., 2013b, Characterization of hyperalkaline fluids produced by low-temperature serpentinization of mantle peridotites in the Oman and Ligurian ophiolites: *Geochemistry Geophysics Geosystems*, v. 14, p. 2496–2522.
- CIPOLLI, F., GAMBARDILLA, B., MARINI, L., OTTONELLO, G., AND ZUCCOLINI, M., 2004, Geochemistry of high-pH waters from serpentinites of the Gruppo di Voltri (Genova, Italy) and reaction path modelling of CO₂ sequestration in serpentinite aquifers: *Applied Geochemistry*, v. 19, p. 787–802.
- CLARK, I.D., AND FONTES, J.-C., 1990, Paleoclimatic reconstruction in Northern Oman based on carbonates from hyperalkaline groundwaters: *Quaternary Research*, v. 33, p. 320–336.
- CLARK, I.D., FONTES, J.-C., AND FRITZ, P., 1992, Stable isotope disequilibria in travertine from high pH waters: laboratory investigations and field observations from Oman: *Geochimica et Cosmochimica Acta*, v. 56, p. 2041–2050.
- COLEMAN, R., 1981, Tectonic setting for ophiolite obduction in Oman: *Journal of Geophysical Research*, v. 86, p. 2497–2508.
- CREMASCHI, M., ZERBONI, A., SPÖTL, C., AND FELLETTI, F., 2010, The calcareous tufa in the Tadart Acacus Mt. (SW Fezzan, Libya), an early Holocene palaeoclimate archive in the central Sahara: *Palaeogeography, Palaeoclimatology, Palaeoecology*, v. 287, p. 81–94.
- DANSGAARD, W., 1964, Stable isotopes in precipitation: *Tellus*, v. 16, p. 436–468.
- DARLING, W.G., BATH, A.H., GIBSON, J.J., AND ROZANSKI, K., 2006, Chapter 1, Isotopes in Water, in Leng, M.J., ed., *Isotopes in Palaeoenvironmental Research*: Dordrecht, 66 p.
- DIETZEL, M., USADOWSKI, E., AND HOEFS, J., 1992, Chemical and ¹³C/¹²C- and ¹⁸O/¹⁶O-isotope evolution of alkaline drainage waters and the precipitation of calcite: *Applied Geochemistry*, v. 7, p. 177–184.
- DUBININA, E., CHERNYSHYEV, I., BORTNIKOVA, N., LEIN, A., SAGALEVICH, A., GOULTSMAN, Y., BAIROVA, E., AND MOKHOV, A., 2007, Isotopic-geochemical characteristics of the lost city hydrothermal field: *Geochemistry International*, v. 45, p. 1131–1143.
- FAIRCHILD, I., BORSATO, A., TOOTH, A.F., FRISIA, S., HAWKESWORTH, C., HUANG, Y., McDERMOTT, F., AND SPIRO, B., 2000, Controls on trace element (Sr-Mg) compositions of carbonate cave waters: implications for speleothem climatic records: *Chemical Geology*, v. 166, p. 255–269.
- FAIRCHILD, I.J., SMITH, C.L., BAKER, A., FULLER, L., SPÖTL, C., MATTEY, D., McDERMOTT, F., AND EDINBURGH ION MICROPROBE FACILITY (E.I.M.F.), 2006, Modification and preservation of environmental signals in speleothems: *Earth-Science Reviews*, v. 75, p. 105–153.
- FLEITMANN, D., BURNS, S.J., NEFF, U., MANGINI, A., AND MATTER, A., 2003, Changing moisture sources over the last 330,000 years in Northern Oman from fluid-inclusion evidence in speleothems: *Quaternary Research*, v. 60, p. 223–232.
- FLEITMANN, D., BURNS, S.J., NEFF, U., MUDELSEE, M., MANGINI, A., AND MATTER, A., 2004, Palaeoclimatic interpretation of high-resolution oxygen isotope profiles derived from annually laminated speleothems from Southern Oman: *Quaternary Science Reviews*, v. 23, p. 935–945.
- FLEITMANN, D., BURNS, S.J., MANGINI, A., MUDELSEE, M., KRAMERS, J., VILLA, I., NEFF, U., AL-SUBBARY, A.A., BUETTNER, A., HIPPLER, D., AND MATTER, A., 2007, Holocene ITCZ and Indian monsoon dynamics recorded in stalagmites from Oman and Yemen (Socotra): *Quaternary Science Reviews*, v. 26, p. 170–188.
- FLÜGEL, E., 2004, *Microfacies of Carbonate Rocks: Analysis, Interpretation and Application*: Berlin, Springer-Verlag, 996 p.
- FORD, T.D., AND PEDLEY, H.M., 1996, A review of tufa and travertine deposits of the world: *Earth-Science Reviews*, v. 41, p. 117–175.
- FOUKE, B., 2011, Hot-spring systems geobiology: abiotic and biotic influences on travertine formation at Mammoth Hot Springs, Yellowstone National Park, USA: *Sedimentology*, v. 58, p. 170–219.
- FOUKE, B., FARMER, J., DES MARAIS, D., PRATT, L., STURCHIO, N., BURNS, P., AND DISCIPULO, M., 2001, Depositional facies and aqueous-solid geochemistry of travertine-depositing hot springs (Angel Terrace, Mammoth Hot Springs, Yellowstone National Park, USA): *Journal of Sedimentary Research*, v. 70, p. 565–585.
- FRUH-GREEN, G.L., KELLEY, D.S., BERNASCONI, S.M., KARSON, J.A., LUDWIG, K.A., BUTTERFIELD, D.A., BOSCHI, C., AND PROSKUROWSKI, G., 2003, 30,000 years of hydrothermal activity at the Lost City vent field: *Science*, v. 301, p. 495–498.
- FUCHS, M., AND BUEKERT, A., 2008, A 20 ky sediment record from the Hajar Mountain range in N-Oman, and its implication for detecting arid-humid periods on the southeastern Arabian Peninsula: *Earth and Planetary Science Letters*, v. 265, p. 546–558.
- GANDIN, A., AND CAPEZZUOLI, E., 2008, Travertine versus calcareous tufa: distinctive petrologic features and related stable isotopes signature: *Il Quaternario*, v. 21, p. 125–136.
- GANDIN, A., AND CAPEZZUOLI, E., 2014, Travertine: distinctive depositional fabrics of carbonates from thermal spring systems: *Sedimentology*, v. 61, p. 264–290.
- GROSSMAN, E., 2012, Applying oxygen isotope paleothermometry in deep time, in Ivany L.C., and Huber, B.T., eds., *Reconstructing Earth's Deep-Time Climate: The State of the Art in 2012*: Paleontological Society Short Course, The Paleontological Society Papers, v. 18, p. 39–67.
- GUO, L., ANDREWS, J., RIDING, R., DENNIS, P., AND DRESSER, Q., 1996, Possible microbial effects on stable carbon isotopes in hot travertine: *Journal of Sedimentary Research*, v. 66, p. 468–473.
- HUANG, H., FAIRCHILD, I., BORSATO, A., FRISIA, S., CASSIDY, N., McDERMOTT, F., AND HAWKESWORTH, C., 2001, Seasonal variations in Sr, Mg and P in modern speleothems (Grotta di Ernesto, Italy): *Chemical Geology*, v. 175, p. 429–448.
- JANSEN, A., SWENNEN, R., PODOOR, N., AND KEPPEND, E., 1999, Biological and diagenetic influence in Recent and fossil tufa deposits from Belgium: *Sedimentary Geology*, v. 126, p. 75–95.
- JOHNSON, K., HU, C., BELSHAW, N., AND HENDERSON, G., 2006, Seasonal trace-element and stable-isotope variations in a Chinese speleothem: the potential for high-resolution paleomonsoon reconstruction: *Earth and Planetary Science Letters*, v. 244, p. 394–407.
- JUTEAU, T., ERNEWEIN, M., REUBER, I., WHITECHURCH, H., AND DAHL, R., 1988, Duality of magmatism in the plutonic sequence of the Semail Nappe, Oman: *Tectonophysics*, v. 151, p. 107–126.
- KELLE, S., DEMÉNY, A., SIKLOS, Z., NÉMETH, T., TOT, M., AND KOVACS, M., 2008, Chemical and stable isotope composition of recent hotwater travertines and associated thermal waters, from Egerszalók, Hungary: depositional facies and non-equilibrium fractionation: *Sedimentary Geology*, v. 211, p. 53–72.
- KELEMEN, P.B., AND MATTER, J., 2008, *In situ* carbonation of peridotite for CO₂ storage: National Academy of Sciences [U.S.A.], *Proceedings*, v. 105, p. 17295–17300.
- KELEMEN, P.B., MATTER, J., STREIT, E.E., RUDGE, J.F., CURRY, W.B., AND BLUSZTAJN, J., 2011, Rates and mechanisms of mineral carbonation in peridotite: natural processes and recipes for enhanced, *in situ* CO₂ capture and storage: *Annual Review of Earth and Planetary Sciences*, v. 39, p. 545–576.
- KELLEY, S.D., KARSON, J.A., BLACKMAN, D.K., FRUH-GREEN, G.L., BUTTERFIELD, D.A., LILLEY, D.M., OLSON, E.J., SCHRENK, M.O., ROELL, K.K., LEBON, G.T., RIVIZZIGNO, P., AND THE AT3-60 SHIPBOARD PARTY, 2001, An off-axis hydrothermal vent field near the Mid-Atlantic Ridge at 30° N: *Nature*, v. 412, p. 145–149.

- KWARTENG, A.Y., DORVLO, A.S., AND KUMAR, G.T.V., 2009, Analysis of a 27-year rainfall data (1977–2003) in the Sultanate of Oman: *International Journal of Climatology*, v. 29, p. 605–617.
- LACHNIET, M.S., 2009, Climatic and environmental controls on speleothem oxygen-isotope values: *Quaternary Science Reviews*, v. 28, p. 412–432.
- LAINAY, J., AND FONTES, J.C., 1985, Les sources thermales de Prony (Nouvelle Calédonie) et leurs précipités chimiques exemple de formation de brucite primaire: *Géologie de France*, v. 1, p. 83–100.
- MATTER, J.M., WABER, H.N., LOEW, S., AND MATTER, A., 2005, Recharge areas and geochemical evolution of groundwater in an alluvial aquifer system in the Sultanate of Oman: *Hydrogeology Journal*, v. 14, p. 203–224.
- MATTEY, D.P., FAIRCHILD, I.J., AND ATKINSON, T.C., 2009, Seasonal microclimate control on calcite fabrics, stable isotopes and trace elements in modern speleothem from St. Michaels Cave, Gibraltar: *Geochimica et Cosmochimica Acta*, v. 73, p. A849.
- McMILLAN, E., FAIRCHILD, I., FRISIA, S., BORSATO, A., AND McDERMOTT, F., 2005, Annual trace element cycles in calcite–aragonite speleothems: evidence of drought in the western Mediterranean 1200–1100 yr BP: *Journal of Quaternary Science*, v. 20, p. 423–433.
- MERVINE, E.M., HUMPHRIS, S.E., SIMS, K.W.W., KELEMEN, P.B., AND JENKINS, W.J., 2014, Carbonation rates of peridotite in the Samail Ophiolite, Sultanate of Oman, constrained through ^{14}C dating and stable isotopes: *Geochimica et Cosmochimica Acta*, v. 126, p. 371–397.
- MICKLER, P.J., STERN, L.A., AND BANNER, J.L., 2006, Large kinetic isotope effects in modern speleothems: *Geological Society of America, Bulletin*, v. 118, p. 65–81.
- MONNIN, C., CHAVAGNAC, V., BOULARI, C., MÉNEZ, B., GÉRARD, M., GÉRARD, E., PISAPIA, C., QUÉMENEUR, M., ERAUSO, G., POSTEC, A., QUENTAS-DOMBROWSKI, L., PAYRI, C., AND PELLETIER, B., 2014, Fluid chemistry of the low temperature hyperalkaline hydrothermal system of Prony Bay (New Caledonia): *Biogeosciences*, v. 11, p. 5687–5706.
- NEAL, C., AND STANGER, G., 1983, Hydrogen generation from mantle source rocks in Oman: *Earth and Planetary Science Letters*, v. 66, p. 315–320.
- NEAL, C., AND STANGER, G., 1984, Calcium and magnesium hydroxide precipitation from alkaline groundwaters in Oman, and their significance to the process of serpentinization: *Mineralogical Magazine*, v. 48, p. 237–241.
- O'NEIL, J.R., AND BARNES, I., 1971, C^{13} and O^{18} compositions in some fresh-water carbonates associated with ultramafic rocks and serpentinites: western United States: *Geochimica et Cosmochimica Acta*, v. 35, p. 687–697.
- PALLISTER, J., AND HOPSON, C., 1981, Samail ophiolite plutonic suite: field relations, phase variation, cryptic variation and layering, and a model of a spreading ridge magma chamber: *Journal of Geophysical Research*, v. 86, p. 2593–2644.
- PAUCKERT, A.N., MATTER, J.M., KELEMEN, P.B., SHOCK, E.L., AND HAVIG, J.R., 2012, Reaction path modeling of enhanced in situ CO_2 mineralization for carbon sequestration in the peridotite of the Samail Ophiolite, Sultanate of Oman: *Chemical Geology*, v. 330–331, p. 86–100.
- PENTECOST, A., 2005, *Travertine*: Berlin, Springer-Verlag, 445 p.
- PENTECOST, A., AND VILES, H., 1994, A review and reassessment of travertine classification: *Géographie Physique et Quaternaire*, v. 48, p. 305–314.
- POLA, M., GANDIN, A., TUCCIMEL, P., SOLIGO, M., DEIANA, R., FABBRI, P., AND ZAMPIERI, D., 2014, A multidisciplinary approach to understanding carbonate deposition under tectonically controlled hydrothermal circulation: a case study from a recent travertine mound in the Euganean hydrothermal system, northern Italy: *Sedimentology*, v. 61, p. 172–199.
- PYTHON, M., AND CEULENEER, G., 2003, Nature and distribution of dykes and related melt migration structures in the mantle section of the Oman ophiolite: *Geochemistry Geophysics Geosystems*, v. 4, p. 1–34.
- RENAUT, R.W., AND JONES, B., 1997, Controls on aragonite and calcite precipitation in hot spring travertines at Chemurkeu, Lake Bogoria, Kenya: *Canadian Journal of Earth Sciences*, v. 34, p. 801–818.
- SADER, J.A., LEYBOURNE, M.I., McCLENAGHAN, M.B., AND HAMILTON, S.M., 2007, Low-temperature serpentinization processes and kimberlite groundwater signatures in the Kirkland Lake and Lake Timiskiming kimberlite fields, Ontario, Canada: implications for diamond exploration: *Geochemistry: Exploration, Environment, Analysis*, v. 7, p. 3–21.
- SANO, Y., URABE, A., WAKITA, H., AND WUSHIKI, H., 1992, Origin of hydrogen–nitrogen gas seeps, Oman: *Applied Geochemistry*, v. 8, p. 1–8.
- SCHWARZENBACH, E.M., LANG, S.Q., FRUHL-GREEN, G.L., LILLEY, M.D., BERNASCONI, S., AND MÉHAY, S., 2013, Sources and cycling of carbon in continental, serpentinite-hosted alkaline springs in the Voltri Massif, Italy: *Lithos*, v. 177, p. 236–244.
- SINCLAIR, D.J., 2011, Two mathematical models of Mg and Sr partitioning into solution during incongruent calcite dissolution: *Chemical Geology*, v. 283, p. 119–133.
- SINCLAIR, D.J., BANNER, J.L., TAYLOR, F.W., PARTIN, J., JENSON, J., MYLROIE, J., GODDARD, E., QUINN, T., JOCSON, J., AND MIKLAČIĆ, B., 2012, Magnesium and strontium systematics in tropical speleothems from the Western Pacific: *Chemical Geology*, v. 294–295, p. 1–17.
- TEBOUL, P.A., DURLET, C., GAUCHER, E.C., VIRGONE, A., GIRARD, J.-P., CURIE, J., LOPEZ, B., AND CAMOIN, G.F., 2016, Origins of elements building travertine and tufa: new perspective provided by isotopic and geochemical tracers: *Sedimentary Geology*, v. 334, p. 97–114.
- VAN DER LEE, J., 1998, Thermodynamic and mathematical concepts of CHESS: technical report LHM/RD/98/3, Ecole des Mines de Paris, Centre d'Informatique Géologique, Fontainebleau, France.
- VEYSEY, J., FOUKE, B., KANDIANIS, M., SCHICKEL, T., JOHNSON, R., AND GOLDENFELD, N., 2008, Reconstruction of water temperature, pH, and flux of ancient hot springs from travertine depositional facies: *Journal of Sedimentary Research*, v. 78, p. 69–76.
- WEYHENMEYER, C.E., 2000, Origin and Evolution of Groundwater in the Alluvial Aquifer of the Eastern Batinah Coastal Plain, Sultanate of Oman [Ph.D. Thesis]: Universität Bern, 202 p.
- WEYHENMEYER, C.E., BURNS, S.J., WABER, H.N., AESCHBACH-HERTIG, W., KIPFER, R., LOOSLI, H.H., AND MATTER, A., 2000, Cool glacial temperatures and changes in moisture source recorded in Oman groundwaters: *Science*, v. 287, p. 842–845.
- WEYHENMEYER, C.E., BURNS, S.J., WABER, H.N., MACUMBER, P.G., AND MATTER, A., 2002, Isotope study of moisture sources, recharge areas, and groundwater flow paths within the eastern Batinah coastal plain, Sultanate of Oman: isotopes study of groundwater movement in Oman: *Water Resources Research*, v. 38, p. 1–22.

Received 10 February 2015; accepted 26 September 2016.

Résumé

Cette thèse présente une étude détaillée de la composition des fluides de haute température du champ hydrothermal de Lucky Strike (37°N, dorsale médio atlantique) s'appuyant sur 3 campagnes d'échantillonnage réalisées dans le cadre de l'observatoire fond de mer EMSO-Açores. Ce champ hydrothermal s'est développé autour d'un lac de lave fossile bordé au Nord-Ouest, Nord Est et Sud Est par des cônes volcaniques plus anciens. En 2013, la découverte du site hydrothermal de Capelinhos à l'Est, et présentant des compositions de fluides inédites à Lucky Strike (concentration faible en Cl et forte en Fe et Mn), nous permet de proposer un nouveau modèle de circulation hydrothermale basé sur l'application de géothermobaromètres (Si ; Si-Cl ; Fe-Mn) chimiques sur 13 événements hydrothermaux. Nous avons défini 5 groupes de sites selon leur chlorinité et leur position par rapport au lac de lave. Les fluides de Capelinhos, dominés par la phase vapeur, sont rapidement extraits de la zone de séparation de phase (estimée à 2600 m sous le plancher océanique). Les fluides à proximité du lac de lave, avec des chlorinités variables, suggèrent un rééquilibrage à des pressions et températures plus faibles qu'à Capelinhos, cohérent avec des processus de refroidissement conductif et/ou d'entraînement de saumures prenant place lors de la remontée des fluides jusqu'à la base de la couche 2A. La fluctuation de la chlorinité témoigne de la variabilité du temps de résidence du fluide dans la zone de remontée, et ses relations avec les caractéristiques physiques de la croûte océanique. Nous avons évalué la variabilité temporelle de la composition des fluides collectés au cours des campagnes effectuées entre 2009 et 2015. Deux échelles de temps sont mises en évidence. (1) l'échelle de l'échantillonnage, i.e. de l'heure, répond à des phénomènes de subsurface, et révèle qu'un fluide hydrothermal refroidi conductivement ($T < 150^{\circ}\text{C}$) est stocké dans la roche poreuse entourant le site de décharge. (2) l'échelle de temps pluri-annuelle montre une fluctuation des conditions de P et T apparentes de la zone de séparation de phase et du degré d'altération du substratum dans la zone de réaction. Les variations intersites du rapport Ca/Na (indicateur du degré d'albitisation) sont dues à la séparation de phase, à l'exception des sites du Sud-Est du lac de lave qui indiquent un degré d'altération plus élevé. La concentration en Li et sa composition isotopique indiquent que le basalte du substratum est relativement frais avec des rapports W/R proches de 1 pour tous les groupes, avec des $\delta^7\text{Li}$ du fluide identiques au substratum. Pour le Sr nous calculons des rapports W/R plus élevés, autour de 7-8, qui sont dus au Sr de l'eau de mer initiale qui est partiellement stocké et à la formation de minéraux secondaires (l'albite et l'anhydrite) lors des interactions eau-roche dans le faciès schiste vert. La faible teneur en métaux des fluides situés autour du lac de lave est probablement due à un piégeage en subsurface, équivalent à ~65% du Fe mobilisé dans la zone de réaction (basé sur les teneurs des fluides de Capelinhos). La variabilité de chlorinité des fluides de Lucky Strike offre l'opportunité d'étudier le comportement des terres rares à l'échelle d'un site hydrothermal. Ainsi, nous montrons l'effet de la séparation de phase sur les terres rares légères et lourdes ainsi que le lien entre l'Eu et le cycle géochimique du Sr. Les terres rares dissoutes dans le panache hydrothermal montrent une perte au cours du mélange ainsi que des phénomènes de redissolution visible via la signature isotopique en Nd. Cette modification des compositions isotopiques en Nd de l'eau de mer profonde est similaire au « boundary exchange » observé aux interfaces océan-plateforme continentale. Au vue de la répartition des champs hydrothermaux sur les dorsales océaniques, ce phénomène pourrait avoir un impact sur le bilan océanique du Nd et donner lieu à un phénomène de « ridge exchange ».

Mots-clés : Fumeur noir ; séparation de phase ; isotope ; circulation hydrothermale ; variabilité spatio-temporelle.

Abstract

This thesis presents a detailed study of the composition of high temperature fluid from the Lucky Strike hydrothermal field (37°N, Mid Ocean Ridge) collected during three sampling campaigns within the framework of the deep sea observatory EMSO-Azores. The hydrothermal field has developed around a fossil lava lake framed by three ancient volcanic cones. In 2013, the discovery of a new active site to the East of the system, and presenting an unprecedented fluid composition at Lucky Strike (low Cl concentration and high Fe and Mn concentration), led to a new model of hydrothermal circulation based on chemical geothermobarometer (Si; Si-Cl) and geothermometer (Fe-Mn) applied to 13 venting sites. We defined 5 groups of sites based on their chlorinity and location around the lava lake. It appears that vapor-dominated Capelinhos fluids were extracted relatively fast from the phase separation zone (estimated at ~2600mbsf). Nevertheless, fluids in the vicinity of the lava lake, both vapor and brine dominated, display P and T conditions of equilibration lower than for Capelinhos fluids. This highlights on-going equilibration process through conductive cooling and/or brine entrainment in the upflow zone up to the layer 2A of the oceanic crust. Chlorinity variations highlight the varying residence time in the upflow of the fluids between vents which depends on physical characteristics of the crust. We studied the temporal variability of fluid composition collected between 2009 and 2015. Two time scales have been evidenced. The first is the sampling scale, i.e. ~1h, and corresponds to subsurface processes indicating that a hydrothermal fluid, conductively cooled ($T < 150^{\circ}\text{C}$), was stored in the porous substratum close to the discharge. The second is at the scale of the year. It shows fluctuations of P and T conditions in the phase separation and different degree of alteration of the substratum in the reaction zone. Intersites variations of Ca/Na ratios (proxies for albitisation) are related to phase separation expected the South Eastern sites that display a more altered substratum. To avoid this issue, we use Li and Sr isotopes which are not affected phase separation. Li concentration and isotopic composition indicates that basalt substratum is relatively fresh with W/R ratio close to 1 calculated for all groups with $\delta^7\text{Li}$ of fluid equivalent to substratum. Sr concentration and isotopic composition suggest higher W/R ratio (~7-8) because of seawater Sr partially removed in the recharge. Moreover, other parameters are at play such as secondary mineral formation (albite, anhydrite) during water rock interaction in the greenschist facies. Because the basalt is relatively fresh, the low metal content in the fluid around the lava lake is due to storage, in the subsurface, of approximately ~60-70% of Fe that is mobilized in the reaction zone compared to Fe-Mn rich Capelinhos fluids. Furthermore, the Cl variability from the fluids at Lucky Strike brings a unique opportunity to study the REE distribution from the reaction zone to the discharge into the deep ocean. We show that the LREE are preferentially concentrated into the brine phase. Furthermore, the Eu is linked to the Sr geochemical cycle. Dissolved REE from buoyant plume fluids highlight a scavenging effect. The Nd isotopic compositions indicate redissolution process. This Nd isotopes modification of the deep seawater is similar to the process of "boundary exchange" that occurs at the ocean/continents interface. Considering the global distribution of submarine hydrothermalism, the Nd modification at the ridge could have an impact on the global Nd cycle in the oceans and act as a "ridge exchange".

Keywords: Black Smoker; phase separation; isotope; hydrothermal circulation; time-serie.